PREFACE
Maria Gritsevich, Alberto J. Castro-Tirado, Petr Kubánek, Shashi B. Pandey, and David Hiriart vii

LIST OF PARTICIPANTS ix

GROUP PHOTOGRAPH xi

DEVELOPMENT OF ASTRONOMICAL OBSERVATORIES FROM THE LATE 19TH TO THE 21ST CENTURY *M. A. Castro Tirado* 1

CHARACTERIZATION OF THE KL4040 SCMOS FOR USE ON THE BOYDEN RESEARCH TELESCOPES
W. Smit, H. J. van Heerden, & B. van Soelen 9

CONSIDERATIONS ON AUTOMATING OLDER TELESCOPES: THE BOYDEN 1.5 M TELESCOPE
H. J. van Heerden, P. J. Meintjes, B. van Soelen, W. Smit, I. P. van der Westhuizen, & H. Szegedi 13

MODERNIZATION OF COLOTI OPTICAL OBSERVATORY: REMOTE CONTROL AND AUTOMATION FOR MULTIMESSENGER FOLLOW-UP
P. Cristarella Orestano, S. Cutini, S. Germani, S. Palmerini, & G. Tosti 19

DON: AUTOMATION OF THE VATICAN ADVANCED TECHNOLOGY TELESCOPE *P. Gabor* 23

AUTONOMOUS TELESCOPE AND SCIENTIFIC INFRASTRUCTURE DEVELOPMENTS AT TUG *O. Erece, Y. Kilic, & K. Uluc* 27

OAUJ-CDK500: A NEW KRAKÓW ROBOTIC TELESCOPE
S. Zola, G. Stachowski, S. Kurowski, T. Kundera, W. Waniak, D. E. Reichart, V. Kouprianov, J. B. Haislip, Ł. Wyrzykowski, & P. J. Mikołajczyk 31

BUILDING A LIMITED BUDGET ROBOTIC OBSERVATORY *M. Odeh* 37

TOWARDS A FULLY ROBOTIC SOLAR OBSERVATORY AT THE UNIVERSITY OF GÖTTINGEN *S. Martens & T. O. Husser* 43

THE IMPACT OF THE SITE QUALITY OF THE ZADKO OBSERVATORY ON ITS SCIENTIFIC RESULTS
B. Gendre, R. Tonello, M. Studdert, D. Coward, A. Klotz, E. Moore, J. Moore, & F. Panther 49

ADVANCED WEATHER CONTROL SYSTEM AT THE TJO TELESCOPE
F. Domene, E. Herrero, P. Gil, D. Baroch, & A. Rojas 55

SKY BRIGHTNESS MEASUREMENTS WITH THE ALLSKY CAMERA AT THE UNIVERSITY OF GÖTTINGEN *K. J. Schimpf & T. O. Husser* 63

ZERO POINT MAGNITUDES OF ALL-SKY IMAGES FOR DETERMINING CLOUD CONDITIONS
C. H. D. van Gend, N. Erasmus, J. Tonry, L. Denneau, M. Hlakola, & S. B. Potter 69

OBSERVATORY CONTROL SYSTEM AT SOUTH AFRICAN ASTRONOMICAL OBSERVATORY
Sunil Chandra, Steve B. Potter, Carel van Gend, Nicolas Erasmus, & Roufurd Julie 71

MANAGEMENT OF A MULTI-USER ROBOTIC OBSERVATORY
J. Moore, B. Gendre, D. Coward, F. Panther, & E. Moore 77

AUTONOMOUS SCHEDULING AT THE TJO TELESCOPE
D. Baroch, E. Herrero, P. Gil, F. Domene, A. Rojas, & N. Ribó 81

UNSYNCHRONIZED FIREBALL ANALYSIS AND CHALLENGES IN DIMENSIONLESS ATMOSPHERIC FLIGHT PARAMETRIZATION:THE SPMN230522 SUPERBOLIDE AS A CASE STUDY
E. Peña-Asensio, P. Grèbol-Tomàs, J.M. Trigo-Rodríguez, M. Gritsevich, A. Rimola, M. Corretgé-Gilart, C. Guasch, C. Alcaraz, V. Ibáñez, A. Gómez, & J. Gómez 87

COMETARY OUTBURSTS AND EVOLUTION OF EJECTED PARTICLES
M. Gritsevich, M. Nissinen, J. Ryske, A. J. Castro-Tirado, I. Pérez-García, M. Weso, J. M. Trigo-Rodríguez, E. Peña-Asensio, I. Boaca, T. Prystavski, M. Husárik, O. Ivanova, A. Sánchez, & J. M. Llenas 93

INTERSTELLAR VISITORS AND ELUSIVE EXTRASOLAR METEORITES
E. Peña-Asensio, J. M. Trigo-Rodr', M. Gritsevich, H. Socas-Navarro, J. Visuri, & A. Rimola 101

EARLY-TIME OPTICAL SPECTRAL SHAPE MEASUREMENTS OF GRB 200925B
Z. Abdullayev, T. Komesh, B. Grossan, E. Abdikamalov, Z. Maksut, M. Krugov, S. Myrzakul, D. Tuiakbayeva, & A. Kostangeldinova 109

AN INTERMEDIATE LUMINOSITY GRB 210210A: THE EARLY ONSET OF THE EXTERNAL FORWARD SHOCK IN THE X-RAY?
R. Gupta, A. K. Ror, S. B. Pandey, J. Racusin, M. Moss, A. Aryan, N. Klingler, & A. J. Castro-Tirado 115

PROMPT AND AFTERGLOW ANALYSIS OF THE *FERMI-LAT DETECTED GRB 230812B*
A. K. Ror, S. B. Pandey, A. Aryan, S. Kumar, & A. J. Castro-Tirado 133

THE CORE COLLAPSE OF A $16.5\,M_\odot$ STAR
A. Aryan, S. B. Pandey, R. Gupta, A. K. Ror, & A. J. Castro-Tirado 145

VII Workshop on Robotic Autonomous Observatories (October 16-20, 2023)
Editors: Maria Gritsevich, Alberto J. Castro-Tirado, Petr Kubánek, Shashi B. Pandey, and David Hiriart

CONTENTS

EARLY EMISSION OF SHORT OPTICAL TRANSIENTS
S. Wu, V. M. Lipunov, A. J. Castro-Tirado, Y.-D. Hu, K. Zhirkov, & N. V. Tyurina 153

GERRY : FINDING ELECTROMAGNETIC COUNTERPARTS IN GRAVITATIONAL WAVES FOLLOW-UP CAMPAIGNS *D. O'Neill* 161

BLACK HOLE TOM – AN AUTOMATIC TOOL FOR PHOTOMETRIC TIME-DOMAIN DATA
P. J. Mikołajczyk, P. Zieliński, Ł. Wyrzykowski, A. Krawczyk, & K. Kotysz 167

ATTITUDE CONTROL STUDY ON ARTIFICIAL SATELLITES AND SPACE DEBRIS USING LASER DATA *R. Martínez & M. Á. Sánchez* 173

A UNIQUE LOOK ON MICROMETEORITES: WHEN SPECTROSCOPY MEETS CITIZEN SCIENCE
M. R. López-Ramírez, J. Laserna, M. Hanna, J. Moilanen, & M. Gritsevich 179

USING ARTIFICIAL INTELLIGENCE AND MACHINE LEARNING IN EDUCATION OF ASTRONOMY, PHYSICS AND MATHEMATICS
F. Bahrani 183

DEVELOPING SCHOOL SCIENCE SKILLS THROUGH THE SCIENCE-IES ROBOTIC TELESCOPE PROJECTS *J. R. Girón-Gambero* 187

TULANCINGO-I: THE K BAND MEXICAN RADIOTELESCOPE
D. Hiriart, E. Colorado, F. Diaz, T. Calvario, H. Serrano, D. Rojas, & S. Kurtz 193

IMAGING STOKES PHOTOMETER-POLARIMETER FOR THE BOOTES GLOBAL TELESCOPE NETWORK
S. Guziy, I. Syniavsky, Ye. Oberemok, O. Ivanova, & A. J. Castro-Tirado 197

THE INTELLIGENT OBSERVATORY
N. Erasmus, S. B. Potter, C. H. D. van Gend, S. Chandra, H. L. Worters, M. Hlakola, & R. Julie 201

SOFTWARE COMPONENTS OF THE INTELLIGENT OBSERVATORY
C. H. D. van Gend, S. B. Potter, N. Erasmus, S. Chandra, M. Hlakola, H. Worters, & R. Julie 209

NEW ROBOTIC TELESCOPE: THE BIG EYE TO OBSERVE THE TRANSIENT UNIVERSE
C. M. Gutiérrez, J. Barrera, J. Bento, D. Copley, C. M. Copperwheat, F. J. De Cos, M. Escriche, J. J. Fernández-Valdivia, A. P. Garner, J. Gracia, D. G. Heffernan-Clarke, H. E. Jermak, J. León Gil, A. M. McGrath, C. Miossec, A. Oria, A. Ranjbar, R. Rebolo, C. Rodríguez-Pereira, F. Sánchez-Lasheras, R. J. Smith, I. A. Steele, & M. Torres 217

AUTHOR INDEX 225

PREFACE

AstroRob2023 – A Continuing Tradition of Innovation and Collaboration

Fifteen years have passed since the inaugural Workshop on Robotic Autonomous Observatories was held in Málaga, Spain. In that time, the field of robotic astronomy has evolved at an unprecedented pace, marked by the rapid growth in the number and sophistication of autonomous astronomical facilities worldwide. As we approach the publication of the AstroRob2023 Proceedings—featured in a special issue of the Revista Mexicana de Astronomía y Astrofísica Conference Series in early 2025—it is fitting to reflect on the remarkable advancements and the workshop's vital role in fostering innovation and collaboration within this dynamic field.

The AstroRob series has become a cornerstone international forum, drawing researchers from across the globe to share the latest technological and scientific developments. The workshop, held from October 16th to 20th, 2023, at the Hotel Occidental Torremolinos Playa in Málaga, Spain, was no exception. Situated along the picturesque Costa del Sol, the venue provided an inspiring backdrop for a week of insightful presentations, engaging discussions, and invaluable networking opportunities.

The 2023 workshop arrived at a key moment for the astronomical community. The advent of new gravitational wave detectors in recent years and the anticipated discovery of electromagnetic counterparts have underscored the urgent need for highly autonomous and networked observatories. These facilities are essential not only for gravitational wave astronomy but also for a wide range of space research. From detecting fireballs and minor planets to monitoring variable stars and active galactic nuclei, robotic observatories are at the forefront of modern astronomy. Their contributions to the detection and monitoring of supernovae, gamma-ray bursts, and neutrino counterparts further highlight their importance in advancing our understanding of the universe.

Beyond traditional astrophysics, robotic observatories are increasingly vital in areas like space debris surveillance and tracking, where their ability to monitor and predict the movements of debris is critical for ensuring the safety of current and future space missions. The workshop also emphasized the educational potential of robotic observatories, showcasing how they inspire and engage the next generation of scientists.

The workshop's sessions reflected the field's breadth and depth, with topics ranging from hardware and software development to real-time data analysis, wide-field imaging, and follow-up observations. Discussions highlighted the integration of these technologies into global networks of observatories, enabling unprecedented coordination and data sharing, especially for transient event responses. The workshop also addressed challenges related to data archiving, quality control, and the development of advanced control systems for telescopes and observatories.

In addition to technical and scientific sessions, the workshop served as a platform for discussions on public outreach, citizen science, and future strategies to drive Robotic Astronomy forward. These initiatives are crucial for maintaining public interest and support for astronomical research.

We are grateful for co-organizing the workshop to the Instituto de Astrofísica de Andalucía (IAA-CSIC) and the Department of System Engineering and Automatics at Universidad de Málaga (UMA). We extend our heartfelt thanks to the Scientific Organizing Committee (SOC)—I. Andreoni, M. D. Caballero-García, A. J.

Castro-Tirado (chair), M. Gritsevich, S. Guziy, L. Hanlon, D. Hiriart, R. Hudec, P. Kubánek, D. Martínez-Delgado, F. F. Özeren, S. B. Pandey, C. Pérez del Pulgar, and B.-B. Zhang—for curating an exceptional scientific program. We are equally grateful to the Local Organizing Committee (LOC)—led by A. J. Reina (LOC chair), with M. E. Alcoholado-Feltström (LOC secretary), I. M. Carrasco-García, A. Castellón, S. Castillo, E. Fernández-García, Y.-D. Hu, M. Carmen López-Casado, I. Pérez-García, R. Sánchez-Ramírez, and S. Wu—for ensuring a flawlessly executed event.

This sixth workshop marked a significant milestone, with 80 registered participants representing 22 nationalities—a remarkable increase in both participation and internationalization since the inaugural event in 2009. The tradition of combining rigorous scientific engagement with cultural experiences continued, highlighted by the cherished midnight swim following the conference dinner—a hallmark of AstroRob workshops for the past 15 years.

We especially thank Irina Guziy for designing the vibrant workshop announcement poster and María Eva Alcoholado-Feltström (assisted by Javier Alberto Castro Alcoholado) for her outstanding efforts as workshop secretary, ensuring the event's smooth organization.

Last but not least, we express our heartfelt gratitude to the referees for their dedicated reviews and to the team behind the Revista Mexicana de Astronomía y Astrofísica for their meticulous editorial work in preparing and publishing this issue. As the AstroRob2023 Proceedings are finalized, we are reminded of the critical role these gatherings play in advancing the field. The contributions presented at this workshop not only capture the current state of robotic astronomy but also serve as a foundation for future breakthroughs.

The continued success of the AstroRob series is a testament to the dedication, creativity, and collaboration of the global community of researchers driving innovation in autonomous astronomical observations. We look forward to the insights and advancements that will emerge from these proceedings and the ongoing growth of this exciting field. May the AstroRob series continue to stand as a pillar of collaboration, driving both technological and scientific progress in the years to come.

Maria Gritsevich, Alberto J. Castro-Tirado, Petr Kubánek, Shashi B. Pandey, and David Hiriart
Helsinki, Málaga, Praha, Nainital, and Ensenada
Editors of the proceedings

VII Workshop on Robotic Autonomous Observatories (October 16-20, 2023)
Editors: Maria Gritsevich, Alberto J. Castro-Tirado, Petr Kubánek, Shashi B. Pandey, and David Hiriart

LIST OF PARTICIPANTS

ADAMČÁK, Ján, Astronomical Institute of Slovak Academy of Sciences, Vysoké Tatry,	Slovakia
ALCOHOLADO-FELSTRÖM, Eva, Málaga,	Spain
ARYAN, Amar, ARIES, NainiTal,	India
BAHRANI, Fatemeh, AstroTech,	Iran
BAROCH LÓPEZ, David, Montsec Observatory (IEEC),	Spain
BARROS BLANCO, Beatriz, UMA, Málaga,	Spain
CABALLERO-GARCÍA, María D., AA-CSIC, Granada,	Spain
CARRASCO-GARCÍA, Irene M., UMA, Málaga,	Spain
CASTELLÓN SERRANO, Alberto, UMA, Málaga,	Spain
CASTRO-SEGURA, Noel, Univ. of Southampton,	UK
CASTRO-TIRADO, Alberto J., IAA-CSIC Granada,	Spain
CASTRO TIRADO, Miguel Ángel, Málaga Planetarium,	Spain
CHANDRA, Sunil, SAAO,	South Africa
CHEN, Zong, Shanghai Astronomical Observatory, CAS,	China
CONVERSI, Luca, ESA,	France
CORREAL OLMO, Alba, UMA, Málaga,	Spain
CRISTARELLA ORESTANO, Paolo, UNIPG and INFN,	Italy
DELOMÉNIE, Guillaume, Ariana Group,	France
DOMENE, Francesc, Montsec Observatory,	Spain
ERASMUS, Nicolas, SAAO,	South Africa
ERECE, Orhan, Tübitak National Observatory,	Türkiye
FERNÁNDEZ CENTENO, Alejandro, Quasar Science Resources SL, Madrid,	Spain
FERNÁNDEZ-GARCÍA, Emilio, IAA-CSIC Granada,	Spain
GABOR SJ, Paul, Vatican Observatory,	USA
GENDRE, Bruce, University of Western Australia,	Australia
GIMÉNEZ, Álvaro, CAB/INTA-CSIC, Madrid,	Spain
GIRÓN GAMBERO, Jesús R., UMA,	Spain
GORSKI, Marek, Nicolaus Copernicus Astronomical Center, Warsaw,	Poland
GRITSEVICH, Maria, University of Helsinki,	Finland
GUPTA, Rahul, ARIES, NainiTal,	India
GUTIÉRREZ DE LA CRUZ, Carlos M., IAC, La Laguna,	Spain
GUZIY, Sergiy, IAA-CSIC, Granada,	Spain
HIRIART, David, UNAM, Ensenada,	México
HU, Youdong, IAA-CSIC Granada,	Spain
HUSSER,Tim-Oliver, Göttingen University,	Germany
JELÍNEK, Martin, ASU-CAS, Ondřejov,	Czech Rep.
JIMÉNEZ-IBARRA, Felipe, Monash University,	Australia
JOHNSON, Chris, Vatican Observatory,	USA

KAŁUSZYŃSKI, Mikolaj, Nicolaus Copernicus Astronomical Center, Warsaw, Poland
KICIA, Miroslaw, Nicolaus Copernicus Astronomical Center, Warsaw, Poland
KOMESH, Toktarkhan, Nazarbayev University, Kazakhstan
KUBÁNEK, Petr, LSST, USA and Czech Rep.
KUMAR, Amit, Warwick University, UK
KUMAR ROR, Amit, ARIES, NainiTal, India
LE MONTAGNER, Roman, IJCLab Orsay, France
LEIVA, Rodrigo, IAA-CSIC Granada, Spain
LIPUNOV, Vladimir, MSU, Moscow, Russia
LÓPEZ-RAMÍREZ, Ma. Rosa, UMA, Málaga, Spain
LÓPEZ-VALVERDE, Miguel Ángel, IAA-CSIC, Granada, Spain
MANJUNATH, Bestha, IIAP, Bengaluru, India
MARTENS, Sven, University of Göttingen, Germany
MEERWART, Leon, Institute for Astrophysics and Geophysics, Göttingen, Germany
MIKOŁAJCZYK, Przemysław, Astronomical Observatory, University of Warsaw, Poland
MOORE, John, University of Western Australia, Australia
MUTLAQ, Jasem, Ikarus Technologies, Kuwait
NÚÑEZ, José Manuel, SMA, Spain
ODEH, Mohammad, International Astronomical Center, UAE, United Arab Emirates
O'NEILL, David, University of Warwick, UK
ORTIZ, José Luis, IAA-CSIC Granada, Spain
ÖZEREN, Ferhat Fikri, APSCO, TUA and ERCİYES University, Türkiye
PEÑA-ASENSIO, Eloy, Universidad Autónoma de Barcelona, Spain
PÉREZ DEL PULGAR MANCEBO, Carlos, UMA, Málaga, Spain
PÉREZ-GARCÍA, Ignacio, IAA-CSIC Granada, Spain
POZANENKO, Alexei, IKI, Moscow, Russia
REINA TEROL, Antonio Jesús, UMA, Málaga, Spain
SÁNCHEZ PIEDRA, Manuel, ROA, San Fernando Naval, Cádiz, Spain
SANTANA-ROS, Toni, Universidad de Alicante, Spain
SCHIMPF, Karsten Johann, University of Göttingen, Germany
SINGER, Leo P., NASA, Greenbelt, USA
VAN GEND, Carel, SAAO, South Africa
VAN HEERDEN, Hendrik J., University of the Free State, South Africa
VILARDELL, Francesc, GMV, Spain
VITEK, Stanislav, Czech Technical University, Prague, Czech Rep.
WILDI, Markus, Obs. Vermes, Switzerland
WU, Siyu, IAA-CSIC Granada, Spain
XU, Yang, National Astronomical Observatories, CAS, China
ZHANG, Binbin, Nanjing University, China
ZIELENSKI, Pawel, Institute of Astronomy, Nicolaus Copernicus University, Torun, Poland
ZOLA, Staszeck, Jagiellonian University, Poland

GROUP PHOTOGRAPH



Revista Mexicana de Astronomía y Astrofísica Serie de Conferencias (RMxAC), **59**, 1–8 (2025)
© 2025: Instituto de Astronomía, Universidad Nacional Autónoma de México
https://doi.org/10.22201/ia.14052059p.2025.59.01

VII Workshop on Robotic Autonomous Observatories (October 16-20, 2023)
Editors: Maria Gritsevich, Alberto J. Castro-Tirado, Petr Kubánek, Shashi B. Pandey, and David Hiriart - DOI: https://doi.org/10.22201/ia.14052059p.2025.59.01

DEVELOPMENT OF ASTRONOMICAL OBSERVATORIES FROM THE LATE 19TH TO THE 21ST CENTURY

Miguel Ángel Castro Tirado[1]

RESUMEN

Este artículo atiende a la transición desde el observatorio moderno al contemporáneo así como su evolución hasta principios del siglo XXI. Asimismo analiza las variaciones en los diseños de estos edificios hasta que algunas de estas características se consolidan definiendo los rasgos propios del observatorio contemporáneo.

ABSTRACT

This work explores the transition from modern to contemporary astronomical observatories and traces their evolution up to the early 21st century. It examines the gradual changes in architectural and functional designs of these structures, highlighting how certain features evolved and eventually became standardized, shaping the defining characteristics of the contemporary observatory.

Key Words: instrumentation: detectors — methods: observational — techniques: photometric — telescopes

1. INTRODUCTION

The development of the observatories up to the 19th century reached a series of characteristics or constructive solutions that were established as substantial features of the architectural definition of the astronomical observatory. In this sense, several aspects were consolidated, such as the search for the greatest possible structural stability, the independence of the optical instrument supports from the rest of the structure of the complex, the separation of main and secondary uses, attention to thermal stability, the specialisation of the façade and its openings according to the contained use, and the installation of the mobile dome as a roof-covering solution through which the entire sky can be made visible (Castro Tirado 2021a), a solution adopted in many robotical observatories (see for instance Hu et al. 2023).

Beyond the particularities of their construction, the substantial changes in the observatories up to this point range from their genesis to their purpose. In this way, they went from the nobleman or monarch as promoter to the institutions or public benefactors. Likewise, it would progress from the purely scientific interest to its practical application or the incorporation of propagandistic or informative functions. Historically, the enlargement of observatories has been linked to the increase in the number of their instruments and the increase in their size as technical advances made this possible. In the case of royal or state centres, Newcomb stated that "whenever a monarch has wished to associate his name with science, he has designed an observatory commensurate with the magnitude of his ambition, filling it with instruments of the corresponding scaler" (Newcomb 1881). This assertion can be extrapolated to contemporary observatories, regardless of the benefactor or promoter of their foundation, with the qualification that the design and scale of the building will be proportional to the scientific ambition and research project behind it. On the other hand, from the 19th century onwards, the development of cities began to cause problems in some nineteenth-century observatories, which not only began to move away from the large capitals towards smaller towns but also began to consider their situation in environments far from the urban environment as something favourable. This trend would continue and intensify in the following decades, underlining a physical distance from the ordinary citizen that would lead to intellectual dissociation. These astronomical centres with spaces such as lecture halls, classrooms or exhibitions, open to visitors, amateurs and experts, or even public observatories, will gradually lose prominence in favour of highly specialised scientific complexes in which, increasingly, almost exclusively the astronomical function will have its place (Castro Tirado 2019). Both the need to move away from urban centres and the new architectural and structural demands required by the new astronomical instruments were causes of obsolescence of the observatories. As a result, many observatories, especially the more modest ones, which emerged during the previous period, ended up abandoning re-

[1]Málaga Planetarium, Victoria de los Ángeles 12, 29004 Málaga, Spain (mact@malagaplanetarium.com).

VII Workshop on Robotic Autonomous Observatories (October 16-20, 2023)
Editors: Maria Gritsevich, Alberto J. Castro-Tirado, Petr Kubánek, Shashi B. Pandey, and David Hiriart - DOI: https://doi.org/10.22201/ia.14052059p.2025.59.01

search in order to reconvert to another type of use, taking advantage of the construction itself, or they were closed down altogether (Eelsalu 1999).

2. DETACHMENT/DISENGAGEMENT FROM URBAN/CITY

The massive movement from the rural world to the cities that occurred after the Industrial Revolution led to a continuous growth of populations throughout the 19th century. This movement was accompanied by some changes in human activity that already at the beginning of the new century compromised the good performance of observatories (Bourgeois 2017) in urban or peri-urban environments. The emergence of new industry and the increase in motorised transport by land and sea led to an increase in vibrations and pollution. In addition, public street lighting brought with it light pollution that limited the visibility of faint objects. Likewise, this change of century coincided with the transition from refractors, as the paradigm of the telescope typical of any astronomical centre worthy of significance, to large reflectors. This evolution went hand in hand with the rise of astrophysics, although without leaving behind classical astronomy, which relied on meridian circles, transit instruments and astrographs to continue its studies related to the measurement of time or navigation itself (at least until the middle of the 20th century). This meant that the observatories had to attend to different lines of work, which meant that they had to have markedly heterogeneous equipment (Hünsch et al. 2012). Thus, at the end of the 19th century, almost simultaneously in America (near San José, California) and Europe (near Nice, France), the newly-born observatories (both the Lick and Nice ones) presented some of the defining features of what was to become the contemporary observatory. These complexes were to be set up isolated from urban centres, in remote and elevated areas such as mountaintops where, far from the fumes and lights of the city, they would find the best possible conditions for observation.

The boundary between the modern and the contemporary observatory is clearly marked by the ambivalent Lick Observatory (Figure 1). Both its architectural configuration and its main design features are typical of the earlier period, yet it would become the first astronomical centre completely detached from the urban with its permanent mountain installation. The remoteness of the cities meant that the general population was isolated and lost contact with this science. In contrast, during the first part of the 20th century, public observatories were built in large European cities (Berlin, Vienna...) to inform the public about astronomy and the universe (Markkanen 2013). These institutions, being disconnected from the scientific avant-garde, moved away from the new design trends and remained stagnant in the features of the modern observatory. On the other hand, despite their high degree of professionalism and greater secrecy, there are still some astronomical complexes that are occasionally open to an initiated (or at least interested) public, which include guided tours and museum spaces in their complexes. There will even be some centres that consider tourism as a value or recognition (such as the Mount Wilson in the US or the BTA-6 in Russia) and even as a means of financing their research programme (such as the Pic du Midi Observatory or the above mentioned one in Nice, both in France) (Figure 2).

In this regard, the same Director of the Nice Observatory (now the Observatory of the Côte d'Azur) emphasises the natural environment, the panoramic views and the architecture of the complex as values to be highlighted in order to broaden the potential visitor base beyond the amateur public or school excursions, acquiring a national and international tourist vocation (Heudier 2006).

3. FRAGMENTATION

The new needs of science were to lead to some variations in the design principles of buildings devoted to astrophysics, in particular spectroscopy and photometry (Markkanen 2013). While the modern observatory tends to be configured as a unitary building in which a complex programme of heterogeneous uses (observation rooms, offices, libraries, workshops, dwellings...) shares a roof in a single building in which one or more domes and a meridian room that conditioned the orientation of the construction were evidence of its raison d'être, the contemporary observatory will be organised in a less regulated and rigid way (Hünsch et al. 2012). The very size of the new large reflectors, the differences in scale, the different needs intrinsic to the multiple uses or the orography of the mountainous terrain itself, which makes it difficult to have large leveled floors, will be aspects that will cause the segregation of the building into a series of independent constructions. This separation will allow a liberty of layout and orientation in the territory that will favour the conditions for observation, as well as exempting the astronomical function from some of the interferences (vibrations, smoke, light, heating) inherent to other uses.

In addition to being located on a mountain, the Nice Observatory (Figure 3) would be the forerunner

VII Workshop on Robotic Autonomous Observatories (October 16-20, 2023)
Editors: Maria Gritsevich, Alberto J. Castro-Tirado, Petr Kubánek, Shashi B. Pandey, and David Hiriart - DOI: https://doi.org/10.22201/ia.14052059p.2025.59.01

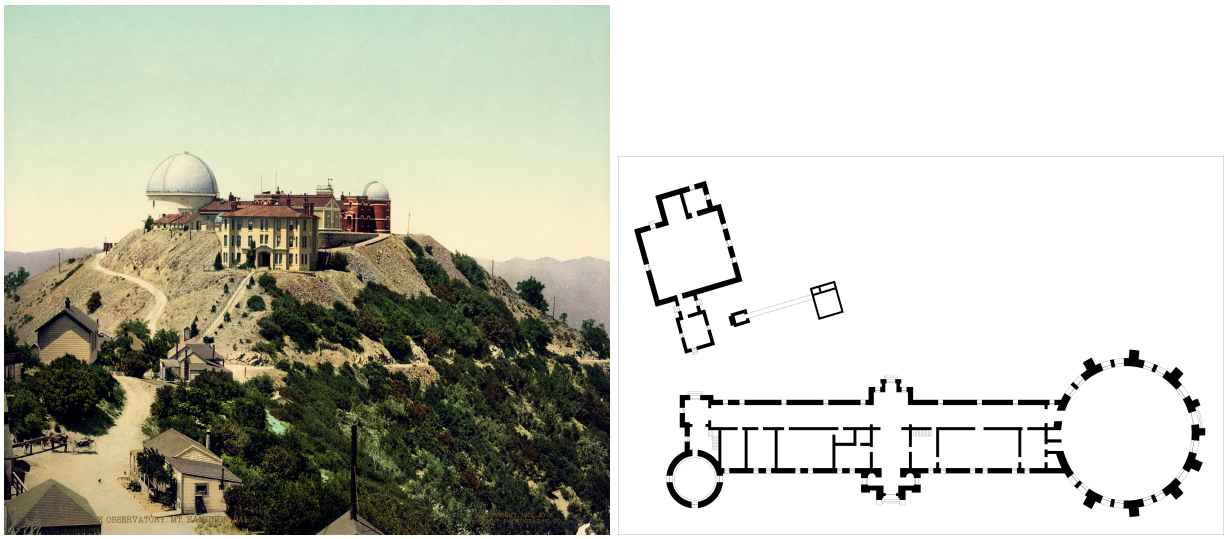


Fig. 1. *Left:* Lick Observatory perspective. *Right:* Lick Observatory plan. Adapted from Castro Tirado (2019).



Fig. 2. Tourism at the Pic du Midi Observatory.

in being intentionally and permanently conceived, designed and constructed as a set of independent buildings with a high level of specialisation. Although over the next few years, several astronomical institutions would emerge that fulfilled one of these two characteristics, it would be a quarter of a century before both were replicated simultaneously. This marks him out as a man ahead of his time who should be recognised as a benchmark. The aforementioned distance from urban centres will entail the disconnection of public installations from urban areas (electricity, water, etc.) so that, although there are solutions to this isolation (such as electricity generators or water tanks), the truth is that experience has shown in cases such as the Pic du Midi Observatory that connection to the supply networks is essential for the acceptable development of the research activity (Davoust 1998). On the other hand, the occupation of land that is isolated and disconnected from the population is evidence of the effects that such a facility can have on its surroundings. As the landowners who gave the land for the construction of the Mount Wilson Observatory have already warned, a large observatory becomes an important point of interest that gives its surroundings renown and prestige, attracting scientists and tourism, and catalysing the development of the industry directly and indirectly linked to this activity; in short, increasing the wealth of the place and its inhabitants. Shortly after 1900, the Mount Wilson and Hamburg observatories joined the trend set by the Nice observatory, which was to become consolidated throughout the 20th century: the formalisation of an independent building for each telescope, allowing an absolute level of specialisation by defining each of the characteristics that would condition the project on the basis of the functional requirements of its single instrument.

4. CONSEQUENCES OF UPSCALING

The inauguration of the Hamburg-Bergedorf Observatory preceded a period of instability from the First World War (1914-1918) to the Second World War (1939-1945), including the interwar years. During this period, both the possible funding and the thoughts of a large part of scientists, and of the population in general, will be focused on the war conflicts, their unforeseeable consequences or on the recovery

VII Workshop on Robotic Autonomous Observatories (October 16-20, 2023)
Editors: Maria Gritsevich, Alberto J. Castro-Tirado, Petr Kubánek, Shashi B. Pandey, and David Hiriart - DOI: https://doi.org/10.22201/ia.14052059p.2025.59.01

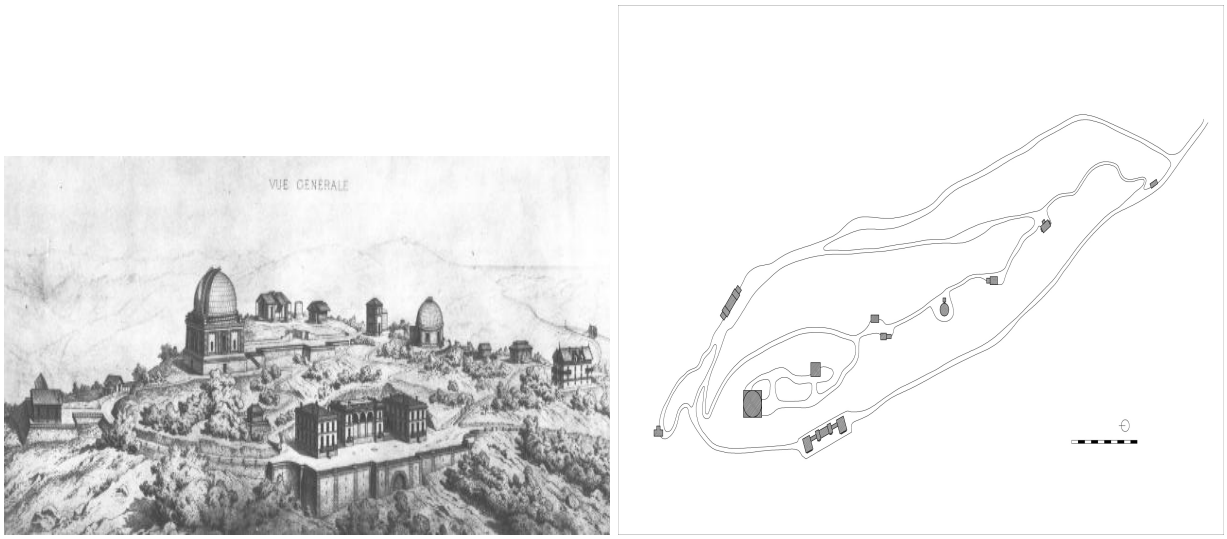


Fig. 3. *Left:* Nice Observatory perspective. *Right:* Nice Observatory ensemble plan. Adapted from Castro Tirado (2019).

from them. For all these reasons, no new astronomical observatory of any significance will be built until almost the middle of the 20th century. The only exception worth mentioning is the Griffith Observatory in Los Angeles, which was built between the two conflicts thanks to the tenacious efforts of a private investor (Krupp 2011). Prior to this parenthesis, during the 19th century there had been a race for the world's largest telescope which, perhaps, rather than scientific ambition, represented an ambition for fame, prestige or recognition. Thus, this competition was active from the installation of the large 76 cm diameter refractor telescope at Pulkovo Observatory (Russia) in 1839 until the 102 cm diameter refractor at Yerkes Observatory (US) in 1897, still holding the record of being the largest refracting telescope in the world. See also Castro Tirado (2021b). In addition to the technical difficulties that complicated this redundant growth of instruments, it would be a change in the prevailing telescope system that would eventually put an end to this competition. Although mirror-based telescopes had been installed in observatories for decades, their role had always been secondary to the importance of the large refractors. However, their relevancy was to increase thanks to the technological advances that would make it possible to manufacture the required mirrors in parallel with the development of astrophysics itself. Thus, with the installation of the large reflector at the Mount Wilson Observatory (152 cm) in 1908 and, above all, with the inauguration of the large Hooker reflector (254 cm) (see both in Figure 4) at the same complex in 1917, a new race began to build the largest reflecting telescope in the world. An aspiration that has been maintained to the present day.

Regardless of the type of instrument being referred to, the exponential growth achieved during these disputes reached such magnitudes of telescopes that it rivalled the very scale of the architecture that contained them. This would mean an increase in the size of the buildings housing the telescopes that would produce a large amount of contained space that could be taken up by other uses. Similarly, the large instruments would require larger structural supports. To such an extent that the scale they would acquire would generate interior voids or spaces that would even allow for the accommodation of some functions. In this way, the projects for these large telescopes would or could incorporate enough secondary functions (offices, workrooms, meeting rooms, laboratories, storerooms, workshops, rest rooms, toilets, etc.) to be able to contain almost the entire programme required for an entire observatory. Thus, each building planned for a particular instrument could have sufficient autonomy to constitute an entire astronomical observatory in its own right. At the same time, this independence allowed absolute freedom in the design of the project, which could be adjusted and specialised according to the specific observation needs of the instrument it would house, optimising its observation solution, adapting to its location and environment, and accommodating the rest of the secondary uses required to its architecture. From this point onwards, the most important observatories would be constituted as groups of independent structures which would usually include

VII Workshop on Robotic Autonomous Observatories (October 16-20, 2023)
Editors: Maria Gritsevich, Alberto J. Castro-Tirado, Petr Kubánek, Shashi B. Pandey, and David Hiriart - DOI: https://doi.org/10.22201/ia.14052059p.2025.59.01

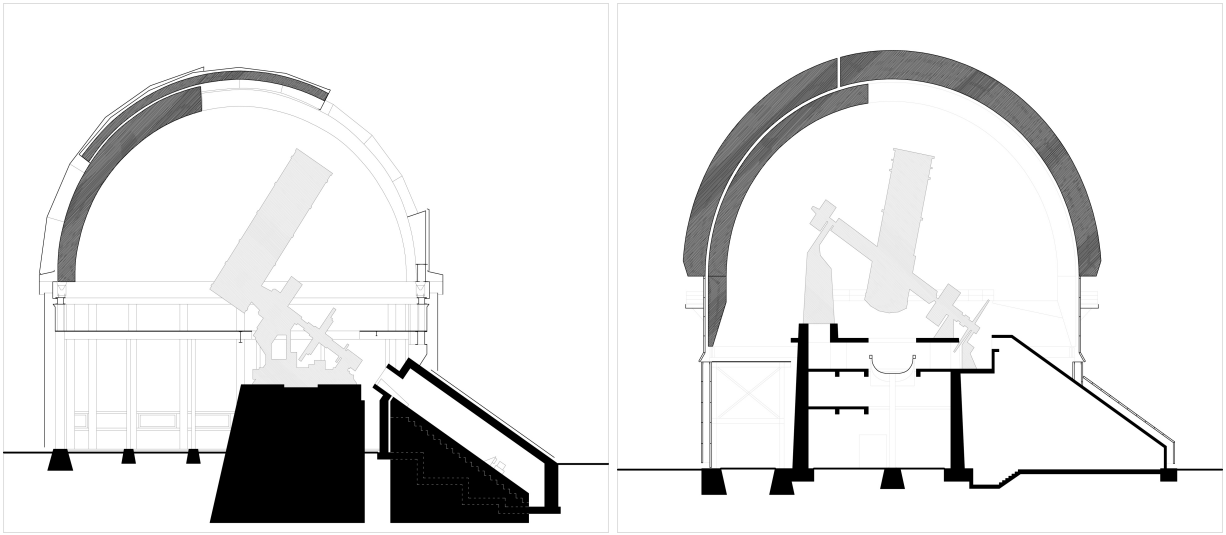


Fig. 4. *Left:* Mount Wilson Observatory section. Adapted from Castro Tirado (2019). *Right:* the Hooker Great Reflector section at Mount Wilson Observatory. Adapted from Castro Tirado (2019).

buildings containing some accessory uses (residences, coffee shops, exhibitions, rooms for visitors...), other constructions for astronomical instruments and the main buildings for the large telescopes together with the primary functions (meeting rooms, work rooms, laboratories, offices...), which would constitute the very essence of the observatory itself.

5. BUILDING-SIZE TELESCOPES

The war years would reduce investment in this science to a minimum, causing a standstill in the construction of new astronomical centres. This pause would lead, after its conclusion, to new projects for observatories with telescopes, and therefore larger and more ambitious buildings. Likewise, this parenthesis had allowed us to take a certain perspective on the latest advances in astronomical centres, discerning the values implemented by some observatories (it should be remembered that during the first half of the century both observatories typical of the previous period and others incorporating contemporary aspects were inaugurated). Thus, by the middle of the 20th century, the principles that would shape the characteristic features of the contemporary observatory had become apparent: location in the mountains, far from the population, and the configuration of the observatories as groups of autonomous buildings of high technical specificity destined for a particular instrument or function. In addition, the new century brought with it a paradigm shift in this science, from classical astronomy to contemporary astrophysics. This evolution brought the telescope back into the spotlight, which as a refractor seemed to be reaching insurmountable limits, but as a reflector had many possibilities for improvement and enlargement. The increase in the number of reflectors leads to a upscale in the building that contains them and in the structure that supports them. The size of the telescopes soon reaches dimensions that bring them into the range of buildings and their structural supports and foundations become so large that, since it would make no sense for them to be massive, the space they contain exceeds the architectural scale of man, so that they can be inhabited and occupied by all kinds of functions. Then some of the uses that had been broken up to make way for buildings exclusively for large telescopes are eventually reintroduced into their bases to take advantage of the space created by their increased scale. This leap in scale is first evident at the Hale Telescope (Figure 5), at the inauguration of which almost a thousand people were seated under the dome around the reflector mount supports in front of a stage.

The enlargement of telescopes went hand in hand with the upsize of their mirrors, which became larger, heavier and more complex to manufacture, maintain and move. For this reason, it became increasingly essential to have facilities for the handling and maintenance of the large mirrors, and so they were eventually added to the telescope building itself. This incorporation of new functions will not be an isolated event, but on the contrary will become a recurrent feature as new developments are implemented as basic standards. In this way, various rooms for specific facilities or storage will be incorporated into the programme of essential uses of the observatories. Just

VII Workshop on Robotic Autonomous Observatories (October 16-20, 2023)
Editors: Maria Gritsevich, Alberto J. Castro-Tirado, Petr Kubánek, Shashi B. Pandey, and David Hiriart - DOI: https://doi.org/10.22201/ia.14052059p.2025.59.01

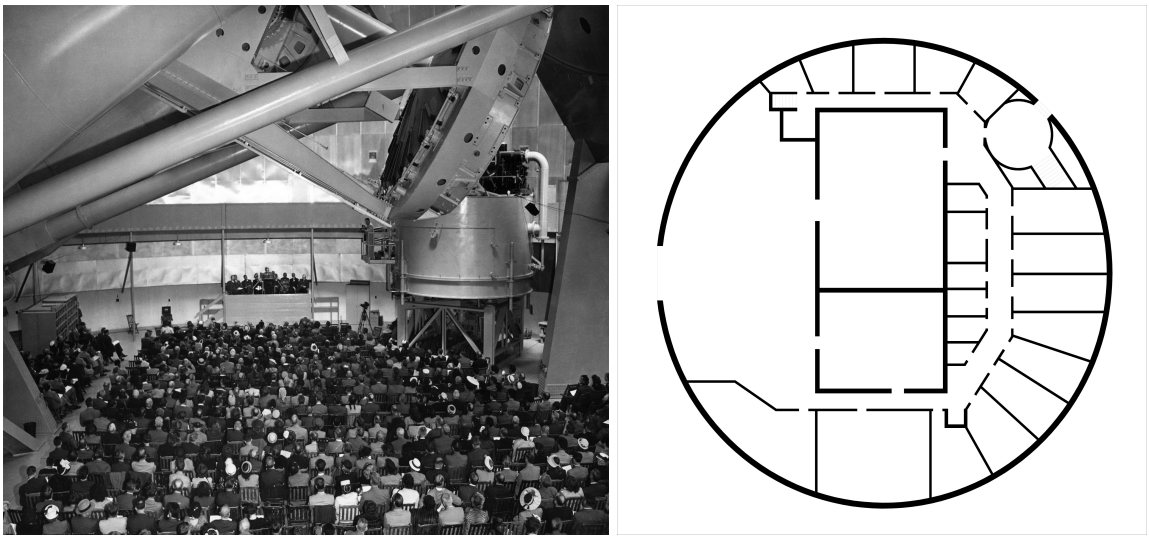


Fig. 5. *Left:* The Hale Telescope inauguration. *Right:* Hale Telescope plan. Adapted from Castro Tirado (2019).

as with the modern observatory there was a competition for the world's largest refractor, so the era of the large reflector saw the beginning of a similar competition, which has continued throughout the 20th century and into the present day. If around the turn of the century the orientation of science towards astrophysics would boost the weight of reflectors in research, then this type of telescope would remain modest until George Hale promoted the most powerful reflector of its time (1.52 m diameter), installed in 1908 at the Mount Wilson Observatory. However, his ambition led him to surpass his own milestone by promoting the Hooker (2.54 m diameter) at the same complex in 1917. This race continued with the inauguration of the Hale Telescope (5.08 m diameter) at Palomar Observatory (California) in 1948, followed by the BTA-6 (6 m diameter) at Zelenchuk (Russia) in 1975 and surpassed by the Keck I (9.8 m diameter) at Mauna Kea (Hawaii) in 1993. The current holder of the honour of being the largest reflector in the world is the Gran Telescopio Canarias (10.4 m diameter) in Spain since 2007. However, it is already known that this prerogative is about to expire as new observatories with reflectors larger than the GTC are already planned. For example, the Giant Magellan Telescope (24.5 m diameter) at Las Campanas Observatory (Chile) is under construction and is expected to start operations in 2030[2]. The Thirty Meter Telescope (30 m diameter) at the Mauna Kea Observatory is also in the pipeline, although it has been announced that work will begin in 2019 and it is expected to start operations in 2027[3]. And the Extremely Large Telescope (39 m diameter) at Cerro Armazones (Chile) is under construction too and is expected to be operational from 2027[4]. There were even plans for such a huge project as the Overwhelmingly Large Telescope (100 m diameter), which is, at least for now, cancelled[5]. Since the transition from monolithic mirrors to composite solutions, either of hexagonal or circular pieces, the weight of the reflector element has been reduced and its structure lightened, giving the possibility to continue with a growth, so far, without limit.

6. STAGNATION DESPITE TECHNICAL PROGRESS

Leaving aside improvements in optical systems or technological aspects, designers were so strongly influenced by the Hale Telescope design that almost all post-World War II astronomical centres were devoted to replicating the Hale Observatory pattern without a critical eye or study of other possible variations (Leverington 2017). In this sense, such transcendental advances for astronomy as the altazimuth mount or the incorporation of the computer control of the BTA-6 had little impact on its architectural definition (see for instance, Figure 6) beyond the not very significant displacement of the structural support of the telescope from a lateral position to the centre of the building's floor plan. In other words, although there have been some significant advances

[2] https://www.gmto.org/.

[3] https://www.tmt.org/.

[4] https://www.eso.org/public/teles-instr/elt/.

[5] http://www.eso.org/sci/facilities/eelt/owl/index.html.

VII Workshop on Robotic Autonomous Observatories (October 16-20, 2023)
Editors: Maria Gritsevich, Alberto J. Castro-Tirado, Petr Kubánek, Shashi B. Pandey, and David Hiriart - DOI: https://doi.org/10.22201/ia.14052059p.2025.59.01

in this science after Hale, such as the altazimuthal configuration of the mount, computerised tracking, and even remote access to observations, the fact is that the architecture of the buildings has hardly had any representative evolution beyond some minor and specific variations that become the exception, such as the recovery of the dwellings in the construction of some observatories.

Just as the modern observatory paid attention to details such as structural independence or thermal stability as resources to reduce the constraints that reduced its resolution, the contemporary observatory, in addition to technical advances to improve the results of its observations (such as automated tracking or optical improvements through the controlled deformation of its mirrors), also pays attention to the impact of the complex itself on the nearby atmosphere. Experience has shown that the most unfavourable source of atmospheric turbulence for observation usually comes from the observatory itself, as the unattainable thermal inhomogeneity between parts of the building or even the telescope is detrimental to such precise instruments (Finn 1985). Therefore, some observatories already incorporate air-conditioning and/or ventilation to equalise temperatures and carefully control their own heat sources. While each new improvement in telescopes or in the tools for analysing their observations leaves their predecessors a little more outdated, the reality is that these reflectors that are not at the forefront of global research are still in high demand for use. After all, there are more lines of astronomical work than there are state-of-the-art observatories, and many projects do not depend on extremely high resolution observations[6]. Beyond all this, the importance of technological evolution in terms of computerisation and communication systems should be emphasised and reiterated. Although a priori it may seem a minor change with no particular impact on the observatories, both remote control and remote access to observations mark a decisive turning point for these complexes, since it seems to offer the possibility of abandoning all physical presence in the observatories, which would end up stripping them of their status as buildings.

7. CONCLUSIONS

Despite the many and far-reaching advances in the 20th century observatories, the changes from mid-century onwards have always been driven by technical issues, which has not meant a major transgression in their architecture, so that there has been no impediment for the projects of these buildings to adapt to this evolution in order to achieve designs that would incorporate these changes and, as far as possible, take advantage of them favourably. Even so, although during the beginnings of this period of contemporary development some design strategies for astronomical centres were occasionally manifested in terms of their spatial configuration or their arrangement on the ground, on many occasions these practices were limited to the replication of building envelopes with outdated architectural languages (neo-baroque in the Nice Observatory or art deco in the Hale Telescope) that had little or nothing to do with the activity for which they were intended, with the exception of their domes: those iconic features whose uniqueness was to make them a symbol of the astronomical function. However, although the hemispherical dome is the most common and popular, it is not the only existing solution for an observation building, and there are other less common alternatives such as the polyhedral or cylindrical dome, the vault, the folding or retractable roof, or even the completely movable covering (used in many autonomous and robotic observatories nowadays). The existing dissociation between container and content, between astronomy and architecture, which almost only the domes link in some way, has not been remedied in the development up to the present, but has increased. The ever-increasing budgets allocated to telescopes reduce to a minimum the funds allocated to the buildings in which they are installed, so that a hierarchical imbalance is created whereby architecture is completely eclipsed by science and the buildings lose all sense or meaning and become mere carcasses. Whereas the modern observatory achieved a perfect communion between astronomy and architecture, thanks to which observatory projects were developed in parallel to the construction of the instruments and the design of the buildings was based on generating the most propitious scenarios for observation on the basis of the equipment provided, the contemporary observatory perverts this relationship. The transition from a functionalist attitude, which demanded that every architectural decision should be based on the conditions of use, to a misunderstood utilitarianism, in which any design criterion must be justified solely and exclusively on the basis of its scientific convenience, ignoring users and surroundings, leaving architecture in a situation of absolute submission. Thus, the contemporary observatory is characterised by being governed almost exclusively by scientific-technological crite-

[6] "25 years of Calar Alto Observatory", Max Planck Institute for Astrophysics: `http://www.mpia.de`

VII Workshop on Robotic Autonomous Observatories (October 16-20, 2023)
Editors: Maria Gritsevich, Alberto J. Castro-Tirado, Petr Kubánek, Shashi B. Pandey, and David Hiriart - DOI: https://doi.org/10.22201/ia.14052059p.2025.59.01



Fig. 6. *Left:* Mount Wilson Observatory. *Right:* Calar Alto Observatory.

ria, reducing the architectural impact to the bare minimum and stripping architecture of its autonomy and leaving it subjugated to astronomy.

Acknowledgements: I want to thank M. Gritsevich and A.J. Castro-Tirado for very useful conversations. I also acknowledge the support of both the Spanish Ministry project PID2020-118491GB-I00 and Junta de Andalucía project P20_01068.

REFERENCES

Bourgeois, N. 2017, "Category of Astronomical Heritage: tangible immovable". Pic du Midi de Bigorre Observatory. France, Portal to Heritage of Astronomy (UNESCO official website: `https://www3.astronomicalheritage.net/index.php`)

Castro Tirado, M. A. 2019, PhD Thesis, Universidad de Málaga, Spain, pp. 289-317

Castro Tirado, M. A. 2021a, RMxAC, 53, 6

Castro Tirado, M. A. 2021b, RMxAC, 53, 4

Davoust, E. 1998, ASPC, 141, 42

Eelsalu, H. 1999, Journal of Astronomical History and Heritage, Vol. 2, No. 2, p. 111

Finn, R. 1985, Keck Observatory, Engineering and Science, 48 (3), 9

Heudier, J.L. 2006, "De l'Observatoire à l'Observatorium", La lettre de l'OCIM 106, 8

Hu, Y.-D., Fernández-García, E. J., Caballero-García, M. D. et al. 2023, Frontiers in Astronomy and Space Sciences, vol. 10, id. 952887

Hünsch, M., Seemann, A., Wolfschmidt, G. 2012, The Hamburg Observatory, Justification of Outstanding Universal Value (from City of Hamburg official website: `www.hamburg.de`)

Krupp, E.C. 2011, Going public, p. 463

Leverington, D. 2017, Observatories and Telescopes of Modern Times, Cambridge University Press, UK, p. 109

Markkanen, T. 2013, Acta Baltica Historiae et Philosophiae Scientiarum, 1 (2), 48

Newcomb, S. 1881, Sci, 2 (59), 378

Revista Mexicana de Astronomía y Astrofísica Serie de Conferencias (RMxAC), **59**, 9–12 (2025)
© 2025: Instituto de Astronomía, Universidad Nacional Autónoma de México
https://doi.org/10.22201/ia.14052059p.2025.59.02

VII Workshop on Robotic Autonomous Observatories (October 16-20, 2023)
Editors: Maria Gritsevich, Alberto J. Castro-Tirado, Petr Kubánek, Shashi B. Pandey, and David Hiriart - DOI: https://doi.org/10.22201/ia.14052059p.2025.59.02

CHARACTERIZATION OF THE KL4040 SCMOS FOR USE ON THE BOYDEN RESEARCH TELESCOPES

W. Smit[1,2], H. J. van Heerden[1,3], and B. van Soelen[1]

RESUMEN

Recientemente, los sensores sCMOS se han vuelto más populares en la investigación astrofísica debido a su asequibilidad y disponibilidad en comparación con los sensores CCD, pero también debido a su rápida velocidad de lectura y bajo ruido de lectura. Sin embargo, la tecnología que utiliza sCMOS es diferente a la CCD, por lo que es importante una caracterización completa para garantizar una reducción y un procesamiento válidos para los procesos científicos. Se muestran los resultados de las pruebas de laboratorio y en el cielo para el comportamiento de parámetros como la polarización, corriente oscura y respuesta fotográfica del modelo Kepler KL4040 de la casa Finger Lake Instruments. Las imágenes de bias analizadas mostraron un aumento en los recuentos medios del bias de un 8,24 por ciento a medida que la temperatura aumenta de -15 a 10 C, lo que indica una relación con la temperatura. Se investigó la corriente oscura promedio en función del tiempo de exposición, entre 0,1 s a 60 s, en un rango de temperaturas absolutas de -15 a 10 C, con una clara indicación de una correlación entre la corriente oscura y la temperatura del sensor. La tasa de aumento del ruido de corriente oscura muestra claramente tendencias lineales para todas las temperaturas. La curva de respuesta es lineal hasta el rango completo de profundidad del pozo de potencial, con una tendencia similar tanto en el modo de baja ganancia como en el de alta ganancia. Utilizando tanto las filas como las columnas de las imágenes, se muestra el procesamiento de reducción desde imágenes sin procesar hasta imágenes científicas listas para el análisis fotométrico. Los resultados indican que los sensores sCMOS son opciones viables para las observaciones astronómicas, dado que están bien caracterizados, a sabiendas de sus ventajas y posibles inconvenientes.

ABSTRACT

Recently sCMOS sensors have become more popular in astrophysics research due to affordability and availability versus CCDs, but also due to their fast readout speed and low read noise. However, the technology that sCMOS utilize is different than CCD, because of this, full characterization is important to ensure valid reduction and processing for science pipelines. In lab as well as on-sky testing results for the bias, dark current and photo response behavior of the Kepler KL4040 by Finger Lake Instruments will be shown. Analyzed bias frames showed an increase in mean bias counts by 8.24 percent as the temperature increases from -15 to 10 C, indicating a temperature relation. The average dark current as a function of exposure time was investigated, from 0.1 s to 60 s, at an absolute temperatures range of -15 to 10 C, with a clear indication of a correlation between dark current and sensor temperature. The rate of the Dark Noise increase clearly shows linear trends for all temperatures. The photo response curve is linear up to full well depth range, with a similar trend to both low-gain and high-gain modes. Using images with row and column plots, the reduction processing from raw to science images ready for photometric analysis is shown. The results indicates that sCMOS sensors are viable options for astronomical observations given that a thorough understanding of the characteristics and possible drawbacks of sCMOS sensors are understood and compensated for.

Key Words: instrumentation: detectors — instrumentation: photometers — techniques: image processing — techniques: photometric — telescopes

1. INTRODUCTION

Scientific Complementary Metal-oxide-Semiconductor (sCMOS) cameras have become as good, or for some use cases better performing, than Charge Coupled Devices (CCDs). sCMOS cameras are also more affordable than CCDs for similar specifications. Although they work on the same principles, one big difference is that sCMOS sensors show more pixel to pixel variability due to each pixel and each row of pixels having its own readout amplifier. The sCMOS however has the benefit of low readout noise, unlike CCDs where

[1]Boyden Observatory, University of the Free State, Bloemfontein, South Africa.
[2]smitw@ufs.ac.za
[3]vanheerdenhj@ufs.ac.za

VII Workshop on Robotic Autonomous Observatories (October 16-20, 2023)
Editors: Maria Gritsevich, Alberto J. Castro-Tirado, Petr Kubánek, Shashi B. Pandey, and David Hiriart - DOI: https://doi.org/10.22201/ia.14052059p.2025.59.02

the cumulative read-noise is amplified by a single readout amplifier. Some sCMOS sensors have 12-bit readout amplifiers, whereas high quality CCDs use 16-bit, which leads to sCMOS sensors having a lower dynamic range than CCDs. To enhance the dynamic range, these sCMOS sensors reads the pixels out at a high and a low gain. The camera driver software of the sCMOS then merges these images into a single high dynamic 16-bit image.

A benefit of using sCMOS is the ability of taking science grade images with low noise at 20 frames per second for low dynamic range images and 10 frames per second for high dynamic range images. This gives an observer the ability to undertake very high speed photometry, with a low cost instrument. This can be especially useful for objects like active galactic nuclei (AGN), Blazars and cataclysmic variable (CV) systems. This research aims to characterise the Kepler KL4040 sCMOS sensor from Finger Lake Instruments (FLI), which is implemented at the Boyden Observatory near Bloemfontein. The limits and parameters of the sensor are studied. A processing pipeline specific to the sensor is being developed.

2. OBSERVATION & ANALYSIS

The Kepler KL4040 sCMOS camera was tested both in laboratory and on-sky. Laboratory tests include: Bias current response to operation and environment conditions. Dark current response at different temperatures and exposure times. The plots for the dark current versus temperature versus exposure time was generated by processing individual dark frames and correcting for bias and Fixed Pattern Noise (FPN) (as per the FLI Kepler Manual[4]), and then averaging them together to create relevant master dark frames. For more on FPN in CMOS cameras refer to Zhang et al. (2020).

Photo-Response Curves (PRC) were also produced for the camera by exposing the camera to simulated spectral light using a VeraSol-2 LED Class AAA Solar Simulator[5] and an integrating sphere in combination with neutral density (ND) and colour filters. The PRC reveals the saturation level, high and low gain switch over and any pixel to pixel and frame to frame variation in the sCMOS sensor. Refer to Karpov et al. (2021); Wocial et al. (2022) regarding PRC and cross-over regions for CMOS sensors.

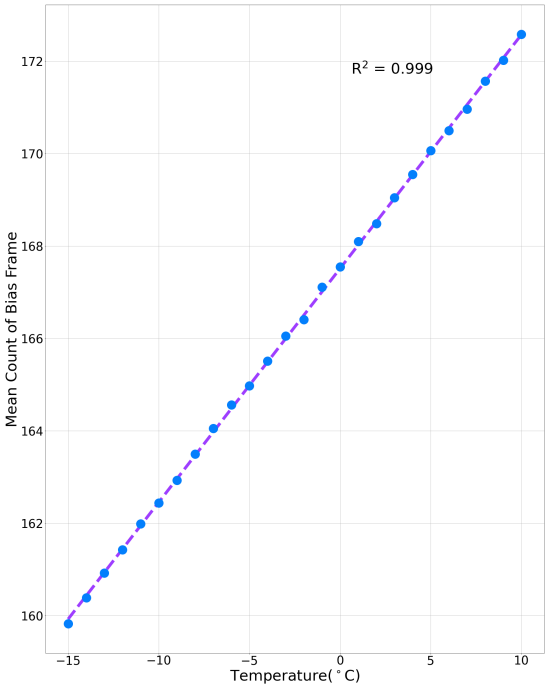


Fig. 1. Temperature dependence of mean bias based on initial in-lab testing results. Mean bias increases with a linear trend with an increase in sensor temperature.

On-sky testing was completed using both a 14 Celestron and the 1.5 m Boyden reflector telescope. Beside flat-fielding tests, observational tests included standard photometry fields (AAVSO-SA107[6]), time-domain CV stars and limiting magnitude tests on Blazars/AGN.

3. RESULTS

Based on initial analysis of the in laboratory testing results, the temperature dependence of the mean bias count (Figure 1) shows a linear trend, indicating that the sCMOS bias is dependant on the temperature. The strong dependence of the dark current to temperature (Figure 2) as is documented for sCMOS electronic architecture due to each pixel hosting an analog to digital converter (ADC) can be observed, i.e. at specific temperatures, the mean dark current increases relative to the exposure times. This indicates that careful notation must

[4] https://www.flicamera.com/downloads/KeplerManual.pdf.

[5] https://www.newport.com/f/class-aaa-led-solar-simulators.

[6] https://app.aavso.org/vsp/chart/?title=SA107&ra=234.7025&dec=-0.224722&fov=70&maglimit=14.5&special=std_field&all=on&north=down&east=right.

VII Workshop on Robotic Autonomous Observatories (October 16-20, 2023)
Editors: Maria Gritsevich, Alberto J. Castro-Tirado, Petr Kubánek, Shashi B. Pandey, and David Hiriart - DOI: https://doi.org/10.22201/ia.14052059p.2025.59.02

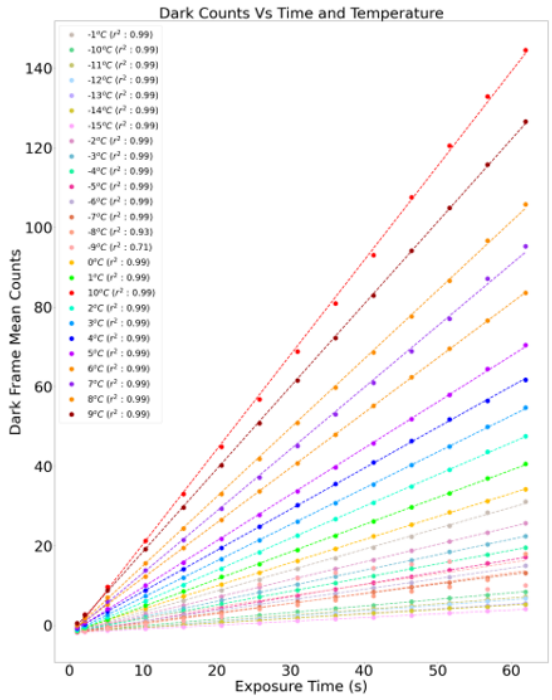


Fig. 2. Temperature dependence of mean Dark Current based on initial in-lab testing results. As can be seen, the dark current increases based on both temperature and exposure times. Sensor temperature indicated by legends.

be made of the absolute sensor temperature during observations to compensate for strong dark current temperature dependence. Relatively good linearity of the photo response of the camera (Figure 3) for both modes of operation up to full well depth was found.

To inspect and compare pre- and post-reduction images, column and row profiles were used to evaluate pixel variations and trends across the sensor for the various data types, i.e. BIAS, DARK, FLAT and SCIENCE. Figures 4, 5 & 6 are the column summed side profiles of master calibration/reduction images and Figures 7 & 8 are raw and cleaned science/star frame side profiles after using the master reduction frames to remove electronic as well as optics effects. Figure 9 is a composite image to compare a raw (left) vs cleaned (right) sky image.

4. CONCLUSION

Based on results from both in laboratory as well as on-sky testing, the sCMOS seems to be a good option for science on a low budget as long as the dependence on temperature is fully understood and considered during post acquisition processing. Thankfully

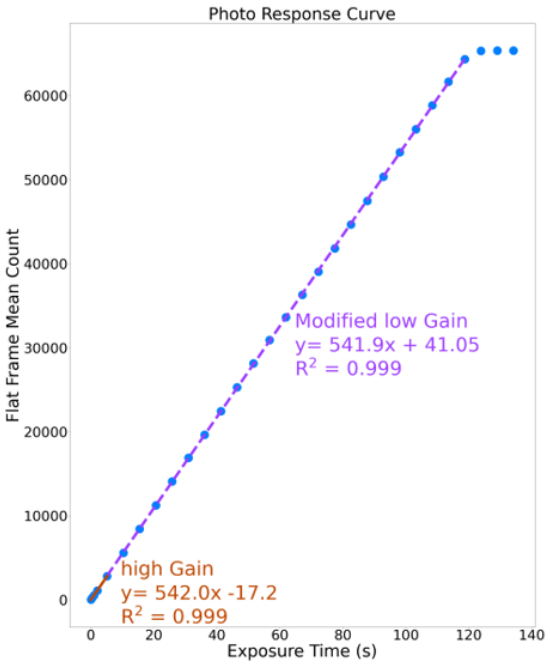


Fig. 3. Photo response curve based on initial in-lab testing results. Both high gain and low gain indicated. Transition point is at 3800 counts from high gain to modified low gain.

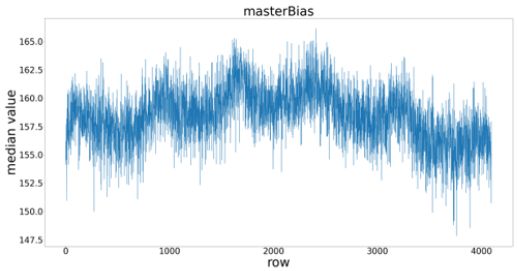


Fig. 4. Summed column profile for Master BIAS images.

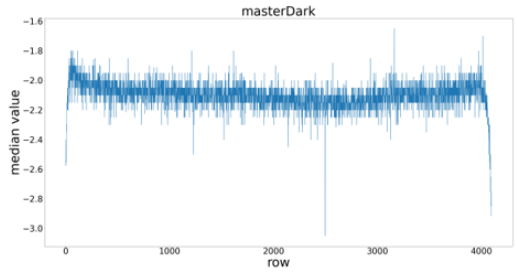


Fig. 5. Summed column profile for Master DARK images.

VII Workshop on Robotic Autonomous Observatories (October 16-20, 2023)
Editors: Maria Gritsevich, Alberto J. Castro-Tirado, Petr Kubánek, Shashi B. Pandey, and David Hiriart - DOI: https://doi.org/10.22201/ia.14052059p.2025.59.02

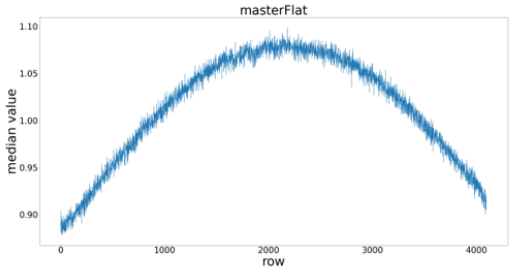


Fig. 6. Summed column profile for Master FLAT images.

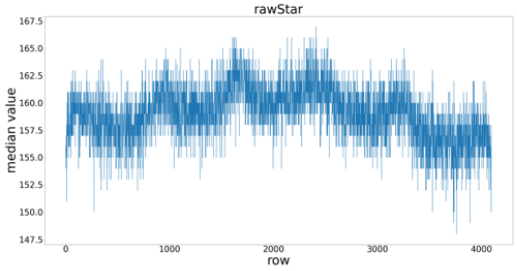


Fig. 7. Summed column profile for raw science/star images.

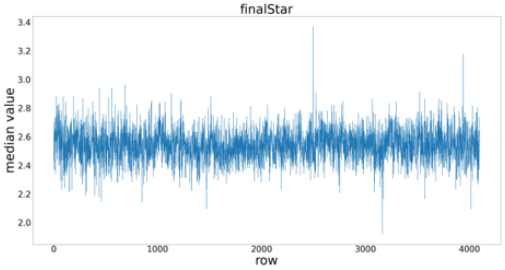


Fig. 8. Summed column profile for final reduced science/star images.

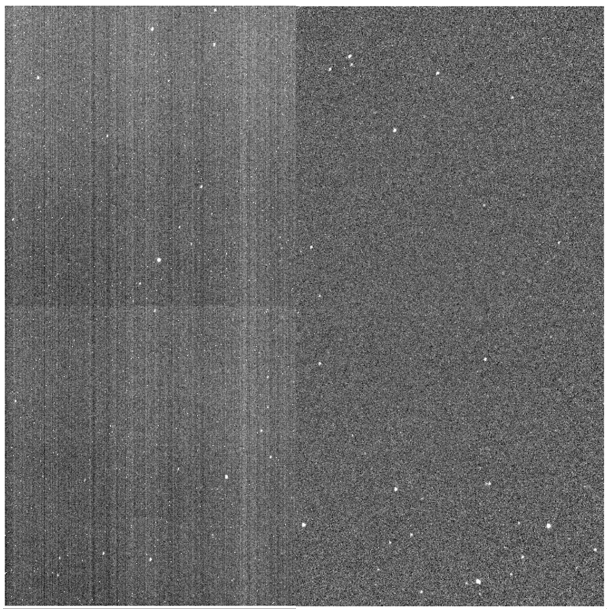


Fig. 9. Composite image to indicate the difference between a raw (left) vs cleaned (right) science / star image.

these additional considerations that have to be applied during processing can be incorporated into custom pipelines that can easily be developed in python using AstroPy[7] packages.

REFERENCES

Karpov, S., Christov, A., Bajat, A., et al. 2021, RMxAC, 53, 190, doi:10.22201/ia.14052059p.2021.53.38

Wocial, T., Stefanov, K. D., Martin, W. E., et al. 2022, IEEE Sensors Journal, 22, 21619, doi:10.1109/JSEN.2022.3211152

Zhang, T., Li, X., Li, J., & Xu, Z. 2020, Appl. Sci., 10, 3694, doi:10.3390/app10113694

[7] https://www.astropy.org/.

Revista Mexicana de Astronomía y Astrofísica Serie de Conferencias (RMxAC), **59**, 13–17 (2025)
© 2025: Instituto de Astronomía, Universidad Nacional Autónoma de México
https://doi.org/10.22201/ia.14052059p.2025.59.03

VII Workshop on Robotic Autonomous Observatories (October 16-20, 2023)
Editors: Maria Gritsevich, Alberto J. Castro-Tirado, Petr Kubánek, Shashi B. Pandey, and David Hiriart - DOI: https://doi.org/10.22201/ia.14052059p.2025.59.03

CONSIDERATIONS ON AUTOMATING OLDER TELESCOPES: THE BOYDEN 1.5 M TELESCOPE

H. J. van Heerden[1,2], P. J. Meintjes[1], B. van Soelen[1], W. Smit[1], I. P. van der Westhuizen[1], and H. Szegedi[1]

RESUMEN

En este momento, el desarrollo y la puesta en servicio de un nuevo sistema de telescopio autónomo o remoto es fácilmente realizable debido a la cantidad de opciones disponibles para el constructor. Las consideraciones más difíciles serían la ubicación del sitio y la disponibilidad de servicios. Teniendo en cuenta el telescopio en sí, existen multitud de tecnologías como monturas, sensores, software de control y controladores disponibles, lo que supone pueda convertirse en un ejercicio complejo el encontrar cómo ajustar todo de la mejor forma. La pregunta que debe hacerse al considerar la automatización de un telescopio tan antiguo es: ¿Cuáles son los parámetros que deben investigarse? ¿Cuáles son los pros y los contras a considerar para el proceso? ¿Cuál es el estado tecnológico actual del telescopio? Con estas preguntas, y otras muchas, se examina el estado actual del telescopio reflector de 1,5 m del Observatorio de Boyden, así como lo que se necesitaría para hacerlo operativo bien de forma remota o bien completamente autónomo.

ABSTRACT

At this point in time, the development and commissioning of a new autonomous or remote telescope system is easily achievable due to the number of choices available to the builder. The most difficult considerations would be site location and availability of services. Considering the telescope itself, there is such a multitude of technologies such as mounts, sensors, control software and drivers available that it can become a complex exercise to find the best integrated fit. The question that must be asked when considering the automation of an older established telescope include: what are the parameters that needs to be investigated? What are the pros and cons to be considered for the process? What is the current technological state of the telescope? With these questions, and many more, the 1.5 m Boyden Reflector telescope will be examined as to its current state, as well as what would be required to either make it remotely operable, or fully autonomous.

Key Words: history of astronomy — instrumentation: photometers — instrumentation: spectrographs — instrumentation: polarimeters — software: development — telescopes

1. INTRODUCTION

1.1. *Boyden Observatory and 1.5 m telescope*

The Boyden Observatory is currently located 24 km to the east of Bloemfontein, South Africa (Boyden GPS: -29.0382 S, 26.4036 E). The history of the observatory can be traced to 1879 when Uriah A. Boyden left funding for astronomical research to Harvard College. The observatory was first established on Mount Harvard during 1889 in South America, but within a year moved to Arequipa, Peru where it was run until its relocation. The relocation to South Africa in 1927 led to the opportunity to establish a 1.5 m (60 inch) telescope which was built between 1930 and 1933. The initial optical configuration of the telescope was a Newtonian focus (775.6 cm) telescope on an English equatorial mount. During the 1960s the mirror cell and optics were upgraded to allow for a Cassegrain focus (2382 cm). In 2001 the telescope control system was upgraded to a DFM[3] telescope control system (TCS) interface. During it's operational lifetime the telescope also hosted various instruments, including photo-metric plates, a Zeiss spectrograph and up to recent developments an Apogee U55 CCD. More information regarding the observatory's history and equipment can be found in Van Heerden (2008), Jarret (1979) and Andrews (1998).

1.2. *Current state of the 1.5 m telescope*

The telescope is operational and is used for Astrophysical Research inline with the research interests of the Department of Physics' Astrophysics group. These include transient phenomena, cataclysmic variable (CV) systems, quasars and active galactic nuclei (AGN) as well as occasional occultation events. The telescope is also used for

[1]Boyden Observatory, University of the Free State, Bloemfontein, South Africa.
[2]vanheerdenhj@ufs.ac.za

[3]`https://www.dfmengineering.com/index.html`.

VII Workshop on Robotic Autonomous Observatories (October 16-20, 2023)
Editors: Maria Gritsevich, Alberto J. Castro-Tirado, Petr Kubánek, Shashi B. Pandey, and David Hiriart - DOI: https://doi.org/10.22201/ia.14052059p.2025.59.03

student training during undergraduate and post-graduate research programs. The telescope has 2 instrument configurations or "packs" available that can be mounted on the back-end. A photometer with either an Apogee U55 CCD or a new Finger Lakes Instrumentation Kepler KL4040 sCMOS[4] sensor and Johnson-Cousins UBVRcIc filters & a Spectro-polarimeter with a microline CCD[5] and various gratings and wave-plates available. The observations are undertaken using a custom built python GUI that interfaces between the TCS and the instrument hardware (see Figure 1).

The various systems are continually optimised as better solutions or processes are found during operational use and active Research and Development (R&D). Components that are currently actively being worked on are: optimization of the auto-guiding capabilities, best observational parameters and equipment settings relative to instrument pack being utilised; as well as data analysis pipelines. Recent upgrades and maintenance services include the re-aluminization of the primary mirror, the commissioning of the spectro-polarimeter, the testing of the FLI sCMOS, and general maintenance to the mount and turret dome.

2. UPGRADE PROJECT

The addition of the spectro-polarimeter as well as recent developments in the research group regarding observational requirements and opportunities for collaborative work have resulted in the identification of a need for remote observing capabilities. This requirement will also then be inline with recent international trends regarding remote or even automated observations. This has resulted in a new project being initiated with the goal of making the 1.5 m telescope remotely operable, with full automation a final endeavor. The project will be implemented using a phased approach, as the telescope is an operational system, and cannot be put in an offline state for long periods to allow for a single long continuous upgrade and commissioning process. Observations still need to be made by researchers and students alike. The 5 phases that have been identified will be discussed in more detail next.

2.1. *Phase 0: Research, funding, planning and testing*

The start of the project, as with any project, is to do thorough research on what is available, what has been done and how it matches with the requirements and expected outcomes of said project, or to put it more basic: What is required to convert the current system to a remotely operable telescope and prepare for full automation.

The 1.5 m telescope system was compared to known systems that the team has either collaborated with or utilised. These include the Watcher Robotic Telescope (Martin-Carrillo 2019) and BOOTES-6 which is part of the BOOTES network (Castro-Tirado 2023; Hu et al. 2023), which are both hosted at and maintained by Boyden Observatory. Utilisation and collaborations with the South African Astronomical Observatory (SAAO)[6] also give the group access to telescopes at SAAO such as the 1.0 m, Lesedi and the 1.9 m Telescopes. These telescopes are either in process of becoming or are already remotely operable. The research as well as in-house knowledge by professional staff, especially in the divisions of Instrumentation and Electronics, on development of research equipment has led to the identification of core components that will have to be addressed, as well as some preliminary solutions. These include: fixing the dome, fixing the telescope controls, programming and prepping for remote observing and finally coding and commissioning for full automation. Each of these components will be addressed in more detail in the following sections and will become additional phases of the project.

2.2. *Phase 1: Fixing the dome*

The turret dome of the telescope building currently uses a 2-motor push-pull cable design to rotate the dome. The motors are housed 180 degrees apart at north and south, with the north motor hosting a relative encoder on the connection rod between the motor and cable pulley. This encoder counts pulses, with a set ratio converting rotational motion to angular motion on the dome. This encoder also determines direction of rotation. Because the encoder is relative the dome does not have a set zero or home position and needs to be "told" where it is pointing. This can be corrected by mounting "home" position indicators or limit switches on the dome at north and south, or even north, south, east and west. The dome system can therefore re-orientate itself if it loses its "known" position by just rotating until it finds the nearest position indicator.

There is an additional problem with the dome in that the determined azimuth position of the dome based on the right ascension - declination of the telescope pointing does not match for certain positions.

[4] https://www.flicamera.com/kepler/kepler.html.
[5] https://www.flicamera.com/microline/index.html.
[6] https://www.saao.ac.za/astronomers/#tab-1567162218737-5-7.

VII Workshop on Robotic Autonomous Observatories (October 16-20, 2023)
Editors: Maria Gritsevich, Alberto J. Castro-Tirado, Petr Kubánek, Shashi B. Pandey, and David Hiriart - DOI: https://doi.org/10.22201/ia.14052059p.2025.59.03

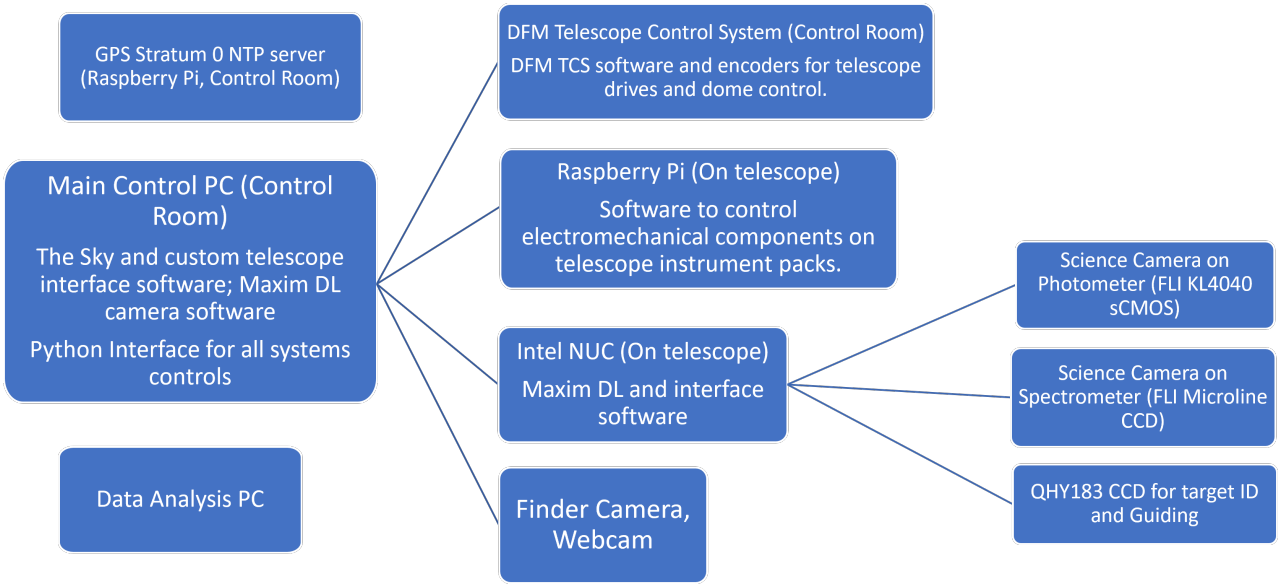


Fig. 1. A schematic layout of the various system components and their interfaces/connections utilised on the 1.5 m telescope.

This discrepancy in the synchronizing could be an inaccuracy in the geometry calculation of the telescope pointing, or a time or epoch miscalculation or even an error in the electronics. This problem has to be corrected. The conversion calculations is complicated by the fact that the dome centre and therefore dome azimuth and geometric pointing centre of the telescope (centre of the primary mirror) has an offset. The telescope centre and azimuth also moves relative to the stationary dome centre. A basic principle of how to match the telescope azimuth and dome azimuth can be found in (Suszynski 2009). Referring to figure 2, the horizontal telescope coordinates, can be used to calculate the dome azimuth through the use of the following equations:

$$\beta = \alpha - \varphi$$

where

$$\sin\varphi = \frac{r}{R}\sin\alpha\,.$$

The final problem with the dome is that there is no electrical power on the dome. Because of this the dome shutters are still opened and closed manually with a hand lever and pulley system. To make the system remote operable will require the dome shutters to be powered and controllable from a computer interface. There are various options to get power on the dome to operate the shutters electromechanically. Options include: slip rings, wiping contacts, battery system with charging contacts or solar cells on the roof are the most commonly used. An optimal solution is still to be determined, but a solution on how to operate the shutters has been proposed, which is 24V DC Centurion Shutter roller door motors and controllers with a 500 kg rating. These are off the shelve systems that come with relative easy to integrate and monitor controllers that have already been utilised onsite at another telescope building with success. Adaptation of the mechanical components to integrate with the motors, i.e. how to drive the pulley and cable system using the motors, could also provide its own challenges.

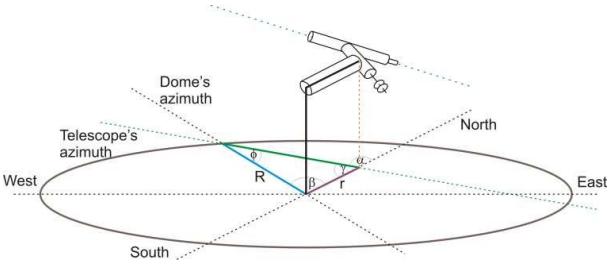


Fig. 2. Geometric calculation to match dome and telescope azimuths. Adapted from (Suszynski 2009)

The current dome motion and positioning is controlled via the DFM TCS. For optimal system design and future proofing the new dome control systems will be required to run independently from the current DFM TCS, with dedicated dome software developed that can integrate into the current user interfaces, or even integrate into potential future robotic

VII Workshop on Robotic Autonomous Observatories (October 16-20, 2023)
Editors: Maria Griffsevich, Alberto J. Castro-Tirado, Petr Kubánek, Shashi B. Pandey, and David Hiriart - DOI: https://doi.org/10.22201/ia.14052059p.2025.59.03

control systems or standardised software such as ASCOM[7].

2.3. *Phase 2: Fixing the telescope controls*

There are various components on the telescope that needs attention to optimise the system for remote and potential automation. The first that needs attention is to convert the telescope tube shutter from a manual control to an elctromechanical system that is controlled via a computer. The most difficult part could be exactly what mechanical changes would be required for a smooth operation (open and close) of the shutter within the cylindrical structure, and whether the current shutter would require extensive modification?

The second main component that would need attention is the Right Ascension - Declination (RA & Dec) encoders. The telescope system currently uses relative encoders without a "home" position indicator or limit switch. Thus if the telescope experiences a system shutdown without adequate parking procedures, the telescope loses its position. Re-pointing of the telescope then requires the use of finder telescopes for field identification and fine adjustment or re-centering with the main camera system. This would prove to be a major problem for remote or automation purposes.

The TCS system used on the telescope is a PC Dos based application developed by DFM Engineering. Although the TCS still functions adequately the hardware running the TCS is beyond end of life and the danger lays in that if the hardware fails, the telescope becomes inoperable, as the TCS cannot be run on newer computer hardware. The options available are to get an upgraded DFM system (which takes control and adaptation out of the owner's hands), or to develop a whole new custom TCS system that matches what is required by the research group in terms of control of the telescope and peripheral systems. A custom TCS could also be made to match standardised protocols better for future remote or automation purposes.

The new TCS will have to control the following components:

- RA and Dec motors. Slew speed and direction.
- RA and Dec encoders (will have to upgrade to absolute, or add limit/home position switches).
- Current dual speed focus driver.
- Tracking control. Rated tracking or interface with auto-guider cameras.
- Pointing model. Optimization of pointing model based on feedback from imaging systems.
- Telescope tube shutter.
- Interface with the dome control driver for effective telescope-dome syncing.
- Accurate time systems and coordinate calculators for target acquisition and tracking given any standard astronomical target parameters.

2.4. *Phase 3: Commissioning remote observing*

Once all manual systems have been "converted" to computer controllable and current systems upgraded and optimised to match newer available technologies (hardware and software) then the system can be set up for remote capabilities. The various system interfaces will have to be adapted for optimal remote interaction, which will require an analysis of best operating procedures: What experience will make the remote observer effective and comfortable. The system must be easy to use, which will require some systems to run as black boxes. The remote observer must have adequate control with a simple command interface.

The remote observer must also have adequate feedback from site, i.e. what is the status of the various telescope systems and environment. This will require status values such as telescope pointing, telescope motion, various science camera values and imaging as well as guiding systems. Or simple feedback, such as a live webcam showing the telescope in the dome. Other environmental feedback systems should include a live weather update (connect with the weather stations onsite or a dedicated station such as a Davis[8] weather station specifically just for the 1.5 m telescope) as well as a live star-cam system to check sky quality and seeing conditions.

On the other end must be an effective remote observing computer station. Fortunately this has already been acquired and configured. A new remote observing station consisting of a high end multi screen computer system with a quality internet connection has been established at the Department of Physics in Bloemfontein. This system has already been used to do remote observations utilising telescope systems at SAAO, with the experience used to start planning the interface requirements for a remote observer session from Bloemfontein to Boyden Observatory.

[7] `https://www.ascom-standards.org/`.

[8] `https://www.davisinstruments.com/collections/weather-stations`.

VII Workshop on Robotic Autonomous Observatories (October 16-20, 2023)
Editors: Maria Gritsevich, Alberto J. Castro-Tirado, Petr Kubánek, Shashi B. Pandey, and David Hiriart - DOI: https://doi.org/10.22201/ia.14052059p.2025.59.03

2.5. *Phases 4&5: System automation*

For full system automation the observer needs to be replaced by an automated system that can manage the observations. Robotic systems manage the respective observations via a queue or scheduler. This scheduler uses parameters to determine observation setup, i.e. camera settings, filter or grating selection, telescope position and tracking, etc. The scheduler will be monitored by a master control system that monitors environmental parameters that determines whether the telescope and weather conditions are conducive for observations or not, and can start or stop the scheduler as needed. With subsystems interfacing in an interconnected web of links that communicates various statuses and events that can impact the scheduled observations, thus replacing the human link.

Such a complex system can be designed from scratch to fit exactly to a custom setup, but it would be better to utilise systems that are already being used. A system that was developed for various robotic telescope systems and initially used on Watcher was RTS2 (Kubánek et al. 2004). It is a very comprehensive control system coded in C++ that have been tested over many years, but at the same time very complex to manage and maintain and could be daunting for a first time user that needs to setup and manage queues and schedules. Another option that is python based and that could fit better with the more modern mix of science and python is pyobs (Husser et al. 2022). Whichever system is to be implemented, a thorough schedule of testing and debugging will have to be planned during commissioning, and might have to be done in stages.

3. FINAL THOUGHTS

The project is daunting, but nothing is impossible. The options are: Buy a new telescope system already fully robotic and just use as is, OR, use what is available in a new configuration after a period of R&D and hard work and perseverance. Old does not mean cold. Stars are millions of years old, and they still burn bright. Therefore the case can be made to upgrade, develop and re-utilise older telescopes for more advanced work than that for which they were initially build.

REFERENCES

Andrews, A. D. 1998, IrAJ, 25, 129

Castro-Tirado, A. J. 2023, Nature Astronomy, 7, 1136. doi:10.1038/s41550-023-02075-w

Hu, Y.-D., Fernández-García, E., Caballero-García, M. D., et al. 2023, Frontiers in Astronomy and Space Sciences, 10, 952887. doi:10.3389/fspas.2023.952887

Husser, T.-O., Hessman, F. V., Martens, S., et al. 2022, Frontiers in Astronomy and Space Sciences, 9, 891486. doi:10.3389/fspas.2022.891486

Jarret, A. H. 1979, *Boyden Observatory (A Concise History)*, Acta Academica, 12

Kubánek, P., Jelínek, M., Nekola, M., et al. 2004, Gamma-Ray Bursts: 30 Years of Discovery, 727, 753. doi:10.1063/1.1810951

Martin-Carrillo, A., Murphy, D., Salmon, L., & Hanlon, L. Sept 2019, Workshop on Future Astronomical Instrument Development, Dublin Institute for Advanced Studies, Dublin, {\url{https://www.dias.ie/techdev/images/4_Martin-Carrillo.pdf}}

Suszynski, R. 2009, Stand-alone station for deep space objects astrophotography, In: 52nd Proc. IEE International Midwest Symposium on Circuits and Systems, 333, doi:10.1109/MWSCAS.2009.5236086

Van Heerden, H. J. 2008, MNSSA, 67, 116

Revista Mexicana de Astronomía y Astrofísica Serie de Conferencias (RMxAC), **59**, 19–22 (2025)
© 2025: Instituto de Astronomía, Universidad Nacional Autónoma de México
https://doi.org/10.22201/ia.14052059p.2025.59.04

VII Workshop on Robotic Autonomous Observatories (October 16-20, 2023)
Editors: Maria Gritsevich, Alberto J. Castro-Tirado, Petr Kubánek, Shashi B. Pandey, and David Hiriart - DOI: https://doi.org/10.22201/ia.14052059p.2025.59.04

MODERNIZATION OF COLOTI OPTICAL OBSERVATORY: REMOTE CONTROL AND AUTOMATION FOR MULTIMESSENGER FOLLOW-UP

P. Cristarella Orestano[1,2], S. Cutini[2], S. Germani[1,2], S. Palmerini[1,2,3], and G. Tosti[1,2]

RESUMEN

En 2017, dos eventos cósmicos nos condujeron a la era de la astronomía de multi-mensajeros: por un lado, el evento de ondas gravitacionales GW 170817 (detectado por LIGO y VIRGO) con contrapartida electromagnética en todo el espectro y por otro, el evento de neutrinos cósmicos IC 170922A (detectado por IceCube) y asociados a una llamarada de un blazar. Ambos también fueron detectados por *Fermi*-LAT en el rango de los rayos gamma. El estudio de este tipo de eventos transitorios necesita de observaciones coordinadas entre los telescopios o detectores espaciales y los terrestres. El objetivo de este proyecto es contribuir a la comprensión de los eventos de multimensajeros mediante la restauración del Observatorio Coloti, permitiendo el control remoto y la automatización: desarrollando estrategias observacionales, sistemas de adquisición de datos y automatización de análisis de imágenes. El paso obligatorio para ello es una actualización del hardware y, con ello, también es necesaria una renovación del software. Todos los subsistemas del observatorio estarán conectados entre sí a través de un Internet de las Cosas por medio de un protocolo de Arquitectura Unificada de Comunicaciones de Plataforma Abierta (OPCUA). Los programas de control de cada objeto están escritos en `JAVA`, desde las comunicaciones serie de bajo nivel hasta la Interfaz Gráfica de Usuario (GUI). El protocolo OPCUA permite una personalización completa y un control remoto flexible de cada objeto. En el futuro próximo, la automatización se implementará fácilmente en el nuevo software y consistirá en la búsqueda automática de objetos para ser monitoreados y la respuesta automática a alertas de multi-mensajeros.

ABSTRACT

In 2017 two cosmic events led us into the multimessenger astronomy era: the gravitational wave event GW 170817 (detected by both LIGO and VIRGO) with electromagnetic counterpart in the whole spectrum on one side, and the cosmic neutrino IC 170922A (detected by IceCube) associated to a blazar flar on the other side, both also seen by *Fermi*-LAT in the gamma-ray band. This proved that the study of transient multimessenger events needs synergy between space-borne and ground-based telescopes or detectors. The goal of this project is to contribute to the understanding of multimessenger events by restoring the Coloti Observatory, enabling remote control and automation: develop observation strategies, data acquisition system and image analysis pipeline. The mandatory step is a hardware upgrade, and with it a software renewal is necessary too. All the objects of the observatory will be connected to each other in an Internet of Things via a protocol of Open Platform Communications Unified Architecture (OPCUA). The control programs for each object is written in `JAVA`, from the low-level serial communications to the Graphical User Interface (GUI). The OPCUA protocol enables complete customization and flexible remote control of each object. In the next future the automation will be easily implemented in the new software, and it will consist of automatic search for targets to monitor and automatic response to multimessenger event alerts.

Key Words: Multimessenger — Optical Observatory — Remote Control and Automation

1. INTRODUCTION

In 2017 two cosmic events led us into the multimessenger astronomy era (Branchesi et al. 2016): the gravitational wave event GW 170817 (Abbott et al. 2017) detected by both LIGO (Harry et al. 2010) and VIRGO (Acernese et al. 2014) with an electromagnetic counterpart in the whole spectrum on one side, and the event of cosmic neutrinos IC 170922A (IceCube Collaboration 2018) detected by IceCube (Aartsen et al. 2017) and associated to a blazar flare on the other side. Both events were also seen by *Fermi*-LAT in the gamma-ray band. This proved that the study of transient multimessenger events needs synergy between space-borne and ground-based telescopes or detectors.

[1]Università degli Studi di Perugia, Italy.
[2]Istituto Nazionale di Fisica Nucleare, Sezione di Perugia, Italy.
[3]Istituto Nazione di Astrofisica, Osservatorio Astronomico di Roma, Italy.

VII Workshop on Robotic Autonomous Observatories (October 16-20, 2023)
Editors: Maria Gritsevich, Alberto J. Castro-Tirado, Petr Kubánek, Shashi B. Pandey, and David Hiriart - DOI: https://doi.org/10.22201/ia.14052059p.2025.59.04



Fig. 1. The observatory is located near Perugia (Italy), alt-azimuthal mount telescope with Cassegrain configuration ($f/10$) and 80 cm primary mirror.

2. INITIAL STATE

The Coloti Observatory was inaugurated in 1999 in Coloti, an ancient uninhabited village near Perugia, in central Italy, 470 m a.s.l., and far from the light pollution of the cities. Unfortunately, it closed its scientific and divulgation activities in 2010.

The telescope (Figure 1), inside a rotating dome, has an alt-azimuthal mount and a Cassegrain optical configuration with an 80 cm primary mirror having a focal ratio of $f/3$; the resulting focal length of the telescope is 8 m ($f/10$). Considering the CCD detector size, we have a current field of view of $7.7' \times 5.1'$.

The telescope has a motorized analog focuser that works on the position of the secondary mirror, not the optimal way to focus since there is only one position of the mirrors where the number of photon captured is maximized. In the room below the telescope there are three motor encoders: for dome, azimuth and elevation.

The original telescope control program was written in `Microsoft Visual C++ 6.0`.

In the multimessenger astronomy era, ground telescopes can contribute to the study of extragalactic transient sources with more focused and long-duration observations. With these purposes, it was decided to reactivate the observatory, hence the need for upgrades to respond to alerts from gravitational wave interferometers and neutrino detectors. We need hardware upgrades (Figure 2) to improve observation quality and software upgrades for a fully automated remote control of the observatory.

3. HARDWARE UPGRADE

The first step of the upgrades was to replace the old workstation, which previously managed the telescope directly, with a Main Workstation (MW) in the observatory control room and two industrial computers: Telescope Motors Controller (TMC), Camera and Data acquisition Controller (CDC).

The MW and the TMC are both placed inside the control room, so we do not drastically change the position of the serial cables that run from the wall down into the room below the telescope, where there are encoders that communicate with the telescope motors. The CDC on the other hand, being connected to the camera subject to three movements (azimuth, elevation, and field rotation), will be attached to the telescope to decrease cable movements. The data acquisition camera, a Charged Coupled Device (CCD), and the Pointing Monitoring Camera (PMC) are connected to the CDC, this means we are going to manage many cables around the telescope. The PMC uses a $12,5\ cm$ diameter refractor telescope; so, thanks to the larger field of view, it is used for astrometry.

The primary mirror had to be re-aluminized, a needed process to restore the mirror to the original condition: vaporization of aluminum inside a vacuum bell, which will uniformly cover the entire surface of the mirror.

The ruined Weather Station is replaced by a newer one (WS). A Field Derotator (FD) is going to be added to the telescope where the camera will be mounted, and in the future also a new focuser to be managed digitally to allow remote and automated focusing. All these objects form a complex structure, schematized in Figure 3, they will be connected to each other in an Internet Of Things via the Open Platform Communications Unified Architecture (OPCUA) protocol, all controlled from the MW.

4. SOFTWARE RENEWAL

We are currently developing the new software in `JAVA`, starting from the low-level programming with the serial communication for many objects (motor encoders, WS, CCD, FD, PMC) up to the high level Graphical User Interface (GUI).

The hierarchy tree is shown in Figure 4, at base level we have a serial communication protocol common to all objects, then we have the Axis Control

VII Workshop on Robotic Autonomous Observatories (October 16-20, 2023)
Editors: Maria Gritsevich, Alberto J. Castro-Tirado, Petr Kubánek, Shashi B. Pandey, and David Hiriart - DOI: https://doi.org/10.22201/ia.14052059p.2025.59.04



Fig. 2. (a) Two identical industrial computers (TMC, CDC). (b) CCD: Moravian G2-1600 Mark II: Full Frame, 9×9 μm pixels, resolution 1536×1024 pixels, it has a Bessel filter wheel (U, B, V, R, I) and a cooling system. (c) PMC: FLIR FL3-U332S2M sensor CMOS 1/2.8", resolution 3.2 MP. (d) Davis Vintage 2 Weather Station.

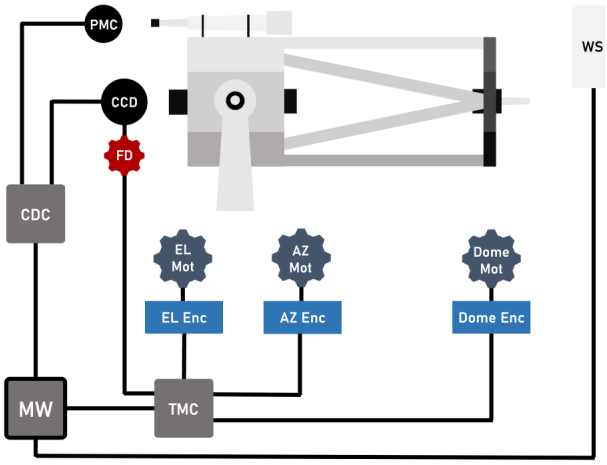


Fig. 3. Observatory hardware scheme. All the objects are connected to the main workstation in the control room. The PMC uses the refractor Apo ED Tecnosky 125/975. For each motors (Mot) there is an encoder (Enc).

System (ACS) for controlling each axis (azimuth, elevation and dome motors), above it the Telescope Control System (TCS), which manages the logic and the complex functions of the telescope-dome system. The Weather Control System (WCS), the Pointing Control System (PCS) with the astrometry and the Camera Control System (CCS), for data acquisition, complete the observatory logic. A state machine structure is used in the TCS, to make the system

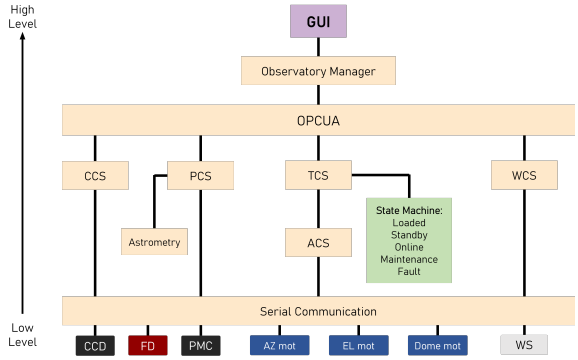


Fig. 4. Software hierarchy tree. From the low level we have the Serial Communication, then many programs converge in the TCS, above it we have the OPCUA server where everything is mapped, and then the GUI.

more organized and secure, it has 5 states: Loaded, Standby, Online, Maintenance, Fault, the same state machine structure will be added in the other scripts too.

In order to write the ACS and the TCS it was necessary to work directly with the previous scripts doing a massive translation process, from `Visual C++ 6.0` to `JAVA`, starting with the serial communication with the encoders up to the complex pointing functions.

The tracking program is already implemented in the encoders, as is the *set-zero* command, which searches for the telescope limit switches to calibrate the positions of the axes.

`JAVA` turned out to be perfect for the software since it simplifies the development of the GUI and the management of the low-level communication, indeed the debugging process was very easy and short and during the preliminary tests we were able to move the telescope without any problems.

Above all the other programs there is the OPCUA, where nodes corresponding to each individual high-level function are created, thus the objects can communicate with each other.

5. CONCLUSIONS

The observatory is already reactivated, especially for outreach activities. The hardware upgrade is in the assembly phase. It is also necessary to replace the analogue focuser with a new, more precise electronic step-by-step focuser.

Currently, it is difficult to correctly measure the seeing, the sharpness of astronomical images, from the observatory, because the focus still needs to be improved and the primary mirror re-aluminized. The seeing depends on atmospheric turbulence and is measured as the Full Width at Half Maximum

VII Workshop on Robotic Autonomous Observatories (October 16-20, 2023)
Editors: Maria Gritsevich, Alberto J. Castro-Tirado, Petr Kubánek, Shashi B. Pandey, and David Hiriart - DOI: https://doi.org/10.22201/ia.14052059p.2025.59.04

(FWHM) of the star profiles and is therefore expressed in arcseconds. Considering the observatory site and the pictures taken in these months, we can expect to measure a the seeing at least under $4''$.

Concerning the renewal of the software, we are close to achieving the remote control and automation objectives. Thanks to the OPCUA protocol the remote control is already usable. We are completing the GUI and we have to implement the data acquisition software, then we will organize everything in order to automate the observatory with scheduled observation and with automatic response to multi-messenger event alerts.

Acknowledgements: The Ministero dell'Università e della Ricerca (MUR) is acknowledged for financial support through the program "Dipartimenti di Eccellenza 2018-2022" (Grant SUPER-C). Author Paolo Cristarella Orestano acknowledges the financial support of the "Agenzia della Coesione Territoriale" through the doctoral scholarship. We acknowledge the Dipartimento di Fisica e Geologia - Università degli Studi di Perugia for the support through the funding of the projects: "COLOTI" and "COLOTI2".

REFERENCES

Aartsen, M. et al. 2017, JInst, 12, P03012
Abbott, B. P. et al. 2017, AJ, 848, L12
Acernese, F. A. et al. 2014, CQGra, 32, 024001
Branchesi, M. 2016, JPhCS, 718, 022004
Harry, G.M. & the LIGO Scientific Collaboration 2010, CQGra, 27, 084006
IceCube Collaboration 2018, Sci, 361, 147

Revista Mexicana de Astronomía y Astrofísica Serie de Conferencias (RMxAC), **59**, 23–26 (2025)
© 2025: Instituto de Astronomía, Universidad Nacional Autónoma de México
https://doi.org/10.22201/ia.14052059p.2025.59.05

VII Workshop on Robotic Autonomous Observatories (October 16-20, 2023)
Editors: Maria Griffsevich, Alberto J. Castro-Tirado, Petr Kubánek, Shashi B. Pandey, and David Hiriart - DOI: https://doi.org/10.22201/ia.14052059p.2025.59.05

DON: AUTOMATION OF THE VATICAN ADVANCED TECHNOLOGY TELESCOPE

P. Gabor[1]

RESUMEN

El telescopio Alice P. Lennon y la infraestructura astrofísica Thomas J. Bannan, conjuntamente conformando el Telescopio de Tecnología Avanzada del Vaticano (VATT), fue inaugurado hace algo más de 30 años en el Monte Graham, en Arizona. Se trata de un telescopio gregoriano con un primario de f/1 y un sistema óptico completo a f/9. Ya presentamos las modernizaciones completadas y planificadas del VATT en un congreso anterior (AstroRob 2017, ver Swindell 2019). El propósito de este artículo es presentar los últimos avances. En particular, contratamos a la empresa ProjectSoft HK (República Checa) para revisar el sistema de control. El nuevo sistema, denominado `Don`, utiliza PLC. La revisión del diseño ha concluido, el sistema se está montando en ProjectSoft HK y se realizó una prueba de aceptación en fábrica en enero de 2024. El sistema se instaló y puso en marcha en abril-mayo de 2024. `Don` permite un funcionamiento por script, sin necesidad de operadores in situ. También estamos trabajando en la colimación y el enfoque automatizados.

ABSTRACT

The Alice P. Lennon Telescope and the Thomas J. Bannan Astrophysics Facility, informally the Vatican Advanced Technology Telescope (VATT), was dedicated 30 years ago on Mount Graham in Arizona. It is a Gregorian telescope with an f/1 primary and an f/9 full system optics. We presented the completed and planned upgrades of the VATT at the AstroRob 2017 (Swindell 2019). The purpose of this paper is to present the latest developments. In particular, we have contracted ProjectSoft HK (Czech Republic) to overhaul the control system. The new system, named `Don`, uses PLCs. The design review was completed, the system was assembled at ProjectSoft HK, and a factory acceptance test was carried out in January 2024. The system was installed and commissioned in April and May 2024. `Don` allows for scripted operation based, with no need for on-site operators. We are also working on automated collimation and focusing.

Key Words: Vatican Advanced Technology Telescope — VATT — automation — control system — ProjectSoft

1. INTRODUCTION

The 1.8m diameter Vatican Advanced Technology Telescope (VATT)'s M1 primary mirror was a proof-of-concept project by the team of J. Roger Angel at what was to become Steward Observatory's Mirror Laboratory at the University of Arizona: the first mirror to be made in a spinning furnace and the first mirror to be lap-stress polished at f/1.0 (Blanco 1990; West 1997). The mirror's and the telescope's success paved the way to the production of larger mirrors of similar optical speed and a new generation of telescopes (WIYN, MMT, Magellan, LBT, GMT).

While there have been numerous upgrades over the years, VATT's control system still runs on the original hardware from the early 1990s. Steward Observatory and the Vatican Observatory agreed on a concept of an Arizona Robotic Telescope Network (ARTN) in 2013 (MOU signed in 2016), intended to include the Bok 90-inch Telescope on Kitt Peak, the Kuiper 61-inch Telescope on Mt Bigelow, and the VATT.

We presented the completed and planned upgrades of the VATT at the 2017 AstroRob (Swindell 2019). Changes at Steward Observatory led both parties to recognize that an outside contractor was needed to complete the VATT's automation. The Vatican Observatory Foundation contracted ProjectSoft HK to carry out the work (Table 1).

2. DON

The VATT's new automated control system is named `Don` (Fig. 1) in honor of Donald M. Alstadt (1921-2007). Designed and built by ProjectSoft HK, it is modular, based on Beckhoff industrial PLCs (Programmable Logic Controllers; Fig. 2), absolute Renishaw encoders and ELMO drives. The mount control ought to achieve pointing precision of 4 to 8 arcsec rms.

Apart from the telescope's mount, `Don` also controls numerous support systems: the weather sta-

[1]Vatican Observatory, Specola Vaticana, V-00120 Città del Vaticano (pgabor@specola.va).

VII Workshop on Robotic Autonomous Observatories (October 16-20, 2023)
Editors: Maria Gritsevich, Alberto J. Castro-Tirado, Petr Kubánek, Shashi B. Pandey, and David Hiriart - DOI: https://doi.org/10.22201/ia.14052059p.2025.59.05

TABLE 1

TIMELINE OF THE VATT AUTOMATION EFFORT

1993	dedication	
2010	remote-operation capable	
2012	received first automation quote from ProjectSoft	
2013	Steward's attempt at VATT's automation begins	Steward intends ARTN
2016		Steward-Vatican MOU
2022	ProjectSoft contract signed, financing secured	
2024	commissioning of Don	



Fig. 1. The Don figurine played an important role in our fundraising. Credit: Robert Macke, S.J.

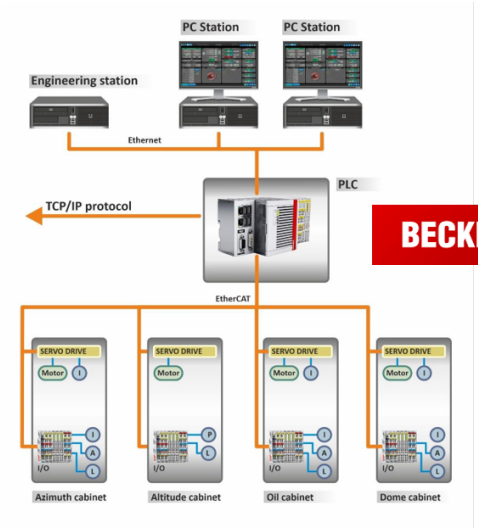


Fig. 2. Don's architecture is based on PLCs by Beckhoff. Credit: ProjectSoft.

tion, the dome and the dome slit shutters, the hydraulic oil system of the Azimuth's axis hydrostatic bearing, the primary mirror's cooling system, etc. The units communicate within Don by EtherCAT and externally by TCP/IP (Transmission Control Protocol/Internet Protocol).

Don's operational modes include a legacy mode with fully automated startup and shutdown, a local mode, a remote mode, and a scripted mode. In Don's first months, users will be using the VATT in the legacy mode, on site or remotely, while developing scripts for their own science cases.

While Don itself, i.e., the control system, runs on Beckhoff PLCs, Don's GUI (Graphical User Interface) is ProjectSoft's TomPack (Fig. 3) running exclusively on Windows. TomPack makes a minimal use of Windows libraries, which renders it stable across OS updates. Although TomPack would allow us to run the facility from a laptop, for added security, we shall use a remote sessions on a rack-

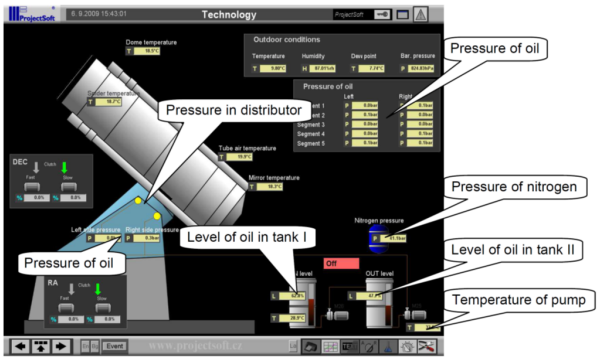


Fig. 3. Don's GUI is TomPack. The illustration show a sample page. Credit: ProjectSoft.

mounted Windows server residing on-site.

Don can be run from the command line using ProjectSoft's ASCOL (AStronomical COmmunication Language). It is based on the TCP/IP protocol, and the commands are ASCII strings. Don also contains an implementation of ASCOM/Alpaca.

VII Workshop on Robotic Autonomous Observatories (October 16-20, 2023)
Editors: Maria Gritsevich, Alberto J. Castro-Tirado, Petr Kubánek, Shashi B. Pandey, and David Hiriart - DOI: https://doi.org/10.22201/ia.14052059p.2025.59.05

3. OTHER SYSTEMS

In addition to the installation of `Don`, other systems running at the VATT include:

- the secondary mirror (M2) Physik-Instrumente hexapod (see Sec. 4),
- the instrument interface (so-called Guide Box) with smart motors positioning a stage carrying a flip-in tertiary mirror and a U-shaped offset guiding mirror, the three filter wheels, and the three axes of the translation stage supporting the guider camera,
- guider camera and guider software (PHD2), and
- the scientific instruments, i.e.,
  - the VATT 4k CCD Imager,
  - the VATTspec spectrograph with its optomechanical systems and its CCD camera,
  - the GUFI-Marana CMOS camera, and

Currently, these systems have their own GUIs, user-end software, and can be operated using various TCP/IP-based protocols (e.g., the GUFI-Marana camera uses Andor's SOLIS proprietary software; the 4k CCD Imager and the VATTspec use the AzCam camera control software, and, in addition, the frames are displayed in DS9, exported to a data server, and they can be inspected and analyzed using IRAF). Some of these systems will be adjusted so that they can be operated within the same platform as `Don`.

4. AUTOMATED COLLIMATION

Service and/or engineering algorithms are being developed as ready-to-use scripts. In particular, the f/1 primary calls for an alignment with the secondary mirror at the micron and arcsec level (Fig. 4). While M2 can be positioned with a repeatability at the micron level thanks to a hexapod by PhysikInstrumente, the mutual position and orientation of the primary mirror and the focal plane instrument are fixed. This means that the alignment is not a simple geometry problem with a unique solution but rather an optimization problem. We are developing a collimation routine, intended to be deployed periodically. During ordinary operations, the alignment is maintained by monitoring the thermal expansion of the struts, the mechanical sag of the struts with elevation, as well as the changes in M1's position (6 axes monitored) and compensating for these perturbations by adjusting M2's position and orientation in a 1 Hz loop.

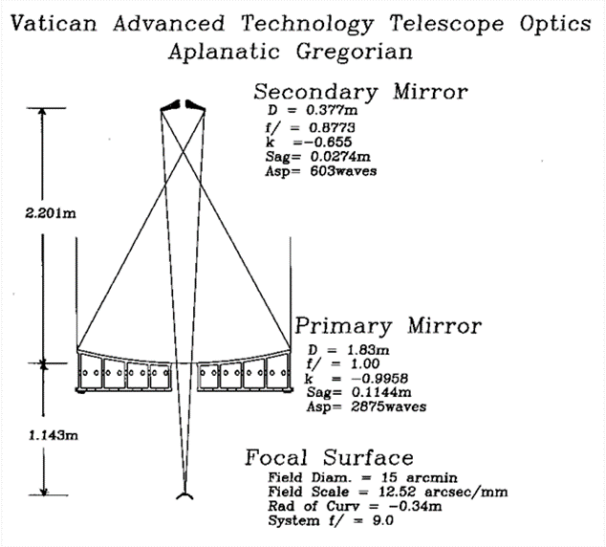


Fig. 4. VATT's optical layout.

5. CONCLUSION

By way of a conclusion, here is the status of the project as of September 2024, the last update of this manuscript. `Don` has passed a Factory Acceptance Test on January 17. It was installed and commissioned in April and May. The Final Acceptance Protocol was signed on June 3. We continue working on the automated collimation, on configuring the software environment for the astronomical instruments (mostly ASCOM/Alpaca), as well as working towards fully autonomous operations (which will require some experience with various weather conditions, tuning environmental triggers for automated shutdown).

Acknowledgements: The authors gratefully acknowledge the contributions of Tomáš Turek, Vít Talácko, Petr Langer, Vlastislav Andrle (ProjectSoft), Christopher Johnson, Michael Franz, Gary Gray, Daewook Kim, Heejoo Choi (University of Arizona), Petr Kubánek (LSST). The project is carried out with the assistance of the Vatican Observatory Foundation, the Thomas Lord Charitable Trust, and Mrs Judith Alstadt in memory of Mr Donald Alstadt.

REFERENCES

Blanco, D., Corbally, C., Nagel, R., et al. 1990, Proc. SPIE, 1236, 905.
Swindell, S. R., Johnson, C. S., Franz, M. H., et al. 2019, RMxAC, 51, 54
West, S. C., Nagel, R. H., Harvey, D. A., et al. 1997, Proc. SPIE, 2871, 74



Fig. 5. Moonlit VATT in winter, view from the East. Credit: Paul Schulz.

VII Workshop on Robotic Autonomous Observatories (October 16-20, 2023)
Editors: Maria Gritsevich, Alberto J. Castro-Tirado, Petr Kubánek, Shashi B. Pandey, and David Hiriart - DOI: https://doi.org/10.22201/ia.14052059p.2025.59.05

Revista Mexicana de Astronomía y Astrofísica Serie de Conferencias (RMxAC), **59**, 27–30 (2025)
© 2025: Instituto de Astronomía, Universidad Nacional Autónoma de México
https://doi.org/10.22201/ia.14052059p.2025.59.06

VII Workshop on Robotic Autonomous Observatories (October 16-20, 2023)
Editors: Maria Gritsevich, Alberto J. Castro-Tirado, Petr Kubánek, Shashi B. Pandey, and David Hiriart - DOI: https://doi.org/10.22201/ia.14052059p.2025.59.06

AUTONOMOUS TELESCOPE AND SCIENTIFIC INFRASTRUCTURE DEVELOPMENTS AT TUG

Orhan Erece[1,2], Yucel Kilic[1], and Kadir Uluc[1]

RESUMEN

En este estudio, se proporciona una breve descripción de los telescopios ubicados en el Observatorio Nacional TÜBİTAK (TUG). Se describe el software NightAssistant (NA), desarrollado como una aplicación de escritorio fácil de usar para controlar las operaciones del telescopio T100 y del observatorio. Además, se presenta la plataforma web denominada Occultation Portal (OP), que se ejecuta en servidores del TUG, con el fin de anunciar, recopilar y analizar observaciones de ocultaciones estelares que deseen realizar diferentes proyectos desde una plataforma compartida.

ABSTRACT

In this study, a brief overview of the telescopes located at the TÜBİTAK National Observatory (TUG) is provided. The NightAssistant (*NA*) software, developed as a user-friendly desktop application for controlling both the T100 telescope and observatory operations, is described. Additionally, the web-based platform named Occultation Portal (*OP*), running on TUG servers, is introduced for the purpose of announcing, collecting, and analyzing stellar occultation observations desired to be conducted by different projects from a shared platform.

Key Words: occultations — telescopes

1. INTRODUCTION

The TÜBİTAK National Observatory (TUG) is located in Bakırlıtepe, Antalya, in the southern part of Türkiye, at an altitude of 2500 m (latitude 36°49' N, longitude 30°20' E). Established in 1997, the observatory hosts four main telescopes, as well as other smaller telescopes and scientific instruments that actively participate in scientific observations. The 1.5-meter RTT150 and the 1.0-meter T100 telescopes are fully automatic and operated remotely from the TUG Administration Building in Antalya, while the 0.6-meter T60 telescope and the 0.45-meter ROTSE III-d telescope are fully robotic. To date, numerous software development studies have been undertaken to automate these telescopes and enhance astronomical data collection, processing, and data services.

In this paper, we will present the NightAssistant software, the main telescope and observatory control software for the T100 telescope and the Occultation Portal[3](Kilic et al. 2022), a web-based platform for data collection and analysis of stellar occultations, both developed at TUG.

2. T100 TELESCOPE AND NIGHTASSISTANT

The T100 telescope was installed in 2009 at the south peak of the Bakırlıtepe mountain. The telescope has a large field of view and is dedicated to wide-field imaging and high-precision photometric and astrometric observations, mainly used in multi-band photometric observations of variable stars, galaxies, exoplanets, minor planets, stellar occultations, as well as follow-up observations (see Table 1). The main software used for the T100 telescope was the ACE Connector running on Windows OS, developed by the company named ACE[4]. However, the ACE Connector did not fully meet our demands due to its complex modular structure. Consequently, we explored alternative solutions to enhance the performance of the T100 telescope and developed a new graphical user interface (GUI) called *NightAssistant* (*NA*) using PyQt5, a cross-platform Python binding of the GUI toolkit Qt[5]. The *NA* software consists of a single window with different tabs (see Fig. 1). It is capable of not only controlling telescope parts but also of assigning specific coordinates of the project for the night, creating nightly directories, setting saving paths, offsetting the telescope, generating ephemerides of minor planets, displaying

[1]The Scientific and Technological Research Council of Türkiye (TÜBİTAK) National Observatory, Akdeniz University, 07058, Antalya, Türkiye (orhan.erece@tubitak.gov.tr).
[2]Türkiye National Observatories, Antalya Campus, Antalya, Türkiye.
[3]`https://occultation.tug.tubitak.gov.tr`

[4]`https://www.astronomical.com`
[5]Qt, a widely-used GUI toolkit, provides a framework for creating cross-platform graphical user interfaces `https://www.qt.io/`

VII Workshop on Robotic Autonomous Observatories (October 16-20, 2023)
Editors: Maria Gritsevich, Alberto J. Castro-Tirado, Petr Kubánek, Shashi B. Pandey, and David Hiriart - DOI: https://doi.org/10.22201/ia.14052059p.2025.59.06

TABLE 1

T100 TECHNICAL SPECIFICATIONS

Optical design	Ritchey-Chrétien
Main Mirror diameter	1000 mm
Focal Length	10000 mm
Focal Ratio	f/10
Resolving Capacity	0.11”
Plate Scale	20”/mm
Field of view	21’x21’
CCD Camera	SI 1100 4Kx4K

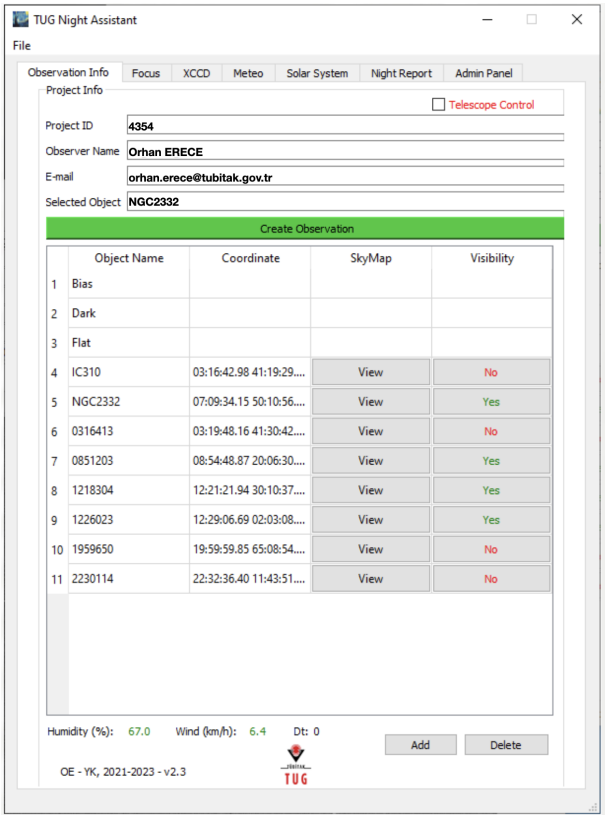


Fig. 1. The *NA* software *Observation Info* tab

instant meteorological values and all-sky camera images, and automatically creating and sending nightly reports to the database.

The *NA* employs the ACE Connector as an interface to manage and control various telescope components. The other information is obtained either through functions embedded within the software or from real-time data retrieved from the web. It consists of seven tabs at the top of the GUI, as seen in Fig. 1, designed for different purposes. On the *Observation Info* tab, observers can slew the telescope by clicking on one of the listed coordinates after activating the telescope control checkbox located in the top right of the tab. Additionally, the dynamically updated visibility of the coordinates is indicated as ”Yes” in green or ”No” in red, along with the visibility chart and the sky map of the coordinates.

Another notable functionality of the *NA* is its automated focusing capability. Within the *Focus* tab, a distinct focusing model is presented for each filter, determined on the basis of the telescope’s altitude. The *NA* promptly retrieves the current altitude of the telescope. Consequently, when the auto-focus checkbox, located on the bottom left, is enabled, the *NA* optimizes the focus to its ideal setting during the observation sessions. This streamlines the process for observers and contributes to improved telescope performance. The *NA* offers also the option to specify an offset value for observers interested in conducting defocused observations. Additionally, real-time images from the all-sky camera at the observatory are visible within this tab (see Fig. 2).

On the *XCCD* tab, users can provide an offset value for minor adjustments. Once coordinates are selected in the *Observation Info* tab, they are displayed on the *XCCD* tab. The sole task remaining is to input the physical coordinates corresponding to specific points on the image, indicating the starting and ending corner positions. On the *Meteo* tab, real-time wind and humidity values are displayed. These values are presented in green if they fall within predefined limits; otherwise, they appear in red to indicate conditions outside the acceptable range.

On the *Solar System* tab, ephemerides can be generated for all small objects, found in the *JPL/Horizon* database[6]. These ephemerides include instantaneous equatorial coordinates and apparent magnitudes, along with related data obtained from this database. Such information encompasses the object’s sky motion and direction, which can be depicted in the sky image.

On the *NightReport* tab, the nightly report is automatically generated and sent to the database. It includes information such as observers, technicians, night assistants, weather conditions, comment sections, and the number of total hours of observations. In the *Admin Panel* tab, tasks such as specifying the file path for the focus model, selecting the weather station for weather information, defining weather condition limits, and determining the path for storing scientific data can be carried out. We showcase all the tabs of the *NA* on *GitHub*[7].

[6] https://ssd.jpl.nasa.gov/horizons/
[7] https://github.com/orhanerece/nightassistant-

VII Workshop on Robotic Autonomous Observatories (October 16-20, 2023)
Editors: Maria Gritsevich, Alberto J. Castro-Tirado, Petr Kubánek, Shashi B. Pandey, and David Hiriart - DOI: https://doi.org/10.22201/ia.14052059p.2025.59.06

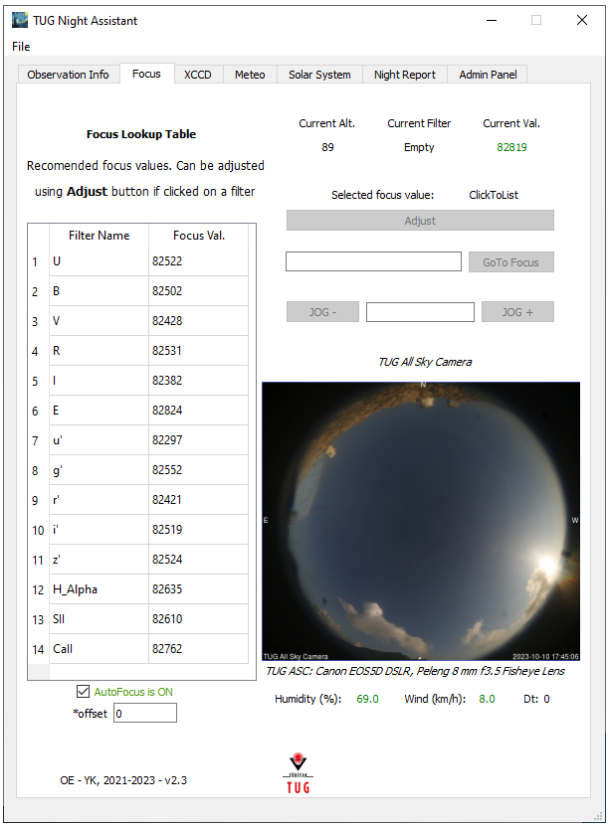


Fig. 2. The *NA* software *Focus* tab

3. OCCULTATION PORTAL

A stellar occultation is a celestial event that occurs when a Solar System object obscures a source from the perspective of an observer (Kilic et al. 2022). When this event is recorded simultaneously from more than two locations across the occultation path, it becomes possible to obtain detailed information about the foreground object (Braga-Ribas et al. 2013; Souami et al. 2020). However, coordinating different observers and collecting data from them posed challenges. To address these issues, the *Occultation Portal*[8] (*OP*) was developed at TUG (Kilic et al. 2022), as shown in Fig. 3. Currently, the *OP* manages campaigns for the *ERC Lucky Star*[9], *Across*[10] and *Gaiamoons*[11] projects and efficiently gather and analyze data from many contributing observers distributed along the occultation path. Through its coordination of occultation observations for various projects, the *OP* encompasses occultation events involving a range of objects within the Solar System, from NEAs (Near-Earth

[8]https://occultation.tug.tubitak.gov.tr/
[9]https://lesia.obspm.fr/lucky-star/
[10]https://lagrange.oca.eu/fr/home-across
[11]https://www.oca.eu/fr/gaiamoons

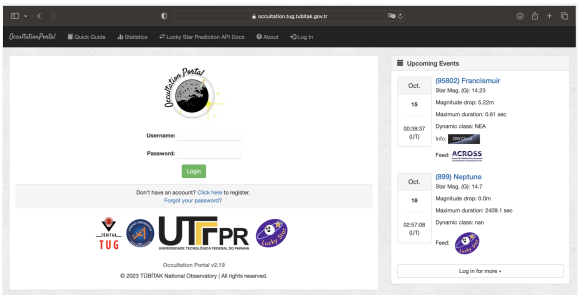


Fig. 3. The login screen of the *OP* website

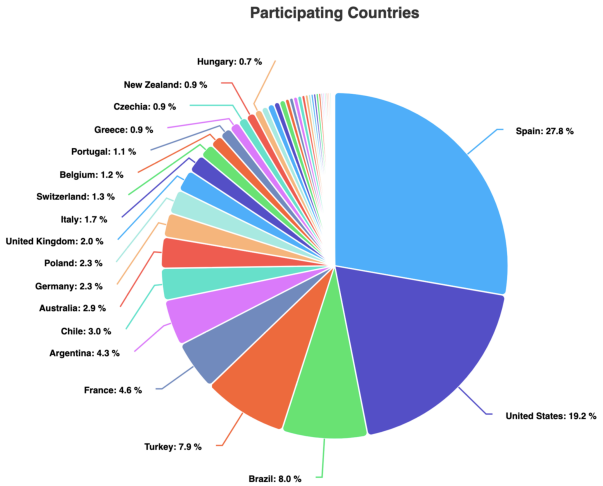


Fig. 4. The percentage of participating countries on the *OP* platform

Objects) to TNOs (TransNeptunian Objects). As a result, the *OP* contributes significantly to numerous scientific endeavours aimed at exploring the physical and dynamic characteristics of objects throughout the Solar System.

To date, there are 953 observation sites from 46 different countries registered in the *OP* (see Fig. 4). Considering the brightness of the occulted star in the observation campaigns announced to date, the number of stars brighter than the 14th magnitude is %55.5[12]. This statistic is quite noteworthy, as it demonstrates that telescopes participating in the campaign can be operated with amateur-level equipment. From this perspective, the contribution of the *OP* to citizen science is also highly significant.

The high-precision stellar occultation predictions enabled by the European Space Agency's (ESA) star-mapping satellite *Gaia* and its high astrometric accuracy (Gaia Collaboration 2021) contribute significantly to the increase in successful occultation event observations (Braga-Ribas et al. 2019; Fer-

[12]https://occultation.tug.tubitak.gov.tr/statistics/

VII Workshop on Robotic Autonomous Observatories (October 16-20, 2023)
Editors: Maria Gritsevich, Alberto J. Castro-Tirado, Petr Kubánek, Shashi B. Pandey, and David Hiriart - DOI: https://doi.org/10.22201/ia.14052059p.2025.59.06

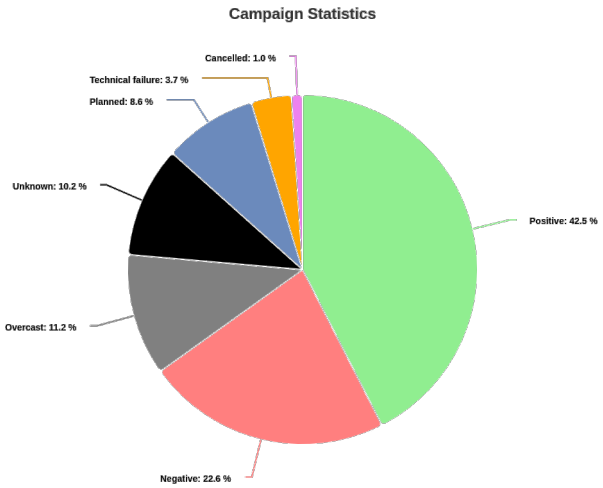


Fig. 5. The percentage of campaigns conducted through the *OP* platform

reira et al. 2022). As expected, the positive observation rates in the OP are higher, and they continue to rise during overall organized campaigns, as shown in Fig. 5. So far, after reviewing all the campaigns organized within the *OP*, it has been discovered that 42.5% of occultation events were observed positively, 22.6% were negative, and 10.2% were unknown. The total percentage of observers who planned to observe, but experienced technical difficulties, bad weather, or cancelled their observations has been approximately 25%.

4. CONCLUSION

In conclusion, the TÜBİTAK National Observatory (TUG), located in Bakrltepe, Antalya, has been a leader in advancing astronomical observations since its creation in 1997 in Türkiye. Equipped with a range of telescopes and scientific instruments, including the fully automated T100 and RTT150 telescopes along with the robotic T60 and ROTSE telescopes. After a significant amount of work in software development, the NightAssistant (*NA*) software has streamlined the telescope operations and data collection processes, increasing efficiency and accuracy of astronomical studies.

Moreover, the development of the Occultation Portal (*OP*) demonstrates TUG's commitment in promoting collaborative research efforts. By providing a centralized platform for announcing, collecting, and analyzing stellar occultation observations, the *OP* has made coordinated observations straightforward, thus encouraging international cooperation. Observers from 46 countries have participated in this global engagement, highlighting the significance of TUG's contributions to professional research and citizen science initiatives.

TUG's dedication in advancing astronomical research and promoting international collaboration is evident from the development of the *NA* software and *OP* platform, among others.

REFERENCES

Braga-Ribas, F., et al. 2013, ApJ, 773, 26
Braga-Ribas, F., et al. 2019, JPhCS, 1365, 012024
Ferreira, J. F., et al. 2022, A&A, 658, A73
Gaia Collaboration, Brown, A. G. A., et al. 2021, A&A, 649, A1
Kilic, Y., et al. 2022, MNRAS, 515, 1346
Souami, D., et al. 2020, A&A, 643, A125

Revista Mexicana de Astronomía y Astrofísica Serie de Conferencias (RMxAC), **59**, 31–36 (2025)
© 2025: Instituto de Astronomía, Universidad Nacional Autónoma de México
https://doi.org/10.22201/ia.14052059p.2025.59.07

VII Workshop on Robotic Autonomous Observatories (October 16-20, 2023)
Editors: Maria Griffsevich, Alberto J. Castro-Tirado, Petr Kubánek, Shashi B. Pandey, and David Hiriart - DOI: https://doi.org/10.22201/ia.14052059p.2025.59.07

OAUJ-CDK500: A NEW KRAKÓW ROBOTIC TELESCOPE

S. Zola[1], G. Stachowski[1], S. Kurowski[1], T. Kundera[1], W. Waniak[1], D. E. Reichart[2], V. Kouprianov[2], J. B. Haislip[2], Ł. Wyrzykowski[3], and P. J. Mikołajczyk[3,4]

RESUMEN

Describimos el pequeño telescopio óptico más nuevo de los pertenecientes al Observatorio Astronómico de la Universidad Jagellónica. Este telescopio está actualmente instalado en una cúpula Zeiss en el observatorio de Cracovia (Polonia). Damos detalles de la configuración del hardware, así como del software, lo que le permite funcionar de forma autónoma como telescopio asociado dentro de la Red de Telescopios Robóticos Skynet.

ABSTRACT

We describe the newest small optical telescope belonging to the Astronomical Observatory of the Jagiellonian University. This telescope is currently installed in a Zeiss dome at the observatory site in Kraków, Poland. We give details of the hardware configuration as well as the software which enables it to work autonomously as a partner telescope within the Skynet Robotic Telescope Network. The telescope working in this configuration is an efficient tool supporting the scientific, educational and outreach projects.

Key Words: telescopes — instrumentation: detectors — methods: observational — techniques: photometric

1. INTRODUCTION

Until nearly the end of the 20th century, observations with ground-based optical telescopes required the presence of an on-site observer, who decided if the weather conditions were suitable and who had to manually open the dome and point and operate the telescope. Subsequent progress in computing power and networking made remote observing possible, but still required continuous monitoring by the observer and a night assistant to be present on-site.

The decreasing costs and improving capabilities of computers, sensors and microcontrollers around the 1990s led to the development of hardware and software capable of controlling telescopes working autonomously from a target list. The first individual robotic telescopes were soon followed by the creation of robotic telescope networks, eventually spanning the entire globe (Woźniak 2013).

Several of these networks were initially created to facilitate rapid follow-up observations of the optical afterglows of γ-ray bursts (GRBs). Examples include the Bootes network created in 1998, with global coverage of seven telescopes completed in 2023 (Castro-Tirado et al. 1999; Castro-Tirado 2023), and the Skynet Robotic Telescope Network (Zola et al. 2021) created in 2004. The latter currently consists of a few dozen optical telescopes located on five continents and one radiotelescope (Greenbank–20) which has also been integrated into the network. A review of the ground based GRB follow-up facilities was published recently by Tsevtkova et al. (2022).

Until 2019, the Astronomical Observatory of the Jagiellonian University in Kraków, Poland, had three small telescopes used for photometry, all of which were originally manually operated. An attempt was made to automate the 1970s-era 50 cm Cassegrain telescope, however full automation turned out to not be economically viable and the telescope still requires remote operation by the observer and some manual setup. Therefore, the decision was made to purchase a more modern 50 cm telescope which could be used both for automated scientific observations and for teaching students at the astronomy department.

The new telescope, built by PlaneWave, arrived at the end of 2019 and was fully commissioned and collecting data at the Astronomical Observatory site in the suburbs of Kraków in early 2020.

In the next section of this paper we describe the hardware of the new telescope, followed by a description of the Skynet software on the client computer side. Next we present the performance of this telescope under typical Central European weather conditions.

[1]Astronomical Observatory of the Jagiellonian University, ul. Orla 171, PL 30-244 Kraków, Poland, (szola@oa.uj.edu.pl).
[2]University of North Carolina at Chapel Hill, Chapel Hill, North Carolina, NC 27599, USA.
[3]Astronomical Observatory, University of Warsaw, Al. Ujazdowskie 4, 00-478 Warszawa, Poland.
[4]Astronomical Institute, University of Wrocław, Kopernika 11, 51-622 Wrocław, Poland.

VII Workshop on Robotic Autonomous Observatories (October 16-20, 2023)
Editors: Maria Gritsevich, Alberto J. Castro-Tirado, Petr Kubánek, Shashi B. Pandey, and David Hiriart - DOI: https://doi.org/10.22201/ia.14052059p.2025.59.07



Fig. 1. The dome of the OAUJ-CDK500 telescope.

2. OBSERVATORY HARDWARE

2.1. *Weather Sensors*

Two crucial pieces of hardware must be present for a fully autonomous telescope to operate safely and be aware of changing weather conditions: a cloud sensor and a weather station providing rainfall, wind, temperature and humidity measurements. Our observatory is equipped with the AAG cloud sensor [5] and a Davis WeatherPro station [6] which provide continuous monitoring of weather status at the site. Current weather conditions and the dome position can be visually checked with a SBIG Allsky-340C camera mounted next to the dome and a nearby security camera.

2.2. *Telescope and Dome Hardware*

The telescope is a 20 inch (50.8 cm) diameter f/6.8 Corrected Dall-Kirkham (CDK), manufactured by PlaneWave[7]. The CDK optical design consists of an ellipsoidal primary mirror, spherical secondary and additional lenses to correct off-axis aberrations.

[5]https://eu.lunaticoastro.com/product/aag-cloudwatcher-cloud-detector

[6]https://www.davisinstruments.com/

[7]https://planewave.com/product/cdk500-telescope-system/

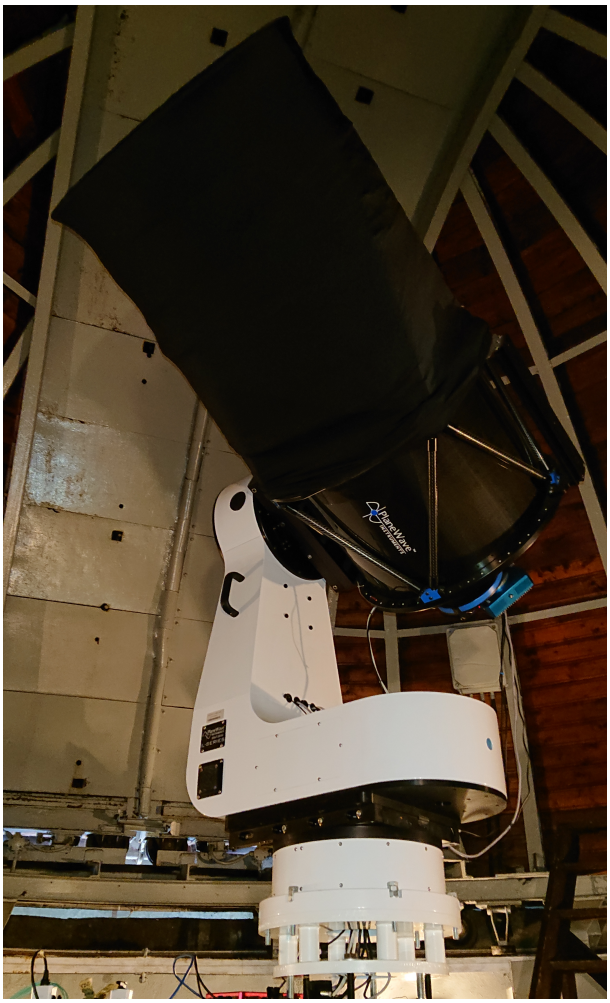


Fig. 2. The OAUJ-CDK500 telescope inside the Zeiss dome.

The telescope works on the PlaneWave L-500 direct-drive mount, ensuring high pointing precision and fast slewing speeds up to 50° per second. The alt-azimuth type mount necessitates a field derotator, which in our case is integrated with the focuser (PlaneWave IRF90). Due to the low expansion coefficient of the carbon-fiber truss tube, the focus position only needs to be corrected a few times a year when the temperature changes very significantly.

The telescope is installed in the 6-meter Zeiss dome formerly housing an astrograph, which has been automated with a Technical Innovations Digital Dome Works (DDW) system[8]. This consists of a set of sensors and relays for both azimuthal rotation and shutter control. The DDW software interface includes some safety features, such as the control software querying the DDW processor every few

[8]https://www.homedome.com/

VII Workshop on Robotic Autonomous Observatories (October 16-20, 2023)
Editors: Maria Gritsevich, Alberto J. Castro-Tirado, Petr Kubánek, Shashi B. Pandey, and David Hiriart - DOI: https://doi.org/10.22201/ia.14052059p.2025.59.07

minutes and automatically parking and closing the dome if the connection to the computer is lost.

2.3. *CCD and Filters*

Two CCD cameras are currently configured for, and can be installed on, the OAUJ-CDK500 telescope: an Apogee Alta U47 and Apogee Alta F42. Both cameras have CCD chips with 13 μm pixels, however the Alta U47 has a 1k×1k chip, while the chip of the Alta F42 is twice as large, providing a field view of $27.7' \times 27.7'$. A Finger Lakes Instrumentation (FLI) seven-position filter wheel is mounted in front of the camera. It accomodates 3 filters in the Strömgren system (Sv, Sb and Sy) and 4 wide band (B, V, R, I) ones manufactured according to Bessell's specification (Bessell 1990, 2005).

3. SOFTWARE

The Skynet Robotic Telescope Network consists of two parts: the server side which is hosted at the University of North Carolina (UNC) at Chapel Hill (USA), and software running on a data gathering computer at each site. The former was described in more detail by Zola et al. (2021). The server is responsible for submission of observation requests, their prioritization and scheduling, and dispatch to one or more telescopes for execution. After the observations are completed, the client computers transfer images to the server for calibration. Once calibration is completed, the images are ready for download by the user in both JPEG and FITS formats. The Skynet client computer software for the OAUJ-CDK500 runs under the Windows 10 operating system on a PrimaLuce Labs Eagle computer. In the following subsections, we describe the software modules needed to operate the telescope in robotic mode within the Skynet Network.

3.1. *Weather control programs*

To enable fully autonomous and unsupervised operation, OAUJ-CDK500 uses weather monitoring software to retrieve information from the sensors described in section 2.1. The central part of this software is WeatherMan, a custom weather data collection service created by the Skynet team at UNC. It talks to the AAG cloud sensor driver via the Component Object Model (COM) server built into the AAG cloud sensor driver and to the Davis weather station via the freely available Cumulus software, using its ability to log current sensor readings to a text file. WeatherMan has configurable thresholds and wait times for all available weather parameters, most important of which are humidity, precipitation, wind speed and sky temperature. This data is analyzed to determine whether the conditions are safe; failure to retrieve data from a particular sensor is also considered an unsafe situation. WeatherMan communicates this safe/unsafe decision to the telescope control software described below by means of a custom HTTP-based application programming interface (API).

3.2. *Telescope control software*

The current Skynet telescope software architecture is built around the ASCOM ecosystem[9]. All hardware components, including the mount, dome, imaging camera, focuser, filter wheel, and field derotator, are controlled either directly via their ASCOM drivers or through MaxIm DL (from Diffraction Limited) using its COM API. Terminator is a custom Skynet telescope client LabView application which is responsible for integrating all other software components and communicating with the Skynet servers at UNC. It 1) reports the current state of the telescope to Skynet, including the weather safety flag and the status of all telescope subsystems, 2) receives calibration and science observation requests from Skynet, 3) commands the hardware components via ASCOM and MaxIm DL to perform their respective tasks running the job from opening the dome, through pointing the telescope, to obtaining the images from the CCD camera, and 4) transfers the resulting images to the UNC data storage servers. Terminator is responsible for coordinating the work of all hardware components and for maintaining the safety of the observatory by closing the dome and suspending observations if the weather becomes unsafe. As an additional safety measure, telescope administrators have the ability to flag the telescope as "locked" via the Skynet website to prevent the dome from opening and all observations (excluding bias and dark calibration tasks which are performed with a closed dome) from running in the (unlikely) event that the weather is wrongly reported as safe by WeatherMan, or there are other issues that Terminator cannot detect such as mechanical damage to the dome.

From the users' perspective, observations within the Skynet network are submitted via a web-based interface[10]. This is suitable for users with all levels of experience, from school pupils, through students to professional astronomers. The interface allows for target objects to be chosen via map, name search or by directly entering coordinates. Restrictions such as altitude or lunar phase and separation

[9] `https://www.ascom-standards.org`
[10] `https://skynet.unc.edu`

VII Workshop on Robotic Autonomous Observatories (October 16-20, 2023)
Editors: Maria Gritsevich, Alberto J. Castro-Tirado, Petr Kubánek, Shashi B. Pandey, and David Hiriart - DOI: https://doi.org/10.22201/ia.14052059p.2025.59.07

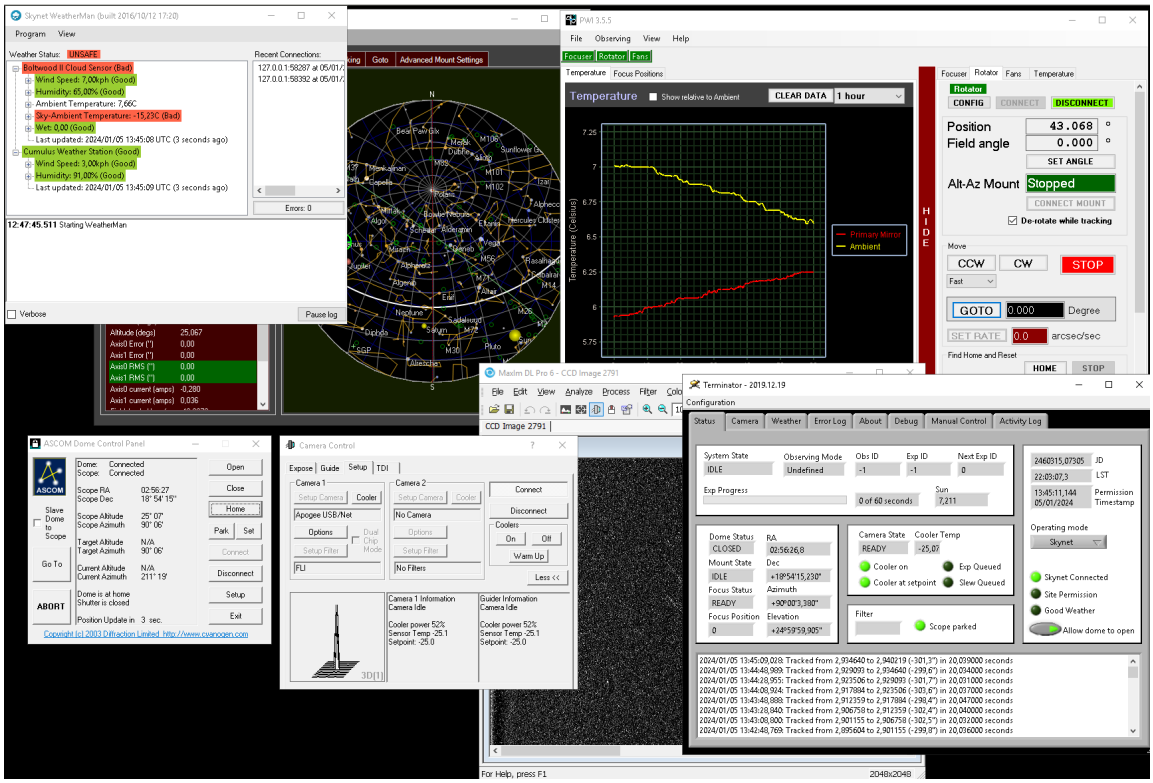


Fig. 3. Programs running on the data gathering computer.

can be set, and for exposure sequences and intervals (both within one night and over multiple nights) to be defined. Filters can be set for each exposure (depending on their availability on the given telescope). The interface can easily and conveniently be used to set up observations ranging from 'pretty pictures' to carefully-planned long-duration photometric studies. Once submitted the process is fully automated. The Skynet server will allocate time on the certain telescope or a subset of telescopes until the desired observation sequence is completed. Users of the Skynet network do not have to take bias, dark and flatfield calibration images themselves, as this task is automatically scheduled by the Skynet server and image calibration is performed automatically. When the observations are done, the calibrated images appear in the user's account ready for downloading, typically within a few days but sometimes in almost real time, depending on weather and number of jobs submitted.

4. TELESCOPE PERFORMANCE AND EFFICIENCY

Since commissioning at the beginning of 2020, the telescope has operated in the robotic mode continuously with just few small glitches, most of which were due to mechanical issues with the old dome. It has collected several thousand images and was used for a combination of scientific programs, teaching and outreach. The scientific programs mostly consisted of long term monitoring of extragalactic targets, as these are most suitable for unpredictable weather conditions.

Here we present data taken during 2023 of the supernova SN2023ixf, discovered in the nearby galaxy Messier 101 in May (Perley et al. 2023). Soon after its discovery, a long observing run request was submitted through Skynet and data were collected over the entire summer vacation without any human supervision. In early October all the obtained images were tentatively reduced using the BHTOM project led by L. Wyrzykowski[11] (Zieliński at al. 2019, 2020). The result is shown in Fig. 4.

5. CONCLUSIONS

After several attempts at automating the Zeiss 50 cm Cassegrain telescope, originally installed in 1970, we were only able to make it partially remotely operable. Full automation turned out to be extremely costly and therefore, after being granted

[11] https://bh-tom2.astrolabs.pl

VII Workshop on Robotic Autonomous Observatories (October 16-20, 2023)
Editors: Maria Gritsevich, Alberto J. Castro-Tirado, Petr Kubánek, Shashi B. Pandey, and David Hiriart - DOI: https://doi.org/10.22201/ia.14052059p.2025.59.07



Fig. 4. Photometric observations of the supernova SN2023ixf in M101. Data were taken in four filters. The vast majority of the points represent observations taken with the OAUJ-CDK500 robotic telescope.

funds, it was instead decided to buy a new automatic telescope. A PlaneWave CDK-500 telescope and mount system was chosen and arrived at the site in Kraków at the end of 2019. We considered several possibilities for operating it autonomously, and eventually joined the Skynet Robotic Telescope Network as a partner telescope. Using the mature Skynet software we were able to start observing in the robotic mode from early 2020. This proved extremely fortuitous as it allowed students and pupils to carry on observations from their homes during the subsequent COVID-19 pandemic lockdown, using the convenient and intuitive Skynet web interface. Long-term photometric monitoring programs could also be continued without interruption.

The ability to observe autonomously whenever the weather was clear turned out to be very efficient in our prevailing weather patterns. The telescope often automatically opened, collected data and closed during short windows of good weather which appeared during the night, when a manually-operated telescope would have remained closed and missed the opportunity. Compared to fully manual operation, we estimate the gain in efficiency was twofold, and especially suitable for very long term brightness monitoring of targets for which just a short series of images is needed every clear night. This can be seen in the case of the observations of the recent supernova SN2023ixf (see Fig. 4), with many data points being obtained despite the absence of on-site observing staff during the summer vacation.

In summary, since installation in 2020, the OAUJ CDK500 operating within the Skynet network has proven itself to be a reliable and efficient tool supporting the scientific, educational and outreach missions of the Jagiellonian University Astronomical Observatory.

Acknowledgements: This project used data obtained via BHTOM (https://bhtom.space [bhtom.space]), which has received funding from the European Union's Horizon 2020 research and innovation program under grant agreements No. 730890 (OPTICON) and 101004719 (OPTICON-RadioNET Pilot). Funding for the OAUJ-CDK500 telescope was provided by the Jagiellonian University which we gratefuly acknowlege.

REFERENCES

Bessell, M. S. 1990, PASP, 102, 1181
Bessell, M. S. 2005, ARA&A, 43, 293
Castro-Tirado, A. J., Soldán, J., Bernas, M., Páta, P., Rezek, T. et al. 1999, A&AS, 138, 449
Castro-Tirado, A. J. 2023, Nature Astronomy, 7, 1136
Perley, D. A., Gal-Yam, A., Irani, I., Zimmerman, E. 2023, Transient Name Server AstroNote 2023-119

Tsvetkova, A., Svinkin, D., Karpov, S., Frederiks, D. 2022, Universe, 8, 373
Woźniak, P. 2013 in Planets, Stars and Stellar Systems. Volume 1: Telescopes and Instrumentation, 43
Zieliński, P., Wyrzykowski, Ł., Rybicki, K., et al. 2019, CoSka, 49, 125
Zieliński, P., Wyrzykowski, Ł., Mikolajczyk, P., Rybicki, K., & Kolaczkowski, Z. 2020, past.conf, 190
Zola, S., Kouprianov, V., Reichart, D. E., Bhatta, G., & Caton, D. B. 2021, RMxAC, 43, 293

VII Workshop on Robotic Autonomous Observatories (October 16-20, 2023)
Editors: Maria Gritsevich, Alberto J. Castro-Tirado, Petr Kubánek, Shashi B. Pandey, and David Hiriart - DOI: https://doi.org/10.22201/ia.14052059p.2025.59.07

Revista Mexicana de Astronomía y Astrofísica Serie de Conferencias (RMxAC), **59**, 37–41 (2025)
© 2025: Instituto de Astronomía, Universidad Nacional Autónoma de México
https://doi.org/10.22201/ia.14052059p.2025.59.08

VII Workshop on Robotic Autonomous Observatories (October 16-20, 2023)
Editors: Maria Gritsevich, Alberto J. Castro-Tirado, Petr Kubánek, Shashi B. Pandey, and David Hiriart - DOI: https://doi.org/10.22201/ia.14052059p.2025.59.08

BUILDING A LIMITED BUDGET ROBOTIC OBSERVATORY

M. Odeh[1]

RESUMEN

Proporcionamos una visión general del Observatorio Astronómico Al-Khatam (AKO), situado en el desierto de Abu Dhabi, Emiratos Árabes Unidos, y operado por el Centro Astronómico Internacional (IAC). AKO es un observatorio robótico que realiza observaciones astronómicas preprogramadas. Utilizando AKO como ejemplo, mostramos cómo se puede establecer un observatorio robótico con un presupuesto bajo y mano de obra mínima. Se describen los diversos componentes necesarios para montar un observatorio robótico. Además, mostramos algunas de las observaciones y logros notables del observatorio, particularmente en observaciones fotométricas y astrométricas, como la colaboración con organizaciones internacionales para monitorear asteroides recién descubiertos, contribuyendo a los esfuerzos de defensa planetaria. El observatorio pone un gran énfasis en las observaciones fotométricas de contrapartidas ópticas de GRB, especialmente inmediatamente después de su descubrimiento por parte de observatorios espaciales. Además, alberga un exitoso programa de búsqueda de supernovas, que condujo al descubrimiento de la supernova SN 2023rve después de nueve meses de esfuerzo continuado.

ABSTRACT

This paper provides an overview of the Al-Khatam Astronomical Observatory (AKO) situated in the Abu Dhabi desert, United Arab Emirates, and operated by the International Astronomical Center (IAC). AKO is a robotic observatory that conducts pre-programmed astronomical observations. Using AKO as an example, the paper shows how a robotic observatory can be established with a low budget and minimal workforce. The paper outlines the various components required for setting up a robotic observatory. Furthermore, the paper shows some of the observatorys notable observations and achievements, particularly in photometric and astrometric observations, such as collaborating with international organizations to monitor recently discovered asteroids, contributing to planetary defense efforts. The observatory places a strong emphasis on photometric observations of GRB optical counterparts, especially immediately following their discovery by space-based observatories. Additionally, it hosts a successful supernova search program, leading to the discovery of supernova SN 2023rve after nine months of continuous effort.

Key Words: astrometry — gamma-ray burst: general — methods: observational — supernovae: general — techniques: photometric — telescopes

1. INTRODUCTION

AKO is a fully remote and robotic observatory, which was established in January 2021 within the Abu Dhabi desert, situated approximately 50 kilometers away from the capital city of Abu Dhabi in the United Arab Emirates (UAE). It is registered with the Minor Planet Center (MPC) of the International Astronomical Union (IAU) and was assigned the code M44. It is noteworthy that the entire observatory, including both the building and the sliding roof, was entirely designed, and constructed by the members of the International Astronomical Center (IAC).

2. SITE CONDITIONS

Utilizing data from a nearby location[2], the observatory benefits from ∼275 clear nights per year, with estimated seeing values in the range 1.0″-1.25″. The altitude of AKO is 90 meters above mean sea level. Initially, it was located under moderately dark skies around Bortle class 5, the observatory's location has since experienced an increase in light pollution, now falling under Bortle class 6. For unfiltered 30-s exposure times gathered with our 0.36m telescope, the limiting magnitude is approximately 18.5. Increasing the exposure time to 180-s raises the limiting magnitude to around 19.5. Additionally, by stacking several 180-s exposure time images, the limiting magnitude can be further improved, reaching up to about 20.5.

[1]International Astronomical Center (IAC), Abu Dhabi, P.O. Box 45015, UAE.

[2]`https://weatherspark.com`

VII Workshop on Robotic Autonomous Observatories (October 16-20, 2023)
Editors: Maria Gritsevich, Alberto J. Castro-Tirado, Petr Kubánek, Shashi B. Pandey, and David Hiriart - DOI: https://doi.org/10.22201/ia.14052059p.2025.59.08

3. MAIN WORK AND OBJECTIVES

The primary focus of our observatory revolves around photometric and astrometric observations. Photometric observations entail studying variable stars, asteroids, GRBs optical afterglows, and kilonovae. Astrometric observations, on the other hand, primarily target newly discovered asteroids and complementing observations from space missions. We also dedicate significant effort to lunar crescent observations, crucial for commencing the new lunar month in many Islamic countries. Additionally, we conduct solar observations utilizing a specialized Hydrogen-α telescope. We aim to establish a remote-operated observatory for swift response during urgent observations and to develop a robotic observatory for streamlined, multi-observation sessions within the same night, without human intervention. Through these initiatives, we aim to create an efficient observatory that actively shares its findings and data with the global scientific community, contributing to international scientific endeavors.

4. EQUIPMENT AND SOFTWARE

In this section, we delve into the essential equipment and software necessary for establishing a robotic observatory, using the infrastructure of AKO as a prime example.

4.1. *The Telescope*

Needless to say, one of the primary components of an observatory is the telescope, and contrary to common misconceptions, a small telescope can indeed facilitate serious scientific work. In AKO, our astronomical journey began with a 5-inch diameter apochromatic refractor, through which we conducted photometric and astrometric observations, subsequently published in refereed journals. However, the advantages of a larger instrument are undeniable, providing observers with the capability to detect fainter objects and obtain more accurate results. The current main telescope at AKO is a 0.36m diameter Schmidt-Cassegrain telescope, with a focal length of 2,737 mm and a focal ratio of 7.7. In addition to this primary instrument, we maintain the 5-inch apochromatic refractor telescope on the same mount, a 90mm diameter Coronado solar telescope on a separate mount, and a dedicated small refractor telescope for lunar crescent observations, particularly during the daytime.

4.2. *The Mount*

It is not an exaggeration to emphasize the critical role of the mount within an observatory. A superior telescope paired with subpar mount risks producing compromised data that could prove challenging to rectify later on. Therefore, our advice is to prioritize investing in a high-quality mount, as it's the most challenging component to upgrade afterward. We initially utilized a commercially available, budget-friendly German equatorial mount and gradually upgraded it. Presently, our observatory is equipped with a 10 Micron GM3000 HPS mount.

4.3. *The Camera and Filters*

We commenced our work with a color camera, which, although it imposed limitations on conducting serious scientific work, we managed to overcome at times. For instance, in photometric tasks, we extracted the green channel from the images and conducted subsequent analysis, closely resembling the utilization of a standard green photometric filter. Presently, our primary camera is the ZWO ASI2600MM Pro cooled mono camera, which provides decent results with very low noise and high-efficiency characteristics.

Regarding filters, we have LRGB filters, HSO narrowband filters, U, V, and Ic Johnson-Cousin photometric filters, and finally a clear filter. All filters have the same thickness to make sure they have the same focus point, and they are hosted in a large 11-position filter wheel. Using BIN1, our image scale is $0.28''$/pixel and the field of view is $29.5' \times 19.7'$.

4.4. *The Guider*

Most mounts require guiding to ensure precise tracking during long exposures. Two common guiding methods exist: the off-axis guider (OAG), which sends starlight to your guide camera using an internal pick-off prism that collects light running of the telescope axis, or to guide using a small telescope attached to the main telescope. Each method has its pros and cons. For long focal lengths, the OAG method is preferred due to its effectiveness in guiding. This is the method employed in AKO. However, for high-end mounts, guiding may not be necessary for short to medium exposures. This is the case in AKO since we upgraded our mount to the current one.

4.5. *Dew Heater and Dew Shield*

These items are strongly recommended. A dew heater is essential on nights when dew formation could otherwise hinder observations. While a dew heater alone may suffice in many cases, a dew shield offers additional protection. Initially, it delays dew formation and safeguards the telescope's mirror or

VII Workshop on Robotic Autonomous Observatories (October 16-20, 2023)
Editors: Maria Gritsevich, Alberto J. Castro-Tirado, Petr Kubánek, Shashi B. Pandey, and David Hiriart - DOI: https://doi.org/10.22201/ia.14052059p.2025.59.08

plate from dust accumulation. Moreover, it shields the telescope from nearby lights, particularly beneficial if the observatory is situated in a light-polluted area.

4.6. *Power & USB Hub and Focuser Motor*

The telescope and its various components, including the camera, filter wheel, dew heater, and focuser, require power and/or USB connections for control. However, numerous cables can potentially affect the tracking accuracy of the mount, also some items might not work properly if connected to a long cable. To mitigate this issue, two solutions are commonly employed: installing a small PC at the telescope or using a power and USB hub.

Given the high temperatures in our desert location and since we use our lunar and solar telescope during the daytime, installing a PC at the telescope is not feasible, leaving us with the option of utilizing a power and USB hub. This setup involves running just one USB cable from the telescope to a PC located inside the control room, approximately 5 meters away.

It is crucial to note that the quality and length of cables play a significant role in the observatory's functionality. Poor-quality cables or those exceeding specified length limitations can lead to issues that require extensive troubleshooting. In a robotic observatory, the focuser motor is particularly important as it enables automatic focusing multiple times throughout the night, ensuring optimal image quality. Therefore, it is essential for the telescope's focuser to be equipped with such a motor for efficient operation.

4.7. *Weather Station and Video Cameras*

A weather station is an indispensable component of any robotic observatory, providing crucial information about environmental conditions such as cloud coverage, rain, temperature, pressure, humidity, and wind speed. This data is essential for ensuring the safety of operations, especially in remote sessions where observatories may be operated from another country. Before opening the observatory dome or roof, it is imperative to verify that conditions are safe. Furthermore, in a robotic observatory, all weather parameters are integrated into the automation software to determine whether to initiate or proceed with programmed observations.

In addition to a weather station, employing multiple cameras to monitor the telescope's position and the dome or roof is highly recommended. This precaution becomes especially important when the telescope lacks encoders and the automation software may potentially lose track of the telescope's position. Without visual monitoring, there is a risk of damaging the telescope. Moreover, installing an all-sky camera is beneficial for assessing sky quality and cloud coverage, enhancing the overall effectiveness of observations.

4.8. *Observatory Controller*

This item serves at least dual purposes within the observatory. Firstly, it acts as the power controller for all observatory components, including the roof motor. Secondly, it is linked to various sensors throughout the observatory, such as the roof limit switches and telescope level sensor. Through integration with the automation software, this controller sends commands to different components to switch on or off. It also acts as a safety measure, preventing the roof shutter from closing if the telescope is not in the desired position.

Additionally, this controller can be utilized for other safety commands due to its connection to the weather station. For instance, it can park the telescope and close the roof shutter during risky weather conditions, although similar actions can also be programmed directly into the automation software.

4.9. *Automation Software*

The automation software acts as the observatory's brain, connecting to all previously mentioned components, it is also used to determine the objects to be observed during the night, including the exposure time, gain, filter, number of frames, ... etc. Advanced scripting allows for detailed observation routines with specific constraints. Various software options are available, with some being free. The choice depends on the observatory's components and desired level of automation. Certain software can fully automate observatory operations efficiently.

5. OBSERVATIONS

This section demonstrates the scientific capabilities of a low-budget robotic observatory. It will be highlighted that such an observatory can indeed participate in several important observations and share its results to others, where they can be used along with others data in publishing papers to find out certain parameters such as the rotational period of asteroids, or orbital period of binary stars, or establishing accurate orbit for a newly discovered asteroid.

5.1. *Asteroid Astrometry and Planetary Defense Program*

One of AKO's initial observations involved astrometric observations of several asteroids, utilizing

VII Workshop on Robotic Autonomous Observatories (October 16-20, 2023)
Editors: Maria Gritsevich, Alberto J. Castro-Tirado, Petr Kubánek, Shashi B. Pandey, and David Hiriart - DOI: https://doi.org/10.22201/ia.14052059p.2025.59.08

the small 5-inch refractor telescope. Subsequently, a paper was published showcasing the remarkable accuracy achievable with such a modest telescope size, demonstrating its efficacy in establishing asteroid orbits and calculating future coordinates with precision (Odeh & Al-Wardat 2023).

In 2022, AKO received an invitation from the Catalina Sky Survey, operated by the University of Arizona, to contribute to planetary defense efforts via the NEOfixer website[3]. This platform aids observers in optimizing their observing lists to maximize the utility of telescope time, with priorities automatically updated based on new observations posted by the Minor Planet Center.

Granted access to the NEOfixer website, AKO began observing critical and newly discovered asteroids of importance. Since then, AKO has confirmed the discovery of over 30 new asteroids and comets (Amrum 2024).

5.2. *Spectroscopic Observations*

While spectroscopic observations are not among AKO's primary objectives, the observatory has conducted basic spectroscopic studies using cost-effective tools. These observations hold significant educational value for public outreach initiatives and university students, providing practical demonstrations of astrophysical principles through live observations.

Using a high-efficiency diffraction grating, AKO obtained spectra from various astronomical objects. Notably, the Balmer series was clearly visible when observing an A-type star, while TiO absorption lines were distinguishable in observations of an M-type star. Methane absorption lines were observed in Uranus and Neptune, while HI and HeI emission lines were detected in a blue hypergiant. Additionally, C2 Swan band absorption lines were identified in observations of a red giant carbon star. Further details regarding these spectroscopic observations were published in a paper by AKO (Odeh 2021).

5.3. *Public Outreach*

AKO places a strong emphasis on public outreach, occasionally observing intriguing phenomena and sharing the results, along with images and simple descriptions, through its social media channels. One such example is the phenomenon of gravitational lensing, where AKO observed the twin quasar PGC 2518326. This quasar, the first identified gravitationally lensed object, appears as two distinct images due to gravitational lensing caused by the galaxy YGKOW G1 situated between Earth and the quasar.

Another observation is the relativistic jet of the galaxy M87 in the Virgo constellation. This galaxy's central black hole ejects a relativistic jet, or plasma jet, outward at velocities close to the speed of light. Both of these events were clearly captured in images taken by the observatory's main telescope, showcasing captivating astronomical phenomena to the public.

5.4. *Astrometric and Photometric Observations for Space Missions*

AKO diligently monitors new space missions and aims to observe them, especially immediately after launch. At this stage, astrometric and photometric data are crucial for some researchers. For instance, AKO observed the *James Webb Space Telescope* (JWST) during its journey to its final orbit, conducting photometric and astrometric observations on 06 January 2022. These observations revealed fluctuations in *JWST*'s magnitude, changing by approximately 1.5 magnitude within half an hour.

Similarly, AKO observed the Orion spacecraft from the *Artemis-1* mission as it returned to Earth on 07 December 2022. Astrometric data provided by AKO along with others were utilized by researchers to construct the spacecraft's trajectory. Additionally, AKO observed the *Jupiter Icy Moons Explorer* (JUICE) shortly after its launch on 14 April 2023, contributing to trajectory calculations alongside data from other observers.

Furthermore, AKO observed the asteroid Dimorphos minutes before the impact of the *DART* mission on 26 September 2022. Despite foggy conditions preventing observation of the impact itself, AKO conducted subsequent observations and detected three tails for the asteroid.

5.5. *Novae and Supernovae Photometry*

Photometric observations of novae and supernovae hold high priority in our observatory. To ensure our results are accessible to interested researchers, we regularly submit our data to the American Association of Variable Star Observers (AAVSO) website[4]. Noteworthy observations include those of the nova U Scorpii on 06 June 2022. Our data from this observation were utilized for detailed analysis reported by Muraoka et al. (2024). In addition to this we conducted photometry for several supernovae, such as SN 2022hrs, SN 2023rve, and SN 2023wrk.

[3] https://neofixer.arizona.edu/

[4] https://www.aavso.org/

VII Workshop on Robotic Autonomous Observatories (October 16-20, 2023)
Editors: Maria Gritsevich, Alberto J. Castro-Tirado, Petr Kubánek, Shashi B. Pandey, and David Hiriart - DOI: https://doi.org/10.22201/ia.14052059p.2025.59.08

5.6. *Photometry for Asteroids and Binary Stars*

Several photometric observations were conducted for asteroids to determine their rotational period, as well as for eclipsing binary stars to ascertain their orbital period. The detailed results of these observations were published in a dedicated paper (Odeh & Al-Wardat 2023).

5.7. *GRB Optical Afterglows and Kilonovae Observations*

Since October 2022, AKO has started photometric observations for GRB optical afterglows, with results being sent to Gamma-ray Coordinates Network (GCN). Among the notable GRBs observed was GRB 221009A, considered the strongest GRB in history. AKO was among the first observatories to follow up on this event. For instance, on 09 October 2023 at 19:30 local time, its magnitude was 14.0, which subsequently dropped to magnitude 14.6 after 45 minutes.

Additionally, AKO is participating in the Kilonova Catcher Program, supported by GRANDMA and the University of Paris. Members of this program contribute to the optical follow-up of gravitational wave (GW) events detected by the worldwide network of GW detectors. These follow-up campaigns aim to detect kilonova emissions arising from the coalescence of two compact objects.

5.8. *Supernovae Search Program*

AKO launched its supernovae search program on 26 November 2022, systematically observing around 90 galaxies daily. The following day, a thorough analysis of the collected data was conducted to identify any potential new supernovae in the images. After nine months of consistent effort, on the evening of 08 September 2023, a bright new star with a magnitude of 14 was observed within the galaxy NGC 1097. Promptly, the team reported this discovery to the International Astronomical Union. The IAU officially documented the discovery and designated it as SN 2023rve (Odeh 2023).

6. CONCLUSION

A fully robotic observatory can indeed be built by enthusiastic astronomers or amateurs with limited budgets. It is not necessary to have all the required components from the beginning. For instance, AKO started with a basic equatorial mount and a 5-inch telescope without any filters and gradually upgraded its equipment over time. Even smaller and moderate-sized telescopes can contribute significantly to serious scientific work. Observers must carefully select objects suitable for their available equipment. Sharing results with others by submitting them to dedicated websites or groups is crucial. This ensures that the efforts put into the observatory yield the maximum benefit to the scientific community.



Fig. 1. The different subsystems of the AKO observatory.

Acknowledgements: I extend my heartfelt gratitude to the exceptional team of AKO for their invaluable contributions to the construction and ongoing dedication to observation and maintenance tasks at the observatory. Special thanks to Khalfan Al-Noimy, Anas Mohammad, Osama Ghannam, Sameh Al-Ashi, and Mohammad Mudallal for their unwavering commitment and hard work.

REFERENCES

Amrum, J. 2024, MPEC statistics, `https://mpec.jostjahn.de/M44-stat.html`
Muraoka, K. et al. 2024, PASJ, 76, 293
Odeh, M. 2023, Transient Name Serv Discov Rep, 1, 2023
Odeh, M. & Al-Wardat, M. 2023, Emir J Space Astron Sci, 1, 4
Odeh, M. 2021, JInst, 16, T12009
Odeh, M. & Al-Wardat, M. 2023, JASS, 40, 19

Revista Mexicana de Astronomía y Astrofísica Serie de Conferencias (RMxAC), **59**, 43–47 (2025)
© 2025: Instituto de Astronomía, Universidad Nacional Autónoma de México
https://doi.org/10.22201/ia.14052059p.2025.59.09

VII Workshop on Robotic Autonomous Observatories (October 16-20, 2023)
Editors: Maria Griffsevich, Alberto J. Castro-Tirado, Petr Kubánek, Shashi B. Pandey, and David Hiriart - DOI: https://doi.org/10.22201/ia.14052059p.2025.59.09

TOWARDS A FULLY ROBOTIC SOLAR OBSERVATORY AT THE UNIVERSITY OF GÖTTINGEN

S. Martens[1] and T. O. Husser[1]

RESUMEN

El Instituto de Astrofísica y Geofísica de Gotinga opera un observatorio solar que permite observaciones del Sol integradas y espacialmente resueltas con una resolución espectral muy alta. La instalación consta de un siderostato de 50 cm en el techo del edificio de la Facultad que alimenta un telescopio vertical de vacío y también un espectrógrafo de transformada de Fourier (ETF) con un poder de resolución > 700.000 a 600 nm. Al implementar y ampliar el sistema de control del telescopio (pyobs), podemos controlar de forma remota el siderostato y el ETF para adquirir y guiar con precisión cualquier objetivo en el disco solar mientras realizamos observaciones espectrales. Actualmente, estamos poniendo en marcha un modo de observación totalmente robótico que nos permitirá explotar aún más las capacidades de este observatorio. En particular, el modo robótico nos permitirá realizar observaciones de alta resolución de fenómenos variables en el tiempo, como manchas solares y fáculas solares.

ABSTRACT

The Institute for Astrophysics and Geophysics in Göttingen operates a solar observatory that allows for integrated and spatially resolved observations of the Sun with very high spectral resolution. The setup consists of a 50 cm siderostat on the roof of the faculty building that feeds a vacuum vertical telescope and, finally, a Fourier Transform Spectrograph (FTS) with a resolving power of $> 700,000$ at 600 nm. By implementing and extending the telescope control system `pyobs` we are able to remotely control the siderostat and FTS to accurately acquire and guide on any target on the solar disk while performing spectral observations. Currently, we are commissioning a fully robotic observation mode that will allow us to exploit the capabilities of this observatory even further. In particular, the robotic mode will enable us to make high-resolution observations of time-dependent phenomena such as sunspots and solar faculae.

Key Words: Sun — Spectroscopy — Telescopes

1. INSTRUMENTAL SETUP

The solar telescope at the Institute for Astrophysics and Geophysics in Göttingen consists of two components: a siderostat and a vertical vacuum telescope (VTT). The siderostat is installed on top of the 5th floor of the physics building and is shown in Fig. 1. It consists of two rotating and tilting mirrors that feed light to the VTT below. The vacuum tube of the VTT is built directly into the building, so that its primary mirror is located below the 3rd floor. This telescope has been in operation since September 2008 (Schäfer et al. 2020).

From the VTT, the light enters our optical setup, which is located on the fourth floor of the building and shown in Fig. 2. The light exits the VTT through a collimator onto a parabolic mirror, which reflects the light onto our fiber pickup. The fiber pickup is a circular steel disc with a 2.5 mm hole in the center. Behind the hole is an FC/PC fiber connector such that the fiber head is parallel to the image plane. The fiber finally leads to a Fourier Transform Spectrograph, which was described by Schäfer et al. (2020) to take spectra with a resolution of $R > 7 \cdot 10^5$ at 600 nm. The light that is reflected by the steel disk is again focused by another parabolic mirror and a collimator. The light is then filtered using a neutral-density filter with an optical density of 5. Using a focus lens followed by a flat mirror, the light hits the CMOS detector of our camera. The light collected by this camera is used for acquisition and guiding.

2. SCIENCE CASES

The two science cases that are presented here both consider the Sun as a star. This means that we do not try to learn specifics about the Sun itself, but use the Sun as a very convenient test case and relate our findings to other stars. In particular,

[1]Institute for Astrophysics and Geophysics, University of Göttingen, Friedrich-Hund-Platz 1, 37077 Gttingen, GER, (sven.martens@uni-goettingen.de).

VII Workshop on Robotic Autonomous Observatories (October 16-20, 2023)
Editors: Maria Gritsevich, Alberto J. Castro-Tirado, Petr Kubánek, Shashi B. Pandey, and David Hiriart - DOI: https://doi.org/10.22201/ia.14052059p.2025.59.09



Fig. 1. Siderostat on top of the roof of the physics building in Göttingen. M1 on the right is tracking the target and M2 on the left is feeding the light into the vertical vacuum telescope.

the structure of the photosphere of a star can have a large impact on its spectrum. By observing the Sun with a high-resolution spectrograph, we are able to quantify the line-by-line effects of different features that are currently only observable for solar spectral data. This enables us to inform spectroscopic observations of other stars based on our findings.

2.1. *The Quiet Sun*

Non-active, quiet regions of the Sun still show granulation due to convection. Granulation induces changes to the observed spectral lines. This effect is relevant for stellar radial velocity measurements and exoplanet transit spectroscopy and has already been studied using the solar observatory in Göttingen by Ellwarth et al. (2023). In particular, they performed centre-to-limb observation of the sun to analyze how spectral line shapes and positions change due to granulation as a function of position on the solar disk. We can improve on the results by Ellwarth et al. (2023) by robotizing our solar observatory to enable more efficient raster observations of the solar disk.

2.2. *The Active Sun*

Observing the sun reveals many active regions such as sunspots and solar faculae. In particular, sunspots affect the wavelength and shape of spectral lines and can add such variation as to obscure exoplanets altogether. Regarding solar faculae there is currently little to no time resolved data to study any potential effect on stellar spectra. Sets of data on both these types of features from such a high resolution spectrograph would be a large step in addressing the current international effort to separate stellar

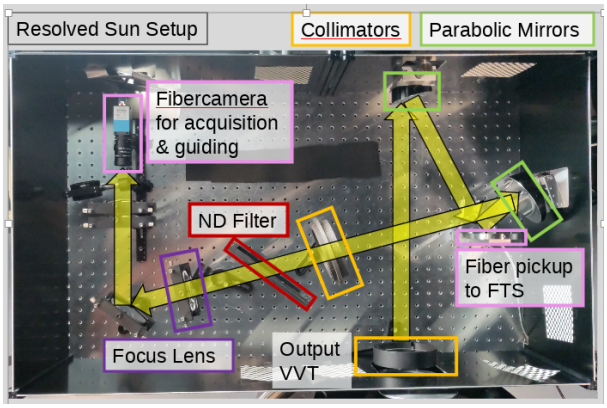


Fig. 2. Resolved sun setup. The path of the light exiting the vertical vacuum telescope to the fiber pickup and finally the fibercamera is shown.

activity from exoplant signals. To observe these features, we employ robotics to allow for efficient and importantly time-dependent observations.

3. OBSERVATION CONTROL SYSTEM

The observation control system (OCS) we use is the Python-based and open source `pyobs`[2] by Husser et al. (2022). Out of the box, it supports many popular cameras and includes common functionality like focusing, sky-flatfielding, acquisition and guiding and pipeline calibration. `pyobs` enables remote and fully autonomous control and is fully configurable and extendable. It follows the principle of one process per block of functionality, where these blocks are called modules. It was designed for night-time observations and is run on three night-time telescopes currently. To extend `pyobs` to solar observations, we simply implemented new modules that give us the functionality we need. In the following, we will describe the modules we added and how they work.

3.1. *Sun Camera*

As described in Sec. 1 and shown in Fig. 2, we use a camera for acquisition and guiding. This camera is implemented in `pyobs` as a simple camera module called fibercamera. The sun camera is implemented as a virtual camera that forwards all calls to the fibercamera, but it adds a world coordinate system (WCS) to each image. To do so, the sun camera needs the solar position and radius on the image. To find these parameters, we employ a solar disk detection.

[2] `https://www.pyobs.org/`

VII Workshop on Robotic Autonomous Observatories (October 16-20, 2023)
Editors: Maria Gritsevich, Alberto J. Castro-Tirado, Petr Kubánek, Shashi B. Pandey, and David Hiriart - DOI: https://doi.org/10.22201/ia.14052059p.2025.59.09

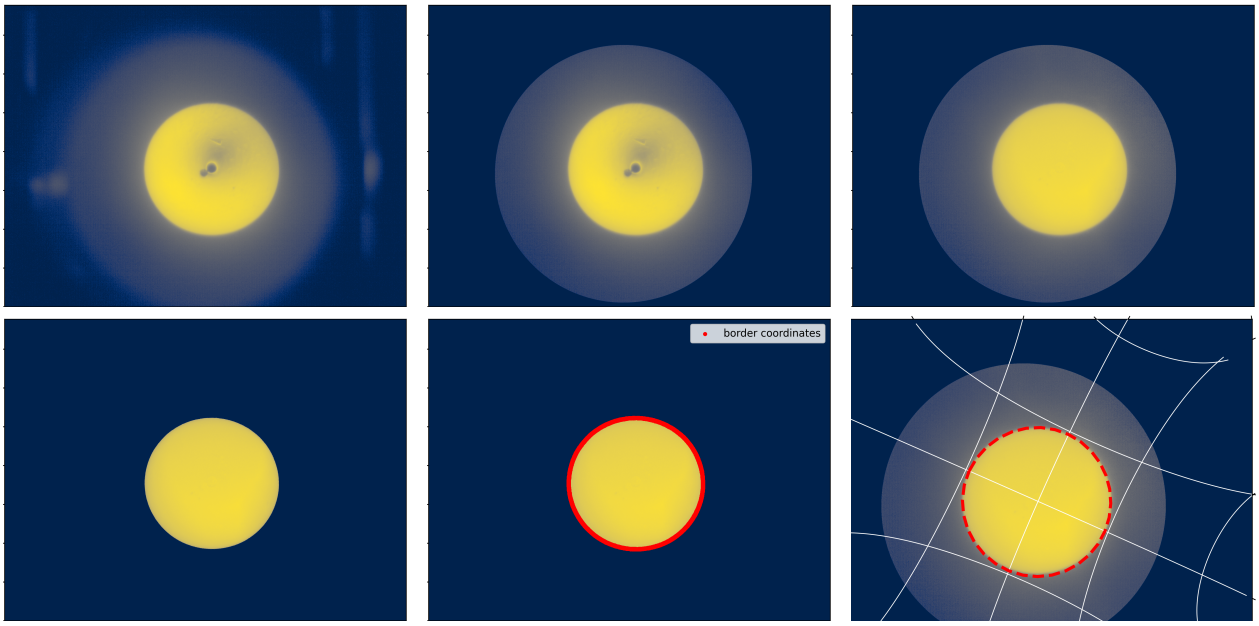


Fig. 3. Illustration of the different analysis steps for the solar disk detection, starting with the raw image from the fibercamera in the upper left panel, to the detected solar disk shown in the bottom right panel.

3.2. *Solar Disk Detection*

The aim of the solar disk detection is to derive the center and radius of the solar disk on an image taken by the fibercamera. Figure 3 illustrates the different steps of this analysis. First, we filter the background of the image that contains reflection from parts of our optical setup using a predefined mask. Then we apply a flatfield correction, which most notably causes the holes of the fiber pickup to seemingly disappear in the image.

Next, we derive a sun mask by creating a histogram of the current image, which can be seen in Fig. 4. This histogram always shows two peaks: One peak around zero that is caused by pixel that do not belong to the solar disk, and one peak offset from zero that contains the solar disk pixels. To separate these distributions, we find the minimum between them and use it as a cutoff value. Pixels with values below the cutoff value are defined to not belong to the solar disk and are filtered from the image. After that, we find the border coordinates of the solar disk pixels, which describe the outline of the sun in our image.

Due to our optical setup described in Sec. 1, the image recorded by the fibercamera contains large distortions, especially towards the edges of the image. To correct for this distortion, we use an image of a regular point grid, which is shown in Fig. 5. We detect the dots in this image using a cutoff and derive the simple imaging polynomial (SIP). By applying the SIP, we can finally fit a circle to the distortion corrected border coordinates of the solar disk pixels to derive the solar position and radius in the image.

3.3. *Solar Acquisition and Guiding*

We use a helioprojective radial coordinate frame to define the position of each point on the solar disk. This coordinate frame is defined by a radial coordinate ranging from 1 to 0 from the center of the solar disk to its limb and a counter-clockwise angular coordinate that is 0 at solar north (Thompson 2006). To acquire and guide on any target on the solar disk given this coordinate frame, we simply derive offsets between the current positions of the telescope and the target coordinates.

3.4. *Fourier Transform Spectrograph*

The Fourier Transform Spectrograph is conventionally controlled via LabVIEW using a computer that is located in the laboratory. To allow for remote control of the FTS, we added a webserver that allows us to communicate with it via `pyobs` through LabVIEW. To start and observation via `pyobs`, a setup file is needed that contains all relevant settings. The result of an observation is a FITS file that contains the spectrum, the interferogram and the field of view image from the sun camera.

VII Workshop on Robotic Autonomous Observatories (October 16-20, 2023)
Editors: Maria Gritsevich, Alberto J. Castro-Tirado, Petr Kubánek, Shashi B. Pandey, and David Hiriart - DOI: https://doi.org/10.22201/ia.14052059p.2025.59.09

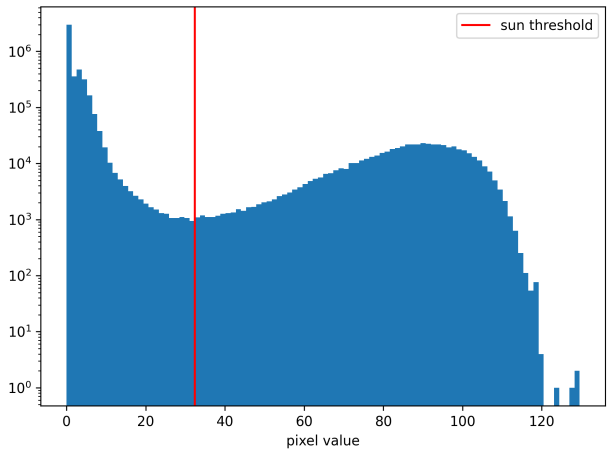


Fig. 4. Histogram of pixel values for the background filtered and flatfield corrected fibercamera image. The peak on the left corresponds to pixels that are not part of the solar disk, whereas pixels on the right belong to the solar disk. The sun threshold in red is derived as the minimum between these peaks. Pixels above the threshold are considered to be part of the solar disk.

3.5. *Robotic Solar Observatory*

We use the observation portal from Las Cumbres Observatory (LCO)[3] to manage observation requests. We modified it to allow for day-time observations and added a command-line interface to add requests and see the status of submitted requests. The robotic control of the solar observatory is implemented via the *Mastermind* module from `pyobs`. This module runs tasks that an additional scheduler module provides it with. In our case, the scheduler checks the observation portal for new requests and creates tasks based on these requests. If there is currently no active request, the scheduler will create a default task to minimize downtime. Currently, the default task is to observe the center of the Sun. Finally, the task runner executes the tasks provided by the scheduler. It has full control over the telescope, including acquisition and guiding, the cameras and the FTS.

Other remote and robotic solar observatories exist, such as the Swedish Solar Telescope (Scharmer et al. 1985), the Global Oscillation Network Group (Kennedy & GONG Team 1994) and the Laser-based Absolute Reference Spectrograph at the Vacuum Tower Telescope at the Observatorio del Teide on Tenerife (Löhner-Böttcher et al. 2017) to name just a few. However, to our knowledge, the setup presented here is one of the first ground-based robotic observatories that is capable of taking high-resolution spectra of the Sun over a large spectral range.

[3] `https://github.com/observatorycontrolsystem/observation-portal`

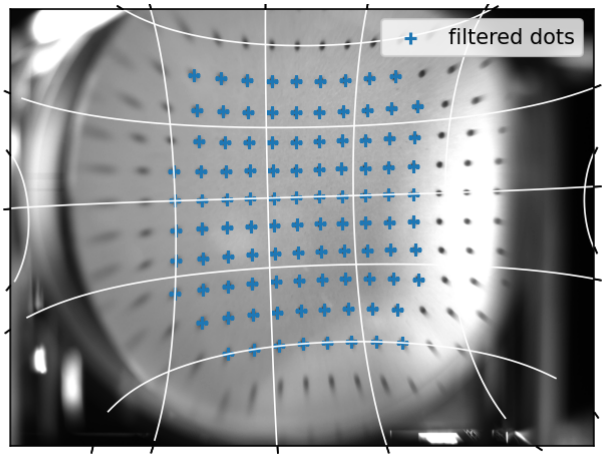


Fig. 5. Image of a regular point grid taken with the fibercamera. The distortion in the image is accounted for as shown by the white lines based on the analysis of the filtered dots.

4. SUMMARY & OUTLOOK

We presented the solar observatory at the University of Göttingen, which consists of a 50 cm siderostat, vertical vacuum telescope and a high-resolution Fourier Transform spectrograph. We demonstrated that there are multiple science cases that benefit from robotic observations with our observatory. Furthermore, we described our implementation of `pyobs` as an OCS, by extending it to support solar observations. `pyobs` allows us to remote control the observatory, and we are currently commissioning the robotic mode.

As described in Sec. 3.5, currently the default task that the scheduler creates is to observe the center of the Sun. We are working on having different observing modes for observations of the faculae, sunspots or the quiet Sun. Each mode would define and create a corresponding task. For example, in the sunspot observation mode we work out which sunspots are currently observable on the solar disk based on publicly available space weather data. The scheduler will then create default tasks to observe these sunspots. This approach still allows for the observation of specific objects by users, but minimizes downtime when there are no user defined requests.

REFERENCES

Ellwarth, M., Schäfer, S., Reiners, A., & Zechmeister, M. 2023, A&A, 673, A19

Husser, T.-O., Hessman, F. V., Martens, S., Masur, T., Royen, K., & Schäfer, S. 2022, FrASS, 9, 891486
Kennedy, J. R. & GONG Team. 1994, in ASPC, 55, 188
Löhner-Böttcher, J., Schmidt, W., Doerr, H. P., Kentischer, T., Steinmetz, T., Probst, R. A., & Holzwarth, R. 2017, A&A, 607, A12
Schäfer, S., Royen, K., Huster Zapke, A., Ellwarth, M., & Reiners, A. 2020, in Proc. SPIE Conference Series, 11447A9
Scharmer, G. B., Brown, D. S., Pettersson, L., & Rehn, J. 1985, ApOpt, 24, 2558
Thompson, W. T. 2006, A&A, 449, 791

VII Workshop on Robotic Autonomous Observatories (October 16-20, 2023)
Editors: Maria Gritsevich, Alberto J. Castro-Tirado, Petr Kubánek, Shashi B. Pandey, and David Hiriart - DOI: https://doi.org/10.22201/ia.14052059p.2025.59.09

Revista Mexicana de Astronomía y Astrofísica Serie de Conferencias (RMxAC), **59**, 49–53 (2025)
© 2025: Instituto de Astronomía, Universidad Nacional Autónoma de México
https://doi.org/10.22201/ia.14052059p.2025.59.10

VII Workshop on Robotic Autonomous Observatories (October 16-20, 2023)
Editors: Maria Gritsevich, Alberto J. Castro-Tirado, Petr Kubánek, Shashi B. Pandey, and David Hiriart - DOI: https://doi.org/10.22201/ia.14052059p.2025.59.10

THE IMPACT OF THE SITE QUALITY OF THE ZADKO OBSERVATORY ON ITS SCIENTIFIC RESULTS

Bruce Gendre[1,2,3], Richard Tonello[4,5], Mitchell Studdert[4,5], David Coward[1], Alain Klotz[6], Eloise Moore[1], John Moore[1], and Fiona Panther[1,7]

RESUMEN

Presentamos el estudio de la calidad del cielo del Observatorio Zadko, centrándonos en el brillo del cielo y los efectos del clima en la eficiencia del observatorio. Discutimos estos efectos y sus consecuencias para los objetivos científicos del observatorio. Como se esperaba, la calidad general del cielo ha disminuido durante la última década. Sin embargo, esta disminución se debe principalmente al patrón climático en el emplazamiento más que a la contaminaciń lumínica. Ponemos énfasis en que lo importante es la preservación de la oscuridad del cielo para los observatorios pequeños, con el fin de estabilizar la degradación global de la calidad del sitio, ya que esto impacta directamente el retorno científico de las observaciones.

ABSTRACT

We present the site quality of the Zadko Observatory, focusing on the brightness of the sky and the effects of the weather on the efficiency of the Observatory. We discuss these effects and their consequences for the scientific goals of the Observatory. Without surprise, the overall sky quality had decreased during the last decade. However, this decrease is mostly due to the weather pattern at the Observatory rather than the light pollution. We put an emphasis on how important the preservation of the sky darkness is for small observatories, in order to stabilize the global degradation of the site quality, as this directly impacts the scientific return of the observations.

Key Words: History and philosophy of astronomy — Site testing — Atmospheric effects — Light pollution

1. INTRODUCTION

The Zadko Observatory is located approximately 70 kilometres north of Perth in the Shire of Gingin, Western Australia (Coward et al. 2017; Moore et al. 2021). It hosts the 1.0 m RitcheyChrtien f/4 Zadko Telescope, which was installed in June 2008; this telescope is the only fully robotic telescope hosted by a Western Australian University (UWA), and is the only metreclass optical facility at this southern latitude between the east coast of Australia and South Africa. At the time of its construction, the Zadko Observatory was a state-of-the-art facility, and for many years the Zadko Telescope performed observation campaigns in collaboration with various Australian and international research teams (Coward et al. 2011). This is mostly due to the Observatory being in a very desirable location: some parts of the sky can be observed only from the west coast of Australia in night conditions in the early morning. This has provided a niche opportunity for engaging in pure research collaborations, international partnerships and research training on site (Laas-Bourez et al. 2011), with approximately one hundred scientists both National and International having worked with the Observatory. Since that time, the observatory has expanded to host several other instruments, which are devoted to various research or commercial programs.

In a companion paper (Moore et al., these proceedings), we have described how the global operations of the observatory are managed. In this paper, instead, we will focus on the scientific goals of the observatory, and how the quality of the site impacts those goals. In Section 2 we will explain the scientific goals of the Observatory. In Section 3 we will explain how the darkness of the sky is impacting our goals and how we try to mitigate this effect. In Section 4 we show the effect of celestial bodies on the observations. In Section 5 we will describe in more detail the effects of the weather on the assets of the

[1]University of Western Australia, OzGrav ARC Centre of Excelence, 35 Stirling Highway, M013, 6009 Crawley, WA, Australia.
[2]Present address: University of the Virgin Islands, 2 John Brewer's Bay, St Thomas, 00802, VI, USA.
[3]Email: bruce.gendre@gmail.com
[4]Gravity Discovery Center, 1098 Military Road, 6503 Yeal, WA, Australia.
[5]Chiro Observatory, IAU code 320.
[6]IRAP, Universite de Toulouse, CNRS, CNES, UPS, 31401, Toulouse, France.
[7]Forest Fellow.

VII Workshop on Robotic Autonomous Observatories (October 16-20, 2023)
Editors: Maria Gritsevich, Alberto J. Castro-Tirado, Petr Kubánek, Shashi B. Pandey, and David Hiriart - DOI: https://doi.org/10.22201/ia.14052059p.2025.59.10

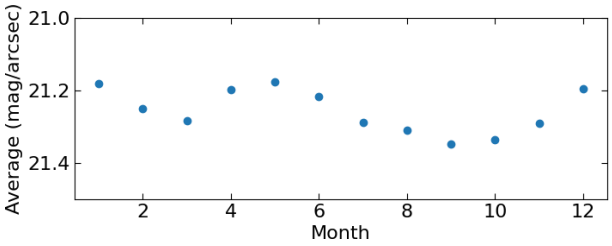


Fig. 1. Evolution of the mean darkness of the sky along the year, with the effect of the Galactic bulge clearly visible. The measurements have been taken at the start of the night, explaining why the effect of the Galactic bulge is at its maximum a couple of months before it reaches the zenith.

Observatory, before concluding. A forthcoming paper (Gendre et al., in preparation) will explore in more detail the weather patterns at the Observatory which are not addressed here.

2. SCIENTIFIC GOALS OF THE OBSERVATORY

Historically, the Zadko Observatory has been used to study the transient sky (Coward et al. 2010), and particularly explosive events, such as gamma-ray bursts, supernovae, and the emitters of gravitational wave sources (LIGO Scientific Collaboration et al. 2012; Andreoni et al. 2017; Antier et al. 2020; Gendre et al. 2021). However, due to the transient and random nature of these events, the Observatory was using fillers such as asteroid observations, long term monitoring of red dwarf stars, satellite follow-up, or even space junk monitoring (Zic et al. 2020; Micheli et al. 2021).

However, Australia is expanding its role in the space sector, both commercially and in strategic defence. Space situational awareness programs, for instance, are an increasing priority. Space debris can be a serious hazard for commercial, communications, military and research satellites.

Potential Earth colliders, so-called hazardous Near-Earth Objects (NEOs) (Gladman et al. 2000) are another well-known threat and are usually detected only a few hours before impact, and can pose a direct hazard to human activities. Space agencies, such as ESA, monitor the sky continuously to provide an early warning for such an event, of which the Zadko Telescope has been utilized for this task in the preceding few years (Conversi et al. 2021). All of those programs are now routinely run at the Observatory, and with the current upgrade of the facility, it is foreseen they will take more and more importance.

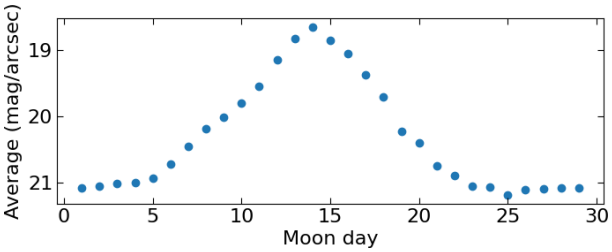


Fig. 2. Breakout of the sky luminosity along one Moon cycle, averaged over 12 months. The new moon is located at phase 0.

One of those programs, for instance, uses the Zadko Telescope to perform follow-up of radio observation of asteroids (Kruzins et al., in preparation). This kind of program requests a long duration follow-up, as the celestial body is in rotation, with a stable sky transparency, and a low brightness of the sky, due to the objects being very faint. In the following, we will use this program as a template for our considerations.

3. IMPACT OF THE DARK SKY AND HOW TO MITIGATE LIGHT POLLUTION

The Zadko Observatory has been established on a pre-existing scientific precinct, beside another Observatory aimed at outreach activities, the Gravity Discovery Center Observatory (hereafter the GDC observatory)[8]. It was constructed in 2009 with, at that time, no controls to evaluate or mitigate the effects of light pollution. However, with the continued expansion of Perths northern suburbs it was noted there has been a significant increase in light pollution on the southern horizon (Falchi et al. 2016). In fact, under favourable conditions of low humidity and no cloud the light dome extends to an altitude of approximately 25 degrees above the southern horizon. In the case of unfavourable conditions, the light pollution can reach an altitude of 35 degrees above the southern horizon.

Starting in 2018, astronomers at the GDC observatory, preoccupied by the increasing glow of the sky and its impact on the outreach activities, began monitoring of the sky brightness and management of onsite lighting to reduce the effects of local light pollution on both the Zadko and GDC observatories. For this purpose, they established the Gingin Dark Sky Reserve, which encompasses 3211 Km^2 of protected dark sky, centered around the GDC and Zadko Observatories.

[8] See https://gravitycentre.com.au/wp-content/uploads/2023/12/Annual-Report-2022-2023-Final-2-1.pdf for more information

VII Workshop on Robotic Autonomous Observatories (October 16-20, 2023)
Editors: Maria Gritsevich, Alberto J. Castro-Tirado, Petr Kubánek, Shashi B. Pandey, and David Hiriart - DOI: https://doi.org/10.22201/ia.14052059p.2025.59.10

They started by replacing the majority of outdoor lighting on the site, and brought them into compliance with international dark sky standards. The impact of that local light pollution on the observatories was however insignificant, as one could expect: most of the issues arises from the diffused light and not the direct sources (Hänel et al. 2018). In fact, observations taken in 2023 (Gendre et al. in preparation) have shown that with all onsite lighting turned on, the the limiting magnitude at zenith was reduced by only 0.1 magnitude.

The GDC astronomers also started to continually monitor the sky quality, in order to record any changes, establish trends, and assess whether local light pollution has increased/decreased within the reserve. For that purpose, a Unihedron SQM-LU sky quality instrument has been installed on the roof of the GDC observatory, together with an array of detectors within the reserve itself. These observations demonstrated that the light pollution dome from Perth is the largest factor in limiting magnitude (as it can be also infered from Falchi et al. 2016), with an effect of 0.5 magnitudes.

With the dark sky reserve, centred around the Gingin Gravity Precinct to help mitigate the ingress of light pollution towards the observatories, and a strict lighting management plan in place within 40 kilometres around the observatories, the sky quality started to stabilize. With all those efforts, the current sky brightness is at mimimum 21.4 magnitude.arcsec^{-1}, which gives the limit of what can be observed on site.

4. EFFECT OF CELESTIAL BODIES ON OUR SCIENTIFIC GOALS

Natural celestial bodies can also affect the sky background (Falchi et al. 2016; Hänel et al. 2018). While this is barely noticeable within cities, in a modern observatory, established at a reasonable distance from light pollution, the sky transparency allows one to notice the effect of the Galaxy bulge, which rises in the sky in April, and passes close to the zenith in June-July in the Southern hemisphere. In Figure 1, it is possible to see that the Galaxy has a 0.2 magnitude effect on the sky luminosity, and that the best period to observe faint objects is during the Southern Hemisphere's Spring.

Another effect clearly at play is the effect of the Moon, as anybody could guess. We present it on Figure 2. Following the standard naming convention (clear nights being the nights close to the full moon, and dark ones being close to the new moon), clear nights are about 3 magnitudes brighter than dark nights, and this has some obvious consequences on the faintest objects one can detect with the Zadko telescope: during clear nights with full moon, it is very difficult to detect objects fainter than about 18.5 magnitudes.

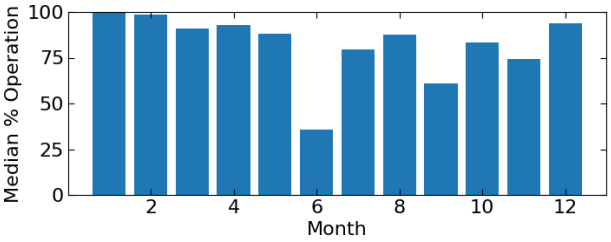


Fig. 3. Mean efficiency of the Zadko Observatory during a typical year, averaged over one month, and using the same method than in Figure 4. One can clearly see the effect of the wet season.

This has some consequences, as the asteroids observed for the current program are ranging in luminosity between 12 and 20. While there is no restrictions for bright objects, this can bias our observation program toward nearby or large events (i.e. those which are reflecting more light and/or presenting less attenuation due to the distance). For this reason, it is clear that it is impossible to dedicate the Zadko telescope to a single class of event, and that the scientific scheduling of the observations has to be carefully planned.

5. IMPACT OF THE WEATHER AND HOW TO PROTECT THE ASSETS

The second important effect one has to consider is that of the weather, particularly the rain and the humidity (Abbot et al. 2021). It is obviously not desirable to have the roof of an observatory open whilst it is raining, which in turn can have a serious impact on available viewing time. As most modern observatories use electronic cameras which have a given working range for temperature, humidity and pressure, it is the responsibility of the observatory operators to maintain those parameters in the correct range to protect these valuable assets. A normal operation efficiency is of the order of 60% for a professional observatory not located on a top quality site (Abbot et al. 2021). In Figure 3 we present the efficiency of the site for the year 2023.

Our overall operation efficiency is of the order of 80%, which is very good for an observatory like the Zadko Observatory, with some months being near an efficiency of 100%. Those nights are mainly during the hot, dry season (traditionally known as "Birak" by the Noongar People). This is confirmed with more granularity (as displayed in Figure 4): for a

VII Workshop on Robotic Autonomous Observatories (October 16-20, 2023)
Editors: Maria Gritsevich, Alberto J. Castro-Tirado, Petr Kubánek, Shashi B. Pandey, and David Hiriart - DOI: https://doi.org/10.22201/ia.14052059p.2025.59.10

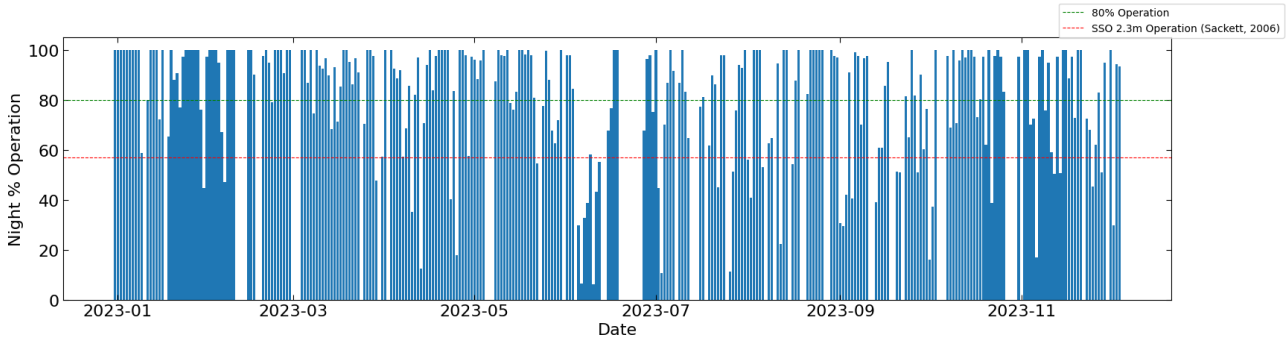


Fig. 4. Efficiency of the Zadko Observatory, expressed as the amount of time the roof was opened vs the amount of available time during a given night. The dotted red line represent the Siding Spring Observatory efficiency measured in 2006, as indicated in Sackett (2006)

fair amount of nights within the year we reach an efficiency of 100%. However, one can clearly see that most nights have a period of some minutes to a couple of hours of closure, due to the humidity coming from the sea. In winter there are many rainy and foggy nights preventing operation during the whole night.

This has some consequences on how long a continuous observation can be. While during the summer it is possible to have long observations, this is not the case during the winter. Indeed, one effect not presented on these figures is the rapid evolution of the seeing of the site (which can change dramatically within minutes), indicating that there are cloud sheets passing through the sky (see Gendre et al. for a full discussion of this effect). Each of them can trigger the closure of the roof to protect the observatory assets, blocking a continuous observation. One can consider that observations undertaken at the Zadko Observatory need to factor in that they won't be continuous, except during the good season. This has consequences for all observation policies, and requests specific methods of data analysis to correct its effects within the data.

6. CONCLUSION

The Gingin Gravity Precinct, despite it being close to a major source of Light Pollution (Perths northern suburbs), was the logical place to locate the Zadko Observatory. With its established infrastructure, education and research programs, the Precinct is the perfect place to instigate, demonstrate and educate people. However, this has not taken into account the scientific goals set for an Observatory. Without constant evaluation and monitoring of the site parameters, it is clear from the recent data collected that the scientific astronomical activities of the Zadko Observatory may be at risk.

The current measures to continue to improve the darkness of the sky include that all external light fixtures are to be shielded or mounted underneath the awning of buildings to mitigate the amount of stray light scattered up into the air, and to have a colour corrected temperature of 3000K or less. At greater distance from the Observatory, a buffer zone of 3211 square kilometres had been created, in which the GDC astronomers are working with the local government to change public lighting to be dark sky compliant. Finally, a public education campaign is also in place to educate the locals on the effects of light pollution which can assist in mitigating its locally.

Albeit the dark sky reserve project was initiated to protect:

- Astronomical Education and Tourism;
- Astronomical/ Astrophysical Research;
- Local Aboriginal Cultural Heritage;
- Local Wildlife, Bird, Insect, amphibian and Coastal marine life and habitats found within the local ecosystem

it has been of great help to mitigate the degradation of the dark sky quality. Future monitoring with upgraded equipment will give a better sample of the effect of local and distant light pollution domes and their impact. It will also assist in the annual reporting required by Dark Sky International (formerly International Dark Sky Association) to demonstrate the continual protection of the accredited Dark Sky Reserve.

Unfortunately, the climate change within the last few years has had some more serious effects, with some years being particularly humid, and an increasing trend of rainy nights preventing the observatory

VII Workshop on Robotic Autonomous Observatories (October 16-20, 2023)
Editors: Maria Gritsevich, Alberto J. Castro-Tirado, Petr Kubánek, Shashi B. Pandey, and David Hiriart - DOI: https://doi.org/10.22201/ia.14052059p.2025.59.10

to stay operating the whole night. It is not possible to really mitigate this effect, but rather to take it into account when defining the future priorities and scientific goals of the observatory: the scientific policy of any observatory has to be revised from time to time to reflect changes in local conditions. Not doing so will only bring frustrations when the previous goals are not fulfilled or no longer attainable.

Acknowledgements: This research was supported by the Australian Research Council Centre of Excellence for Gravitational Wave Discovery (OzGrav), through project number CE170100004. E.M. acknowledges support support from the Zadko Postgraduate Fellowship and International Space Centre (ISC).

At the Gravity Precinct, located in the Shire of Gingin, the Gravity Discovery Centre & Observatory, and the University of Western Australia acknowledge the Yued Noongar people as the traditional owners of the land on which it is situated. The Yued Noongar remain the spiritual and cultural custodians of this land, where they continue to practise their values, languages, beliefs and knowledge.

REFERENCES

Abbot, H. J., Munro, J., Travouillon, T., et al. 2021, PASP, 133, 095001. doi:10.1088/1538-3873/ac1f3b

Antier, S., Agayeva, S., Aivazyan, V., et al. 2020, MNRAS, 492, 3904. doi:10.1093/mnras/stz3142

Andreoni, I., Ackley, K., Cooke, J., et al. 2017, PASA, 34, e069. doi:10.1017/pasa.2017.65

LIGO Scientific Collaboration, Virgo Collaboration, Abadie, J., et al. 2012, A&A, 539, A124. doi:10.1051/0004-6361/201118219

Conversi, L., Koschny, D., Micheli, M., et al. 2021, ESA's NEO Coordination Centre Observational Network, in 7th IAA Planetary Defense Conference, Vienna

Coward, D. M., Todd, M., Vaalsta, T. P., et al. 2010, PASA, 27, 331, doi:10.1071/AS09078

Coward, D. M., Gendre, B., Sutton, P. J., & Howell, E. J. 2011, MNRAS, 415, L26

Coward, D. M., Gendre, B., Tanga, P., et al. 2017, PASA, 34, 16

Falchi, F., Cinzano, P., Duriscoe, D., et al. 2016, Science Advances, 2, e1600377, doi:10.1126/sciadv.1600377

Gendre, B., Coward, D., Moore, J., et al. 2021, RMxAC, 53, 124, doi:10.22201/ia.14052059p.2021.53.24

Gladman, B., Michel, P., and Froeschl, C. 2000, Icar, 146, 176

Hänel, A., Posch, T., Ribas, S. J., et al. 2018, J. Quant. Spec. Radiat. Transf., 205, 278. doi:10.1016/j.jqsrt.2017.09.008

Laas Bourez, M., Coward, D. M., Klotz, A., Boer, M. 2011, Advances in Space Research, 47, 3

Micheli, M., Koschny, D., Conversi, L., et al. 2021, Acta Astronautica, 184, 251, doi:10.1016/j.actaastro.2021.04.022

Moore, J. A., Gendre, B., Coward, D. M., et al. 2021, RMxAC, 53, 35, doi:10.22201/ia.14052059p.2021.53.08

Sackett, P. D. 2006, Report to the Australian Academy of Science, available at https://www.atnf.csiro.au/nca/sso.pdf

Zic, A., Murphy, T., Lynch, C., et al. 2020, ApJ, 905, 23, doi:10.3847/1538-4357/abca90

Revista Mexicana de Astronomía y Astrofísica Serie de Conferencias (RMxAC), **59**, 55–61 (2025)
© 2025: Instituto de Astronomía, Universidad Nacional Autónoma de México
https://doi.org/10.22201/ia.14052059p.2025.59.11

VII Workshop on Robotic Autonomous Observatories (October 16-20, 2023)
Editors: Maria Griffsevich, Alberto J. Castro-Tirado, Petr Kubánek, Shashi B. Pandey, and David Hiriart - DOI: https://doi.org/10.22201/ia.14052059p.2025.59.11

ADVANCED WEATHER CONTROL SYSTEM AT THE TJO TELESCOPE

F. Domene[1], E. Herrero[1], P. Gil[1], D. Baroch[1], and A. Rojas[1]

RESUMEN

Los observatorios robóticos terrestres desempeñan un papel clave en la astronomía moderna al permitir la recogida automatizada y continua de datos de objetos celestes. Sin embargo, su funcionamiento depende en gran medida de las condiciones ambientales. Una respuesta automatizada y rápida del Sistema de Control Meteorológico (WCS) cuando las condiciones ambientales se vuelven adversas es fundamental para preservar la integridad del hardware del observatorio y garantizar datos astronómicos de alta calidad. Para hacer frente a estos retos, el nuevo WCS del Telescopio Joan Oró (TJO) del Observatorio del Montsec incorpora redundancia multisensor con varios algoritmos de redundancia, y mecanismos robustos de filtrado y validación de datos, mejorando la fiabilidad y precisión de los procesos de toma de decisiones relacionados con la meteorología y la calidad observacional.

La integración de estas características en el WCS permite al Sistema de Control del Observatorio (OCS) tomar decisiones informadas y oportunas sobre la programación de las observaciones, la protección del hardware y la adquisición de datos. Este sistema mejora significativamente la eficiencia y fiabilidad de los programas de observación astronómica llevados a cabo en el TJO. Tras un año de operaciones con el nuevo sistema, los resultados han sido excelentes, con una notable mejora de las observaciones. El uso de múltiples sensores redundantes y el filtrado de datos han demostrado ser particularmente efectivos, demostrando la eficacia del sistema en la mejora de las capacidades operativas del observatorio bajo diversas condiciones meteorológicas y fallos de hardware.

ABSTRACT

Ground-based robotic observatories play a key role in modern astronomy by enabling automated and continuous data collection of celestial objects. However, their operation is highly dependent on environmental conditions. An automated and rapid response of the Weather Control System (WCS) when environmental conditions become adverse is critical to preserve the integrity of the observatory hardware and ensure high quality astronomical data. To address these challenges, the new WCS of the Joan Oró Telescope (TJO) of the Montsec Observatory incorporates multi-sensor redundancy with various redundancy algorithms, and robust data filtering and validation mechanisms, improving the reliability and accuracy of weather-related decision-making processes and observational quality.

The integration of these features into the WCS enables the Observatory Control System (OCS) to make informed and timely decisions about observing scheduling, hardware protection, and data acquisition. This system significantly improves the efficiency and reliability of astronomical observing programs conducted at the TJO. After one year of operations with the new system, the results have been excellent, with a marked improvement in observations. The use of multiple redundant sensors and data filtering has proven to be particularly effective, demonstrating the system's effectiveness in improving the observatory's operational capabilities under various weather conditions and hardware malfunctions.

Key Words: telescope — weather control system — multi-sensor redundancy — data filtering

1. INTRODUCTION

Environmental monitoring is essential in ground-based astronomical observations. The observatory control system must be agile at responding to different environmental scenarios and the dynamic nature of meteorological variables. In the past, and even nowadays, observatories have depended on human staff to monitor weather conditions during observations. This approach, while functional, often leads to compromises in precision and is prone to human error.

Technology offers significant enhancements in accuracy, precision, and the reduction of errors. These improvements include continuous monitoring, sophisticated data storage, and retrieval mechanisms for comprehensive statistical analysis. The adop-

[1]Institut d'Estudis Espacials de Catalunya (IEEC), c/ Gran Capità 2-4, E-08034 Barcelona, Spain.

VII Workshop on Robotic Autonomous Observatories (October 16-20, 2023)
Editors: Maria Gritsevich, Alberto J. Castro-Tirado, Petr Kubánek, Shashi B. Pandey, and David Hiriart - DOI: https://doi.org/10.22201/ia.14052059p.2025.59.11



Fig. 1. Night view of the OdM. Image credit: E. Herrero.

tion and adaptation of robotic and autonomous telescopes have led to the automation of these tasks, typically relying on weather stations. However, challenges arise when these stations experience errors, malfunctions, or when sensor data becomes biased or unreliable. Such issues can impact the quality of observations, the integrity of hardware, and even the mechanics of the observatory's infrastructure. The repercussions of errors in the weather control system (WCS) range from data loss due to inability to observe, to catastrophic situations involving hardware and mechanical failures. Therefore, the implementation of a robust system that relies on redundancy and data filtering is critical. Such a system should be capable of detecting and rectifying errors, thereby ensuring worry-free observations.

The motivation for developing a new WCS arises from the limitations and inefficiencies of the previous system. The old system depended solely on various sensors from different weather stations installed over time to measure new variables or replace faulty sensors. However, this setup relied on a single sensor for each weather variable. This approach was not only inefficient but also wasteful, as it ignored the potential of utilizing multiple other sensors from different stations.

Moreover, the system required manual intervention whenever a sensor malfunctioned. If a sensor used for measuring a specific weather variable encountered problems, operations had to be paused. This interruption was due to the need for human operators to replace the malfunctioning sensor with another one. That process not only led to operational delays but also resulted in the loss of valuable data during the transition period.

In essence, the need for a new Weather Control System was driven by the desire to overcome these challenges: to make better use of the available sensors, reduce dependency on manual intervention, and minimize data loss due to sensor or device failures.

Furthermore, the new WCS benefits of increased precision in weather variable data through the use of multiple redundant sensors. In the previous system, relying on a single sensor for each weather variable not only limited the system's efficiency but also its accuracy. With the implementation of multiple sensors for the same variable, the new system can cross-verify data, leading to more accurate and reliable measurements.

This redundancy is crucial in weather monitoring for astronomical observations, where precise data is vital. By integrating multiple sensors, the system can compare and contrast the readings from these sensors to identify any anomalies or errors. This approach not only enhances the overall precision of the weather data but also provides a fail-safe mechanism. If one sensor fails or provides inaccurate data, the system can automatically rely on the other sensors without the need for manual intervention, ensuring continuous and accurate monitoring. This improvement is a key factor in the decision to develop a new, more sophisticated Weather Control System.

In this proceedings, we present a comprehensive overview of the Weather Control System employed by the Joan Oró Telescope (TJO). We discuss its design, redundancy and data filtering.

VII Workshop on Robotic Autonomous Observatories (October 16-20, 2023)
Editors: Maria Gritsevich, Alberto J. Castro-Tirado, Petr Kubánek, Shashi B. Pandey, and David Hiriart - DOI: https://doi.org/10.22201/ia.14052059p.2025.59.11

2. THE MONTSEC OBSERVATORY

The TJO telescope is mounted at the Montsec Observatory[2] (OdM), located at an altitude of 1570 m in Sant Esteve de la Sarga, 50 km north of the city of Lleida (Catalonia, Northeastern Spain). This site was carefully selected for its exceptional conditions for astronomical observation. First of all, it is in a region certified as an UNESCO Starlight Reserve[3], and explicitly protected from light pollution by a law of the Catalan Parliament. The night sky brightness at the site reaches values as low as 22.0 mag arcsec^{-2} at the zenith, and between 21.520.6 mag arcsec^{-2} at a height of 45° above the horizon, both in the Johnson V band (Colomé et al. 2008). Secondly, the weather conditions are quite good during the year, allowing operations in around 70% of all the night time. Finally, it has a very low astronomical seeing, with a median value of 0.82" and better than 0.7" during 32% of the night time (Colomé et al. 2010), as reported by five months of measurements using a Robotic Differential Image Motion Monitor (DIMM Sarazin & Roddier 1990).

The observatory has multiple facilities that are devoted to different areas, such as:

- Research: two telescopes offered to the scientific community, the TJO (0.8 m) and the TFRM[4] (0.5 m), and an All-Sky Camera for fireball and meteor detection.
- Teleport: S-band and UHF/VHF facilities for communication with satellites.
- Services to the community: a weather monitoring station of the Catalan Meteorological Service, an atmospheric pollution and quality monitoring station, firefighter surveillance cameras, and radiolinks to provide internet access to hydroelectric generating systems and nearby towns.

3. THE TJO TELESCOPE

The main facility at the OdM is the Joan Oró telescope (TJO), which has been operated by the Institute for Space Studies of Catalonia[5] (IEEC) since its construction in 2004. It is a Ritchey-Chrétien telescope with an aperture of 80 centimeters, and is fully robotic, with no human intervention required apart from supervision and maintenance.

The TJO is equipped with two simultaneous instruments. The main instrument is the Large Area Imager for Astronomy (LAIA), an Andor iKon XL imaging camera with a 4096×4096 back-illuminated sensor, a pixel size of 0.4 arcsec, and a field of view of 30 arcmin. LAIA is mounted together with a rotating filter wheel that contains 5 standard Johnson-Cousins photometric filters (U, B, V, R, and I), 4 Sloan Digital Sky Survey photometric filters (g, r, i, and z), and a narrow filter centered at the Hα line.

The other instrument mounted at the TJO is the Astronomical Mid-Resolution Spectrograph (ARES), an optical spectrograph with a resolution of R=12'000 divided in two spectral windows, one centered at the magnesium triplet (495 to 529 nm) and another centered at the Hα alpha line (634 to 678 nm).

The primary functions of the TJO include satellite surveillance and tracking (SST) activities and scientific research, offering observation time to the scientific community via a Time Allocating Committee (TAC) in two yearly semestral calls for proposals. As for the research areas, the TJO is a multi-purpose telescope, with proposals aimed at stellar variability (e.g. Ribas et al. 2018), stellar activity (e.g. Baroch et al. 2020), transiting exoplanets (e.g. Herrero et al. 2011), Gaia follow-up (e.g. Wyrzykowski et al. 2020), transient sources (e.g. Morales-Garoffolo et al. 2014), or Solar System objects (e.g. Trigo-Rodríguez et al. 2008), among others.

The TJO has been working on a completely unattended control since 2013, requiring minimal human supervision. In order to achieve this level of autonomy, it requires having a reliable, secure, and efficient system that is able to plan, execute, and reduce images completely unattended.

The current system present at the TJO, the Robotic Observatory Control System (ROCS), is divided in two main nodes: one off-site and another on-site, as depicted in Fig. 2. Each of the nodes is equipped with its own database containing identical information, which is synchronized on a routine basis.

The offsite node, located at the IEEC offices in Barcelona, is in charge of the storage and distribution of data. The main system there is the Management for Users in ROCS (MUR), which is the interface where the users can submit proposals, define the observations, and access and download the observed data. Additionally, as part of an agreement with the Spanish Virtual Observatory (SVO), all the images older than a year stored in our database are

[2] https://www.montsec.ieec.cat/
[3] https://en.fundacionstarlight.org/contenido/46-list-starlight-reserves.html
[4] https://www.racab.cat/es/observatori-fabra/tfrm
[5] https://www.ieec.cat/

VII Workshop on Robotic Autonomous Observatories (October 16-20, 2023)
Editors: Maria Griffsevich, Alberto J. Castro-Tirado, Petr Kubánek, Shashi B. Pandey, and David Hiriart - DOI: https://doi.org/10.22201/ia.14052059p.2025.59.11

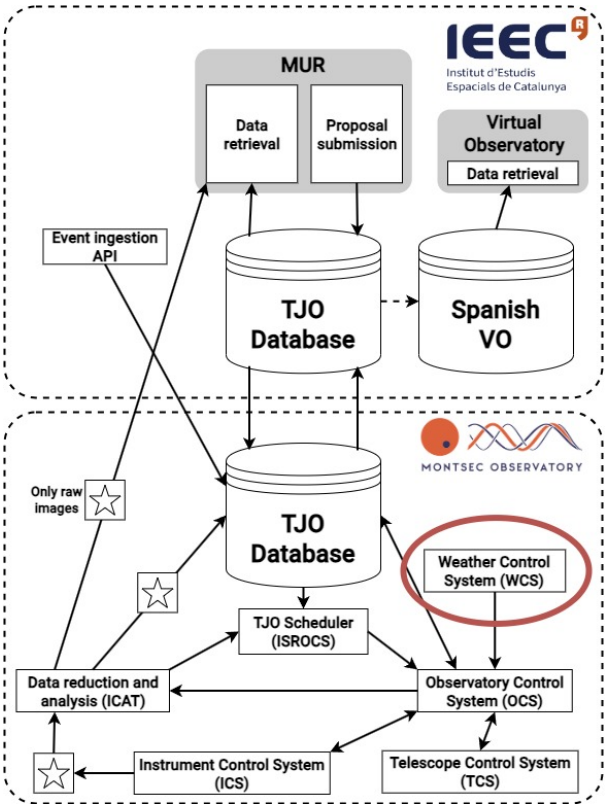


Fig. 2. Schematic diagram of the architecture of the Robotic Observatory Control System (ROCS) of the TJO.

made publicly available through the SVO webpage[6], where more than 300'000 images spanning 10 years are available to the community.

The onsite node is located at the OdM, and it is in control of unattended operations. The main system in this node is the Observatory Control System (OCS), which is responsible for issuing commands to the dome, telescope, and the instrument (via the Telescope Control System, TCS, and the Instrument Control System, ICS) based on the night plan issued by the scheduler and on the weather conditions. Additionally, the system contains a collection of pipelines (The IEEC Calibration and Analysis Tool, ICAT) used to perform data reduction and quality control. Finally, this node also contains the Weather Control System (WCS), which is the one highlighted in red in Fig. 2.

4. DESIGN AND IMPLEMENTATION

The behaviour of the overall system is fundamental to understanding the Weather Control System. The WCS is responsible for retrieving sensor data from weather devices, processing this data, and generating a validated output for each weather variable, which ultimately determines the WCS's overall status. This validated output is subsequently utilized by the Observatory Control System (OCS) to make informed decisions regarding the operation of the Telescope Control System (TCS) and, by extension, the observatory hardware.

When dealing with the challenges of this weather control system, it is important to consider a few key aspects. These include setting up a standard interface for easy communication with various drivers from different weather stations. Also, utilizing all available sensors effectively, including redundancy strategies. Additionally, ensuring that the data collected from many sensors is accurate by strong validation and filtering mechanisms to catch and fix errors and outliers before using it in the system. Lastly, the system needs to be flexible enough to add new weather devices and improvements as needed.

The WCS of the TJO considers the

4.1. *Structure and status*

The system's architecture is based on a Device-Sensor-Variable framework, coupled with state definitions. Each device is equipped with a range of weather sensors, each measuring distinct weather variables. For example, a basic device may have three sensors, measuring variables such as temperature, humidity, and pressure.

The management of the state for each system component is contingent on various factors. At the highest level, the overall status of the weather control system relies on a selected set of required weather variable statuses. Each individual weather variable, in turn, depends on a group of sensor states and the redundancy mechanisms applied to those sensors. Concurrently, the status of each device hinges on the states of its respective sensors.

The system's architecture is organized into five essential modules, the configuration, input, filter, redundancy, and output modules. Each of these modules serves a specific function within the WCS:

- **Configuration Module:** This module is responsible for establishing a connection with the database to retrieve and apply user-defined configuration parameters for all system components.

- **Input Module:** The Input Module is tasked with collecting sensor values from different drivers associated with various weather devices.

[6] https://sdc.cab.inta-csic.es/joro

VII Workshop on Robotic Autonomous Observatories (October 16-20, 2023)
Editors: Maria Gritsevich, Alberto J. Castro-Tirado, Petr Kubánek, Shashi B. Pandey, and David Hiriart - DOI: https://doi.org/10.22201/ia.14052059p.2025.59.11

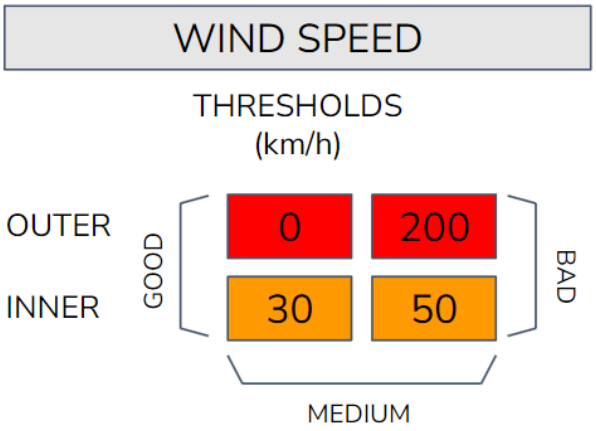


Fig. 3. Example of wind sensor thresholds for data validation and state determination.

- **Filter Module:** Responsible for processing raw data extracted from the weather stations and filtering and validating this data to ensure its accuracy and reliability.
- **Redundancy Module:** Leveraging the validated data and the redundancy configuration, the Redundancy Module generates values for each weather variable.
- **Output Module:** The Output Module is responsible for managing the delivery of data to external systems, such as databases or external software applications.

4.1.1. *Configuration module*

The Configuration Module is responsible for establishing the system's behaviour. It connects to the database and retrieves configuration parameters for devices, sensors, and variables. These parameters govern the system's operation across all modules. Specifically:

For the Input Module, configuration parameters dictate the selection of drivers and specify the location of configuration files that map devices to their respective drivers for sensor data retrieval.

In the Filter Module, configuration parameters are utilized to customize thresholds, limits, conversion factors, and validation algorithms for sensor data.

In the Redundancy Module, configuration parameters determine which redundancy algorithms are applied to weather variables.

Lastly, the Output Module's configuration governs the system's operating frequency for data publication to external software or databases.

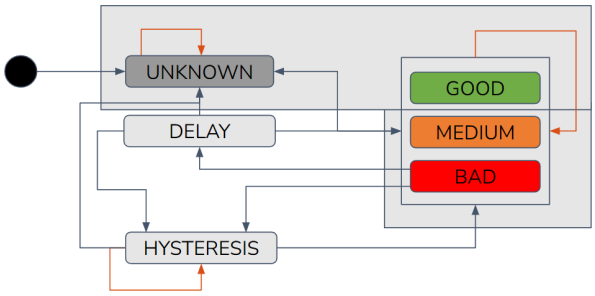


Fig. 4. High-level diagram of the WCS state machine. The gray area is only for sensors whether variables have DELAY and HYSTERESIS additional states.

4.1.2. *Input Module*

The Input Module interfaces with various drivers associated with different devices to collect sensor data. It employs a common interface, allowing multiple drivers, including APIs, SERIAL communication drivers, and web scrapers, to integrate seamlessly with the WCS.

4.1.3. *Filter Module*

The Filter Module is responsible for validating sensor and variable values, ensuring that the WCS processes accurate and precise data while determining the state of sensors and variables. Multiple validation algorithms are employed:

- **Sensor Level Validation:** This includes the Spike Validator, Unit Conversion, and Threshold and Limits.
- **Variable Level Validation:** After sensor data validation, variables undergo additional scrutiny through algorithms such as Threshold and Limits and Simple Moving Median (SMM). These algorithms not only validate data but also assign statuses to sensors and variables.

The Threshold and Limit algorithm maps sensor or variable values to states based on user-configured parameters, including two outer limits indicating erroneous data and two inner thresholds separating GOOD, MEDIUM, and BAD states as depicted in Fig. 3. Values outside this range are discarded.

Additionally, variables adhere to the same threshold definitions, and they may include DELAY and HYSTERESIS states (Fig. 4) based on user configurations, allowing for delayed transitions or hysteresis-based state changes that can be combined.

The Spike Validator's purpose is to detect and discard data spikes within a specified window. This is achieved by using a window reference translated

VII Workshop on Robotic Autonomous Observatories (October 16-20, 2023)
Editors: Maria Griffsevich, Alberto J. Castro-Tirado, Petr Kubánek, Shashi B. Pandey, and David Hiriart - DOI: https://doi.org/10.22201/ia.14052059p.2025.59.11

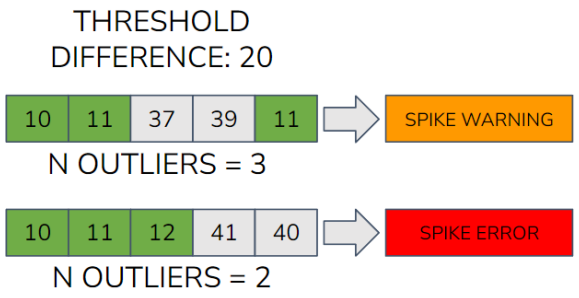


Fig. 5. Two examples of spike behaviour in a window of 4 values with a threshold difference of 20 and a configured maximum number of outliers.

into an array of values, along with a minimum threshold difference criterion for identifying outliers. When a specified number of outliers are detected within the defined window, these are considered errors and are not incorporated into the WCS as shown in Fig. 5.

The Simple Moving Median (SMM) algorithm is employed at the variable level to smooth data and prevent the WCS from making the observations stop when certain variables report a BAD state for a very short period of time (for example, gusts of wind short humidity peaks or small clouds passing by as in Fig. 6).

4.1.4. *Redundancy Module*

The Redundancy Module is responsible for delivering the final output for each weather variable, particularly when multiple devices provide the same variable. To facilitate diverse user requirements and in alignment with the WCS's design philosophy, users have to configure the redundancy settings for different variables. The Redundancy Module offers several algorithms, including:

- **Mean:** This algorithm calculates the mean of sensor values and assigns it to the corresponding variable.
- **Fallback:** Users define a preferred priority order for sensors from 1 to N, and if one sensor fails or produces an error, the subsequent sensor in the priority order is used for the weather variable.
- **Least Restrictive:** Only when all sensors report a BAD state is the weather variable assigned a BAD state.
- **Most Restrictive:** In contrast to the least restrictive algorithm, when one or more sensors report a BAD state, the variable is assigned a BAD state.

The Redundancy Module also offers an interface to facilitate the development and integration of new redundancy algorithms.

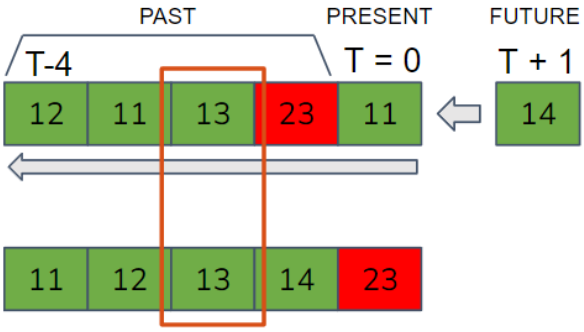


Fig. 6. Example that shows how the SMM works given a user-defined window and with a short-lived BAD state.

4.1.5. *Output Module*

Lastly, the Output Module determines the frequency of data publication and is responsible for delivering raw sensor data (prior to validation), validated variable data, and the overall WCS status. This data is transmitted to the Observatory Control System (OCS) for integration with the observatory's overall structure and is concurrently stored in a database for visualization and statistical analysis.

5. SUMMARY

The proceedings highlighted the successful implementation of the Weather Control System employed by the TJO telescope at the OdM, showcasing its capabilities and contributions to the field of weather control systems.

The WCS, which has been in production for over a year, demonstrated exceptional versatility by using various weather devices, eliminating the need for manual intervention when dealing with different sensors and drivers. This extended period of practical application proves the system's reliability and effectiveness in real-world scenarios. The WCS is notably fault-tolerant, handling device or sensor failures smoothly to ensure continuous data collection and system operations.

In terms of data accuracy, the WCS has a robust filtration and validation process, ensuring that sensor values are consistently and accurately represented. The system's ability to manage redundancy is another strong point, reliably producing accurate weather variable outputs even with overlapping data from multiple devices, which is crucial for data integrity and system dependability.

VII Workshop on Robotic Autonomous Observatories (October 16-20, 2023)
Editors: Maria Gritsevich, Alberto J. Castro-Tirado, Petr Kubánek, Shashi B. Pandey, and David Hiriart - DOI: https://doi.org/10.22201/ia.14052059p.2025.59.11

Customizability is another key attribute highlighted during the proceedings. The WCS allows users to tailor and define the system's behaviour to suit their specific requirements. This adaptability ensures that the system can be fine-tuned to meet the unique needs of various applications. Moreover, the WCS is committed to ongoing improvement, regularly incorporating new methods and algorithms to enhance its performance and expand its capabilities.

Acknowledgments: The Joan Oró Telescope (TJO) of the Montsec Observatory (OdM) is owned by the Catalan Government and operated by the Institute for Space Studies of Catalonia (IEEC).

REFERENCES

Baroch, D., Morales, J. C., Ribas, I., et al. 2020, A&A, 641, A69

Colomé, J., Ribas, I., Fernández, D., et al. 2008, Proc. SPIE, 7019, 70192k

Colomé, J., Ribas, I., Francisco, X., et al. 2010, AdAst, 2010, 183016

Herrero, E., Morales, J. C., Ribas, I., & Naves, R. 2011, A&A, 526, L10

Morales-Garoffolo, A., Elias-Rosa, N., Benetti, S., et al. 2014, MNRAS, 445, 1647

Ribas, I., Tuomi, M., Reiners, A., et al. 2018, Natur, 563, 365

Sarazin, M. & Roddier, F. 1990, A&A, 227, 294

Trigo-Rodríguez, J. M., García-Melendo, E., Davidsson, B. J. R., et al. 2008, A&A, 485, 599

Wyrzykowski, Ł., Mróz, P., Rybicki, K. A., et al. 2020, A&A, 633, A98

Revista Mexicana de Astronomía y Astrofísica Serie de Conferencias (RMxAC), **59**, 63–68 (2025)
© 2025: Instituto de Astronomía, Universidad Nacional Autónoma de México
https://doi.org/10.22201/ia.14052059p.2025.59.12

VII Workshop on Robotic Autonomous Observatories (October 16-20, 2023)
Editors: Maria Griffsevich, Alberto J. Castro-Tirado, Petr Kubánek, Shashi B. Pandey, and David Hiriart - DOI: https://doi.org/10.22201/ia.14052059p.2025.59.12

SKY BRIGHTNESS MEASUREMENTS WITH THE ALLSKY CAMERA AT THE UNIVERSITY OF GÖTTINGEN

K. J. Schimpf[1] and T. O. Husser [2]

RESUMEN

El telescopio de 50 cm utilizado por el Instituto de Astrofísica y Geofísica (IAG) de la Universidad de Göttingen está ubicado en la azotea de la Facultad de Física en las afueras de la ciudad. Esto significa que las ventanas de observación disponibles no sólo están limitados por la nubosidad, sino también por la contaminación lumínica provocada por la ciudad, lo que también afecta a la calidad de las mediciones. Al ampliar las capacidades de nuestro sistema de control de telescopios 'pyobs', este proyecto implementará una medición en tiempo real del brillo del cielo y la cobertura de nubes, brindando la capacidad de seleccionar los objetos a ser observados de acuerdo con estas mediciones. Se creará un módulo de control de cámara Allsky, 'pyobs-allsky', que gestionará el tiempo de exposición y la configuración de ganancia, y utilizará un canal de reducción de las imágenes y las coincidencias con los catálogos para así poder cumplir con los requisitos.

ABSTRACT

The 50-cm telescope used by the Institute for Astrophysics and Geophysics (IAG) at the University of Göttingen is located on the roof of the physics faculty on the outskirts of the city. This means that the available observing targets are not only limited by cloud cover, but also by the light pollution caused by the city, which also affects the quality of the measurements. By extending the capabilities of our telescope control system 'pyobs', this project will implement a real-time measurement of sky brightness and cloud cover, providing the ability to select observation targets according to these measurements. An Allsky camera control module 'pyobs-allsky' will be created, which will manage the exposure time and gain settings, and will use an image reduction pipeline and catalogue matching to meet the requirements.

Key Words: Allsky camera — Sky brightness — Cloud detection — pyobs

1. INTRODUCTION

Robotic telescopes and automatic target scheduling are considered solved problems; predicting target visibility is one of the next frontiers for optimising observing time. While remote observation locations with dry climates face target altitude as the primary limiting factor for visibility, urban European observation sites must also factor in cloud coverage and light pollution from nearby towns and cities when planning observations. The Institute for Astrophysics and Geophysics (IAG) operates a fully robotic 50 cm Cassegrain telescope on the roof of the institute using the observation control system pyobs[3] (Husser et al. 2022a,b). With only a few photometric nights per year and significant light pollution from the town of Göttingen, it is a good example of the challenging telescope sites described above. Next to the telescope is a suite of weather sensors, already used by the pyobs-weather[4] weather control system. These are complemented by an allsky camera, which is currently only used for manual weather confirmation. Automated analysis of the allsky images, together with the existing weather data, should enable spatially resolved sky brightness measurements and cloud detection, as well as prediction of cloud cover for short time periods. This paper presents the preliminary results of this analysis.

2. METHODS

The data collection process is described by two layers. The physical hardware used to measure the weather at IAG and the software responsible for managing and analysing the obtained weather data.

2.1. *Sensors*

As described above, the sensors are located next to the 50 cm telescope on the roof of the Faculty of Physics building. A Boltwood III cloud sensor is mainly used for sky temperature measurements and

[1]Institute for Astrophysics and Geophysics, University of Göttingen, Friedrich-Hund-Platz 1, 37077 Göttingen, GER, (k.schimpf@stud.uni-goettingen.de).

[2]Institute for Astrophysics and Geophysics, University of Göttingen, Friedrich-Hund-Platz 1, 37077 Göttingen, GER, (thusser@uni-goettingen.de).

[3]`https://pyobs.org`

[4]`https://github.com/pyobs/pyobs-weather`

VII Workshop on Robotic Autonomous Observatories (October 16-20, 2023)
Editors: Maria Gritsevich, Alberto J. Castro-Tirado, Petr Kubánek, Shashi B. Pandey, and David Hiriart - DOI: https://doi.org/10.22201/ia.14052059p.2025.59.12

rain detection. The sky temperature is determined by measuring the surface brightness of the zenith in an infrared band. Similarly, a Sky Quality Meter (SQM) measures the surface brightness of the zenith in the visible band, resulting in a measurement of sky brightness. Both sensors cannot spatially resolve the sky. In addition, a weather station measures temperature, humidity, wind direction and speed. The allsky camera, a ASI 120 MC-S Color from ZWO, is located next to the other sensors. It has a field of view of 150, allowing it to capture most of the sky. To allow better control of exposure times, it operates at a cadence of 1 frame per minute. To prevent dew formation on the camera housing, the housing is heated by a 12 W heating element. As the dew point temperature in Göttingen does not exceed 15 °C, the heater is only switched on when the temperature inside the housing falls below 15 °C. An 80 mm cooling fan is used above 40 °C to reduce the risk of overheating in summer.

2.2. *Software Architecture*

The architecture connecting all the sensors mentioned above follows the micro-service architecture also used by pyobs. The pyobs-allsky module controls a pyobs camera module to which it is connected via pyobs. While the pyobs camera module only provides an interface for the allsky camera, the pyobs-allsky module is responsible for exposure time control, imaging cadence and file output. The file output includes the raw fits image and a compressed version with an overlay to be used on the Institute's public website. These files are then hosted by a static file server so that they can be accessed remotely. The weather sensor data is aggregated by the pyobs-weather module and stored in a time series database (InfluxDB). The current and historical weather data can be retrieved via a A REpresentational State Transfer Application Programming Interface (REST API) provided by the pyobs-weather module. The allsky-analyser module, currently under development, will access both the weather API and raw allsky imagery to compute the current sky brightness and cloud map, and to predict cloud movement. This will then be used to provide a REST API for checking current and future target visibility.

3. RESULTS

First, a relationship between the celestial and image coordinates is established by fitting a World Coordinate System (WCS). This is subsequently used to determine the visibility of catalogue stars in an image. Sorting the visible and invisible stars around each pixel by visual magnitude and calculating the limiting magnitude between these groups produces a limiting magnitude map. Subtracting the map for the ideal scenario, where all stars are visible, results in a map that showcases the change in limiting magnitude compared to a perfectly clear sky. Assuming that clouds are causing this change, the map corresponds to the cloud cover. A sky brightness map is derived from the limiting magnitude map using the linear relationship between limiting magnitude and sky brightness and the sky brightness data collected by the SQM. Furthermore, the sky brightness data obtained from the SQM is correlated with the sky temperature measurements of the Boltwood III sensor to explore the potential substitution of a sky temperature sensor with a sky brightness sensor.

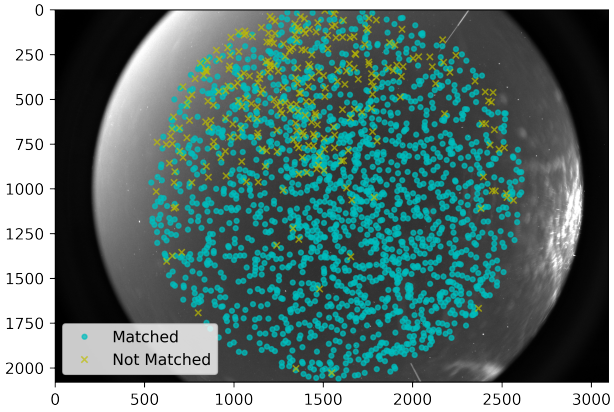


Fig. 1. Allsky image of a clear sky. Matched and not matched stars are marked with circles and crosses respectively for ALT > 30°.

3.1. *World Coordinate System (WCS)*

In order to relate pixel positions in the image to celestial coordinates, it is required to define a World Coordinate System (WCS). For the allsky camera, an hour angle-declination model has been adopted, with an Airy projection and a simple imaging polynomial (SIP) of third degree. A list of coordinate pairs is required to fit this model, but since a WCS is crucial to find these pairs, multiple iterations are required to determine the final WCS. The stars in each image are identified using using the Python library for Source Extraction and Photometry (SEP) (Bertin & Arnouts 1996; Barbary 2016). Then, in the initial iteration, a limited number of bright stars are matched with their respective catalogue counterparts manually. This minimal set of pairs is adequate for fitting a basic astrometric model for the allsky camera (Barghini et al. 2019). In the second

VII Workshop on Robotic Autonomous Observatories (October 16-20, 2023)
Editors: Maria Gritsevich, Alberto J. Castro-Tirado, Petr Kubánek, Shashi B. Pandey, and David Hiriart - DOI: https://doi.org/10.22201/ia.14052059p.2025.59.12

iteration, the simplified model is employed to match all stars found in all images of a photometric night to increase the number of pairs. These are then used to fit the WCS model. The fit results in a root mean square error of 3.10 pixels on the x-axis and 3.06 pixels on the y-axis in the image, and 11.81' in altitude and 17.48' in azimuth in the sky.

3.2. *Reverse matching*

The next objective is to determine if a catalogue star is visible in an image $I(v, w)$, which pixels can be indexed by the pixel coordinates (v, w). Using the WCS described in § 3.1, the stars are projected onto the image in the sky, resulting in pixel coordinates (x, y). These coordinates then define a window area

$$W_I[i] : [0..2i + 1]^2 \to \mathbb{N},$$
$$W_I[i](a, b) = I(x - i + a, y - i + b),$$

where $2i + 1$ is the length of one side of the area. A catalogue star is found in the image if a significant peak is found in the window area, so

$$\exists a, b \in [0..2i + 1]^2 : W[i](a, b) \geq \overline{W} + 3\sigma,$$

where $\overline{W}$ is the mean of the window and σ is the standard deviation of that mean. Applying this to all stars in the catalogue that are above the horizon at the time the image was taken will give a list of visible and invisible stars in the image. Figure 1 shows the resulting matches for a clear and cloudy sky for stars with ALT $> 30°$. For the cloudy sky the invisible stars match well with the visible clouds, while for the clear sky they match up with the areas of high sky brightness.

3.3. *Limiting magnitude map*

The limiting visual magnitude can be determined using the lists of visible and invisible stars in the image from § 3.2. For a pixel position (x, y) in the image, both lists are filtered for stars that are within a distance R of the pixel position. Ordering these stars by their visual magnitude gives four cases for the resulting lists, as can be seen in Figure 3. The limiting magnitude can be calculated for these cases using the following algorithm:

1. If all stars are visible, the limiting visual magnitude is assumed to be equal to the highest magnitude star in the list.

2. If all stars are invisible, the limiting magnitude is assumed to be equal to the lowest magnitude star in the list.

3. If all the invisible stars are of lower magnitude than the visible stars, the limiting magnitude is assumed to be the average of the magnitude of the lowest visible star and the highest invisible star. The stars are weighted by their distance from the pixel position.

4. If there are invisible stars with magnitudes greater than the visible stars, the limiting magnitude is assumed to be the average magnitude of all the invisible stars with magnitudes greater than the lowest visible star, and vice versa. The stars are weighted according to their distance from the position of the pixel.

For the last two cases, this also gives an estimated error in the form of the standard deviation of the averages. Applying this to all the pixels in the image produces a map of the limiting magnitude, accompanied by an error map, displayed in Figure 2. As expected from the algorithm, regions of low visual magnitude and high standard deviation correspond to regions with many invisible stars.

3.4. *Cloud map*

Assuming that limiting visual magnitude is solely influenced by cloud coverage and all stars in the catalogue are visible during clear skies, a cloud coverage map may be generated by subtracting the limiting magnitude map acquired in § 3.3 from the corresponding map that represents the situation where all stars are visible. The resulting map will express the change in visible magnitude with respect to the ideal case. A threshold value can be determined to discern when a difference in visual magnitude signifies a cloud. Overlaying this image using a threshold of 0.5 generates Figure 4a. Figure 4b shows the same image, but with marked invisible stars. Comparing Figure 4a to Figure 4b, indicates that the detected clouds are mostly consistent with the visible clouds where the catalogue has a high enough star density. The large chosen radius R, in which the visibility of stars is still taken into account for a given pixel, results in insufficient spatial resolution of the clouds. Also Figure 1 shows invisible stars for a clear sky, which means, that the assumption of all stars being visible for a clear sky is violated.

3.5. *Sky brightness map*

The relation between the limiting magnitude m_0 and the sky surface brightness μ can be described by a linear function (Crumey 2014). The measured limiting magnitude in § 3.3 is limited by the camera optics and the star catalogue used to match the stars,

VII Workshop on Robotic Autonomous Observatories (October 16-20, 2023)
Editors: Maria Gritsevich, Alberto J. Castro-Tirado, Petr Kubánek, Shashi B. Pandey, and David Hiriart - DOI: https://doi.org/10.22201/ia.14052059p.2025.59.12

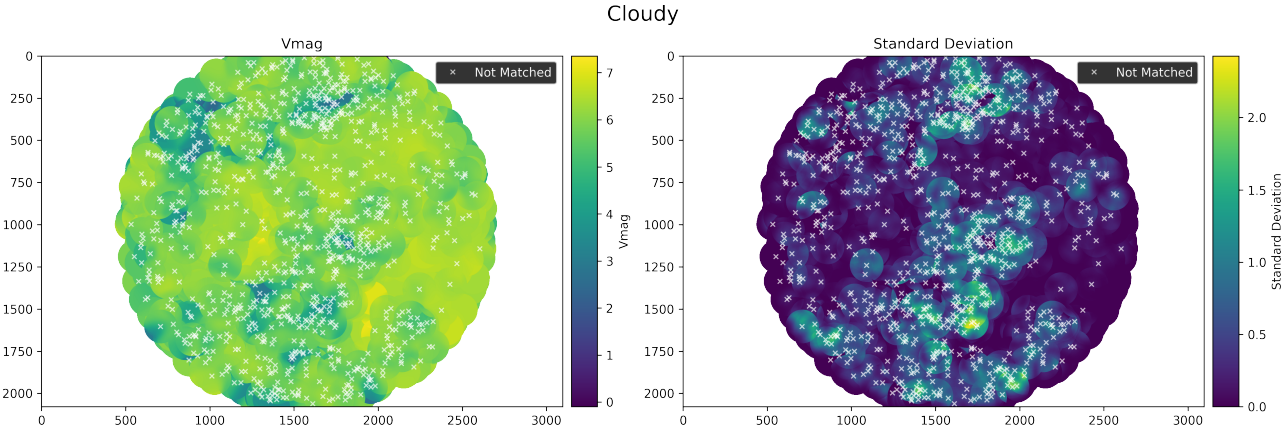


Fig. 2. Limiting visual magnitude map (left) and standard deviation (right) generated from a cloudy allsky image. In both plots crosses mark not matched stars.

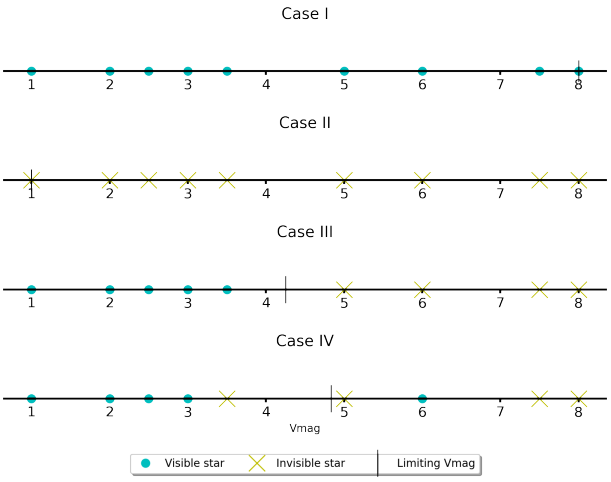


Fig. 3. Four examples of calculating the limiting magnitude from a group of nearby stars. The visual magnitude for the stars and the calculated limiting visual magnitude are shown.

which implies a maximum limiting magnitude above a limiting sky brightness μ_{limit}. This yield the fit function

$$m_0(\mu) = \begin{cases} a \cdot \mu + b & x \leq \mu_{\text{limit}} \\ a \cdot \mu_{\text{limit}} + b & x \geq \mu_{\text{limit}} \end{cases}, \qquad (1)$$

where a, b are free fit parameters. The free parameters are found by fitting this function with the surface brightness measurements made by the SQM described in § 2.1 and the limiting magnitude found by the algorithm described in § 3.3. Using the data of one night to fit this function results in $a = (1.523 \pm 0.006)\,\text{arcsec}^2$,$b = (-22.7 \pm 1.3)\,\text{mag}$ and $\mu_{\text{limit}} = (19.08 \pm 0.07)\,\text{mag/arcsec}^2$. Figure 5 illustrates the data for the fitted night and function. It can be seen that the function fits the data well, but also that measurements were made with $\mu > \mu_{\text{limit}}$. This means that using this configuration only a sky brightness below $\mu_{\text{limit}} = (19.08 \pm 0.07)\,\text{mag/arcsec}^2$ can be measured correctly.

3.6. *Sky brightness and temperature*

The IAG currently operates a Boltwood sensor for cloud detection. This is described in § 2.1. However, a comparison of the Boltwood sensor with the SQM shows that both sensors effectively measure the surface brightness of the zenith, but at different wavelengths and price ranges: While the SQM measures brightness in the range $300 - 1100\,\text{nm}$, the Boltwood sensor operates in the range $8 - 15\,\mu\text{m}$, but costs about ten times as much. This leads to the question of whether the SQM could be a more economical alternative to the Boltwood sensor for cloud detection. Figure 6 shows both the sky temperature measured by the Boltwood sensor and the sky brightness measured by the SQM over a period of one night. The figures shows some correlation between the sensors, but it is noticeable that in the darkest conditions the sky brightness lacks features that are visible in the sky temperature. Plotting sky brightness against sky temperature for one month, as shown in Figure 7, also suggests this imperfect correlation. This can be quantified by the Pearson r-value $r = -0.81$ with a p-value $p = 0.0$, which also supports the suggestion.

4. DISCUSSION

The WCS presented in § 3.1 provides sufficient accuracy above ALT $> 30°$ for the reverse matching algorithm shown in § 3.2. By visual inspection, the results of the reverse matching algorithm appear to match the actual visibility of the stars. The algorithm used to compute the limiting magnitude map

VII Workshop on Robotic Autonomous Observatories (October 16-20, 2023)
Editors: Maria Gritsevich, Alberto J. Castro-Tirado, Petr Kubánek, Shashi B. Pandey, and David Hiriart - DOI: https://doi.org/10.22201/ia.14052059p.2025.59.12

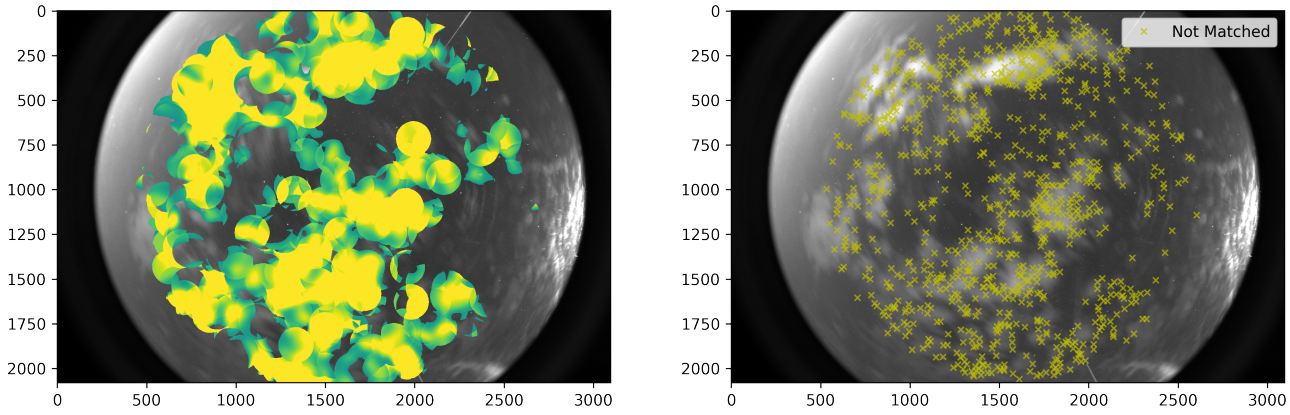


Fig. 4. Comparison between the cloud map on the left and the allsky image with the not matched stars. The cloud map is superimposed on the Allsky image, while values < 0.5 have been made transparent in the cloud map.

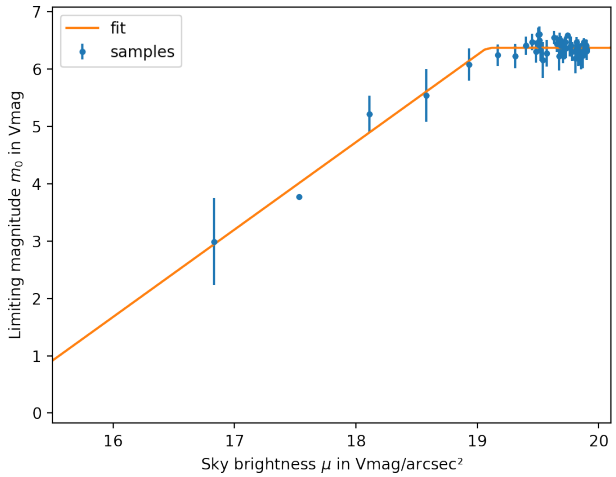


Fig. 5. The limiting visual magnitude at the zenith calculated in § 3.3 plotted against the sky brightness measured by the SQM for one evening. The data are fitted with the linear relation described by Equation 1.

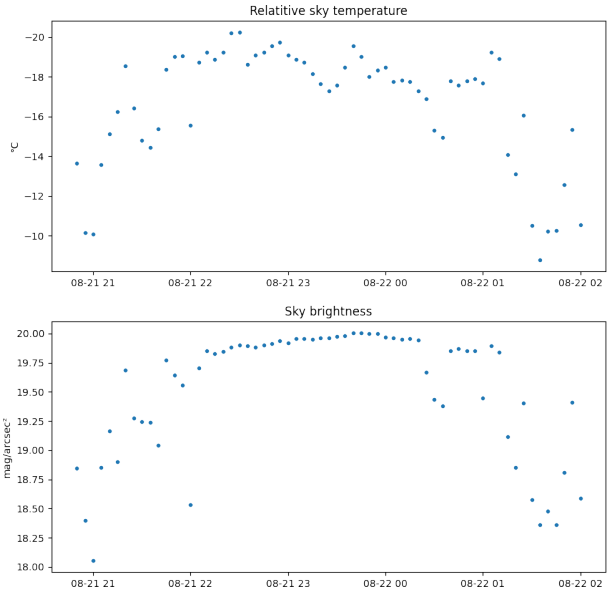


Fig. 6. Relative sky temperature measured with the Boltwood III and sky brightness measured with the SQM for one night with samples every 5 minutes.

described in § 3.3 produces plausible results, but when used to compute the sky magnitude it fails to reproduce the sky magnitude measured by the SQM. This is probably due to the limited magnitude of the catalogue used for the reverse matching or the limited exposure time of the allsky camera. In addition, the algorithm only approximates the limiting magnitude, as the catalogue visual magnitude used differs from the actual apparent magnitude of the stars due to air mass and star type. Using the limiting magnitude map for cloud detection by subtracting the limiting magnitude map for a perfect sky in § 3.4 also gives useful results. However, the clear sky image in Figure 1 shows that the assumption of a perfect sky does not correspond to the clear sky found in Göttingen, as not all stars are detected. This could be solved by taking the light pollution into account, when generating the cloudless map. That would also require accounting for time variable source as the sun and moon. The cloud map is also poorly spatially resolved because the radius used to group stars for the limiting magnitude map generation algorithm needs to be large enough to include enough stars. Using a continuous star visibility instead of the binary might alleviate this problem by providing more information per star. Determining the star visibility using a Laplacian of Gaussian filter (Adam et al. 2017) or point source photometry could be possible solutions. The sky brightness and sky temperature analysed in § 3.6 show a clear correlation. Whether this is sufficient to replace a sky temperature sensor with a sky

VII Workshop on Robotic Autonomous Observatories (October 16-20, 2023)
Editors: Maria Gritsevich, Alberto J. Castro-Tirado, Petr Kubánek, Shashi B. Pandey, and David Hiriart - DOI: https://doi.org/10.22201/ia.14052059p.2025.59.12

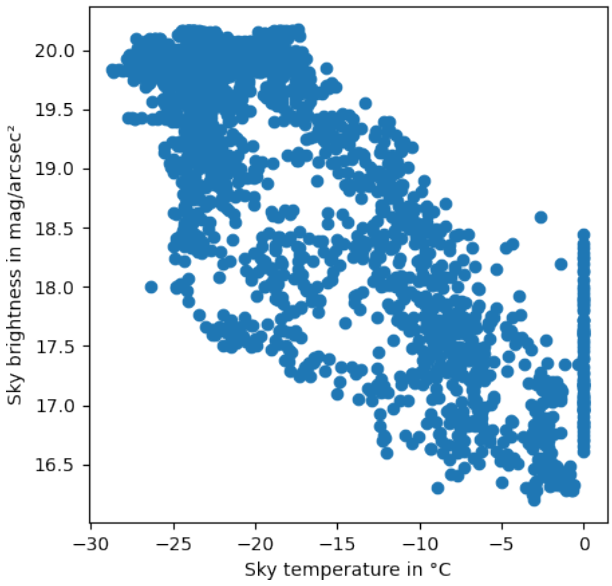


Fig. 7. Sky brightness measured with the SQM plotted against relative sky temperature measured with the Boltwood III for one month. The data is filtered for solar altitudes below $< -18°$.

quality meter needs further investigation. In the future, a cloud tracking system will be implemented by utilising a clustering algorithm, as previously demonstrated by Adam et al. 2017. Measuring the cloud height with the allsky camera (Jechow et al. 2019) and using the wind speed and direction data from our weather station would then allow for better prediction of cloud movement.

5. CONCLUSION AND SUMMARY

We presented the operational setup of the allsky camera and weather sensor at the IAG. The data gathering and hardware components of the project are functional, although the analysis module is still in the prototyping phase. We demonstrated an initial attempt to estimate star visibility and produce maps of sky brightness and cloud coverage using, at present, solely binary star visibility. However, the resulting maps are limited to ALT $> 30°$ and not spatially well-resolved. This must be addressed to enhance accuracy and monitor clouds over multiple images. We examined the potential estimation of sky temperature based on sky brightness measurements, and while a clear correlation is evident, further research is necessary to apply this method. In conclusion we showed that external weather sensors can be used to improve allsky image analysis.

REFERENCES

Adam, J., Buss, J., Brügge, K., et al. 2017, EPJWC, 144, 01004, doi:10.1051/epjconf/201714401004
Barbary, K. 2016, asci.soft, 1, 58, doi:10.21105/joss.00058
Barghini, D., Gardiol, D., Carbognani, A., et al. 2019, A&A, 626, A105, doi:10.1051/0004-6361/201935580
Bertin, E. & Arnouts, S. 1996, A&AS, 117, 393, doi:10.1051/aas:1996164
Crumey, A. 2014, MNRAS, 442, 2600, doi:10.1093/mnras/stu992
Husser, T.-O., Hessman, F. V., Martens, S., et al. 2022, FrASS, 9, 891486, doi:10.3389/fspas.2022.891486
Husser, T.-O., Hessman, F. V., Martens, S., et al. 2022, Astrophysics Source Code Library, ascl:2203.012
Jechow, A., Hölker, F., & Kyba, C. C. M. 2019, NatSR, 9, 1391, doi:10.1038/s41598-018-37817-8

Revista Mexicana de Astronomía y Astrofísica Serie de Conferencias (RMxAC), **59**, 69–70 (2025)
© 2025: Instituto de Astronomía, Universidad Nacional Autónoma de México
https://doi.org/10.22201/ia.14052059p.2025.59.13

VII Workshop on Robotic Autonomous Observatories (October 16-20, 2023)
Editors: Maria Gritsevich, Alberto J. Castro-Tirado, Petr Kubánek, Shashi B. Pandey, and David Hiriart - DOI: https://doi.org/10.22201/ia.14052059p.2025.59.13

ZERO POINT MAGNITUDES OF ALL-SKY IMAGES FOR DETERMINING CLOUD CONDITIONS

C. van Gend[1], N. Erasmus[1], J. Tonry[2], L. Denneau[2], M. Hlakola[1], and S. Potter[1]

RESUMEN

Brevemente explicamos el método del punto cero para determinar el porcentaje de nubes, comparando las imágenes obtenidas con las que se esperarían en condiciones de cielo despejado, proporcionando valores del porcentaje cubierto por cada sector del cielo.

ABSTRACT

We briefly explain the zero-point method of determining cloud cover, by comparing recent all-sky images with what would be expected in cloudless conditions, obtaining values for the cloudiness of each sky sector.

Key Words: All-sky image — Zero point data — Cloud condition detection

1. INTRODUCTION

Why do we need to know the sky conditions? When operating autonomously we need to ensure that we do not proceed with observing if the target is obscured by heavy cloud.

Traditional cloud sensors provide a single value for the cloudiness of the sky. They are subject to degradation over time, eventually returning erroneous values.

We would like a more reliable solution that reports how much cloud there is in each part of the sky.

Our method compares recent all-sky images with what would be expected in cloudless conditions, obtaining values for the cloudiness of each sky sector.

2. METHOD

2.1. *Using the zero-point magnitude*

We make use of the zero-point magnitude, considering that the zero-point magnitude is the magnitude of a star that would result in one count per second measured by the detector for a given system so it is direct measurement of the efficiency (or throughput) of a system.

In other words for a higher throughput system (e.g. a larger aperture, fewer lossy optics, or a more sensitive detector) the zero-point magnitude will be a larger value.

If the throughput of the system remains constant the next biggest contributor to a change in the counts per second measured by the detector would be losses through the atmosphere (e.g thin clouds).

2.2. *Determining the reference zero-point*

We use all-sky images and zero-point magnitudes provided by the all-sky camera of the Asteroid Terrestrial-impact Last Alert System (ATLAS)[3] at our Sutherland site.

ATLAS does full astrometric and photometric calibration of each night-time image.

We first determined a "reference" zero-point map of the sky taking all archival zero-point data where the sky was clear and the seeing was recorded to be below 1.2 arcseconds (the median seeing at Sutherland is about 1.5 arcseconds).

We then divide the sky into segments and obtain a reference zero-point value for each segment.

2.3. *Mapping the cloud cover*

From the calibrated all-sky image we can obtain a live zero-point map. We then compare this live zero-point map to the reference map.

If no live zero-point data is available in a segment (e.g no stars detected) or the difference between live and reference values is above 0.5 we flag that segment as "bad". If not, the segment is flagged as "good".

This leads to a table of good/bad values, describing the current state of each sky segment.

If more than a predetermined number of segments is bad, we abort ongoing observations and close the dome until conditions improve.

[1]South African Astronomical Observatory, 1 Observatory Rd, Observatory, Cape Town 7925, South Africa, (ch.vangend@saao.nrf.ac.za).
[2]Institute for Astronomy, 2680 Woodlawn Drive, Honolulu, HI 96822-1839 USA.

[3]`https://atlas.fallingstar.com/`

VII Workshop on Robotic Autonomous Observatories (October 16-20, 2023)
Editors: Maria Gritsevich, Alberto J. Castro-Tirado, Petr Kubánek, Shashi B. Pandey, and David Hiriart - DOI: https://doi.org/10.22201/ia.14052059p.2025.59.13

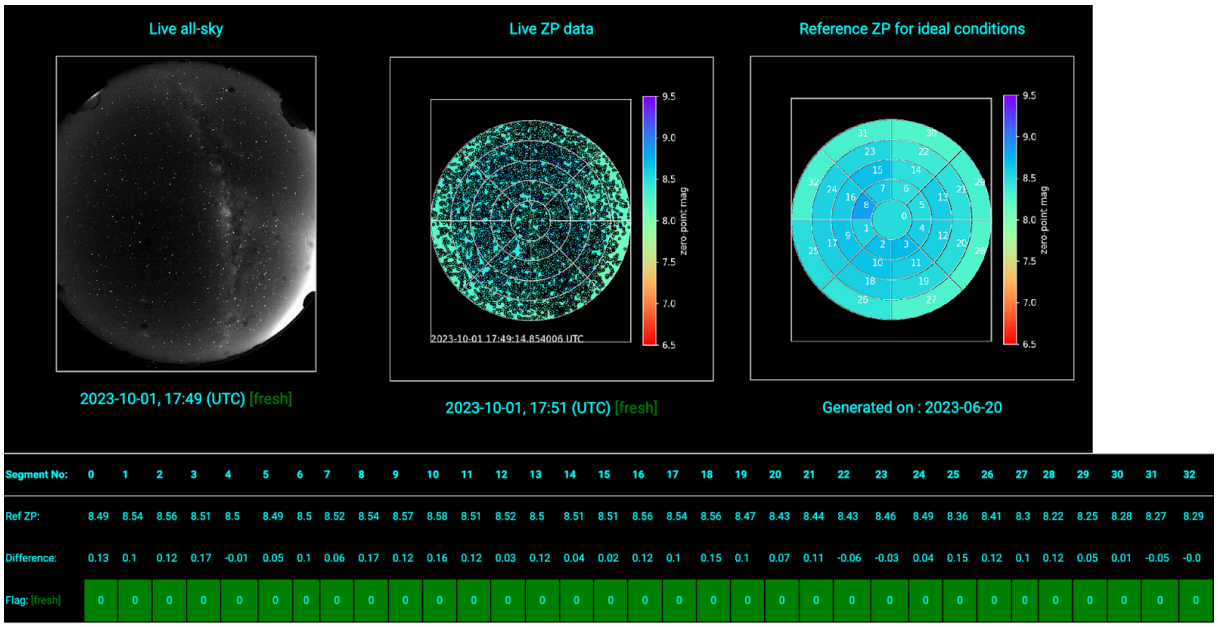


Fig. 1. Example of GOOD sky-conditions.

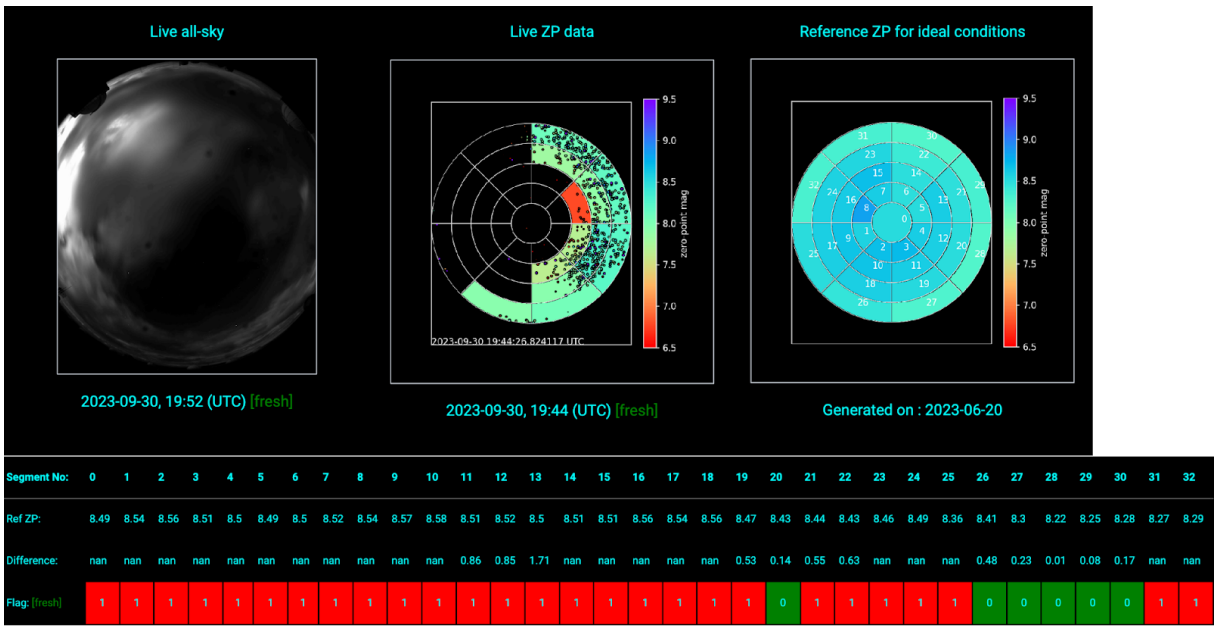


Fig. 2. Example of BAD sky-conditions.

3. CONCLUSIONS AND FUTURE WORK

We show our zero-point method of determining cloud cover, by comparing recent all-sky images with what would be expected in cloudless conditions, obtaining values for the cloudiness of each sky sector. Currently we use the zero-point data to make a simple do/dont observe decision. However, data is available for each segment of the sky. We could refine this to decide which part of the sky is clear enough for observing, and constrain the system to accept only observation requests for this part of the sky.

Revista Mexicana de Astronomía y Astrofísica Serie de Conferencias (RMxAC), **59**, 71–76 (2025)
© 2025: Instituto de Astronomía, Universidad Nacional Autónoma de México
https://doi.org/10.22201/ia.14052059p.2025.59.14

VII Workshop on Robotic Autonomous Observatories (October 16-20, 2023)
Editors: Maria Gritsevich, Alberto J. Castro-Tirado, Petr Kubánek, Shashi B. Pandey, and David Hiriart - DOI: https://doi.org/10.22201/ia.14052059p.2025.59.14

OBSERVATORY CONTROL SYSTEM AT SOUTH AFRICAN ASTRONOMICAL OBSERVATORY

S. Chandra[1,2,3], S. B. Potter[1], C. G. Gend[1], N. Erasmus[1], and R. Julie[1,4]

RESUMEN

El programa de Observatorio Inteligente (IO) del Observatorio Astronómico de Sudáfrica (SAAO) tiene como objetivo operar la mayoría de sus telescopios de forma robótica y desde un sistema de control centralizado equipado con tecnologías modernas para coordinar las observaciones de seguimiento de alertas proporcionadas por otros telescopios y observatorios tales como LSST, ROMAN, zTF, CTA, etc. Con los recientes desarrollos en el SAAO, el sistema de control del observatorio (OCS) ha demostrado ser un subsistema ya integrado de la compleja arquitectura del IO. El OCS, considerando sus distintos componentes: telescopios, instrumentos, observaciones como tal, registros, etc., facilitó a la arquitectura IO el poder integrar de manera única telescopios e instrumentos más antiguos, originalmente no diseñados para operaciones automatizadas. Al utilizar lenguajes populares como Python como componente principal, también resulta fácil cambiar según sean los requerimientos e igualmente el poder comunicarse mediante robots. También se ha reducido gran parte de la carga del equipo de gestión del observatorio al proporcionar una base de datos con un protocolo de comunicación fácil para la gestión y visualización de los datos.

ABSTRACT

The intelligent observatory (IO) programme at SAAO aims to operate most of its hosted telescopes robotically from a centralized control system equipped with modern technologies to coordinate the followup observations triggered by the most sophisticated global facilities like LSST, ROMAN, zTF, CTA etc. With the recent developments at SAAO, the observatory control system (OCS) has proven to be an integrated sub-component of the complex IO architecture. The OCS, because of a simplistic fragmentation in terms of the definitions of the various components: such as telescopes, instruments, observations, logging; helped the IO architecture uniquely to integrate very old telescope and instruments, originally not designed for the automated operations. Using popular languages like Python as a major component, it also become easy to change as per need and also to communicate using robots. It has also reduced a lot of burden of the observatory management team by providing a communicable database for managements and data visualization

Key Words: IO Architecture — Observatory: Observatory Control System

1. GENERAL

In the current era of the multi-messenger astronomy the coordinated multi-wavelength campaigns have become an effective tool for a wide range of astronomical research. Being either variable stars in our galaxy, outbursts in galactic compact objects, active galaxies, or distant gamma-ray bursts, etc., wherever variability is a crucial characteristic, the coordinated monitoring provides only ways to uncover a complete picture of the system and underlying physical processes. Depending on the astrophysical systems the campaigns may become very time critical and to involve real-time coordination between various international observing facilities from ground and the space. A well structured campaign with real-time feedback system has served backbone for reporting ice-breaking discoveries such as kilonovae as the optical counterparts to some gravitational wave events (Abbott et al. 2017), and the first electromagnetic (EM) counterparts of neutrino sources (IceCube Collaboration et al. 2018; Andreoni et al. 2024). The coordinated campaigns have historically helped many traditional research fields to uncover deep hidden details of the physical processes (Plucinsky et al. 2017; Yao et al. 2021; EHT MWL Science Working Group et al. 2021). The upcoming mega facility Vela Rubin Observatory or LSST (Ivezić et

[1]South African Astronomical Observatory (SAAO), 1 Observatory Road, Observatory, Cape Town, 7925, South Africa (sunil.chandra355@gmail.com).

[2]Centre for Space Research, North-West University, Potchefstroom Campus, 11 Hoffman St., Potchefstroom, 2520, North-West, South Africa (chandra@saao.ac.za).

[3]Physical Research Laboratory, Mt. Abu Observatory, Mount Abu, Rajasthan, 507501, India (schandra@prl.res.in).

[4]South African Radio Astronomy Observatory, 2 Fir Street, Cape Town, 7925, South Africa.

VII Workshop on Robotic Autonomous Observatories (October 16-20, 2023)
Editors: Maria Gritsevich, Alberto J. Castro-Tirado, Petr Kubánek, Shashi B. Pandey, and David Hiriart - DOI: https://doi.org/10.22201/ia.14052059p.2025.59.14

al. 2019) shall be streaming millions of triggers every night with many new exotic unknown breeds of astrophysics systems.

For example, characterizing and classifying optical transients or electromagnetic counterparts of neutrinos and gravitational waves, variable nature of broad-band emitters pose a huge challenge of covering entire accessible energy spectrum with best possible simultaneity. These coverage may need many repetitions in similar of different orders based on the requirements of the scientific objectives and telescope times. Such complex observing plans not only demand rapid actions but also a nearly real-time communications between different participating facilities or collaborations. Intelligent observatory (IO) programme[5](Potter 2021) is an effort to upgrade the existing observing facilities at SAAO in Sutherland to robotize and convert the South African plateau as a rapid followup machine in the LSST era. The IO's flexible architecture (van Gend et al. 2020) has provisions of switchable robotic and manual modes of telescopes operations. This also enables a centralized computer brain for communicating with the observer (or robots) and multiple observing facilities. The IO architecture can be split between three major components **1) The Local Control Unit (LCU):** set of modules to communicate with telescope control, instrument control and auxiliary services attached to the instrument (guider, focusser etc), **2) IO Observatory Control System (IO OCS or OCS):** modules to enable **Application Programming Interface (API)** driven communications between observer and the observatory, and **3) The IO Interfacing Layer (IOIL):** set of modules converting the instructions from the OCS to the frameworks of individual telescopes-instruments pairs. The LCUs are very different for the instrument and telescopes combinations. The IO team has developed layers (e.g., thrift or python wrapper) to communicate original control software (cameras, filter-wheels, telescope drives, dome drives etc) and avoid re-development from scratch, wherever possible (Erasmus, N., et. al., 2024). The IOIL are mostly Python libraries developed in-house to establish a general format communication, preferably by converting the incoming instructions in the JSON format (e.g., `schedule_poller` at SAAO) to small scripts with settings forwarded to the LCUs. The OCS as per the design, is very important component of the IO architecture (refer to Figure 1) because this aims to provide easy, descriptive and robotic two-way communications, support multi-platform access

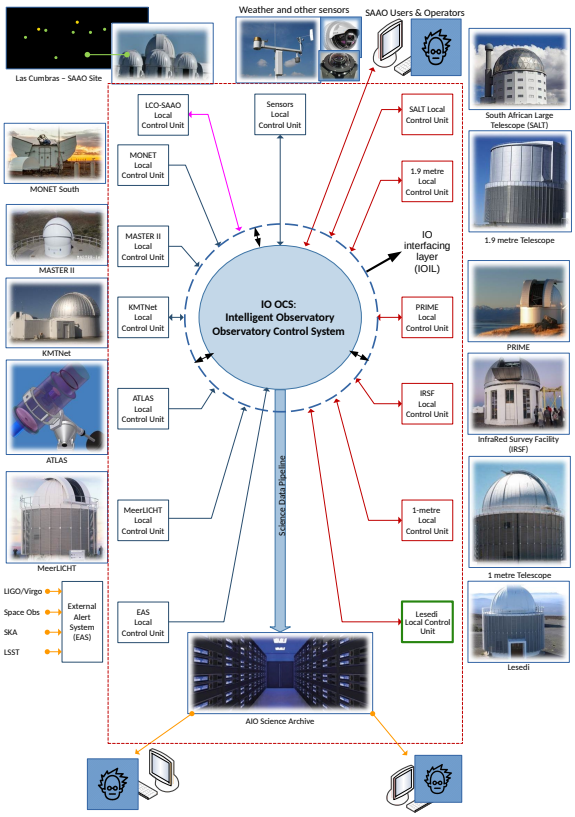


Fig. 1. The high-level design of the Intelligent Observatory Architecture. The IO OCS or OCS serves as the central server which communicates the users/admin and local control units (LCUs). The communication with the LCUs are mediated through IO interfacing layer. The green box around Lesedi telescope indicates that it is already operated in a robotic mode.

(API controlled), and easy to be integrated with other systems and layers. This manages various databases and serves as the brain of the IO system at SAAO.

2. OBSERVATORY CONTROL SYSTEM (OCS) AT SAAO

The OCS at SAAO (henceforth referred as OCS, mentioned otherwise) primarily consists of the modules developed by the Las Cumbres Observatory (LCO), with the same name[6], enabling the networking of 25 telescopes of the LCO network in the different geographical locations. A subset of publicly available modules with a minimal optimization and added layering for the networking using Python, in close collaborations with the development team at

[5]`https://io.saa.ac.za`

[6]`https://observatorycontrolsystem.github.io`

VII Workshop on Robotic Autonomous Observatories (October 16-20, 2023)
Editors: Maria Gritsevich, Alberto J. Castro-Tirado, Petr Kubánek, Shashi B. Pandey, and David Hiriart - DOI: https://doi.org/10.22201/ia.14052059p.2025.59.14

LCO, serves as the brain of the OCS. Having a generalized structure, vast ranges of the basic functionalities, robotic communications for the admin and user related activities, network based communications for almost internal and external activities, the OCS is very easy to add more intelligent layers to the IO structure in-near future such as weather based decision making, analysis pipelines, and artificial intelligence (AI) driven characterization, cataloging and alerts etc. The adoption of the LCO's modules are integrated in such a way that the future upgrades of these can be easily used without any major change of other communicating layers. These justifies the use of the local production of the LCO's modules a best suited publicly available resource to serve the vision of IO at SAAO.

2.1. *Modules adopted from the LCO's OCS*

The recent versions of the following modules make the complete OCS being used for the IO:

- `configdb`:[7] This is Django, HTML and Python based module to create, maintain and communicate the database related to the site, telescope, instruments, detectors, and optical components. The module, because of defining the sub-components of the instruments at a very fundamental level of information (with additional controls in the form of validation schema), is capable of creating a complex and shared telescope-instrument combinations. The database used by this is freely available (`PostgreSql` and hence adds to its applicability for the general use. The `configdb` database (see Figure 2 for different sub-components and the flow-chart) stores information in a multi-layered JSON format which is easily callable for the API requests through GET instances. Figures 3 and 4 refer to the snapshots of various instances in the JSON format. The customization of the this database to apply the local requirements of the SAAO telescopes and instruments are done through using generic modes, optical path elements, and specific custom validation_schema. We also had defined several specific 'tags' while defining the 'instrument' and 'instrument type' to apply many complex settings and availing those to the users. These tags are interpreted by IIL in a comprehensive and machine readable instructions before forwarding it to the LCUs.

- `downtime`: A library to create, manage and communicate a database of downtime of the telescope and instruments. This database enable telescope operation team to keep records of the duration of unavailability of telescope-instrument pairs (due to maintenance, upgradation or technical glitches) and which is accessed by the operational modules in real-time manner through network. This module is used at SAAO in its original format without any modification. It is used to disable the telescopes from the robotic network if it is used for the manual operation, student training programs, and the maintenance.

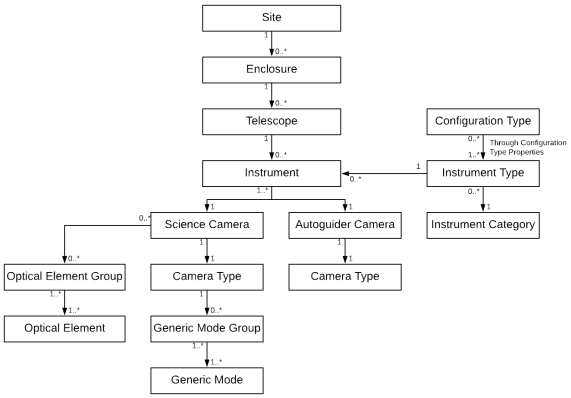


Fig. 2. The schematic drawing, borrowed from the LCO official page, showing different components used in the configdb database. It also represent a flow of defining the database. These basic components are used for the formation of the telescope-instrument pairs.

- `observation_portal`:[8] This library (Python and HTML) is the central package managing an API driven portal to create semester, collaboration, proposal, configurations, and many other useful tasks related to the operations for any observatory. It also has capabilities of sending out automated notifications for the new proposal calls, status of an active proposal, and communication between telescope control about the status of the data acquisition etc. It generates and maintain a comprehensive database which can be accessed for automated data archiving and visualization. In order to meet the compatibility of the SAAO's observing facilities, telescope operation guidelines, and user requirements, the first level of customization was made through applying 'validation_schema' and by defining specific 'configurations' and without making any actual changes to

[7] `https://observatorycontrolsystem.github.io/components/configuration_database/`

[8] `https://observatorycontrolsystem.github.io/components/observation_portal/`

VII Workshop on Robotic Autonomous Observatories (October 16-20, 2023)
Editors: Maria Gritsevich, Alberto J. Castro-Tirado, Petr Kubánek, Shashi B. Pandey, and David Hiriart - DOI: https://doi.org/10.22201/ia.14052059p.2025.59.14



```
GET /sites/1/

HTTP 200 OK
Allow: GET, PUT, PATCH, DELETE, HEAD, OPTIONS
Content-Type: application/json
Vary: Accept

{
    "id": 1,
    "name": "SAAO Sutherland",
    "code": "saa",
    "active": true,
    "timezone": 3,
    "restart": "16:00:00",
    "tz": "SAST",
    "lat": -32.3743318,
    "long": 20.80641,
    "elevation": 1798,
    "enclosure_set": [

GET /telescopes/1/

HTTP 200 OK
Allow: GET, PUT, PATCH, DELETE, HEAD, OPTIONS
Content-Type: application/json
Vary: Accept

{
    "id": 1,
    "serial_number": "telsa0001",
    "name": "Lesedi 1m",
    "code": "1m0a",
    "active": true,
    "aperture": 1.0,
    "lat": -32.374331,
    "slew_rate": 10.0,
    "minimum_slew_overhead": 30.0,
    "instrument_change_overhead": 0.0,
    "long": 20.80641,
    "enclosure": "http://10.1.100.96/enclosures/1/",
    "horizon": 19.0,
    "ha_limit_pos": 5.0,
    "ha_limit_neg": -5.0,
    "telescope_front_padding": 90.0,
    "zenith_blind_spot": 0.0,

GET /opticalelementgroups/1/

HTTP 200 OK
Allow: GET, PUT, PATCH, DELETE, HEAD, OPTIONS
Content-Type: application/json
Vary: Accept

{
    "name": "SDSS filters",
    "type": "filters",
    "optical_elements": [
        {
            "name": "OUT",
            "code": "out",
            "schedulable": true
        },
        {
            "name": "u'",
            "code": "u'",
            "schedulable": true
        },
        {
            "name": "g'",
            "code": "g'",
            "schedulable": true
        },
        {
            "name": "r'",
            "code": "r'",
            "schedulable": true
        },
        {
            "name": "i'",
            "code": "i'",
            "schedulable": true
        },
        {
            "name": "z'",
            "code": "z'",
            "schedulable": true
        }
    ],
    "element_change_overhead": 0.0,
    "default": "out"
}
```

Fig. 3. The snapshots of the 'site' (top), 'telescope' (middle), and 'optical elements': filters, slits, grating, half-wave plates etc (bottom) stored in the database and accessible through the observation_portal API.



```
GET /cameratypes/

HTTP 200 OK
Allow: GET, POST, HEAD, OPTIONS
Content-Type: application/json
Vary: Accept

{
    "count": 3,
    "next": null,
    "previous": null,
    "results": [
        {
            "id": 1,
            "size": "10.07",
            "pscale": 0.58,
            "name": "Mookodi-CAM",
            "code": "Mookodi-CAM",
            "pixels_x": 1024,
            "pixels_y": 1024,
            "max_rois": 30
        },
        {
            "id": 2,
            "size": "120",
            "pscale": 0.6,
            "name": "Mookodi-AutoG",
            "code": "Mookodi-AutoG",
            "pixels_x": 1024,
            "pixels_y": 1024,
            "max_rois": 0
        },
        {
            "id": 3,
            "size": "5",
            "pscale": 0.75,
            "name": "Spupnic_SciCAM",
            "code": "Spupnic_SciCAM",
            "pixels_x": 1024,
            "pixels_y": 1024,
            "max_rois": 4
        }
    ]
}
```

Fig. 4. The API instance of the list of science cameras loaded in the database at SAAO.

the codes. Another advanced level of customization is also possible via overriding any serializer in the project (observation portal project by LCO with forking options), or overriding the as_dict methods of models which are used for generating API responses. The detailed example and methods can be found on the official page of the LCO's project. We may need to adapt more specific customization using overrides for the integration of old telescopes to the IO network. Note that the telescopes we are integrating with the IO network, were not originally meant for the robotic modes of operations.

The SAAO's implementation of these packages are made using dockers, hosted in the virtual machines at different servers at SAAO headquarter in Cape Town, South Africa. The APIs in the dockers are accessed through their respective IPs and ports (for example http://10.1.100.96:7000 for the `configdb` service). The 'api' and 'admin' components are accessible by using these tags in the front of the IP:PORT combination. The Django web framework server based centralized authentication (`OAUTH` scheme hosted at the observation portal database) is

VII Workshop on Robotic Autonomous Observatories (October 16-20, 2023)
Editors: Maria Gritsevich, Alberto J. Castro-Tirado, Petr Kubánek, Shashi B. Pandey, and David Hiriart - DOI: https://doi.org/10.22201/ia.14052059p.2025.59.14

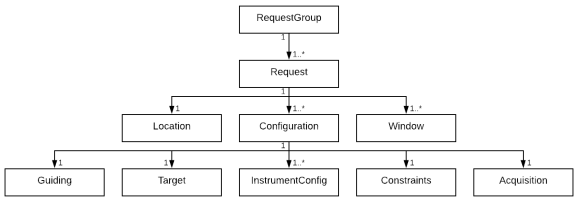


Fig. 5. The schematic borrowed from the official page by the LCO describing the hierarchy of properties of a RequestGroup. These requests can be made through the submission forms or programmatically using the API.

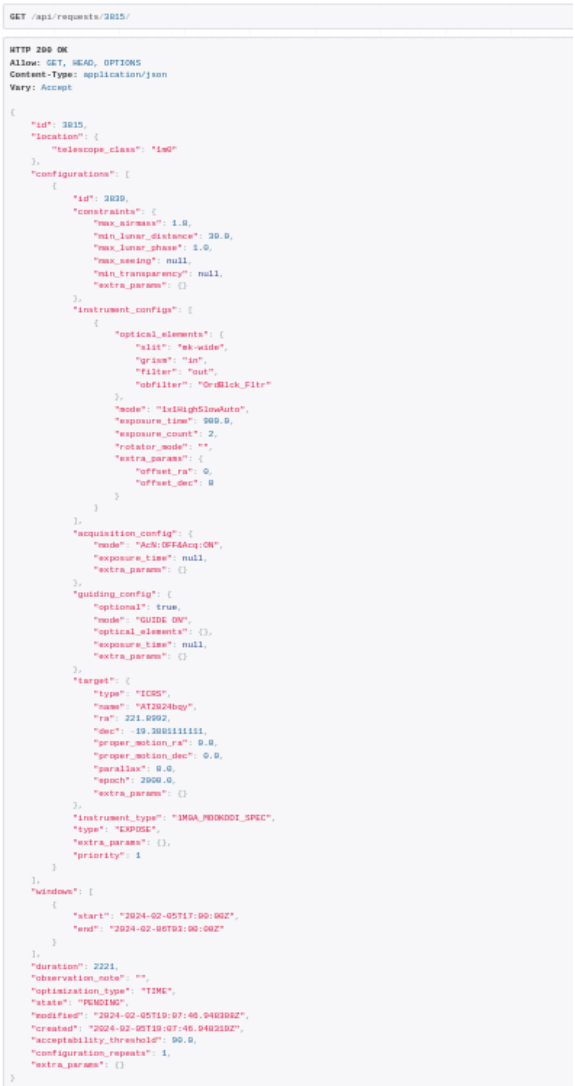


Fig. 6. The snapshot of a submitted request structured in JSON format.

used for managing the user accounts for all the modules. Various important tasks from different services such as, admin: management of users & proposals, adding new telescopes, instruments, changing status of existing pairs, etc; and users: registration, submitting new observing requests, checking the status of submitted requests, getting proposal metric etc; can easily be performed by sending requests to corresponding APIs either in batch mode or pragmatically as part of alert management systems. All these modules are equipped with interactive python shells preloaded with a list of useful libraries for debugging, updates etc. Within the OCS structure: the `configdb` and `downtime` runs the databases of the instruments and their availability and they are communicated in realtime using internal network communications. The `observation_portal` runs all the API back-ends related to the members, observation requests, proposals, logs, schedule information, status record of submitted requests etc. For any communication to `observation_portal`, it sends queries to `configdb` and `downtime` to verify and framing any observing request. Any submitted request, for example the one shown in Figure6, can be broken into different parts as shown in Figure 5. The LCUs, hosted at the computers controlling the different telescopes and instruments, are communicated through two way API requests by the OCS as soon the schedule is uploaded on the OCS server. In order to schedule the submitted requests we are using a python module '`adaptive_scheduler`[9] developed by the LCO team. This scheduler uses Google's OR-Tools[10] as kernel and avails configurations to support the SCIP, CBC and GLPK free algorithms. It also supports the optimization using premium services like GUROBI[11], but based on our local traffic of the requests, the free algorithms serves the purpose.

The robotic communications sent form the `io_robot`, either as direct submissions (calibrations: bias, flats & arcs) or regular submission (transient monitoring from the Transient Name Server (TNS) triggers after quality filtering) are already tested and being used since last two trimesters. The `io_robot`, which is an auxiliary service replacing human interventions at the top level with pre-defined setup, currently filters triggers from both the TNS and GCN and submits requests to the IO, as applicable. We are testing other trigger resources like BAWG[12] and FINK[13] to enable full compliance for following up observations of the triggers from the LSST. A more technical paper on IO OCS is in preparation

[9] `https://github.com/observatorycontrolsystem/adaptive_scheduler`
[10] `https://developers.google.com/optimization`
[11] `https://www.gurobi.com/`
[12] `https://t.me/+lfchnd4klOdmYTYy`
[13] `https://fink-broker.org/`

VII Workshop on Robotic Autonomous Observatories (October 16-20, 2023)
Editors: Maria Gritsevich, Alberto J. Castro-Tirado, Petr Kubánek, Shashi B. Pandey, and David Hiriart - DOI: https://doi.org/10.22201/ia.14052059p.2025.59.14

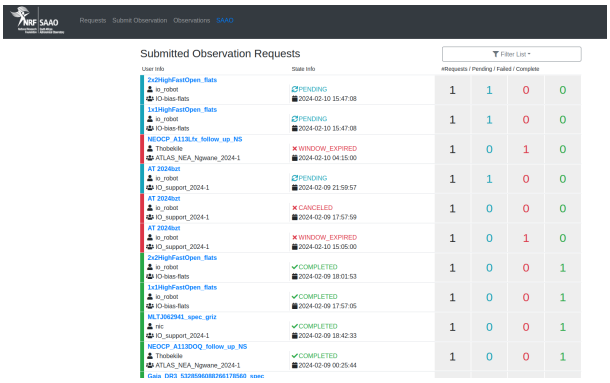


Fig. 7. The snapshot of the IO front-end (`https://ocsio.saao.ac.za`) showing a list of submitted requests. A mojor part of the design of this front-end is taken from the OCS-EXAMPLE[15] project by the LCO.

for the Journal of Astronomical Telescopes, Instruments, and Systems (JATIS).

3. WORK-FLOW AND SUMMARY

The demands of the IO architecture to serve a centralized brain for communicating the users and LCUs are best met by the current verison of the OCS at SAAO. The local production of the LCO's modules, because of its flexibility, have been a vital components of the OCS. The telescope operations (TOPS) and telescope time allocation committee (TAC) at SAAO are responsible for managing the proposal submission and time allocation for any trimester. The respective proposer(s) need to register at IO frontend[16]. Any user with already approved instrument time, submits observation requests to their assigned proposals. The submission can be made through the said portal or programmatically. The requests framed in formats supported by the pre-defined validation schema are validated in realtime and only the successful ones are submitted. The submitted requests are stored in the `observation_portal` database. The `adaptive_scheduler` runs every 2 minutes to generate an optimized schedule for all active instruments and update it on the OCS API. The IOIL analyses the schedules on a regular interval to check for any urgent time-critical or rapid response submissions. It can cancel the ongoing monitoring, if urgent action is needed otherwise before every new telescope pointing the most updated schedule is used. For every pointing the IOIL communicates with the LCUs for observing instructions and also to get updates about the data acquisition. It is also responsible for updating the status tags at the OCS server such as 'PENDING', 'ATTEMPTED' and 'COMPLETED' with a short summary. Once the observation is tagged as 'COMPLETED', a trigger is generated for the real-time analysis procedures (pipelines) and the SAAO Science Archive to ingest the data. The pipelines and archiving system are under commissioning phase.

Figure 7 shows a glimpse of the IO front-end showcasing the active IO system, listing various requests from manual and robotic submissions.

Acknowledgements: The IO programme is supported by the National Research Foundation, South Africa. SC acknowledges the discussions with Mr. Jon Nation from the LCO which were very helpful in adapting the OCS into IO architecture. SC also acknowledges the discussions with Dr. Christain Hettlage and Mr. Iriwaan Simon related to debugging of networking the different dockerized services. The authors also acknowledge entire efforts of the LCO team for this Open Source Observatory Control System Project, which is supported with the generous financial support from the Heising-Simons Foundation.

REFERENCES

Abbott, B. P., Abbott, R., Abbott, T. D., et al. 2017, ApJ, 848, L12, doi:10.3847/2041-8213/aa91c9

Andreoni, I., Coughlin, M. W., Criswell, A. W., et al. 2024, APh, 155, 102904, doi:10.1016/j.astropartphys.2023.102904

EHT MWL Science Working Group, Algaba, J. C., Anczarski, J., et al. 2021, ApJ, 911, L11, doi:10.3847/2041-8213/abef71

Erasmus, N., Potter, S. B., van Gend, C. H. D., et al. 2025, RMxAC, 59,

van Gend, C. H. D. R., Sickafoose, A. A., Potter, S. B., et al. 2020, Proc. SPIE, 11452, 1145206, doi:10.1117/12.2562161

IceCube Collaboration, Aartsen, M. G., Ackermann, M., et al. 2018, Sci, 361, 147, doi:10.1126/science.aat2890

Ivezić, Ž., Kahn, S. M., Tyson, J. A., et al. 2019, ApJ, 873, 111, doi:10.3847/1538-4357/ab042c

Potter, S. 2021, AFAS2 2021: AfAS, 34

Plucinsky, P. P., Beardmore, A. P., Foster, A., et al. 2017, A&A, 597, A35, doi:10.1051/0004-6361/201628824

Yao, Y., Kulkarni, S. R., Burdge, K. B., et al. 2021, ApJ, 920, 120, doi:10.3847/1538-4357/ac15f9

[16] `https://ocsio.saao.ac.za`

Revista Mexicana de Astronomía y Astrofísica Serie de Conferencias (RMxAC), **59**, 77–80 (2025)
© 2025: Instituto de Astronomía, Universidad Nacional Autónoma de México
https://doi.org/10.22201/ia.14052059p.2025.59.15

VII Workshop on Robotic Autonomous Observatories (October 16-20, 2023)
Editors: Maria Gritsevich, Alberto J. Castro-Tirado, Petr Kubánek, Shashi B. Pandey, and David Hiriart - DOI: https://doi.org/10.22201/ia.14052059p.2025.59.15

MANAGEMENT OF A MULTI-USER ROBOTIC OBSERVATORY

John Moore[1,2], Bruce Gendre[1,3], David Coward[1], Fiona Panther[1,4], and Eloise Moore[1]

RESUMEN

El Observatorio Zadko, ubicado aproximadamente a 70 km al norte de Perth, en la reserva natural de Yeal dentro de la Comarca de Gingin, Australia Occidental, albergó inicialmente el Telescopio Zadko de rápido movimiento y con un diámetro de 1,0 m a f/4, que se puso en servicio en junio de 2008. Desde entonces, el telescopio Zadko ha demostrado su eficacia al detectar numerosos estallidos de rayos gamma, dos de los cuales han sido las "fuentes transitorias ópticas" más distantes fotografiadas por un telescopio australiano. El telescopio Zadko también contribuyó al descubrimiento de la fusión de dos estrellas de neutrones en 2017, hecho que tuvo gran repercusión. Otro uso importante del Telescopio Zadko es el seguimiento y cartografiado de basura espacial, que consisten en todos los objetos fabricados por el ser humano, incluidos sus fragmentos o partes, distintos de los vehículos espaciales activos y con un tamaño de más de 10 micras y que orbitan la Tierra en el espacio exterior. El telescopio Zadko forma parte del Centro de Excelencia ARC para el Descubrimiento de Ondas Gravitacionales (OzGrav). Con miras a apoyar las actualizaciones en curso de los instrumentos científicos y el mantenimiento de los observatorios, ha resultado fundamental atraer financiación adicional y buscar colaboración con socios internacionales. En este artículo detallamos los detalles administrativos y técnicos del Observatorio, centrándonos en la sostenibilidad del Observatorio y su continuo potencial para el crecimiento futuro hasta convertirse en un Centro de Vigilancia Espacial reconocido internacionalmente. También se comenta la evolución del Observatorio, desde su estado inicial albergando un único instrumento, hasta sus capacidades actuales con múltiples telescopios e instrumentos, para terminar esbozando el futuro del Observatorio y su emplazamiento.

ABSTRACT

The Zadko Observatory located approximately 70 kilometres north of Perth in the Yeal nature reserve within the Shire of Gingin, Western Australia, initially housed the 1.0 metre f/4 fast-slew Zadko Telescope which was commissioned in June 2008. Since the Zadko telescope has been in operation it has proven its worth by detecting numerous Gamma Ray Burst afterglows, two of these being the most distant optical transients imaged by an Australian telescope. The Zadko telescope also contributed to the discovery of colliding neutron stars in 2017 capturing the imagination of the public. Another important use for the Zadko Telescope is the tracking and mapping of Space Debris which consist of all man-made objects, including their fragments or parts, other than active space vehicles larger than 10 microns and orbiting the Earth in outer space. The Zadko telescope forms part of the ARC Centre of Excellence for Gravitational Wave Discovery (OzGrav). With a view to supporting ongoing scientific instrument upgrades and observatory maintenance it has proven critical to attract additional funding and seek out collaboration with international partners. In this article, we will focus on the administrative and technical details of the Observatory, focusing on the sustainability of the Observatory and its ongoing potential for future growth into an internationally recognized Space Surveillance Hub. We will review the evolution of the Observatory, from its early, single instrument state, to its current multi-telescope and multi-instrument capabilities. We will finish by outlining the future of the Observatory and surrounds.

Key Words: Miscellaneous — Telescopes

1. INTRODUCTION

The Zadko Observatory is a unique fully automated robotic observatory (Moore et al. 2021) located at the Gingin Gravity Precinct, Western Australia (see Figure 1). The Observatory is of National and International importance, with more than 100 scientists utilizing it routinely and it remains the

[1]University of Western Australia, OzGrav ARC Centre of Excellence, 35 Stirling Highway, M013, 6009 Crawley, WA, Australia.
[2]Email address: john.moore@uwa.edu.au
[3]Present address: University of the Virgin Islands, VI, USA.
[4]Forest Fellow.

VII Workshop on Robotic Autonomous Observatories (October 16-20, 2023)
Editors: Maria Gritsevich, Alberto J. Castro-Tirado, Petr Kubánek, Shashi B. Pandey, and David Hiriart - DOI: https://doi.org/10.22201/ia.14052059p.2025.59.15

only facility operating a metre class telescope with deep imaging capability between the east coast of Australia and South Africa in the Southern hemisphere. Indeed, this facility is the only observatory worldwide able to study Southern astronomical events after 02:00 AWST, placing it in high demand both Nationally and Internationally (Coward et al. 2017).

Due to the Zadko Observatorys longitude, it has become apparent that many Eastern States Universities and International Space Agencies are keen to utilize our unique geographical location. This is due to the West coast being the last place in Australia to observe the night sky in the early morning: it is still night in Perth while it is already the day on the East coast. For this reason alone, the Zadko Observatory has been identified as a premium site by other astronomical groups and commercial entities to compliment sites located in the East. As a consequence, this can only lead to further demand and development of the Space Surveillance Hub at Gingin.

The purpose of this short paper is to highlight the management of a multi-user robotic observatory, and how the various conflicting scientific goals are balanced in order to extract as much data from the site as possible. In a companion paper (Gendre et al., this proceeding), we will present how the site location can impact the scientific goals and how we try to mitigate some of them. This paper is organised as follow. In Section 2 we recall the historical aspects of the observatory, from its initial design to its current one. In Section 3 we present the current upgrade of the observatory and how we will use the Zadko Telescope. Finally, in Section 4, we indicate how we expect the Observatory to grow.

2. HISTORICAL ASPECTS

The 1.0 metre f/4 Ritchey-Chrétien Zadko Telescope was constructed by DFM Engineering Inc. in Longmont Colorado USA and donated to the University of Western Australia by Resource Company Claire Energy CEO, Jim Zadko. The Zadko Observatory is located at Longitude 115°42′49″E and Latitude 31°21′24″S with Observatory Code D20. Due to operational issues, the original 6.7 metre fibreglass domed observatory, which the Zadko Telescope was initially housed, was replaced in 2011 with a state of the art purpose built robotic rolling roof autonomous observatory with a dedicated 21 m^2 constant temperature climate controlled operations room. In addition to this, a climate controlled telescope service room to mirror the operation room was also added. This had the benefit of allowing for possible future conversion into a second control room when other telescopes were added to the increased 63 m^2 telescope observation room. Robotic control of the rolling roof is performed using a PLC-Burgess system designed and manufactured by the electronics workshop at Observatoire de Haute-Provence, France. A brief system overview is explained here: The PLC is connected to a dedicated server via an Ethernet connection. The weather station and the cloud sensor are connected to the serial ports of the server. The PC processes this data and sends commands to the PLC in order to control the roof in a safe condition. The PLC receives these commands from the server and sends its status through a socket connection. All the safety devices (rain detectors, humidity and temperature sensors, power probe before the UPS unit) are controlled by the PLC. In the event of a communication failure with the PC, the PLC closes the roof.

3. CURRENT UPGRADE OF THE OBSERVATORY

To realize the high potential of the site, we have initiated a project aimed at transforming the Zadko Observatory and surrounds into a Space Surveillance Hub in Western Australia that can be used by major international space agencies and commercial partners. The project is driven by a partnership with the European Space Agency (ESA), the Polish Space Agency (POLSA) and the Japan Aerospace Exploration Agency (JAXA). Each of these entities require observations of the Near-Earth environment at the specific location of the Zadko Observatory which are not currently feasible owing to the ageing of the observatory and its outdated components. Indeed, most of the electronic control systems within the Zadko Observatory were designed and manufactured in the late 1990s and require urgent upgrades to ensure the longevity of this critically important facility. The existing computers cannot provide the level of cyber-security required by a modern observatory, and its instrumentation is becoming obsolete and degraded due to more than ten years of continuous operation.

The global commercial investment in space-related technology is rapidly increasing (Gladman et al. 2000). The Australian Government has recognized the economic benefits of this evolution, and is actively promoting links between defence, the space industry and the university sector. This investment outcome depends critically on the successful operation of space assets owned and operated by commercial entities and other international partners. One of the core topics covered by our current project is

VII Workshop on Robotic Autonomous Observatories (October 16-20, 2023)
Editors: Maria Gritsevich, Alberto J. Castro-Tirado, Petr Kubánek, Shashi B. Pandey, and David Hiriart - DOI: https://doi.org/10.22201/ia.14052059p.2025.59.15



Fig. 1. An overview of the Zadko Observatory showing an aerial shot with the rolling roof open and various images of instruments within including (from left to right) the Zadko, Ariane Group, POLSA-1, JAXA and Slingshot telescopes, hosted within the Observatory.

the possibility to track space hazards, allowing for pre-emptive actions such as an anticipated alert to a population, or planning an action to avoid collision and potential destruction of space and ground assets. Another topic is the possible use of the facility into the study of the degradation of satellites in orbit, in particular how payloads, structural components and solar panels react to space conditions over time, with vital information obtained used to assist space and satellite manufacturing commercial industry growth. In fact, this Project would enable a versatile Hub offering numerous benefits to the space sector.

Due to the aforementioned reasons, we have decided to upgrade the IT structure, critical to sustaining the activities of the Observatory, and the Telescope Control System (TCS) of the Zadko Telescope itself (including its motor, allowing for fast, precise tracking of satellites and Near-Earth Orbiters). These activities also involve an upgrade of the instrument chain, in order to increase the field of view of the telescope, in case of observations of objects with a poorly constrained position.

We do expect that these modifications will increase the request of observation time on the Zadko Telescope, due to its improved versatility, enabling further diversification of its scientific program. This will obviously also potentially lead to an over subscription of the telescope viewing time. For this reason, all requests for use of the Zadko Telescope will be handled by a scientific committee, granting access to the instrument based on the scientific merit of the request for 700 hours per year. This committee will also define a core program of 900 hours per year, based on collaborations signed between the Observatory and other research institutions, and a contributed program of 1000 hours per year, which will request a fee for observation time. This will provide additional funding for specific future improvements and upgrades. All of these programs will be open to any organization upon request.

In addition, the Zadko Observatory has been able to attract commercial contracts and associated funding since 2016 due to its unique location and its expert support team. As part of the refurbishment process, climate control of the observation room and roof operations have been upgraded in order to maximize the roof open time, where any instrument can perform observations, while still allowing for some protection against inclement weather (see Gendre et al., these proceedings). These commercial contracts will continue with the potential for further development going forward. Some discussions have commenced with another entity for hosting of a new instrument. All the funds obtained by the commercial contracts and the paid contributed program using the Zadko Telescope will be used to support the ongoing daytoday operation of the Zadko Observatory.

4. FUTURE PLANS

Having now secured consistent funding for the Zadko Observatory, considered critical for its ongoing operations and maintenance, we can now look to the future with confidence. As the nature of space situational awareness and space defence is rapidly changing, we consider ourselves to be in a transition phase to participate in this sector. One area

VII Workshop on Robotic Autonomous Observatories (October 16-20, 2023)
Editors: Maria Gritsevich, Alberto J. Castro-Tirado, Petr Kubánek, Shashi B. Pandey, and David Hiriart - DOI: https://doi.org/10.22201/ia.14052059p.2025.59.15

that we have recently been invited to collaborate in, is the International Asteroid Warning Network (IAWN, United Nations 2014) with the aim to establish a worldwide network of instruments used to detect, track and physically characterize near-Earth objects (NEOs) to determine those that are potential impact threats to Earth. Consequently, in partnership with the University of New South Wales (UNSW), the JPL-NASA/CSIRO group based at Tidbinbilla and the University of Tasmania we have formed 'The Australian Consortium for Planetary Defence' using both optical and radar. The consortium of JPL-NASA/CSIRO/UNSW/UTAS/UWA, offers a wide baseline radio frequency and optical capability stretching from the West to East coast of Australia (Kruzins et al., in preparation). Another project we are about to commence in partnership with the Polish space agency (POLSA) is to understand how defunct satellites degrade over time to produce space debris. To accomplish this the project will employ low resolution spectroscopy to measure the surface degradation of geostationary satellites.

As mentioned previously once the upgrades to the Zadko Telescope are complete we expect an increase in demand from various users. This increased use of telescope viewing time has several benefits being increased revenue, potential for collaboration, improved international visibility for the observatory plus maximum output from our scientific asset. Now referring to the site where the Zadko Observatory is situated as a 'Space Surveillance Hub' we are looking to expand beyond the Zadko Observatory to its surrounds. We are hosting another instrument for the USAFA's Falcon Telescope Network (Chun et al. 2018) in close proximity to the Zadko Observatory and are currently in discussion with another international partner to host one other instrument onsite.

Acknowledgements: This research was supported by the Australian Research Council Centre of Excellence for Gravitational Wave Discovery (OzGrav), through project number CE170100004. E.M. acknowledges support from the Zadko Postgraduate Fellowship and International Space Centre (ISC).The Zadko Observatory is also supported by the University of Western Australias Office of Research and forms part of UWAs International Space Centre (ISC).

REFERENCES

Chun, F. K., Tippets, R. D., Strong, D. M., et al. 2018, PASP, 130, 095003, doi:10.1088/1538-3873/aad03f

Coward, D. M., Todd, M., Vaalsta, T. P., et al. 2010, PASA, 27, 331, doi:10.1071/AS09078

Coward, D. M., Gendre, B., Sutton, P. J., & Howell, E. J. 2011, MNRAS, 415, L26

Coward, D. M., Gendre, B., Tanga, P., Turpin, D., Zadko, J., Dodson, R., Devogéle, M., Howell, E. J. , Kennewell, J. K., Boer, M., Klotz, A., Dornic, D., Moore, J. A., & Heary, A. 2017, PASA, 34, 16

Gladman, B., Michel, P., & Froeschlé, C. 2000, Icar, 146, 176

Moore, J. A., Gendre, B., Coward, D. M., et al. 2021, RMxAC, 53, 35, doi:10.22201/ia.14052059p.2021.53.08

United Nations Office for outer space affairs, 2014, description available at `https://iawn.net/documents/18-03593\_NEO\_Brochure\_Ebook.pdf`

Revista Mexicana de Astronomía y Astrofísica Serie de Conferencias (RMxAC), **59**, 81–85 (2025)
© 2025: Instituto de Astronomía, Universidad Nacional Autónoma de México
https://doi.org/10.22201/ia.14052059p.2025.59.16

VII Workshop on Robotic Autonomous Observatories (October 16-20, 2023)
Editors: Maria Griffsevich, Alberto J. Castro-Tirado, Petr Kubánek, Shashi B. Pandey, and David Hiriart - DOI: https://doi.org/10.22201/ia.14052059p.2025.59.16

AUTONOMOUS SCHEDULING AT THE TJO TELESCOPE

D. Baroch[1], E. Herrero[1], P. Gil[1], F. Domene[1], A. Rojas[1], and M. Ribó[1,2]

RESUMEN

Disponer de un planificador autónomo y eficiente es un aspecto fundamental para cualquier telescopio robótico, dada su influencia directa en el rendimiento científico de un observatorio. Un sistema de este tipo debería priorizar e identificar observaciones críticas, tener en cuenta las coordenadas de los cuerpos celestes, considerar las condiciones meteorológicas y asegurar que las observaciones cumplan con diversas restricciones definidas por el usuario. Todo esto debe lograrse a la vez que se optimiza la lista de objetos a observar dentro de un intervalo de tiempo predefinido, todo ello sin requerir intervención humana.

En este artículo presentamos ISROCS, el programa de planificación autónoma del telescopio Joan Oró (TJO), un telescopio totalmente robótico de 0,8 m de apertura, situado en el Observatorio del Montsec y dedicado a la investigación astrofísica y a actividades de vigilancia y seguimiento espacial. Explicamos cuales son los procesos empleados por ISROCS para producir planificaciones eficientes y revelamos mejoras recientes destinadas a hacer posible la planificación dinámica durante la propia ejecución de las observaciones. Esto incluye la capacidad de planificar rápidamente nuevas observaciones enviadas por los usuarios, logrando tiempos de reacción de menos de 2 minutos. Esta nueva función permitirá a los usuarios el uso de alertas de eventos transitorios emitidas por sistemas externos para enviar observaciones en tiempo real de manera automática, la cual será crucial para la rápida observación de fenómenos astrofísicos de corta duración.

ABSTRACT

Efficient autonomous scheduling is a paramount aspect of a fully robotic telescope, given its direct influence on the scientific yield of an observatory. Such a system should prioritize tasks and identify critical observations, factor in the coordinates of celestial bodies, consider weather conditions, and ensure that the tasks meet various user-defined constraints. All of this must be achieved while optimizing the list of tasks to be observed within a predefined time interval, all without requiring human intervention.

In this proceedings we introduce ISROCS, the autonomous scheduling software of the Joan Oró telescope (TJO), a fully-robotic 0.8m telescope at the Montsec Observatory dedicated to astrophysical research and Space Surveillance and Tracking activities. We explain the processes employed by ISROCS to deliver time-efficient schedules and reveal recent upgrades aimed at enabling dynamic planning during the observations. This includes the capability to swiftly include new tasks submitted by users, with a reaction time of under 2 minutes. This new feature will enable users to use alerts issued by external alert systems for real-time observations with minimal oversight, which will be crucial for the rapid observation of short-lived astrophysical phenomena.

Key Words: telescopes — instrumentation: miscellaneous

1. INTRODUCTION

Observing time on multi-million telescopes represents a valuable and limited resource in astronomy. As these instruments operate within finite lifetimes, the efficient utilization of their observing time becomes of the upmost importance. The optimization of observing schedules is therefore crucial not only for maximizing the scientific return of these telescopes but also for justifying the substantial investments made in these facilities.

Traditionally, the creation of observation schedules has been an intensive manual process, often referred to as queue scheduling, which needs to select tasks meeting various constraints and objectives. While this manual approach is capable of producing decent results it has its drawbacks: it is time-consuming and requires a continuous supervision by the staff, hindering the ability to rapidly respond to changing observing conditions, weather losses, and target-of-opportunity events (Bellm et al. 2019).

[1]Institut d'Estudis Espacials de Catalunya (IEEC), c/ Gran Capità 2-4, E08034 Barcelona, Spain.
[2]Departament de Física Quàntica i Astrofísica, Institut de Ciències del Cosmos (ICCUB), Universitat de Barcelona, c/ Martí i Franquès 1, E08028 Barcelona, Spain.

VII Workshop on Robotic Autonomous Observatories (October 16-20, 2023)
Editors: Maria Gritsevich, Alberto J. Castro-Tirado, Petr Kubánek, Shashi B. Pandey, and David Hiriart - DOI: https://doi.org/10.22201/ia.14052059p.2025.59.16



Fig. 1. Night view of the OdM. Image Credit: E. Herrero.

Given the surge of new fully-robotic telescopes in the last decades (Steele & Carter 1997; Bakos et al. 2002), there have been a growing interest in exploring different automated scheduling techniques (see e.g. Granzer 2004; Colomé et al. 2012). This interest is not only aimed at reducing the workload on human operators, but also at optimizing scheduling strategies for enhanced scientific outcomes.

One of the most used automated scheduling algorithms is the dispatch scheduling (Denny 2004). This method involves selecting the most advantageous task based on current conditions and a merit function. The dispatch scheduler is notably fast, and therefore can easily handle changes in observing conditions and the addition of target-of-opportunity events autonomously. This technique, however, only focuses on scheduling one task at a time, potentially overlooking the broader, long-term objectives outlined in various research proposals, such as survey completeness. Another challenge is the difficulty in scheduling calibration observations, since the scheduler does not know ahead of time the tasks to observe.

Another common scheduling algorithm is optimal scheduling (Granzer 2004). Similar to queue-scheduling, it autonomously constructs a schedule prior to actual observations by evaluating many possible combinations of tasks and selecting the one with the highest yield. This has the advantage that minimizes the slewing time over the whole night, while also defining calibration tasks. However, the computational requirements for computing an optimal schedule make this technique vulnerable to unexpected changes in conditions, such as changing weather or the addition of new urgent observation of transient events.

In this proceedings, we provide a brief overview of the scheduling algorithm employed at the fully-robotic Joan Oró Telescope (TJO). Furthermore, we describe the recent upgrades made to the scheduler, combining the strenghts of both dispatch and optimal scheduling algorithms. This new approach ensures a global and adaptable scheduling strategy, enabling the use of the TJO telescope for the observation of target-of-opportunity events in combination with long term monitoring programs.

2. THE MONTSEC OBSERVATORY

The TJO telescope is mounted at the Montsec Observatory[3] (OdM), located at an altitude of 1570 m in Sant Esteve de la Sarga, 50 km north of the city of Lleida (Catalonia, Northeastern Spain). This site was carefully selected for its exceptional conditions for astronomical observation. First of all, it is in a region certified as an UNESCO Starlight Reserve[4], and explicitly protected from light pollution by a law of the Catalan Parliament. The night sky brightness at the site reaches values as low as 22.0 mag arcsec^{-2} at the zenith, and between 21.520.6 mag arcsec^{-2} at a height of 45° above the horizon, both in the Johnson V band (Colomé et al. 2008). Secondly, the weather conditions are quite good during the year, allowing operations in around 70% of all the night time. Finally, it has a very low astronomical seeing, with a median value of 0.82" and better than 0.7" during 32% of the night time

[3] https://www.montsec.ieec.cat/

[4] https://en.fundacionstarlight.org/contenido/46-list-starlight-reserves.html

VII Workshop on Robotic Autonomous Observatories (October 16-20, 2023)
Editors: Maria Griffsevich, Alberto J. Castro-Tirado, Petr Kubánek, Shashi B. Pandey, and David Hiriart - DOI: https://doi.org/10.22201/ia.14052059p.2025.59.16

(Colomé et al. 2010), as reported by five months of measurements using a Robotic Differential Image Motion Monitor (DIMM Sarazin & Roddier 1990).

The observatory has multiple facilities that are devoted to different areas, such as:

- Research: two telescopes offered to the scientific community, the TJO (0.8 m) and the TFRM[5] (0.5 m), and an All-Sky Camera for fireball and meteor detection.
- Teleport: S-band and UHF/VHF facilities for communication with satellites.
- Services to the community: a weather monitoring station of the Catalan Meteorological Service, an atmospheric pollution and quality monitoring station, firefighter surveillance cameras, and radiolinks to provide internet access to hydroelectric generating systems and nearby towns.

3. THE TJO TELESCOPE

The main facility at the OdM is the Joan Oró telescope (TJO), which has been operated by the Institute for Space Studies of Catalonia[6] (IEEC) since its construction in 2004. It is a Ritchey-Chrétien telescope with an aperture of 80 centimeters and a focal ratio of F/9.8, and is fully robotic, with no human intervention required apart from supervision and maintenance.

The TJO is equipped with two simultaneous instruments. The main instrument is the Large Area Imager for Astronomy (LAIA), an Andor iKon XL imaging camera with a 4096×4096 back-illuminated sensor, a pixel size of 0.4 arcsec, and a field of view of 30 arcmin. LAIA is mounted together with a rotating filter wheel that contains 5 standard Johnson-Cousins photometric filters (U, B, V, R, and I), 4 Sloan Digital Sky Survey photometric filters (g, r, i, and z), and a narrowband filter centered at the Hα line.

The other instrument mounted at the TJO is the Astronomical mid-REsolution Spectrograph (ARES), an optical spectrograph with a resolution of R=12'000 divided in two spectral windows, one centered at the magnesium triplet (495 to 529 nm) and another centered at the Hα alpha line (634 to 678 nm).

The primary functions of the TJO include satellite surveillance and tracking (SST) activities and scientific research, offering observation time to the scientific community via a Time Allocating Committee (TAC) in two yearly semestral calls for proposals. As for the research areas, the TJO is a multi-purpose telescope, with proposals aimed at stellar variability (e.g. Ribas et al. 2018), stellar activity (e.g. Baroch et al. 2020), transiting exoplanets (e.g. Herrero et al. 2011), Gaia follow-up (e.g. Wyrzykowski et al. 2020), transient sources (e.g. Morales-Garoffolo et al. 2014), or Solar System objects (e.g. Trigo-Rodríguez et al. 2008), among others.

The TJO has been working on a completely unattended control since 2013, requiring minimal human supervision. In order to achieve this level of autonomy, it requires having a reliable, secure, and efficient system that is able to plan, execute, and reduce astronomical data completely unattended.

The current system present at the TJO, the Robotic Observatory Control System (ROCS), is divided in two main nodes: one off-site and another on-site, as depicted in Fig. 2. Each of the nodes is equipped with its own database containing identical information, which is synchronized on a routine basis.

The offsite node, located at the IEEC offices in Barcelona, is in charge of the storage and distribution of data. The main system there is the Management for Users in ROCS (MUR), which is the interface where the users can submit proposals, define the observations, and access and download the observed data. Additionally, as part of an agreement with the Spanish Virtual Observatory (SVO), all the data outside the ownership period (1 year) are made publicly accesible through the SVO webpage[7], where more than 300'000 images spanning 10 years are available to the community.

The onsite node is located at the OdM, and it is in control of unattended operations. The main system in this node is the Observatory Control System (OCS), which is responsible for issuing commands to the dome, telescope, and the instrument (via the Telescope Control System, TCS, and the Instrument Control System, ICS) based on the night plan issued by the scheduler and on the weather conditions. Additionally, the system contains a collection of pipelines (The IEEC Calibration and Analysis Tool, ICAT) used to perform data reduction and quality control. Finally, this node also contains the Intelligent Scheduler for ROCS (ISROCS), which is the autonomous scheduler used to create the night plans.

[5] https://www.racab.cat/es/observatori-fabra/tfrm
[6] https://www.ieec.cat/
[7] https://sdc.cab.inta-csic.es/joro

VII Workshop on Robotic Autonomous Observatories (October 16-20, 2023)
Editors: Maria Gritsevich, Alberto J. Castro-Tirado, Petr Kubánek, Shashi B. Pandey, and David Hiriart - DOI: https://doi.org/10.22201/ia.14052059p.2025.59.16

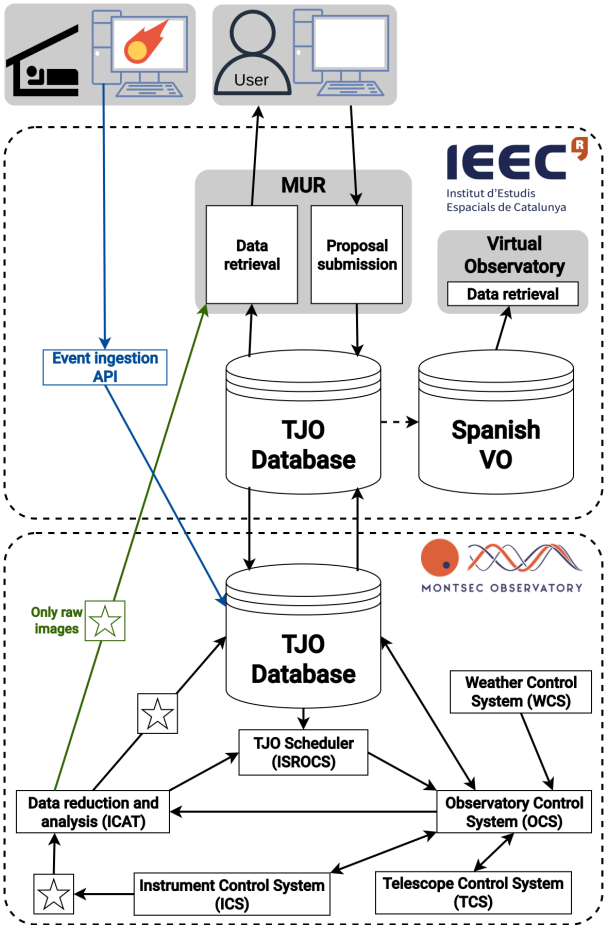


Fig. 2. Schematic diagram of the architecture of the Robotic Observatory Control System (ROCS) of the TJO. The blue and green arrows and icons correspond to new upgrades to the system to allow the ingestion of transient events.

4. ISROCS

The main function of the scheduler is to compute an efficient schedule of astronomical observation tasks that optimizes the available time, which has a direct impact on the scientific return. The scheduler used for the TJO, ISROCS, is a custom layer on top of the Scheduling Telescopes as Autonomous Robotic Systems (STARS, Colomé et al. 2020), which is the scheduler presently in use or soon to be adopted by several ground and space-based observatories, such as CARMENES, CTA, PLATO, and ARIEL, and is being used by the TJO since 2020.

At the TJO, ISROCS is responsible for accessing to the observation tasks that the users have defined in MUR, computing the visibility windows of these tasks based on the observing constraints specified by the users, such as the maximum solar elevation and airmass, the minimum distance to the moon, or the time-delay between to observations of the same object, among others. Then, all the tasks that comply with the observing constraints for the current night are sent to STARS, which uses an optimal scheduling algorithm that tries to maximize the figure-of-merit of the entire schedule, defined as:

$$\mathcal{F} = \sum_i f_i \sigma(t_i), \tag{1}$$

where $\sigma(t_i)$ is a correction factor that depends on the time t at which the target i has been scheduled and is used to penalize tasks scheduled at relatively high airmass values, and f is the figure-of-merit of each individual observation task, given by:

$$f = \begin{cases} p\Delta t \left(1 + \frac{G-R}{\alpha}\right) & \text{if } G \geq R \\ p\Delta t \left(1 - \frac{G-R}{\alpha}\right)^{-1} & \text{if } G < R \end{cases}. \tag{2}$$

In this equation, Δt is the duration in seconds of the observation, p is the priority assigned to the proposal as defined by the TAC, G is the fraction between amount of time already observed and the total time granted to the proposal, and R is the fraction of semester passed. Finally, α is a configurable parameter that is used to control the weight of the different parameters in the function. In that way, for example, the tasks of a proposal that has not been observed yet at the end of the semester will have a higher figure-of-merit than a proposal that has been normally observed.

Finally, once the schedule that optimizes the figure-of-merit is found by STARS, ISROCS sends the night plan with the tasks to be observed during the night to the OCS, which will trigger the observations at the specified time.

5. OBSERVING TRANSIENT EVENTS AT THE TJO

As outlined in Sect. 1, one of the major limitations of using an optimal scheduling algorithm, as the one used at the TJO, is its inability to rapidly react to urgent observation of transient events. These unpredictable and short-lived astronomical phenomena, such as stellar flares, near earth objects, supernovae, gamma ray bursts, microlensing events, and more, require instantaneous follow-up observations.

Recognizing the critical need for swift responses to observe these events, we have performed significant enhancements across all subsystems involved in the scheduling system of the TJO. With these improvements, we achieved a reaction time for photometric observations of around 1-2 minutes since the

VII Workshop on Robotic Autonomous Observatories (October 16-20, 2023)
Editors: Maria Gritsevich, Alberto J. Castro-Tirado, Petr Kubánek, Shashi B. Pandey, and David Hiriart - DOI: https://doi.org/10.22201/ia.14052059p.2025.59.16

alerts are issued, corresponding to the time required to move the dome and point the telescope. The key updates include:

- **Dynamic nighttime scheduling:** ISROCS can now dynamically generate new schedules during the night, using real-time information about the progress of ongoing observations, such that completed or partially observed tasks are not included in the new plan. Nighttime scheduling is triggered only in two scenarios: firstly, after returning from bad weather conditions, enabling the rescheduling of high-priority observations that could not be observed before due to adverse weather conditions. Secondly, in response to the addition of new tasks to our database, providing a prompt option for urgent observations.

- **API for programmatic observations:** The creation of a new API enables users subscribed to transient event alert distribution services to programmatically submit observation requests. Users can use their codes that are continuously monitoring these alerts to automatically trigger new photometric observations at the TJO. When the observation is received, it is immediately scheduled at the earliest time allowed by the observing constraints, and sent to the OCS to start the observation. In parallel, a new night plan is requested to ISROCS, which will schedule the remaining tasks around the newly received observation with a reaction time of under 2 minutes.

- **Immediate raw image access:** Users now have the option to download raw images in real-time as they are being observed. This immediate access to raw data gives the user the ability to respond effectively to evolving astronomical phenomena. This feature is particularly valuable in scenarios such as imminent impactor observations, allowing users to analyze data immediately and adjust observing strategies as needed.

6. SUMMARY

In this proceedings, we provide an overview of the scheduling system employed by the TJO telescope at the OdM, and introduce significant enhancements aimed at enabling photometric observations of transient events. These new upgrades strategically align the TJO with the current trend toward rapid-response observational capabilities.

Acknowledgments: The Joan Oró Telescope (TJO) of the Montsec Observatory (OdM) is owned by the Catalan Government and operated by the Institute for Space Studies of Catalonia (IEEC).

REFERENCES

Bakos, G. Á., Lázár, J., Papp, I., Sári, P., & Green, E. M. 2002, PASP, 114, 974
Baroch, D., Morales, J. C., Ribas, I., et al. 2020, A&A, 641, A69
Bellm, E. C., Kulkarni, S. R., Barlow, T., et al. 2019, PASP, 131, 068003
Colomé, J., Nakhjiri, N., García-Piquer, Á., Morales, J. C., & Vilardell, F. 2020, ASPC, 527, 313
Colomé, J., Ribas, I., Fernández, D., et al. 2008, Conf. SPIE, 70192K
Colomé, J., Ribas, I., Francisco, X., et al. 2010, AdAst, 2010, 183016
Colomé, J., Sanz, J., Vilardell, F., Ribas, I., & Gil, P. 2012, Conf. SPIE, 845127
Denny, R. B. 2004, SASS, 23, 35
Granzer, T. 2004, AN, 325, 513
Herrero, E., Morales, J. C., Ribas, I., & Naves, R. 2011, A&A, 526, L10
Morales-Garoffolo, A., Elias-Rosa, N., Benetti, S., et al. 2014, MNRAS, 445, 1647
Ribas, I., Tuomi, M., Reiners, A., et al. 2018, Natur, 563, 365
Sarazin, M. & Roddier, F. 1990, A&A, 227, 294
Steele, I. A. & Carter, D. 1997, Proc SPIE, 3112, 222
Trigo-Rodríguez, J. M., García-Melendo, E., Davidsson, B. J. R., et al. 2008, A&A, 485, 599
Wyrzykowski, Ł., Mróz, P., Rybicki, K. A., et al. 2020, A&A, 633, A98

Revista Mexicana de Astronomía y Astrofísica Serie de Conferencias (RMxAC), **59**, 87–91 (2025)
© 2025: Instituto de Astronomía, Universidad Nacional Autónoma de México
https://doi.org/10.22201/ia.14052059p.2025.59.17

VII Workshop on Robotic Autonomous Observatories (October 16-20, 2023)
Editors: Maria Gritsevich, Alberto J. Castro-Tirado, Petr Kubánek, Shashi B. Pandey, and David Hiriart - DOI: https://doi.org/10.22201/ia.14052059p.2025.59.17

UNSYNCHRONIZED FIREBALL ANALYSIS AND CHALLENGES IN DIMENSIONLESS ATMOSPHERIC FLIGHT PARAMETRIZATION: THE SPMN230522 SUPERBOLIDE AS A CASE STUDY

E. Peña-Asensio[1,2], P. Grèbol-Tomàs[2,3], J. M. Trigo-Rodríguez[2,3], M. Gritsevich[4,5,6,7], A. Rimola[1], M. Corretgé-Gilart[8], C. Guasch[8], C. Alcaraz[8], V. Ibáñez[8], A. Gómez[8], and J. Gómez[8]

RESUMEN

La triangulación de las trayectorias de bólidos facilita la reconstrucción del vuelo atmosférico y la determinación de la órbita heliocéntrica. La sincronización de fotogramas entre estaciones de observación no es trivial, especialmente con equipos de bajo rendimiento. Para abordar esto, implementamos un enfoque desincronizado compensando con una calibración de cámara robusta. En el contexto del análisis de entrada atmosférica, el método α-β ofrece un modelo adimensional efectivo, aunque sus resultados son sensibles a las técnicas de suavizado de datos. Esto se subraya con el evento del superbólido SPMN230522 que cruzó Cataluña el 23 de mayo de 2022, analizado por la Red de Investigación sobre Bólidos y Meteoritos (SPMN). Además, el diagrama α-β se ha revelado como una herramienta valiosa para la identificación de bólidos con potencial de generar meteoritos, demostrando su eficacia mediante su aplicación a la extensa base de datos de la red FRIPON.

ABSTRACT

Triangulation of fireball trajectories facilitates atmospheric path reconstruction and heliocentric orbit determination. Frame synchronization across networks with varied equipment capabilities presents a challenge. To address this, we implement an unsynchronized approach, underpinned by robust camera calibration. For atmospheric entry analysis, the α-β method offers an effective dimensionless model, though its outcomes are sensitive to the data smoothing techniques employed. This is underscored by the SPMN230522 superbolide event crossing Catalonia on 23 May 2022, analyzed by the Spanish Fireball and Meteorite Network (SPMN). Furthermore, the α-β diagram has proven to be a useful tool for pinpointing meteorite-producing fireballs, with its application to the FRIPON network's comprehensive dataset further validating its utility.

Key Words: Ablation — Atmospheric flight — Fireballs — Meteorites — Meteors — Superbolides

1. INTRODUCTION

Ground-based meteor networks offer in-depth studies of meteoric activity and facilitate campaigns aimed at recovering recently fallen meteorites (Wetherill & Revelle 1981; Brown et al. 2013). These meteorites provide valuable scientific insights into the origin and evolution of our Solar System (Ceplecha et al. 1998; Trigo-Rodríguez et al. 2015; Kyrylenko et al. 2023). Optical devices used for fireball multistation triangulation enable the reconstruction of atmospheric trajectory, luminosity, possible strewn field, and heliocentric orbit (Ceplecha 1987; Gritsevich & Koschny 2011; Dmitriev et al. 2015; Moilanen et al. 2021).

One critical and non-trivial aspect of research in this field involves determining the velocity curve (along with its associated uncertainty) of a meteoroid as it undergoes ablation upon entering Earth's atmosphere (Egal et al. 2017). Extracting spatial-temporal information from recordings captured by different cameras and merging them can be challenging due to occasional unsynchronized stations and data storage errors, which are more prevalent in pro-am collaborations that often involve equipment of varying performance. Consequently, it becomes imperative to employ methods not reliant on

[1]Departament de Química, Universitat Autònoma de Barcelona, 08193 Bellaterra, Catalonia, Spain (eloy.peas@gmail.com, eloy.pena@uab.cat).
[2]Institut de Ciències de l´Espai (ICE, CSIC), Campus UAB, C/ de Can Magrans s/n, 08193 Cerdanyola del Vallès, Catalonia, Spain (trigo@ice.csic.es).
[3]Institut d´Estudis Espacials de Catalunya (IEEC), 08034 Barcelona, Catalonia, Spain.
[4]Swedish Institute of Space Physics (IRF), Bengt Hultqvists vg 1, SE-98192, Kiruna, Sweden.
[5]Finnish Fireball Network, Ursa Astronomical Association, Kopernikuksentie 1, Helsinki FI-00130, Finland.
[6]Faculty of Science, University of Helsinki, Gustaf Hällsrömin katu 2, FI-00014 Helsinki, Finland.
[7]Institute of Physics and Technology, Ural Federal University, Mira str. 19, 620002 Ekaterinburg, Russia.
[8]Spanish Fireball and Meteorite Network (SPMN-CSIC) citizen team, Institut de Ciències de l´Espai (ICE, CSIC), Campus UAB, C/ de Can Magrans s/n, 08193 Cerdanyola del Vallès, Catalonia, Spain.

VII Workshop on Robotic Autonomous Observatories (October 16-20, 2023)
Editors: Maria Gritsevich, Alberto J. Castro-Tirado, Petr Kubánek, Shashi B. Pandey, and David Hiriart - DOI: https://doi.org/10.22201/ia.14052059p.2025.59.17

achieving precise timing synchronization. Thanks to robust lens calibration techniques (Borovicka et al. 1995), we can achieve a high level of spatial accuracy when observing fireballs. This, in conjunction with the plane intersection method, enables us to consistently arrange the captured frames based on meteoroid height, thereby facilitating the collection of point-by-point, combineable velocity measurements.

A neat approach to assess the trajectory without making assumptions about any parameters is through the α-β method (Gritsevich 2007, 2009) with its latest modification applicable to arbitrary atmospheric models or weather conditions (Lyytinen & Gritsevich 2016). It relies on dimensionless equations resulting from scaling laws applied to the single-body flight theory (Stulov 1997), providing the ballistic coefficient α and mass-loss parameter β for any event with a certain level of deceleration, using only height y and velocity v data. Due to observational constraints that yield velocity dispersion and nonlinearity of the formulas, this approach benefits from smoothing the data. However, results may be sensitive to this pretreatment.

2. THE SPMN230522 SUPERBOLIDE

We demonstrate and discuss the application of this methodology to the recent meteorite-dropping event recorded by the Spanish Fireball and Meteorite Network (SPMN; Trigo-Rodríguez et al. 2004). The superbolide occurred on May 23, 2022, at 00:42:50 UTC and reached an absolute magnitude of -17. This spectacular event was recorded from 17 SPMN fireball stations, being cataloged as SPMN230522. It was produced by an asteroidal rock experiencing ablation during a luminous path over 100 km to finally suffer an ending explosion near Barcelona at an altitude of 25.4 km (Fig. 1). We analyzed the event with our *3D-FireTOC* software (Peña-Asensio et al. 2021a,b, 2023b).

It has been suggested to employ a three-point moving average technique for data smoothing, which can be applied iteratively and include initial velocity as a free parameter (Sansom et al. 2019, 2021). Figure 2 illustrates the α-β fit for three distinct smoothing scenarios concerning the SPMN230522 event. Despite their apparent similarities, these scenarios yield varying estimates of the meteoroid's mass: ranging from an initial preatmospheric mass exceeding 200 kg with a final mass of ∼6 g to an initial mass of ∼7 kg with a final mass of ∼1.4 kg. The solution with the largest initial mass yields the lowest ending mass as it features a greater mass loss parameter and smaller ballistic coefficient. In contrast, the solution with the smallest initial mass showcases a lower mass loss parameter and greater ballistic coefficient, resulting in the largest terminal mass.

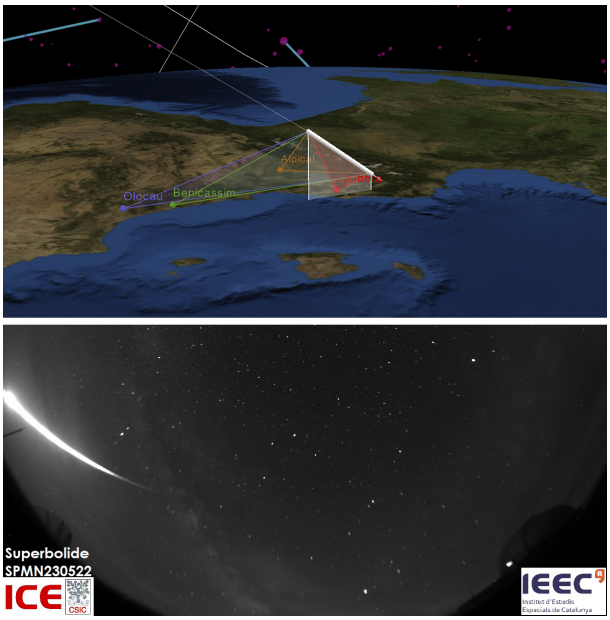


Fig. 1. A fraction of the all-sky camera image showing the SPMN230522 superbolide (bottom) and its 3D reconstruction (top). The device in placed at the Observatori Astronòmic del Montsec (OdM).

These variations occur due to the application of different smoothing techniques to raw (y, v) data, yielding distinct datasets (y_i, v_i) that are then used as input in the α-β model. Note that an increase in α is counteracted by a decrease in β in the solution. This is because the contribution of α in the $y = y(v)$ equation is additive, which effectively shifts the curve's position higher in the plot. The β value dictates the curvature of the fit. Consequently, any modifications in the initial data, with a notable emphasis on the initial velocity (as it is employed for the normalization of all velocity measurements), lead to subsequent alteration in the fitted curve. It is worth noting that much of the previously published data, such as MORP by Halliday et al. (1996), primarily consists of pre-smoothed values, for which α-β provides nearly flawless fits (Gritsevich 2009).

3. α-β DIAGRAM IN FRIPON DATABASE

On the other hand, it has been shown that α-β diagram serves as a straightforward yet potent tool for visualizing which fireball events are probable candidates for possessing tangible terminal masses and subsequently can be used to identify the meteorite-producing fireballs (Gritsevich et al. 2012, 2013; Turchak & Gritsevich 2014). This is especially useful

VII Workshop on Robotic Autonomous Observatories (October 16-20, 2023)
Editors: Maria Gritsevich, Alberto J. Castro-Tirado, Petr Kubánek, Shashi B. Pandey, and David Hiriart - DOI: https://doi.org/10.22201/ia.14052059p.2025.59.17

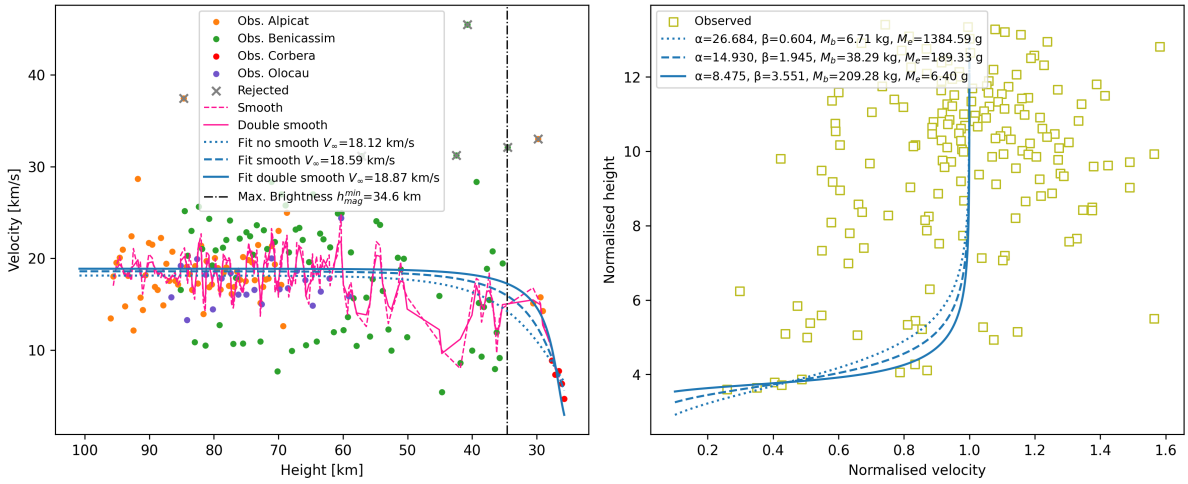


Fig. 2. α-β of SPMN230522 with initial (M_b) and terminal (M_e) masses for different smoothing cases.

when large fireball databases are available. Such analysis has proven valuable when applied to MORP, PN, DFN, MOROI, SPMN, FFN, and EN fireball network data (Gritsevich et al. 2012; Moreno-Ibáñez et al. 2020; Boaca et al. 2022; Peña-Asensio et al. 2023a, 2024b), where meteorite falls including Pribram, Lost City, Innisfree, Neuschwanstein (ABC 2003), Benesov (Gritsevich 2007), Park Forest (Meier et al. 2017), Annama (Trigo-Rodríguez et al. 2015), Bunburra Rockhole (Sansom et al. 2015), Kosice (Gritsevich et al. 2017), Dingle Dell (Devillepoix et al. 2018), Murrili (Sansom et al. 2020), Cavezzo (Gardiol et al. 2021), Arpu Kuilpu (Shober et al. 2022), Madura Cave (Devillepoix et al. 2022), and Traspena (Andrade et al. 2023). Nevertheless, its application to non-decelerating meteor could be further optimized (Peña-Asensio et al. 2024a).

Values of α and β can be used to infer the degree of deepening of meteors in the atmosphere and determine terminal heights of their luminous flight (Gritsevich & Popelenskaya 2008; Moreno-Ibáñez et al. 2015, 2017). In Figure 3, we present an α-β distribution based on the observed terminal height of the luminous phase and the atmospheric trajectory slope using a large data sample from the FRIPON database, which consists of 646 events recorded from June 2018 to December 2021. The FRIPON project, initiated in 2016 by IMCCE at Observatoire de Paris, boasts an impressive network comprising more than 150 cameras and 25 European radio receivers (Colas et al. 2020). Our representation of the acquired data in Fig. 3 provides a clear depiction of the likelihood of meteorite recovery.

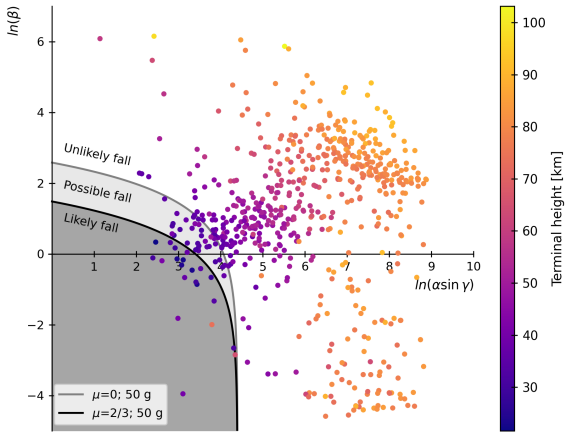


Fig. 3. α-β distribution for FRIPON data, post removal of trajectory slope dependence, plotted against terminal height. It includes meteorite fall regions and meteoroid spin limits. 50 g terminal mass is used as a threshold for meteorite production. μ represents meteoroid rotation, with 0 for no spin and 2/3 for uniform ablation across the surface.

4. CONCLUSIONS

Ground-based meteor networks play a vital role in our understanding of meteoric phenomena and the recovery of fresh meteorites. Our methodology addresses the challenges posed by unsynchronized multistation data. We implement the α-β method, which provides a versatile means of assessing meteoroid atmospheric trajectories. However, the sensitivity to data smoothing techniques is evident, as demonstrated in our analysis of SPMN230522 superbolide. The choice of smoothing technique alters estimates of meteoroid mass. Additionally, the α-β

diagram, exemplified using FRIPON database data, offers a powerful visual tool to assess the likelihood of fresh meteorite recovery, which would benefit from advances in the method.

Acknowledgments: The SPMN-CSIC network initiative has been funded by several CSIC and MICIN grants (PGC2018-097374-B-I00, PGC2018-097374-B-I00, AYA2015-67175-P, and AYA2011-26522). This study was supported by the European Research Council (ERC grant agreement No. 865657) and the Academy of Finland project No. 325806. We also thank Observatori del Montsec IEEC personnel for all-sky camera maintenance.

VII Workshop on Robotic Autonomous Observatories (October 16-20, 2023)
Editors: Maria Gritsevich, Alberto J. Castro-Tirado, Petr Kubánek, Shashi B. Pandey, and David Hiriart - DOI: https://doi.org/10.22201/ia.14052059p.2025.59.17

REFERENCES

Andrade, M., Docobo, J. Á., García-Guinea, J., et al. 2023, MNRAS, 518, 3850, doi:10.1093/mnras/stac2911

Boaca, I., Gritsevich, M., Birlan, M., et al. 2022, ApJ, 936, 150, doi:10.3847/1538-4357/ac8542

Borovicka, J., Spurny, P., & Keclikova, J. 1995, A&AS, 112, 173

Brown, P., Marchenko, V., Moser, D. E., et al. 2013, M&PS, 48, 270, doi:10.1111/maps.12055

Ceplecha, Z. 1987, BAICz, 38, 222

Ceplecha, Z., Borovička, J., Elford, W. G., et al. 1998, SSRv, 84, 327, doi:10.1023/A:1005069928850

Colas, F., Zanda, B., Bouley, S., et al. 2020, A&A, 644, A53, doi:10.1051/0004-6361/202038649

Devillepoix, H. A. R., Sansom, E. K., Bland, P. A., et al. 2018, M&PS, 53, 2212, doi:10.1111/maps.13142

Devillepoix, H. A. R., Sansom, E. K., Shober, P., et al. 2022, M&PS, 57, 1328, doi:10.1111/maps.13820

Dmitriev, V., Lupovka, V., & Gritsevich, M. 2015, P&SS, 117, 223, doi:10.1016/j.pss.2015.06.015

Egal, A., Gural, P. S., Vaubaillon, J., et al. 2017, Icar, 294, 43, doi:10.1016/j.icarus.2017.04.024

Gardiol, D., Barghini, D., Buzzoni, A., et al. 2021, MNRAS, 501, 1215, doi:10.1093/mnras/staa3646

Gritsevich, M. 2007, SoSyR, 41, 509, doi:10.1134/S003809460706007X

Gritsevich, M., Dmitriev, V., Vinnikov, V., et al. 2017, in: Trigo-Rodríguez, J., Gritsevich, M., Palme, H. (eds) Assessment and Mitigation of Asteroid Impact Hazards, ASSP, 46, 153, doi:10.1007/978-3-319-46179-3_8

Gritsevich, M. & Koschny, D. 2011, Icar, 212, 877, doi:10.1016/j.icarus.2011.01.033

Gritsevich, M. I. & Popelenskaya, N. V. 2008, DokPh, 53, 88, doi:10.1134/S1028335808020092

Gritsevich, M. I. 2008, Moscow University Mechanics Bulletin, 63, 1, doi:10.1007/s11971-008-1001-5

Gritsevich, M. I. 2009, AdSpR, 44, 323, doi:10.1016/j.asr.2009.03.030

Gritsevich, M. I., Stulov, V. P., & Turchak, L. I. 2012, CosRe, 50, 56, doi:10.1134/S0010952512010017

Gritsevich, M. I., Stulov, V. P., & Turchak, L. I. 2013, DokPh, 58, 37, doi:10.1134/S1028335813010059

Halliday, I., Griffin, A. A., & Blackwell, A. T. 1996, M&PS, 31, 185, doi:10.1111/j.1945-5100.1996.tb02014.x

Kyrylenko, I., Golubov, O., Slyusarev, I., et al. 2023, ApJ, 953, 20, doi:10.3847/1538-4357/acdc21

Lyytinen, E. & Gritsevich, M. 2016, P&SS, 120, 35. doi:10.1016/j.pss.2015.10.012

Meier, M. M. M., Welten, K. C., Riebe, M. E. I., et al. 2017, MAPS, 52, 1561, doi:10.1111/maps.12874

Moilanen, J., Gritsevich, M., & Lyytinen, E. 2021, MNRAS, 503, 3337, doi:10.1093/mnras/stab586

Moreno-Ibáñez, M., Gritsevich, M., & Trigo-Rodríguez, J. M. 2015, Icar, 250, 544, doi:10.1016/j.icarus.2014.12.027

Moreno-Ibáñez, M., Gritsevich, M., & Trigo-Rodríguez, J. M. 2017, ASSP, 46, 129, doi:10.1007/978-3-319-46179-3_7

Moreno-Ibáñez, M., Gritsevich, M., Trigo-Rodríguez, J. M., et al. 2020, MNRAS, 494, 316, doi:10.1093/mnras/staa646

Peña-Asensio, E., Trigo-Rodríguez, J. M., Gritsevich, M., et al. 2021, MNRAS, 504, 4829, doi:10.1093/mnras/stab999

Peña-Asensio, E., Trigo-Rodríguez, J. M., Langbroek, M., et al. 2021, Astrodynamics, 5, 347, doi:10.1007/s42064-021-0112-2

Peña-Asensio, E., Trigo-Rodríguez, J. M., Rimola, A., et al. 2023, MNRAS, 520, 5173, doi:10.1093/mnras/stad102

Peña-Asensio, E., Trigo-Rodríguez, J., Grèbol-Tomàs, P., Regordosa-Avellana, D. & Rimola, A., 2023, P&SS, 238, 105802, doi:10.1016/j.pss.2023.105802

Peña-Asensio, E., Visuri, J., Trigo-Rodríguez, J. M., et al. 2024a, Icar, 408, 115844, doi:10.1016/j.icarus.2023.115844

Peña-Asensio, E., Grèbol-Tomàs, P., Trigo-Rodríguez, J. M., Ramírez-Moreta, P., Kresken, R. 2024b, MNRAS, 533, L92-L99, doi:10.1093/mnrasl/slae065

Sansom, E. K., Bland, P., Paxman, J., et al. 2015, MAPS, 50, 1423, doi:10.1111/maps.12478

Sansom, E. K., Bland, P. A., Towner, M. C., et al. 2020, MAPS, 55, 2157, doi:10.1111/maps.13566

Sansom, E. K., Gritsevich, M., Devillepoix, H. A. R., et al. 2019, ApJ, 885, 115, doi:10.3847/1538-4357/ab4516

Sansom, E. K., Gritsevich, M., Devillepoix, H. A. R., et al. 2021, 84th Annual Meeting of the Meteoritical Society, 84, 6199

Shober, P. M., Devillepoix, H. A. R., Sansom, E. K., et al. 2022, MAPS, 57, 1146, doi:10.1111/maps.13813

Stulov, V. P. 1997, ApMRv, 50, 671, doi:10.1115/1.3101678

Trigo-Rodríguez, J. M., Castro-Tirado, A. J., Llorca, J., et al. 2004, EM&P, 95, 553, doi:10.1007/s11038-005-4341-9

Trigo-Rodríguez, J. M., Lyytinen, E., Gritsevich, M., et al. 2015, MNRAS, 449, 2119, doi:10.1093/mnras/stv378

Turchak, L. I. & Gritsevich, M. I. 2014, JTAM, 44, 15, doi:10.2478/jtam-2014-0020

Wetherill, G. W. & Revelle, D. O. 1981, Icar, 48, 308, doi:10.1016/0019-1035(81)90112-3

VII Workshop on Robotic Autonomous Observatories (October 16-20, 2023)
Editors: Maria Gritsevich, Alberto J. Castro-Tirado, Petr Kubánek, Shashi B. Pandey, and David Hiriart - DOI: https://doi.org/10.22201/ia.14052059p.2025.59.17

Revista Mexicana de Astronomía y Astrofísica Serie de Conferencias (RMxAC), **59**, 93–100 (2025)
© 2025: Instituto de Astronomía, Universidad Nacional Autónoma de México
https://doi.org/10.22201/ia.14052059p.2025.59.18

VII Workshop on Robotic Autonomous Observatories (October 16-20, 2023)
Editors: Maria Gritsevich, Alberto J. Castro-Tirado, Petr Kubánek, Shashi B. Pandey, and David Hiriart - DOI: https://doi.org/10.22201/ia.14052059p.2025.59.18

COMETARY OUTBURSTS AND EVOLUTION OF EJECTED PARTICLES

M. Gritsevich[1,2,3,4], M. Nissinen[2], J. Ryske[2], A. J. Castro-Tirado[5,6], I. Pérez-García[6], M. Wesołowski[7], J. M. Trigo-Rodríguez[8,9], E. Peña-Asensio[8,10], I. Boaca[11], T. Prystavski[12], M. Husárik[13], O. Ivanova[13,14], A. Sánchez[15], and J. M. Llenas[16]

RESUMEN

El modelo Dust Trail es un marco robusto desarrollado recientemente para comprender el comportamiento complejo de las colas de polvo cometario resultantes de los estallidos. El modelo tiene en cuenta factores como la presión de radiación solar, las perturbaciones gravitacionales de los cuerpos celestes y las interacciones entre partículas y el cometa progenitor. La precisión del modelo depende de suposiciones sobre las características de las partículas de la erupción, lo que motiva la recopilación oportuna de observaciones de eventos recientes, tal como fue el caso de los estallidos del cometa 12P/Pons-Brooks. Dado que la utilización de observatorios remotos y robóticos resulta crucial para la eficiente recopilación de datos en tiempo real, incorporamos estas observaciones contemporáneas e incluimos una revisión de eventos pasados, como fue el caso de cometas anteriores, el cometa 17P/Holmes por ejemplo. Estos datos sirven para validar el modelo mediante comparaciones con observaciones anteriores y para mejorar las predicciones sobre el comportamiento de las colas de polvo. A través de la comparación de estas predicciones con observaciones recientes, demostramos la eficiencia del modelo para describir la evolución a largo plazo de las colas de polvo cometario.

ABSTRACT

The Dust Trail kit model is a recently developed robust framework for understanding the complex behavior of cometary dust trails resulting from outbursts. The model takes into account factors such as solar radiation pressure, gravitational perturbations from celestial bodies, and interactions between particles and the parent comet. The model accuracy relies on assumptions about outburst particle characteristics, prompting the timely collection of observations from recent events such as the comet 12P/Pons-Brooks outbursts. As the utilization of remote and robotic observatories proves crucial for the efficient collection of real-time data, we incorporate these contemporary observations and include a review of past cases, such as the comet 17P/Holmes. These data serve to validate the model through comparisons with earlier observations and to enchance predictions for dust trail behavior. Through the comparison of these predictions with recent observations, we demonstrate the model efficacy in describing the long-term evolution of cometary dust trails.

Key Words: cometary outbursts — comets — dust trails — dynamical evolution and stability — meteoroid streams — meteors

1. INTRODUCTION

Cometary outbursts, marked by sudden increases in brightness, provide captivating opportunities to observe these relatively small celestial bodies and deduce their characteristics. These outbursts occur among periodic comets and those traversing

[1]Swedish Institute of Space Physics (IRF), Box 812, SE-98128 Kiruna, Sweden.
[2]Ursa Astronomical Association, Kopernikuksentie 1, FI-00130 Helsinki, Finland.
[3]Faculty of Science, University of Helsinki, Gustaf Hallströmin katu 2, FI-00014 Helsinki, Finland.
[4]Institute of Physics and Technology, Ural Federal University, Mira str. 19, 620002 Ekaterinburg.
[5]Instituto de Astrofísica de Andalucía (IAA-CSIC), Glorieta de la Astronomía s/n, E-18008, Granada, Spain.
[6]Ingeniería de Sistemas y Automática, Unidad Asociada al CSIC por el IAA, Escuela de Ingenierías, Universidad de Málaga, c/ Dr. Ortiz Ramos s/n, E-29071, Málaga, Spain.
[7]University of Rzeszów, College of Natural Sciences, Institute of Physics, Pigonia 1 Street, 35-310 Rzeszów, Poland.
[8]Institut de Ciéncies de l'Espai (ICE, CSIC), Campus UAB, C/ de Can Magrans s/n, E-08193 Cerdanyola del Vallès, Catalonia, Spain.
[9]Institut d'Estudis Espacials de Catalunya (IEEC), E-08034 Barcelona, Catalonia, Spain.
[10]Departament de Química, Universitat Autònoma de Barcelona (UAB), 08193 Bellaterra, Catalonia, Spain.
[11]Astronomical Institute of the Romanian Academy, Str. Cutitul de Argint 5, 040557 Bucharest, Romania.
[12]Department of Inorganic Chemistry, Ivan Franko National University of Lviv, Kyryla i Mefodiya St. 6, 79005 Lviv, Ukraine.
[13]Astronomical Institute of the Slovak Academy of Sciences, SK-05960 Tatranská Lomnica, Slovak Republic.
[14]Main Astronomical Observatory of National Academy of Sciences, 27 Akademika Zabolotnoho St., Kyiv, 03143, Ukraine.
[15]Observatori de Gualba, MPC 442, Barcelona, Spain.
[16]Observatori de Pujalt, Barcelona, Spain.

VII Workshop on Robotic Autonomous Observatories (October 16-20, 2023)
Editors: Maria Gritsevich, Alberto J. Castro-Tirado, Petr Kubánek, Shashi B. Pandey, and David Hiriart - DOI: https://doi.org/10.22201/ia.14052059p.2025.59.18

hyperbolic paths, with comet 29P/Schwassmann-Wachmann 1 being a notable example. During outburst events, vast amounts of dust particles and gas are expelled from the cometary nucleus coma, diffusing into elliptical orbits around the Sun. While initially appearing to dissipate, the particle cloud progressively expands. After half a revolution, this meteoroid stream reconverges on the opposite side of the Sun near the mutual node of their orbits, (Lyytinen et al. 2013). Subsequently, a single revolution brings these particles back to their original outburst location, which we refer to as the near-side common node. The hourglass-shaped trail that forms is a result of variations in particle orbits (Lyytinen et al. 2013; Gritsevich et al. 2022). This can be illustrated by considering individual meteoroid orbits with orbital planes differing by up to 3 degrees, a crucial factor contributing to the formation of the apparent hourglass shape (Figure 1). The crossing of these planes results in a distinct contraction and increased brightness at the mutual nodes, and despite the extended duration of meteoroids passing through these regions, the effect remains visible. Figure 1 illustrates how the orbits appear to intersect in the sky, forming a narrow hourglass pattern when observed from inside the orbit near the Sun and close to the plane itself. The brightness distribution exhibits the same hourglass shape, with the center being narrower and having higher surface brightness than the far-side common node.

Cometary outbursts are complex phenomena with various proposed causes, as detailed in the literature (Wesołowski 2020a, 2021, 2022). The concentration of vapors resulting from the sublimation of volatile compounds beneath the cometary surface is one possible mechanism leading to the destruction of surface layers and intensifying sublimation. Other mechanisms involve impacts with small solar system bodies, shock waves from solar flares, and the polymerization of HCN, initiated by UV or high-energy solar photons, releasing energy and causing surface layer disruption. The presence of cavities in comets, filled with pressurized gas, can also contribute to surface layer destruction, exposing deeper layers and rapidly increasing the sublimation rate. Additionally, the melting of solid CH_4 in cavities, releasing heat, may potentially rupture surface layers, resulting in heightened brightness. These mechanisms often work in combination, with the ejection of surface layers revealing subsurface layers rich in volatile materials as a common factor in sudden comet brightening. The importance of characterizing cometary outbursts is evident, as multiband spectroscopy unveils the ongoing processes occurring in the coma (Trigo-Rodríguez et al. 2008, 2010).



Fig. 1. Schematic diagram illustrating the intersection of dust trail particle orbits at common nodes when modeling the long-term evolution of the trail (Lyytinen et al. 2013).

The key physics behind cometary outbursts can be summarized as follows:

i. **Comet Nucleus and Structure:** Comets consist of a nucleus, which is a solid, icy core typically a few kilometers in diameter. The nucleus is composed of a mixture of water ice, frozen gases (like carbon dioxide and carbon monoxide), dust, and other volatile compounds. The nucleus may have a layered structure with subsurface regions and terrain layers on the surface.

ii. **Volatile Sublimation:** As the comet approaches perihelion, the Sun's heat causes the volatile ices on and beneath its surface to sublimate-directly transitioning from solid to gas. This sublimation releases gas and dust into space, forming a temporary atmosphere, or coma, around the nucleus.

iii. **Pressure Build-Up:** Sublimation of ices generates gas pressure beneath the surface, creating stress and tension within the comet's interior. Trapped volatile gases, especially carbon monoxide, play a crucial role in this process.

iv. **Crystallization Process:** Within the comet's nucleus, amorphous (disordered) water ice transforms into a more stable cubic crystalline structure. This crystallization process is exothermic, releasing heat and additional gas.

v. **Exponential Temperature Growth:** As the crystallization progresses, the temperature of the nucleus begins to rise exponentially.

vi. **Self-Feeding Mechanism:** The exponential temperature increase leads to a self-feeding mechanism, where larger quantities of transformed ice release more energy. This results in a rapid jump in temperature within the nucleus.

vii. **Superheated Volatiles:** The rising temperature causes trapped superheated volatile gases to expand explosively, further increasing pressure.

viii. **Terrain Layer Disruption:** Terrain layers on the surface of a comet may not lift as a whole. Instead, they can break up into smaller pieces and get lifted in separate episodes. The level of cohesion

VII Workshop on Robotic Autonomous Observatories (October 16-20, 2023)
Editors: Maria Gritsevich, Alberto J. Castro-Tirado, Petr Kubánek, Shashi B. Pandey, and David Hiriart - DOI: https://doi.org/10.22201/ia.14052059p.2025.59.18



Fig. 2. Observation of comet 12P/Pons-Brooks on November 20, 2023 (16:50UT), 20min integration time in RGB filters using a QHY600 CCD, taken by Michael Jger.

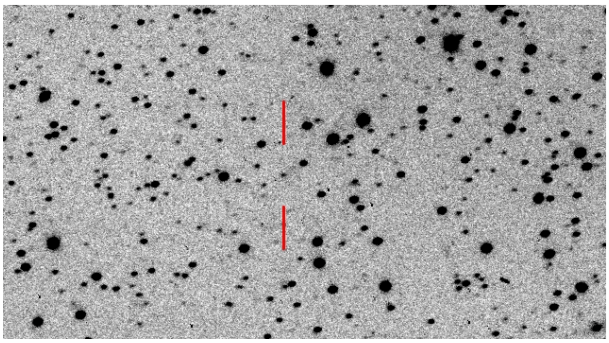


Fig. 3. Early image of comet 12P/Pons-Brooks received remotely on June 13, 2023 using a 0.25-m f/3.4 hyperbolic astrograph (Great Basin Desert, Beryl Junction, Utah, USA). Cometary activity is clearly visible.

within the comet plays a crucial role in determining whether these layers collapse or are ejected.

2. METHODS AND INSTRUMENTS

In our recent publication (Gritsevich et al. 2022), we introduced the Dust Trail kit model, a robust framework capable of elucidating this intricate behavior of cometary dust trails produced by outbursts. The model adeptly considers the influence of solar radiation pressure, gravitational perturbations induced by celestial bodies such as Venus, Earth, Moon, Mars, Jupiter, and Saturn, as well as the gravitational interaction of the particles and the parent comet. By applying the model, we demonstrate the importance of accurately deducing the characteristics of particles released during an outburst to model the subsequent evolution of the dust trail. Therefore, obtaining meticulous observations from the onset of the outburst event is paramount.

To exemplify the model's utility, we took the opportunity to investigate the comet 12P/Pons-Brooks, a Halley-type comet with a 71-year period, Figure 2. This comet is set to return to perihelion on April, 21, 2024 and during this return it has already experienced a series of notable outbursts (Table 1).

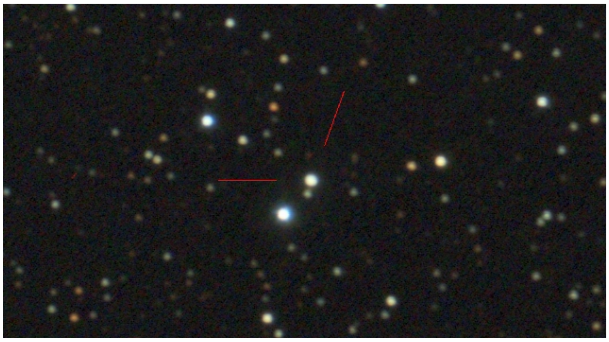


Fig. 4. Coloured image of the comet 12P/Pons-Brooks in the first outburst taken on July 21 with a 0.28−mf/2.2 RASA astrograph (Great Basin Desert, Beryl Junction, Utah, USA). 12P appears very condensed with an increase of ~ 5 mag.



Fig. 5. Appearance of the coma of comet 12P/Pons-Brooks which followed most of the outbursts. 0.61-m f/6.5 astrograph (Auberry, California, USA).

We report findings based on the extensive period of observations conducted on comet 12P/Pons-Brooks, starting from the onset of noticeable activity on June 13, 2023, and continuing until December 17, 2023 (Figures 2-7). The observational span covers heliocentric distances ranging from 4.26 to 2.19 AU. The facilities used in observations include the BOOTES (Burst Observer and Optical Transient Exploring System) a Global Network of Robotic Astronomical Observatories (Castro-Tirado et al. 1999; Castro-Tirado 2023), the 0.3 m Viestikallio remote observatory in Finland, the new remote 0.3 m Makroskooppi observatory in Spain, remote telescopes at the iTelescope observatories in Utah and California (MPC codes U94 and U69, respectively), as well as the 1.3 m and 0.61 m telescopes at the Skalnat Pleso Observatory in Slovakia

VII Workshop on Robotic Autonomous Observatories (October 16-20, 2023)
Editors: Maria Gritsevich, Alberto J. Castro-Tirado, Petr Kubánek, Shashi B. Pandey, and David Hiriart - DOI: https://doi.org/10.22201/ia.14052059p.2025.59.18

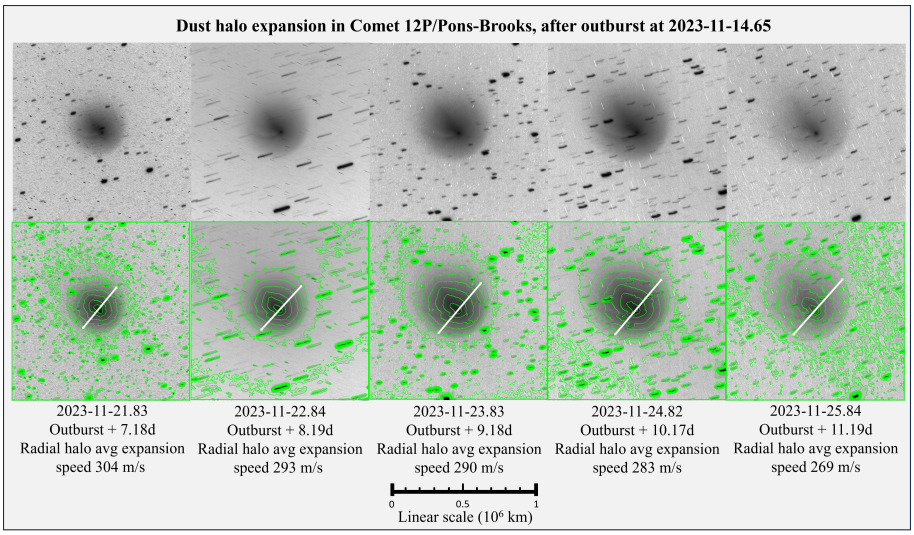


Fig. 6. Dust halo radial expansion speeds of 12P/Pons-Brooks measured and calculated using Viestikallio remote observatory data and the outburst beginning time.

TABLE 1

Date	Brightness change	Amplitude	notes
2023 07 20.37 ± 0.08 UT	17.18G ⇒ 11.68G	5.50	strong outburst
2023 09 04.00 ± 0.60 UT	16.97G ⇒ 16.59G	0.36	mini outburst
2023 09 23.87 ± 0.02 UT	16.74G ⇒ 15.84G	0.90	mini outburst
2023 10 05.16 ± 0.03 UT	16.37G ⇒ 11.37G	5.00	strong outburst
2023 10 22.52 ± 0.21 UT	16.07G ⇒ 15.67G	0.40	mini outburst
2023 10 31.46 ± 0.20 UT	15.90G ⇒ 13.00G	2.90	possibly double event, second outburst on Nov 1.40
2023 11 01.40 ± 0.15 UT	13.70G ⇒ 11.23G	2.50	
2023 11 14.65 ± 0.05 UT	15.00G ⇒ 10.00G	5.00	strong outburst; based on Peter Carson (BAA) observations
2023 11 30.60 ± 0.02 UT	14.00G ⇒ 10.60G	3.40	based on Nick James (BAA) observations
2023 12 14.57 ± 0.11 UT	14.70R ⇒ 13.05R	1.65	

(employing broadband BVR filters). These observations allowed to study the expansion characteristics of the dust halo in comet 12P/Pons-Brooks. The expansion rates triggered by the approximately 5-magnitude outburst on October 05, 2023 (Usher et al. 2023) are presented in Figure 7. Radial expansion speeds of the dust cloud were both measured and calculated based on these observations and the initiation time of the outburst (for additional details, see also Ryske et al. 2023).

In addition to conducting photometric analysis on broadband images, encompassing both nuclear and total magnitudes, we investigated comet 12P/Pons-Brooks for its dust production rate, afrho. Our findings reveal significant variations in comet appearance, estimated magnitude, and dust production activity during outburst periods. Specifically, afrho measured during quiescence on July 01, 2023, was 284±12 cm, a notably lower value compared to the 17295±1081 cm recorded during the outburst on November 02, 2023, shortly after another major outburst occurred.

The estimated nucleus radius from these observations is 21 km, aligning well with the findings of Ye et al. (2020). Additional follow-up images of the evolving dust cloud of the comet 12P were obtained from the two observatories in Barcelona: Observatori de Gualba and Observatori de Pujalt (Barcelona) as

VII Workshop on Robotic Autonomous Observatories (October 16-20, 2023)
Editors: Maria Gritsevich, Alberto J. Castro-Tirado, Petr Kubánek, Shashi B. Pandey, and David Hiriart - DOI: https://doi.org/10.22201/ia.14052059p.2025.59.18

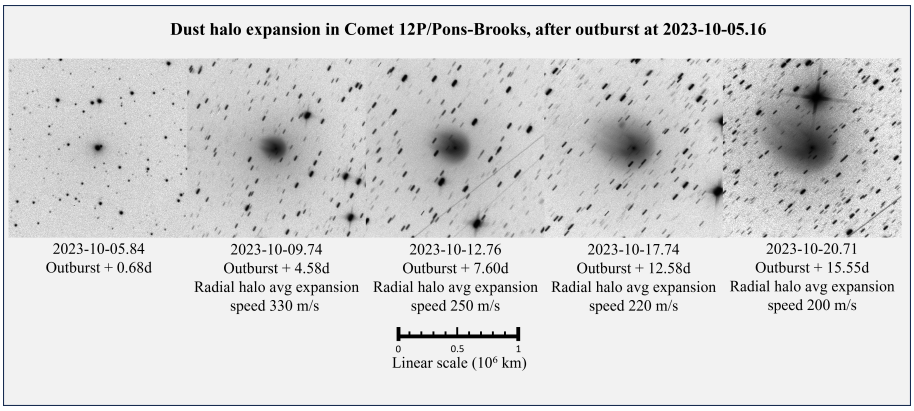


Fig. 7. Dust halo expansion in comet 12P/Pons-Brooks, following a 5 mag outburst on Oct 5, 2023 (Usher et al. 2023), see also Ryske et al. (2023).

part of an Institut d'Estudis Espacials de Catalunya minor bodies monitoring consortium. These observations facilitated the determination of physical parameters of the dust environment, including dust color and productivity, and allowed for analysis of active structural morphology.

The intersection of Earth with a cometary dust trails gives rise to meteor showers. Notably, certain parent bodies of meteoroid streams, like 12P/Pons-Brooks, have been observed to be linked to more than one observable meteor shower in Earth's atmosphere (Tomko & Neslušan 2016). The dust particle orbits within these dust trails evolve, shifting to locations far from the orbit of their parent body to intersect with Earth's orbit. Conducting a realistic simulation of the dust trail evolution is essential to unveil intricate complex of showers that may be associated with the given parent body. The meteoroid stream associated with 12P/Pons-Brooks includes the December k-Draconids and Northern June Aquilids, providing a unique opportunity to study cometary material within Earth's orbit. Observing these meteor showers offers additional insights into the recent evolutionary history of the parent comet.

3. OTHER NOTABLE EXAMPLES

Not all comets possess the same internal structure or behavior. Some comets may never experience outbursts or fragmentation events due to differences in their composition and thermal properties. Hyperbolic comets contribute to this diversity (Seligman et al. 2023; Peña-Asensio et al. 2024a; Peña-Asensio 2024b). Depending on the degree of cohesion and the specific conditions within the comet, various types of outbursts can occur, ranging from localized outgassing to major fragmentation events. In major fragmentation events, substantial portions of the nucleus may be ejected, forming companions or debris clouds. These fragments may undergo secondary and higher-order fragmentation, leading to a cascading process where progressively smaller fragments are generated.

Notable examples that illustrate various aspects of cometary behavior and their impact on their observable characteristics include:

1. Comet Holmes (17P/Holmes), Montalto et al. (2008); Moreno et al. (2008):

- Experienced a giant explosion in October 2007.
- Brightness shot up ~ 14 magnitudes (or nearly 400,000 times) in a matter of two days.
- Formation of a sharply bounded dust halo and a bright extended feature often referred to as a "blob".
- An estimated 10^{14} grams of dust ejected during the event.
- Intrinsic brightness remained significantly elevated more than a year after the explosion.
- Sustained another giant outburst in 18921893 at the time of its discovery.

2. Halley's Comet (1P/Halley), Gronkowski (2002):

- Underwent a giant explosion in the second half of January 1836, less than 10 weeks after perihelion.
- Accompanied by a sharply bounded, rapidly expanding halo and visible with the naked eye for at least two months after the event.
- Magnitude peak measured at 0.3, indicating a significant brightness increase.

3. Comet C/1996 Q1 (Tabur), Ferrin and Penuelas (2022):

- Suddenly "dissolved" after three months.
- Displayed a physical behavior remarkably similar to that of companions of split comets.

VII Workshop on Robotic Autonomous Observatories (October 16-20, 2023)
Editors: Maria Gritsevich, Alberto J. Castro-Tirado, Petr Kubánek, Shashi B. Pandey, and David Hiriart - DOI: https://doi.org/10.22201/ia.14052059p.2025.59.18

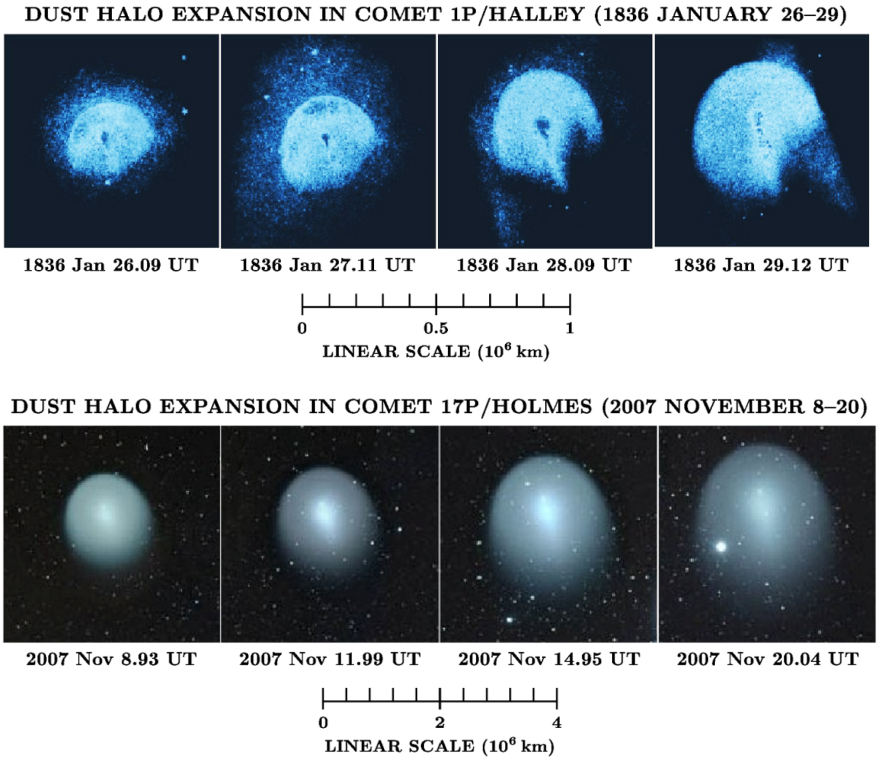


Fig. 8. Dust halo expansion in other cases. Adopted from Sekanina (2008).

- Shared a practically identical orbit with a much brighter comet, C/1988 A1 (Liller).

4. Comet C/1999 S4 (LINEAR), Wolk et al. (2009):

- Disintegrated as it approached the Sun, reaching perihelion on July 26, 2000, at a distance of 0.765 AU. The disintegration was meticulously observed and well-documented.
- Hubble Space Telescope (HST) observations on July 6 revealed a brief outburst and a minor fragmentation event.
- Shortly before perihelion, significant changes in appearance were noted. The comet transformed into a fuzzy, elongated, and faint object.

5. Comet 29P/Schwassmann-Wachmann 1, Gronkowski (2004) & Miles et al. (2016):

- Orbits in a transitional "Gateway" region between the Centaur and Jupiter-family comet (JFC) regions, often referred to as a comet-centaur.
- Estimated nucleus diameter is 60.4 ± 7.4 kilometers.
- Undergoes around seven outbursts per year with a brightness increase of 2-5 magnitudes. Its high level of activity is noteworthy given its nearly circular orbit ($e = 0.04$) and large semi-major axis ($a = 6.05$ AU).
- During outbursts, the coma undergoes a drastic change from being diffuse to very condensed. In the post-outburst periods it exhibits a characteristic horseshoe or spiral shape.
- The last strong outburst occurred on December 23, 2023, with a brightness increase of 2 magnitudes.
- In the 20th century, it experienced two minor approaches to Jupiter. The 21st-century approach on October 11, 2037, will result in an increase in perihelion distance from 5.71 AU to 5.87 AU and an orbital period from 14.37 to 15.87 years.

The timescale for major outburst events is governed by the mean exposure lifespan of terrain layers on the comet surface. The interval between giant outbursts in some comets can be in the order of centuries, providing insights into heat transfer and cometary structure.

4. DUST TRAIL KIT MODELING RESULTS

To illustrate the efficacy of our model in describing long-term dust trail evolution, we studied the comet 17P/Holmes, with an orbital period of close

VII Workshop on Robotic Autonomous Observatories (October 16-20, 2023)
Editors: Maria Gritsevich, Alberto J. Castro-Tirado, Petr Kubánek, Shashi B. Pandey, and David Hiriart - DOI: https://doi.org/10.22201/ia.14052059p.2025.59.18

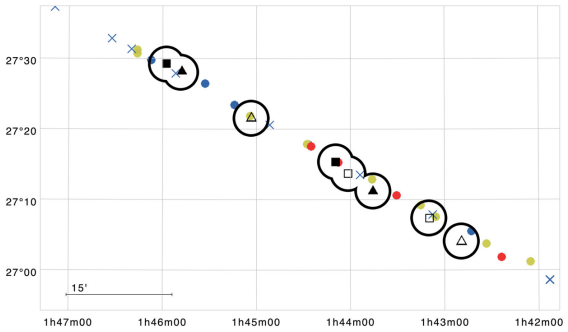


Fig. 9. The positions on the celestial sphere of dust trail resulting from 2007 outburst of the comet 17P/Holmes, depicting color-coded modeled particle population sizes (larger particles (red) with 0.11 mm radius, medium-sized particles (yellow) with 0.010.1 mm radius, and small particles (blue) with 0.0010.01 mm radius). The modeled distribution of particles ejected during the outburst within each of the three groups is uniform. In the first modeling scenario, we assumed spherically symmetric ejection of particles at the start of the outburst. Second scenario for the same particle populations, shown in crosses, only considers particles oriented toward the Sun during the outburst. The modeling results are compared to the observed positions of the trails obtained on dates February 26-28, 2022 and March 01-03, 2022, which are illustrated with black-colored squares and triangle markers. The X-axis denotes Right Ascension (RA), while the Y-axis represents Declination (DEC).

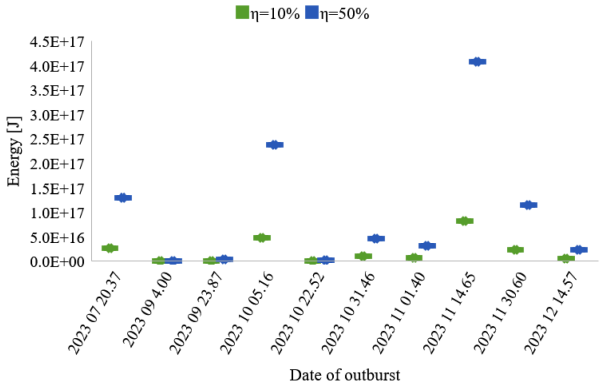


Fig. 10. The energy released during the outbursts of comet 12P/PonsBrooks. The calculations assume two values of the active surface in the quiet sublimation phase (η), which result from observations from comet 1P/Halley to comet 67P/Churyumov-Gerasimenko.

to 7 years, which experienced a massive outburst in October 2007 the largest so far in the documented comet history (Gritsevich et al. 2022). Our simulations encompass various particle populations, ranging in size from 0.001 to 1 mm, with assumptions about ejection speed distributions at the onset of the outburst being subject to variation. The model is implemented in Orekit [17], enabling high computational accuracy through the use of Dormand-Prince numerical integration methods with higher precision. The model's accuracy is validated by comparisons with earlier observations of the trail gathered at common nodes for 0.5 and 1 revolutions. Using this dataset, we formulated predictions concerning the two-revolution dust trail's behavior in proximity to the outburst point and its observability from Earth (Gritsevich et al. 2022).

To enhance practicality, we developed and made available a suite of Python scripts for calculating the dust trail's position based on observatory topographical coordinates (Nissinen & Gritsevich 2022, 2023). Using these predictions, we conducted a series of observations of the 2007 outburst dust trail in February (Ryske et al. 2022), March (Ryske et al. 2022), October, December 2022, and February 2023 (Figure 9). The observability of the dust trail hinges on sunlight scattering by myriad micron-sized particles arising from the outburst phenomenon. Notably, both the brightness of the trail and its spatial coordinates closely align with our earlier published predictions made using the Dust Trail kit model (Gritsevich et al. 2022; Nissinen & Gritsevich 2022).

[17] https://www.orekit.org

5. ENERGY OUTBURST

The cometary outburst is associated with the destruction of a nucleus fragment, accompanied by the emission of dust and gases into the coma. This causes an increase in the total scattering cross-section, which leads to an increase in the efficiency of scattering incident sunlight (Wesołowski 2022). When analysing individual outburst cases, one of the most important parameters is determining the energy released during the outburst (Figure 10). The amount of energy released means that the outburst is a high-energy process, that may be responsible for the presence of fine particles in the coma (Wesołowski 2024). The obtained energy values depend on the mass ejected, the expansion velocity and the fraction of the active surface (η). The cometary outburst causes local destruction and rejuvenation of the core, which involves the exposure of the original subsurface layer (Wesołowski et al. 2020b).

6. CONCLUSIONS

This study includes an extended synopsis of the physics underlying cometary outbursts, extreme

VII Workshop on Robotic Autonomous Observatories (October 16-20, 2023)
Editors: Maria Gritsevich, Alberto J. Castro-Tirado, Petr Kubánek, Shashi B. Pandey, and David Hiriart - DOI: https://doi.org/10.22201/ia.14052059p.2025.59.18

events in the life cycle of comets driven by a complex interplay of physical processes involving the cometary nucleus, dust particles, volatile materials, and solar radiation. The comprehension of cometary outbursts offers insights into the evolution and physical properties of comets and their dust trails as they interact with the surrounding environment. It enhances our current understanding of the diversity of cometary behavior and the fundamental physics shaping the fate of these intriguing celestial objects.

Dedication. This paper is dedicated to the memory of our dear friend and colleague, Esko Lyytinen, a man of extraordinary mind with a lifelong passion for science (Jenniskens et al. 2021; Gritsevich et al. 2021). Remarkably, Esko shares a birthday with the discovery date of comet 17P/Holmes (discovered by the British amateur astronomer Edwin Holmes during the 1892 outburst), separated by a span of 50 years a comet that has greatly captivated his mind and deeply inspired for modeling!

Acknowledgements: This work received partial support from the Academy of Finland project no. 325806 (PlanetS) at the Finnish Geospatial Research Institute, the Spanish Ministry project PID2020-11, Junta de Andalucía grant P20_010168, the Severo Ochoa grant CEX2021-001131-S funded by MCIN/AEI/ 10.13039/501100011033, project PID2021-128062NB-I00 funded by MCIN/AEI/10.13039/501100011033, the Slovak Grant Agency for Science VEGA (Grant No. 2/0059/22, No. 2/0009/22). The program of development within Priority-2030 (04.89) is acknowledged for supporting the research at UrFU.

REFERENCES

Castro-Tirado, A. J., Soldán, J., Bernas, M., et al. 1999, A&A SS, 138, 583
Castro-Tirado, A. J., 2023, Nat Ast, 7, 1136
Ferrin, I. ; Penuelas, G., 2022, The Astronomer's Telegram, 15352
Gritsevich, M., Nissinen, M., Moilanen, J., et al. 2021, WGN, Journal of the International Meteor Organization, 49, 3
Gritsevich, M., Nissinen, M., Oksanen, A., Suomela, J. & Silber, E. A. 2022, MNRAS, 513, 2
Gronkowski, P., 2002, P&SS, 50, 247
Gronkowski, P., 2004, MNRAS, 354, 142
Jenniskens, P., Trigo-Rodríguez, J. M. & Gritsevich, M. 2021, WGN, JIMO, 49, 23
Lyytinen, E., Nissinen, M. & Lehto, H. J. 2013, WGN, JIMO, 41, 77
Miles, R., Faillace, G. A., Mottola, S., et al., 2016, Icar, 272, 327
Montalto, M., Riffeser, A., Hopp, U., Wilke, S., Carraro, G., 2008, A&A, 479, 45
Moreno, F. J. L., Santos-Sanz, P., Morales, N., et al., 2008, ApJ, 677, 63
Nissinen M., & Gritsevich M., 2022, Instructions on where and how to observe the comet 17P/Holmes dust trail. Zenodo. `https://doi.org/10.5281/zenodo.6977358`
Nissinen M., & Gritsevich M., 2023, Instructions for Ongoing Observations of the Dust Trail from the 2007 Outburst of Comet 17P/Holmes. Zenodo. `https://doi.org/10.5281/zenodo.8319474`
Peña-Asensio, E., Visuri, J., Trigo-Rodríguez, J. M., et al. 2024, Icar, 408, 115844
Peña-Asensio, E., Trigo-Rodríguez, J. M., Gritsevich, M., et al. 2025, RMxAC (this issue)
Ryske, J., Gritsevich, M., & Nissinen, M. 2022, EPSC, EPSC2022-60
Ryske, J., Gritsevich, M., Nissinen, M., Pérez-García, I., & Castro-Tirado, A. J. 2023, ATel, 16343
Sekanina, Z. 2008, ICQ, 30, 63
Seligman, D. Z., & Moro-Martín, A. 2023, arXiv e-prints, arXiv:2304.00568
Tomko, D. & Neslušan, L. 2016, A&A, 592, A107
Trigo-Rodríguez, J. M., García-Melendo, E., Davidsson, B. J. R., et al., 2008, A&A, 485, 2
Trigo-Rodríguez, J. M., García-Hernández, D. A., Sánchez, A., et al., 2010, MNRAS, 409, 4
Usher, H., Miles, R., Redondo, J. M. P., et al., 2023, ATel, 16270
Wesołowski, M. 2020a, Icar, 351, 113950
Wesołowski, M., Gronkowski, P., Tralle, I., 2020b, Icar, 352, 114005
Wesołowski, M., 2021, RAA, 21, 69
Wesołowski, M., 2022, Icar, 375, 114847
Wesołowski, M., 2024, Icar, 411, 115937
Wolk, S. J., Lisse, C. M., Bodewits, D., et al., 2009, ApJ, 694, 1293
Ye, Q., Farnham, T. L., Knight, M. M., Holt, C. E. & Feaga, L. M. 2020, RNAAS, 4, 101

Revista Mexicana de Astronomía y Astrofísica Serie de Conferencias (RMxAC), **59**, 101–108 (2025)
© 2025: Instituto de Astronomía, Universidad Nacional Autónoma de México
https://doi.org/10.22201/ia.14052059p.2025.59.19

VII Workshop on Robotic Autonomous Observatories (October 16-20, 2023)
Editors: Maria Gritsevich, Alberto J. Castro-Tirado, Petr Kubánek, Shashi B. Pandey, and David Hiriart - DOI: https://doi.org/10.22201/ia.14052059p.2025.59.19

INTERSTELLAR VISITORS AND ELUSIVE EXTRASOLAR METEORITES

E. Peña-Asensio[1,2], J. M. Trigo-Rodríguez[2,3], M. Gritsevich[4,5,6,7], H. Socas-Navarro[8,9], J. Visuri[5], and A. Rimola[1]

RESUMEN

A pesar del inmenso vacío y las distancias que separan las estrellas, nuestro vecindario cósmico sigue siendo un escenario dinámico donde nuevos fenómenos desafían nuestra comprensión. El descubrimiento de visitantes en nuestro Sistema Solar supone una oportunidad científica sin precedentes. En este artículo proporcionamos una introducción al ámbito de los "intrusos interestelares": 1I/'Oumuamua y 2I/Borisov. Además, exploramos la naturaleza de objetos que parecen haberse originado en otras nebulosas solares pero, en realidad, pertenecen a nuestro propio sistema planetario, apodados "impostores interestelares". Asimismo, explicamos por qué los meteoros hiperbólicos han sido sistemáticamente categorizados como errores de medición. Por último, cuestionamos las afirmaciones sobre los presuntos meteoros interestelares: IM1 e IM2. Nuestro objetivo es arrojar luz sobre la siguiente paradoja: dada la creciente evidencia que indica la presencia de una población visitante de origen interstellar, ¿por qué los meteoritos extrasolares han eludido nuestro descubrimiento?

ABSTRACT

Despite the immense voids and vast distances that separate stars, our cosmic neighborhood remains a dynamic stage where emerging phenomena consistently challenge our present comprehension. One of the most intriguing enigmas involves the appearance of objects originating from distant stellar systems. We provide an introduction to the realm of "interstellar interlopers", focusing on the first two documented sizable visitors: 1I/'Oumuamua and 2I/Borisov. Additionally, we explore the nature of objects that seem to have originated in other solar nebulae but, in reality, belong to our own planetary systemdubbed "interstellar impostors". We explain why hyperbolic meteors have been systematically categorized as measurement errors. Lastly, we raise questions about the contentious assertions concerning the alleged interstellar meteors: IM1 and IM2. By pursuing these inquiries, our objective is to resolve the following paradox: given the growing body of evidence indicating the presence of an interstellar visiting population, why have authentic extrasolar meteorites eluded our discovery?

Key Words: Fireballs — Hyperbolic orbits — Interstellar — Meteorites — Oort cloud

1. 1I/'OUMUAMUA AND 2I/BORISOV

1I/'Oumuamua represents the inaugural macroscopic interstellar object confirmed within our Solar System, initially cataloged as C/2017 U1 (Williams et al. 2017), see Fig. 1. The discovery was made on October 19, 2017, by Robert Weryk at the Haleakal Observatory in Maui, Hawaii. Observational data yielded an effective radius estimate ranging from 55 to 114 meters for this object. In telescopic imaging, 1I manifested merely as a point source, with no discernible outgassing or material ejection detectable in the optical spectrum. One of the more perplexing characteristics was the detection of non-gravitational acceleration. A remarkable aspect of its observational profile was the extreme amplitude of its light curve, indicating variability in brightness by a factor of 10 (Meech et al. 2017). These unusual characteristics prompted the consideration of exotic hypotheses regarding its nature and origin (Loeb 2022, 2023).

The celestial mechanics of 1I were defined by an orbit with a semi-major axis (a) of -1.272 au, an eccentricity (e) of 1.201, and an inclination (i) of 122.8°. Prior to its identification, 1I had passed within a proximity of 0.16 au to Earth, a mere three days earlier. The orbit of this object was deter-

[1]Departament de Química, Universitat Autònoma de Barcelona, 08193 Bellaterra, Catalonia, Spain (eloy.peas@gmail.com, eloy.pena@uab.cat).
[2]Institut de Ciències de l´Espai (ICE, CSIC), Campus UAB, C/ de Can Magrans s/n, 08193 Cerdanyola del Vallès, Catalonia, Spain.
[3]Institut d´Estudis Espacials de Catalunya (IEEC), 08034 Barcelona, Catalonia, Spain.
[4]Swedish Institute of Space Physics (IRF), Bengt Hultqvists väg 1, SE-98192, Kiruna, Sweden.
[5]Finnish Fireball Network, Ursa Astronomical Association, Kopernikuksentie 1, Helsinki FI-00130, Finland.
[6]Faculty of Science, University of Helsinki, Gustaf Hällsrömin katu 2, FI-00014 Helsinki, Finland.
[7]Institute of Physics and Technology, Ural Federal University, Mira str. 19, 620002 Ekaterinburg, Russia.
[8]Instituto de Astrofísica de Canarias, Avda. Vía Láctea S/N, La Laguna, 38205, Tenerife, Spain.
[9]Departamento de Astrofísica, Universidad de La Laguna, La Laguna, 38205, Tenerife, Spain.

VII Workshop on Robotic Autonomous Observatories (October 16-20, 2023)
Editors: Maria Gritsevich, Alberto J. Castro-Tirado, Petr Kubánek, Shashi B. Pandey, and David Hiriart - DOI: https://doi.org/10.22201/ia.14052059p.2025.59.19

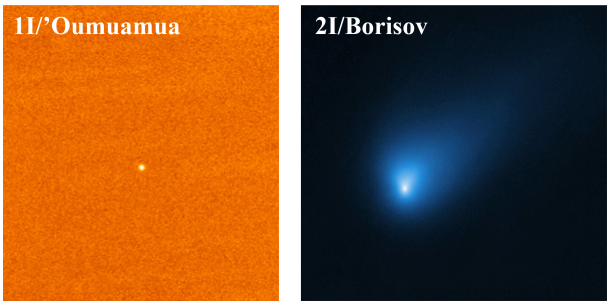


Fig. 1. 1I/'Oumuamua observed by the Nordic Optical Telescope in 2017 and 2I/Borisov observed by the Hubble Space Telescope in 2019.

mined from approximately 2.5 months of observational data. Initial shape estimates suggested an extreme axis ratio of 10:1, a figure that permeated popular representations with the dissemination of a 10:1:1 shape. However, subsequent refinements in shape assessments proposed a more oblate ellipsoid with a 6:6:1 axis ratio (Mashchenko 2019). The dominant component of the observed non-gravitational acceleration was radially aligned in opposition to the solar vector. Potential mechanisms for this acceleration include the sublimation of volatile substances such as solid hydrogen (H_2), nitrogen (N_2), or carbon monoxide (CO) (Jewitt & Seligman 2023). Alternatively, radiation pressure effects could be invoked, implying an extremely low-density, porous structure for the object (Bialy & Loeb 2018). A further hypothesis posits the release of molecular hydrogen, potentially accumulated through cosmic ray interactions during its interstellar voyage, which may have commenced with the object's outgassing upon solar approach (Bergner & Seligman 2023). 1I may be a planetesimal shaped by low-temperature, high-energy irradiation during its journey through interstellar space, undergoing significant outgassing when subjected to solar radiation.

2I/Borisov, the second macroscopic interstellar object officially recognized within our Solar System, was identified as C/2019 Q4 before its interstellar origin was confirmed (Borisov 2019), see Fig. 1. The discovery was credited to Gennadiy Borisov on August 30, 2019, who utilized a self-built 0.65-meter telescope for the observation. The nucleus of 2I was estimated to range between 0.2 and 0.5 km in diameter. Similar to 1I, 2I exhibited non-gravitational acceleration, but unlike its predecessor, it showed a clear and continuous mass loss, as well as a coma with distinct gas emission bands, indicating active processes commonly associated with comets. The nature and behavior of 2I do not seem as extraordinary as those of 1I.

The orbital parameters for 2I included a semi-major axis of -0.851 au, an eccentricity of 3.357, and an inclination of 44.05°. This interstellar visitor was first observed approximately three months before reaching its closest approach to the Sun, or perihelion. Observational efforts extended over a year (Jewitt & Seligman 2023). A bright coma around 2I hampered the direct observation of its nucleus. The radial acceleration exhibited by 2I was consistent with its observed mass loss. The detection of a high concentration of CO within the coma suggested that the object was likely formed under extremely cold conditions, possibly in the distant reaches of a protoplanetary disk (Jewitt & Seligman 2023). This origin provides a plausible explanation for the object's gravitational unbinding and its eventual incursion into our Solar System. The prospect of lasting dust trails from interstellar visitors, akin to those produced by cometary outbursts, presents a fascinating line of inquiry. Although comets are recognized for generating dust trails that can persist and remain visible over prolonged durations (Gritsevich et al. 2022), the behavior of these hyperbolic objects differs markedly in their dynamics.

2. HYPERBOLIC ≠ INTERSTELLAR

While dynamically probable, the interstellar provenance of 1I and 2I is not without contention. Numerical simulations suggest that massive bodies, with masses down to approximately ∼0.2 M_J (Jupiter masses), traversing the Oort cloud can gravitationally perturb resident comets, catapulting them into hyperbolic trajectories that propel them into interstellar space or the planetary region (Higuchi & Kokubo 2020), see Fig 2. Statistical analyses indicate that roughly 0.1% of such perturbed objects could adopt orbital characteristics akin to those of 1I, while a mere 0.01% might attain the highly eccentric orbits that are characteristic of 2I.

The actual number density of such sub-stellar and sub-Jovian perturbers in the vicinity of the Solar System remains inadequately quantified. This uncertainty raises pivotal questions about the broader dynamics of Solar Systems and their role in the ejection of material into the galactic milieu. It is plausible to consider whether such interactions are an efficient mechanism through which systems lose material to the interstellar medium.

Furthermore, the potential for these hyperbolic objects to become Earth impactors cannot be overlooked. If planetary systems regularly eject debris

VII Workshop on Robotic Autonomous Observatories (October 16-20, 2023)
Editors: Maria Gritsevich, Alberto J. Castro-Tirado, Petr Kubánek, Shashi B. Pandey, and David Hiriart - DOI: https://doi.org/10.22201/ia.14052059p.2025.59.19

in this manner, it could have significant implications for understanding the frequency and nature of hyperbolic impactors on Earth. Besides, interstellar impactors would elude our asteroid surveillance, preventing any possible prediction and planetary defense. These considerations underscore the importance of constraining the abundance and properties of massive perturber objects to better comprehend the dynamical processes governing the transfer of material between planetary systems, the broader interstellar environment, and the dynamics of our Solar System.

In this context, exploring the extensive meteor data collected by fireball networks today proves valuable. We focused on analyzing selected data from the Spanish Fireball and Meteorite Network (SPMN-CSIC; Trigo-Rodríguez et al. 2004) and the Finnish Fireball Network, FFN (Gritsevich et al. 2014; Lyytinen & Gritsevich 2016; Moilanen et al. 2021; Visuri & Gritsevich 2021). The FFN, in particular, observed an exceptional meteor On October 23, 2022, at 19:38:34 (UTC), a meteoroid (named FH1) was detected penetrating the atmosphere above Finland at a velocity marginally exceeding the escape speed of the Solar System by 200–700 m/s (Peña-Asensio et al. 2024a,b). This event was documented by three video stations within the FFN and a single image from an independent observer. The trajectory and physical parameters of the meteor were subsequently analyzed using the *3D-FireTOC* software (Peña-Asensio et al. 2021a,b, 2023).

The trajectory of FH1 is particularly notable due to its coincidence with the plane of the ecliptic, which is unusual for objects that are presumed to be interstellar in origin. Typically, interstellar objects are anticipated to exhibit a random distribution of orbital inclinations relative to the ecliptic plane. The absence of any detectable close planetary encounters before its detection reinforces the peculiarity of its orbital path. Given the modest velocity excess above the parabolic limit, we posit that FH1 is more likely an object originating from the Oort cloud that has been perturbed into a hyperbolic orbit, rather than an interstellar visitor.

Statistical analysis suggests that the probability of an interstellar object coincidentally sharing the same orbital inclination as FH1 is approximately 0.12%, further substantiating the likelihood that FH1 is of Solar System origin. Specifically, FH1 was found to be compatible with having undergone a gravitational perturbation by the close passage of the Scholz star binary system 80,000 years ago (Mamajek et al. 2015; Dupuy et al. 2019; de la Fuente Marcos et al. 2018; de la Fuente Marcos & de la Fuente Marcos 2022).

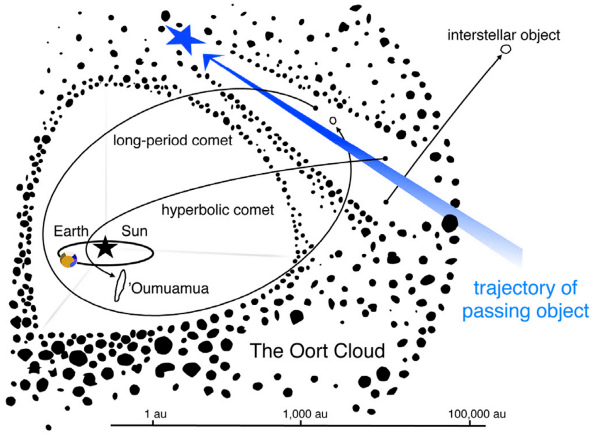


Fig. 2. Schematic illustration of a star penetrating the Oort cloud. Adapted from Higuchi & Kokubo (2020).

The detection and analysis of FH1 underscore a critical lesson: hyperbolic Earth impactors may not exclusively originate from interstellar space; instead, they may also be objects native to our own Solar System that have been accelerated to hyperbolic velocities. This realization has significant implications for assessing impact risks and understanding the processes governing the dynamics of our Solar System's Oort cloud and its interactions with the planetary region.

3. INTERSTELLAR METEORS

The detection of meteors possessing hyperbolic orbits is not a recent phenomenon; reports date back to the 1950s. Despite their consistent detection over decades, such hyperbolic meteors have historically been dismissed as observational or computational errors (Hajduková et al. 2014). This skepticism is partly due to the complex dynamics involved in accurately measuring the high velocities at which these objects enter Earth's atmosphere. In large automated databases of meteor observations, approximately 10% of recorded events exhibit non-elliptical, hyperbolic trajectories. Such a significant percentage suggests a systematic presence rather than sporadic anomalies.

Observational data indicate a tendency for these hyperbolic meteors to align closely with the ecliptic plane, which is the apparent path of the Sun across the sky where the Earth's orbital motion is also situated. There is a notable correlation between the direction from which these meteors appear to approach and the Earth's apex (the direction towards which Earth is moving in its orbit). Impacts that

VII Workshop on Robotic Autonomous Observatories (October 16-20, 2023)
Editors: Maria Gritsevich, Alberto J. Castro-Tirado, Petr Kubánek, Shashi B. Pandey, and David Hiriart - DOI: https://doi.org/10.22201/ia.14052059p.2025.59.19

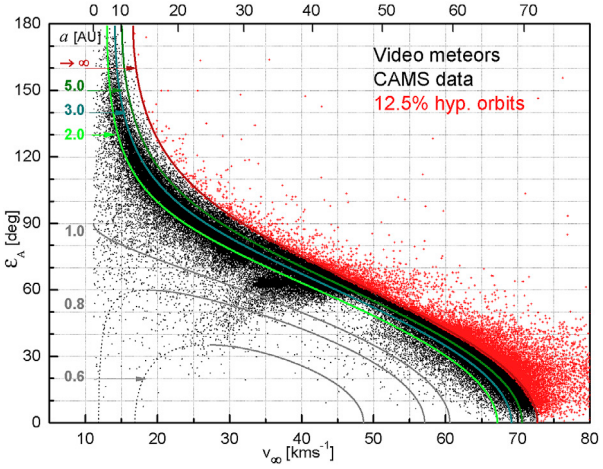


Fig. 3. Angular difference of the meteor apparent radiant and the Earths apex (ϵ_A) in CAMS database versus the geocentric pre-atmosperic velocity (v_∞) of the meteor. Reproduced from Hajdukova et al. (2020).

occur head-on, relative to Earth's apex, are more likely to be measured as hyperbolic because the relative velocities at impact are higher, which can result in spurious hyperbolic excess measurements, as depicted in Figure 3. These high-speed encounters increase the likelihood of measurement errors, potentially misclassifying the trajectory of an object as hyperbolic. Consequently, many hyperbolic orbits reported in meteor network databases could be artifacts of this high-velocity impact geometry.

3.1. *IM1 and IM2 CNEOS fireballs*

The identification of interstellar meteors presents a significant challenge in astrometric analysis and interpretation. The first two instances of such detections, referred to as IM1 and IM2 (Siraj & Loeb 2022a,b), were proclaimed based on luminous events captured by space sensors on United States Department of Defense (DoD) satellites, with their data subsequently published on the Center for Near-Earth Object Studies (CNEOS) website. Notably, IM2 was first recognized by Peña-Asensio et al. (2022). It is worth mentioning that within this database, a minuscule proportion (1%) of events are characterized by hyperbolic orbits. However, the data of these events is classified, rendering external verification infeasible.

IM1 was detected on January 8, 2014, near Papua New Guinea's northeast coast. The U.S. Space Command affirmed that the velocity estimate reported to NASA is sufficiently accurate to indicate an interstellar trajectory. This object had an asymptotic velocity of 42 km/s and disintegrated at an altitude of 18.7 km, with an estimated mass of around 500 kg and a diameter of approximately 0.5 m. Remarkably, IM1 exhibited a dynamic strength (the ram pressure at break up) twice that of known iron meteorites and maintained a heliocentric orbital inclination of 10°.

IM2 was observed on March 9, 2017, above the Atlantic Ocean near Portugal. The event peaked in radiance at an altitude of 23 km, with the object estimated to be 1 m in diameter and weighing 5,000 kg. Its aerodynamic strength was recorded as the third highest in the CNEOS catalog. IM2 entered the Solar System with an initial velocity of 26 km/s and had a heliocentric orbital inclination of 24°.

The strength anomaly presented by the interstellar meteor candidates IM1 and IM2 raises significant questions regarding our understanding of interstellar objects. Both events display an unexpectedly high aerodynamic strength, implying that only the most robust materials may endure the rigors of interstellar travel to reach our Solar System (Peña-Asensio et al. 2022). This observed robustness could point towards a detection bias, where only the sturdiest of objects are detected, as less resilient materials may not survive the journey intact. The calculation of aerodynamic strength, dependent on the atmospheric density and the square of the velocity, i.e., $\rho_{air} v^2$ (Trigo-Rodríguez & Llorca 2006; Vida et al. 2021), suggests that any overestimation in the velocity measurement could artificially inflate the perceived strength of these meteors. Consequently, the tremendous dynamic strength attributed to IM1 and IM2 could be a byproduct of inflated velocity measurements.

Furthermore, the heliocentric orbital inclinations for IM1 and IM2 are curiously low at 10° and 24°, respectively. This stands in marked contrast to the highly inclined orbits of the previously identified interstellar objects 1I and 2I, whose inclinations are -57.2° and 44.05°, respectively. The lower inclinations of IM1 and IM2 diverge from the expected distribution for an incoming interstellar population, which on average would exhibit inclinations closer to 45 degrees.

Theoretical models that aim to replicate the observed light curve of IM1 suggest that such observations could be consistent with an object possessing chondritic properties, albeit assuming velocities that are lower than those recorded (Brown & Borovička 2023)[10]. For IM1, aligning its observational data

[10]The authors contend that selecting errors to render IM1 elliptical is feasible, but requires a specific combination representing merely about ∼0.1% of all possible combination. Additionally, their assumption of velocity error being pro-

VII Workshop on Robotic Autonomous Observatories (October 16-20, 2023)
Editors: Maria Gritsevich, Alberto J. Castro-Tirado, Petr Kubánek, Shashi B. Pandey, and David Hiriart - DOI: https://doi.org/10.22201/ia.14052059p.2025.59.19

with theoretical models necessitates assumptions of exceptionally low luminous efficiency, a highly aerodynamic shape, and materials with substantial inherent strength. Nevertheless, the event's uniqueness is further underscored by discrepancies between these observations and the measurements recorded by an infrasound station. Fernando et al. 2024 state that the reported seismic signals are spurious: one likely originates from local vehicular traffic, while the other is statistically indistinguishable from background noise. Additionally, Hajduková et al. 2024 conclude that the interstellar origin of IM1 is unsupported by available data, as all CNEOS hyperbolic fireballs show significant velocity component deviations, indicating mismeasurements potentially producing parameters statistically similar to IM1.

3.2. *Interstellar flux*

The estimation of interstellar flux, specifically through the detection of hyperbolic meteors, remains a subject of debate within the astronomical community. Radar-based detections of such meteors have frequently been challenged or dismissed as erroneous. Reports from radar systems like AMOR (Advanced Meteor Orbit Radar, Baggaley et al. 1993) and CMOR (Canadian Meteor Orbit Radar, Weryk & Brown 2004) have identified interstellar impactors in the 10-100 μm size range among millions of impacts.

Moreover, the Arecibo Observatory's radar system has reported the atmospheric entry of particles that appear to be of interstellar origin (Meisel et al. 2002). Complementing these ground-based observations, in-situ dust detections have been documented by spaceborne instruments aboard the *Galileo* and *Ulysses* spacecraft (Grun et al. 1993), lending credence to the presence of such particles within our Solar System.

In the six years that have passed since the groundbreaking discovery of 1I, the utilization of the Pan-STARRS (Panoramic Survey Telescope and Rapid Response System) survey has enabled astronomers to calculate an approximate number density of these interstellar objects. The number density is estimated to be 0.1 au^{-3} for 1I-like objects (Jewitt et al. 2017). Extrapolating from this density, it is inferred that there could be around 10^4 such objects within the vicinity of the Sun up to the orbit of Neptune at any given time. This translates to an influx of approximately 10^3 such objects per year, or about three per day entering the Solar System.

portional to velocity lacks statistical support ($R^2 = 0.027$; Peña-Asensio et al. 2024a).

Emerging global surveys with broader sky coverage, such as Vera C. Rubin Observatory (formerly the Large Synoptic Survey Telescope or LSST) and the Global Network of Robotic Astronomical Observatories (BOOTES), have the potential to significantly enhance today's statistical data (Vinkovi et al. 2016; Bektešević et al. 2018; Vinkovic et al. 2020; Castro-Tirado 2023).

4. EXTRASOLAR METEORITES

The possibility of extrasolar meteorites reaching Earth's surface presents a captivating yet formidable challenge for detection and verification. Cometary objects, which originate at substantial distances from their stars, are more prone to becoming interstellar as they are weakly gravitationally bound to their host systems. However, these bodies are often composed of fragile icy conglomerates, which are unlikely to withstand the intense ablation of Earth's atmosphere if they impact at hypervelocities. More than half of the interstellar objects that enter our Solar System are traveling at velocities greater than 40 km/s (Cabot & Laughlin 2022). Should these objects impact Earth, they would do so at velocities exceeding 100 km/s, resulting in high-altitude airbursts rather than delivering meteorites to the surface.

In terms of frequency, based on the density number it is estimated that fewer than 50 impacts by 100-meter-sized interstellar objects have occurred over Earth's history (Jewitt et al. 2020). This rate is small compared to the impact frequency of similar-sized objects originating from within our Solar System, which is about 10,000 times higher. This discrepancy is reflected in the geological record, with only around 200 confirmed impact structures (Schmieder & Kring 2020) and approximately 70,000 meteorites found on Earth (according to The Meteoritical Society database). This suggests that, if asteroidal in nature, our collections would contain seven extrasolar meteorites (0.01%).

The identification of extrasolar meteorites poses a significant challenge. According to the nebular hypothesis, such objects would carry a distinct isotopic signature. However, the critical question remains: Are we adequately verifying this unique signature? And if so, is it sufficiently distinct to be discernible from Solar System materials?

The recent announcement of the recovery of mm-sized spherules in the Pacific Ocean has sparked interest (Loeb et al. 2023). To substantiate the claim that these spherules are indeed interstellar in origin and are associated with the IM1 fireball, several

VII Workshop on Robotic Autonomous Observatories (October 16-20, 2023)
Editors: Maria Gritsevich, Alberto J. Castro-Tirado, Petr Kubánek, Shashi B. Pandey, and David Hiriart - DOI: https://doi.org/10.22201/ia.14052059p.2025.59.19

crucial points require demonstration: firstly, that the IM1 event was interstellar incursion and that the object did not completely disintegrate in the atmosphere; secondly, that there is a direct link between the collected material and the IM1 event; and thirdly, that these spherules display an unusual isotopic composition indicative of an interstellar origin.

To date, none of these points have been conclusively proven, although full data is still pending peer-reviewed publication. The chemical anomalies levels of nickel, beryllium, lanthanum, and uranium detected in the spherules are reminiscent of those previously described in micrometeorites of Solar System origin (Rudraswami et al. 2016; Van Ginneken et al. 2021) and have been reported to align with anthropogenic coal ash (Gallardo 2023). Additionally, the search region is known for debris from artificial satellite re-entries, which could potentially contaminate the area with refractory materials exhibiting atypical element concentrations (Moreno-Ibáñez et al. 2016).

The spherules' isotopic signatures align with the Terrestrial Fractionation Line (TFL), a characteristic consistent with other materials from within our Solar System. In contrast, interstellar spherules would be expected to display significant deviations in Fe isotope ratios and align along a distinct line, parallel to but separate from the TFL. The alignment with the TFL shown in Figure 4 strongly suggests that these spherules do not pertain to interstellar visitors but are indigenous to our solar nebula. Should the materials be of natural origin, it is more likely that they are conventional micrometeorites derived from common asteroids altered by prolonged interaction with seawater and terrestrial contamination (Desch 2023).

5. CONCLUSIONS

Whether Earth receives impacts of interstellar provenance can be affirmedobjects from outside the Solar System visit our planet. The evidence strongly suggests that both 1I and 2I are of interstellar origin, given their hyperbolic orbits and other properties that cannot be easily explained by conventional mechanisms within our Solar System. The anomalies associated with 1I, such as its non-gravitational acceleration and extreme elongation, have plausible explanations that do not necessarily require the invocation of an exotic nature.

While a hyperbolic orbit is a strong indicator of an interstellar trajectory, it is not a definitive criterion, as such orbits can also result from interactions within the Solar System, such as close encounters with stars as exemplified by the hyperbolic Finnish fireball FH1.

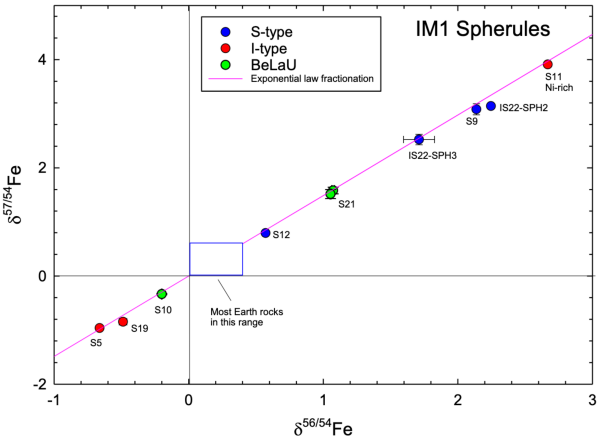


Fig. 4. Fe isotope ratios reported of the found spherules in the Pacific Ocean near the IM1 site. Reproduced from Loeb et al. (2023).

The classification of specific meteors as interstellar, including events such as IM1 and IM2, remains ambiguous. While initial assessments may suggest an interstellar pathway, further analysis often reveals inconsistencies with this interpretation. As such, there is no absolute certainty about the interstellar nature of IM1 and IM2, especially the latter.

The existence of extrasolar meteorites on Earth is a concept that continues to captivate the imagination of the scientific community. However, based on current detections, the likelihood of such discoveries remains extremely unlikely, primarily due to their low frequency and the challenges faced during atmospheric entry.

Regarding the spherules attributed to the IM1 event, their connection to IM1 and their interstellar nature is uncertain. The isotopic analysis does not support an interstellar origin, as their signatures are consistent with known Solar System materials.

In summary, while the pursuit of macroscopic interstellar samples is a scientific imperative, the likelihood of success increases when we turn our gaze upwards. Our endeavors should be directed toward enhancing sky surveillance capabilities and developing ready-to-launch interceptor missions. Such strategies will likely yield more definitive results in the quest to capture and study interstellar objects, as opposed to searching on the ground or in the seas.

Acknowledgements: This study was supported by the European Research Council (ERC) grant agreement No. 865657, projects PID2021-128062NB-I00 funded by MCIN/AEI /10.13039/501100011033, Unidad de Excelencia María de Maeztu CEX2020-001058-M,

FEDER/Ministerio de Ciencia e Innovación Agencia Estatal de Investigación PID2021-126427NB-I00, and Academy of Finland project no. 325806.

VII Workshop on Robotic Autonomous Observatories (October 16-20, 2023)
Editors: Maria Gritsevich, Alberto J. Castro-Tirado, Petr Kubánek, Shashi B. Pandey, and David Hiriart - DOI: https://doi.org/10.22201/ia.14052059p.2025.59.19

REFERENCES

Baggaley, W. J., Taylor, A. D., & Steel, D. I. 1993, mtpb.conf, 53

Bektešević, D., Vinković, D., Rasmussen, A., et al. 2018, MNRAS, 474, 4837, doi:10.1093/mnras/stx3085

Bergner, J. B. & Seligman, D. Z. 2023, Natur, 615, 610, doi:10.1038/s41586-022-05687-w

Bialy, S. & Loeb, A. 2018, ApJ, 868, L1, doi:10.3847/2041-8213/aaeda8

Borisov, G., 2019, MPEC, 2019-R106

Brown, P. G. & Borovička, J. 2023, ApJ, 953, 167, doi:10.3847/1538-4357/ace421

Cabot, S. H. C. & Laughlin, G. 2022, PSJ, 3, 172, doi:10.3847/PSJ/ac77e9

Castro-Tirado, A. J. 2023, NatAs, 7, 1136, doi:10.1038/s41550-023-02075-w

de la Fuente Marcos, C., de la Fuente Marcos, R., & Aarseth, S. J. 2018, MNRAS, 476, L1, doi:10.1093/mnrasl/sly019

de la Fuente Marcos, R. & de la Fuente Marcos, C. 2022, RNAAS, 6, 152, doi:10.3847/2515-5172/ac842b

Desch, S. J., Jackson, A. P., & Hartnett, H. E. 2023 The Challenges of Recovering Interstellar Meteorites, in Asteroids, Comets, Meteors Conference 2023, LPI Contrib, No. 2851

Dupuy, T. J., Liu, M. C., Best, W. M. J., et al. 2019, AJ, 158, 174, doi:10.3847/1538-3881/ab3cd1

Fernando, B., Mialle, P., Ekström, G., et al. 2024, GeoJI, 181, doi:10.1093/gji/ggae202

Gallardo, P. A. 2023, RNAAS, 7, 220, doi:10.3847/2515-5172/ad03f9

Gritsevich, M., Lyytinen, E., Moilanen, J., et al. 2014, pim4.conf, France, 18-21 September 2014, 162

Gritsevich, M., Nissinen, M., Oksanen, A., et al. 2022, MNRAS, 513, 2201, doi:10.1093/mnras/stac822

Grun, E., Zook, H. A., Baguhl, M., et al. 1993, Natur, 362, 428, doi:10.1038/362428a0

Hajduková, M., Kornoš, L., & Tóth, J. 2014, M&PS, 49, 63, doi:10.1111/maps.12119

Hajdukova, M., Sterken, V., Wiegert, P., et al. 2020, Planet. Space Sci., 192, 105060, doi:10.1016/j.pss.2020.105060

Hajduková, M., Stober, G., Barghini, D., et al. Accepted A&A

Higuchi, A. & Kokubo, E. 2020, MNRAS, 492, 268, doi:10.1093/mnras/stz3153

Jewitt, D., Luu, J., Rajagopal, J., et al. 2017, ApJ, 850, L36, doi:10.3847/2041-8213/aa9b2f

Jewitt, D., Hui, M.-T., Kim, Y., et al. 2020, ApJ, 888, L23, doi:10.3847/2041-8213/ab621b

Jewitt, D. & Seligman, D. Z. 2023, ARA&A, 61, 197, doi:10.1146/annurev-astro-071221-054221

Lyytinen, E. & Gritsevich, M. 2016, P&SS, 120, 35, doi:10.1016/j.pss.2015.10.012

Loeb, A. 2022, AsBio, 22, 1392, doi:10.1089/ast.2021.0193

Loeb, A. 2023, RNAAS, 7, 43, doi:10.3847/2515-5172/acc10d

Loeb, A., Adamson, T., Bergstrom, S., et al. 2023, arXiv:2308.15623, doi:10.48550/arXiv.2308.15623

Mamajek, E. E., Barenfeld, S. A., Ivanov, V. D., et al. 2015, ApJ, 800, L17, doi:10.1088/2041-8205/800/1/L17

Mashchenko, S. 2019, MNRAS, 489, 3003, doi:10.1093/mnras/stz2380

Meech, K. J., Weryk, R., Micheli, M., et al. 2017, Natur, 552, 378, doi:10.1038/nature25020

Meisel, D. D., Jnches, D., & Mathews, J. D. 2002, ApJ, 567, 323, doi:10.1086/322317

Moilanen, J., Gritsevich, M., & Lyytinen, E. 2021, MNRAS, 503, 3337, doi:10.1093/mnras/stab586

Moreno-Ibáñez, M., Trigo-Rodríguez, J. M., Martínez-Jiménez, M., et al. 2016, LPI Contribution, 1903, 1430

Peña-Asensio, E., Trigo-Rodríguez, J. M., Gritsevich, M., et al. 2021, MNRAS, 504, 4829, doi:10.1093/mnras/stab999

Peña-Asensio, E., Trigo-Rodríguez, J. M., Langbroek, M., et al. 2021, Astrodynamics, 5, 347, doi:10.1007/s42064-021-0112-2

Peña-Asensio, E., Trigo-Rodríguez, J. M., & Rimola, A. 2022, AJ, 164, 76, doi:10.3847/1538-3881/ac75d2

Peña-Asensio, E., Trigo-Rodríguez, J. M., Rimola, A., et al. 2023, MNRAS, 520, 5173, doi:10.1093/mnras/stad102

Peña-Asensio, E., Visuri, J., Trigo-Rodríguez, J. M., et al. 2024a, Icar, 408, 115844, doi:10.1016/j.icarus.2023.115844

Peña-Asensio, E., Visuri, J., Trigo-Rodríguez, J. M., et al. 2024b, LPI Contribution, 3036, 6386

Rudraswami, N. G., Shyam Prasad, M., Babu, E. V. S. S. K., et al. 2016, M&PS, 51, 718, doi:10.1111/maps.12618

Schmieder, M. & Kring, D. A. 2020, ABio, 20, 91, doi:10.1089/ast.2019.2085

Seligman, D. Z. & Moro-Martín, A. 2022, ConPh, 63, 200, doi:10.1080/00107514.2023.2203976

Siraj, A. & Loeb, A. 2022, ApJ, 939, 53, doi:10.3847/1538-4357/ac8eac

Siraj, A. & Loeb, A. 2022, ApJ, 941, L28, doi:10.3847/2041-8213/aca8a0

Trigo-Rodríguez, J. M., Castro-Tirado, A. J., Llorca, J., et al. 2004, EM&P, 95, 553, doi:10.1007/s11038-005-4341-9

Trigo-Rodríguez, J. M. & Llorca, J. 2006, MNRAS, 372, 655. doi:10.1111/j.1365-2966.2006.10843.x

Van Ginneken, M., Goderis, S., Artemieva, N., et al. 2021, EPSC, doi:10.5194/epsc2021-679

Vida, D., Brown, P. G., Campbell-Brown, M., et al. 2021, Icar, 354, 114097, doi:10.1016/j.icarus.2020.114097

Vinković, D., & Gritsevich, M. 2020, Geographical Institute "Jovan Cvijić" of the Serbian Academy of Sciences and Arts, 1, 45-55
Vinković, D., Gritsevich, M., Srećković, V., et al. 2016, primo.conf, 319
Visuri, J. J. & Gritsevich, M. I. 2021, LPI Contribution, 2609, 6093
Weryk, R. J. & Brown, P. 2004, EM&P, 95, 221, doi:10.1007/s11038-005-9034-x
Williams, G. V., Sato, H., Sarneczky, K., et al. 2017, CBET, 4450, 1

VII Workshop on Robotic Autonomous Observatories (October 16-20, 2023)
Editors: Maria Gritsevich, Alberto J. Castro-Tirado, Petr Kubánek, Shashi B. Pandey, and David Hiriart - DOI: https://doi.org/10.22201/ia.14052059p.2025.59.19

Revista Mexicana de Astronomía y Astrofísica Serie de Conferencias (RMxAC), **59**, 109–113 (2025)
© 2025: Instituto de Astronomía, Universidad Nacional Autónoma de México
https://doi.org/10.22201/ia.14052059p.2025.59.20

VII Workshop on Robotic Autonomous Observatories (October 16-20, 2023)
Editors: Maria Griffsevich, Alberto J. Castro-Tirado, Petr Kubánek, Shashi B. Pandey, and David Hiriart - DOI: https://doi.org/10.22201/ia.14052059p.2025.59.20

EARLY-TIME OPTICAL SPECTRAL SHAPE MEASUREMENTS OF GRB 200925B

Zhavlonbek Abdullayev[1,2], Toktarkhan Komesh[1,3,*], Bruce Grossan[1,4], Ernazar Abdikamalov[1,5], Zhanat Maksut[1], Maxim Krugov[6], Shynaray Myrzakul[2], Duriya Tuiakbayeva[1,7], and Alma Kostangeldinova[7]

RESUMEN

Las mediciones para determinar los espectros ópticos en banda ancha de posluminescencias de estallidos de rayos-gamma (GRB) generalmente se realizan una hora o más tras del evento desencadenante. Con nuestro sistema automatizado de respuesta rápida, el generador de imágenes de tres canales simultáneos (BSTI) en el telescopio de fuentes transitorias de la Universidad de Nazarbayev en el Observatorio Astrofísico Assy-Turgen (NUTTelA-TAO), comenzamos las mediciones del estallido GRB 200925B a los 129 s después de la alerta proporcionada por *Swift*-BAT. Las pendientes del declive de la curva de luz en las bandas g', r' e i' en el intervalo de tiempo de 129 s a 1029 s son -0,43 ± 0,31, -0,43 ± 0,15 y -0,72 ± 0,14 respectivamente. Durante la fase de declive, se midió un cambio de color de rojo a azul y un cambio en la pendiente logarítmica β de -2,73 a -1,52. La evolución de la pendiente espectral óptica es consistente con una disminución de la extinción provocada por la destrucción del polvo circundante.

ABSTRACT

Optical broad-band spectral shape measurements of gamma-ray bursts (GRBs) are typically made starting an hour or more after the trigger event. With our automated, rapid-response system, the Burst Simultaneous Three-channel Imager (BSTI) on the Nazarbayev University Transient Telescope at Assy-Turgen Astrophysical Observatory (NUTTelA-TAO), we began measurements of GRB 200925B 129 s after the *Swift* BAT trigger. The temporal decay log slopes in the g', r', and i' bands in the time interval 129 s to 1029 s are -0.43 0.31, -0.43 0.15, and -0.72 0.14, respectively. During the decay phase, a shift in color from red to blue, a change in log slope of β from -2.73 to -1.52 was measured. The evolution in the optical spectral slope is consistent with a decrease in extinction caused by dust destruction.

Key Words: dust, extinction — gamma-ray burst: individual: GRB 200925B

1. INTRODUCTION

While the single-band optical flux of gamma-ray bursts (GRBs) has been detected as early as ∼10 s after the onset of gamma-ray emission (e.g., Akerlof et al. 1999; Kobayashi & Sari 2000; Racusin et al. 2008; Vestrand et al. 2005, 2014; Oganesyan et al. 2023; Xin et al. 2023; Jin et al. 2023), the earliest measurements of the spectral shape are typically made much later, starting an hour or more after trigger (e.g., Filgas et al. 2011; Krühler et al. 2011; Pozanenko et al. 2020). In order to study the early-time optical behavior of GRBs, our group developed an automated, rapid-response system, the Burst Simultaneous Three-channel Imager (BSTI) on the 700 mm diameter Nazarbayev University Transient Telescope at Assy-Turgen Astrophysical Observatory (Grossan & Maksut 2020). The system responds to *Swift* Burst Alert Telescope (BAT) and other high-quality GRB alert positions and begins simultaneous imaging in i', r', and g' typically 20-100 s after trigger.

Komesh et al. (2023) describes the measurement of the broad-band spectral shape of GRB 201015A with this instrument. The authors found pronounced colour evolution from 58 s to 4140 s after trigger, and concluded that the likely cause was dust destruction due to powerful UV emission in the event. Morgan

[1]Energetic Cosmos Laboratory, Nazarbayev University, Astana 010000, Kazakhstan. *E-mail: toktarkhan.komesh@nu.edu.kz
[2]Department of General & Theoretical Physics, L. N. Gumilyov Eurasian National University, Astana, 010008, Kazakhstan.
[3]Institute of Experimental and Theoretical Physics, Al-Farabi Kazakh National University, Almaty, 050040, Kazakhstan.
[4]Space Sciences Laboratory, University of California, Berkeley, CA 94720, USA.
[5]Department of Physics, School of Sciences and Humanities, Nazarbayev University, 53 Kabanbay Batyr Ave., 010000 Astana.
[6]Fesenkov Astrophysical Institute, Almaty, 050020, Kazakhstan.
[7]Sh. Ualikhanov Kokshetau University, 76 Abaya str., 020000, Kokshetau, Kazakhstan.

VII Workshop on Robotic Autonomous Observatories (October 16-20, 2023)
Editors: Maria Gritsevich, Alberto J. Castro-Tirado, Petr Kubánek, Shashi B. Pandey, and David Hiriart - DOI: https://doi.org/10.22201/ia.14052059p.2025.59.20

et al. (2014) also found red to blue color evolution in GRB 120119A, but in the initial 200 s following the trigger.

In this paper, we present and analyze our NUTTelA-TAO optical measurements of GRB 200925B. We include the archival X-γ ray measurements in our analysis. Our observations of GRB 200925B began 129 s after the BAT trigger. We observe in the Sloan filter bands g', r', and i' (Grossan et al. 2020). In the initial phase spanning from 129 s to ∼1029 s after trigger, we observe variations in the light curve that differ from those typically observed at later times. These measurements serve as diagnostic tools for probing both the physical mechanisms within the outflow and the environment surrounding the progenitor (e.g., Zaninoni et al. 2013; Melandri et al. 2008).

In this paper, we focus on the evolution of the temporal and broad-band spectral slopes during the early afterglow phase. We use the temporal parameter α and the spectral log slope parameter β defined via: $f_\nu \propto t^\alpha \nu^\beta$. Our observations are presented in Section 2. Our results are described in Section 3, and conclusion is provided in Section 4.

2. OBSERVATIONS

We observed GRB 200925B beginning at 21:52:46 UT on September 25, 2020, 129 s after the BAT trigger. Detailed observational parameters can be found in Table 1. Our cameras recorded 15 s exposures, but we co-added the images to the exposure time of 225 s in the time interval 129 s to 1029 s after trigger. The five sigma upper limit sensitivities achieved for the g', r', and i' filter images are 18.5, 19.1 and 18.6 magnitudes, respectively. The weather was clear during the observation. The calibration process was performed using five Pan-STARRS catalog stars identified in our images. We verify the accuracy of our measurements by comparing standard star magnitudes and colors with catalog values. The standard deviation of our magnitude values compared to catalog values of the five standard stars were 0.08, 0.04 and 0.03 mag in the g', r', and i' filters, respectively. We also verify our measurements by examining simulated stars of known actual brightness that we included in our images.

The BAT and XRT data were obtained through the Burst Analyser (Evans et al. 2010), which is provided by the UK Swift Science Data Centre at the University of Leicester (hereafter "SSDCUL")[8].

[8] https://www.swift.ac.uk

3. RESULTS AND DISCUSSION

3.1. *Optical light curve and spectral log slope*

Figure 1 (upper panel) shows the optical light curve. In all filters, g', r', and i' , we see a monotonic decay (see Table 1 for values). Temporal decay log slopes for the g', r', and i' bands are -0.43 0.31, -0.43 0.15 and -0.72 0.14, respectively.

To determine the intrinsic log slope of the GRB emission, we account for extinction effects originating from both within our Milky Way galaxy and local surrounding of the burst. The Galactic extinction toward GRB 200925B is 0.133, 0.092 and 0.068 magnitudes in the Sloan g', r' and i' filters, respectively (Schlafly & Finkbeiner 2011). We use the mean value $A_v^{\rm local}$= 0.15 determined by Li et al. (2018) for the local extinction and the empirical extinction curve from Pei (1992) for the Small Magellanic Cloud (SMC). We obtain the local extinction values for the Sloan g', r' and i' filters as 0.06, 0.04 and 0.03 magnitudes, respectively.

Figure 1 (lower panel) shows the spectral log slope as a function of time. The determination of the optical spectral log slope involves fitting a power law spectrum to the g', r' and i' data captured during time interval ranging from 129 s to 580 s and to the r' and i' data captured during time interval of 580 and 1029 s (note that g' is not detected in this time interval). The obtained spectral log slopes are -2.73 0.28, -2.27 0.32, and -1.52 0.06, respectively.

3.2. *γ-X-ray light curve*

Data of 10 keV values of XRT and BAT were obtained by the SSDCUL. These values were derived through spectral and temporal fits encompassing both the BAT and XRT measurements, ensuring a uniform basis for comparison as described in detail in Evans et al. (2007, 2009, 2010). Figure 2 (upper panel) displays the γ-X-ray light curves alongside the optical light curves. Dashed lines indicate best fit model with 2 breaks (Evans et al. 2009). Flares and plateau are noticeable in the X-ray light curve during the initial time interval until approximately 1100 s relative to the BAT trigger time. The early-phase temporal decay log slope is -4.5 (+1.2, -0.9) until 125 s. Subsequently, following the second break at 4100 s, the decay transitions to a log slope of 0.07 (+0.11, -0.12). In the sunsequent phase, it undergoes decay with a temporal decay log slope of -1.4 (+0.25, -0.21).

3.3. *Color Evolution*

The temporal decay value of longer wavelength band i' is steeper than those in shorter wavelength

VII Workshop on Robotic Autonomous Observatories (October 16-20, 2023)
Editors: Maria Gritsevich, Alberto J. Castro-Tirado, Petr Kubánek, Shashi B. Pandey, and David Hiriart - DOI: https://doi.org/10.22201/ia.14052059p.2025.59.20

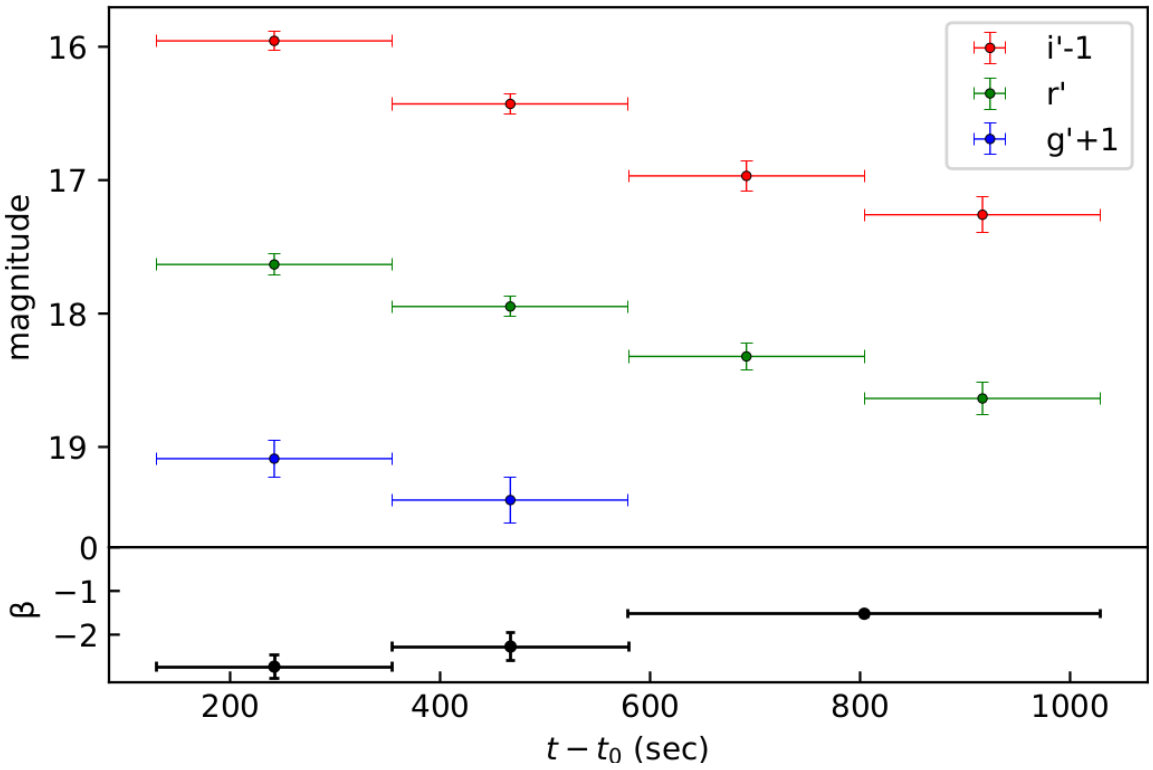


Fig. 1. Optical light curve (upper panel) and spectral log slope β (lower panel) of GRB 200925B. t_0 = 21:52:46 UT on September 25, 2020. In this plot, the magnitudes have not been corrected for Galactic extinction. For clarify, we shift the i' and g' bands by -1 and +1 mag, respectively.

TABLE 1

NUTTELA-TAO OBSERVATION OF GRB200925B.

T_{mid} (s)	t_{exp} (s)	Magnitudes			Flux density (mJy)		
		g' (error)	r' (error)	i' (error)	g' (error)	r' (error)	i' (error)
242	225	18.08 (0.13)	17.63 (0.07)	16.95 (0.06)	0.23 (0.03)	0.34 (0.02)	0.63 (0.04)
467	225	18.39 (0.17)	17.94 (0.07)	17.42 (0.07)	0.17 (0.02)	0.26 (0.01)	0.41 (0.03)
692	225	UL 18.62	18.32 (0.01)	17.96 (0.11)	UL 0.14	0.18 (0.01)	0.25 (0.02)
1029	225	UL 18.74	18.63 (0.12)	18.25 (0.13)	UL 0.13	0.13 (0.01)	0.19 (0.02)

UL indicates the error value is a 5 sigma upper limit. The mJy flux values are corrected for extinction effects from both within our Milky Way galaxy (Schlafly & Finkbeiner 2011) and local to the burst (see Section 3.1 for details).

bands g' and r'. This is what one might observe from fading emission behind a dust column that decreased with time, causing decreasing reddening with time. The blue channel would appear to decay slower than the more red ones, which are less affected by reddening. Eventually when the reddening no longer changed, the spectral and temporal slopes would converge to their intrinsic values. Here at late times we do observe these constant slope values, both in the optical and, after 4100 s, in the X-ray.

In order to determine the changing local reddening, we assume a constant intrinsic spectral and temporal log slope as observed during later stages, with a value of β=-1.52 and α=-0.72. This is the same procedure used in Komesh et al. (2023). Using these intrinsic values, we derive the local reddening as given in Fig. 3 shows a decrease in A_v^{local} from 0.30 $\pm$ 0.09 mag to -0.01 $\pm$ 0.14 mag in the time interval 129 s to 580 s. This amounts to a change of 1.87 σ. Subsequently, A_v^{local} appears to remain constant.

VII Workshop on Robotic Autonomous Observatories (October 16-20, 2023)
Editors: Maria Gritsevich, Alberto J. Castro-Tirado, Petr Kubánek, Shashi B. Pandey, and David Hiriart - DOI: https://doi.org/10.22201/ia.14052059p.2025.59.20

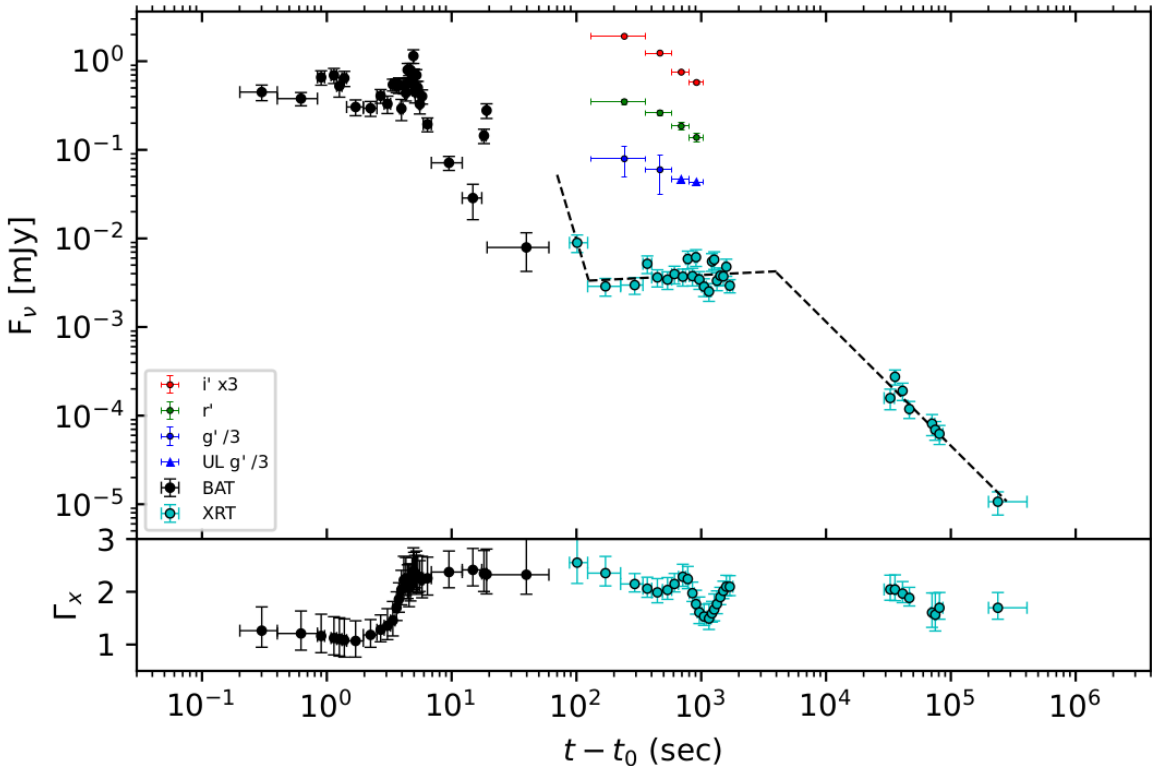


Fig. 2. X-ray and optical light curves of GRB 200925B. UL refers to the 5σ upper limit. BAT refers to the 10 keV X-ray flux extrapolated from BAT data, and XRT gives the 10 keV flux from XRT data (Evans et al. 2010). Dashed lines indicate the best fit model (χ^2=29.8, dof=24) with two breaks obtained by SSDCUL (Evans et al. 2009).

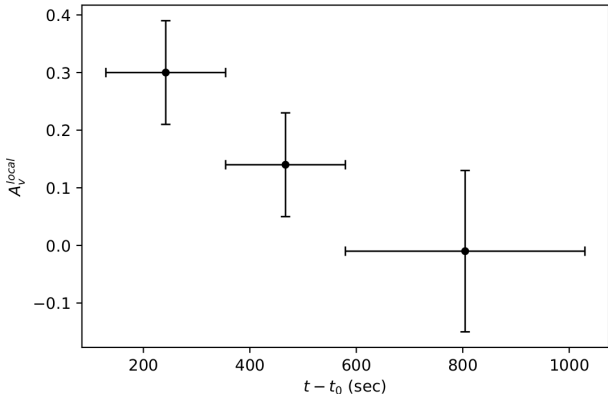


Fig. 3. Local extinction, $A_v^{\rm local}$, as a function of time for GRB 200925B. See the main text for definition and method.

Long GRBs are observed in regions with active star formation (Woosley 1993; Woosley & Bloom 2006). The majority of GRBs exhibit a moderate level of dust extinction around ~ 1000 s, with occasional cases of heavier extinction Perley et al. (2009). Red-to-blue color evolution of the color of GRBs has been observed in GRB and attributed to destruction of dust grains in at least the two cases given in the introduction. We observed a monotonic red-to-blue color evolution which is *consistent* with dust destruction, but the weakness of the statistical significance does not allow us to make a definite conclusion that it is present.

4. CONCLUSION

We studied the early-time optical behavior of GRB 200925B, starting 129 s after the BAT trigger. Our analysis revealed variations in the light curve from 129 s to approximately 1029 s after the trigger. We accounted for extinction effects from both within our Milky Way galaxy and the local environment of the burst. The spectral log slope analysis revealed monotonic change from red to blue during the early afterglow phase. This is *consistent* with decreasing reddening with time, but this change had low statistical significance. Consistency with dust destruction is conceptually significant, however, as we have only observed and analyzed a small number (total 4 including soon-to-be-published) of early light curves, and one was a clear case (Komesh et al. 2023), and one consistent with dust destruction. If this trend continues, it will become clear that this is a common and important process.

VII Workshop on Robotic Autonomous Observatories (October 16-20, 2023)
Editors: Maria Gritsevich, Alberto J. Castro-Tirado, Petr Kubánek, Shashi B. Pandey, and David Hiriart - DOI: https://doi.org/10.22201/ia.14052059p.2025.59.20

Additionally, we presented X-ray and optical light curves, highlighting flares and plateaus in the X-ray light curve during the initial time interval until around 1100 s relative to the BAT trigger time. The temporal decay log slope exhibited changes during different phases of the afterglow.

Ackowledgements: This research has been funded by the Science Committee of the Ministry of Science and Higher Education of the Republic of Kazakhstan (Grant Nos. AP14870504) and partially supported by the Nazarbayev University Faculty Development Competitive Research Grant Program (No 11022021FD2912). MK is supported by the Science Committee of the Ministry of Science and Higher Education of the Republic of Kazakhstan (Grant No. BR21881880). The NUTTelA-TAO Team expresses gratitude to the personnel of the Assy-Turgen Astrophysical Observatory in Almaty, Kazakhstan, and the Fesenkov Astrophysical Institute, Almaty, Kazakhstan, for their assistance. Special appreciation is extended to the ATO staff. The research utilized data provided by the UK Swift Science Data Centre at the University of Leicester.

REFERENCES

Akerlof, C., Balsano, R., Barthelmy, S., et al. 1999, Natur, 398, 400
Evans, P., Beardmore, A., Page, K., et al. 2009, MNRAS, 397, 1177
Evans, P., Beardmore, A. P., Page, K. L., et al. 2007, A&A, 469, 379
Evans, P., Willingale, R., Osborne, J., et al. 2010, A&A, 519, A102
Filgas, R., Greiner, J., Schady, P., et al. 2011, A&A, 535, A57
Grossan, B. & Maksut, Z. 2020, SPIE, 11447
Grossan, B., Maksut, Z., Kim, A., et al. GCN, 28511, 1
Jin, Z.-P., Zhou, H., Wang, Y., et al. 2023, NatAs, 7, 1108
Kobayashi, S. & Sari, R. 2000, ApJ, 542, 819
Komesh, T., Grossan, B., Maksut, Z., et al. 2023, MNRAS, 520, 6104
Krühler, T., Greiner, J., Schady, P., et al. 2011, A&A, 534, A108
Li, L., Wang, Y., Shao, L., et al. 2018, ApJS, 234, 26
Melandri, A., Mundell, C., Kobayashi, S., et al. 2008, ApJ, 686, 1209
Morgan, A. N., Perley, D. A., Cenko, S. B., et al. 2014, MNRAS, 440, 1810
Oganesyan, G., Karpov, S., Salafia, O. S., et al. 2023, NatAs, 7, 843
Pei, Y. C. 1992, ApJ, 395, 130
Perley, D. A., Cenko, S., Bloom, J., et al. 2009, AJ, 138, 1690
Pozanenko, A., Belkin, S., Volnova, A., et al. 2020, GRB Coordinates Network, 29033, 1
Racusin, J. L., Karpov, S., Sokolowski, M., et al. 2008, Natur, 455, 183
Schlafly, E. F. & Finkbeiner, D. P. 2011, ApJ, 737, 103
Vestrand, W., Wozniak, P., Wren, J., et al. 2005, Natur, 435, 178
Vestrand, W., Wren, J., Panaitescu, A., et al. 2014, Sci, 343, 38
Woosley, S. E. 1993, ApJ, 405, 273
Woosley, S. & Bloom, J. 2006, ARA&A, 44, 507
Xin, L., Han, X., Li, H., et al. 2023, NatAs, 7, 724
Zaninoni, E., Bernardini, M. G., Margutti, R., Oates, S., & Chincarini, G. 2013, A&A, 557, A12

Revista Mexicana de Astronomía y Astrofísica Serie de Conferencias (RMxAC), **59**, 115–131 (2025)
© 2025: Instituto de Astronomía, Universidad Nacional Autónoma de México
https://doi.org/10.22201/ia.14052059p.2025.59.21

VII Workshop on Robotic Autonomous Observatories (October 16-20, 2023)
Editors: Maria Gritsevich, Alberto J. Castro-Tirado, Petr Kubánek, Shashi B. Pandey, and David Hiriart - DOI: https://doi.org/10.22201/ia.14052059p.2025.59.21

AN INTERMEDIATE LUMINOSITY GRB 210210A: THE EARLY ONSET OF THE EXTERNAL FORWARD SHOCK IN THE X-RAY?

Rahul Gupta[1,2,3], A. K. Ror[1,4], S. B. Pandey[1], J. Racusin[2], M. Moss[2,3], A. Aryan[1,5], N. Klingler[2], and A. J. Castro-Tirado[6,7]

RESUMEN

Hemos analizado las carcterísticas de la emisión de la posluminiscencia del estallido de rayos gamma de luminosidad intermedia GRB 210210A. Nuestro análisis de la emisión de la misma indica que GRB 210210A es uno de los GRB largos más suaves detectados por *Swift*-BAT. El espectro de emisión de dicha posluminiscencia integrado en el tiempo de la duración de GRB 210210A se describe adecuadamente mediante una función de ley de potencias con un corte exponencial. La energía del pico espectral ($E_{p,z}$) en el sistema de referencia de reposo y el valor de la energía (asumiendo isotropía) $E_{\gamma,\rm iso}$ para este GRB satisfacen marginalmente (2σ) la correlación de Amati, una caracterstica común observada en GRBs de luminosidad baja/intermedia. Cabe destacar que se observa un declive temprano en la curva de luz de *Swift*-XRT (una caracterstica poco común); mientras que la curva de luz de la posluminiscencia en el óptico, por otro lado, parece seguir un decaimiento en forma de ley de potencias. Sin embargo, debido a la falta de suficientes observaciones ópticas tempranas, no podemos descartar por completo la posibilidad de una protuberancia temprana en la curva de luz óptica. Para la protuberancia observada en la curva de luz de rayos X temprana, calculamos parámetros como el tiempo de pico, el tiempo de ascenso, el tiempo de decaimiento y el factor de Lorentz ($\Gamma_0 \sim 156$), que satisface perfectamente la correlación entre los parámetros del inicio de la posluminiscencia en los GRB. Tanto la curva de luz óptica como la de rayos X (incluidas nuestras observaciones) exhiben una ruptura cromática tardía para dicha posluminiscencia. Con base en los parmetros de dicha protuberancia y postluminiscencia, confirmamos que la luminosidad intermedia del GRB 210210A favorece un escenario de colapso y que posiblemente sea debido a un magnetar subyacente.

ABSTRACT

We have analyzed the prompt and afterglow characteristics of the intermediate luminosity burst "GRB 210210A". Our prompt emission analysis indicates that GRB 210210A is among the softest long GRBs detected by the *Swift*-BAT. The time-integrated prompt emission spectrum of GRB 210210A is aptly described by a power law function with an exponential cutoff. The spectral peak energy ($E_{p,z}$) in rest-frame and the $E_{\gamma,\rm iso}$ for this GRB marginally satisfy the 2σ Amati correlation, a common feature observed in low/intermediate luminosity GRBs. Notably, an early bump is observed in the *Swift*-XRT light curve (a rare feature); the optical afterglow light curve, on the other hand, appears to follow a power law decay. However, due to the lack of sufficient early optical observations, we cannot completely rule out the possibility of an early bump in the optical light curve. For the bump observed in the early X-ray light curve, we calculated parameters such as peak time, rise time, decay time, and bulk Lorentz factor ($\Gamma_0 \sim 156$), which perfectly satisfy the correlation between the parameters of the onset of the afterglow in GRBs. Both the optical and X-ray (including our observations) light curves exhibit a chromatic break in the late afterglow. Based on the prompt and afterglow parameters, we confirm that the intermediate luminosity GRB 210210A favors a collapsar scenario and is possibly powered by a magnetar.

Key Words: gamma-ray burst: general — gamma-ray burst: individual (GRB 210210A) — methods: data analysis — stars: jets — techniques: photometric

1. INTRODUCTION

Gamma-ray bursts (GRBs) are among the most energetic and luminous events in the cosmos, typically observed as brief flashes of gamma-ray light

[1]Aryabhatta Research Institute of Observational Sciences (ARIES), Manora Peak, Nainital-263002, India.
[2]Astrophysics Science Division, NASA Goddard Space Flight Center, Mail Code 661, Greenbelt, MD 20771, USA.
[3]NASA Postdoctoral Program Fellow.
[4]Department of Applied Physics/Physics, Mahatma Jyotiba Phule Rohilkhand University, Bareilly-243006, India.
[5]Graduate Institute of Astronomy, National Central University, 300 Jhongda Road, 32001 Jhongli, Taiwan.
[6]Instituto de Astrofisica de Andalucía (IAA-CSIC), Glorieta de la Astronomía s/n, E-18008, Granada, Spain.
[7]Ingeniería de Sistemas y Automática, Unidad Asociada al CSIC por el IAA, E.T.S. de Ingenierías Industriales, Universidad de Málaga, Arquitecto Francisco Peñalosa, 6, E-29071, Spain.

VII Workshop on Robotic Autonomous Observatories (October 16-20, 2023)
Editors: Maria Gritsevich, Alberto J. Castro-Tirado, Petr Kubánek, Shashi B. Pandey, and David Hiriart - DOI: https://doi.org/10.22201/ia.14052059p.2025.59.21

(prompt emission), originating from distant galaxies. They are broadly classified into two categories based on their duration: long-duration GRBs, which endure for more than two seconds and are believed to result from the collapse of massive stars (Galama et al. 1998; MacFadyen & Woosley 1999; Hjorth et al. 2003; Piran 2004), while short-duration GRBs, generally lasting less than two seconds, are commonly attributed to the merger of compact binaries comprising either two neutron stars or a neutron star and a black hole (Perna & Belczynski 2002; Abbott et al. 2017). However, recently, a few outliers/hybrid events (long bursts from merger and short bursts from collapsar) have also been discovered (Ahumada et al. 2021; Troja et al. 2022; Lü et al. 2022; Levan et al. 2024).

In addition to the traditional classification based on duration, GRBs can also be categorized based on their prompt emission luminosities, such as high ($\geq 10^{51}$ erg s^{-1}), intermediate ($\sim 10^{49}$ - 10^{51} erg s^{-1}), and low ($\leq 10^{49}$ erg s^{-1}) luminosity GRBs. High-luminosity GRBs have been extensively studied, while low and intermediate-luminosity GRBs have emerged as an intriguing and less-explored domain (Liang et al. 2007; Kumar & Zhang 2015).

Following the initial burst, i.e., the spiky prompt emission phase, there is a steadily diminishing broadband afterglow phase originating from external shocks produced in the surrounding medium due to the interaction of the relativistic fireball with the circumburst medium (Kumar & Zhang 2015). In the pre *Swift* era, afterglow light curves across all energies typically decayed following power laws with one or more breaks, as predicted by various physical mechanisms, such as synchrotron emission from forward shocks in the external medium (Sari & Piran 1999). In the *Swift* era, the early afterglow light curves sometimes exhibit features such as flares (mainly due to internal origin), bumps (mainly due to external origin), and plateaus, which are not explained by the external shock model and need additional components (Kann et al. 2010; Oates 2023). Flares, indicative of late central engine activity, commonly appear in both X-ray and optical light curves (Burrows et al. 2005; Swenson et al. 2013). However, bumps are more frequently observed in optical/NIR light curves than in X-ray ones (Liang et al. 2010). According to several studies (Sari & Piran 1999; Molinari et al. 2007), when the relativistic fireball interacts with the surrounding medium, it begins to accumulate material from that medium. Initially, the energy of the fireball remains nearly constant until it has accumulated a sufficient amount of material so that the rest mass energy equals the initial kinetic energy corresponding to the bulk Lorentz factor (Γ_0). At this point, the light curve reaches its peak time ($t_{\rm p}$). The corresponding distance at this point is defined as the deceleration radius ($R_{\rm dec}$) and is seen as a peak in the afterglow light curve at a time t_p (Gao et al. 2013). Following this, the fireball enters a self-similar phase, and the observed afterglow emission begins to wane following a power law, as predicted by the external forward shock model (Blandford & McKee 1976). Liang et al. 2010 analyzed the onset features in 17 optical and 12 X-ray afterglow light curves. They also investigated correlations among the parameters derived from the onset bump, finding that many of these parameters exhibited significant correlations with each other.

The early bump could also be due to the reverse shock that travels back into the ejecta when the fireball interacts with the surrounding medium (Zhang & Kobayashi 2005). Reverse shocks can occur in the thick shell or thin shell regime, depending on whether the shock travel time is shorter or greater than the prompt emission duration (Gao & Mészáros 2015). The presence of a reverse shock can be seen as a bump in the early afterglow light curve and can be helpful in constraining the magnetic properties of the fireball. Therefore, early observations of GRB afterglows are crucial to witness such features (Gupta et al. 2021). The launch of the *Swift* satellite in 2004 revolutionized early afterglow observations by providing the precise localization of bursts within a few arcminutes, allowing for ground-based robotic optical telescopes to obtain the earliest possible observations for many GRB. Nevertheless, there have been a few instances (e.g., GRB 080319B) where wide-field cameras have coincidentally captured the prompt emission within their fields of view before *Swift* even slewed to the target (Racusin et al. 2008).

As discussed above, afterglow light curves from external forward shocks are predicted to follow a power-law decay with an index of approximately 1. However, at late times ($> 10^4$ s), the emission often begins to exhibit a sharp decline with an index (α) of about 2, generally characterized by a sharp break in the light curve known as a "jet break." This jet break provides crucial information about the geometry and dynamics of the GRB event. A statistical study of 138 GRBs with observed jet break features was conducted by Zhao et al. 2020. Although the concept of a jet break in afterglow light curves is well-established for bright GRBs, its manifestations and implications in the context of low and intermediate-luminosity events remain relatively unexplored. Un-

VII Workshop on Robotic Autonomous Observatories (October 16-20, 2023)
Editors: Maria Gritsevich, Alberto J. Castro-Tirado, Petr Kubánek, Shashi B. Pandey, and David Hiriart - DOI: https://doi.org/10.22201/ia.14052059p.2025.59.21

derstanding jet breaks in these GRBs not only gives insights into the nature of the collimated relativistic outflows responsible for the observed gamma-ray emission but also provides essential insights into the central engines and the interaction between GRBs and their surrounding environments.

GRB 210210A, detected by the *Swift* mission, is an intermediate luminosity GRB. The X-ray afterglow of this burst exhibited a rare early bump and a late-time break. These features motivated us for a detailed exploration of this event. This paper aims to provide a comprehensive description of the properties and origin of GRB 210210A. In Section 2, we give the prompt and afterglow observations of GRB 210210A. In Section 3, the results derived from analyzing the observed data are given. In Section 4, we present our discussion. Finally, Section 5 presents a summary and conclusion of our work.

2. OBSERVATIONS, DATA ANALYSIS, AND RESULTS

2.1. *Prompt observations and data analysis*

On 10 February 2021 at 02:00:27 UT (hereafter referred to as T_0), the Burst Alert Telescope (BAT, Barthelmy et al. 2005) instrument onboard *Swift* first detected GRB 210210A. Due to its rapid slewing capabilities, *Swift*'s X-ray Telescope (XRT) and Ultra-Violet and Optical telescope (UVOT) instruments swiftly localized the burst within a 1.1 ″ error box. GRB 210210A was also detected by *Konus*-Wind during its prompt emission phase. The preliminary analysis of the *Konus*-Wind time-averaged spectrum from T_0-1.685 s to T_0+7.147 s, covering an energy range of 15-1500 keV, indicates that the best fit is achieved with a cutoff power law (CPL) with a power law index Γ_{CPL} = -1.68$^{+0.25}_{-0.23}$ and peak energy $E_{\rm p}$ = 16.6$^{+7.2}_{-10.7}$ keV, indicating that GRB 210210A should be classified as a very soft burst (Frederiks et al. 2021).

2.1.1. *Temporal and Spectral analysis of BAT data*

We have used the methods discussed in Gupta et al. (2021) to download and analyze the BAT observations. The prompt emission multi-wavelength light curve of GRB 210210A is depicted in Fig. 1. The prompt emission's light curve consists of two distinct episodes; the first episode peak around at T_0 s, and the second episode peak around 4.2 s post-trigger, with a quiescent phase of 2 seconds. Most of the energy budget of this burst is concentrated around the second episode. The observed light curve of GRB 210210A is comparable to that of the prompt

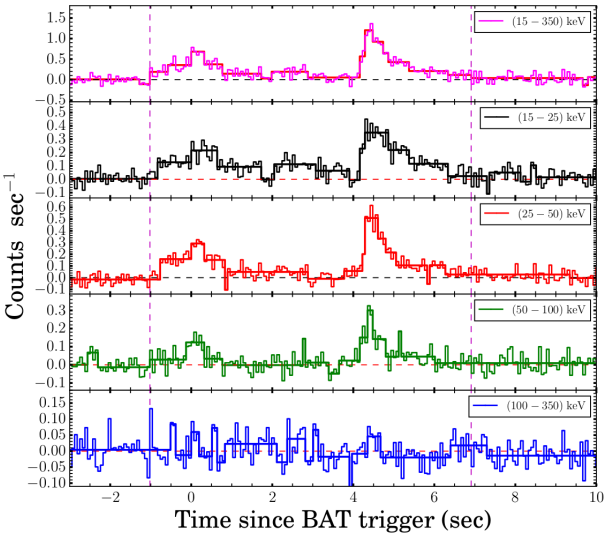


Fig. 1. *Swift* BAT prompt emission multi-channel mask-weighted light curves (temporal bin size of 64 ms) of GRB 210210A along with corresponding Bayesian blocks. The panels from top to bottom represent the light curve in the energy ranges [15-350], [15-25], [25-50], [50-100], and [100-350] keV, respectively. Horizontal lines in each panel illustrate the background level, and the two vertical magenta lines cover the total duration used for the time-averaged spectrum.

emission light curve of another well-studied low luminosity GRB 190829A but has a much shorter T_{90} duration (6.60 ± 0.59 s, Lien et al. 2021).

We modeled the observed *Swift*-BAT spectrum in the 15-150 keV energy range. For this spectral fitting, we used a Python-based package the multi-mission maximum likelihood framework (`3ML`), developed by Vianello et al. (2015). We applied the Bayesian analysis method to fit the spectrum using various built-in models available in `3ML`. We employed a multinest sampler, conducting 10,000 iterations to explore the parameter space thoroughly. To compare the effectiveness of the different fitted models, we utilized the deviance information criterion (DIC). We determined that a cutoff power-law model provides the best fit of the observed BAT spectrum (from T_0-1.02 s to T_0+6.91 s). The resulting parameters are as follows: the spectral index, Γ_{CPL}, is -1.34$^{+0.26}_{-0.26}$, and the spectral peak energy, $E_{\rm p}$, is 22.54$^{+12.54}_{-12.54}$ keV. These findings are compatible with those notified by Lien et al. (2021), and Frederiks et al. (2021). From this spectral analysis, we derived a fluence (in the 15-150 keV range) of 1.04 × 10^{-6} erg cm^{-2}.

VII Workshop on Robotic Autonomous Observatories (October 16-20, 2023)
Editors: Maria Gritsevich, Alberto J. Castro-Tirado, Petr Kubánek, Shashi B. Pandey, and David Hiriart - DOI: https://doi.org/10.22201/ia.14052059p.2025.59.21

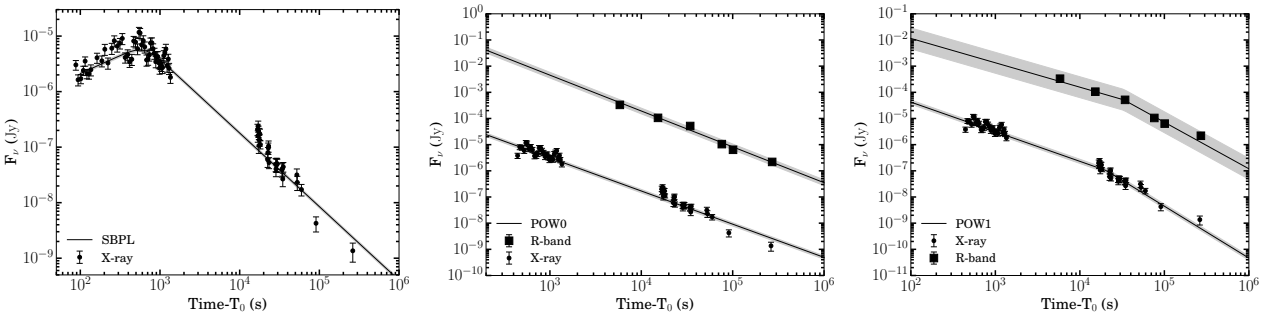


Fig. 2. Left panel: the unabsorbed *Swift*-XRT flux density light curve (at 10 keV) for GRB 210210A. Here, the circles indicate the *Swift*-XRT observations and the solid line shows the best-fit model using a smoothly joined broken power law. Middle panel: The same XRT light curve is now fitted with a simple power law after the initial bump was removed for clarity. The circles depict the XRT data, while the squares represent the optical R-band light curves. Right panel: Same as **the** middle panel but fitted with **a** single break power-law function.

2.2. *Afterglow observations and data analysis*

2.2.1. *X-ray afterglow analysis*

Afterglow follow-up observations for the burst began promptly after *Swift*-XRT identified the potential X-ray counterpart of GRB 210210A at T_0 + 82.1 s. Initially, *Swift*-XRT observed GRB 210210A in window timing mode for approximately 50 seconds before quickly transitioning to photon counting mode based on the low intensity of the burst. We accessed the *Swift*-XRT data from the *Swift* online repository[8] (Evans et al. 2007, 2009). The observed *Swift*-XRT light curve revealed an early bump at approx. 600 s after trigger, followed by a power law decay segment. We fitted the unabsorbed *Swift*-XRT flux density light curve (at 10 keV) using a smoothly joined broken power law and employed the MCMC technique with 10,000 iteration steps for the fitting, discarding the first 500 as burn-in. The best-fit parameters were a rising index α_r = -0.65$^{+0.07}_{-0.07}$, a break time $t_b = 630.79^{+45.85}_{-39.82}$ s, and a decay index $\alpha_d = 1.32^{+0.02}_{-0.02}$. The obtained reduced chi-square value, $\chi^2_\nu = 2.3$, was high, potentially due to deviations in the last two data points from the fit, which might indicate a late time break. Additionally, the XRT count rate light curve (in 0.3-10 keV) could also be successfully fitted with a broken power-law, indicating a plateau phase with parameters $\alpha_1 = 0.31^{+0.05}_{-0.05}$, a break time $t_b = 4529^{+982}_{-883}$ s, and $\alpha_2 = 1.72^{+0.15}_{-0.13}$. To investigate the possibility of a jet break in the X-ray light curve, we re-analyzed the XRT flux density light curve after excluding the data points from the initial rise. Initially, we applied a simple power law fit, which yielded a decay index of $\alpha = 1.27^{+0.01}_{-0.02}$ and a χ^2_ν of 2.83. The elevated χ^2_ν value, influenced by deviations in the last two points, suggested the presence of an additional break. Subsequently, we fitted the light curve with a broken power law, achieving **as** optimal fit parameters: a decay index before the break of $\alpha_1 = 1.13^{+0.09}_{-0.08}$, a break time $t_b = 10000^{+2644}_{-1464}$ s, and a decay index after the break $\alpha_2 = 1.98^{+0.12}_{-0.11}$, with a χ^2_ν of 1.92. The improvement in χ^2_ν indicates an additional break around 10000s, likely representing a jet break in the X-ray light curve. The *Swift*-XRT light curve, along with the various power law models fitted to it, **are** illustrated in Fig. 2. For a uniform external medium and an electron distribution with an index of $p = 2.2$, the expected power-law indices before and after a jet break are $\alpha_1 \sim 0.9$ and $\alpha_2 \sim p$. For a wind medium, the expected values are $\alpha_1 \sim 1.4$ and $\alpha_2 \sim 1.65$.

2.2.2. *UV and Optical afterglow analysis*

The earliest optical observations available for the burst were taken by *Swift*-UVOT in the white filter at around T_0 + 85 s. The UVOT data were analyzed using the standard HEASOFT UVOT tools (e.g., `uvotproduct` and `uvotmaghist`), see more details in Chand et al. (2020), and Gupta et al. (2022). GRB 210210A was successfully detected across all seven UVOT filters (Breeveld et al. 2021), and the results of this photometry are detailed in Table 1 (appendix). No corrections to the UVOT data have been made for the expected extinction in the Milky Way corresponding to a reddening of E_{B-V} of 0.097 mag. in the direction of the GRB (Schlegel et al. 1998), or for the GRB's host galaxy extinction.

In addition to *Swift*-UVOT, GRB 210210A was observed by multiple ground-based observatories, including the 1.3 m Devsthal Fast Optical Telescope (DFOT) located at Devasthal, India (Gupta 2023; Gupta et al. 2022, 2023). The redshift of the burst, determined to be $z = 0.715$, was identified through

[8] `https://www.swift.ac.uk/burst_analyser/01031728/`

VII Workshop on Robotic Autonomous Observatories (October 16-20, 2023)
Editors: Maria Gritsevich, Alberto J. Castro-Tirado, Petr Kubánek, Shashi B. Pandey, and David Hiriart - DOI: https://doi.org/10.22201/ia.14052059p.2025.59.21

spectroscopic observations made by the 10.4 m GTC (de Ugarte Postigo et al. 2021). We monitored the optical afterglow of GRB 210210A using DFOT on 2021-02-13 at 23:20:16 UT, which is 3.89 days after the *Swift*-BAT trigger. During these observations, we observed fifteen frames using the R filter, each with an exposure time of 180 seconds. We followed standard IRAF (Tody 1993) procedures for image cleaning (e.g., bias subtraction, flat field correction, and cosmic ray removal). Subsequent PSF photometry was performed using DAOPHOT (Stetson 1987). However, the optical afterglow was not detected in the final stacked image, with an upper magnitude limit of 21.8.

The observed optical light curve from most of the *Swift*-UVOT filters (v, b, u, uvw1, uvm2, uvw2) exhibit a decay consistent with a simple power law, characterized by the decay indices given in Table 2. However, the white band UVOT light curve shows a significant deviation from a simple power law. A broken power law is found to be the best to describe the light curve in the white band, as shown in Fig. 5 and Table 2. For our analysis, we focused on the R-band light curve, which has a sufficient number of data points after T_0+10000 s. Initially, we modeled the observed R-band light curve with a simple power law, obtaining a decay index of $\alpha = 1.37^{+0.03}_{-0.03}$, with a χ^2_ν/DOF = 13.5/4. Subsequently, we applied a broken power law fit to the same light curve and determined the decay indices to be $\alpha_1 = 0.93^{+0.08}_{-0.10}$ before the break and $\alpha_2 = 1.78^{+0.09}_{-0.08}$ after the break time $t_b = 30000^{+2500}_{-3000}$ s, with a χ^2_ν/DOF = 9.26/2. Although the χ^2_ν values did not approach unity in either fit, which may be attributed to the limited number of data points and the small error bars of the observations, the detection of a break in the optical light curve is statistically significant. The fitted models and the observed R-band light curve are presented in Fig. 2.

3. RESULTS

3.1. *Prompt properties of GRB 210210A*

We discuss the key prompt behavior of GRB 210210A in the context of the larger sample.

3.1.1. *Classical and machine learning-based classification of GRB 210210A*

The classification of GRBs has traditionally been based on their duration and spectral hardness. One commonly used method employs the T_{90} durationthe time during which 90% of the burst's flux is observed, from 5% to 95% of the cumulative flux in the 50 - 300 keV band. There is an observed bimodality in the distribution of T_{90} measurements with a separation at ~ 2 s, leading to the separation of short ($T_{90} \leq 2$ s) and long GRBs ($T_{90} > 2$ s). However, this parameter has significant overlap, and GRB 210210A lies in this T_{90} overlapping region. We further obtained the spectral hardness ratio (HR) for GRB 210210A equal to 0.61 by comparing the fluence values in two different energy bands (50-100 keV/ 25-50 keV). Our analysis helps to classify GRBs and suggests that GRB 210210A is among one of the softest long bursts ever observed using *Swift* BAT (see Fig. 3).

Classification using t-SNE: The t-Distributed Stochastic Neighbor Embedding (t-SNE) is a powerful tool for data visualization that represents high-dimensional data points in a lower-dimensional space. t-SNE is exceptionally effective in capturing non-linear relationships among data points, which makes it highly valuable for visualizing complex datasets. In the case of GRBs, t-SNE has been used to compare the prompt emission light curve of GRBs. Based on similarities and dissimilarities between the observed light curves, it places them on a two-dimensional map (Garcia-Cifuentes et al. 2023). The t-SNE map of *Swift* detected GRBs is shown in Fig. 3. The axes of this map do not have any meaning. However, the effects of T_{90} on the grouping of GRBs are shown with different colors. As indicated with a color bar, the GRBs on the right of the map are short GRBs with $T_{90} < 2$s and mostly lie in the tail of the map. On the other hand, the bulk portion of the map consists of long GRBs. However, there is no sharp boundary between the two groups. GRB 210210A lies in the separation region between two types of GRBs. However, the observed properties of the burst are more consistent with LGRBs (Ror et al. 2024).

3.1.2. *High-energy correlation: Amati and Yonetoku*

The Amati relation suggests that there is a tight correlation between the isotropic energy ($E_{\gamma,\rm iso}$) emitted by a GRB and the peak energy of its gamma-ray spectrum in its rest frame (Amati 2006). In simple terms, brighter bursts tend to have higher spectral peak energies. To estimate the $E_{\gamma,\rm iso}$ for GRB 210210A, we employed the method given in Fong et al. (2015). With the observed spectral peak energy and the isotropic equivalent energy $E_{\gamma,\rm iso}$ = 6.92 $\times$ 10^{51} erg (intermediate energetic), GRB 210210A marginally satisfies the 2 σ of the correlation. Still, it is consistent with 3 σ of the Amati correlation. The position of GRB 210210A within the

VII Workshop on Robotic Autonomous Observatories (October 16-20, 2023)
Editors: Maria Gritsevich, Alberto J. Castro-Tirado, Petr Kubánek, Shashi B. Pandey, and David Hiriart - DOI: https://doi.org/10.22201/ia.14052059p.2025.59.21

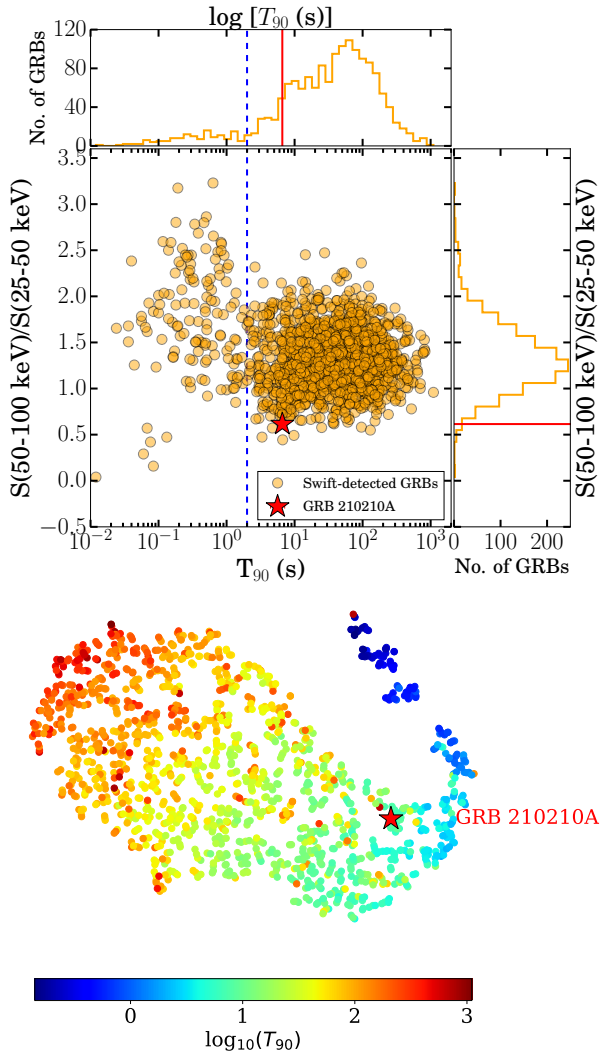


Fig. 3. Classical and machine learning-based classification of GRB 210210A: Top panel represents GRB 210210A in hardness ration (HR) - T_{90} (dashed blue line is the boundary of classical classification) plane. The corresponding histograms of hardness ratio and T_{90} (GRB 210210A is highlighted with a solid red line) are also shown. Bottom panel: T-SNE distribution of *Swift*-detected GRBs. GRB 210210A is shown with a red star lying among the population of LGRBs.

Amati correlation, along with other luminous and low-luminous GRBs, is presented in Fig. 4.

On the other hand, the Yonetoku correlation relates the spectral peak energy ($E_{\rm p}$) of GRBs with the luminosity ($L_{\gamma,\rm iso}$) in their rest frame. Similar to Amati, with the observed spectral peak energy and the isotropic luminosity $L_{\gamma,\rm iso} = 8.73 \times 10^{50}$ erg s^{-1} (intermediate luminosity), GRB 210210A marginally satisfies the 2 σ of the correlation. Still, it is consistent with 3 σ of the Yonetoku correlation (Fig. 4).

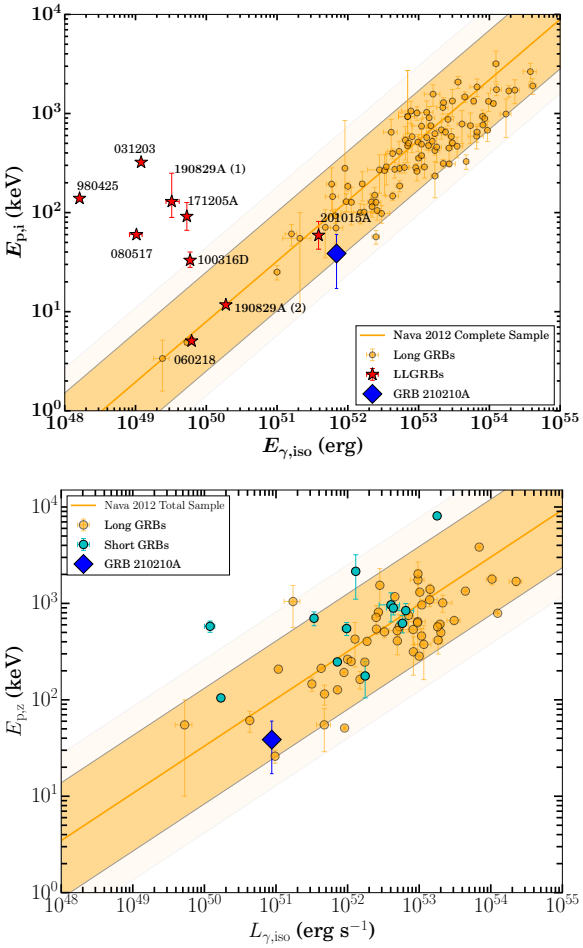


Fig. 4. Prompt emission correlations ($E_{\rm p}$-$E_{\gamma,\rm iso}$, Amati on top and $E_{\rm p}$-$L_{\gamma,\rm iso}$ Yonetoku on bottom) for GRBs along with *Swift* detected GRB 210210A (shown with blue diamond). GRB 210210A marginally satisfies the 2 σ of the correlations but is consistent with 3 σ of both correlations (Nava et al. 2012). In Amati, we have also shown the positions of LLGRBs (with red stars) obtained from Chand et al. (2020).

3.2. *Afterglow properties of GRB 210210A*

In this subsection, by analyzing the afterglow emissions of GRB 210210A, we aim to understand the dynamics of the burst, the nature of its immediate surroundings, and the mechanisms driving the emission processes.

3.2.1. *Afterglow emission and spectral regime*

The X-ray and optical afterglow light curve of GRB 210210A is plotted in Fig. 5. As the temporal analysis of early X-ray and optical emission shows a different behavior (possibly due to a few points during early optical observations), we explored the optical-to-X-ray spectral energy distribution (SED)

VII Workshop on Robotic Autonomous Observatories (October 16-20, 2023)
Editors: Maria Gritsevich, Alberto J. Castro-Tirado, Petr Kubánek, Shashi B. Pandey, and David Hiriart - DOI: https://doi.org/10.22201/ia.14052059p.2025.59.21

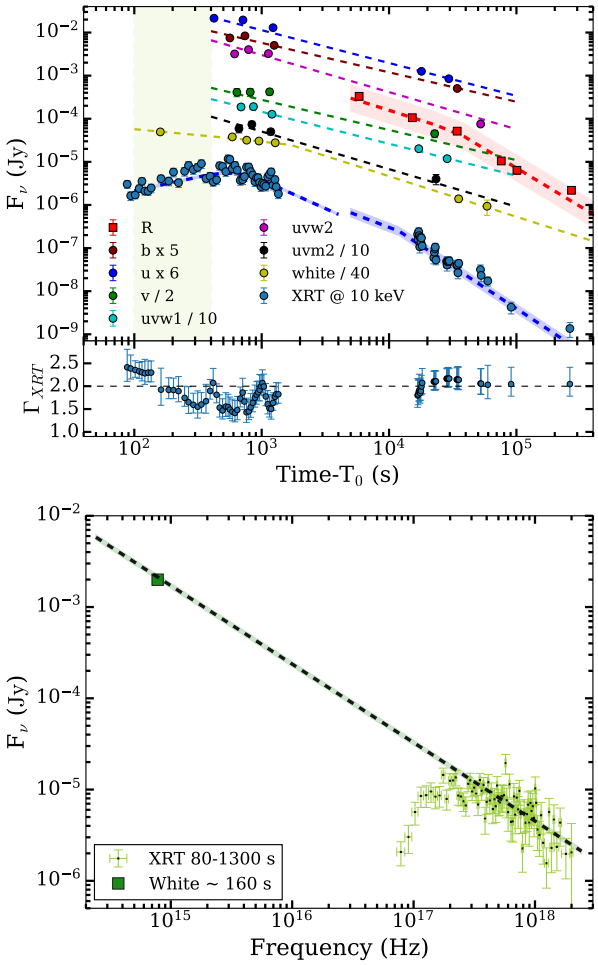


Fig. 5. Upper panel: The multi-wavelength afterglow light curve of GRB 210210A. The colored circles represent the *Swift*-UVOT observations fitted by the power law function, as shown with thin dashed lines. *Swift*-XRT observations, along with a smoothly joined broken power law fitted to it, are shown with a blue circle and thick blue line, respectively. The X-ray photon indices evolution in 0.3-10 keV is shown at the bottom of the plot. The shaded region shows the X-ray and optical SED duration. Lower panel: optical-to-X-ray SED created at 100-1300 s.

at an early time (where the earliest UVOT observations are available). The observed XRT spectrum in 0.3-10 keV was obtained from the *Swift*-XRT GRB spectrum repository (Evans et al. 2007, 2009). We fit the spectrum utilizing an absorbed power law model with Galactic (`phabs`, $N_{H,Gal}$) and host (`zphabs`, $N_{H,z}$) absorption components in `XSPEC` software (Gupta et al. 2022, 2021). First, we used the value of $N_{H,Gal}$ and constrained $N_{H,z}$ by fitting the late-time XRT spectrum. By fixing the $N_{H,Gal} = 8.82 \times 10^{20}$ cm^{-2} and $N_{H,z} = 2.35 \times 10^{21}$ cm^{-2} from the late spectral fitting, we fit the early time X-ray spectra (in the temporal range 85-1350 s and energy range 0.3-10 keV) and determine the observed spectral index is $\beta = 0.79^{+0.09}_{-0.09}$. We extrapolated this index and found that the observed earliest optical (galactic extinction corrected) emission (in UVOT white filter) is consistent with the extrapolation of the X-ray spectral index. This indicates a negligible amount of host extinction if optical and X-ray emissions have similar origins (see Fig. 5). Further, our SED analysis suggests that the observed spectral and temporal indices correspond to the spectral regime $\nu_o < \nu_x < \nu_c$, in the ISM-like medium. We obtained the value of electron energy distribution index $p = \frac{\beta-1}{2} = 2.6$

3.2.2. *Late time possible jet break in GRB 210210A*

The GRB emission is assumed to be produced by a relativistic jet. The evidence of the jet break is observed in the late time afterglow light curve as a steep decay phase ($\alpha \sim 2$) after a normal decay phase ($\alpha \sim 1$) around 10^4 - 10^5 s post-trigger. The observed jet break in the afterglow light curve is utilized to calculate the jet opening angle θ_j and related physical parameters. For GRB 210210A, we found that both X-ray and optical light curves have a statistically significant break around 1E+4 s and 3E+4 s, respectively. The observed slope before and after the break time t_b is $\alpha_1 \sim 1$ and $\alpha_2 \sim 2$ for both X-ray and optical light curves. This indicates that the observed break in the X-ray and optical light curve is possibly due to the jet break. Considering jet break is a geometric effect, we expect that there should not be a change in the spectral index before (β_1) and after (β_2) the break. We calculated β_1 and β_2 to be equal to $0.79^{+0.09}_{-0.09}$ (large variation during this epoch) and $1.01^{+0.13}_{-0.13}$, respectively, using XRT observations. We note that these values are consistent within the error bars, supporting that the jet break model. The jet break in the optical light curve of GRB 210210A is also independently confirmed by Kann et al. (2021). However, we noted that the observed jet break times in the X-ray and optical light curves are not consistent, showing a chromatic nature (although it may not be intrinsic, but due to the less coverage in the optical band, we are not able to precisely constrain the break time). There are several possible reasons for this, such as a structured jet model or two jet components, energy injection, environmental effects, etc. Assuming a two-component jet model for GRB 210210A (if the chromatic jet break is intrinsic), the X-ray emission comes from the narrow jet component, and the optical emission

VII Workshop on Robotic Autonomous Observatories (October 16-20, 2023)
Editors: Maria Gritsevich, Alberto J. Castro-Tirado, Petr Kubánek, Shashi B. Pandey, and David Hiriart - DOI: https://doi.org/10.22201/ia.14052059p.2025.59.21

comes from the wide jet component. Utilizing the jet break time, we have calculated the jet opening θ_j utilizing the method/parameters given in Frail et al. (2001), and Gupta et al. (2022). The calculated values of θ_j from the jet break time in X-ray (narrow jet) and the jet break time in optical (wide jet), respectively, are 2.63° and 3.97°.

4. DISCUSSION

4.1. *Origin of the observed early X-ray bump*

Swift-XRT observations revealed a bump in the X-ray light curve of GRB 210210A. Since we do not have enough simultaneous optical/UV observations corresponding to the X-ray bump, it is hard to discuss any early achromatic behavior between the two bands. However, the earliest observations on the UVOT/white band are slightly inconsistent with a simple power law decay and may hint towards an achromatic bump occurring in both the optical and X-ray light curves. Nevertheless, we do not have enough optical observations to constrain the parameters of a bump (if any) in the early optical light curve. In the next sub-sections, we searched for the possible origin of this X-ray bump. We investigated if this bump could be the signature of a reverse shock, the onset of an external forward shock in the surrounding circumburst medium, or due to an observer viewing the burst slightly outside the narrow jet, i.e., $\theta_{obs} > \theta_J$, energy injection, etc (Kumar & Zhang 2015; Oates 2023).

4.1.1. *Reverse shock*

During the interaction of the relativistic fireball with the surrounding medium, two types of external shock are generally assumed. A forward shock propagates into the surrounding medium and a reverse propagates shock back into the ejecta. Reverse shock emission is characterized by an early sharp rise in the afterglow light curve. However, reverse shock emission is not always visible if the outflow is strongly Poynting flux dominated (Gao & Mészáros 2015). In the case of reverse shock, the early optical/X-ray light curve in the ISM-like medium should rise by the index of -5 in the thin shell case, and -0.5 in the thick shell case, and the decay slope should be around 2 (Gao & Mészáros 2015). For the wind environment, the light curve should show an early rise of -2.5 and the decay slope around 3 (Gao & Mészáros 2015). For GRB 210210A, the observed peak time $t_p = t_b \times \left(\frac{-\alpha_r}{\alpha_d}\right)^{1/w(\alpha_d-\alpha_r)} = 559$ s is much greater than the observed T_{90} duration of the burst, so it is reasonable to assume a thin shell case. The observed

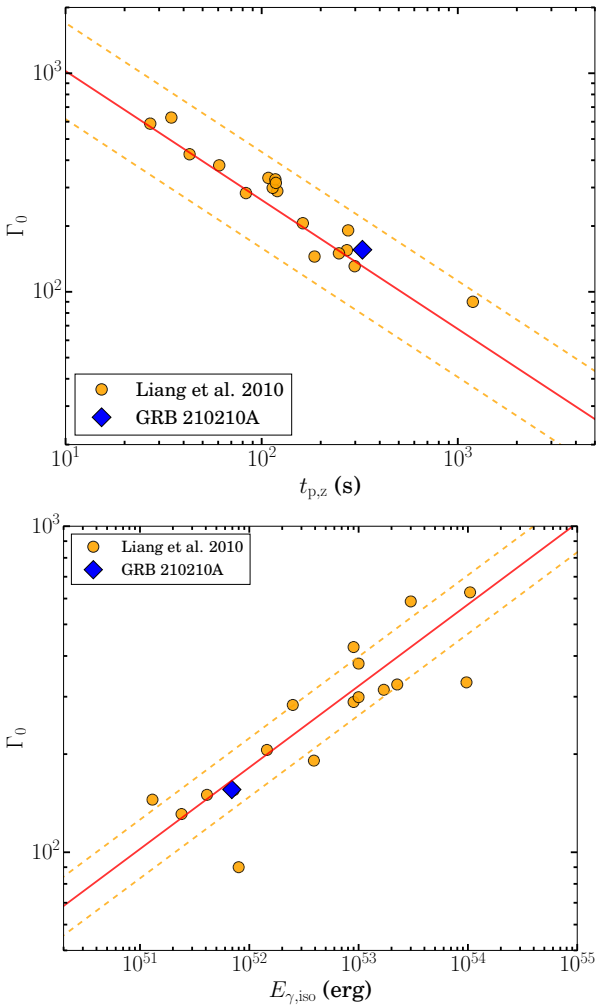


Fig. 6. The top panel represents the distribution of the Lorentz factor (Γ_0) along with the observed peak time (t_p) of the onset bump in the rest frame. Solid and dotted lines represent the correlation found by Liang et al. (2010) and corresponding 2σ region. The lower panel similarly represents the distribution of the Lorentz factor and isotropic gamma-ray energy release (Eγ, iso). GRB 210210A is shown with a blue diamond, and the orange circles are the data points taken from Liang et al. (2010).

parameters of the bump α_r = -0.65 and α_d = 1.32 are not consistent with the above cases in both wind or ISM-like medium. Therefore, we discard the possibility of reverse shock emission dominating early X-ray bump observed in the case of GRB 210210A.

4.1.2. *Onset of afterglow*

Liang et al. 2010 extensively searched for the deceleration feature in the early light curves of X-ray and optical afterglows, and they found 20 optical (17 with redshift measurements) and 12 X-ray (only two with redshift measurements) afterglow light curves

VII Workshop on Robotic Autonomous Observatories (October 16-20, 2023)
Editors: Maria Gritsevich, Alberto J. Castro-Tirado, Petr Kubánek, Shashi B. Pandey, and David Hiriart - DOI: https://doi.org/10.22201/ia.14052059p.2025.59.21

with onset features. The onset feature in optical light curves is common but rare in X-ray light curves. Additionally, they studied several correlations among the parameters of the onset bump obtained based on the temporal fitting of the bump using a smooth broken power-law function. To check the nature of the X-ray bump observed in our case, we fitted the bump using smoothly joined broken power law and calculated the bump parameters (see section 2.2). We utilized these parameters to calculate the bulk Lorentz factor ($\Gamma_0 \sim 156$) from the relation given by Molinari et al. (2007). We placed these parameters in the correlations plane of Liang et al. (2010) see also Ror et al. (2023). In Fig. 6, we can see that the calculated value of the bulk Lorentz factor, t_p, and $E_{\gamma,iso}$ for GRB 210210A perfectly satisfies the observed correlation by Liang et al. (2010), supporting the onset origin for the observed early bump in the X-ray light curves. Additionally, we estimated the rise and decay time of GRB 210210A and investigated the possible correlation of these parameters with peak time along with data points obtained from Liang et al. (2010). GRB 210210A is consistent with these correlations (see Fig. 7), further supporting the onset nature of the early X-ray afterglow bump.

4.1.3. *Off axis observation of* Swift-*XRT*

One of the possible reasons for the early rise in the X-ray light curve could be if the observer is initially looking outside the jet (a GRB jet may be oriented away from Earth's line of sight), i.e., the jet opening angle is smaller than the viewing angle ($\theta_j < \theta_{obs}$). In such a case, when the jet loses its energy, it starts spreading, and the observer begins to observe more flux, and the light curve rises initially. We need detailed afterglow modeling to constrain the viewing angle. However, observational signatures of off-axis observations of X-ray afterglows exhibit distinct temporal and spectral features compared to on-axis observations, such as a typically lower X-ray flux (due to the emission being less beamed and hence appears fainter), a delayed onset of the afterglow (the emission becomes observable only after the jet has decelerated sufficiently for the relativistic beaming effect to expand the emitting region into the observer's line of sight), a shallower decay (the decay slope of the light curve post-peak will be shallower compared to on-axis observations due to the contribution of emission from wider angles becoming visible over time), an extended plateau phase (off-axis afterglows often show an extended plateau phase, where the brightness remains relatively constant for a longer period before declining). This is due to the gradual increase in the observed emitting area as the jet spreads laterally), reduced apparent luminosity (the observed luminosity of an off-axis GRB is lower because the relativistic beaming effect, which concentrates the jet's energy into a narrow cone, is less effective at larger viewing angles), etc. For GRB 210210A, we investigated these features in its afterglow light curve. We noted that the X-ray flux observed at 11 hours and 24 hours post-burst is significantly brighter than the typical X-ray counterpart of long bursts (Gupta et al. 2022). An onset was observed in the early X-ray observations of GRB 210210A, with no shallower decay emission, and no observed extended plateau phase plateau, indicating on-axis observations. We also compared its X-ray and optical afterglow luminosity with nearby GRBs and found that the initial X-ray and optical emission from GRB 210210A has an intermediate luminous afterglow and that its late emission shows the jet break (see Fig. 8). Additionally, we detected the jet break signature in the afterglow light curve of GRB 210210A at the usually expected time from on-axis observations (the observation of a jet break may be less noticeable or occur at a later time in off-

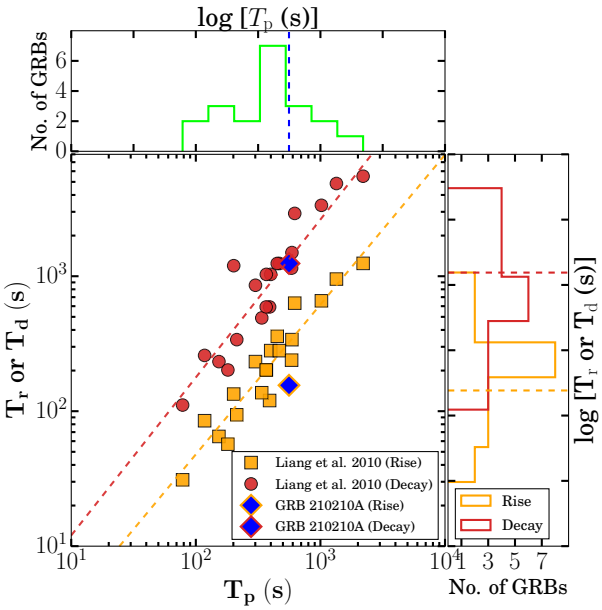


Fig. 7. The distribution of the rise and decay times with the observed peak time (t_p) of the onset bump. The red and orange dotted lines represent the correlation found by Liang et al. (2010). The histograms of the observed peak time (lime), rise time (orange), and decay time (red) are shown in the upper and right panels, respectively. The position of GRB 210210A is shown with vertical dashed lines in these histograms, and orange squares/red circles are the data points taken from Liang et al. (2010).

VII Workshop on Robotic Autonomous Observatories (October 16-20, 2023)
Editors: Maria Gritsevich, Alberto J. Castro-Tirado, Petr Kubánek, Shashi B. Pandey, and David Hiriart - DOI: https://doi.org/10.22201/ia.14052059p.2025.59.21

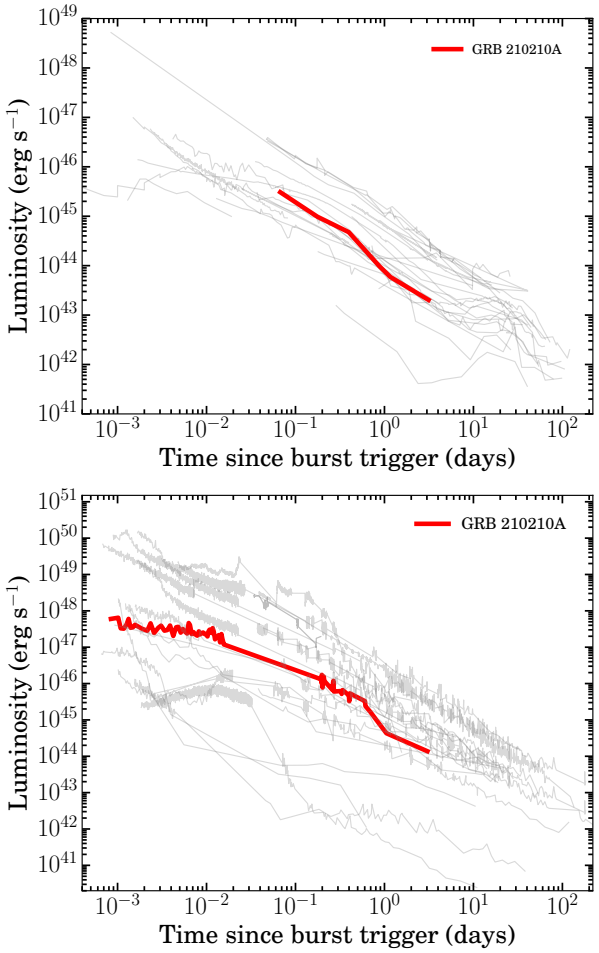


Fig. 8. Upper panel: the R-band optical luminosity afterglow light curve of GRB 210210A (depicted by the red curve) compared with other nearby GRBs (shown in grey). Lower panel: the *Swift*-XRT X-ray luminosity afterglow light curve of GRB 210210A (red curve) compared with other nearby GRBs (grey).

axis observations). This is due to the observer seeing emission from progressively wider angles as the jet slows and expands; further supporting an on-axis jet model for GRB 210210A afterglow and discarding the off-axis scenarios.

4.2. *Origin of Intermediate luminosity of GRB 210210A*

Low-luminosity or intermediate-luminosity gamma-ray bursts can originate from various mechanisms and environments. In the present section, we discuss a few possible scenarios.

4.2.1. *Shock Breakout from Stellar Explosions*

According to the shock breakout model, low-luminosity GRBs may result from the shock breakout of a supernova (SN) explosion (unsuccessful jets). Generally, these bursts are not consistent with the Amati correlation. When the shock wave from a supernova's core collapse reaches the surface of the star, it can produce a brief burst of gamma rays. In such cases, the duration of the burst follows a fundamental correlation $T_{90} \sim 20\ \mathrm{s}\ (1+z)^{-1.68} \left(\frac{E_{\gamma,\mathrm{iso}}}{10^{46}\ \mathrm{erg}}\right)^{1/2} \left(\frac{E_\mathrm{p}}{50\ \mathrm{keV}}\right)^{-2.68}$ (Nakar & Sari 2012). In the case of GRB 210210A, we calculated the expected shock breakout duration to be approximately 56 ks, which is much longer than the observed T_{90} duration, thereby inconsistent with the predictions of the shock breakout scenario. Additionally, the estimated gamma-ray efficiency for GRB 210210A is $\eta \sim 1\,\%$ (typical of long and short GRBs), inconsistent with those expected from shock breakout and LLGRBs ($\eta \sim 10^{-4}\,\%$, Gottlieb et al. 2018). Furthermore, the shock breakout model predicts a very simple light curve with a fast rise and exponential decay without any gap. However, for GRB 210210A, we observed two episodic emissions with a significant gap, which further rules out the shock breakout model.

4.2.2. *"Choked" Jets*

For GRBs, a jet is a highly relativistic outflow of particles and radiation launched by the central engine, usually a collapsing massive star or a merger of compact objects. A choked jet occurs when this jet fails to escape the progenitor star before losing its energy. The jet is "choked" because it does not break out of the stellar envelope, thus preventing a typical high-energy gamma-ray burst from being observed. In such a scenario, the jet's energy is dissipated into the stellar envelope, converting kinetic energy into thermal energy. This results in a sub-relativistic, mildly relativistic shock that can produce observable emissions (also possible neutrinos) different from standard GRBs (Senno et al. 2016; Denton & Tamborra 2018). Due to the shock heating of the stellar envelope, choked jets can produce thermal X-ray emissions that are detectable as a smooth thermal spectrum. Also, choked jets can produce strong radio emissions as the sub-relativistic shock-wave interacts with the surrounding interstellar medium. However, for GRB 210210A, we do not detect any thermal signature in the X-ray regime, and no radio emission is reported, and we clearly detected the signature of jet break, thus discarding the choked jet scenario.

4.2.3. *Magnetar Central Engine?*

Two types of central engines are generally considered in GRB models. Either a black hole with

VII Workshop on Robotic Autonomous Observatories (October 16-20, 2023)
Editors: Maria Gritsevich, Alberto J. Castro-Tirado, Petr Kubánek, Shashi B. Pandey, and David Hiriart - DOI: https://doi.org/10.22201/ia.14052059p.2025.59.21

an accretion disc that utilizes the rotational energy of the disc through the magnetic field (Blandford & Znajek 1977) or a rapidly spinning magnetar (a neutron star with an extremely strong magnetic field) which provides energy through the spin-down of the magnetar. However, a magnetar central energy can only produce a GRB with a maximum energy of 10^{52} erg; any GRBs crossing this must have a black hole central engine. A magnetar can also power a GRB with relatively lower luminosity. To determine the possible central engine of GRB 210210A, we applied the techniques described in Sharma et al. (2021). The key idea of this approach revolves around the maximum potential rotational energy from a millisecond magnetar, which can launch jets with energies around 10^{52} erg. We calculated the beaming-corrected gamma-ray energy ($E_{\gamma,\mathrm{beamed}}$) for GRB 210210A to be 7.30×10^{48} erg, which is within the possible energy budget of a millisecond mangetar central engine.

Furthermore, it might be the case that the observed early X-ray emission (within the 0.3-10 keV band) is not purely synchrotron emission coming from the external forward shock but also has a contribution from the central engine (plateau). In such a scenario, to maintain the level of the observed flux at a constant level, energy must be supplied to the fireball by the inner engine. We applied equation 7 from Li et al. (2018) to calculate the X-ray energy during the early phase, finding it to be 2.12×10^{50} erg, which is within the total energy budget of a magnetar. Additionally, we used equation 11 from the same source to determine the kinetic energy ($\mathrm{E}_{K,iso}$) of the fireball, which resulted in a value of 6.90×10^{53} erg. The measured $\mathrm{E}_{X,iso}$ and $\mathrm{E}_{K,iso}$ for GRB 210210A are consistent with the silver sample from Li et al. (2018), supporting the magnetar central engine hypothesis for this burst (see Fig. 9).

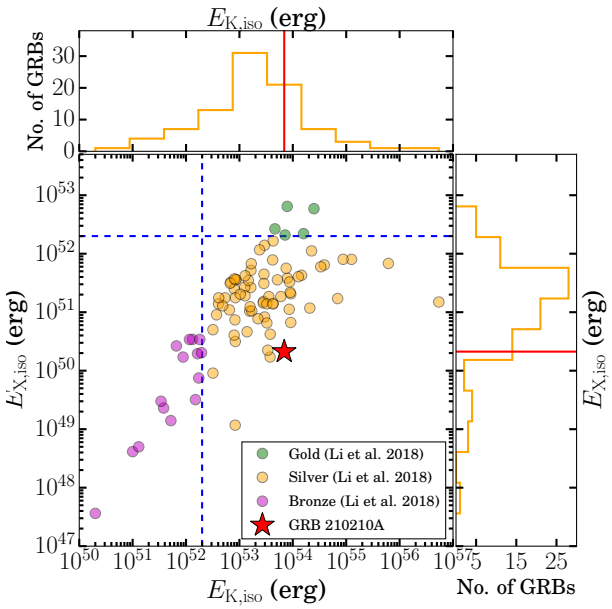


Fig. 9. The distribution of $\mathrm{E}_{X,iso}$ and $\mathrm{E}_{K,iso}$ for gold, silver, and bronze samples of Li et al. (2018), see also Ror et al. (2024). Dashed blue lines represent $\mathrm{E}_{X,iso}$ and $\mathrm{E}_{K,iso}$ values equal to 2×10^{52} erg. GRB 210210A is shown with a red star. The histograms of observed $\mathrm{E}_{X,iso}$ and $\mathrm{E}_{K,iso}$ are shown in the right and upper panels, respectively. The position of GRB 210210A is shown with vertical red solid lines in these histograms.

4.2.4. *Compact Object Mergers*

Though less common, low-luminosity GRBs can also stem from the merger of compact binaries, such as the system of two neutron stars or a neutron star plus a black hole. These mergers may produce a weak jet, resulting in a fainter burst of gamma rays. The direct evidence of such progenitors is the detection of kilonova emission (optical/infrared transient due to the radioactive decay of heavy elements synthesized in the merger ejecta) and gravitational waves (potential detection of gravitational waves coincident with the gamma-ray signal if the event is relatively close). Given that such observations are challenging at the measured redshift of GRB 210210A with current instruments, we aim to determine the origin (collapsar or merger) of GRB 210210A following the indirect methodology of Bromberg et al. (2011) and estimate its non-collapsar probability. The duration of the prompt emission of GRBs, represented by the T_{90} value, must be at least as long as the engine remains active after the jet breakout. Typically, these two durations are considered equal in GRB models, expressed as $T_{90} = \mathrm{T_{Eng}}$ - $\mathrm{t_b}$, where $\mathrm{T_{Eng}}$ is the duration of the engine's activity, and $\mathrm{t_b}$ is the time required for the jet to emerge from the surrounding envelope of the progenitor star. It is highly unlikely that the engine will stop operating exactly after the jet breakout. This condition is a fundamental aspect of the Collapsar model, implying that if GRB 210210A originated from Collapsars, it must meet this criterion. We calculated $\mathrm{t_b}$ ($\sim$ 1.8 s) and the ratio $\mathrm{T_{90}/t_b}$ ($\sim$ 3.6) to identify the potential progenitor of GRB 210210A, supporting the collapsar model. Furthermore, we estimated the non-collapsar probability of the burst using equations 2 and 3 from Bromberg et al. (2013). The non-collapsar probability is 2.61×10^{-3}. Our analysis suggests that GRB 210210A is more likely to be in-

VII Workshop on Robotic Autonomous Observatories (October 16-20, 2023)
Editors: Maria Gritsevich, Alberto J. Castro-Tirado, Petr Kubánek, Shashi B. Pandey, and David Hiriart - DOI: https://doi.org/10.22201/ia.14052059p.2025.59.21

stead explained by of a merger of compact merger scenario.

5. SUMMARY AND CONCLUSIONS

In this paper, we have analyzed the prompt and afterglow features of the intermediate luminosity GRB 210210A. This GRB is identified as one of the softest long-duration bursts detected by the the *Swift* satellite. The prompt emission's time-integrated spectrum is effectively described by a power law with an exponential cutoff. The rest-frame spectral peak energy and the isotropic energy ($E_{\gamma,iso}$) of GRB 210210A marginally satisfy by 2σ of the Amati correlation, which is a typical feature of low to intermediate luminosity GRBs. This observed feature is common in low-luminosity GRBs. The observed characteristics of the prompt emission of GRB 210210A indicate that it is a soft GRB, with $E_p \sim 20$ keV. Thus, GRB 210210A is an X-ray-rich burst belonging to the class of X-ray flashes (Kumar & Zhang 2015). The afterglow observations of this burst show chromatic behaviors. An early bump is observed in the X-ray light curve, which is a rare feature for GRBs. The optical light curve appears to follow a power law decay. However, due to insufficient early optical observations, the possibility of an early optical bump cannot be ruled out completely. We calculated parameters such as peak time, rise time, decay time, and bulk Lorentz factor ($\Gamma_0 \sim 156$) for the early bump observed in the X-ray light curve. These calculated parameters perfectly satisfy the correlation found by Liang et al. (2010) from the study of 17 optical and 12 X-ray afterglows with onset features. LLGRBs/intermediate luminosity GRBs may have jets with lower bulk Lorentz factors, resulting in less relativistic beaming and hence lower observed luminosity, which might be the case for GRB 210210A. Both X-ray and optical afterglows exhibit a chromatic break (although these breaks are not well constrained due to fewer data points during these epochs) in the late afterglow phase, suggesting complex dynamics in the jet structure and surrounding medium. The parameters obtained by fitting the light curve reveal that the observed break is consistent with the jet break.

We calculated the jet opening angle, breakout time, beaming corrected gamma-ray energy, kinetic energy, and X-ray energy during the early emission phase and suggested that the overall properties of GRB 210210A favor a collapsar scenario with a possible magnetar central engine. The analysis of GRB 210210A provides significant insights into the characteristics and behavior of intermediate luminosity GRBs. Further prompt observations of more LLGRBs/intermediate luminosity GRBs with soft X-ray instruments/missions (such as the *Einstein* Probe) and detailed theoretical studies are required to unravel the complexities of these less energetic events (Gupta 2023).

Acknowledgments: We thank the referee for carefully reading the manuscript and the positive report. RG and MM were sponsored by the National Aeronautics and Space Administration (NASA) through contracts with ORAU. The views and conclusions contained in this document are those of the authors and should not be interpreted as representing the official policies, either expressed or implied, of the National Aeronautics and Space Administration (NASA) or the U.S. Government. The U.S. Government is authorized to reproduce and distribute reprints for Government purposes notwithstanding any copyright notation herein. RG and SBP acknowledge the financial support of ISRO under the AstroSat archival data utilization program (DS_2B-13013(2)/1/2021-Sec.2). AJCT acknowledges support from the Spanish Ministry project PID2020-118491GB-I00 and Junta de Andalucia grant P20_010168. AA acknowledges funds and assistance provided by the Council of Scientific & Industrial Research (CSIR), India, under file no. 09/948(0003)/2020-EMR-I. AA also acknowledges the Yushan Fellow Program by the Ministry of Education, Taiwan for the financial support (MOE-111-YSFMS-0008-001-P1). This research has used data obtained through the HEASARC Online Service, provided by the NASA-GSFC, in support of NASA High Energy Astrophysics Programs. This work made use of data supplied by the UK Swift Science Data Centre at the University of Leicester.

VII Workshop on Robotic Autonomous Observatories (October 16-20, 2023)
Editors: Maria Gritsevich, Alberto J. Castro-Tirado, Petr Kubánek, Shashi B. Pandey, and David Hiriart - DOI: https://doi.org/10.22201/ia.14052059p.2025.59.21

APPENDICES

TABLE 1: A log of photometric data for GRB 210210A has been compiled, featuring observations from *Swift* UVOT, DFOT, and various GCN reports. It should be noted that the magnitudes listed have not been corrected for galactic or host galaxy extinction.

FILTER	T_{start}-T_0 (s)	T_{stop}-T_0 (s)	MAG	MAG Error	Telescope	Reference
white	85.1	234.9	16.05	0.03	*Swift* UVOT	Present work
white	578	597.8	16.34	0.06	*Swift* UVOT	Present work
white	753.2	773	16.53	0.06	*Swift* UVOT	Present work
white	877.8	1027.5	16.58	0.03	*Swift* UVOT	Present work
white	1181	1373.8	16.68	0.05	*Swift* UVOT	Present work
white	34748.6	35571.3	19.93	0.09	*Swift* UVOT	Present work
white	58479.6	59166.3	20.36	0.21	*Swift* UVOT	Present work
white	98188.5	98482.3	>20.93	-	*Swift* UVOT	Present work
white	224611.5	224950.3	>20.91	-	*Swift* UVOT	Present work
white	235162.2	367653.1	>21.93	-	*Swift* UVOT	Present work
white	373259.7	373553.5	>20.95	-	*Swift* UVOT	Present work
white	378869.7	385337.9	>20.79	-	*Swift* UVOT	Present work
b	552.9	572.7	16.95	0.12	*Swift* UVOT	Present work
b	728.8	748.5	16.83	0.11	*Swift* UVOT	Present work
b	1156.5	1349.5	17.38	0.13	*Swift* UVOT	Present work
b	33835.4	34743.5	19.88	0.15	*Swift* UVOT	Present work
b	57567.7	98183.8	>21.05	-	*Swift* UVOT	Present work
b	224268.1	367264.5	>21.38	-	*Swift* UVOT	Present work
b	372961.4	373255.2	>20.27	-	*Swift* UVOT	Present work
b	378676.6	385295.1	>20.14	-	*Swift* UVOT	Present work
u	297.6	547.4	15.87	0.04	*Swift* UVOT	Present work
u	703.1	722.9	15.97	0.1	*Swift* UVOT	Present work
u	1131.8	1324.9	16.42	0.1	*Swift* UVOT	Present work
u	17556.6	18366.4	18.95	0.1	*Swift* UVOT	Present work
u	29044.6	29874.4	19.38	0.14	*Swift* UVOT	Present work
u	97591.4	97885.2	>19.97	-	*Swift* UVOT	Present work
u	223923.2	224262	>19.93	-	*Swift* UVOT	Present work
u	234745.1	366875.5	>21.01	-	*Swift* UVOT	Present work
u	372662.5	372956.3	>20.01	-	*Swift* UVOT	Present work
u	378483.1	385251.9	>19.84	-	*Swift* UVOT	Present work
v	628.6	648.4	16.88	0.23	*Swift* UVOT	Present work
v	803	822.8	16.87	0.23	*Swift* UVOT	Present work
v	1058.2	1250.5	16.85	0.17	*Swift* UVOT	Present work
v	22352.7	23259.5	19.28	0.21	*Swift* UVOT	Present work
v	52813.1	98766.5	>19.57	-	*Swift* UVOT	Present work
v	224956.3	368106.6	>20.33	-	*Swift* UVOT	Present work
v	373559.8	373866.5	>19.3	-	*Swift* UVOT	Present work
v	379064.4	385386.5	>19.17	-	*Swift* UVOT	Present work

Continued on next page

VII Workshop on Robotic Autonomous Observatories (October 16-20, 2023)
Editors: Maria Gritsevich, Alberto J. Castro-Tirado, Petr Kubánek, Shashi B. Pandey, and David Hiriart - DOI: https://doi.org/10.22201/ia.14052059p.2025.59.21

FILTER	T_{start}-T_0 (s)	T_{stop}-T_0 (s)	MAG	MAG Error	Telescope	Reference
uvw1	678.8	698.6	16.13	0.16	*Swift* UVOT	Present work
uvw1	852	871.7	16.11	0.16	*Swift* UVOT	Present work
uvw1	1107.5	1300.4	16.55	0.14	*Swift* UVOT	Present work
uvw1	16650.3	17550	18.55	0.09	*Swift* UVOT	Present work
uvw1	28138.3	29038.1	19.13	0.13	*Swift* UVOT	Present work
uvw1	62967.5	63263.3	>19.81	-	*Swift* UVOT	Present work
uvw1	86691.3	93066.5	>20.4	-	*Swift* UVOT	Present work
uvw1	213506.8	213546.6	>18.23	-	*Swift* UVOT	Present work
uvw1	217934.1	218166.5	>19.6	-	*Swift* UVOT	Present work
uvw2	603.4	623.2	16.55	0.2	*Swift* UVOT	Present work
uvw2	778.6	798.3	16.3	0.18	*Swift* UVOT	Present work
uvw2	1033.5	1226.1	16.53	0.14	*Swift* UVOT	Present work
uvw2	1379.5	1386.3	>16.63	-	*Swift* UVOT	Present work
uvw2	51906.9	52806.6	>20.6	-	*Swift* UVOT	Present work
uvw2	85572.6	92105.9	>20.8	-	*Swift* UVOT	Present work
uvw2	161135.1	161288.9	>19.43	-	*Swift* UVOT	Present work
uvw2	213350.1	213423.9	>18.84	-	*Swift* UVOT	Present work
uvw2	217416.6	217670.3	>19.83	-	*Swift* UVOT	Present work
uvm2	652.9	672.7	16.3	0.22	*Swift* UVOT	Present work
uvm2	827.3	847.1	16.06	0.2	*Swift* UVOT	Present work
uvm2	1082.6	1275	16.48	0.17	*Swift* UVOT	Present work
uvm2	23264.7	23526.3	19.22	0.29	*Swift* UVOT	Present work
uvm2	86131.8	92645	>20.61	-	*Swift* UVOT	Present work
uvm2	161293.6	161346.6	>18.22	-	*Swift* UVOT	Present work
uvm2	213428.5	213502.3	>18.56	-	*Swift* UVOT	Present work
uvm2	217675.4	217929.2	>19.58	-	*Swift* UVOT	Present work

FILTER	T-T_0 (s)	Exp time (s)	MAG	MAG Error	Telescope	Reference
R	335989.00	15×180	>21.8	-	DFOT	Present work

Data taken from GCN circular

FILTER	T-T_0 (days)	MAG	MAG Error	Reference
R	0.0674	17.60	0.20	(Jelinek et al. 2021)
R	0.1763	18.84	0.03	(de Ugarte Postigo et al. 2021)
R	0.3967	19.62	0.05	(Strausbaugh & Cucchiara 2021)
R	0.8800	21.35	0.07	(Dimple et al. 2021)
R	1.1674	21.89	0.21	(Kann et al. 2021)
R	3.1294	23.05	0.14	(Kann et al. 2021)

VII Workshop on Robotic Autonomous Observatories (October 16-20, 2023)
Editors: Maria Gritsevich, Alberto J. Castro-Tirado, Petr Kubánek, Shashi B. Pandey, and David Hiriart - DOI: https://doi.org/10.22201/ia.14052059p.2025.59.21

TABLE 2

PARAMETERS OBTAINED FROM THE FITTING *SWIFT*-UVOT LIGHT CURVE WITH POWER LAW AND BROKEN POWER LAW MODEL.

Filter	α_1 or α	t_b	α_2	χ^2_ν
Power law				
b	$-0.68^{+0.04}_{-0.04}$			2.01
u	$-0.76^{+0.02}_{-0.02}$			4.75
v	$-0.70^{+0.07}_{-0.07}$			1.58
uvw1	$-0.74^{+0.03}_{-0.03}$			0.72
uvm2	$-0.86^{+0.01}_{-0.01}$			1.57
uvw2	$-0.87^{+0.08}_{-0.09}$			5.22
Broken Power law				
White	$0.28^{+0.02}_{-0.02}$	$1545.84^{+303.46}_{-303.11}$	$0.94^{+0.05}_{-0.05}$	0.87

VII Workshop on Robotic Autonomous Observatories (October 16-20, 2023)
Editors: Maria Gritsevich, Alberto J. Castro-Tirado, Petr Kubánek, Shashi B. Pandey, and David Hiriart - DOI: https://doi.org/10.22201/ia.14052059p.2025.59.21

REFERENCES

Abbott, B. P., Abbott, R., Abbott, T. D., et al. 2017, ApJ, 848, L13. doi:10.3847/2041-8213/aa920c

Ahumada, T., Singer, L. P., Anand, S., et al. 2021, Nature Astronomy, 5, 917. doi:10.1038/s41550-021-01428-7

Amati, L. 2006, MNRAS, 372, 233. doi:10.1111/j.1365-2966.2006.10840.x

Barthelmy, S. D., Barbier, L. M., Cummings, J. R., et al. 2005, Space Sci. Rev., 120, 143. doi:10.1007/s11214-005-5096-3

Blandford, R. D. & Znajek, R. L. 1977, MNRAS, 179, 433. doi:10.1093/mnras/179.3.433

Blandford, R. D. & McKee, C. F. 1976, Physics of Fluids, 19, 1130. doi:10.1063/1.861619

Breeveld, A. A., Laha, S. L., & Swift/UVOT Team 2021, GRB Coordinates Network, Circular Service, No. 29457, 29457

Bromberg, O., Nakar, E., & Piran, T. 2011, ApJ, 739, L55. doi:10.1088/2041-8205/739/2/L55

Bromberg, O., Nakar, E., Piran, T., et al. 2013, ApJ, 764, 179. doi:10.1088/0004-637X/764/2/179

Burrows, D. N., Romano, P., Falcone, A., et al. 2005, Science, 309, 1833. doi:10.1126/science.1116168

Chand, V., Banerjee, A., Gupta, R., et al. 2020, ApJ, 898, 42. doi:10.3847/1538-4357/ab9606

Evans, P. A., Beardmore, A. P., Page, K. L., et al. 2007, A&A, 469, 379. doi:10.1051/0004-6361:20077530

Evans, P. A., Beardmore, A. P., Page, K. L., et al. 2009, MNRAS, 397, 1177. doi:10.1111/j.1365-2966.2009.14913.x

Denton, P. B. & Tamborra, I. 2018, ApJ, 855, 37. doi:10.3847/1538-4357/aaab4a

D'Elia, V., D'Ai, A., Gropp, J. D., et al. 2021, GRB Coordinates Network, Circular Service, No. 29452, 29452

de Ugarte Postigo, A., Kann, D. A., Thoene, C. C., et al. 2021, GRB Coordinates Network, Circular Service, No. 29450, 29450

Dimple, Ghosh, A., Gupta, R., et al. 2021, GRB Coordinates Network, Circular Service, No. 29488, 29488

Fong, W., Berger, E., Margutti, R., et al. 2015, ApJ, 815, 102. doi:10.1088/0004-637X/815/2/102

Frail, D. A., Kulkarni, S. R., Sari, R., et al. 2001, ApJ, 562, L55. doi:10.1086/338119

Frederiks, D., Golenetskii, S., Lysenko, A., et al. 2021, GRB Coordinates Network, Circular Service, No. 29517, 29517

Galama, T. J., Vreeswijk, P. M., van Paradijs, J., et al. 1998, Nature, 395, 670. doi:10.1038/27150

Gao, H. & Mészáros, P. 2015, Advances in Astronomy, 2015, 192383. doi:10.1155/2015/192383

Garcia-Cifuentes, K., Becerra, R. L., De Colle, F., et al. 2023, ApJ, 951, 4. doi:10.3847/1538-4357/acd176

Gao, H., Lei, W.-H., Zou, Y.-C., et al. 2013, Nature, 57, 141. doi:10.1016/j.newar.2013.10.001

Gottlieb, O., Nakar, E., Piran, T., et al. 2018, MNRAS, 479, 588. doi:10.1093/mnras/sty1462

Gupta, R., Oates, S. R., Pandey, S. B., et al. 2021, MNRAS, 505, 4086. doi:10.1093/mnras/stab1573

Gupta, R., Pandey, S. B., Castro-Tirado, A. J., et al. 2021, Revista Mexicana de Astronomia y Astrofisica Conference Series, 53, 113. doi:10.22201/ia.14052059p.2021.53.23

Gupta, R., Gupta, S., Chattopadhyay, T., et al. 2022, MNRAS, 511, 1694. doi:10.1093/mnras/stac015

Gupta, R., Kumar, A., Pandey, S. B., et al. 2022, Journal of Astrophysics and Astronomy, 43, 11. doi:10.1007/s12036-021-09794-4

Gupta, R., Pandey, S. B., Kumar, A., et al. 2022, Journal of Astrophysics and Astronomy, 43, 82. doi:10.1007/s12036-022-09865-0

Gupta, R., Pandey, S. B., Ror, A. K., et al. 2023, arXiv:2307.15585. doi:10.48550/arXiv.2307.15585

Gupta, R. 2023, arXiv:2312.16265. doi:10.48550/arXiv.2312.16265

Hjorth, J., Sollerman, J., Møller, P., et al. 2003, Nature, 423, 847. doi:10.1038/nature01750

Jelinek, M., Strobl, J., Karpov, S., et al. 2021, GRB Coordinates Network, Circular Service, No. 29469, 29469

Jespersen, C. K., Severin, J. B., Steinhardt, C. L., et al. 2020, ApJ, 896, L20. doi:10.3847/2041-8213/ab964d

Kann, D. A., Klose, S., Zhang, B., et al. 2010, ApJ, 720, 1513. doi:10.1088/0004-637X/720/2/1513

Kann, D. A., de Ugarte Postigo, A., Thoene, C. C., et al. 2021, GRB Coordinates Network, Circular Service, No. 29502, 29502

Kann, D. A., de Ugarte Postigo, A., Thoene, C. C., et al. 2021, GRB Coordinates Network, Circular Service, No. 29476, 29476

Kumar, P. & Zhang, B. 2015, Phys. Rep., 561, 1. doi:10.1016/j.physrep.2014.09.008

Levan, A. J., Gompertz, B. P., Salafia, O. S., et al. 2024, Nature, 626, 737. doi:10.1038/s41586-023-06759-1

Li, L., Wu, X.-F., Lei, W.-H., et al. 2018, ApJS, 236, 26. doi:10.3847/1538-4365/aabaf3

Liang, E., Zhang, B., Virgili, F., et al. 2007, ApJ, 662, 1111. doi:10.1086/517959

Liang, E.-W., Yi, S.-X., Zhang, J., et al. 2010, ApJ, 725, 2209. doi:10.1088/0004-637X/725/2/2209

Lien, A. Y., Barthelmy, S. D., Krimm, H. A., et al. 2021, GRB Coordinates Network, Circular Service, No. 29467, 29467

MacFadyen, A. I. & Woosley, S. E. 1999, ApJ, 524, 262. doi:10.1086/307790

Molinari, E., Vergani, S. D., Malesani, D., et al. 2007, A&A, 469, L13. doi:10.1051/0004-6361:20077388

Nakar, E. & Sari, R. 2012, ApJ, 747, 88. doi:10.1088/0004-637X/747/2/88

Nava, L., Salvaterra, R., Ghirlanda, G., et al. 2012, MNRAS, 421, 1256. doi:10.1111/j.1365-2966.2011.20394.x

Oates, S. 2023, Universe, 9, 113. doi:10.3390/universe9030113

Perna, R. & Belczynski, K. 2002, ApJ, 570, 252. doi:10.1086/339571

Piran, T. 2004, Reviews of Modern Physics, 76, 1143. doi:10.1103/RevModPhys.76.1143

Racusin, J. L., Karpov, S. V., Sokolowski, M., et al. 2008, Nature, 455, 183. doi:10.1038/nature07270

Ror, A. K., Gupta, R., Jelínek, M., et al. 2023, ApJ, 942, 34. doi:10.3847/1538-4357/aca414

Ror, A. K., Gupta, R., Aryan, A., et al. 2024, arXiv:2406.01220. doi:10.48550/arXiv.2406.01220

Sari, R. & Piran, T. 1999, ApJ, 520, 641. doi:10.1086/307508

Schlegel, D. J., Finkbeiner, D. P., & Davis, M. 1998, ApJ, 500, 525. doi:10.1086/305772

Senno, N., Murase, K., & Mészáros, P. 2016, Phys. Rev. D, 93, 083003. doi:10.1103/PhysRevD.93.083003

Sharma, V., Iyyani, S., & Bhattacharya, D. 2021, ApJ, 908, L2. doi:10.3847/2041-8213/abd53f

Strausbaugh, R. & Cucchiara, A. 2021, GRB Coordinates Network, Circular Service, No. 29459, 29459

Stetson, P. B. 1987, PASP, 99, 191. doi:10.1086/131977

Swenson, C. A., Roming, P. W. A., De Pasquale, M., et al. 2013, ApJ, 774, 2. doi:10.1088/0004-637X/774/1/2

Tody, D. 1993, Astronomical Data Analysis Software and Systems II, 52, 173

Troja, E., Fryer, C. L., O'Connor, B., et al. 2022, Nature, 612, 228. doi:10.1038/s41586-022-05327-3

Vianello, G., Lauer, R. J., Younk, P., et al. 2015, arXiv:1507.08343. doi:10.48550/arXiv.1507.08343

Zhao, W., Zhang, J.-C., Zhang, Q.-X., et al. 2020, ApJ, 900, 112. doi:10.3847/1538-4357/aba43a

Zhang, B. & Kobayashi, S. 2005, ApJ, 628, 315. doi:10.1086/429787

Lü, H.-J., Yuan, H.-Y., Yi, T.-F., et al. 2022, ApJ, 931, L23. doi:10.3847/2041-8213/ac6e3a

VII Workshop on Robotic Autonomous Observatories (October 16-20, 2023)
Editors: Maria Gritsevich, Alberto J. Castro-Tirado, Petr Kubánek, Shashi B. Pandey, and David Hiriart - DOI: https://doi.org/10.22201/ia.14052059p.2025.59.21

Revista Mexicana de Astronomía y Astrofísica Serie de Conferencias (RMxAC), **59**, 133–144 (2025)
© 2025: Instituto de Astronomía, Universidad Nacional Autónoma de México
https://doi.org/10.22201/ia.14052059p.2025.59.22

VII Workshop on Robotic Autonomous Observatories (October 16-20, 2023)
Editors: Maria Gritsevich, Alberto J. Castro-Tirado, Petr Kubánek, Shashi B. Pandey, and David Hiriart - DOI: https://doi.org/10.22201/ia.14052059p.2025.59.22

PROMPT AND AFTERGLOW ANALYSIS OF THE *Fermi-LAT DETECTED GRB 230812B*

Amit K. Ror[1,2], S. B. Pandey[1], A. Aryan[1,3], Sudhir Kumar[2], and A. J. Castro-Tirado[4,5]

RESUMEN

La emisión temprana de GRB 230812B se destaca como uno de los eventos más luminosos observados por instrumentos del satélite *Fermi* tales como GBM y LAT. El análisis espectral de emisión temprana (tanto integrado en el tiempo como en sus diversas fases temporales) de esta explosión respalda una componente térmica adicional y otra no térmica, lo que indica una composición híbrida del *jet* (chorro). Los parámetros espectrales α, E_p y kT del modelo espectral de `Band+Blackbody` son los que proporcionan un mejor ajuste. Además, las emisiones de la postluminiscencia a energías más bajas son consistentes con la emisión de sincrotrón del choque externo que se va propagando hacia adelante barriendo el medio del medio interestelar. El instrumento LAT detectó una emisión de muy alta energía (VHE) que se desvía de los esperado del mecanismo de emisión sincrotrón, posiblemente originada por el aumento del factor de Lorentz de los fotones de emisión temprana motivado por electrones acelerados en el choque externo a través de mecanismos de emisión de Compton inverso (IC) o auto sincrotrón Compton (SSC). La comparación de las propiedades de emisión temprana y de la posterior de este estallido reveló que, a diferencia de la emisión simultánea (gamma) y más brillante, la postluminiscencia posterior de GRB 230812B es más débil que la de los otros estallidos de rayos gamma también brillantes y asociados con una supernova (GRB 130427A y GRB 171010A) con desplazamientos al rojo similares.

ABSTRACT

Prompt emission of GRB 230812B stands out as one of the most luminous events observed by both the *Fermi*-GBM and LAT. Prompt emission spectral analysis (both time-integrated and resolved) of this burst supports an additional thermal component together with a non-thermal, indicating the hybrid jet composition. The spectral parameters α, E_p, and kT of the best-fit `Band+Blackbody` model show a tacking behaviour with the intensity. Further, the low energy afterglow emission is consistent with the synchrotron emission from the external forward shock in the ISM medium. LAT detected very high energy emission (VHE) deviating from the synchrotron mechanism, possibly originating from the Lorentz boosting of prompt emission photons by accelerated electrons in the external shock via Inverse Compton (IC) or Synchrotron Self Compton (SSC) emission mechanisms. The comparison of the prompt and afterglow emission properties of this burst revealed that, unlike the bright prompt emission, the afterglow of GRB 230812B is fainter than the other SN-detected bright bursts (GRB 130427A and GRB 171010A) at a similar redshift.

Key Words: Gamma ray burst — mechanism: Blackbody, Synchrotron, Synchrotron self Compton.

1. INTRODUCTION

Gamma-ray bursts (GRBs) are distant and powerful cosmic events characterized by two phases: A highly variable prompt emission in soft γ-rays and hard X-rays with a duration of (T_{90}) seconds (s) to minutes, followed by a smoothly decaying afterglow emission spanning a broad temporal (hours-days) and energy ranges (radio-TeV energies; Kumar & Zhang 2015). GRBs are traditionally classified based on temporal and spectral properties into short/hard (SGRB) and long/soft (LGRBs; Kouveliotou et al. 1993). SGRBs ($T_{90} < 2$ s) come from compact binary mergers, and LGRBs ($T_{90} > 2$ s) are likely originating from a massive star collapse (Galama et al. 1998; Hjorth et al. 2003; Abbott et al. 2017). However, GRB 200826A ($T_{90} \sim 1.2$ s from collapsar; Ahumada et al. 2021), GRB 211211A ($T_{90} \sim 50$ s; Troja et al. 2022), and GRB 230307A ($T_{90} \sim 35$ s; Levan et al. 2023) come from mergers are outlier to the traditional classification. Newly introduced

[1]Aryabhatta Research Institute of Observational Sciences (ARIES), Manora Peak, Nainital-263002, India.
[2]Department of Applied Physics/Physics, Mahatma Jyotiba Phule Rohilkhand University, Bareilly-243006, India.
[3]Graduate Institute of Astronomy, National Central University, 300 Jhongda Road, 32001 Jhongli, Taiwan.
[4]Instituto de Astrofísica de Andalucía (IAA-CSIC), Glorieta de la Astronomía s/n, E-18008, Granada, Spain.
[5]Departamento de Ingeniería de Sistemas y Automática, Unidad Asociada al CSIC por el IAA, Escuela de Ingeniería Industrial, Universidad de Málaga, C. Dr. Ortiz Ramos s/n, 29071 Málaga, Spain.

VII Workshop on Robotic Autonomous Observatories (October 16-20, 2023)
Editors: Maria Gritsevich, Alberto J. Castro-Tirado, Petr Kubánek, Shashi B. Pandey, and David Hiriart - DOI: https://doi.org/10.22201/ia.14052059p.2025.59.22

classifications include intermediate bursts and ultra-long GRBs (ULGRBs, $T_{90} > 1000$ s; Mukherjee et al. 1998; Boër et al. 2015; Ror et al. 2024), broadening the classification beyond traditional LGRBs and SGRBs.

Over the 50 years of study, the GRB prompt emission remains a subject of ongoing exploration (Pe'er 2015). Several theories describe its origin from internal shock or magnetic reconnection in the ultra-relativistic jet. The jet composition can be baryonic or magnetic, and the mechanism of prompt emission from these ultra-relativistic jets (`synchrotron`, non-thermal, thermal, or hybrid) is still an open question (Zhang et al. 2018; Gupta et al. 2024). A widely employed `Band` function (Band et al. 1993), introduced during the *BATSE* era, characterizes the non-thermal spectral components of GRBs. It incorporates four parameters: (1) normalization constant, (2) low-energy spectral index ($\alpha \sim$ -1), (3) high-energy spectral index ($\beta \sim$ -2), and (4) peak energy ($E_p \sim 300$ keV; Preece et al. 2000). However, results of time-resolved spectral analysis from Kaneko et al. (2006) have revealed variations, with a harder $\alpha \sim$ -0.72. Subsequent studies of 1500 time-resolved spectra from 78 bright bursts (Wang et al. 2024) revealed that the α values from 80% of spectra crossing the limit (-3/2,-2/3) are due to the fast and slow cooling limits from `synchrotron` emission mechanism known as `synchrotron` line of death (Preece et al. 2000). Recently, new models have been used to fit complicated spectra like the physical `synchrotron` and `blackbody` to constrain the emission mechanism (Burgess et al. 2020). Studies have shown that in the case of GRBs, where α crosses the limit (-3/2,-2/3), still the physical `synchrotron` model is found to best fit the spectra in some cases (Burgess et al. 2020). In addition, the study of the spectral parameter evolution during the prompt emission serves as a valuable tool to constrain emission mechanisms. The peak energy E_p shows four types of evolution: flux tracking, hard to soft, soft to hard, and a chaotic (Golenetskii et al. 1983; Norris et al. 1986). Time-resolved spectral analysis of bright GRBs from *Fermi*-GBM revealed that the E_p obtained for most of the cases shows flux tracking, but hard to soft evolution is common in single pulse GRBs (Wang et al. 2024; Li et al. 2021). The evolution of α is, on the other hand, less predictable. However, recently Gupta et al. (2021, 2022); Gupta (2023); Ror et al. (2023) and Ror et al. (2024) determined the flux tracking evolution of α in GRB 140201A and GRB 201216C, respectively.

GRB afterglows from the cooling population of accelerated electrons from external shocks generally decay following a simple or broken PL. The late-afterglow light curve (hereafter LC) of some nearby GRBs exhibits a distinct bump, indicating the emergence of the underlying supernova (SN; Galama et al. 1998; Hjorth et al. 2003). Detailed spectroscopic examinations of these underlying SNe reveal that they are predominantly hydrogen-deficient broad-line type Ic-BL, often categorized as striped envelope supernovae (SESNe), for more detail about SESNe please refer to Pandey et al. (2021). Notably, SN-associated GRBs display a luminosity of three to five orders of magnitude less than typical LGRBs, so detectable only in the close proximity up to a redshift of ~ 1. The energy source of GRB-associated SNe is believed to be thermal heating from radioactive Nickel trapped within the ejecta. Recently, the magnetar model has emerged as a compelling framework to explain the power source for GRB-associated SNe (Kumar et al. 2022). Another plausible energy source for GRBs associated with SNe involves the interaction between the ejected material and the circumstellar medium surrounding the burst. In the case of GRB 230812B, Srinivasaragavan et al. (2024) used the radioactive heating model to explain the power source of SN 2023pel to constrain the radioactive Nickel mass $M_{Ni} = 0.38 \pm 0.01$ $M_\odot$ and the total ejecta mass of 1.0 ± 0.6 $M_\odot$. Recently, Wang et al. (2024) demonstrated that GRB 230812B is one of the shortest long-duration GRBs ($T_{90} \sim 3$ s) with a collapsar origin. This event is analogous to GRB 200826A (Ahumada et al. 2021), where a longer jet-bore time through the stellar envelope was proposed to account for the shorter burst duration.

Until 2018, LAT was the only very high-energy instrument that successfully detected GeV emissions from more than 100 GRBs (Fraija et al. 2019). LAT detected the maximum energy photon from GRB 130427A with an energy of ~ 95 GeV (Ackermann et al. 2014). After 2018, six long GRBs (GRB 180720B, GRB 190114C, 190829A, GRB 201015A, GRB 201216C, and GRB 221009A) were detected as having TeV emissions associated with their prompt and afterglow emissions (Gupta et al. 2021; Ror et al. 2023, 2024). A single synchrotron component could not explain the double bump observed in the broad-band SED of VHE-detected GRBs, and an additional Synchrotron Self Compton (SSC) or inverse Compton (IC) component is required (Fraija et al. 2019; MAGIC Collaboration et al. 2019; Fraija et al. 2021; H. E. S. S. Collaboration et al. 2021; Ror et al. 2023). In our work, we have tried to constrain the possible

VII Workshop on Robotic Autonomous Observatories (October 16-20, 2023)
Editors: Maria Gritsevich, Alberto J. Castro-Tirado, Petr Kubánek, Shashi B. Pandey, and David Hiriart - DOI: https://doi.org/10.22201/ia.14052059p.2025.59.22

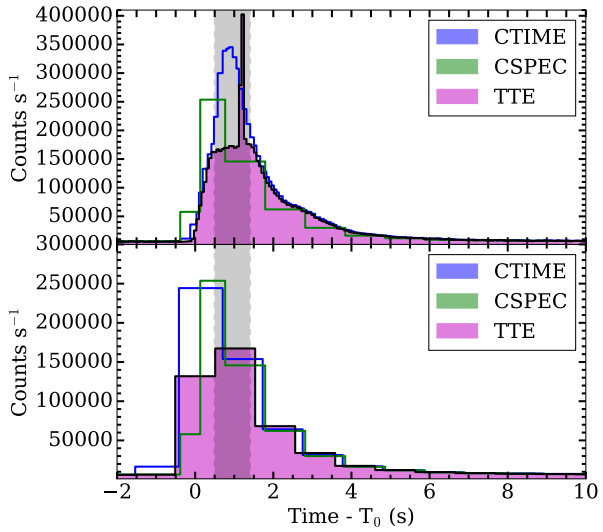


Fig. 1. Represents the *Fermi*-GBM LCs of GRB 230812B, plotted from the CSPEC (green), CTIME (blue), and TTE (magenta) data files. The Upper panel shows the 1s binned LC of CSPEC and 64 ms of CTIME and TTE observation. Similarly, the lower panel shows the LC binned with 1s for all CSPEC, CTIME, and TTE. The vertical gray region corresponds to the pulse pileup, which we removed from our data analysis.

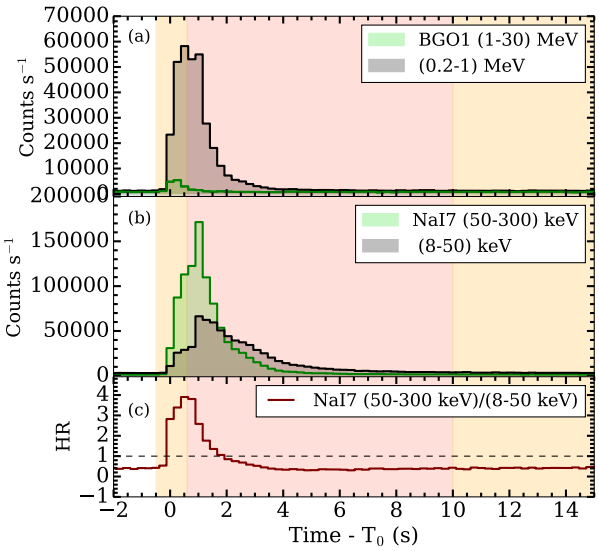


Fig. 2. The multi-wavelength prompt emission LC of GRB 230812B is plotted from the GBM TTE observation. (a) GBM-BGO observation plotted in the 0.2-1 MeV (gray) and 1-30 MeV (green). (b) Similarly, the NaI LCs in the energy ranges 50-300 keV and 8-50 keV are plotted. (c) Evolution of hardness ratio (HR, number of photons detected in 50-300 keV / number of photons in the 8-50 keV) from the combined NaI-3, NaI-6, and NaI-7 scintillation detectors of *Fermi*-GBM.

origin of GeV detection associated with the GRB 230812B.

The content of the paper is as follows: §2 is devoted to multi-band observation and analysis of GRB 230812B, §3 to results, §4 to discussion, and §5 to summary and conclusion. In this paper, the chosen cosmological parameters are the Hubble constant $H_0 = 71$ km s^{-1} Mpc^{-1} and the density parameters $\Omega_\Lambda = 0.73$ and $\Omega_m = 0.27$. Uncertainties are given at 1σ level if not stated otherwise. The representation of afterglow flux follows the convention expressed by $F(\nu, t) = t^{-\alpha}\nu^{-\beta}$.

2. MULTI-WAVELENGTH OBSERVATION AND ANALYSIS

2.1. *Prompt emission observation and analysis*

On August 12, 2023, at 18:58:12.05 UT (hereafter T_0), the Gamma-Ray Burst Monitor (GBM, Meegan et al. 2009) on board Fermi gamma-ray space telescope (*Fermi*) discovered and localised GRB 230812B (Fermi GBM Team 2023; Lesage et al. 2023). During the prompt emission phase, the initial 3.3 ± 0.1 s exhibited 95% of the burst's fluence in γ-rays, hence considered the T_{90} duration. However, a softer tail persisted for approx 10 s post-detection (Lesage et al. 2023; Roberts et al. 2023). Prompt emission's preliminary analysis revealed that the time-integrated spectra within the 0-32 s time-interval were well-described by the band function, yielding parameters of $E_p = 273 \pm 3$ keV, α = -0.80 ± 0.01, and β = -2.47 ± 0.02. The fluence recorded during this period was 2.5201 ± 0.0002 × 10^{-4} erg cm^{-2} by Roberts et al. (2023). In addition to *Fermi*-GBM, *GECAM*-C (Xiong et al. 2023), *Konus*-Wind (Frederiks et al. 2023), and *AGILE*/MCAL (Casentini et al. 2023) also detected the intense prompt emission from GRB 230812B.

GBM observations for this burst were acquired from the official web page of *Fermi* Science Support center[6]. Before analyzing the *Fermi*-GBM data, we carefully check the observed LC from the three types of spectral file (CTIME, CSPEC, and TTE) using the GBM-Tool python package (Goldstein et al. 2023). In the 64 ms bin LC, we found a glitch around [1.12-1.312] s in the TTE data. A thin magenta spike in the TTE LC at around 1.2 s (see upper panel of Figure 1) corresponds to the artificially generated spike mentioned by Roberts et al. (2023). This bright spike is not present in the CSPEC and CTIME data files, which might be due

[6] https://fermi.gsfc.nasa.gov/ssc/data/access/gbm/

VII Workshop on Robotic Autonomous Observatories (October 16-20, 2023)
Editors: Maria Gritsevich, Alberto J. Castro-Tirado, Petr Kubánek, Shashi B. Pandey, and David Hiriart - DOI: https://doi.org/10.22201/ia.14052059p.2025.59.22

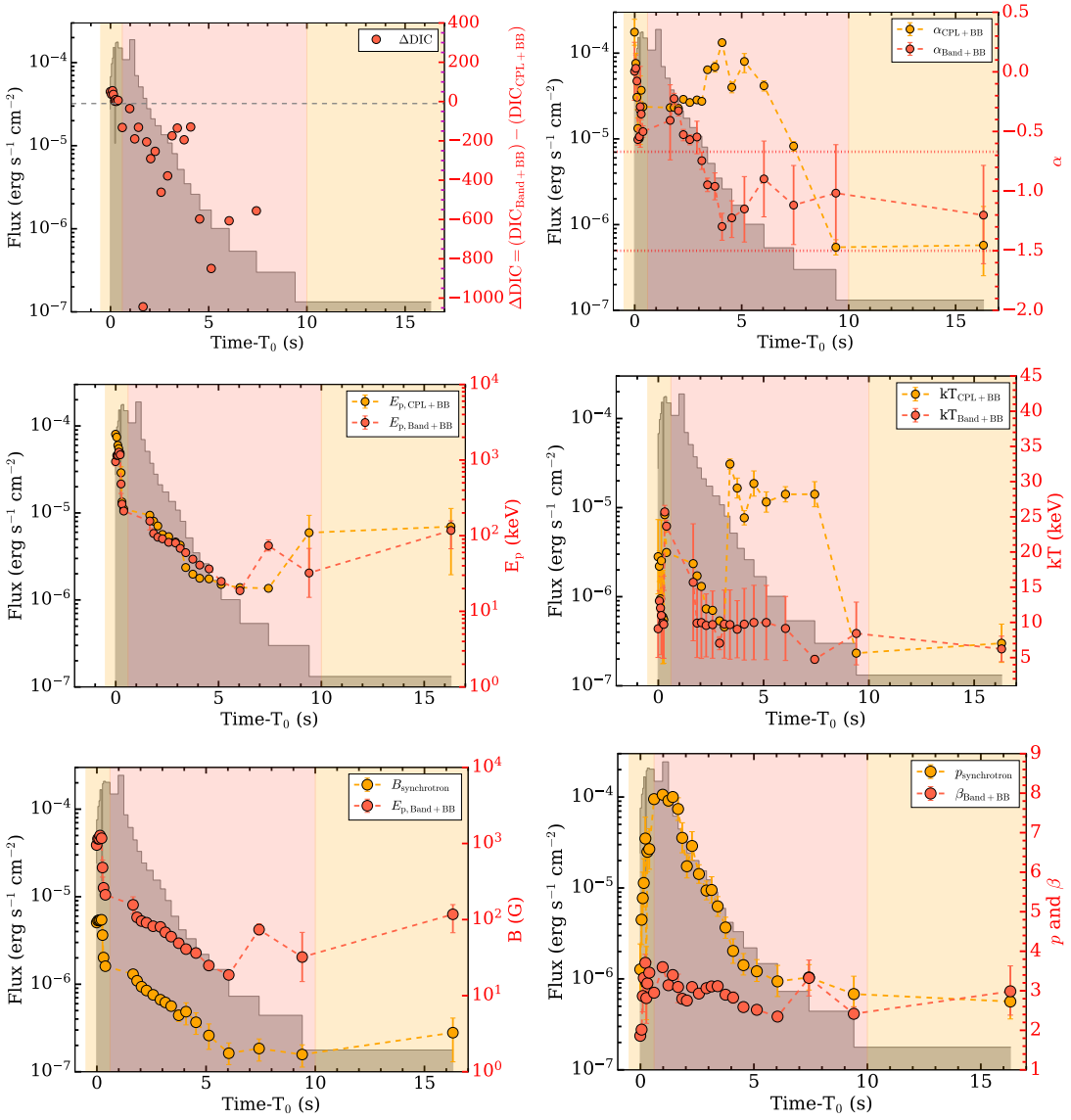


Fig. 3. Represents the evolution of the prompt emission parameter obtained from the time-resolution spectral analysis of GRB 230812B. In each plot, the left Y-axis represents the flux plotted in the background as a step function, where each step represents the width of the Bayesian block in which the spectral parameters are evaluated, and the X-axis ticks are midpoints of the Bayesian block. The orange-shaded region represents the time range where `CPL+BB` is the best fit, and the red-shaded region is the region where `Band+BB` is the best fit. The difference in the DIC ΔDIC= $DIC_{\texttt{Band+BB}}$- $DIC_{\texttt{CPL+BB}}$ is shown in the upper-left panel. A dashed line at -10 is plotted to select the best-fit model. The upper-right panel represents the evolution of low energy spectral index α obtained from `CPL+BB` (orange) and `Band+BB` (red). Two dotted lines at -3/2 and -2/3 represent the limits of `synchrotron` emission from external shock (Preece et al. 2000). Similarly, the middle-left and middle-right panels represent the evolution of E_p and kT, respectively. The lower two panels represent the magnetic field strength B and the energy distribution index p of the shock-accelerated electrons.

to their coarse temporal or spectral resolution. However, the LC plotted with 1.024 s resolution from the TTE, CSPEC, and CTIME data files showed similar results without any discrepancy (see bottom panel of Figure 1). TTE data in the interval [1.12-1.312] s was lost due to its band-width limit, and also, there is observed pileup in all types of data files during the time-interval [0.5-1.4] s (Roberts et al. 2023). We have not utilized the data corresponding to this time range during the time-resolution spectral fitting of GBM data. As recommended by the *Fermi*-GBM team, we have used NaI-3,6,7 and BGO-0 detectors

VII Workshop on Robotic Autonomous Observatories (October 16-20, 2023)
Editors: Maria Gritsevich, Alberto J. Castro-Tirado, Petr Kubánek, Shashi B. Pandey, and David Hiriart - DOI: https://doi.org/10.22201/ia.14052059p.2025.59.22

for the GBM data analysis. All other detectors are blocked by different parts of the spacecraft and cannot be considered reliable (Roberts et al. 2023).

We closely followed the methodology described in Ror et al. (2023), for the prompt emission spectral analysis. The time-integrated spectrum analysis in the temporal range of -0.1s to 5s was performed by combining the detectors NaI-3,6,7 and BGO-0, obtaining a spectrum spanning the energy range of $\sim$ 0.01 - 40 MeV. As usual, we discarded the 33-37 keV range to avoid the sodium K-edge. The time-integrated spectrum in the given temporal and energy range was extracted utilizing the `GtBurst` software (Caballero-García et al. 2023; Castro-Tirado et al. 2024). To employ the Bayesian analysis method for the temporal and spectral analysis of GBM data, we used a Python-based software package, Multi-Mission Maximum Likelihood (`3ML`, Vianello et al. 2015). For the spectral fitting within `3ML`, we utilized a multi-nest sampler with 10,000 iteration steps, as described in Vianello et al. (2018). We have used several empirical models such as Power Law (PL), `Band`, and `Cutoff PL` (`CPL`) and physical `Synchrotron` and `Blackbody` (`BB`) models and their combinations (`PL+BB`, `Band+BB`, `CPL+BB`), to fit the time-integrated spectrum. Burgess et al. (2020) provides the complete details on the physical `synchrotron` model. To compare between the different models, we used the deviance information criteria (DIC).

Further, we performed the time-resolved spectral analysis of *Fermi*-GBM data to study the parameter's evolution during the prompt emission. For the time-resolved spectral analysis, the GBM LC from the brightest detector (NaI-6) was rebinned using the methodology known as Bayesian block binning by setting the false alarm probability at 0.01 (Scargle et al. 2013). The obtained time slices were then applied to all other detectors. The advantages of Bayesian block binning methods are given in Burgess (2014). From this method, we obtained 29 spectra, out of which only 24 are statistically significant with S $>$ 20 (Vianello et al. 2018). After extracting the spectrum using `GtBurst`, we fit each spectrum with several empirical and physical models as discussed above for time-integrated analysis. The results of the spectral analysis for the prompt emission are presented in Figure 3 and elaborated upon in section 3.

2.2. *Afterglow observation and analysis*

Initially, the burst was beyond the observational range of the Burst Alert Telescope onboard *Neil Gehrel Swift Observatory* (*Swift*-BAT, Barthelmy et al. 2005). Following a sequence of tiled observations, the *Swift* X-ray Telescope (XRT) successfully localized the burst at T_0+25 ks (Evans & Swift Team 2023; Kennea & Swift Team 2023; Page & Swift-XRT Team 2023). All *Swift*-XRT observations were taken in photon count (PC) mode. The preliminary XRT LC and spectrum were modeled by a simple PL and absorbed PL with indices $\alpha_x = 1.80 \pm 0.4$ and Γ_x (β_x+1) = 1.82 $\pm$ 0.15 (Beardmore et al. 2023).

To delve into the afterglow characteristic of GRB 230812B, the X-ray temporal and spectral data were obtained from the online repository [7] of UK *Swift* Science Data Centre (Evans et al. 2007, 2009). For the optical data analysis, we obtained the data reported from GCN circulars [8]. The redshift (z=0.36) of the burst was measured from the spectroscopic observations using the 10.4m Gran Telescopio de Canarias (de Ugarte Postigo et al. 2023).

In the case of GRB 230812B, the flux density X-ray LC at 10 keV showed no flare or plateau throughout the XRT observations from T_0+25 ks to T_0+1400 ks. We modeled the X-ray LC with a simple PL using the MCMC technique. We obtained a PL index of $\alpha_x = -1.22^{+0.05}_{-0.05}$. The X-ray flux density LC and the PL model fitted to it are shown in the left panel of Figure 4.

Similarly, the optical LC also seems to decay without breaks. Following a similar methodology, we fitted the optical LC using a simple PL and obtained the decay index of $\alpha_o = 1.08^{0.03}_{-0.03}$. As shown in the left panel of Figure 4, the optical LC starts deviating from the PL decay at $\sim$ 4 days after T_0. This is because the underlying supernova emission began to emerge about four days after the burst trigger (Srinivasaragavan et al. 2024; Hussenot-Desenonges et al. 2023).

We have retrieved the X-ray spectra in the time range of 25 ks to 38 ks and the energy range of 0.3 - 10 keV. For the XRT spectrum fitting, we utilized an absorbed PL model with a multiplicative Galactic absorption component (*phabs*) and the host absorption component (*zphabs*) in the X-ray spectral fitting package (`XSPEC`; Arnaud 1996; Gupta et al. 2022). The galactic hydrogen column density (NH_{Gal}) was fixed at 2.02×10^{20} cm^{-2} during the spectral fitting. There is no flare or any other variation present in the XRT LC. We first calculated the host hydrogen column density ($NH_z = 7.20 \times 10^{20}$ cm^{-2}) along the line of sight by fitting the absorbed PL to the average spectrum. Then, by fixing both NH_{Gal} and NH_z, we again fit the XRT spectrum with the same

[7] `https://www.swift.ac.uk/xrt_curves/00021589/`
[8] `https://gcn.nasa.gov/circulars`

VII Workshop on Robotic Autonomous Observatories (October 16-20, 2023)
Editors: Maria Gritsevich, Alberto J. Castro-Tirado, Petr Kubánek, Shashi B. Pandey, and David Hiriart - DOI: https://doi.org/10.22201/ia.14052059p.2025.59.22

absorbed PL model and obtained a spectral index of $\beta_x = 0.68^{+0.08}_{-0.08}$.

After that, we created an optical r-band to X-ray spectral energy distribution (SED) in the time interval 25 ks - 38 ks. We fit the optical-X-ray SED with the PL and obtained a PL index $\beta_{\rm ox} = 0.74^{0.01}_{0.01}$. The optical r-band to X-ray SED and corresponding PL fit is presented in the right panel of Figure 4.

2.3. Fermi-*LAT observation and analysis*

At the moment of the GBM detection, the LAT boresight angle was 29°. Scotton et al. (2023) reported that *Fermi*-LAT detected the GeV photons from the GRB 230812B. Preliminary LAT spectral analysis above 100 MeV revealed the PL distribution of energy with the photon index $\Gamma_{\rm LAT}$ = 2.16 ± 0.14. *Fermi*-LAT recorded a photon with a maximum energy of 72 GeV at T_0+32.2s (Scotton et al. 2023).

We employed the `GtBurst` software to download *Fermi*-LAT data spanning T_0 to T_0+10 ks. Subsequently, we conducted an unbinned likelihood analysis on the time-integrated LAT data, covering the energy range of 0.1-100 GeV. In our analysis of LAT data, we selected a 10×10 deg^2 region centered around the GRB 230812B. The instrumental response function P8R3_SOURCE, a maximum zenith cut of 100 degrees, and a skybinning of 0.2 degrees were applied. Finally, we utilized the `gtsrcprob` tool to calculate the probability of observed photons associated with GRB 230812B.

The time-integrated spectral analysis of LAT data yielded a photon index $\Gamma_{\rm LAT}$ = -1.99 ± 0.13, with an average flux = 3.79 ± 0.68 × 10^{-9} erg s^{-1} cm^{-2} in the 0.1-10 GeV energy range. Additionally, we extracted the spectral file for `XSPEC`. We again fit the extracted spectra in `XSPEC` and obtained a photon index of $\Gamma_{\rm LAT} = 2.03^{+0.27}_{-0.23}$ and a flux of 3.52 ± 0.98 × 10^{-9} erg s^{-1} cm^{-2}, consistent within the error. We saved the QDP file from the `XSPEC` and plotted the LAT spectra in Figure 5.

Following this, we performed the time-resolved analysis of LAT data. Initially, we binned the LAT data in 5 s bins, and subsequently, the bin width was increased, as illustrated in Figure 6. Up to the initial 100 s, the instrument response function `P8R3_TRANSIENT020` was utilized, followed by a switch to the instrument response function `P8R3_SOURCE`. The outcomes of the time-resolved spectral analysis are presented in Figure 6. The flux obtained in the range 0.1-10 GeV decreased with time following a PL decay, with the decay index $\alpha_{\rm LAT} = 1.04 \pm 0.08$.

3. RESULTS

3.1. *Prompt emission*

The prompt emission multichannel LC of GRB 230812B is presented in the upper and middle panels of Figure 2. The evolution of hardness ratio (HR, i.e. no. of photons in 50-300 keV / no. of photons in 8-50 keV) is presented in the lower panel of Figure 2. The prompt emission LC is the fast rise and exponential decay (FRED) type with a single broad pulse. The HR remains > 1 for almost T_0 to T_0+ 2 s and seems to follow the intensity of the burst, indicating that GRB 230812B is a hard burst.

The time-integrated spectrum of GRB 230812B is best modeled by `Band+BB` with the minimum DIC value of 9531 over `synchrotron`, Band, `CPL`, and `CPL+BB` with DIC values of 9570, 10356, 24725, and 13234, respectively. The best-fit parameter obtained from the best-fit model are α = $-1.02^{+0.01}_{-0.01}$, $E_{\rm p}$ = $411.35^{+8.21}_{-8.18}$ keV, β = $-2.75^{+0.04}_{-0.04}$ and kT = $24.05^{+0.32}_{-0.32}$ keV.

The prompt emission time-resolved spectral fitting results are presented in Figure 3. The upper left panel of Figure 3 illustrates the difference between the DIC values of two best-fit models, `Band+BB` and `CPL+BB`, i.e., ΔDIC = DIC$_{\texttt{Band+BB}}$-DIC$_{\texttt{CPL+BB}}$. ΔDIC < -10 means that the `Band+BB` is best fitting; otherwise, `CPL+BB` is best fitting. The time-resolved spectral analysis revealed that during the rising phase of the LC's prompt emission, the time-resolved spectra are best fitted by the `CPL+BB` model. Conversely, during the decay phase of the LC, all the spectra are best fitted by the `Band+BB` model based on the lower DIC values. In Figure 3, the orange shade region represents the interval during which `CPL+BB` is best fitting, and the red shaded region represents the interval during which `Band+BB` best fits the time-resolved spectra. The total isotropic γ-ray energy release $E_{\gamma,iso} = 8.74 \pm 1.61 \times 10^{52}$ erg along with the $E_{\rm p}$ value is found to be consistent with the Amati correlation for LGRBs (Amati 2006).

3.2. *The prompt emission parameter's evolution*

The evolution of the low energy spectral index α obtained from the best-fit model is presented in the upper right panel of Figure 3. Throughout the prompt emission, α seems to follow the intensity. The α obtained from the `CPL+BB` in the 2-10 s time intervals deviates from the flux tracking. This might be due to the `CPL+BB` model not fitting well in the given time interval. Similar to the α, the peak energy $E_{\rm p}$ of the spectrum is also found to be following the intensity. Hence, the GRB 230812B is a double-tracking burst. The time-integrated and

VII Workshop on Robotic Autonomous Observatories (October 16-20, 2023)
Editors: Maria Gritsevich, Alberto J. Castro-Tirado, Petr Kubánek, Shashi B. Pandey, and David Hiriart - DOI: https://doi.org/10.22201/ia.14052059p.2025.59.22

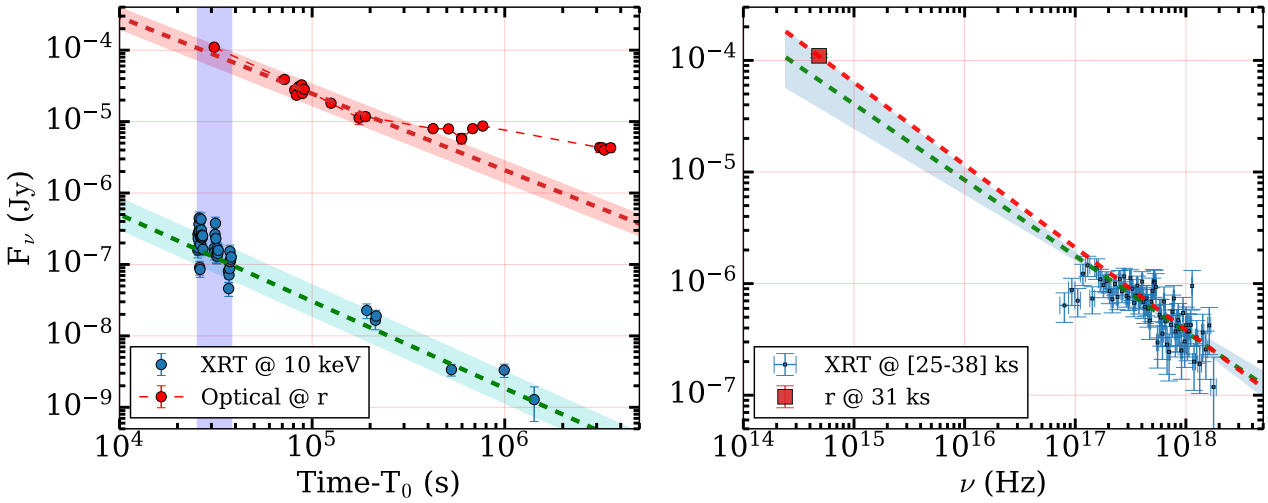


Fig. 4. Left panel: XRT (green) and r-band optical LCs (red) are plotted. The colored dotted line and the shaded area around them represent the PL fit and associated error bar for both LCs. The vertically shaded region corresponds to the time interval used to construct an optical r-band to X-ray SED. Right pane: optical to X-ray SED. Optical r-band data is plotted in a red square, and X-ray observation is shown in blue. The blue dotted line represents the PL fitted to X-ray spectra at 0.3-10 keV. The red dotted line represents the PL model fitted to the combined r-band to X-ray SED. Green squares and the dotted line represent the LAT spectra and corresponding power law fit, respectively.

time-resolved spectral analysis results showed that the single empirical `Band` or `CPL` do not fit well the spectra, but an addition of a thermal component is required. However, the evolution of the thermal energy component kT is somewhat complicated. It closely follows the flux up to T_0+3 s. After that, it shows almost a constant value of $\sim$ 7 keV, but with larger error bars. Nevertheless, the physical `Synchrotron` model did not fit the spectrum well. However, it is still reasonable to check for the evolution of the magnetic field strength (B) obtained from fitting with the `Synchrotron` model. The evolution of B closely matches with the evolution of E_p, as shown in the lower panel of Figure 3. The electron energy distribution in the `synchrotron` model follows a PL with a PL index p. The parameter p is obtained from fitting the `synchrotron` model and is also showing a flux tracking evolution as shown in the lower right panel of Figure 3.

3.3. *Afterglow emission and the closure relations*

The observed X-ray and optical r-band LCs of GRB 230812B do not show any flare, plateau, or bump (see Figure 4). Both X-ray and r-band LCs were fitted with a simple PL obtaining temporal decay indices of $\alpha_x = -1.22^{+0.05}_{-0.05}$ and $\alpha_o = 1.08^{0.03}_{-0.03}$. Both X-ray and optical decay indices are consistent with each other within 3σ. In addition, the spectral indices $\beta_x = 0.68^{+0.08}_{-0.08}$ and $\beta_{ox} = 0.74^{0.01}_{0.01}$ obtained from the fitting of XRT spectra in 0.3-10 keV and combined optical r-band to X-ray SED are also consistent within 1σ. This indicates that both X-ray and optical emissions come from the same spectral regime. We checked the closure relation followed by the GRB external shock (Sari et al. 1998). We found that the optical and X-ray spectral and temporal indices satisfy the relation $\beta = \frac{p-1}{2}$ and $\alpha = \frac{3(p-1)}{4}$ in the spectral regime $\nu_m < \nu_o < \nu_x < \nu_c$ in the ISM-like surrounding medium.

Fermi-LAT data was not included in the Spectral Energy Distribution (SED) due to the absence of optical and X-ray observations during the *Fermi*-LAT detection. From *Fermi*-LAT temporal and spectral analysis we obtained decay indices of $\alpha_{LAT} = 1.04 \pm 0.08$ and β_{LAT} (Γ_{LAT}-1) $= 1.03^{+0.27}_{-0.23}$. The observed β_{LAT} is slightly steeper than β_o and β_x. The difference $\Delta\beta = \beta_{LAT}$-$\beta_x$ is 0.4 ± 0.3, which is consistent with the assumption that ν_c might lie between the X-ray and LAT observation in the ISM medium.

3.4. *Discussion*

3.5. *Afterglow LC comparison*

We compared the X-ray and optical afterglow LCs of GRB 230812B with a set of 15 SN-detected GRB from Kumar et al. (2022) in Figure 7. We found the *Swift*-XRT and optical r-band afterglow LC of GRB 230812B is consistent with other GRBs in the background and does not possess an exceptional bright afterglow or SN emissions. Even the optical and X-ray LC of GRB 230812B is relatively

VII Workshop on Robotic Autonomous Observatories (October 16-20, 2023)
Editors: Maria Gritsevich, Alberto J. Castro-Tirado, Petr Kubánek, Shashi B. Pandey, and David Hiriart - DOI: https://doi.org/10.22201/ia.14052059p.2025.59.22

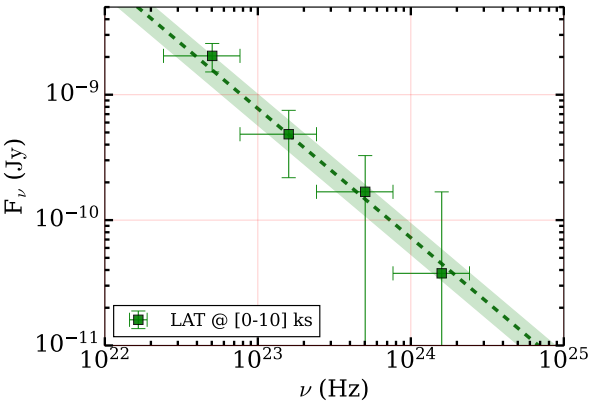


Fig. 5. Represents the fitting results of time average LAT spectra in the energy range 0.1-100 GeV

fainter than the bright bursts of GRB 130427A (Xu et al. 2013) and GRB 171010A (Kumar et al. 2022) at similar redshifts as shown in Figure 7. Our analysis concluded that the afterglow of GRB 230812B and its associated SN 2023pel (Hussenot-Desenonges et al. 2023; Srinivasaragavan et al. 2024) is an intermediate bright GRB/SN compared to other GRBs.

3.6. *Possible origin of GeV emission from* Fermi-*LAT*

The observed power-law decay of the LAT light curve and spectra indicate that the LAT emission originates from an external shock. However, unlike optical and X-ray observations, the emission mechanism of LAT-detected photons still needs to be completely clarified. According to Fraija et al. (2019), the maximum energy of photons from `synchrotron` external shock model can be 10 GeV $\times$ $(\Gamma_0/100)$ $\times$ $(1+z)^{-1}$. Where Γ_0 is the bulk Lorentz factor, and z is redshift. Considering the bulk Lorentz factor $\Gamma_0 = 315$, calculated it from the observed $E_{\gamma,iso}$ using the relation given in Liang et al. (2010). Using the above relations, we calculated that, in the case of GRB 230812B, the `Synchrotron` emission mechanism could only generate a maximum energy photon of 23 GeV, as shown with a red dotted line in the lower panel of the Figure 6. From the lower panel of Figure 6, it is clear that all photons lie below this level except for 72 GeV photons. Thus, the origin of the 72 GeV photons cannot be from `synchrotron` emission. This has been observed earlier for the VHE bursts (GRB 180720B, 190114C, 190829B, GRB 201015A, GRB 201216C: Fraija et al. 2019; MAGIC Collaboration et al. 2019; Fraija et al. 2021; H. E. S. S. Collaboration et al. 2021; Ror et al. 2023), where the observed VHE photons are explained via `synchrotron self Compton (SSC)` or

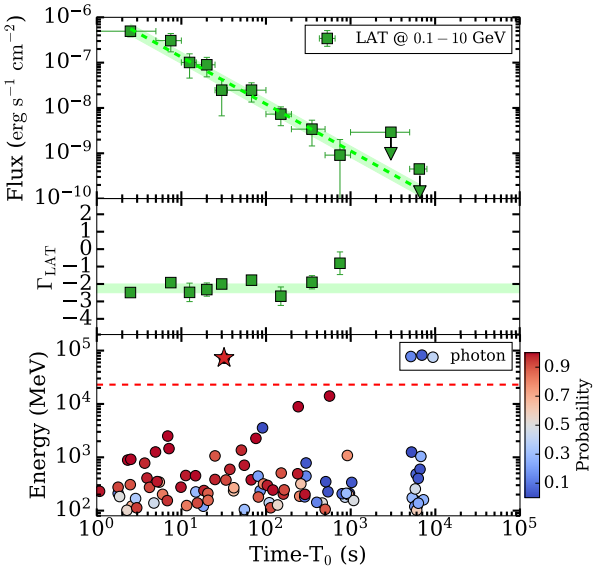


Fig. 6. Top panel: represents the *Fermi*-LAT LC of GRB 230812B in the energy range of 0.1-10 GeV. Squares denote the observed flux, and the dotted line represents the PL fitted to the LC. The shaded area represents the 1σ error associated with the fit. The middle panel represents the evolution of the photon index derived from the time-resolved fitting of LAT spectra. The bottom panel displays the temporal distribution of LAT-detected photons, with the color map indicating the probability of the photons being associated with GRB 230812B. The red star at 32 s represents the maximum energy photon of 72 GeV from *Fermi*-LAT. The red dotted line represents the maximum energy allowed by synchrotron emission for GRB 230812B.

external `Inverse Compton (IC)`. It is possible that the non-thermal photons from the prompt emission were Lorentz boosted by accelerated electrons in the external shock resulting in the observed LAT emission. This suggests that the `IC` and `SSC` are the potential emission mechanisms that could be responsible for the VHE 72 GeV photons observed from GRB 230812B.

3.7. *GRB 230812B compared with other S- and LGRBs*

The characteristics of GRB 230812B compared to the other burst from the IceCube[9] catalog are shown in the Figure 8. In the upper right panel of Figure 8, we compared the $E_{\gamma,iso}$ of redshift detected bursts. The observed $E_{\gamma,iso}$ of the bursts is found to correlate with the luminosity distance (D_L). We fitted a PL and found the relation: $\log_{10}(E_{\gamma,iso}) = (45.42 \pm 0.16) + (1.66 \pm 0.04) \times \log_{10}(D_L)$.

[9] `https://user-web.icecube.wisc.edu/~grbweb_public/Summary_table.html`

VII Workshop on Robotic Autonomous Observatories (October 16-20, 2023)
Editors: Maria Gritsevich, Alberto J. Castro-Tirado, Petr Kubánek, Shashi B. Pandey, and David Hiriart - DOI: https://doi.org/10.22201/ia.14052059p.2025.59.22

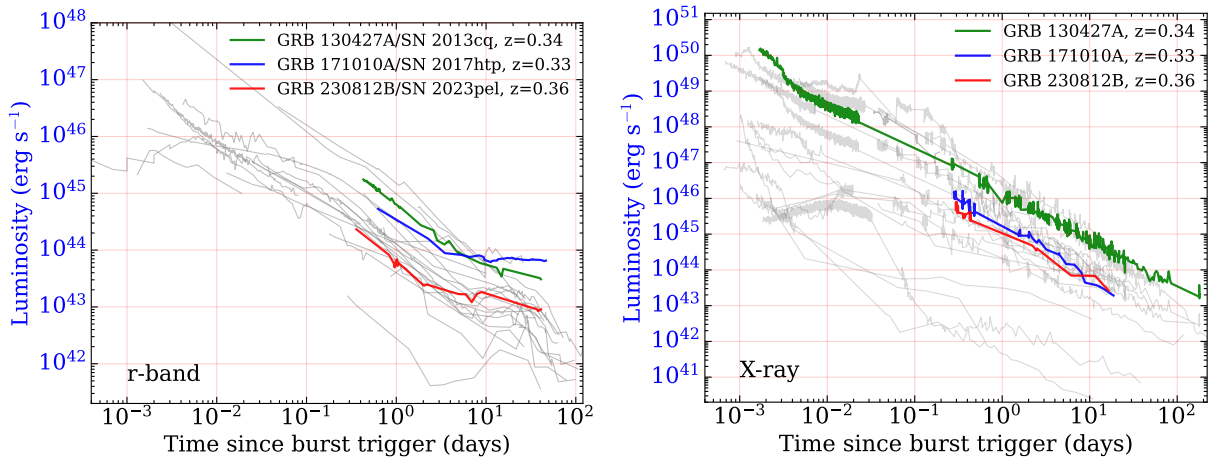


Fig. 7. A comparison of optical r-band (left) and *Swift*-XRT (right) luminosity LCs of GRB 130427A, GRB 171010A, and GRB 230812B (red) with other SN-detected bursts (grey) in the background, see Ror et al. (2023) for more details.

GRB 230812B, with the observed distance of 1.9 Gpc corresponding to the cosmological age of 9.75 Gyr, is inconsistent with the above relation. Along with GRB 130427A and GRB 171010A, GRB 230812B lies outside of the 5σ range of relations, as shown in Figure 8. This is due to its exceptionally high prompt emission brightness at z=0.36. Most of the other GRBs at this redshift are fainter than GRB 230812B, except for GRB 130427A and GRB 171010A. In the lower-left panel of Figure 8, we compared the observed fluence of GRB 230812B (red star), GRB 130427A and GRB 171010A along with other bursts from the IceCube catalog. GRB 230812B is the brightest burst with $T_{90} < 5$ s, and only slightly fainter than GRB 130427A and GRB 171010A at the similar redshift. This huge flux detected in such sort time scale is the possible region for observed pileup in *Fermi*-GBM. The lower right panel compares the E_p (i.e., Hardness) of the *Fermi*-GBM detected bursts. GRB 230812B is harder than the GRB 171010A and softer than the GRB 130427A at a similar redshift. GRB 230812B with $T_{90} > 2$ s lies around the dividing line of the population of SGRBs and LGRBs. However, based on the observed underlying SN and other observed properties, GRB 230812B is classified as a LGRB. Our analysis indicates that GRB 230812B is one of the brightest *Fermi*-GBM and LAT-detected LGRB with the hardest prompt spectra.

4. SUMMARY AND CONCLUSION

This work presents a detailed prompt and afterglow analysis of *Fermi*-LAT GRB 230812B. Due to its extreme brightness, the detecting instruments (*Fermi*-GBM) suffer a pileup in the time range [0.5-1.4] s, which we exclude from our analysis. The time-integrated spectral analysis showed that the spectrum in the *Fermi*-GBM energy range is the best fit by the `Band+BB` function. In addition to this, all the time-resolved spectra favour an additional thermal component along with a dominant non-thermal component. All of these findings indicate the hybrid (baryonic + magnetic) jet composition of the burst. Spectral parameter evolution from our time-resolved analysis showed that the low energy spectral index α crosses the slow and fast cooling limit imposed by the synchrotron emission mechanism. The evolution of α poses a challenge to linking the non-thermal prompt emission with pure synchrotron emission. In addition, both α and E_p were found to track the intensity of the burst throughout the prompt emission duration. The X-ray and optical LCs of this burst do not show any signature of late central engine activity (flare or plateau). Both X-ray and optical emissions are consistent with the closure relation in spectral regime $\nu_m < \nu_o < \nu_x < \nu_c$ in the ISM-like surrounding medium. The *Fermi*-LAT analysis showed that in the early stage (< 10 ks), the LAT spectral index $\beta_{\rm LAT}$ is harder than the $\beta_{\rm x}$, indicating that the LAT emission is coming from a different spectral regime or entirely different origin. With the assumption of synchrotron origin of the LAT photons, we calculated that the break frequency ν_c may lie or remain between the X-ray and LAT frequencies throughout the observations. However, the synchrotron emission mechanism is unable to explain the origin of the 72 GeV photons detected by LAT at $T_0 + 32s >> T_{90}$, i.e., during the afterglow phase. The most plausible explanation for the VHE-detected photons is IC or SSC boost-

VII Workshop on Robotic Autonomous Observatories (October 16-20, 2023)
Editors: Maria Gritsevich, Alberto J. Castro-Tirado, Petr Kubánek, Shashi B. Pandey, and David Hiriart - DOI: https://doi.org/10.22201/ia.14052059p.2025.59.22

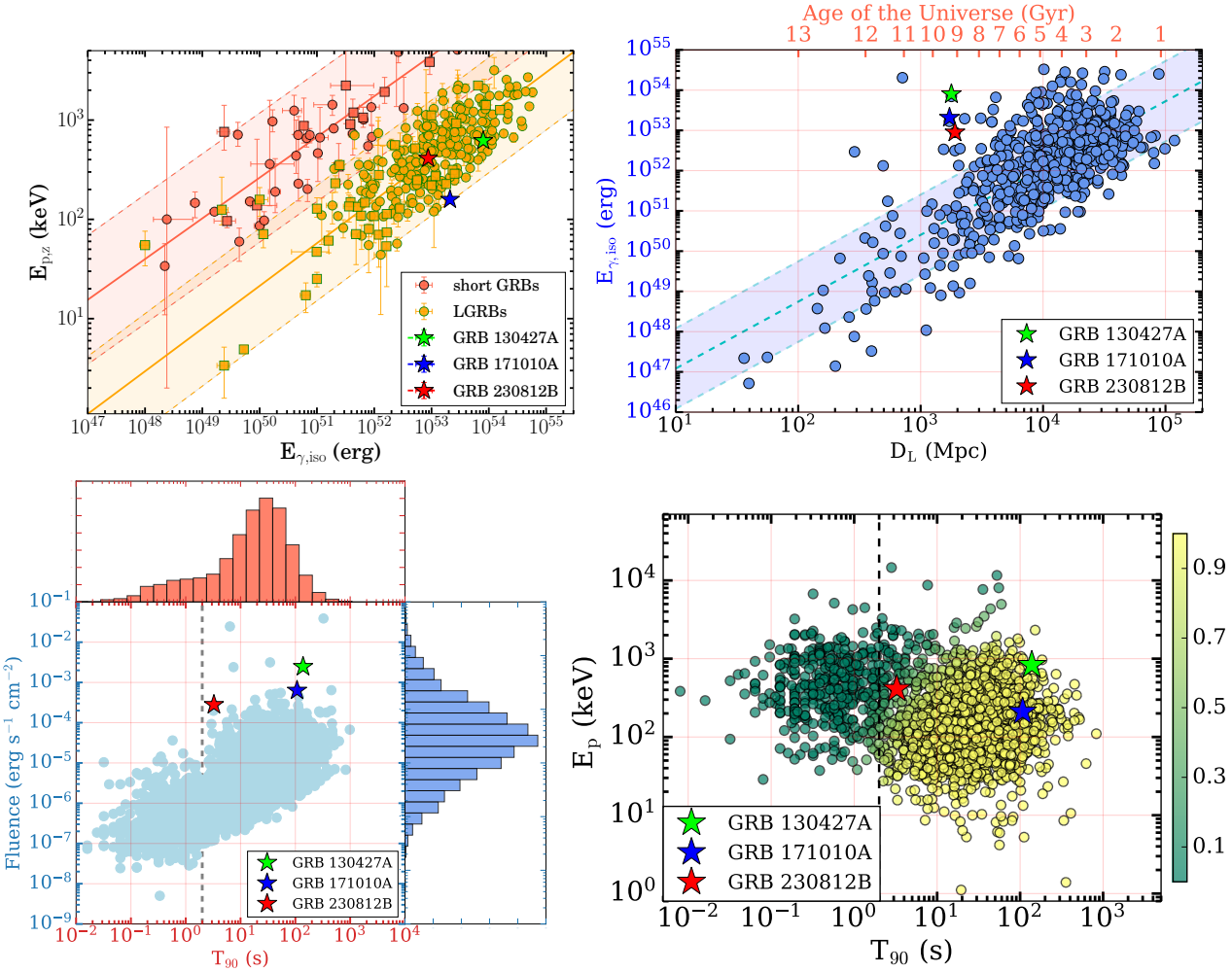


Fig. 8. Prompt emission characteristic of GRB 230812B compared with SN-detected GRB 130427A and GRB 171010A at similar redshift. Upper left panel: represents GRB 230812B in Amati correlation space (Amati 2006). Upper right panel: represents the $E_{\gamma,iso}$ distribution of GRBs plotted against the luminosity distance in Mpc and the universe's age in Gyr. Lower left panel: represents the fluence distribution of GRBs along with the T_{90} duration on the observer frame. Lower right panel: E_p in the observed frames plotted with the T_{90} duration. A vertical dashed line at 2s separates between SGRBs and LGRBs.

ing of prompt or early afterglow photons by the shock-accelerated electrons in the external medium. The comparison of X-ray and optical LCs of GRB 230812B with similar bursts (GRB 130427A and 171010A) revealed that, unlike the bright prompt emission, the afterglow of GRB 230812B was fainter than the other SN-detected GRBs at a similar E_p, $E_{\gamma,iso}$, and redshift. Moreover, previous studies have shown that low-redshift GeV-TeV detected GRBs, such as GRB 130427A and GRB 201015A, are associated with supernovae (Ror et al. 2023). This event further reinforces the idea that the association of low-redshift GeV-TeV detected GRBs with underlying supernovae is a common occurrence.

Acknowledgments: AKR is thankful to Dr. Rahul Gupta for his continuous support during the analysis and writing of the paper. SBP acknowledges the financial support of ISRO under the AstroSat archival data utilization program (DS_2B-13013(2)/1/2021-Sec.2). SBP also acknowledges support from DST grant no. DST/ICD/BRICS/Call-5/CoNMuTraMO/2023(G) for the present work. AA acknowledges funds and assistance provided by the Council of Scientific & Industrial Research (CSIR), India, under file no.

09/948(0003)/2020-EMR-I. AA also acknowledges the Yushan Young Fellow Program by the Ministry of Education, Taiwan, for financial support. AJCT acknowledges support from the Spanish Ministry projects PID2020-118491GB-I00 and PID2023-151905OB-I00 and Junta de Andalucía grant P20_010168. This research has used data obtained through the HEASARC Online Service, provided by the NASA-GSFC, in support of NASA High Energy Astrophysics Programs.

REFERENCES

Abbott, B. P., Abbott, R., Abbott, T. D., et al. 2017, ApJ, 848, L13, doi:10.3847/2041-8213/aa920c

Ackermann, M., Ajello, M., Asano, K., et al. 2014, Sci, 343, 42, doi:10.1126/science.1242353

Ahumada, T., Singer, L. P., Anand, S., et al. 2021, NatAs, 5, 917, doi:10.1038/s41550-021-01428-7

Amati, L. 2006, MNRAS, 372, 233, doi:10.1111/j.1365-2966.2006.10840.x

Arnaud, K. A. 1996, Astronomical Data Analysis Software and Systems V, 101, 17

Band, D., Matteson, J., Ford, L., et al. 1993, ApJ, 413, 281, doi:10.1086/172995

Barthelmy, S. D., Barbier, L. M., Cummings, J. R., et al. 2005, Space Sci. Rev., 120, 143, doi:10.1007/s11214-005-5096-3

Beardmore, A. P., Melandri, A., Sbarrato, T., et al. 2023, GRB Coordinates Network (GCN), Circular Service, No. 34400

Boër, M., Gendre, B., & Stratta, G. 2015, ApJ, 800, 16, doi:10.1088/0004-637X/800/1/16

Burgess, J. M. 2014, MNRAS, 445, 2589, doi:10.1093/mnras/stu1925

Burgess, J. M., Bégué, D., Greiner, J., et al. 2020, NatAs, 4, 174, doi:10.1038/s41550-019-0911-z

Caballero-García, M. D., Gupta, R., Pandey, S. B., et al. 2023, MNRAS, 519, 3201, doi:10.1093/mnras/stac3629

Castro-Tirado, A. J., Gupta, R., Pandey, S. B., et al. 2024, A&A, 683, A55, doi:10.1051/0004-6361/202346042

Casentini, C., Longo, F., Pittori, C., et al. 2023, GCN, Circular Service, No. 34402

de Ugarte Postigo, A., Agui Fernandez, J. F., Thoene, C. C., et al. 2023, GCN, Circular Service, No. 34409

de Ugarte Postigo, A., Horváth, I., Veres, P., et al. 2011, A&A, 525, A109, doi:10.1051/0004-6361/201015261

Evans, P. A. & Swift Team 2023, GCN, Circular Service, No. 34388

Evans, P. A., Beardmore, A. P., Page, K. L., et al. 2007, A&A, 469, 379, doi:10.1051/0004-6361:20077530

Evans, P. A., Beardmore, A. P., Page, K. L., et al. 2009, MNRAS, 397, 1177, doi:10.1111/j.1365-2966.2009.14913.x

Fermi GBM Team 2023, GCN, Circular Service, No. 34386

Fraija, N., Dichiara, S., Pedreira, A. C. C. do E. S., et al. 2019, ApJ, 879, L26, doi:10.3847/2041-8213/ab2ae4

Fraija, N., Veres, P., Beniamini, P., et al. 2021, ApJ, 918, 12, doi:10.3847/1538-4357/ac0aed

Frederiks, D., Lysenko, A., Ridnaia, A., et al. 2023, GCN, Circular Service, No. 34403

Galama, T. J., Vreeswijk, P. M., van Paradijs, J., et al. 1998, Natur, 395, 670, doi:10.1038/27150

Goldstein, A., William H. Cleveland et al. 2023, website: https://fermi.gsfc.nasa.gov/ssc/data/analysis/gbm

Golenetskii, S. V., Mazets, E. P., Aptekar, R. L., et al. 1983, Natur, 306, 451, doi:10.1038/306451a0

Gupta, R., Oates, S. R., Pandey, S. B., et al. 2021, MNRAS, 505, 4086, doi:10.1093/mnras/stab1573

Gupta, R., Pandey, S. B., Castro-Tirado, A. J., et al. 2021, RMxAC, 53, 113, doi:10.22201/ia.14052059p.2021.53.23

Gupta, R., Gupta, S., Chattopadhyay, T., et al. 2022, MNRAS, 511, 1694, doi:10.1093/mnras/stac015

Gupta, R., Kumar, A., Pandey, S. B., et al. 2022, ApA, 43, 11, doi:10.1007/s12036-021-09794-4

Gupta, R. 2023, arXiv:2312.16265, doi:10.48550/arXiv.2312.16265

Gupta, R., Pandey, S. B., Gupta, S., et al. 2024, ApJ, 972, 166, doi:10.3847/1538-4357/ad5a92

H. E. S. S. Collaboration, Abdalla, H., Aharonian, F., et al. 2021, Sci, 372, 1081, doi:10.1126/science.abe8560

Hjorth, J., Sollerman, J., Møller, P., et al. 2003, Natur, 423, 847, doi:10.1038/nature01750

Hussenot-Desenonges, T., Wouters, T., Guessoum, N., et al. 2023, arXiv:2310.14310, doi:10.48550/arXiv.2310.14310

Kaneko, Y., Preece, R. D., Briggs, M. S., et al. 2006, ApJS, 166, 298, doi:10.1086/505911

Kennea, J. A. & Swift Team 2023, GCN, Circular Service, No. 34393

Kouveliotou, C., Meegan, C. A., Fishman, G. J., et al. 1993, ApJ, 413, L101, doi:10.1086/186969

Kumar, A., Pandey, S. B., Gupta, R., et al. 2022, NewA, 97, 101889, doi:10.1016/j.newast.2022.101889

Kumar, P. & Zhang, B. 2015, Phys. Rep., 561, 1, doi:10.1016/j.physrep.2014.09.008

Liang, E.-W., Yi, S.-X., Zhang, J., et al. 2010, ApJ, 725, 2209, doi:10.1088/0004-637X/725/2/2209

Li, L., Ryde, F., Pe'er, A., et al. 2021, ApJS, 254, 35, doi:10.3847/1538-4365/abee2a

Lesage, S., Burns, E., Dalessi, S., et al. 2023, GCN, Circular Service, No. 34387

Levan, A., Gompertz, B. P., Salafia, O. S., et al. 2023, arXiv:2307.02098, doi:10.48550/arXiv.2307.02098

MAGIC Collaboration, Acciari, V. A., Ansoldi, S., et al. 2019, Natur, 575, 459. doi:10.1038/s41586-019-1754-6

Meegan, C., Lichti, G., Bhat, P. N., et al. 2009, ApJ, 702, 791, doi:10.1088/0004-637X/702/1/791

Mukherjee, S., Feigelson, E. D., Jogesh Babu, G., et al. 1998, ApJ, 508, 314, doi:10.1086/306386

Norris, J. P., Share, G. H., Messina, D. C., et al. 1986, ApJ, 301, 213, doi:10.1086/163889

VII Workshop on Robotic Autonomous Observatories (October 16-20, 2023)
Editors: Maria Gritsevich, Alberto J. Castro-Tirado, Petr Kubánek, Shashi B. Pandey, and David Hiriart - DOI: https://doi.org/10.22201/ia.14052059p.2025.59.22

Pandey, S. B., Kumar, A., Kumar, B., et al. 2021, MNRAS, 507, 1229, doi:10.1093/mnras/stab1889
Page, K. L. & Swift-XRT Team 2023, GCN, Circular Service, No. 34394
Pe'er, A. 2015, AdAst, 2015, 907321, doi:10.1155/2015/907321
Preece, R. D., Briggs, M. S., Mallozzi, R. S., et al. 2000, ApJS, 126, 19, doi:10.1086/313289
Roberts, O. J., Meegan, C., Lesage, S., et al. 2023, GCN, Circular Service, No. 34391
Roberts, O. J., Lesage, S., Cleveland, W., et al. 2023, GCN, Circular Service, No. 34694
Ror, A. K., Gupta, R., Jelínek, M., et al. 2023, ApJ, 942, 34, doi:10.3847/1538-4357/aca414
Ror, A. K., Gupta, R., Aryan, A., et al. 2024, ApJ, 971, 163, doi:10.3847/1538-4357/ad5554
Ror, A. K., Bhushan Pandey, S., Gupta, R., et al. 2024, BSRSL, 93, 709, doi:10.25518/0037-9565.11848
Sari, R., Piran, T., & Narayan, R. 1998, ApJ, 497, L17, doi:10.1086/311269
Scargle, J. D., Norris, J. P., Jackson, B., et al. 2013, ApJ, 764, 167, doi:10.1088/0004-637X/764/2/167
Scotton, L., Kocevski, D., Racusin, J., et al. 2023, GCN, Circular Service, No. 34392
Srinivasaragavan, G. P., Swain, V., O'Connor, B., et al. 2024, ApJ, 960, L18, doi:10.3847/2041-8213/ad16e7
Troja, E., Fryer, C. L., O'Connor, B., et al. 2022, Natur, 612, 228, doi:10.1038/s41586-022-05327-3
Vianello, G., Lauer, R. J., Younk, P., et al. 2015, arXiv:1507.08343, doi:10.48550/arXiv.1507.08343
Vianello, G., Gill, R., Granot, J., et al. 2018, ApJ, 864, 163, doi:10.3847/1538-4357/aad6ea
Wang, W.-K., Xie, W., Gao, Z.-F., et al. 2024, RAA, 24, 025006, doi:10.1088/1674-4527/ad16af
Wang, C.-Y., Yin, Y.-H. I., Zhang, B.-B., et al. 2024, arXiv:2409.12613
Xiong, S., Liu, J., Huang, Y., et al. 2023, GCN, Circular Service, No. 34401
Xu, D., de Ugarte Postigo, A., Leloudas, G., et al. 2013, ApJ, 776, 98, doi:10.1088/0004-637X/776/2/98
Zhang, B.-B., Zhang, B., Castro-Tirado, A. J., et al. 2018, NatAs, 2, 69, doi:10.1038/s41550-017-0309-8

VII Workshop on Robotic Autonomous Observatories (October 16-20, 2023)
Editors: Maria Gritsevich, Alberto J. Castro-Tirado, Petr Kubánek, Shashi B. Pandey, and David Hiriart - DOI: https://doi.org/10.22201/ia.14052059p.2025.59.22

Revista Mexicana de Astronomía y Astrofísica Serie de Conferencias (RMxAC), **59**, 145–152 (2025)
© 2025: Instituto de Astronomía, Universidad Nacional Autónoma de México
https://doi.org/10.22201/ia.14052059p.2025.59.23

VII Workshop on Robotic Autonomous Observatories (October 16-20, 2023)
Editors: Maria Gritsevich, Alberto J. Castro-Tirado, Petr Kubánek, Shashi B. Pandey, and David Hiriart - DOI: https://doi.org/10.22201/ia.14052059p.2025.59.23

THE CORE COLLAPSE OF A 16.5 $M_\odot$ STAR

Amar Aryan[1,2], Shashi Bhushan Pandey[1], Rahul Gupta[1,3,4], Amit Kumar Ror[1], and A. J. Castro-Tirado[5,6]

RESUMEN

Investigamos la evolución estelar 1D de una estrella de secuencia principal de edad cero de 16,5 $M_\odot$ que tiene diferentes rotaciones iniciales. A partir de la secuencia previa a la principal, los modelos evolucionan hasta el inicio de la etapa de colapso del núcleo. El colapso de una estrella tan masiva puede dar lugar a varios tipos de fuentes transitorias de alta energía, como explosiones de rayos gamma (GRB), supernovas, etc. Utilizando los parámetros de la simulación, calculamos sus escalas de tiempo de caída libre cuando los modelos alcanzan la etapa de inicio del colapso del núcleo. Estimar la escala de tiempo de caída libre es crucial para comprender la duración durante la cual se puede alimentar el motor central, lo que nos permite comparar la escala de tiempo de caída libre con la duración T_{90} de los GRB. Nuestros resultados indican que, dadas las limitaciones de los parámetros y las condiciones iniciales en nuestros modelos, las estrellas masivas que giran rápidamente podrían servir como progenitores potenciales de GRB ultralargos ($T_{90} >> 500$ s). Por el contrario, los modelos en los cuales los progenitores no giran o que giran lentamente son más propensos a que se produzcan supernovas de colapso del núcleo de clase IIP que son ricas en hidrógeno.

ABSTRACT

We investigate the 1D stellar evolution of a 16.5 $M_\odot$ zero-age main-sequence star having different initial rotations. Starting from the pre-main-sequence, the models evolve up to the onset of the core collapse stage. The collapse of such a massive star can result in several kinds of energetic transients, such as Gamma-Ray Bursts (GRBs), Supernovae, etc. Using the simulation parameters, we calculate their free-fall timescales when the models reach the stage of the onset of core collapse. Estimating the free-fall timescale is crucial for understanding the duration for which the central engine can be fueled, allowing us to compare the free-fall timescale with the T_{90} duration of GRBs. Our results indicate that, given the constraints of the parameters and initial conditions in our models, rapidly rotating massive stars might serve as potential progenitors of Ultra-Long GRBs ($T_{90} >> 500$ s). In contrast, the non-rotating or slowly rotating models are more prone to explode as hydrogen-rich Type IIP-like core-collapse supernovae.

Key Words: Simulation tools: MESA — Simulation tools: STELLA — Stars: Zero-age Main-sequence — Stars: Collapsing — Transients: Gamma-Ray Bursts — Transients: Core-collapse Supernovae

1. INTRODUCTION

The core collapse of massive stars could result in several classes of transients. Usually, the collapse of massive stars having initial masses $\gtrsim 8\,M_\odot$ produces the catastrophic transient phenomena known as core-collapse supernovae (CCSNe; for review, please see Woosley & Weaver 1986; Gilmore 2004; Woosley & Janka 2005, etc.); however, the association of SN component with a few long gamma-ray bursts (LGRBs; for review on SN-GRB connection, please see Bloom et al. 1999; Woosley & Bloom 2006; Modjaz et al. 2016, etc.) have opened new avenues of transients resulting from the collapse of massive stars. Such identified connections of SN and GRB have indicated that a fraction of GRBs come from the collapse of massive stars (Cano et al. 2017). In recent years, observational technologies and theoretical modeling advancements have significantly enhanced our understanding of the evolution of massive stars as the progenitors of CCSNe and a special class of GRBs. The detection of SN progenitors in high-resolution pre-explosion images has enabled us to put important constraints over the evolution and terminating phases of massive stars (Smartt 2015; Van Dyk 2017). Besides the direct detection of pro-

[1]Aryabhatta Research Institute of Observational Sciences (ARIES), Manora Peak, Nainital-263002, India.
[2]Graduate Institute of Astronomy, National Central University, 300 Jhongda Road, 32001 Jhongli, Taiwan.
[3]Astrophysics Science Division, NASA Goddard Space Flight Center, Mail Code 661, Greenbelt, MD 20771, USA.
[4]NASA Postdoctoral Program Fellow.
[5]Instituto de Astrofísica de Andalucía (IAA-CSIC), Glorieta de la Astronomía s/n, E-18008, Granada, Spain.
[6]Departamento de Ingeniería de Sistemas y Automática, Unidad Asociada al CSIC por el IAA, Escuela de Ingeniería Industrial, Universidad de Málaga, C. Dr. Ortiz Ramos s/n, 29071 Málaga, Spain.

VII Workshop on Robotic Autonomous Observatories (October 16-20, 2023)
Editors: Maria Gritsevich, Alberto J. Castro-Tirado, Petr Kubánek, Shashi B. Pandey, and David Hiriart - DOI: https://doi.org/10.22201/ia.14052059p.2025.59.23

genitors in pre-explosion images, serious simulations have been conducted to constrain the properties of massive star evolution. In their simulations, Perna et al. (2018) employed stars with the masses of 30 $M_\odot$ and 40 $M_\odot$ under various initial rotation conditions. Their research revealed that moderately rotating massive stars could conclude their evolution as BSG, capable of launching ultra-relativistic jets to power ULGRBs. Furthermore, Song & Liu (2023) extensively explored the effects of initial mass, metallicity, and rotation on magnetar formation, which could serve as the central engine to power the GRBs. In a very recent study, Ror et al. (2024) studied the evolution of massive stars having initial mass in the range of 15–30 $M_\odot$ to constrain the properties of ULGRB progenitors.

The lower mass limit for typical LGRB progenitors, as suggested by Larsson et al. (2007), is close to 20 $M_\odot$. However, modeling results from Perna et al. (2018) identified BSG stars as ULGRB progenitors, with a standard mass of 15 $M_\odot$ (Dessart & Hillier 2018). Following these studies, the lower limit of mass for a progenitor to produce a GRB could lie in the range of 15–20 $M_\odot$. Supported by this mass range, we choose a 16.5 $M_\odot$ zero-age main-sequence (ZAMS) star and investigate its entire evolution on HR diagram. Based on the minimum mass limits to produce a CCSN or an LGRB, a star with an initial mass of 16.5 $M_\odot$ capable of producing both, a CCSN or an LGRB, depending upon the initial rotation and metallicity. We are also slightly biased to choose a 16.5 $M_\odot$ because one of our nearby Red supergiant (RSG) in the Orion constellation, Betelgeuse, has a similar mass (Joyce et al. 2020).

The entire manuscript is structured as follow; in § 1, we provide a broad overview of the current progress in the massive star evolutions and the motivation behind selecting a 16.5 $M_\odot$ ZAMS star for the present study. In § 2, we provide the details of the numerical setups to evolve the various non-rotating and rotating models up to the core collapse stage. In § 3, we present a broad discussion on the physical properties of models under concern. § 4 presents the details of the collapse of rapidly rotating models and the comparison of their properties with the actual observables of ULGRBs; additionally, the CCSNe resulting from the core-collapse of non/slowly rotating models are also discussed in this section. Finally, in § 5, we provide a brief discussion and major outcomes of the present study.

2. CORE COLLAPSE OF THE 16.5 $M_\odot$ STAR: NUMERICAL SETUPS

In this section, we highlight the specific numerical setups for the simulation of a 16.5 $M_\odot$ ZAMS mass star model having different initial rotations utilizing the state-of-the-art, 1D stellar evolution tool, the Modules for Experiments in Stellar Astrophysics `MESA` of version 23.05. (Paxton et al. 2011, 2013, 2015, 2018, 2019; Jermyn et al. 2023). To evolve the models from their pre-main-sequence (PMS) stages up to the stage of the onset of core collapse, we utilize the `20M_pre_ms_to_core_collapse test_suit` directory. We choose the initial conditions for the models considering various characteristics of exploding stars outlined in literature (Farmer et al. 2016; Perna et al. 2018; Paxton et al. 2018; Aguilera-Dena et al. 2018; Song & Liu 2023).

The variety of `MESA` parameters in this study to evolve our models up to the onset of core collapse stage, closely follow the `MESA` settings employed in our earlier studies (Aryan et al. 2021, 2022a; Pandey et al. 2021; Aryan et al. 2022b,c, 2023a; Ror et al. 2024). However, we mention a few important modifications ahead. The stellar models in our study have the same ZAMS mass of 16.5 $M_\odot$. We employ the metallicity (Z) of 2×10^{-4} for each model (except the one with solar metallicity) in our study, which is favored by host galaxy observations of LGRBs (Le Floc'h et al. 2003; Mannucci et al. 2011; Gupta et al. 2022). Starting from the non-rotating model, we change the initial angular rotational velocity (Ω) in steps of 0.1 Ω_c till 0.7 Ω_c. Here, Ω_c is the critical angular rotational velocity expressed as:

$$\Omega_c^2 = (1 - \frac{L}{L_{edd}})\frac{GM}{R^3} \quad (1)$$

with L_{edd} representing the Eddington luminosity in the above equation (please see Paxton et al. 2011, 2013 for details on how `MESA` implements rotation).

We apply the Ledoux criterion and model convection using the mixing length theory introduced by Henyey et al. (1965), with a fixed mixing length parameter, α_{MLT} of 2.0. To account for semiconvection, we set the semiconvection coefficient, α_{sc} to 0.01, following the approach of Langer et al. (1985). Thermohaline mixing is incorporated based on the formulation given by Kippenhahn et al. (1980), using the efficiency parameter, α_{th} of 2.0 till the stage of the core-He exhaustion and 0 thereafter, as employed in the default `20M_pre_ms_to_core_collapse test_suit` directory of `MESA`. Convective overshooting is modeled using parameters, $f_{ov} = 0.005$ and $f_0 = 0.001$, following Herwig (2000), consistent with

VII Workshop on Robotic Autonomous Observatories (October 16-20, 2023)
Editors: Maria Gritsevich, Alberto J. Castro-Tirado, Petr Kubánek, Shashi B. Pandey, and David Hiriart - DOI: https://doi.org/10.22201/ia.14052059p.2025.59.23

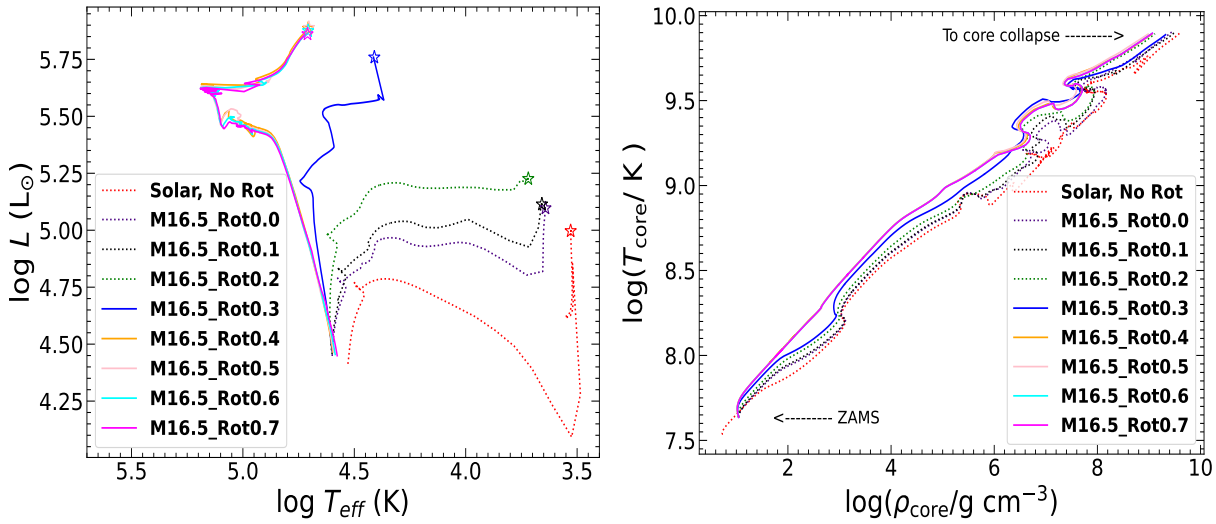


Fig. 1. *Left:* The evolution of our models on the HR diagram. The non/slow rotating models (Rot0.0, Rot0.1, and Rot0.2) have relatively smaller luminosity, and they are also relatively cooler compared to the faster rotating models when they are at the stage of the onset of core collapse (marked with ⋆). The non-rotating solar metallicity model is also shown for comparison purposes. *Right:* The evolution of core-temperature and core-density, as the models evolve in time and reach the stage of the onset of core collapse.

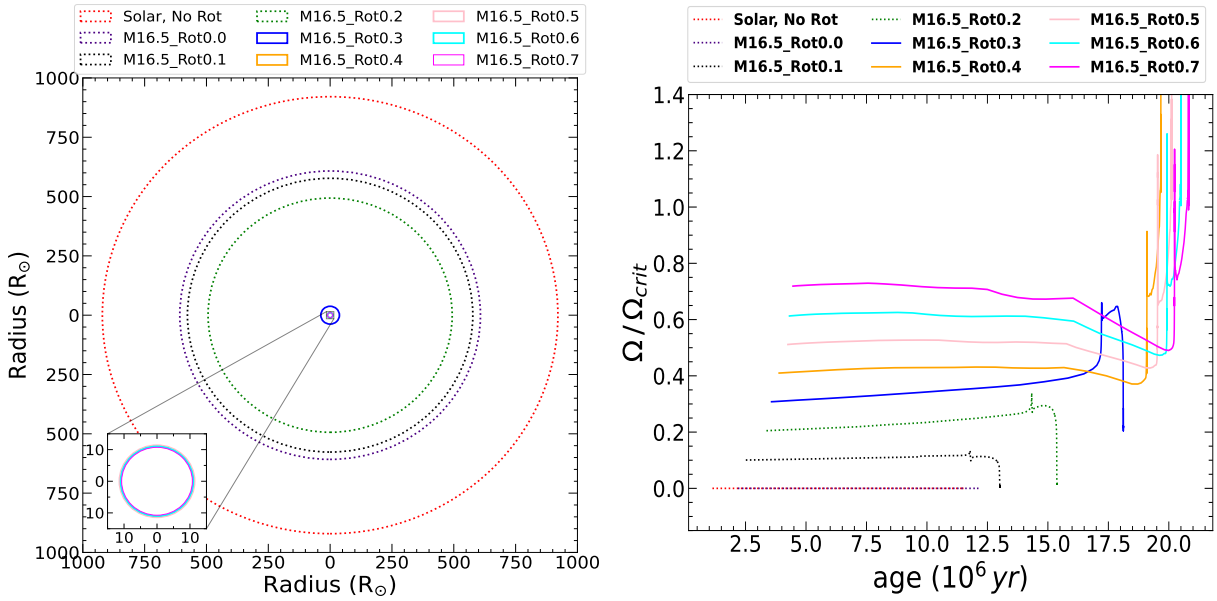


Fig. 2. *Left:* The size of our models when they have arrived at the onset of core collapse. The rapidly rotating models are relatively more compact than the non/slow rotating models. *Right:* The variation of the rotational velocity throughout the course of the evolution of the models from the MS up to the stage of the onset of core collapse. The rapidly rotating models (except the model with Rot0.3) exceed their critical rotational velocity limits during the last stages of their evolution.

prior studies like Farmer et al. (2016) and Aryan et al. (2023b). The 'Dutch' wind scheme, with a wind scaling factor ($\eta_{\rm wind}$) of 0.5, is employed to incorporate wind effects, aligning with previous works

VII Workshop on Robotic Autonomous Observatories (October 16-20, 2023)
Editors: Maria Gritsevich, Alberto J. Castro-Tirado, Petr Kubánek, Shashi B. Pandey, and David Hiriart - DOI: https://doi.org/10.22201/ia.14052059p.2025.59.23

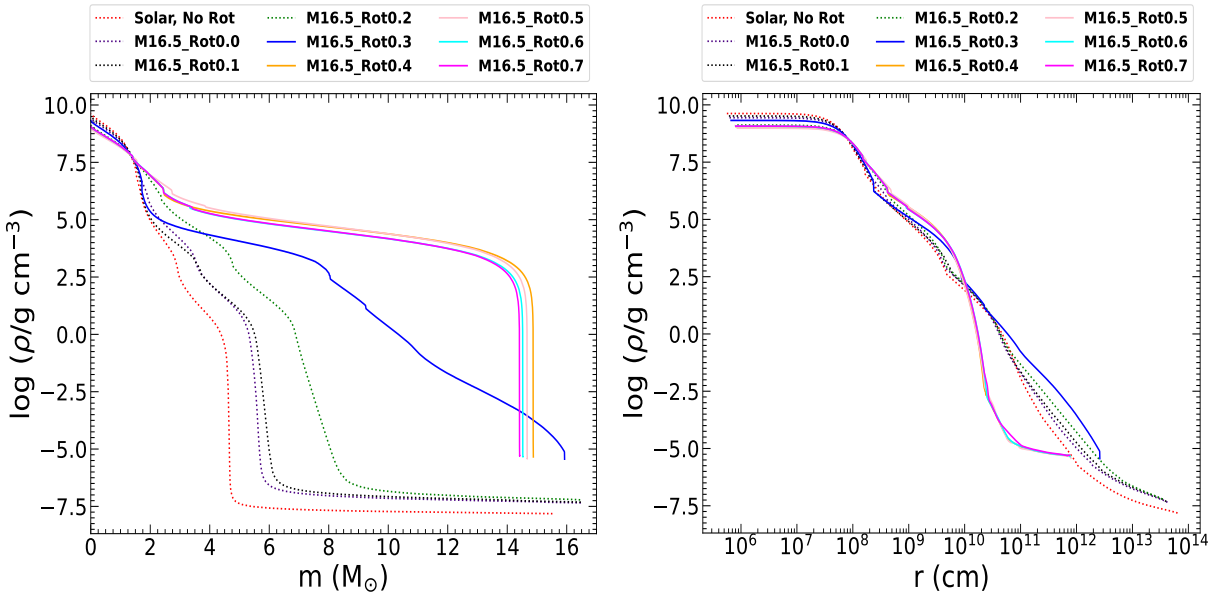


Fig. 3. *Left:* The progenitor mass density profile of the models as a function of mass coordinate. Beyond the inner cores, the rapidly rotating models maintain a relatively higher density than the slow-rotating models. *Right:* The progenitor mass density profile of the models as a function of radius. The rapidly rotating models appear to maintain more compactness than the slow-rotating models; both of these profiles have been derived when all the models have reached the stage of the onset of core collapse.

such as Perna et al. (2018), Aguilera-Dena et al. (2018), and Song & Liu (2023). A summary of some initial parameters can be found in Table 1.

3. CORE COLLAPSE OF THE 16.5 $M_\odot$ STAR: PHYSICAL PROPERTIES

With the above-mentioned `MESA` settings of initial parameters, we evolve all the models from PMS up to the stage of the onset of core collapse. Following the default `MESA` settings, the arrival of a model on ZAMS is marked at a stage when the ratio of the luminosity from nuclear reactions and the overall luminosity of the model becomes 0.4. Further, the beginning of the core collapse of the model is marked when the infall velocity of its Iron-core exceeds a limit of 100 $\mathrm{km\,s^{-1}}$. The left panel of Figure 1 illustrates the evolutionary trajectory of the models in the current study on the HR diagram. Owing to the low initial metallicity, rotation, and a moderate wind scaling factor ($\eta_{\rm wind}$=0.5), the rapidly rotating models (with $\Omega \geq 0.3\,\Omega_{\rm c}$) terminate their evolution towards the relatively hotter end on the HR diagram in comparison to the slowly rotating models. The final temperatures of rapidly rotating models and their corresponding positions on HR diagram are more consistent with Blue supergiant (BSG) stars ($\Omega = 0.3\,\Omega_{\rm c}$) or stripped Wolf-Rayet (WR) stars (models with $\Omega > 0.3\,\Omega_{\rm c}$). On the other hand, the positions of the slowly rotating models on HR diagram are consistent with the locations of RSG stars ($\Omega < 0.3\,\Omega_{\rm c}$). The right panel of Figure 1 shows the variation of the core-temperature, $\log(T_{\rm core}/{\rm K})$ and the core-density, $\log(\rho_{\rm core}/{\rm g\ cm^{-3}})$ as the models pass through the various stages of their evolution starting from main-sequence (MS) upto the onset of core collapse. During the last evolutionary stages, the models seem to exceed the $\log(T_{\rm core}/{\rm K})$ of 9.9 and corresponding $\log(\rho_{\rm core}/{\rm g\ cm^{-3}})$ of 9. Such high temperatures and densities of the cores are considered ideal conditions for stars to collapse under their own gravity.

The left panel of Figure 2 displays the final radii of our models at the stage of the onset of core collapse. The rapidly rotating models are quite compact having final radii of 10 $R_\odot$ (models with $\Omega > 0.3\,\Omega_{\rm c}$) or a few 10 $R_\odot$ (the model with $\Omega = 0.3\,\Omega_{\rm c}$). On the other hand, the non/slowly rotating models are enormous, having final radii of several 100 $R_\odot$. The non-rotating solar metallicity model is much bigger than the low metallicity models. For a given mass and other simulation parameters, the radius decreases with a corresponding decline in metallicity due to the competing effects of compressional heating and radiative cooling (for details, please see Kasen & Woosley 2009). These final sizes of the rapidly rotating and non/slowly rotating

VII Workshop on Robotic Autonomous Observatories (October 16-20, 2023)
Editors: Maria Gritsevich, Alberto J. Castro-Tirado, Petr Kubánek, Shashi B. Pandey, and David Hiriart - DOI: https://doi.org/10.22201/ia.14052059p.2025.59.23

TABLE 1

SUMMARY OF THE INITIAL AND FINAL PARAMETERS EMPLOYED IN AND DERIVED FROM MESA CODE

Ω/Ω_c	M_{final} ($M_\odot$)	R_{final} ($R_\odot$)	$M_{Fe-core}$ ($M_\odot$)	log(T_{eff}) (K)	Log (L) ($L_\odot$)	t_{ff} (s)	t_b (s)
0.0	16.474	607.8	1.539	3.644	5.097	1385926.3	141.8
0.1	16.475	577.0	1.490	3.659	5.115	1281711.9	134.6
0.2	16.452	493.6	1.733	3.721	5.226	1014838.8	115.1
0.3	15.928	37.6	1.501	4.414	5.759	21663.6	8.8
0.4	14.878	11.2	1.937	4.708	5.885	3636.7	2.6
0.5	14.674	11.4	1.923	4.705	5.890	3773.7	2.7
0.6	14.528	11.0	1.840	4.709	5.875	3600.7	2.6
0.7	14.418	10.7	1.899	4.712	5.865	3477.0	2.5
Solar, No Rot							
0.0	15.519	921.0	1.520	3.529	4.998	2663287.0	214.8

Note: Starting from the PMS phase, these models evolve until they arrive at the onset of core collapse stage. Here, M_{ZAMS} represents the model's mass at ZAMS, while Ω/Ω_c is the ratio between initial angular rotational velocity and critical angular rotational velocity at ZAMS. Moreover, M_{final} denotes the final mass, R_{final} indicates the final radius, $M_{Fe-core}$ represents the mass of the iron core, T_{eff} denotes the effective temperature, and L stands for the corresponding luminosity of the model at the onset of core collapse. Additionally, t_{ff} and t_b refer to the free-fall time of the model and the bore time of the weak jet, respectively.

models are seemingly governed by the corresponding mass losses they suffer during their late evolutionary stages. As evident from the right panel of Figure 2, the rapidly rotating models either exceed their critical angular rotational velocities (model with $\Omega > 0.3\,\Omega_c$) or their angular rotational velocities become much higher than initial values (model with $\Omega = 0.3\,\Omega_c$). As a result, they suffer enormous mass loss, which almost completely strips off their outer hydrogen envelope, or a significant amount of their outer hydrogen envelope is lost (Aryan et al. 2023b; Ror et al. 2024). As a result, the corresponding final models are relatively much more compact when compared to the non/slowly rotating models, which have their outer hydrogen envelope (almost) intact.

Figure 3 illustrates the density profiles of the models as a function of their mass coordinates (left panel) and their radii (right panel) at the stage of the onset of core collapse. As seen in the left panel, the rapidly rotating models ($\Omega \geq 0.3\,\Omega_c$) have slightly smaller densities near the core when compared to non/slowly rotating models, however, as we move towards the surface, the rapidly rotating models maintain an overall higher density profile than the non/slowly rotating models. The reason for the non/slowly rotating models having an overall shallow density profile compared to rapidly rotating models can be attributed to their large hydrogen envelope. Moreover, the right panel shows that the rapidly rotating models have relatively higher densities and smaller final radii, which in turn implies that they are compact.

4. CORE COLLAPSE OF THE 16.5 $M_\odot$ STAR

4.1. *As the Progenitors of Ultra-long GRBs*

Using the simulation parameters of the models at the onset of core collapse, we calculate the free fall timescales (t_{ff}) by applying Equation 1 from Perna et al. (2018). The t_{ff} for each model is detailed in Table 1. Estimating t_{ff} is crucial for understanding how long the central engine can be powered, enabling its comparison with the T_{90} duration of GRBs. In a recent study by Song & Zhang (2023), a two-stage model for GRB 221009A is proposed, linking the precursor pulse with the weak jet resulting from the core collapse of massive stars. Therefore, we also calculate the bore-time (t_b) of the weak jet for each of the models to estimate the duration of the precursor pulse. The t_b for each model is estimated utilizing a simple equation given in Ror et al. (2024):

$$t_b = \frac{R_{final}}{(u\Gamma)} \tag{2}$$

In the equation above, u represents the weak jet velocity corresponding to a Lorentz factor of Γ. Including Γ in the denominator accounts for relativistic length contraction. When calculating t_b using Equation 2, we simplify by assuming the weak jet moves with a constant Γ of 10. This choice is also supported by the analysis of Song & Zhang (2023)

VII Workshop on Robotic Autonomous Observatories (October 16-20, 2023)
Editors: Maria Gritsevich, Alberto J. Castro-Tirado, Petr Kubánek, Shashi B. Pandey, and David Hiriart - DOI: https://doi.org/10.22201/ia.14052059p.2025.59.23

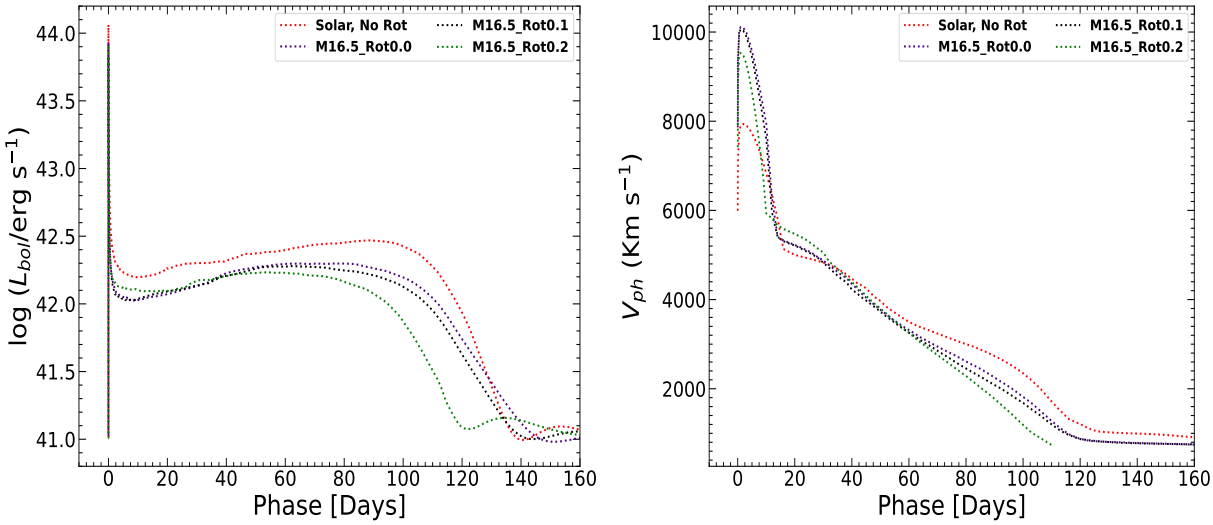


Fig. 4. *Left:* The bolometric light curve of of CCSNe resulting from the explosion of slow rotating models. These light curves are identical to the Type IIP SNe light curve. *Right:* The corresponding photospheric velocity evolution. Once again, the photospheric velocity evolutions follow the trends of Type IIP SNe. The early and plateau phases luminosities of such SNe are well suitable to be observed by the BOOTES network of telescopes (Castro-Tirado et al. 1999; Hu et al. 2023).

and Ror et al. (2024). With these assumptions, the estimated t_b for each model is presented in Table 1.

Now, we compare the t_{ff} derived from our simulation parameters with the T_{90} duration of a few actual ULGRBs selected out of the Gold sample listed in Table A1 of Ror et al. (2024). The `M_16.5_Rot0.3` model (having 16.5 $M_\odot$ of ZAMS mass and $\Omega = 0.3\,\Omega_c$) exhibits a t_{ff} of approximately 21600 s, which closely aligns with the T_{90} duration of GRB 111209A ($T_{90} \sim 18200$s). Similarly, the `M_16.5_Rot0.5` model displays a t_{ff} of around 3800 s, close to the T_{90} duration of GRB 090404 ($T_{90} \sim 4500$s). Furthermore, the t_{ff} values obtained from the rapidly rotating models in our current study are of a comparable order when contrasted with the actual T_{90} duration of the Gold sample of ULGRBs presented in Ror et al. (2024).

As discussed in earlier sections, the non/slowly rotating models have large final radii (R_{final}) at their terminating stage, moreover, their positions on HR diagram are consistent with massive RSG stars. The models terminating their evolution as RSGs cease to serve as the progenitors for the GRBs/ULGRBs since their enormous final radii ($>$ several 100 $R_\odot$, Table 1) do not allow successful penetration of the jet. Rather, the non/slowly rotating models are more prone to explode as CCSNe. In the next section, we investigate the properties when the non/slowly rotating models explode as CCSNe.

4.2. *As the Progenitors of CCSNe*

As mentioned, the parameters of non/slowly rotating models conflict for them to be the progenitors of ULGRBs; however, their core collapse can result in catastrophic CCSNe. To simulate their synthetic explosions for generating the bolometric light curves and corresponding photospheric velocity (V_{ph}) evolutions, we utilize a combination of `MESA` and `STELLA` (Blinnikov et al. 1998; Blinnikov & Sorokina 2004; Baklanov et al. 2005; Blinnikov et al. 2006) following the process described by Paxton et al. (2018, in section 6). We utilize a nickel mass of 0.032 $M_\odot$ and an explosion energy of 1.0×10^{51} for all the non/slowly rotating models. The choice of considered nickel mass and explosion energy are backed by Anderson (2019, for nickel mass) and Nadyozhin (2003, for explosion energy).

The left panel of Figure 4 shows the light curves of CCSNe resulting from the explosion of non/slowly rotating models. The light curves show plateaus similar to the Type IIP CCSNe. The right panel of Figure 4 shows the corresponding photospheric velocity evolution of the models. Since these models have retained almost all of their outer hydrogen envelope, their light curves and photospheric velocity evolution are similar to Type IIP CCSNe.

5. DISCUSSION AND CONCLUSIONS

In this work, we investigated the evolution of a 16.5 $M_\odot$ ZAMS star with different initial rotations.

VII Workshop on Robotic Autonomous Observatories (October 16-20, 2023)
Editors: Maria Gritsevich, Alberto J. Castro-Tirado, Petr Kubánek, Shashi B. Pandey, and David Hiriart - DOI: https://doi.org/10.22201/ia.14052059p.2025.59.23

Starting from the PMS, the models evolved until they arrived at the onset of core collapse. The physical properties of the models were then utilized to constrain whether they could serve as the progenitors of ULGRBs or CCSNe. Enumerated below were the findings from our analysis:

1. The rapidly rotating models suffered significantly higher mass loss than the non/slowly rotating models. We noticed that the angular rotational velocities of rapidly rotating models exceeded their corresponding critical angular rotational velocities, resulting in enormous mass loss during the late evolutionary stages.

2. The physical properties of rapidly rotating models were consistent with the BSG and WR stars. The comparison of their t_{ff} with the T_{90} durations of ULGRBs mentioned in Ror et al. (2024) showed close resemblances. As an example, the t_{ff} duration for `M16.5_Rot0.5` was found to be close to the T_{90} duration of GRB 111209A. The rest of the rapidly rotating models also showed the t_{ff} timescales having similar orders as the T_{90} durations of several ULGRBs. Thus, the rapidly rotating models could serve as the progenitors of ULGRBs.

3. The physical properties of non/slowly rotating models were consistent with RGS stars. Their final radii were too high for them to be ULGRB progenitors. Rather, these non/slowly rotating models could explode as CCSNe, and the resulting light curves resembled the light curves of hydrogen-rich Type IIP SNe.

Acknowledgements: AA acknowledges funds and assistance provided by the Council of Scientific & Industrial Research (CSIR), India, under file no. 09/948(0003)/2020-EMR-I. AA also acknowledges the Yushan Fellow Program by the Ministry of Education, Taiwan for the financial support (MOE-111-YSFMS-0008-001-P1). RG and SBP acknowledge the financial support of ISRO under AstroSat archival Data utilization program (DS_2B-13013(2)/1/2021-Sec.2). AA, SBP, RG and AKR acknowledge support from DST grant no. DST/ICD/BRICS/Call-5/CoNMuTraMO/2023(G) for the present work. AJCT acknowledges support from the Spanish Ministry projects PID2020-118491GB-I00 and PID2023-151905OB-I00 and Junta de Andalucía grant P20_010168 and from the Severo Ochoa grant CEX2021-001131-S funded by MCIN/AEI/10.13039/501100011033. RG was sponsored by the National Aeronautics and Space Administration (NASA) through a contract with ORAU. The views and conclusions contained in this document are those of the authors and should not be interpreted as representing the official policies, either expressed or implied, of the National Aeronautics and Space Administration (NASA) or the U.S. Government. The U.S. Government is authorized to reproduce and distribute reprints for Government purposes, notwithstanding any copyright notation herein.

REFERENCES

Aguilera-Dena, D. R., Langer, N., Moriya, T. J., & Schootemeijer, A. 2018, ApJ, 858, 115
Anderson, J. P. 2019, A&A, 628, A7
Aryan, A., Bhushan Pandey, S., Gupta, R., Nath Tiwari, S., & Ror, A. K. 2023a, arXiv e-prints, arXiv:2307.03234
Aryan, A., Pandey, S. B., Gupta, R., & Ror, A. K. 2023b, MNRAS, 521, L17
Aryan, A., Pandey, S. B., Kumar, A., et al. 2022a, JApA, 43, 87
Aryan, A., Pandey, S. B., Yadav, A. P., Gupta, R., & Tiwari, S. N. 2022b, JApA, 43, 2
Aryan, A., Pandey, S. B., Zheng, W., et al. 2022c, MNRAS, 517, 1750
Aryan, A., Pandey, S. B., Zheng, W., et al. 2021, MNRAS, 505, 2530
Baklanov, P. V., Blinnikov, S. I., & Pavlyuk, N. N. 2005, AstL, 31, 429
Blinnikov, S. & Sorokina, E. 2004, Ap&SS, 290, 13
Blinnikov, S. I., Eastman, R., Bartunov, O. S., Popolitov, V. A., & Woosley, S. E. 1998, ApJ, 496, 454
Blinnikov, S. I., Röpke, F. K., Sorokina, E. I., et al. 2006, A&A, 453, 229
Bloom, J. S., Kulkarni, S. R., Djorgovski, S. G., et al. 1999, Natur, 401, 453
Cano, Z., Wang, S.-Q., Dai, Z.-G., & Wu, X.-F. 2017, AdAst, 2017, 8929054
Castro-Tirado, A. J., Soldán, J., Bernas, M., et al. 1999, A&AS, 138, 583
Dessart, L. & Hillier, D. J. 2018, arXiv e-prints, arXiv:1812.07620
Farmer, R., Fields, C. E., Petermann, I., et al. 2016, ApJS, 227, 22
Gilmore, G. 2004, Sci, 304, 1915, `\href{https://www.science.org/doi/abs/10.1126/science.1100370}`
Gupta, R., Pandey, S. B., Kumar, A., et al. 2022, JApA, 43, 82
Henyey, L., Vardya, M. S., & Bodenheimer, P. 1965, ApJ, 142, 841
Herwig, F. 2000, A&A, 360, 952
Hu, Y. D., Fernández-García, E., Caballero-García, M. D., et al. 2023, FrASS, 10, 952887
Jermyn, A. S., Bauer, E. B., Schwab, J., et al. 2023, ApJS, 265, 15
Joyce, M., Leung, S.-C., Molnár, L., et al. 2020, ApJ, 902, 63

Kasen, D. & Woosley, S. E. 2009, ApJ, 703, 2205
Kippenhahn, R., Ruschenplatt, G., & Thomas, H. C. 1980, A&A, 91, 175
Langer, N., El Eid, M. F., & Fricke, K. J. 1985, A&A, 145, 179
Larsson, J., Levan, A. J., Davies, M. B., & Fruchter, A. S. 2007, MNRAS, 376, 1285
Le Floc'h, E., Duc, P. A., Mirabel, I. F., et al. 2003, A&A, 400, 499
Mannucci, F., Salvaterra, R., & Campisi, M. A. 2011, MNRAS, 414, 1263
Modjaz, M., Liu, Y. Q., Bianco, F. B., & Graur, O. 2016, ApJ, 832, 108
Nadyozhin, D. K. 2003, MNRAS, 346, 97
Pandey, S. B., Kumar, A., Kumar, B., et al. 2021, MNRAS, 507, 1229
Paxton, B., Bildsten, L., Dotter, A., et al. 2011, ApJS, 192, 3
Paxton, B., Cantiello, M., Arras, P., et al. 2013, ApJS, 208, 4
Paxton, B., Marchant, P., Schwab, J., et al. 2015, ApJS, 220, 15
Paxton, B., Schwab, J., Bauer, E. B., et al. 2018, ApJS, 234, 34
Paxton, B., Smolec, R., Schwab, J., et al. 2019, ApJS, 243, 10
Perna, R., Lazzati, D., & Cantiello, M. 2018, ApJ, 859, 48
Ror, A. K., Gupta, R., Aryan, A., et al. 2024, arXiv e-prints, arXiv:2406.01220
Smartt, S. J. 2015, PASA, 32, e016
Song, C.-Y. & Liu, T. 2023, arXiv e-prints, arXiv:2301.05401
Song, X.-Y. & Zhang, S.-N. 2023, ApJ, 957, 31
Van Dyk, S. D. 2017, RSPTA, 375, 20160277
Woosley, S. & Janka, T. 2005, NatPh, 1, 147
Woosley, S. E. & Bloom, J. S. 2006, ARA&A, 44, 507
Woosley, S. E. & Weaver, T. A. 1986, ARA&A, 24, 205

VII Workshop on Robotic Autonomous Observatories (October 16-20, 2023)
Editors: Maria Gritsevich, Alberto J. Castro-Tirado, Petr Kubánek, Shashi B. Pandey, and David Hiriart - DOI: https://doi.org/10.22201/ia.14052059p.2025.59.23

Revista Mexicana de Astronomía y Astrofísica Serie de Conferencias (RMxAC), **59**, 153–159 (2025)
© 2025: Instituto de Astronomía, Universidad Nacional Autónoma de México
https://doi.org/10.22201/ia.14052059p.2025.59.24

VII Workshop on Robotic Autonomous Observatories (October 16-20, 2023)
Editors: Maria Gritsevich, Alberto J. Castro-Tirado, Petr Kubánek, Shashi B. Pandey, and David Hiriart - DOI: https://doi.org/10.22201/ia.14052059p.2025.59.24

EARLY EMISSION OF SHORT OPTICAL TRANSIENTS

S. Wu[1,2], V. M. Lipunov[3], A. J. Castro-Tirado[1,4], Y.-D. Hu[1,2], K. Zhirkov[3], and N. V. Tyurina[3]

RESUMEN

Este estudio presenta un análisis exhaustivo de la emisión óptica temprana de fuentes transitorias ópticas de corta duración, aprovechando los datos de los telescopios robóticos de la red GLOBAL MASTER de la Universidad Estatal de Moscú (MSU). Estos transitorios, que se han detectado relacionados con fenómenos cósmicos como estallidos de rayos gamma (GRBs), estallidos huérfanos de GRBs, precursores de supernovas, y ocasionalmente alertas de ondas gravitacionales y eventos de neutrinos de alta energía, plantean desafíos importantes debido a su naturaleza breve y a su ocurrencia impredecible en el tiempo. El núcleo de nuestra investigación se centra en la detección y caracterización de fenómenos transitorios, utilizando las capacidades únicas de los telescopios de la Red MASTER. Estos incluyen una rápida capacidad de apuntado, posibilidad de proporcionar imágenes de gran campo con polarizadores y así como un procesamiento de datos en tiempo real. Hacemos hincapié en la capacidad de esta red para capturar y estudiar estos fenómenos, contribuyendo a la comprensión de su origen y mecanismos asociados. Asímismo, discutimos en detalle la contrapartida óptica de GRB 210731A, la llamarada óptica del blázar BZQ J0526-4830, el estallido de 2022 de la nova enana AT2019axa, una nova (MASTER OT J010603.18-744715.8) en la Nube Pequeña de Magallanes (SMC), una supernova de tipo IIb (MASTER OT J091344.71762842.5 / SN2017gkk) y finalmente la fuente SWIFT J0840.7-3516.

ABSTRACT

This study presents a comprehensive analysis of early emissions of short optical transients, leveraging data from the GLOBAL MASTER MSU Network's robotic telescopes. These transients, often accompanying cosmic phenomena like gamma-ray bursts, orphan bursts, gravitational wave bursts, high-energy neutrino events, and supernova precursors, pose significant challenges due to their brief nature and unpredictable timings. The core of the research focuses on the transient phenomena's detection and characterization, utilizing the unique capabilities of the MASTER network's telescopes. These include rapid targeting, wide-field imaging in multiple polarizations, and real-time data processing. Emphasis is placed on the network's ability to capture and study these phenomena, contributing to the understanding of their origins and mechanisms. Several targets are discussed: the detected GRB 210731A optical counterpart,the BZQJ0526-4830 optical flare, the 2022 outburst of the dwarf nova AT2019axa 2022, the newly discovered Nova MASTER OT J010603.18-744715.8 in the SMC, the IIb Supernova MASTER OT J091344.71762842.5 / SN2017gkk and the SWIFT J0840.7-3516 X-ray transient

Key Words: astrophysical phenomena — telescope networks — transients GRBs, SOTs

1. INTRODUCTION

Short-term optical flashes accompany gamma-ray bursts (Akerlof et al. 1999), orphan bursts (Ho et al. 2022, Lipunov et al. 2022), gravitational-wave bursts (Abbott et al. 2017ab, Lipunov et al. 2017a), high-energy neutrino detections –blazar flare TXS 0506+056, detected by MASTER (Aartsen et al. 2014, Lipunov et al. 2020), the initial stage of supernova explosions (Matsumoto, Metzger 2022), and others. The global network of robotic telescopes MASTER of Moscow State University (Lipunov et al. 2010, 2019, 2022, Kornilov et al. 2012) regularly detects optical transients of explosive and non-explosive nature (e.g., flares on red dwarfs) during its own, inspectional, and alert surveys. The search and study of specifically short transient phenomena will help us better understand the interaction of matter and energy in the Universe, and investigate the behavior of matter in extreme physical conditions.

The complexity in studying short optical transients is related to the brevity of their availability for observation; they are recorded at unforeseen

[1]Instituto de Astrofísica de Andalucía (IAA-CSIC), Glorieta de la Astronomía s/n, E-18008, Granada, Spain.
[2]Universidad de Granada, Facultad de Ciencias Campus Fuentenueva, s/n, CP, 18071 Granada, Spain.
[3]M. V. Lomonosov Moscow State University, Leninskie Gory, GSP-1, 119991 Moscow, Russia.
[4]Unidad Asociada CSIC Departamento de Ingeniería de Sistemas y Automática, Escuela de Ingenieros Industriales, Universidad de Málaga, C. Dr. Ortiz Ramos sn, 29071 Málaga, Spain.

VII Workshop on Robotic Autonomous Observatories (October 16-20, 2023)
Editors: Maria Gritsevich, Alberto J. Castro-Tirado, Petr Kubánek, Shashi B. Pandey, and David Hiriart - DOI: https://doi.org/10.22201/ia.14052059p.2025.59.24

times and at previously unknown coordinates, therefore the physical mechanisms of the processes occurring are still not fully understood. To detect and study the optical sources of gamma-ray bursts (Figure 1), wide-field telescopes are created (historically: ROTSE, BOOTES, MASTER, TAROT). The key distinction of the robotic telescopes of the MASTER Global Network of Moscow State University lies in the distribution of identical twin telescopes around the globe, capable of quickly (30 degrees per second) aiming based on target indications, obtaining wide-field images simultaneously in two polarizing (or BVRI) filters and processing them in real-time(Figures 2 and 3). This allows for the rapid discovery (and publication) of sources and leads the research in the early optical emission of gamma-ray bursts / GRBs (Ershova et al. 2020). The BOOTES system successfully provided rapid follow-up observations for GRBs detected by BATSE on CGRO, covering 95% to 100% of GRB error boxes within 30 to 255 minutes post-detection, showcasing its efficiency in capturing transient events quickly. BOOTES-1 achieved its "first light" on 1 July 1998, marking the commencement of its operations in detecting and observing gamma-ray bursts(Castro-Tirado et al., 1999).

2. CURRENT STATUS OF RESEARCH

2.1. *Gamma-ray bursts (GRBs)*

Phenomenologically, gamma-ray bursts are classified into short and long bursts with a conventional limit on the duration of $\sim 2-4$ s. The nature of the gamma-ray spectrum is taken into account: short bursts show a tighter spectrum than long bursts. There are exceptions explained either by observational selection - short gamma-ray bursts can be mistaken for long gamma-ray bursts that are not observed completely, or the possibility of the existence of a third group of gamma-ray bursts associated with the merger of black holes and neutron stars is discussed. After 17 August 2017 (registration of gravitational waves from the merger of two neutron stars at a late stage of evolution just before the formation of a black hole as a result of the process), it can be considered proven that short bursts are the result of neutron star mergers (Blinnikov1984, Lipunov1995a, Paczynski1997). Short gamma-ray bursts can also result from the merger of pairs consisting of a neutron star and a black hole (BH+BH). Long GWs are associated with the collapse of the core of a rapidly rotating massive star (Mszros & Rees 1999, Woosley & Heger 2006, Lipunov & Gorbovskoy, 2007).

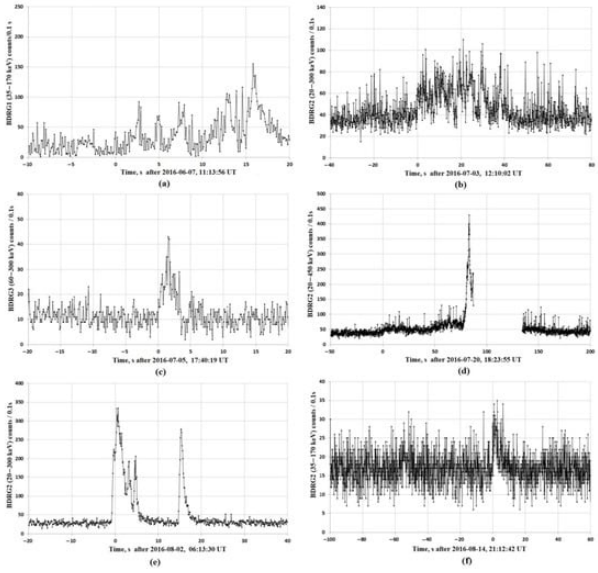


Fig. 1. Long and short (right) gamma-ray bursts registered by the Fermi-GBM detector. At the bottom are 6 bursts recorded by the Lomonosov spacecraft(Sadovnichy et al. 2021).

2.2. *Supernova explosions*

The light curve of supernovae can be traced for several months, the process of the first stage of the explosion itself takes up to 2 weeks, and supernova precursors are sometimes recorded, which can be attributed to short transient events (Tatsuya & Metzer 2022). When the core of a star runs out of nuclear fuel, it collapses into a very dense object, releasing large amounts of energy and material, leading to a supernova explosion.

2.3. *Kilonova*

Kilonova is the result of neutron star and dense star merging (Abbott et al. 2017, Lipunov et al. 2017, Figure 3a) at a late stage of evolution (Barbieri et al. 2019).In 2019, the inclusion of LIGO/VIRGO with increased sensitivity (the O3 set, which has already ended) did not lead to success in the optical localisation of grav-wave sources. Here is events at distances up to 200-300 Megaparsecs in merging neutron star binaries at a good statistical level. At 120 Megaparsecs, a Kilonova like the one detected in the galaxy NGC 4993 will have a stellar magnitude at maximum of about 20m depending on the mass shed. We are ready to inspect error-fields and detect objects on MASTER telescopes, the longitude and latitude distribution of identical MASTER telescopes with proprietary software for real-time detection of optical transients makes it possible to investigate such extreme processes in the Universe.

VII Workshop on Robotic Autonomous Observatories (October 16-20, 2023)
Editors: Maria Gritsevich, Alberto J. Castro-Tirado, Petr Kubánek, Shashi B. Pandey, and David Hiriart - DOI: https://doi.org/10.22201/ia.14052059p.2025.59.24

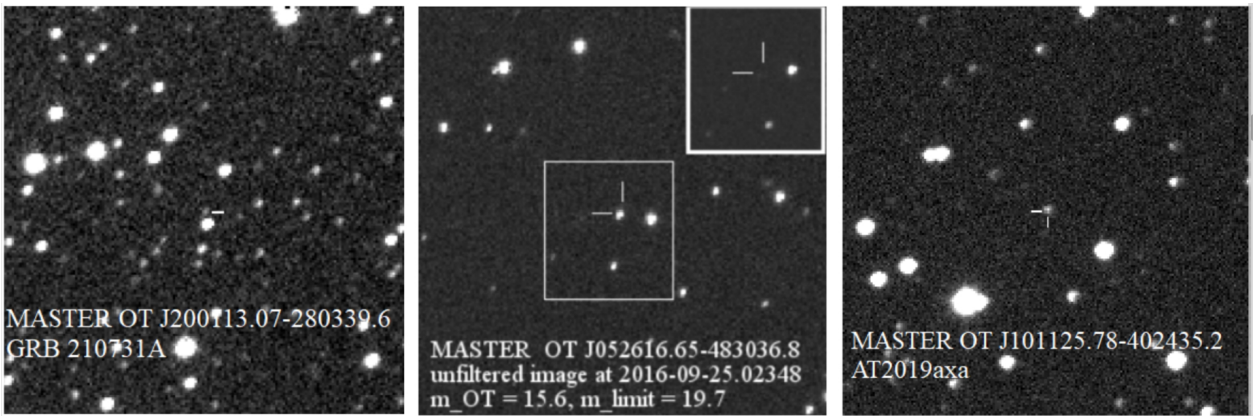


Fig. 2. On the left there is the MASTER OT J200113.07-280339.6, which is identified as the optical counterpart of GRB 210731A, as mentioned in GCN Circulars 30567, 30571, and 30578. The image in the center captures a Blazar flare (with reference image), as reported in ATel 9578. The right image shows dwarf nova (also known as AT2019axa) oturbust in 2023-04-27 00:23:12 by MASTER auto-detection system with an amplitude > 4.5. `www.wis-tns.org/object/2019axa`

3. RESEARCH METHODOLOGY

In this study, we utilized the MASTER network, a cutting-edge facility comprising robotic telescopes strategically positioned around the globe. The data collected from MASTER were subjected to rigorous analysis with the aim of advancing our understanding of the observed celestial phenomena.

3.1. *MASTER Global Robotic Net*

MASTER is very fast positioning alert, follow up and survey twin telecopes global network with own real-time auto-detection software. MASTER goal is One Sky in One Night up to 20-21m (C)(Lipunov et al. 2010). To discover optical transient there are as minimum 2 images in 2 times (there is a small shift between images to exclude any artefacts). MASTER software make initial reduction, detects all optical sources at every wide-field image (4 sq.degrees in 1 tube), compares them with catalogued ones and detected flare of known, or new outburst, or mooving object during the next exposition (30 sec). The second possibility of online auto-detection system is the difference between current and archive images and analysis of detected OT. When GCN (Barthelmy 1998) alert comeby socket, MASTER telescopes are pointing (during previous exposition is finishing) and quickly starts observation of earlier or prompt optical emission of GRB sources (Troja et al. 2017, Ershova et al. 2020, Fig. 2a with MASTER OT of GRB210731A and Fig.3a with Kilonova /short GRB 170817A optical counterpart, independently discovered by MASTER).

3.2. *Research Step*

Following telescope observations, we conduct initial screenings to identify objects for in-depth analysis, selecting appropriately sized frames for sufficient detail. These images are automatically calibrated and readied for examination. We then verify the coordinates of each object against astronomical databases and use these coordinates to extract corresponding catalog data. With Python scripts, we process this data to obtain magnitudes and errors, and subsequently plot light curves. By comparing these curves with those of known transients, we infer the nature of the observed objects.

We used the following procedure to perform the photometry. The optical transient flux is measured in a 6" aperture calibrated against several reference stars with similar colour and G values from GAIA EDR372-74. We used the following formula to estimate the errors:

$$\Delta m = \sqrt{\frac{\sum_{i=1}^{N}(m_i - m_{ij})^2}{N}},$$

where m_i is the stellar magnitude of the reference star i averaged over the observation time, m_{ij} is the stellar magnitude of the reference star i in frame j, and N is the number of reference stars.

At Figure 2 and 3 there are the examples of automatically detected optical transients: GRB optical counterpart, Blazar flare, dwarf nova outburst, SN, Nova and Kilonova outbursts.

MASTER OT J200113.07-280339.6 was found in Swift (GCN 30568) GRB 210731A error-box by MASTER-SAAO pointed 67 after trigger time (GCN 30567, started at 22:22:16UT), by MASTER-IAC (started at 2021-07-31 22:22:57UT), and by MASTER-Kislovodsk (Fig. 2a). This OT was discovered in 4 min after trigger time at 22:25:54UT

VII Workshop on Robotic Autonomous Observatories (October 16-20, 2023)
Editors: Maria Gritsevich, Alberto J. Castro-Tirado, Petr Kubánek, Shashi B. Pandey, and David Hiriart - DOI: https://doi.org/10.22201/ia.14052059p.2025.59.24

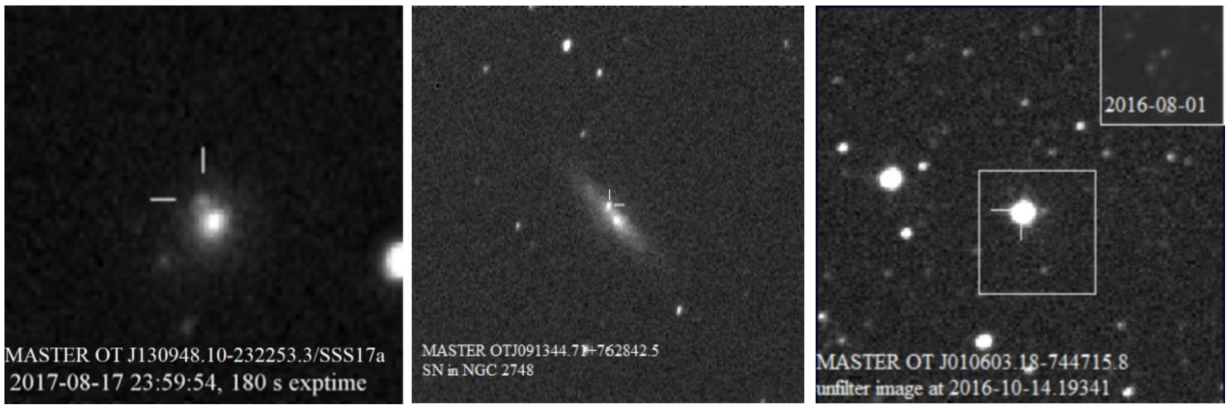


Fig. 3. The left image features the Kilonova MASTER OT J130948.10-232253.3 is at the site of the neutron star merger GW170817 detected by the LIGO/Virgo gravitational-wave interferometers on 17 August 2017 (Abbott et al. 2017, Lipunov et al. 2017). The central image depicts a Type IIb Supernova, as detailed in the Astronomer's Telegram 10698 by Onori et al. On the right is an image of a Nova in the Small Magellanic Cloud, reported in Astronomer's Telegram 9621.

by MeerLICHT (GCN 30570) and observed also by Swift-UVOT (since 210s after trigger time), GROND 4.2h after trigger (GCN 30574), KAIT (GCN 30583), VLT (GCN 30583, z=1.2525).

MASTER OT J101125.72-402435.0 was found by MASTER auto-detection system during regular survey on 2023-04-27.02815 UT (its position coincidents with AT2019axa in TNS) with unfiltered m_{OT}=15.9. The OT is seen in 6 images during previous outburst (2018-02-14 21:48:02-23:41:31) and in 8 images in April 2023. We used reference image from 2018-02-14.98218 UT with unfiltered $m_{lim} = 20.8^m$.

MASTER OT J052616.65-483036.8, a bright blazar BZQJ0526-4830 flare, was detected on 2016-09-25.01638 UT with unfiltered $m_{OT} = 15.6^m$. Using MASTER archive reference image on 2014-12-25.95740 UT with unfiltered $m_{lim} = 20.1^m$ current flare amplitude was $> 4.5^m$.

MASTER OT J010603.18-744715.8, a Nova in SMC discovery (ATel 9621) on 2016-10-14.19341 UT with $m_{OT} = 10.9^m$ (amplitude $> 9^m$).

IIb Supernova (ATel 10698) MASTER OT J091344.71762842.5 was discovered in 3" from the center of NGC2748 galaxy by MASTER-Kislovodsk regular survey with $m_{OT} = 15.6^m$ (ATel 10667). The spectroscopic classification was made by NOT (ATel 10698), BVRI photometry made by Konkoly Observatory (ATel 10686).

4. MASTER OBSERVATIONS AND TRANSIENTS PHOTOMETRY

MASTER online reduction includes photometry, based on USNO-B1 and Gaia comparison stars, taken them a lot in 4 sq.degrees of each images (Lipunov et al. 2010, 2019, Kornilov et al. 2012).

The light curve of MASTER OT J123248.62-012924.5 (figure 4) a transient celestial phenomenon, characterized by a swift rise in magnitudedenoting a dimming of the objectbefore reaching a steady state over the course of roughly two hours. Pronounced error bars at lower brightness levels indicate a higher degree of measurement uncertainty in these observations. The pattern of the curve, marked by an abrupt decline in luminosity followed by a leveling off, is indicative of an explosive astrophysical event, potentially a supernova or nova eruption, which transitions into a phase of equilibrium after the initial outburst.

The MASTER OT J183315.33+623157.0, which corresponds to GRB 200412B, displays a characteristic dimming trend commonly seen in GRB afterglows. Over a span of approximately 8.33 hours, the brightness progressively decreases. The near-constant error bars throughout this period reflect a high level of measurement precision. Notably, when plotted on a logarithmic scale, the trend appears linear, indicative of a power-law decay. This pattern aligns well with established models of GRB afterglow behavior.

The MASTER OT J201048.64-452006.7 associated with GRB 200612A reveals a dynamic event, where the object initially brightens, then experiences a brief dimming before undergoing a rapid fade, all within a span of about 12 seconds. The consistent error bars suggest reliable measurements, though uncertainty increases as the object fades. This behav-

VII Workshop on Robotic Autonomous Observatories (October 16-20, 2023)
Editors: Maria Gritsevich, Alberto J. Castro-Tirado, Petr Kubánek, Shashi B. Pandey, and David Hiriart - DOI: https://doi.org/10.22201/ia.14052059p.2025.59.24

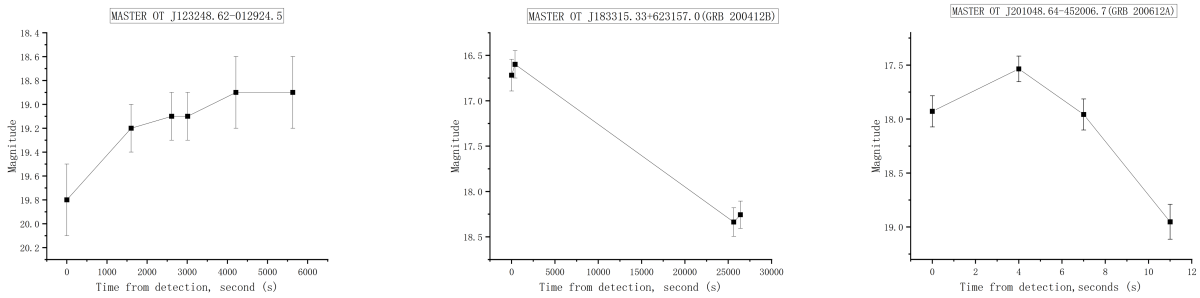


Fig. 4. Photometry of some sources discovered by MASTER.

ior is characteristic of explosive astrophysical events, such as a gamma-ray burst.

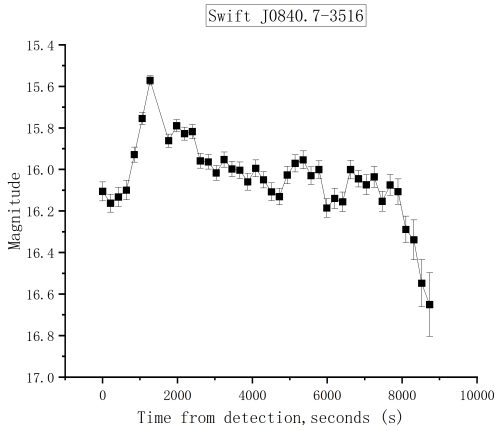


Fig. 5. Light curve of magnitude change with time for Swift J0840.7-3516

5. SWIFT J0840.7-3516

Among the sources observed by MASTER, there is a special source - Swift J0840.7-3516.An analysis of the light curve obtained with the Argentine MASTER-OAFA telescope of the MASTER Global Network shows that the brightness of the source starts to increase rapidly at $T \sim 10^3$ s, and then at $T \sim 10^4$ s it rapidly decreases to approximately the same brightness as at the beginning. During the brightness decay, an even period from $T \sim 4 \times 10^3$ s to $T \sim 7 \times 10^3$ s is maintained. The brightness remains almost constant for nine months after the decline, which also indicates a non-periodic brightness variation of this source.

The photometric profile of Swift J0840.7-3516 captures a sequence of initial brightness variations, a prolonged stable phase, and a distinct dimming towards the end, across a timespan of over two and a half hours. The error margins, relatively uniform throughout, hint at a solid measurement consistency, albeit with a slight rise in variability during transitions in luminosity. This nuanced light curve is characteristic of transient celestial events, such as eruptive stellar behavior or binary system dynamics.

This research was also conducted by a group of researchers from various institutions in Spain, Italy, and Denmark. They began by providing some reference information about ultracompact X-ray binaries (UCXBs) - a subclass of low-mass X-ray binaries (LMXBs) characterized by orbital periods shorter than 80 minutes and a donor star deficient in hydrogen, for example, a non-degenerate helium star or a white dwarf. They utilized data from several telescopes and instruments to study this object across different wavelength ranges, including X-ray, optical, and near-infrared. They also performed spectroscopic analysis to characterize the accretion disk around this compact object. One of the key findings of the study is that Swift J0840.7-3516 exhibits transitional behavior both in the X-ray and in the optical/near-infrared ranges. This is consistent with expectations that UCXBs experience thermal-viscous instabilities in their accretion disks. They suggest that this object might be a new member of the UCXB population (Coti Zelati et al. 2021).

Another group investigated the nature of the unusual X-ray transient Swift J0840.7-3516 to determine whether it is an unusual low-mass X-ray binary or a tidal disruption event(Shidatsu et al. 2021). They conducted X-ray observations of the source using various tools, including MAXI, Swift, NICER, and NuSTAR, and analyzed the X-ray data to determine the photometric and spectroscopic properties of the source during its outburst and fading phase. The team also searched for any radio emission from the source and compared it with the known correlation between radio and X-ray fluxes from low-mass X-ray binaries. Based on the analysis of these observations, they concluded that Swift J0840.7-3516 possesses unusual X-ray properties that are difficult

VII Workshop on Robotic Autonomous Observatories (October 16-20, 2023)
Editors: Maria Gritsevich, Alberto J. Castro-Tirado, Petr Kubánek, Shashi B. Pandey, and David Hiriart - DOI: https://doi.org/10.22201/ia.14052059p.2025.59.24

to explain in terms of any known class of objects. They hypothesize that a plausible explanation might be an LMXB with several extreme properties or a tidal event where a star is destroyed by a supermassive black hole or an asteroid by a galactic neutron star. Their estimates suggest that the black hole's mass ranges from 10^4 to 10^5 solar masses, depending on its rotation, which aligns with their previous estimates based on the observed decay period. Following the mass estimation (van Paradijs & McClintock 1994), we conclude that this should be a binary system of low-mass stars with periods ranging from a few minutes to several hours. Compared with the distinctive features of various binary systems, for instance, we suggest that this is a binary system containing a white dwarf. However, due to limitations, we can only determine the period, but not other important properties. Observation and analysis of distant binary systems also require more specialized telescopes, such as the Gaia satellite launched by the European Space Agency (ESA) in 2013, which provides astrometric data with an accuracy of 7-20 microarcseconds for stars brighter than 15th magnitude (Kornilov et al. 2012), as well as larger precise telescopes, particularly a 10-meter optical infrared telescope for medium and high-resolution spectroscopic observations.

6. CONCLUSIONS

The MASTER telescope network excels in observing short optical transients, rapidly detecting and analyzing transient astronomical events like gamma-ray bursts (GRBs). A notable achievement is the swift detection of the Swift J0840.7-3516 source, demonstrating its quick response to space-based alerts and effective ground follow-up. This quick reaction and high sensitivity make MASTER invaluable for observing fleeting cosmic events.

Looking ahead, robotic telescopes in the MASTER network symbolize a major leap in astronomical research. These automated systems operate continuously, responding instantly to transient events without human intervention, enhancing observational efficiency and data quality. Future advancements are expected to increase sensitivity and autonomy, with artificial intelligence playing a key role in decision-making based on real-time data and research needs.

Acknowledgements: This work was supported by the China Scholarship Council (CSC). I am deeply grateful for the generous funding and opportunities provided by the CSC that greatly assisted the research. I also want to express my heartfelt gratitude to the MASTER Telescope team for their invaluable support in assisting with the data collection and analysis for my research. And finally I am deeply grateful to the organizers of the AstroRob2023 conference for granting me the opportunity to participate in this international meeting.

REFERENCES

Aartsen, M. G., Ackermann, M., Adams, J., et al. 2014, ApJ, 796, 109, doi:10.1088/0004-637X/796/2/109

Abbott, B. P., Abbott, R., Abbott, T. D., et al. 2017, ApJ, 848, L12, doi:10.3847/2041-8213/aa91c9

Abbott, B. P., Abbott, R., Abbott, T. D., et al. 2017, Nature, 551, 85, doi:10.1038/nature24471

Akerlof, C., Balsano, R., Barthelmy, S., et al. 1999, Nature, 398, 400, doi:10.1038/18837

Barbieri, C., Salafia, O. S., Colpi, M., et al. 2019, ApJ, 887, L35, doi:10.3847/2041-8213/ab5c1e

Barthelmy, S. D., Butterworth, P., Cline, T. L., et al. 1998, Gamma-Ray Bursts, 4th Hunstville Symposium, 428, 99, doi:10.1063/1.55426

Castro-Tirado, A. J., Soldán, J., Bernas, M., et al. 1999, A&AS, 138, 583, doi:10.1051/aas:1999362

Coti Zelati, F., de Ugarte Postigo, A., Russell, T. D., et al. 2021, A&A, 650, A69, doi:10.1051/0004-6361/202140573

Ershova, O. A., Lipunov, V. M., Gorbovskoy, E. S., et al. 2020, Astronomy Reports, 64, 126, doi:10.1134/S1063772920020018

Klioner, S. A., Seidelmann, P. K., & Soffel, M. H. (eds.) 2010, Relativity in Fundamental Astronomy (IAU S261): Dynamics, Reference Frames, and Data Analysis, No. 261 (Cambridge: Cambridge Univ. Press)

Kornilov, V. G., Lipunov, V. M., Gorbovskoy, E. S., et al. 2012, Exp Astron, 33, 173

Lipunov, V. & Gorbovskoy, E. 2007, ApJ, 665, L97, doi:10.1086/521099

Lipunov, V. M., Gorbovskoy, E., Kornilov, V. G., et al. 2017, ApJ, 850, L1, doi:10.3847/2041-8213/aa92c0

Lipunov, V. M., Kornilov, V. G., Topolev, V. V., et al. 2022, Astronomy Letters, 48, 623, doi:10.1134/S1063773722110093

Lipunov, V., Kornilov, V., Gorbovskoy, E., et al. 2010, Advances in Astronomy, 2010, 349171, doi:10.1155/2010/349171

Lipunov, V., Kornilov, V., Zhirkov, K., et al. 2022, MNRAS, 516, 4980

Lipunov, V. M., Kornilov, V. G., Zhirkov, K., et al. 2020, ApJ, 896, L19, doi:10.3847/2041-8213/ab96ba

Lipunov, V. M., Kornilov, V. G., Zhirkov, K., et al. 2022, Universe, 8, 271, doi:10.3390/universe8050271

Lipunov, V. M., Vladimirov, V. V., Gorbovskoi, E. S., et al. 2019, Astronomy Reports, 63, 293, doi:10.1134/S1063772919040073
Matsumoto, T., & Metzger, B. D. 2022, ApJ, 936, 114
Mészáros, P., & Rees, M. J. 1999, MNRAS, 306, L39
Sadovnichy, V. A., Panasyuk, M. I., Svertilov, S. I., et al. 2021, Universe, 7, 375, doi:10.3390/universe7100375
Shidatsu, M., Iwakiri, W., Negoro, H., et al. 2021, ApJ, 910, 144, doi:10.3847/1538-4357/abe6a1
Troja, E., Piro, L., van Eerten, H., et al. 2017, Nature, 551, 71, doi:10.1038/nature24290
van Paradijs, J. & McClintock, J. E. 1994, A&A, 290, 133
Woosley, S. E. & Heger, A. 2006, ApJ, 637, 914, doi:10.1086/498500

VII Workshop on Robotic Autonomous Observatories (October 16-20, 2023)
Editors: Maria Gritsevich, Alberto J. Castro-Tirado, Petr Kubánek, Shashi B. Pandey, and David Hiriart - DOI: https://doi.org/10.22201/ia.14052059p.2025.59.24

Revista Mexicana de Astronomía y Astrofísica Serie de Conferencias (RMxAC), **59**, 161–166 (2025)
© 2025: Instituto de Astronomía, Universidad Nacional Autónoma de México
https://doi.org/10.22201/ia.14052059p.2025.59.25

VII Workshop on Robotic Autonomous Observatories (October 16-20, 2023)
Editors: Maria Griffsevich, Alberto J. Castro-Tirado, Petr Kubánek, Shashi B. Pandey, and David Hiriart - DOI: https://doi.org/10.22201/ia.14052059p.2025.59.25

GERry : FINDING ELECTROMAGNETIC COUNTERPARTS IN GRAVITATIONAL WAVES FOLLOW-UP CAMPAIGNS

D. O'Neill[1]

RESUMEN

El campo de la astrofísica es cada vez más rico en datos, especialmente en la astronomía del dominio temporal, donde el número de telescopios robóticos para observaciones de gran campo sigue incrementándose. En parte, esto se ha debido al creciente interés en detectar las contrapartidas electromagnéticas (EM) de los eventos de ondas gravitacionales (GWs), en particular la contrapartidas ópticas de las fusiones de estrellas binarias de neutrones (BNS) que dan como consecuencia a las kilonovas (KNe). Se han diseñado nuevos telescopios como GOTO específicamente para este propósito. Sin embargo, el seguimiento robótico de GWs presenta dos desafíos: cómo optimizar su estrategia de observación para maximizar la probabilidad de recuperar una KN en sus observaciones e identificar qué campañas de seguimiento pueden haber producido un evento detectable. En este trabajo presentamos cómo el 'código de recuperación electromagnética de ondas gravitacionales' (GERry) puede ayudar en estos aspectos al proporcionar un método para permitir rápidamente un análisis en profundidad de la campaña de seguimiento de GWs. Los datos que proporciona se pueden utilizar para determinar si es probable que haya una contrapartida óptica entre las fuentes detectadas, así como para probar la eficacia de la estrategia de observación para un evento determinado.

ABSTRACT

The field of astrophysics is increasingly becoming data rich, especially in time domain astronomy, where the number of wide field robotic survey telescopes is continuing to accelerate. In part, this has been due to the rapidly growing interest in detecting the electro-magntic (EM) counterparts to gravitational wave (GW) events, in particular the optical counterpart to binary neutron star (BNS) events: Kilonovae (KNe). New telescopes such as GOTO have been designed specifically for this purpose. However, robotic GW follow-up presents two challenges: How to optimise your observing strategy in order to maximise the probability of recovering a KN in your observations, and, identifying which follow-up campaigns may have produced a detectable event. In this work I demonstrate how the 'Gravitational wave Electromagnetic RecoveRY code' (GERry) can help in these respects by providing a method to rapidly provide an in-depth analysis of GW follow-up campaign. The data it provides can be used to determine whether an optical counterpart is likely to be among the detected sources as well as to test the effectiveness of the observing strategy for a given event.

Key Words: gravitational waves — methods: observational — surveys

1. INTRODUCTION

The first detection of gravitational waves paved the way for a new era of multi-messenger astronomy through the combination of traditional electromagnetic (EM) datasets complimented by gravitational wave (GW) data. However, challenges remain in the detection of the optical counterparts. The interferometric design of gravitational wave detectors such as the Laser Interferometric Gravitational-wave Observatory (LIGO) and Virgo detectors can often result in poor localisations (∼ 100s - 10,000 sq deg). This poor localisation coupled with the rapid nature of KNe, typically rising and fading within ∼3–5 days makes it exceedingly difficult for traditional telescopes to find and identify these counterparts due to their limited field of view (∼sq arcminutes). Any counterpart will have likely faded before being imaged and identified. Therefore wide field survey instruments such as ATLAS, ZTF, PanSTARRs with fields of view in the 1-10s sq deg range are much more capable of identifying any EM counterparts and yet these events remain elusive. This could be set to change in the near future with the advent of new robotic wide field surveys such as BlackGEM, GOTO, LSST, etc

1.1. *GOTO*

Advances in CCD technologies has resulted in increasing supply of affordable, sensitive, large-scale CCDs allowing for the construction of increasingly sophisticated and cost-effective wide field telescope

[1]University of Warwick, Coventry, CV4 7AL.

VII Workshop on Robotic Autonomous Observatories (October 16-20, 2023)
Editors: Maria Gritsevich, Alberto J. Castro-Tirado, Petr Kubánek, Shashi B. Pandey, and David Hiriart - DOI: https://doi.org/10.22201/ia.14052059p.2025.59.25

arrays. Motivated by this, the rapidly growing interest in GW optical counterparts as well as the aforementioned challenges they pose, the Gravitational wave Optical Transient Observer (GOTO) was born (Steeghs et al. 2022). GOTO has specifically designed to maximise the chances of recovering an EM counterpart signal. It consists of 4 mounts located across two sites, with two mounts in the northern hemisphere at Roque de los Muchachos Observatory in La Palma and the other pair in the southern hemisphere at Siding Spring Observatory in New South Wales, Australia. Each mount consists of 8 0.4m Telescopes each with a field of view of ∼5.8 sq deg. Allowing for a small amount of overlap between each of the telescopes, the field of view of a single mount is therefore approximately 44 sq deg. Images are currently taken in the L-band, a broad filter that covers Sloan r',g' and Johnson V (4000 − 7000Å). When a GW wave trigger is received, GOTO will automatically start imaging the 90% contour skymap, images are 4x60s mean-combined image stacks which typically an image depth of ∼20.5±0.5 mag depending on conditions and moon brightness. This setup should therefore be able to recover any 2017gfo-like KNe happening within $<$ 100 Mpc with possible detections out to ∼150 Mpc which is comparable LIGO's O4 estimated detection threshold for a BNS event.

2. MOTIVATION

At the onset of LIGO's O4a observing run, the northern node of GOTO was completed and operational while the southern node was still under construction. During this time, many low significance GW alerts had been released which were promptly followed up by GOTO where possible. It quickly became apparent that the number of sources detected for each gravitational wave event could span anywhere between 1 to 4 orders of magnitude, in particular this was a problem for single GW detector events which have localisations spanning half the sky. One example is that of S230529ay[2], an event at 197±62 Mpc with $P_{NSBH} = 62\%$, $P_{BNS} = 30\%$. While not statistically significant, its relatively low FAR of 1/160 years still garnered some interest. GOTO did not perform a dedicated follow-up campaign but instead continued in the default all-sky imaging mode. However, due to the very large localisation area, much of the 90% contour area was imaged regardless. Within 1 week post GW trigger, GOTO detected ∼50,000 sources requiring human vetting, which would be a significant time investment. Naturally the feasibility of such a task was questioned and whether it is likely that a KNe would ever have been detected from such a follow-up campaign. Another important consideration is the observing strategy one wishes to employ when observing GW skymaps. Typically the primary choice when considering a strategy is speed vs depth, shorter exposures will result in shallower images, but increases the rate at which you can cover the skymap. Intuitively one might favour longer exposures for further GW events as any counterpart will be fainter, and thus require deeper images to recover the signal. However, with increasing distance comes a lower GW signal-to-noise ratio (SNR) which in turn, results in poorer localisation requiring shorter image exposures to fully map. Finding which strategy to adopt can be difficult even before considering other factors such as airmass, observing conditions etc.

GERRY was developed to address these challenges. It provides a rapid method of quantitatively assessing GW follow-up performance and provide users with a means to quickly determine the probability of detecting an EM counterpart (P_{tr}) in a given GW follow-up campaign. Running the code on simulated observations of skymaps also allows the user to compare the effectiveness of different observing strategies allowing for improvement and refinement which is critical if we want to maximise the probability of detecting these EM counterparts.

3. METHOD

3.1. *Healpix Alchemy*

Upon the detection of a GW signal, LIGO releases a localisation skymap typically generated by the rapid localisation code BAYESTAR. These localisation skymaps utilise Hierarchical Equal Area isoLatitude Pixelization (HEALPix, Górski et al. (2005)), which models the sky as a sphere and subdivides the sky into equal sized pixels. The size of these pixels depend on the resolution. Also contained within each pixel is the probability and GW distance estimates at the position of the pixel. In the past these 'flat' skymaps were the primary format being used by the community. However, more recently 'Multi-Order Coverage' (MOCs) skymaps (Fernique et al. 2022) have become the default. Instead of a single resolution across the entire sky, GW MOC files instead reserve higher resolutions for areas of the sky with higher GW localisation probabilities resulting in significantly less pixels/memory being used for areas of the sky with negligible probabilities leading to a significant reduction in file sizes

[2] https://gracedb.ligo.org/superevents/S230529ay/view/

VII Workshop on Robotic Autonomous Observatories (October 16-20, 2023)
Editors: Maria Gritsevich, Alberto J. Castro-Tirado, Petr Kubánek, Shashi B. Pandey, and David Hiriart - DOI: https://doi.org/10.22201/ia.14052059p.2025.59.25

and the computational resources required to process them.

GERRY is built on healpix-alchemy[3] (Singer et al. 2022), which allows the querying of GW MOCs using SQLalchemy in a PostgreSQL 14 database. healpix-alchemy utilises the mulitrange data type, and uses this to store HEALPix skymap tiles at a given resolution by a number range, also known as a range set. The range set corresponds to the minimum and maximum HEALPix pixel indices at a very high resolution(l=29). Given the sequential nature of these l=29 pixels, one HEALPix tile can therefore be represented by a single range set containing the minimum and maximum indices of the pixels which make up the larger tile which will take the form of e.g. [576460752303423488,577586652210266112). Therefore, the GW skymap can be broken down into a set of rangesets for each tile. These tiles are then stored in the PSQL14 database along with the tiles probability density values, distance estimate and distance uncertainty. The same process is performed for the images in the follow-up campaign, whereby the image is first turned into a MOC, the field of view of the image is broken down into healpix tiles with varying resolution below a maximum limit. They are organised such that the tiles fill the field of view as much as possible while still accurately representing the original field of view with larger resolutions (smaller tiles) at the edges and corners of the images and lower resolution tile (larger tiles) in the centre.

Once the skymap and image tiles have been read into the database, their rangesets can now be trivially queried against each other. If the pixel values in a skymap tile rangeset and an image tile rangeset overlap, then this means the the image tile overlaps the position of the skymap tile on sky. The size of the this overlap can also be found as the l=29 pixels in the rangeset have a fixed size ($3.6\times10^{-18}sr$), multiplying this value by the number of values common in both the skymap and image tile rangesets will give the area of the overlap. Healpix-Alchemy also adds functionality to union field images which can then be used to easily calculate the contained skymap tiles and using the encoded probability values contained within, calculate the total 2D sky probability imaged (P_{fov}) in a follow-up campaign.

3.2. GERRY : *probing 3D probability space*

The issue with simply quoting P_{fov} values is that it is possible for many wide field survey instruments to image a significant fraction of the skymap and achieve high P_{fov} If they do not achieve sufficient depths to ever recover an EM counterpart, or image the sky long after any EM counterpart has faded, then this value can be somewhat meaningless as the chances of detecting with counterpart will be negligible. GERRY builds on Healpix-Alchemy by also utilising the encoded distance information to probe the 3D probability space while folding in the expected temporal evolution of the counterpart and returning meaningful statistics and probability values that directly tie to the probability of detecting an EM counterpart. The temporal evolution of the EM counterpart is estimated using model light curves in the desired filters. In all the following examples we will be using a MOSFiT model L-band light curve generated using the best fitting parameters to KN 2017gfo unless stated otherwise.

The basic flow of operations in GERRY is as follows:

- Find all instances where a skymap tile was imaged by an image tile, and identify what specific area of the tiles was covered and what time the skymap tile was imaged relative to the GW trigger time.
- Using the model light curve, estimate the brightness of the counterpart at the time the skymap tile was imaged by using the encoded GW distance and Milky Way reddening estimate at that position.
- Given the known depth of the image, calculate the fraction of probability that could be recovered at the position of the tile at that time by modelling the brightness probability distribution as a inverse cumulative distribution function and sampling the distribution at the image depth value.
- If a skymap tile was wholly or partially imaged multiple times, combine the probabilities from these overlapping observations and finally sum these probabilities over the entire imaged sky.

When multiple image tiles cover a skymap tile it is vital that it is determined if the image tiles cover the same or different areas of a skymap tile to facilitate precise area and probability calculations for a more meaningful and accurate result. GERRY identifies what specific areas of a skymap tile was covered by an image tile by breaking down the skymap tiles into polygons composed of unique image-skymap tile combinations.

$$P_{tr,poly_i} = P_{max,poly_i}(1-(P_{int_1,img_1}...\times P_{int_n,img_n})) \quad (1)$$

[3] https://github.com/skyportal/healpix-alchemy

VII Workshop on Robotic Autonomous Observatories (October 16-20, 2023)
Editors: Maria Gritsevich, Alberto J. Castro-Tirado, Petr Kubánek, Shashi B. Pandey, and David Hiriart - DOI: https://doi.org/10.22201/ia.14052059p.2025.59.25

Where $P_{tr,poly}$ is the probability of detecting the transient at least once within this polygon, $P_{max,poly}$ is the maximum probability achievable from the polygon and P_{int_n,img_n} is the recovered probability of this polygon from the n^{th} image tile. P_{tr} is then simply the sum of all $P_{tr,poly}$ values for all N polygons:

$$P_{tr} = \sum^{N} P_{tr,poly_i} \quad (2)$$

The primary numerical output of GERRY are three probability values: P_{fov} - the aforementioned 2D probability imaged, P_{vol} - The sum of the maximum probabilities achieved across the entire imaged sky and finally, P_{tr} - the probability of detecting the transient (e.g. KNe) at least once across the imaged sky.

The input required for GERRY is a csv file containing the image corners/vertices in ra/dec, the MJD or JD when the image was taken, the filter, image depth and image depth uncertainty. The primary driver of errors in the returned P_{tr} and P_{vol} values is the uncertainty in the image depths. Image depth will typically vary across an image. In order to simulate this, GERRY will need to be given an image depth uncertainty value for every image. A script is included that will extract the image corners and generate the required csv file from a directory of fits images, however the script will only work on square/rectangular images. The image depths and depths uncertainties will still have to be added manually to the csv file. The images will be converted into MOCs with the maximum resolution set by the user. We strongly recommend avoiding resolutions lower than 10, especially for instruments with smaller (<1 deg) field-of-views. At these lower resolutions, the ability of the larger moc tiles to approximate the image field of view will deteriorate towards the edge of the images resulting in larger errors in the calculated error of the field images. In most cases a value of 11 or 12 should be sufficient. In order to accurately determine the effect of reddening the transmission curve for all the filters used should also be provided. The model light curve of the transient is also required in all of the filters used in the imaging. Finally the GW skymap must be using the new MOC format.

4. RESULTS

In this section I will briefly show the output from GERRY using an example GW event from O3 as well as how it can be used with simulations to optimise observing strategy.

4.1. *O3 example - S190425z*

S190425z was the only statistically significant BNS merger to be detected during LIGO's O3 observing period. The estimated distance to the merger was 157±43 Mpc, it had the potential to produce a detectable, albeit faint, EM counterpart. It was only detected by a single LIGO inferometer as well as Virgo resulting in relatively poor localisation of ∼9000 deg^2.

A GOTO prototype (GOTO-4) was in operation during this time which consisted of a single mount with 4 telescopes at Roque de los Muchachos observatory in La Palma. Observations of the skymap started at 2019-04-25 20:40 to 2019-04-28 05:15 (+0.5 to 2.8 days post trigger) and resulted in 1948 L-band images covering 2155 deg^2. Figure 2 shows a detailed breakdown of the follow-up campaign along with relevant sky-position information such as reddening, image depth, and recovered probability. The total field-of-view probability covered wasP_{fov} = 32%.

GERRY was run to analyse the follow-up campaign and using the aforementioned MOSFiT 2017gfo light curve the resulting volume probed was P_{vol} =$4.45^{+2.9}_{-2.01}$% with a final value for P_{tr} =$7.72^{+4.07}_{-3.07}$%. Therefore, it is perhaps not surprising that no promising counterpart was detected in this follow-up campaign.

Figure 1 shows the expected light curve evolution along with the image depths achieved over the course of the campaign. Top left plot clearly shows that while images were taken at the expected KN peak, they still did not achieve the sufficient depth required to recover a 2017gfo-like KNe. This is primarily due to distance, as the top right plot shows that the majority of the imaged probability suffered little dust reddening.

4.2. *Optimising strategy*

The primary decision when considering strategy for surveys such as GW follow-up is speed vs image depth. More distant BNS mergers require both increasing image exposures due to the fainter counterparts as well as faster skymap coverage due to poorer localisation. Given that both of these requirements cannot be satisfied, knowing which is the optimal strategy as well as identifying possible parameter thresholds which may require different strategies is critical. By comparing the resulting P_{tr} values for each strategy for our simulations, we can compare their performance.

A sample of 60 simulated O4 BNS skymaps with distances <600 Mpc were selected and a 3 day ob-

VII Workshop on Robotic Autonomous Observatories (October 16-20, 2023)
Editors: Maria Gritsevich, Alberto J. Castro-Tirado, Petr Kubánek, Shashi B. Pandey, and David Hiriart - DOI: https://doi.org/10.22201/ia.14052059p.2025.59.25

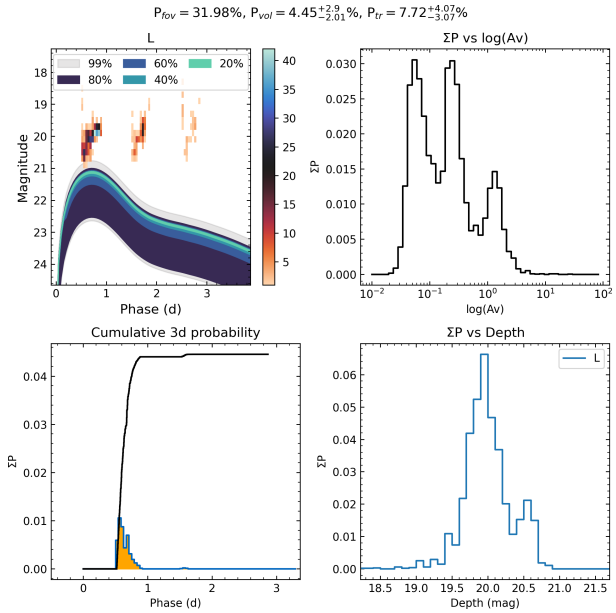


Fig. 1. Top left: The light curve distribution of the model light curve over all parts of the image skymap after accounting for variations in distance and reddening. The squares are a 2D histogram showing the density of images with respect to time and depth. Top right: The reddening distribution over the GW localisation probability. Bottom right: The cumulative 3D probability probed with respect to time. The overwhelming majority of the probability was recovered in the first night when the counterpart would have been brightest. Bottom right: The probability distribution with respect to Depth.

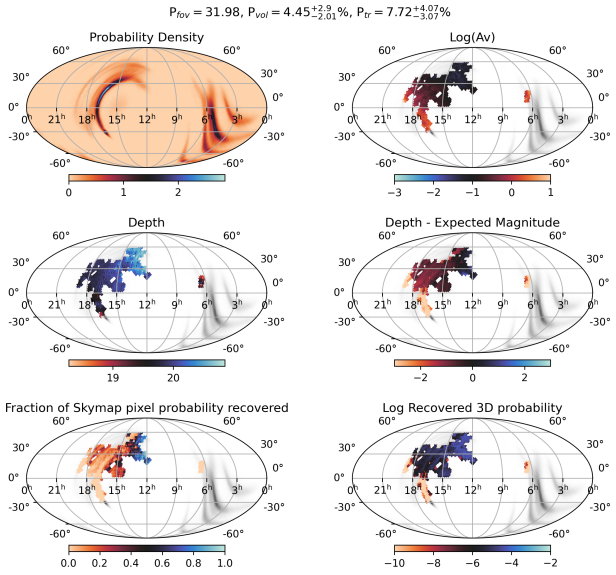


Fig. 2. Results from GERRY showing pointing specific information such as reddening, depths achieved, depths relative to estimated counterpart magnitude and probability recovered.

serving campaign was simulated using the GOTOTILE python package. Users can input the field of view of their instrument, location, number of mounts, exposure times and how long the skymap should be observed. The simulations were run for 2 exposure times, the first was a 4x60s exposure as well as an additional 60s for overheads per pointing resulting in a total pointing time of 300s. The second was 6x90s exposure with the same additional 60s for overheads. These simulations however can not account for sub-optimal observing conditions therefore it is assumed all observations occurred during bright time resulting in estimated depths of 20.3 mag for the 300s scenario and 21.3 mag for the 600s scenario. In both cases we adopt an image depth uncertainty of 0.3 mag. The results are shown in Figure 3. While both exposure scenarios offer similar levels of performance for distances within 100 Mpc, the longer t600s strategy starts to outperform t300s at distances >150 Mpc. Indeed at a distance of 200 Mpc, 600s offers almost a 50% increase in P_{tr} and at 300 Mpc, a factor of 5 increase in performance. While it would be tempting to simply adopt the t600s in all scenarios, given the similarity in performance at distances <100 Mpc, the t300s option would be preferable in this nearby distance range as an increase in cadence can help constrain source rise times, helping to separate any fast rising EM counterpart from more common SNe.

Since the above simulations now give us the average recovery curve over distance, we can use this curve along with the estimated BNS merger rates to estimate the number of KNe that we could expect to recover (assuming the KNe will have a 2017gfo-like light curve) using the 2 different strategies. This is shown in Figure 4.

4.3. *Performance*

Using the S190425z as an example, for a 1948 image follow-up campaign using an image MOC resolution of 10, the runtime of GERRY using a typical laptop with 4 cores, 16GB RAM is ∼7 minutes with an additional 1 minute if the results are plotted. The execution time scales linearly with the number of input images. For each increase in the MOC resolution of the input images typically results in a doubling of image tiles and execution times.

5. CONCLUSION

Identifying GW EM counterparts is difficult due to the typical poor localisations as well as their inherent elusive nature. Here we have shown how GERRY

VII Workshop on Robotic Autonomous Observatories (October 16-20, 2023)
Editors: Maria Gritsevich, Alberto J. Castro-Tirado, Petr Kubánek, Shashi B. Pandey, and David Hiriart - DOI: https://doi.org/10.22201/ia.14052059p.2025.59.25

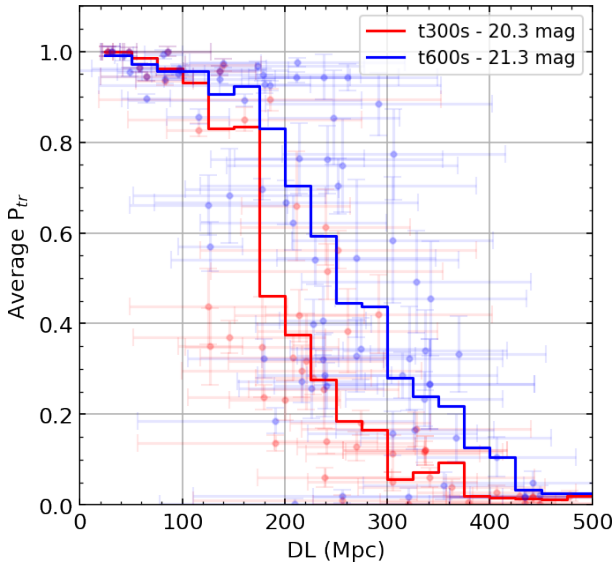


Fig. 3. Results from the follow-up simulations showing the effect of different exposure times on P_{tr} . The blue and red points show individual results from the simulations, the lines show a weighted mean curve binned in 25Mpc intervals.

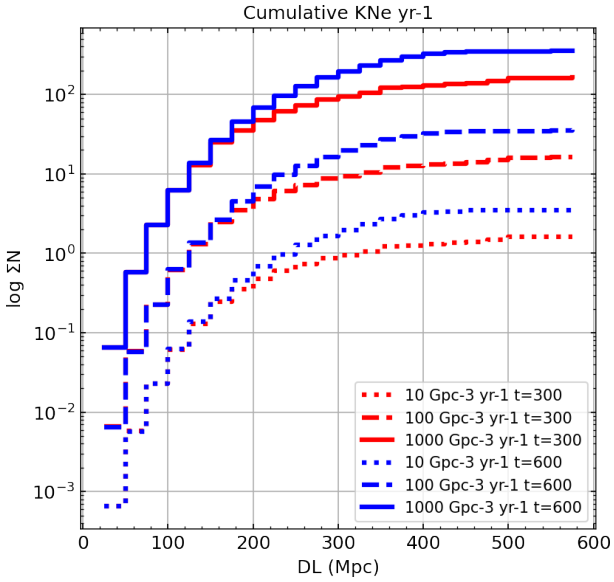


Fig. 4. The expected number of recovered 2017gfo-like KNe using both exposure strategies for different BNS merger rates.

can be a valuable tool in analysing GW follow-up campaigns by providing meaningful probability and follow-up statistics so that the users can determine whether a follow-up campaign should have produced any viable candidates. We have also shown how by leveraging these probability values, one can use simulated GW skymaps and observations to determine the most effective strategy for their instrumentation in order to maximise the potential of their future follow-up campaigns. Much of the work here will be presented in much more detail in an upcoming paper (O'Neill,D & Lyman, J in prep.) as well as showing some of the more advanced capabilities of GERRY and a study of the current and future suite of wide field survey instruments with regards to their expected performance in future GW observing periods. The Code is not yet public but can be found on GitHub when released.

REFERENCES

Fernique, P., Nebot, A., Durand, D., et al. 2022, MOC: Multi-Order Coverage map Version 2.0, IVOA Recommendation 27 July 2022

Górski, K. M., Hivon, E., Banday, A. J., et al. 2005, ApJ, 622, 759

Singer, L. P., Parazin, B., Coughlin, M. W., et al. 2022, AJ, 163, 209

Steeghs, D., Galloway, D. K., Ackley, K., et al. 2022, MNRAS, 511, 2405

Revista Mexicana de Astronomía y Astrofísica Serie de Conferencias (RMxAC), **59**, 167–172 (2025)
© 2025: Instituto de Astronomía, Universidad Nacional Autónoma de México
https://doi.org/10.22201/ia.14052059p.2025.59.26

VII Workshop on Robotic Autonomous Observatories (October 16-20, 2023)
Editors: Maria Gritsevich, Alberto J. Castro-Tirado, Petr Kubánek, Shashi B. Pandey, and David Hiriart - DOI: https://doi.org/10.22201/ia.14052059p.2025.59.26

BLACK HOLE TOM – AN AUTOMATIC TOOL FOR PHOTOMETRIC TIME-DOMAIN DATA

P. J. Mikołajczyk[1,2], P. Zieliński[3], Ł. Wyrzykowski[1], A. Krawczyk[4], and K. Kotysz[1,2]

RESUMEN

Presentamos una nueva herramienta automática para la astronomía del dominio temporal, llamada Black Hole Target and Observation Manager (BHTOM), desarrollada en el marco del programa OPTICON RadioNet Pilot. BHTOM es una herramienta de coordinación para una red global de telescopios capaces de procesar datos fotométricos automatizados para objetos transitorios y en el referido dominio temporal. La herramienta se ha utilizado para procesar alrededor de 150.000 observaciones de varios cientos de objetos transitorios, principalmente reportados por la misión espacial *Gaia*. Demostramos las principales características y ejemplos de uso de BHTOM y presentamos las mejoras que se realizarán en un futuro próximo. Los ejemplos de imágenes y curvas de luz presentados aquí confirman la capacidad de procesar datos de imágenes CCD/CMOS de múltiples telescopios y una gran variedad de instrumentos de manera automatizada.

ABSTRACT

We present a new automatic tool for time-domain astronomy dubbed Black Hole Target and Observation Manager (BHTOM), developed under the OPTICON RadioNet Pilot programme. BHTOM is a coordination tool for a global network of telescopes capable of automated photometric data processing for time-domain and transient targets. The tool has been used to process around 150,000 observations of several hundreds of transients, primarily reported by the *Gaia* space mission. We demonstrate the main features and use cases of BHTOM and present improvements to be made in the near future. The examples of images and light curves presented here confirm the ability to process CCD/CMOS imaging data from multiple telescopes and a whole variety of instruments in an automatic manner.

Key Words: data processing — time-domain astronomy — transients

1. INTRODUCTION

In the era of massive sky surveys, like *Gaia*[5], PTF[6], ASAS-SN[7], OGLE[8], ZTF[9] and forthcoming LSST[10], there are thousands of transient phenomena reported every year. The *Gaia* mission alone published almost 25,000 alerts up to now[11]. The average number of alerts per night that would be observed during a 10-year-long survey by Vera Rubin Observatory/LSST is estimated at 10 million objects. Understanding the nature of as many transients as possible is crucial in modern time-domain astronomy (TDA). It enables, for instance, the selection of the most interesting and promising ones for further follow-up observations (both photometric and spectroscopic). Therefore, first of all, the detailed ground-based monitoring of the transients is fundamental to obtain good coverage of their light curves. Secondly, multi-wavelength photometry informs how an event develops in brightness and colour, allowing for early characterisation and discovery of new types of objects.

To conduct such time-, resource- and manpower-consuming observing programs, one needs to have a global telescope network and dedicated central coordinated system that allows for requesting, managing and processing of the observational data. Transient events, e.g., supernovae, flaring young stellar objects (YSOs), gravitational wave optical counterparts, and microlensing or tidal disruption events, often require immediate follow-up observations, very soon after their discovery. It, in turn, implies the need for automatic reduction processes of the large amount of

[1]Astronomical Observatory, University of Warsaw, Al. Ujazdowskie 4, 00-478 Warszawa, Poland (bhtom@astrouw.edu.pl).
[2]Astronomical Institute, University of Wrocław, Kopernika 11, 51-622 Wrocław, Poland.
[3]Institute of Astronomy, Faculty of Physics, Astronomy and Informatics, Nicolaus Copernicus University in Toruń, Grudzikadzka 5, 87-100 Toruń, Poland.
[4]AkondLab, Wałbrzyska 6-8, 52-314 Wrocław, Poland.
[5]http://sci.esa.int/gaia
[6]https://www.ptf.caltech.edu/iptf
[7]https://www.astronomy.ohio-state.edu/asassn/index.shtml
[8]http://ogle.astrouw.edu.pl
[9]https://www.ztf.caltech.edu
[10]https://www.lsst.org/
[11]http://gsaweb.ast.cam.ac.uk/alerts/home

VII Workshop on Robotic Autonomous Observatories (October 16-20, 2023)
Editors: Maria Gritsevich, Alberto J. Castro-Tirado, Petr Kubánek, Shashi B. Pandey, and David Hiriart - DOI: https://doi.org/10.22201/ia.14052059p.2025.59.26

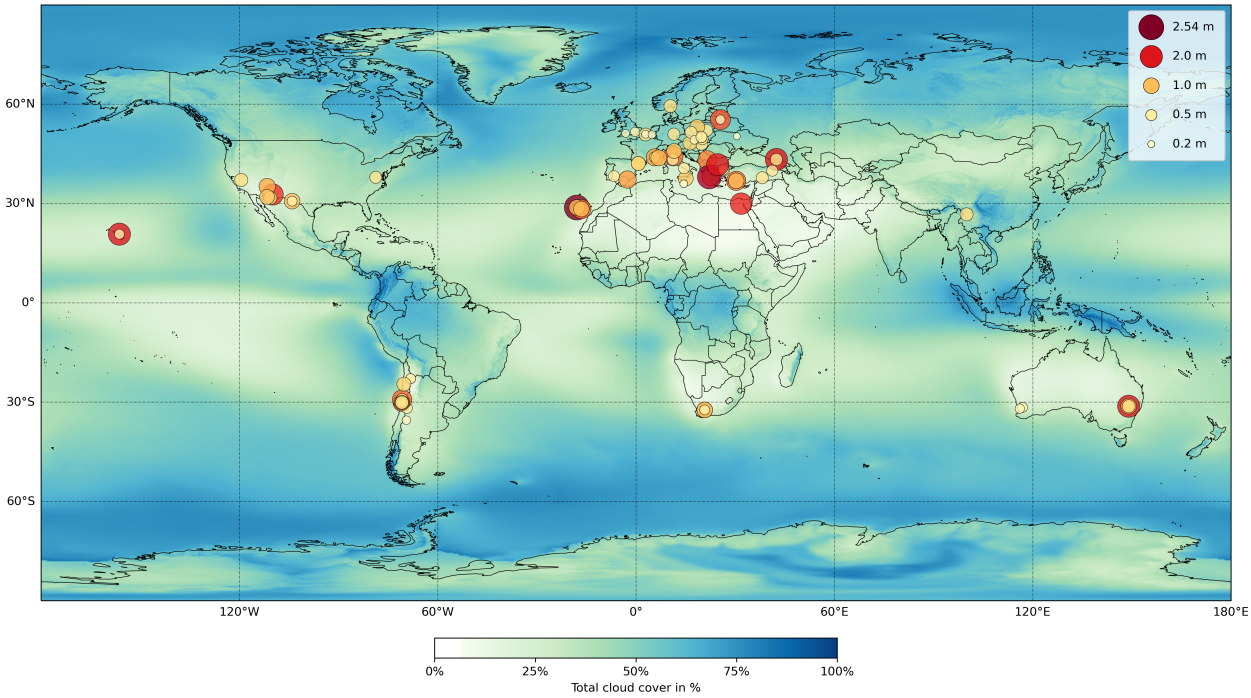


Fig. 1. The global distribution of telescopes involved in the BHTOM follow-up network overplotted on the total average cloud cover (Brun 2022).

photometric data gathered by various telescopes and instruments.

2. TDA FOLLOW-UP NETWORK

The process of preparation, submission and allocation of observing time is inefficient in the context of monitoring thousands of transient events. Observational data must therefore be provided by the active participation of many observers spread around the world. Since 2013, thanks to the EU FP7 and Horizon2020 funds, we have been developing a TDA telescope network for follow-up monitoring of interesting transients, mainly microlensing events alerted by *Gaia*. Within the OPTICON RadioNet Pilot (ORP) programme, we coordinate the operation of about 100 small- and medium-sized telescopes scattered globally. Our activity includes technical support, training, help with the observations, data processing and organizing the annual workshops. However, our main product is the automatic tool, dedicated to TDA, which is described in Sec. 3.

The members of the ORP TDA follow-up network are volunteers (both professional astronomers and amateurs). Some, contributed thousands of observations, while others contributed only a few data points. Figure 1 presents the geographical distribution of our partners. Many of these telescopes are located in Europe (Fig. 2) with poor weather conditions, compared to the best-observing sites like Chile, the Canary Islands, Hawaii, South Africa or Australia. But working in a network, they can still provide extremely useful scientific data and serve as perfect training facilities for young generations of astronomers.

The TDA follow-up network consists of about 20 robotic telescopes, while the rest is operated manually. The main mirror sizes of the telescopes in the network are within the range from 0.2 up to 2.5 m. Certainly, we also use world-class telescopes with apertures $8 - 10$ m for the (spectroscopic) follow-up based on the observing proposals and awarded time. However, the ORP TDA network of telescopes is the core of the available observational infrastructure coordinated by us.

3. BLACK HOLE TOM

The main product of the ORP TDA network is the Black Hole TOM (BHTOM)[12] which allows fast and automatic reduction and calibration of photometric data delivered by various network instruments. Recently, we have been releasing the new version of this software BHTOM 2.0 which improves the old version in several issues.

[12] `bhtom.space`

VII Workshop on Robotic Autonomous Observatories (October 16-20, 2023)
Editors: Maria Gritsevich, Alberto J. Castro-Tirado, Petr Kubánek, Shashi B. Pandey, and David Hiriart - DOI: https://doi.org/10.22201/ia.14052059p.2025.59.26

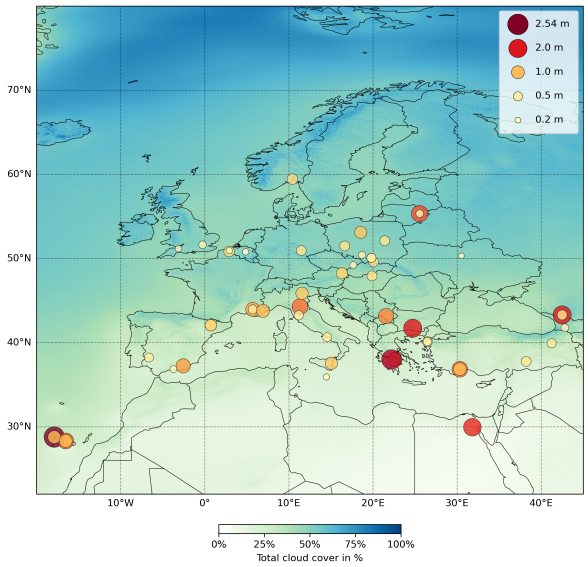


Fig. 2. The distribution of BHTOM telescopes in Europe and beyond overplotted on the total average cloud cover (Brun 2022).

BHTOM is based on the Target and Observation Manager (TOM) – open-source tool developed by Las Cumbres Observatory[13] (Street et al. 2018). It also uses our other, previously developed tools – CCDPhot and CPCS – that are built in the current version (Zieliński et al. 2019, 2020). In general, BHTOM performs the measurements of the target's brightness (photometry) and position (astrometry). It accepts both ASCII or CSV files with photometric measurements provided in a specific format, or FITS[14] files from CCD/CMOS cameras that have to be initially calibrated in the meaning of bias- and dark-subtraction and flat-field correction. This allows less experienced observers, including amateurs and school pupils, to collect scientifically important observations and deliver them to BHTOM directly.

3.1. *Main features*

The main features and workflow of BHTOM processing are as follows:

- automatic photometric and astrometric reduction of CCD/CMOS images by using CCDPhot based on BASH shell and Python scripts, IRAF/PyRAF[15], SExtractor (Bertin & Arnouts 1996), SCAMP (Bertin 2006), DAOPHOT (Stetson 1987) and WCSTools[16];
- direct uploading of photometric data as ASCII, CSV files or images as FITS files, also spectroscopic data possible to upload as simple ASCII or CSV file;
- astrometric solution obtained based on several reference astrometric catalogues: URAT-1 (Zacharias et al. 2015), UCAC-4 (Zacharias et al. 2013), USNOB1 (Monet et al. 2003) and Gaia-DR3 (Gaia Collaboration et al. 2023a) for final astrometric solution;
- photometry calibrated to standard magnitudes based on *Gaia* Synthetic Photometry (GaiaSP, Gaia Collaboration et al. 2023b) and 2MASS (Skrutskie et al. 2006) reference catalogues: transformation of instrumental magnitudes to the standard ones is done by zero-point calibration and colour term application;
- standardization of CCD/CMOS file headers originated from different observatories according to FITS standard[17];
- the Point Spread Function (PSF) model of the whole image constructed in automatic procedure;
- aperture and PSF photometry for all stars detected in the field-of-view based on DAOPHOT calculation procedure obtained with precision ∼0.01 mag (and better);
- final astrometric solution for all stars detected in the image based on Gaia-DR3 coordinates and proper motions obtained with precision ∼0.01 arcsec (and better);
- archival data from optical (*Gaia*, Gaia Collaboration et al. 2023a; ZTF, Masci et al. 2019; CRTS, Drake et al. 2009; LINEAR, Stokes et al. 2002; SDSS, Almeida et al. 2023; Pan-STARRS-DR1, Flewelling et al. 2020; DECAPS, Saydjari et al. 2023; ATLAS, Tonry et al. 2018), infrared (2MASS, Skrutskie et al. 2006; WISE, Wright et al. 2010; NEOWISE, Mainzer et al. 2011) and radio-databases (LOFAR, Shimwell et al. 2022; FIRST, Becker et al.

[13] `https://lco.global/tomtoolkit/`
[14] Flexible Image Transport System, `https://fits.gsfc.nasa.gov`
[15] IRAF is written and supported by the National Optical Astronomy Observatories (NOAO) in Tucson, Arizona. NOAO is operated by the Association of Universities for Research in Astronomy (AURA), Inc. under a cooperative agreement with the National Science Foundation. PyRAF is a product of the Space Telescope Science Institute, which AURA operates for NASA.
[16] `http://tdc-www.harvard.edu/wcstools`
[17] `https://fits.gsfc.nasa.gov/fits_dictionary.html`

VII Workshop on Robotic Autonomous Observatories (October 16-20, 2023)
Editors: Maria Gritsevich, Alberto J. Castro-Tirado, Petr Kubánek, Shashi B. Pandey, and David Hiriart - DOI: https://doi.org/10.22201/ia.14052059p.2025.59.26

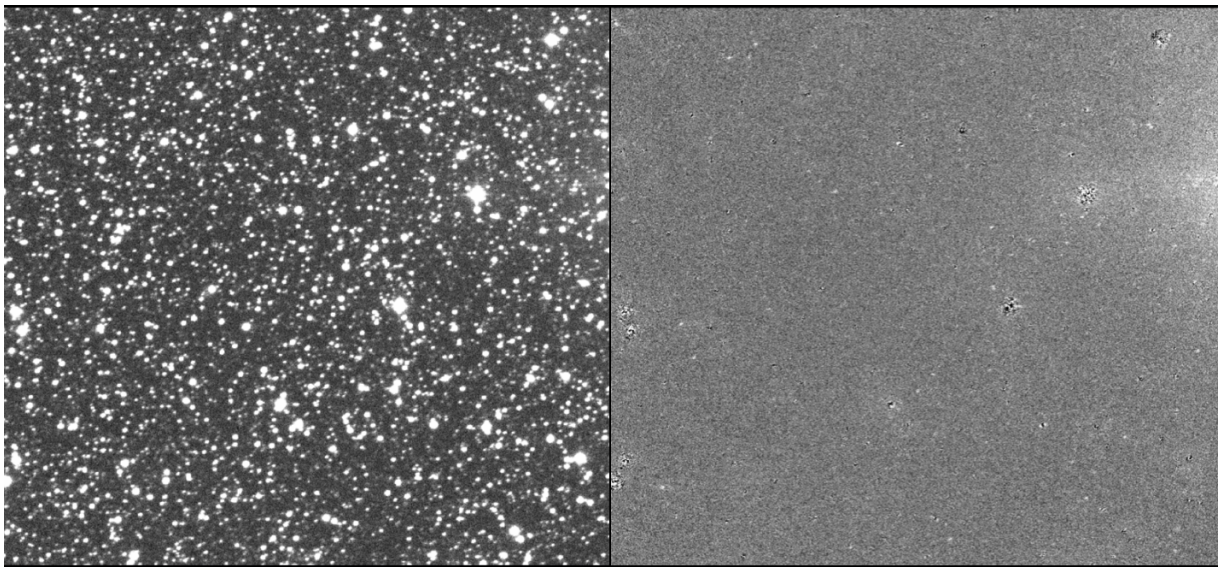


Fig. 3. The example images demonstrating the BHTOM processing result. Left: image of the Gaia16aye stellar field obtained in Bialkow Observatory before uploading to BHTOM; Right – the same image after processing by BHTOM. The result of the subtraction of 14,133 objects identified in the image is visible. The FoV is 13x12 arcmin in both cases.

1994) collected via dedicated brokers for every newly created target in automatic way;

- interactive targets map and easy-to-use target list that can be sorted and filtered by coordinates, magnitudes, priority, number of observations, class of object, etc.; target grouping is also possible;
- interactive light curves for every target (displayed per filter or facility);
- modelling procedure of light curves for microlensing events (at the moment) with and without parallax effect;
- publication feature that uses ChatGPT3.5 from OpenAI[18] to improve the title of the paper, abstract, and portions of the introduction as well as generate the description of the photometric data collected for the target;
- all functionalities of BHTOM are available via Application Programming Interface (API), i.e. data upload, download, target list filtering, standardization results, etc.[19]

3.2. *Future improvements*

The work on the new features and improvements of BHTOM is ongoing. Thanks to the feedback obtained from the users of BHTOM, this tool is getting more and more user-friendly and valuable. The cooperation between observers, astronomers and software engineers leads to continuous improvements, debugging and error detection in the system. In the future we are going to implement the following features, among others:

- live feedback provided for users reducing their FITS files with our dedicated CCDPhot pipeline;
- automatic triggering of robotic observations (already underway for the REM telescope) along with subsequent data reduction;
- introducing other photometric reduction procedures, i.e. SExtractor profile photometry;
- displaying many photometry products (aperture, profile, Kron-like and others);
- database containing light curves for all objects observed in the TOIs field-of-views.

3.3. *Examples*

The examples of processed images (before and after uploading to BHTOM) is presented in Fig. 3. Moreover, the light curves for example targets observed within the TDA follow-up network are shown in Fig. 4

[18] `https://chat.openai.com/auth/login`

[19] `https://github.com/BHTOM-Team/bhtom2/blob/bhtom2-dev/Documentation/Documentation.md`

VII Workshop on Robotic Autonomous Observatories (October 16-20, 2023)
Editors: Maria Gritsevich, Alberto J. Castro-Tirado, Petr Kubánek, Shashi B. Pandey, and David Hiriart - DOI: https://doi.org/10.22201/ia.14052059p.2025.59.26



Fig. 4. The example light curves of transients as presented in BHTOM. From top to bottom: Gaia21fkl microlensing event, 8C0716+714 highly variable quasar, SN2023ixf a supernova in M101. Colour-coded are the photometric follow-up observations in various filters calibrated to GaiaSP bands or from various sky surveys.

VII Workshop on Robotic Autonomous Observatories (October 16-20, 2023)
Editors: Maria Gritsevich, Alberto J. Castro-Tirado, Petr Kubánek, Shashi B. Pandey, and David Hiriart - DOI: https://doi.org/10.22201/ia.14052059p.2025.59.26

4. SUMMARY

Black Hole TOM is the automatic tool for processing photometric follow-up data from various telescopes and instruments. The photometric data from about 100 instruments were already tested successfully and stored in the cloud. In total, we have processed $\sim 150,000$ FITS images since the project's inception. At the moment, there are 257 users registered in BHTOM and the data can be uploaded for more than 2500 targets created.

The tool was already used in several scientific studies of microlensing events (e.g., Kruszyńska et al. 2022, Rybicki et al. 2022), young stellar objects (e.g., Nagy et al. 2022, 2023) or symbiotic stars (e.g., Merc et al. 2020). The papers on many other *Gaia* alerts are in the preparation phase as well. It confirms that the new version of our tool ensures fast and automatic processing of TDA data from various instruments. Nevertheless, the work on developments of other improvements of BHTOM is still in progress.

If you are interested in using Black Hole TOM for your research please visit the BHTOM webpage that can be found under the link `bhtom.space` and join the dedicated Slack channel `slack.bhtom.space` to stay updated.

Acknowledgements: The BHTOM project has received funding from the EU's Horizon 2020 research and innovation programme under grant agreement No. 101004719 (OPTICON RadioNet Pilot, ORP). BHTOM acknowledges the following people who helped with its development: M. Jabłońska, P. Sivak, K. Raciborski, P. Trzcionkowski and AKOND Lab company. This paper made use of the Whole Sky Database (wsdb) created by S. Koposov and maintained at the Institute of Astronomy, Cambridge, by S. Koposov, V. Belokurov and W. Evans with financial support from the Science & Technology Facilities Council (STFC) and the European Research Council (ERC), with the use of the Q3C software (`http://adsabs.harvard.edu/abs/2006ASPC..351..735K`). This work has made use of data from the European Space Agency (ESA) mission *Gaia* (`https://www.cosmos.esa.int/gaia`), processed by the Gaia Data Processing and Analysis Consortium (DPAC, `https://www.cosmos.esa.int/web/gaia/dpac/`). Funding for the DPAC has been provided by national institutions, in particular, the institutions participating in the Gaia Multilateral Agreement.

REFERENCES

Almeida, A., Anderson, S. F., Argudo-Fernández, M., et al. 2023, ApJS, 267, 44
Becker, R. H., White, R. L., & Helfand, D. J. 1994, ASPC, 61, 165
Bertin, E. & Arnouts, S. 1996, A&AS, 117, 393
Bertin, E. 2006, ASPC, 351, 112
Brun, P., Zimmermann, N. E., Hari, C., Pellissier, L., & Nikolaus Karger, D. 2022, ESSD, 14, 5573
Drake, A. J., Djorgovski, S. G., Mahabal, A., et al. 2009, ApJ, 696, 870
Flewelling, H. A., Magnier, E. A., Chambers, K. C., et al. 2020, ApJS, 251, 7
Gaia Collaboration, Vallenari, A., Brown, A. G. A., et al. 2023a, A&A, 674, A1
Gaia Collaboration, Montegriffo, P., Bellazzini, M., et al. 2023b, A&A, 674, A33
Kruszyńska, K., Wyrzykowski, Ł., Rybicki, K. A., et al. 2022, A&A, 662, A59
Mainzer, A., Bauer, J., Grav, T., et al. 2011, ApJ, 731, 53
Masci, F. J., Laher, R. R., Rusholme, B., et al. 2019, PASP, 131, 018003
Merc, J., Mikołajewska, J., Gromadzki, M., et al. 2020, A&A, 644, A49
Monet, D. G., Levine, S. E., Canzian, B., et al. 2003, AJ, 125, 984
Nagy, Z., Ábrahám, P., Kóspál, Á., et al. 2022, MNRAS, 515, 1774
Nagy, Z., Park, S., Ábrahám, P., et al. 2023, MNRAS, 524, 3344
Rybicki, K. A., Wyrzykowski, Ł., Bachelet, E., et al. 2022, A&A, 657, A18
Saydjari, A. K., Schlafly, E. F., Lang, D., et al. 2023, ApJS, 264, 28
Shimwell, T. W., Hardcastle, M. J., Tasse, C., et al. 2022, A&A, 659, A1
Skrutskie, M. F., Cutri, R. M., Stiening, R., et al. 2006, AJ, 131, 1163
Stetson, P. B. 1987, PASP, 99, 191
Stokes, G. H., Evans, J. B., & Shelly, F. C. 2002, AAS, 34, 1315
Street, R. A., Bowman, M., Saunders, E. S., & Boroson, T. 2018, SPIE, 10707, 11
Tonry, J. L., Denneau, L., Heinze, A. N., et al. 2018, PASP, 130, 064505
Wright, E. L., Eisenhardt, P. R. M., Mainzer, A. K., et al. 2010, AJ, 140, 1868
Zacharias, N., Finch, C. T., Girard, T. M., et al. 2013, AJ, 145, 44
Zacharias, N., Finch, C., Subasavage, J., et al. 2015, AJ, 150, 101
Zieliński, P., Wyrzykowski, Ł., Rybicki, K., et al. 2019, CoSka, 49, 125
Zieliński, P., Wyrzykowski, Ł., Mikołajczyk, P., et al. 2020, XXXIX PAS Meeting, 10, 190

Revista Mexicana de Astronomía y Astrofísica Serie de Conferencias (RMxAC), **59**, 173–178 (2025)
© 2025: Instituto de Astronomía, Universidad Nacional Autónoma de México
https://doi.org/10.22201/ia.14052059p.2025.59.27

VII Workshop on Robotic Autonomous Observatories (October 16-20, 2023)
Editors: Maria Gritsevich, Alberto J. Castro-Tirado, Petr Kubánek, Shashi B. Pandey, and David Hiriart - DOI: https://doi.org/10.22201/ia.14052059p.2025.59.27

ATTITUDE CONTROL STUDY ON ARTIFICIAL SATELLITES AND SPACE DEBRIS USING LASER DATA

Rubén Martínez[1] and Manuel Ángel Sánchez[2]

RESUMEN

Satellite Laser Ranging (SLR) es una técnica que permite medir la distancia a un satélite en órbita con alta precisión y, como aplicación particular, caracterizar la actitud y el espín de éste mediante el análisis de los residuos de distancia obtenidos a partir de la medida de tiempo de vuelo de los pulsos láser. Además, esta disciplina tiene aplicaciones en un amplio rango de campos de investigación, como la geofísica y la geodesia, o en la monitorización de objetos orbitales, entre ellos la basura espacial. Aplicando las técnicas de análisis de residuos de distancia, en primer lugar, sobre satélites pasivos y con fines geodésicos, como el *AJISAI*, y, posteriormente, sobre satélites inactivos (basura espacial), como son el *ENVISAT* o el *TOPEX POSEIDON*, se ha logrado observar con gran precisión los diversos movimientos oscilatorios debidos tanto a la rotación sobre el mismo eje de simetría como a la variación del ángulo de incidencia del haz láser sobre los retrorreflectores del satélite. En el desarrollo de este estudio se han comparado y complementado los resultados obtenidos en análisis anteriores examinando la evolución del periodo de rotación de los objetos estudiados. Esta capacidad de obtener información detallada sobre el comportamiento orbital y rotacional de los satélites inactivos, mediante este tipo de técnicas, permitirá desempeñar un papel notable en el entendimiento y la monitorización de la basura espacial, con el objetivo de anticiparse a posibles accidentes y colisiones previniendo la seguridad de las órbitas y la sostenibilidad del espacio. Además, permitirá comprender la dinámica de estos objetos con el fin de desarrollar modelos precisos de perturbaciones orbitales y facilitará ejecutar estrategias efectivas de retirada de satélites inactivos.

ABSTRACT

Satellite Laser Ranging (SLR) is a technique for measuring the distance to an orbiting satellite with high accuracy and, as a particular application, characterising the attitude and spin of the satellite by analysing the range residuals obtained from the time-of-flight (ToF) measurement of the laser pulses. Furthermore, this discipline has applications in a wide range of research fields, such as geophysics and geodesy, or in the monitoring of orbital objects, including space debris. By applying range residual analysis techniques, firstly on passive satellites for geodetic purposes, such as *AJISAI*, and subsequently on defunct satellites (space debris), such as *ENVISAT* or *TOPEX POSEIDON*, it has been possible to observe with great precision the different oscillatory movements due to the rotation around the same axis of symmetry and to the variation of the angle of incidence of the laser beam on the satellite's retroreflectors. In the development of this study, the results obtained in previous analyses have been compared and complemented by examining the evolution of the rotation period of the objects studied. This ability to obtain detailed information on the orbital and rotational behaviour of inactive satellites, using such techniques, will play a significant role in understanding and monitoring space debris, with the aim of anticipating possible accidents and collisions, preventing the safety of orbits and the sustainability of space. In addition, it will allow understanding the dynamics of these objects to develop accurate orbital perturbation models and will facilitate effective de-orbit strategies for the removal of inactive satellites.

Key Words: Attitude control — Satellite Laser Ranging — Space Debris — Space Surveillance and Tracking — Spin period

1. INTRODUCTION

SLR is a laser telemetry technique that uses short pulses of light, typically with a wavelength of 532 nm, to measure the bidirectional ToF from ground stations to satellite reflectors, thus allowing the dis-

[1]Facultad de Ciencias - UNICAN, Avenida de los Castros, 39012, Santander (Cantabria), Spain (rmi648@alumnos.unican.es).
[2]Royal Spanish Navy Observatory, Plaza Tres Marinas, 11100, San Fernando (Cádiz), Spain (msanpie@roa.es).

VII Workshop on Robotic Autonomous Observatories (October 16-20, 2023)
Editors: Maria Gritsevich, Alberto J. Castro-Tirado, Petr Kubánek, Shashi B. Pandey, and David Hiriart - DOI: https://doi.org/10.22201/ia.14052059p.2025.59.27

tance to be determined by applying various corrections.

Corner Cube Reflectors (CCR) are essential elements that are usually installed on the surfaces of satellites in order to implement laser telemetry and to know their orbits with high precision. The particularity of these devices is their ability to reflect light in the same direction in which it strikes them.

To develop this discipline, it is also necessary for ground stations to have three optical systems on a single mount. The first of these is a launching telescope capable of projecting laser pulses onto the observed objects. A second telescope acts as a finder, allowing small deviations of the laser beam to be adjusted. Finally, a receiving telescope, usually with an aperture between 600 mm and 1 m, is needed to capture the reflected photons. This last telescope is connected to an optical path that leads the photons to the optical sensors (photodetector), usually C-SPAD (Compensated Single Photon Avalanche Photodiode) type, in which, without going into too much detail, a single photon-generated carrier can trigger an avalanche current. The signal received at this detector allows the ToF of the beam to be stopped in the event timers. With this measurement it is possible to reconstruct the sensor-object distance at each time instant by applying correction models.

There are currently more than 40 stations distributed around the world that form part of ILRS (International Laser Ranging Service), carrying out their own engineering, operations, and data analysis tasks, among others. This technique has various applications in geophysical and geodetic fields, contributing to the definition of the Earth's centre of mass and monitoring its rotation, or helping to analyse the behaviour of the planet's gravity field, tectonic plates or tides. More recently, due to the high accuracy of this discipline, its use as a Space Surveillance and Tracking system for monitoring orbital objects, including space debris, has been proposed (Greene et al. 2002). Due to this feature it is possible, among other applications, to analyse the orbit of these objects and then compare it with their predicted orbits, thus studying their attitude and rotation period.

In this work, data from various satellites have been analysed, initially of the collaborative type, i.e. passive geodesic satellites, such as *AJISAI* (NORAD ID 16908), due to the precision of their orbits and the high availability of observations. As a result, it has been possible to verify the correct functioning of the developed algorithms. Once this milestone was overcome, these algorithms were applied on space debris objects, specifically on defunct satellites such as *ENVISAT* (27386) inactive since 2012, *TOPEX POSEIDON* (22076) inactive since 2006, among others.

2. METHODOLOGY

The files used in SLR to implement this analysis are two: the Consolidated laser Range Data format (CRD) and the Consolidated Prediction Format (CPF). CRDs provide the observations made by a laser station on a particular satellite during a short period of time that can vary from a few seconds to, under normal conditions, several minutes (Ricklefs & Moore 2009). The second type of file, CPFs, contains the ephemerides of the observed satellites, i.e. accurate predictions of the geocentric positions of that satellite over several days (Ricklefs 2006). These data are generated by several institutions with the necessary computational and technical capabilities, usually known as prediction providers. By having these two sets of files available, it is possible to calculate distance residuals, i.e. the difference between observed and calculated distances, which is very important information in laser telemetry data analysis.

Although this study is focused on space debris, the algorithms have been developed with simpler geodetic satellite passes in order to become familiar with the type of data to work with in this field, as well as to be able to clearly observe the residuals and the expected attitude. Still, the procedure is very similar for both types of objects and has been developed in publications such as that of Kucharski et al. (2014).

The first step in this procedure is to extract the observed data and calculate the distance from the station to the observed satellite. To achieve this, the ToF of the laser pulse must be utilized. After being emitted by the station, the laser pulse is reflected on the satellite reflector panel and then detected by the station once again. It is important to note that the timestamp accompanying the ephemerides positioning data provided by the CPF do not correspond to the observed times, so the next step is to interpolate these predictions into the observation times to obtain the position vector in geocentric coordinates. This has been achieved using a Lagrange 9th degree polynomial function, which is the standard according to the ILRS (Ricklefs 2006).

Then, since the laser propagation conditions in the atmosphere are known, it is possible to relate the speed of light, c, to an index of refraction that varies as a function of various parameters, such as wavelength, pressure, temperature, relative humidity, elevation angle, etc. Various models can be used

VII Workshop on Robotic Autonomous Observatories (October 16-20, 2023)
Editors: Maria Gritsevich, Alberto J. Castro-Tirado, Petr Kubánek, Shashi B. Pandey, and David Hiriart - DOI: https://doi.org/10.22201/ia.14052059p.2025.59.27

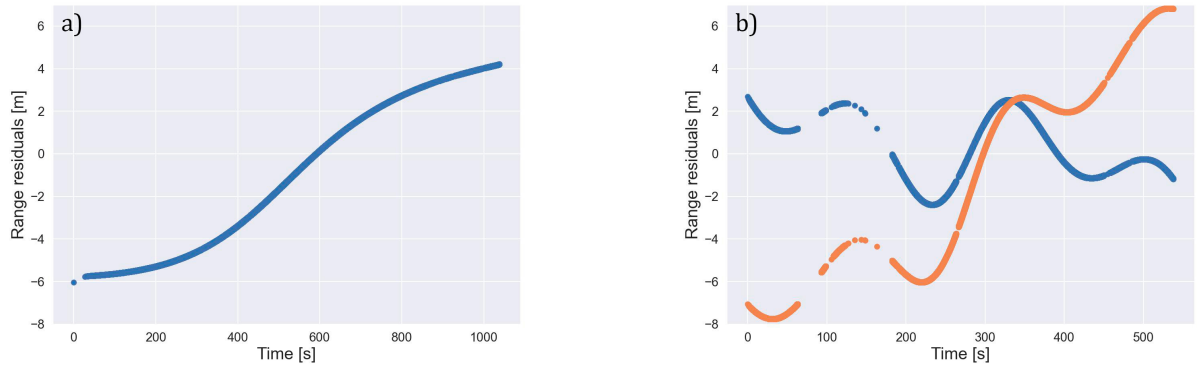


Fig. 1. (a) Range residuals calculated for an *AJISAI* tracking measured by Graz SLR station on December 8, 2023. (b) Range residuals calculated for an *ENVISAT* pass measured by Graz SLR station on January 31, 2018.

to apply this tropospheric correction, such as that of Mendes & Pavlis (2004) or that of Marini & Murray (1973). For this project, the latter model was used; however, it should be noted that below an elevation of 10, its equations become unreliable due to the increased atmospheric errors as light travels further. Because of the dependence on the elevation angle, it is essential to make use of the topocentric coordinates of the satellite, which are extracted from its geocentric coordinates, to solve for the elevation required in the model. Other corrections can be considered in relation to the eccentricity on the ground or on the satellite, or to the delay of the signal at the station, although depending on the case, the error of the measurement may exceed the correction itself due to the characteristics of the laser equipment.

After correcting the data, it is possible to determine the range residuals by the difference between the predicted and observed distance.

In figures 1 (a) (collaborative satellites) and (b) (inactive satellites) there is a clear trend in the data that can be either increasing or decreasing. This variation with time is due to a time bias that may have been caused by both a time lag in the ephemerides and an incorrect time correction in the measurements taken by the station, thus causing a time lag in the observed measurements.

Unlike the case of collaborative satellites, inactive ones show oscillations in the residuals, generally of several metres in amplitude (depending on the size of the satellite) due to their abandonment and the consequent absence of their attitude control. Specifically, the oscillation is due to the displacement, H, between the rotation axis of the retroreflector panel and its symmetry axis, which causes the distance between the CCR panel and the station to vary along the trajectory. This effect is absent in active satellites due to its repositioning systems and in geodetic collaborative satellites, exemplified by *AJISAI*, thanks to its spherical shape. So, as it was being said, in order to be able to work with the range residuals in defunct satellites, it is necessary to eliminate the trend to continue working correctly. Figure 1 (b) shows the range residuals before (orange curve) and after (blue curve) eliminating the trend.

With these oscillations, the period of rotation of the CCRs is determined by applying the Lomb algorithm (or Lomb-Scargle method), which makes it possible to detect the periodicity, as well as to obtain the angular frequency, of irregularly spaced data by means of a spectral analysis. In figure 3 the algorithm is applied to an *ENVISAT* tracking as an example, where a dominant frequency can be seen. There is usually another oscillation in the residuals of several millimetres mainly due to the variation of the distance measured by the laser, as it passes through the individual CCRs as a function of the spin of the satellite and the variation of the angle of incidence (Fig. 2). However, these millimetre-scale distance variations can only be observed with high-precision data, in this case provided by the Graz station, thanks to both its 10 kHz laser and the C-SPAD detector.

3. RESULTS

3.1. *Geodetic Satellites. AJISAI*

For *AJISAI*, a pass on December 8, 2023, measured by Graz laser telemetry station has been studied (Fig. 1 (a)). Figure 2 (a) and (b) show the distance residuals for a section of only 2 seconds duration and, as mentioned above, oscillations of only several millimetres amplitude are shown. On figure

VII Workshop on Robotic Autonomous Observatories (October 16-20, 2023)
Editors: Maria Gritsevich, Alberto J. Castro-Tirado, Petr Kubánek, Shashi B. Pandey, and David Hiriart - DOI: https://doi.org/10.22201/ia.14052059p.2025.59.27

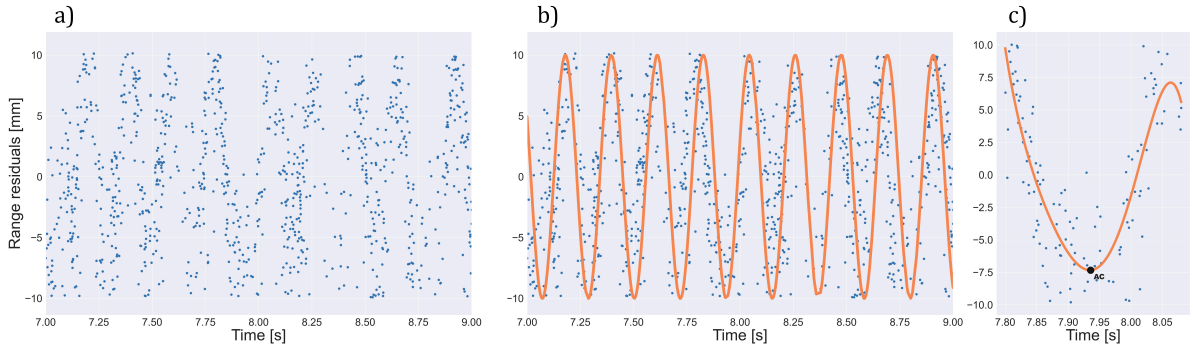


Fig. 2. (a) 2 second section of the *AJISAI* pass shown in figure 1 (a). (b) The same residuals section with a sinusoidal function fitted to the data, to better appreciate the oscillations. (c) Zoom of a peak, given by a single CCR. The curve-fitted polynomial and the CA point marked at the minimum are shown.

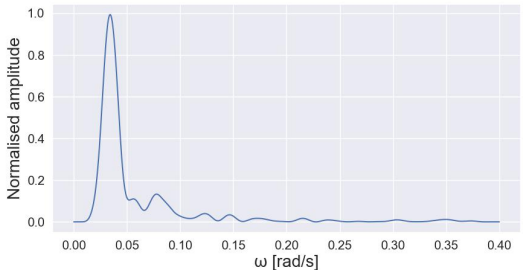


Fig. 3. Dominant frequencies calculated using the Lomb-Scargle method. For an ENVISAT pass measured by Graz SLR station on January 29, 2018, the dominant frequency is 0.0340 rad/s.

2 (c) is shown a zoomed region of one of the minimum residual values that corresponds to a Closest Approach (CA) position of a given CCR. To calculate this point, one can simply fit the curve with a 6th degree polynomial function and determine the minimum. By further study of these residuals it would be possible, knowing the distribution of the CCRs, to identify which ring each minimum corresponds to. In addition, it is known that the *AJISAI* spin axis is nearly parallel to the Earth's spin axis and is stabilised by a passive nutation damper, so it is possible to develop a simulation model capable of predicting the latitude of the satellite at which the laser is always pointing (Kucharski et al. 2010).

3.2. *Space debris. Defunct satellites*

In the case of defunct satellites, we have worked with *ENVISAT* and *TOPEX POSEIDON*, as shown in figures 1 (b) and 5, which show data from a track on 31 January 2018 measured by the Graz station and one on 3 January 2019 observed by the Borowiec station, respectively. From these values we therefore determine the frequency and the apparent spin period of the satellite during both passes, which for *ENVISAT* are 0.026 rad/s and 241.329 seconds respectively, and for *TOPEX POSEIDON* 0.621 rad/s and 10.124 seconds.

In addition to the determination of the period, one could try to estimate the displacement H between the spin axis of the satellite and the symmetry axis of the CCR panel, which is the cause of the oscillations shown. This would require a much more in-depth analysis in which, working in the Body-Centered Satellite, BCS, coordinate system, the incident angles of the laser vector on the CCR panel symmetry axis would have to be calculated to estimate the H-offset from a sinusoidal fit (Kucharski et al. 2014).

By examining several tens of different passes over a given period, it is possible to estimate the apparent rotation rate. In this case, the spin evolution of *ENVISAT* during 2017 and 2018 (Fig. 4 (a)) and of *TOPEX POSEIDON* during 2019 (Fig. 4 (b)) has been studied. The adjustment slope of the *ENVISAT* passes seems to indicate that the apparent spin trend remains approximately constant, with a decreasing trend of approximately 40 ± 30 ms/day, and with an average period of 190 ± 30 seconds. For *TOPEX POSEIDON*, the evolution of the period also seems to remain almost constant throughout the year, with a decrease of 1.1 ± 0.2 ms/day, practically imperceptible, and an average of 10.00 ± 0.15 seconds.

As for *AJISAI*, other oscillations can be found in the *ENVISAT* tracks because of their high accuracy as they are taken by a kHz laser from the Graz station. In this case they have an amplitude of between 6 and 8 mm and as mentioned, each of the peaks represents the change in the angle of incidence between

VII Workshop on Robotic Autonomous Observatories (October 16-20, 2023)
Editors: Maria Gritsevich, Alberto J. Castro-Tirado, Petr Kubánek, Shashi B. Pandey, and David Hiriart - DOI: https://doi.org/10.22201/ia.14052059p.2025.59.27

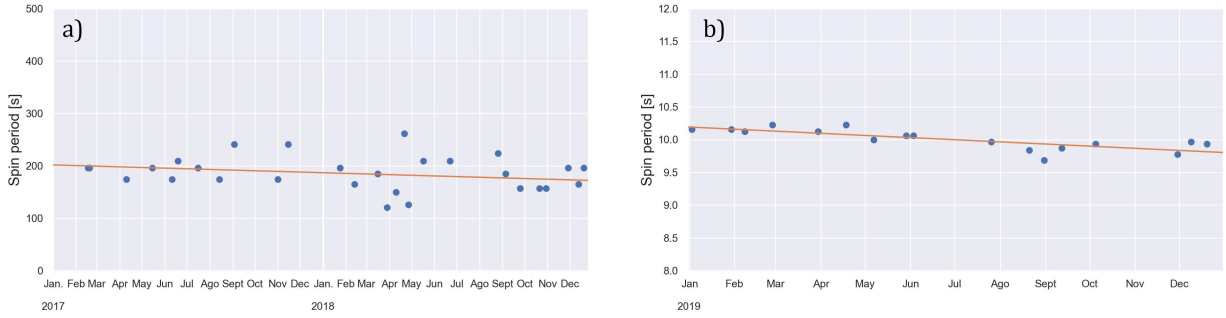


Fig. 4. (a) Evolution of the apparent spin period of *ENVISAT* during years 2017 and 2018. (b) Evolution of the apparent spin period of *TOPEX POSEIDON* during year 2019. The linear function indicates the decreasing trends during time.

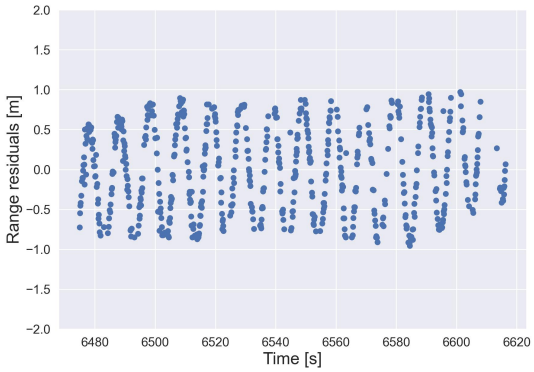


Fig. 5. Range residuals calculated for a *TOPEX POSEIDON* pass measured by Borowiec SLR station on December 8, 2023.

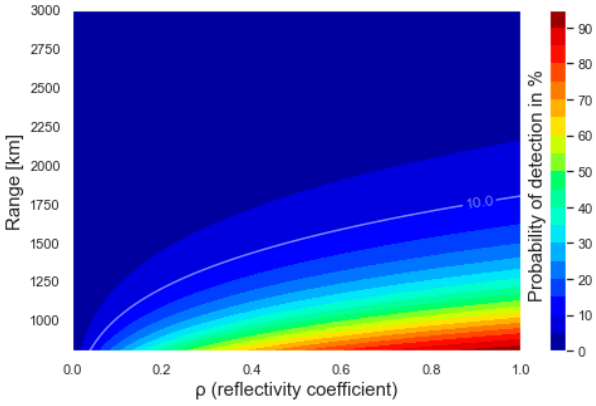


Fig. 6. Probability of detection as a function of the range to the satellite and the reflectivity of its surface (ρ).

the station's laser and the optical axis of the CCR on which the laser is currently incident. As with *AJISAI*, the minimum angle of incidence occurs when the CCRs axis is pointed towards the SLR ground station, this situation indicates the minimum angle of incidence CA between the optical axis of the reflector and the system laser.

Apart from the previous analysis of the residuals, it is interesting to briefly introduce the Laser-Radar transmission equation (Degnan 1993), although in this work the modified equation for space debris (Zhang 2012) has been used. This is very relevant when working with SLR techniques on space debris, as it measures the probability of obtaining laser echoes in tracking various orbital objects, such as satellites or space debris. It takes into account the structural characteristics of the object, such as its radar cross section (RCS); the reflectivity of its surface (ρ), which depends in part on whether it has mirrors and retroreflectors; various atmospheric effects; characteristics of the optical devices involved (transmission and reception efficiency); and the satellite's own position with respect to the station.

Using the Laser-Radar equation, it is then possible to test the probability of detecting laser echoes as a function of various parameters. In this case it is of interest to see the differences between satellites with different reflectivity coefficients ρ. For geodesic satellites it has the highest reflectivity on its surface, $\rho \approx 1$, but for other satellites or space debris in general the reflectivity tends to be lower and very variable from one object to another, $\rho < 1$. This is due, not surprisingly, to the presence of retroreflectors or mirrors or the reflectivity of the surface material. Figure 6 shows the dependence of the probability on the distance to the satellite and on the reflectivity.

4. DISCUSSION

From the various *ENVISAT* data analysed over the years 2017 and 2018, it has been determined that

VII Workshop on Robotic Autonomous Observatories (October 16-20, 2023)
Editors: Maria Gritsevich, Alberto J. Castro-Tirado, Petr Kubánek, Shashi B. Pandey, and David Hiriart - DOI: https://doi.org/10.22201/ia.14052059p.2025.59.27

there appears to be an increase in the apparent spin period of 132 ms/day. This result at first seems to contradict the results shown in the reference article (Kucharski et al. 2014), where it is indicated that in 2013 there seemed to be a clear increase in the period of 36.7 ms/day; however, if this growth rate in 2013 is taken into account and extrapolated to 2017/2018 it seems to be close to the average period of 190 ± 30 seconds corresponding to the evolution during these last years. Perhaps the discrepancy is simply due to the accuracy of the results. As for *TOPEX POSEIDON*, it is estimated that, during 2019, its period has remained approximately constant with a growth of 0.4 ms/day on average and an average period of 10.00 ± 0.15 seconds.

Apart from the actual rotation of the satellites about their centre of mass, another type of movement related to the variation in the angle of incidence between the laser and the optical axis of the CCRs has been observed. This motion is reflected in a series of millimetre-scale oscillations in the debris, only observable with high-precision SLR systems. This is why they have only been observed in *AJISAI* and *ENVISAT*, whose measurements are taken from the Graz laser station, and not in the *TOPEX POSEIDON* tracks.

5. CONCLUSIONS

Ultimately, accurate observation of the orbits of any uncontrolled object, whether by laser telemetry or any other technique, is crucial to gain a better understanding of the space environment. Being able to anticipate possible accidents and collisions between objects allows mitigating the effects and even avoiding such accidents and protecting orbital integrity. Furthermore, understanding rotational dynamics and their evolution not only allows the development of accurate models of orbital perturbations, but also provides the basis for effective automated decommissioning strategies for inactive satellites. This will ensure sustainable orbital space management and the viability of future clean and safe space missions.

Acknowledgements: I acknowledge the SLR stations in Graz (Austria) and Borowiec (Poland) for providing the laser data used in this work. This article is in memory of Dr. Manuel Catalán Morollón, who promoted the collaboration between the authors of the University of Cantabria and the Royal Institute and Navy Observatory, without whom this work would not have been possible.

REFERENCES

Degnan, J. 1993, Millimeter Accuracy Satellite Laser Ranging: A Review, Contributions of Space Geodesy to Geodynamics: Technology, 25, 133

Greene, B., Gao, Y., & Chris, M. 2002, Laser Tracking of Space Debris, in: Proceedings of the 13th International Laser Ranging Workshop, Washington, DC, USA, October 7–11, pp. 198

Kucharski, D., Otsubo, T., Kirchner, G., & Koidl, F. 2010, AdSpR, 46, 251

Kucharski, D., Kirchner, G., Koidl, F., et al. 2014, TGRS, 52, 7651

Marini, J. W., & Murray, C. W. 1973, Correction of laser range tracking data for atmospheric refraction at elevations above 10 degrees, NASA Technical Memorandum X-70555, Goddard Space Flight Center, Greenbelt, MD (USA)

Mendes, V. B. & Pavlis, E. C. 2004, GeoRL, 31, 14602

Ricklefs, R. L., & Moore, C. J. 2009, ILRS Consolidated Laser Ranging Data Format (CRD) Version 1.01

Ricklefs, R. L. 2006, ILRS Consolidated Prediction Format (CPF) Version 1.01

Zhang, Z-P. 2012, RA&A, 12, 212

Revista Mexicana de Astronomía y Astrofísica Serie de Conferencias (RMxAC), **59**, 179–182 (2025)
© 2025: Instituto de Astronomía, Universidad Nacional Autónoma de México
https://doi.org/10.22201/ia.14052059p.2025.59.28

VII Workshop on Robotic Autonomous Observatories (October 16-20, 2023)
Editors: Maria Gritsevich, Alberto J. Castro-Tirado, Petr Kubánek, Shashi B. Pandey, and David Hiriart - DOI: https://doi.org/10.22201/ia.14052059p.2025.59.28

A UNIQUE LOOK ON MICROMETEORITES: WHEN SPECTROSCOPY MEETS CITIZEN SCIENCE

M. R. López-Ramírez[1], J. Laserna[2], M. Hanna[3], J. Moilanen[4], and M. Gritsevich[3,4,5,6]

RESUMEN

Los micrometeoritos (MM) son partículas de polvo extraterrestre que sobreviven a la entrada atmosférica y pueden recuperarse de la superficie de un cuerpo planetario y, en términos de masa, constituyen una parte importante del flujo de material extraterrestre que se acumula en la superficie de la Tierra. Los MM que hemos analizado en este trabajo están compuestos de varios minerales, incluidos metales (como el níquel y el hierro) y silicatos (como el olivino y el piroxeno). Su composición y nivel de alteración pueden variar ampliamente dependiendo de su historia y a partir de su mineralogía y textura (relaciones espaciales y las formas de las fases dentro de las rocas) es posible obtener información sobre su alteración causada por los procesos de entrada atmosférica.

ABSTRACT

Micrometeorites (MMs) are extraterrestrial dust particles that endure atmospheric entry and are recoverable from the surface of a celestial body. In terms of mass, they constitute a significant portion of the extraterrestrial material flux accumulating on the Earth's surface. The MMs examined in this study consist of diverse minerals, encompassing metals such as nickel and iron, as well as silicates like olivine and pyroxene. Their composition and degree of alteration can vary widely, influenced by their unique history. The mineralogy and texture of MMs offer valuable insights into the alterations induced by atmospheric entry processes.

Key Words: instrumentation: spectroscopy — meteorites — methods: observational

1. INTRODUCTION

The extent of heating experienced by micrometeoroids entering Earth's atmosphere varies depending on factors such as size, mass, entry velocity, and angle. This results in flash melting and a diverse array of quench textures, morphologies, and chemical compositions. Combining these textures and chemical compositions enables the standardization of micrometeorite classification (Genge et al. 2008, Rubin & Grossman 2010). Micrometeorites (MMs) complement observations of meteor phenomena (Silber et al. 2018, Moilanen, Gritsevich & Lyytinen 2021), offering precise mineral and compositional determinations through laboratory techniques. This, in turn, provides essential constraints for interpreting spectroscopic data obtained from astronomical observations.

Collecting and identifying MMs need a deep understanding of what to seek and what to discard. Earlier research in this field, from NASA's comparative analysis of cosmic and industrial spherules in the 1960s to contemporary investigations into road dust in India and Hungary, has been fragmented and generally concluded that isolating micrometeorites in populated areas is a formidable challenge (Kurat et al. 1994). Therefore, MMs samples of the extraterrestrial dust flux allow study of the dust population within the early solar system and the nature and evolution of their parent bodies. The preservation of such particles in sediments also provides a record of events occurring beyond our planet over geological time (Dredge et al. 2010).

2. MICROMETEORITE SAMPLES AND INSTRUMENTATION

In 2010, Jon Larsen embarked on a systematic exploration of dust samples from populated areas. Beginning with surfaces oriented skywards, such as roads, roofs, parking lots, and industrial zones, where particles could accumulate over time, Larsen expanded his search to encompass diverse environments around the world, including cities, countries,

[1]Department of Physical Chemistry, Faculty of Science, University of Málaga, Málaga, Spain (melopez@uma.es).
[2]Department of Analytical Chemistry, Faculty of Science, University of Málaga, Málaga, Spain.
[3]Swedish Institute of Space Physics (IRF), Bengt Hultqvists väg 1, SE-98192, Kiruna, Sweden.
[4]Finnish Fireball Network, Ursa Astronomical Association, Kopernikuksentie 1, Helsinki FI-00130, Finland.
[5]Faculty of Science, University of Helsinki, Gustaf Hällsrömin katu 2, FI-00014 Helsinki, Finland.
[6]Institute of Physics and Technology, Ural Federal University, Mira str. 19, 620002 Ekaterinburg, Russia.

VII Workshop on Robotic Autonomous Observatories (October 16-20, 2023)
Editors: Maria Gritsevich, Alberto J. Castro-Tirado, Petr Kubánek, Shashi B. Pandey, and David Hiriart - DOI: https://doi.org/10.22201/ia.14052059p.2025.59.28

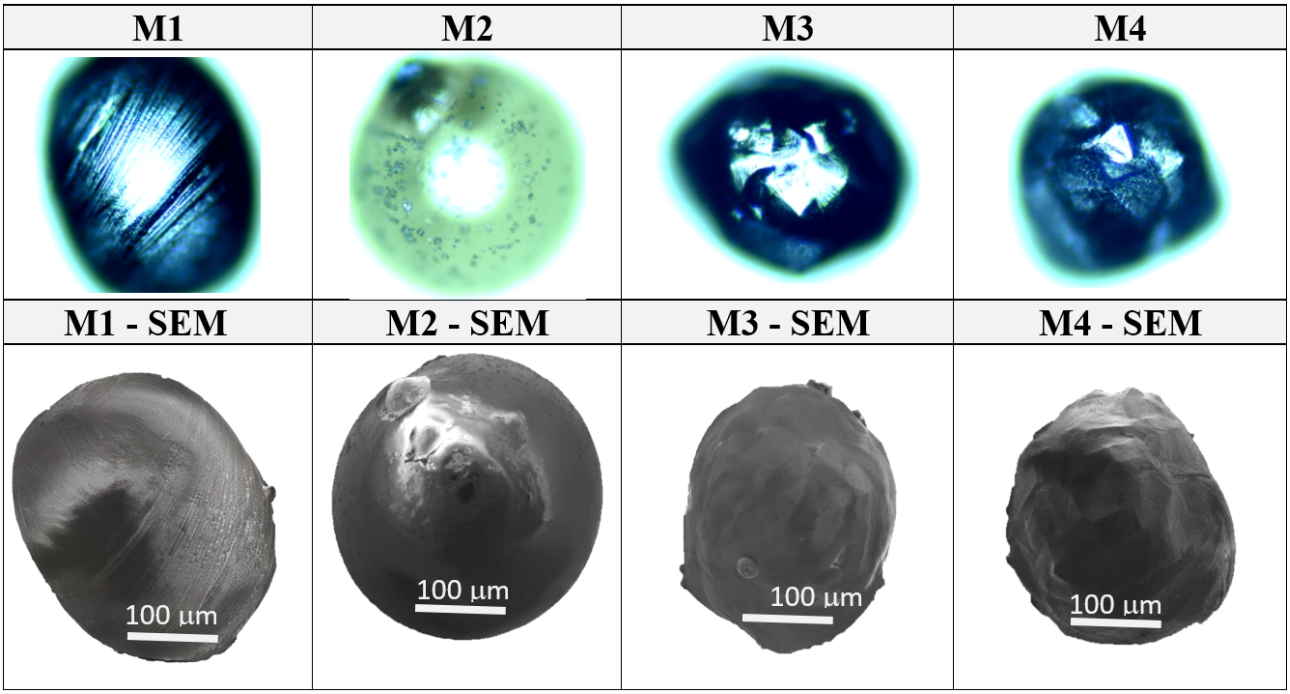


Fig. 1. Optical and scanning electron microscope (SEM) images of the MMs samples studied in this work.

mountains, beaches, and deserts. Now, after over a decade of research, spanning around 50 countries and involving over 1,000 field searches, representatives from every continent, he has amassed a substantial collection. Figure 1 shows the four selected MMs samples (named here M1-M4) from the Jon Larsen collection (Larsen 2017).

We have studied them by scanning electron and Raman microscopies. The scanning electron microscope (SEM) images were acquired by a high-performance scanning electron microscope with a high resolution of 3.0 nm, JEOL JSM-6490LV microscope. The Raman spectra were acquired with an Invia Qontor Confocal Raman microscope with and excitation laser of 532 nm. Its resolution was set at 2 cm^{-1} and the geometry of micro-Raman measurements was 180°. Laser focus diameter, which was of ca. 12 μm, allows measurements on a micrometer scale.

3. RESULTS AND ANALYSIS

The classification of micrometeorites depends on the peak temperature reached during atmospheric entry, caused by frictional heat that induces significant variations in the alteration process. About half of the micrometeoroids with sizes <0.1 mm experience a soft deceleration, ending up on the ground as unmelted MMs. The other half reaches peak temperatures between 1350−2000°C, sufficient to generate various types of melted cosmic spherules through the quenching process during atmospheric flight (Genge et al. 2008, Rubin & Grossman 2010).

The MMs examined in this study belong to the S-type group, which is the most common, characterized by olivine microphenocrysts, silicate glass, and often containing magnetite and/or chromite.

Within this S-type, they can be further subdivided into several subclasses based on their textural and mineralogical characteristics (Genge et al. 2008). In this work, we studied four MMs from three different subclasses: barred olivine spherules dominated by parallel growth dendrites of olivine (Fig. 1, M1), glass (V-type) vesicular spherules featuring a nickel-iron bead (Fig. 1, M2), and cryptocrystalline spherules (Fig. 1, M3 and M4).

We observe that **M1** sample is an aerodynamic ellipsoid micrometeorite that features a dark gray body color and fascinating circular crystal formations on its surface. Raman spectra on sample **M1** (Fig. 2) show distinctive bands of forsterite type olivine recorded at 821 and 853 cm^{-1} with magnetite Raman main band at 679 cm^{-1}. Dark olivine plate crystals interposed by interstitial magnetite crystals that glimmer in the light characterize the body of **M1**.

The sample **M2** is a glass (V-type) vesicular spherule that features a nickel-iron bead. We have acquired the corresponding Raman spectra in the

VII Workshop on Robotic Autonomous Observatories (October 16-20, 2023)
Editors: Maria Gritsevich, Alberto J. Castro-Tirado, Petr Kubánek, Shashi B. Pandey, and David Hiriart - DOI: https://doi.org/10.22201/ia.14052059p.2025.59.28

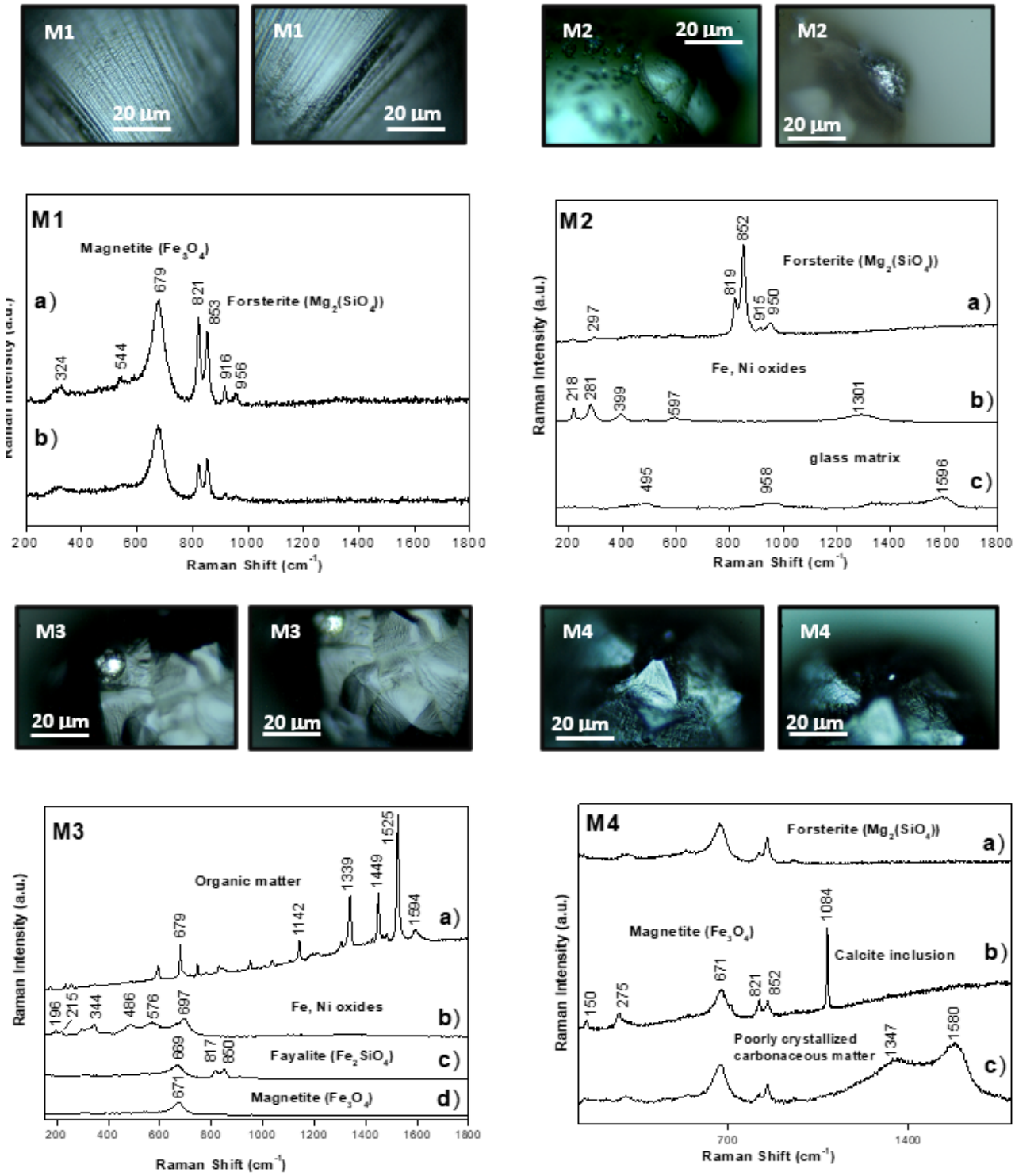


Fig. 2. Raman spectra of MMs studied and optical images (50x objective) showing details of the samples around the recorded area.

VII Workshop on Robotic Autonomous Observatories (October 16-20, 2023)
Editors: Maria Gritsevich, Alberto J. Castro-Tirado, Petr Kubánek, Shashi B. Pandey, and David Hiriart - DOI: https://doi.org/10.22201/ia.14052059p.2025.59.28

bead (Fig. 2, M2b) and in the area around it concluding that there are blends layers of olivine crystals (Fig. 2, M2a) on top of its main glass body (Fig. 2, M2c).

The **M3** sample is a cryptocrystalline spherules dominated by radiating clusters of fine olivine dendrites. In this case we observe that the Raman olivines bands recorder at 817 and 850 cm-1 (Fig. 2, M3c) are wider than the one in Fig. 2, M1a because the Raman spectrum of fayalite, Fe_2SiO_4, is different in appearance from the spectra of other isostructural olivine as i.e. forsterite, Mg_2SiO_4. For example, at ambient temperature the line width FWHH of the mode at 817 cm^{-1} could be about 1.5 times and the mode at 850 cm^{-1} about 3.5 times larger than the equivalent modes in forsterite. This broadening could be related to Fe^{2+} and its magnetic properties in the olivine structure (Kolesov & Geiger 2004). **M3** sample exhibits a nickel-iron bead in which we have detected organic compounds. Fig. 2, M3a shows that besides the weaker signal of olivine the spectrum presented several bands in the typical organic compounds' region of $1050-1650$ cm^{-1}.

The **M4** micrometeorite sample is another cryptocrystalline spherule dominated by phenocrysts of forsterite type olivine (Fig. 2, M4a). We have detected a very strong Raman band at 1084 cm^{-1} corresponding to a calcite inclusion within the olivine matrix. We can observe in Fig. 2, M4c Raman bands of carbonaceous D and G bands, recorded at approximately 1347 cm^{-1} and 1580 cm^{-1}, respectively. These bands reflect the highly disordered carbonaceous phases present in **M4** micrometeorite.

4. CONCLUSIONS

Scanning electron microscopy has been employed to examine the morphology of four selected micrometeorites from the Jon Larsen Collection. MicroRaman spectroscopy was utilized as an appropriate tool to study the chemical composition of these samples, known for their heterogeneous minerals. We identified two isostructural olivines, forsterite and fayalite, along with metal phases and carbonaceous material.

Acknowledgments: This research was supported, in part, by the Academy of Finland, Project No. 325806 (PlanetS) and Finnish Geospatial Research Institute. Special thanks to Jon Larsen for supplying the micrometeorite samples and to the Microscopy area of the Researching Services at the University of Málaga, where we conducted the sample analyses.

REFERENCES

Dredge, I., Parnell, J., Lindgren, P., & Bowden, S., 2010, ScJG, 46, 7

Genge, M. J., Engrand, C., Gounelle, M., & Taylor, S., 2008, M&PS, 43, 497

Kolesov, B. A., & Geiger, C. A., 2004, PCM, 31, 155

Kurat, G., Koeberl, C., Presper, T., Brandstatter, F., & Maurette, M., 1994, GeCoA, 58, 3879

Larsen, J. 2017, In Search of Stardust: Amazing Micrometeorites and Their Terrestrial Imposters, Ed. Voyageur Press

Moilanen J., Gritsevich M., & Lyytinen E., 2021, MNRAS, 503, 3337

Rubin, A. E. & Grossman, J. N., 2010, M&PS, 45, 114

Silber, E. A., Boslough, M., Hocking, W. K., Gritsevich, M., & Whitaker, R. W. 2018, AdSpR, 62, 489

Revista Mexicana de Astronomía y Astrofísica Serie de Conferencias (RMxAC), **59**, 183–185 (2025)
© 2025: Instituto de Astronomía, Universidad Nacional Autónoma de México
https://doi.org/10.22201/ia.14052059p.2025.59.29

VII Workshop on Robotic Autonomous Observatories (October 16-20, 2023)
Editors: Maria Gritsevich, Alberto J. Castro-Tirado, Petr Kubánek, Shashi B. Pandey, and David Hiriart - DOI: https://doi.org/10.22201/ia.14052059p.2025.59.29

USING ARTIFICIAL INTELLIGENCE AND MACHINE LEARNING IN EDUCATION OF ASTRONOMY, PHYSICS AND MATHEMATICS

F. Bahrani[1]

RESUMEN

Presentamos AstroTeach, donde una combinación innovadora de personalización e innovación redefine el panorama educativo en astronomía, física y matemáticas. Nuestra plataforma patentada impulsada por Inteligencia Artificial (IA) est diseñada exclusivamente para transformar la experiencia de aprendizaje, ofreciendo un nivel de individualización sin precedentes. Al comprender primero el conocimiento existente de cada alumno a través de preguntas intuitivas, adaptamos un paquete educativo que se adapta con precisión a su estilo y objetivos de aprendizaje. Este enfoque personalizado, reforzado por nuestra tecnología patentada, garantiza que los conceptos científicos complejos sean accesibles y atractivos para todos los alumnos. Desde profundizar en los misterios del cosmos hasta desentrañar las complejidades de la mecánica cuántica y las matemáticas avanzadas, nuestra plataforma se adapta a cada individuo, haciendo que la exploración científica no sólo sea efectiva sino también estimulante. En AstroTeach, prevemos el uso de telescopios robóticos, y estamos comprometidos a encender la pasión por el aprendizaje y la exploración, brindando a los usuarios un viaje personalizado a través de las maravillas de la ciencia, mejorado por nuestra innovadora y patentada tecnología de IA.

ABSTRACT

Introducing AstroTeach, where a groundbreaking blend of personalization and innovation redefines the educational landscape in astronomy, physics, and mathematics. Our patented AI-driven platform is uniquely designed to transform the learning experience, offering an unprecedented level of individualization. By first understanding each learners existing knowledge through intuitive questioning, we tailor an educational package precisely suited to their learning style and objectives. This personalized approach, bolstered by our patented technology, ensures that complex scientific concepts become accessible and engaging for every learner. From delving into the mysteries of the cosmos to unraveling the intricacies of quantum mechanics and advanced mathematics, our platform adapts to each individual, making scientific exploration not only effective but exhilarating. At AstroTeach, we foresee the use of robotic telescopes, and are committed to igniting a passion for learning and exploration, empowering users with a personalized journey through the wonders of science, enhanced by our innovative and patented AI technology.

Key Words: Artificial Intelligence — Machine Learning — Education

1. INTRODUCTION

In the rapidly evolving landscape of technology, Artificial Intelligence (AI) and Machine Learning (ML) stand as pillars of innovation, reshaping how we interact with the world around us. AI, defined as the simulation of human intelligence processes by machines, particularly computer systems, has become a cornerstone of modern technological advancement. ML, a subset of AI, involves the development of algorithms that enable machines to learn from and make decisions based on data. A groundbreaking work on deep learning is LeCun, Bengio and Hinton (2015).

The transformative power of AI and ML extends far beyond just automation and efficiency. These technologies are key drivers in creating personalized experiences and solving complex problems across industries, from healthcare to education. In the field of education, AI and ML are revolutionizing traditional teaching methodologies, enabling personalized and adaptive learning experiences.

Following our past experience in Shiraz University and with the automatization of astronomical observatories in Iran (Bordbar & Bahrani 2016, Hendi & Bahrani 2019, 2021), we have developed AstroTeach, focusing on a new methodology for teaching science in general and astronomy in particular. At AstroTeach, we harness the potential of AI and ML to redefine educational experiences in astronomy, physics, and mathematics. Our approach,

[1]AstroTeach Ltd., Spark Centre, 2 Simcoe Street South, Suite 300, Oshawa, ON. L1H 8C1, Canada (Bahrani@astroteach.ca).

VII Workshop on Robotic Autonomous Observatories (October 16-20, 2023)
Editors: Maria Gritsevich, Alberto J. Castro-Tirado, Petr Kubánek, Shashi B. Pandey, and David Hiriart - DOI: https://doi.org/10.22201/ia.14052059p.2025.59.29

grounded in the latest advancements in AI and ML, highlighting the future of learning as an adaptive and personalized journey.

2. TRANSFORMING EDUCATION THROUGH AI AND ML

The educational landscape is undergoing a significant transformation,spearheaded by advancements in AI and ML. These technologies are not just supplementary tools; they are reshaping the very fabric of educational methodologies and experiences.

2.1. *Customized Learning Pathways*

One of the most significant impacts of AI and ML in education is the creation of customized learning pathways for students. AI systems can analyze individual learning patterns and tailor the educational content accordingly. This personalized approach ensures that each student's unique learning needs and abilities are addressed. According to Ferguson et al. (2000), personalized learning can be tailored to individual student needs.

2.2. *Enhanced Interactive Learning*

Both AI and ML enable the development of interactive learning environments that engage students in novel ways. These technologies facilitate simulations and game-based learning experiences that enhance understanding and retention of complex concepts.

2.3. *Efficient Educational Administration*

AI also streamlines administrative processes within educational institutions. ML algorithms can efficiently handle tasks such as student enrollment management, grading, and even personalized feedback. This automation reduces the workload on educators, allowing them to dedicate more time to student interaction and teaching.

2.4. *Breaking Language and Accessibility Barriers*

AI is playing a crucial role in breaking down language barriers and enhancing accessibility in education. Tools powered by AI, such as real-time translation and speech-to-text services, make education more inclusive and accessible, especially for students with disabilities or those who are non-native speakers of the instruction language.

At AstroTeach, we embrace these innovative AI and ML technologies to provide an education that is not just informative but also adaptive and engaging. By integrating these cutting-edge tools, we are committed to building a future where education is universally accessible, highly personalized, and profoundly impactful.

3. REVOLUTIONIZING LEARNING: ASTROTEACH'S AI-DRIVEN JOURNEY IN SCIENCE EDUCATION

AstroTeach (2024) is an innovative, AI-powered educational platform, revolutionizing how astronomy, physics, and mathematics are taught and learned. It offers personalized, interactive learning experiences, adapting to individual learners' styles and needs. Its unique approach leverages advanced AI algorithms to create custom learning pathways, enhancing understanding and engagement. Targeting a broad audience, including students, educators, and astronomy enthusiasts, AstroTeach combines technology with education, making complex scientific subjects accessible and exciting. Its business model focuses on membership subscriptions and specialized consultations, aiming to be a leader in the e-learning landscape.

3.1. *Innovative Learning Approach*

At the core of AstroTeach is a commitment to personalized education. Our platform employs sophisticated AI algorithms to analyze individual learning styles and preferences. By doing so, we create customized learning pathways that cater to the unique needs of each student, making the learning process not only more effective but also highly engaging.

3.2. *Interactive and Adaptive Content*

AstroTeach's content is not static; it's dynamic and interactive. We utilize ML to adapt the curriculum in real-time, based on the learners progress and feedback. This adaptability ensures that each learner is consistently challenged at just the right level, facilitating optimal learning outcomes.

3.3. *Bridging Gaps in Education*

Our platform is particularly beneficial for students who might find traditional classroom settings challenging. Whether it's due to different learning abilities, language barriers, or simply a need for a more engaging learning format, AstroTeach provides a solution. We believe that education should be inclusive, and our platform is designed to be just that.

3.4. *Empowering Educators and Institutions*

While our primary focus is on learners, AstroTeach also empowers educators and educational institutions. By providing them with advanced tools and analytics, educators can gain insights into their students' learning processes, enabling more informed teaching strategies and interventions.

VII Workshop on Robotic Autonomous Observatories (October 16-20, 2023)
Editors: Maria Gritsevich, Alberto J. Castro-Tirado, Petr Kubánek, Shashi B. Pandey, and David Hiriart - DOI: https://doi.org/10.22201/ia.14052059p.2025.59.29

3.5. *Looking Towards the Future*

As we continue to grow, AstroTeach remains committed to innovation in education. We are constantly exploring new technologies and methodologies to enhance our platform and stay at the forefront of educational advancements.

AstroTeach is more than just a learning platform; its a gateway to the future of education, where technology and learning converge to create an unparalleled educational experience.

4. A PIONEERING PATENT: ASTROTEACH'S TECHNOLOGICAL EDGE

AstroTeach is not only an innovator in AI-driven education but also a protector of its innovations. Our patented technology is the cornerstone of our unique educational platform, distinguishing us in a competitive market. This patent represents a commitment to originality, quality, and the continuous advancement of our educational tools.

It's this proprietary technology that allows us to offer unrivaled personalized learning experiences. Our patent covers the specific AI and ML algorithms that adapt to each learner's style and pace, ensuring that our educational delivery is as unique as each student who uses our platform.

By securing our methods and systems through intellectual property rights, AstroTeach ensures that we can keep delivering exceptional educational experiences while also investing in the research and development of future innovations. It's a testament to our dedication to excellence and a promise of our ongoing evolution in the edtech space.

5. ENVISIONING THE FUTURE OF ASTROTEACH

As we look toward the horizon, the future of AstroTeach is illuminated by the promise of innovation and the continuous pursuit of knowledge. Our roadmap includes harnessing next-generation AI and ML advancements to deepen the personalization of learning experiences. We are exploring the integration of virtual and augmented realities to bring celestial phenomena into the hands of learners, making the study of the cosmos more interactive and immersive.

An exciting development on the horizon is our plan to provide access to robotic telescopes, enabling learners to experience real-time astronomical observations. This feature will empower users to directly engage with the universe, conducting observations from anywhere in the world. By incorporating robotic telescopes, AstroTeach will create a bridge between theoretical learning and hands-on experience, further enhancing the immersive nature of our platform.

The frontier of space is as vast as the potential of learning, and AstroTeach is committed to expanding its educational offerings, exploring new subjects where AI can make a significant impact. We envision a future where AstroTeach becomes synonymous with lifelong learning and curiosity, where users from around the globe turn to us not just for education, but for an inspiring journey through the wonders of science.

Partnerships with educational institutions, research organizations, and observatories are on the agenda, aiming to create a collaborative ecosystem that fosters discovery and innovation. Our commitment to education extends beyond the present, building a legacy that inspires future generations to reach for the stars.

AstroTeach is not just adapting to the future; we are actively shaping it, creating a world where education, technology, and hands-on astronomical exploration unite to unlock the full potential of every learner.

6. CONCLUSION

In summary, AstroTeach is a trailblazer in the educational technology sector, leveraging AI and ML to tailor learning in astronomy, physics, and mathematics. Its unique platform offers a personalized education journey, making science accessible and engaging. With a commitment to innovation, AstroTeach is not only enhancing the learning experience today but is also poised to shape the future of education. As it expands its offerings and explores new technological frontiers, AstroTeach stands as a beacon of lifelong learning and inspiration, inviting learners worldwide to explore the universe's mysteries with cutting-edge tools at their fingertips.

REFERENCES

AstroTeach. 2024, AstroTeach: AI-Driven Science Education, retrieved from `www.astroteach.ca`.

Bordbar, G. H. & Bahrani, F. 2016, RMxAC, 48, 118

Ferguson, D. L., Ralph, G., Meger, G., et al. 2000, Designing Personalized Learning for Every Student, ASCD Ed.

Hendi, S. H. & Bahrani, F. 2019, RMxAC, 51, 50

Hendi, S. H. & Bahrani, F. 2021, RMxAC, 53, 42

LeCun, Y., Bengio, Y., & Hinton, G. 2015, Natur, 521, 436, doi:10.1038/nature14539

Revista Mexicana de Astronomía y Astrofísica Serie de Conferencias (RMxAC), **59**, 187–192 (2025)
© 2025: Instituto de Astronomía, Universidad Nacional Autónoma de México
https://doi.org/10.22201/ia.14052059p.2025.59.30

VII Workshop on Robotic Autonomous Observatories (October 16-20, 2023)
Editors: Maria Gritsevich, Alberto J. Castro-Tirado, Petr Kubánek, Shashi B. Pandey, and David Hiriart - DOI: https://doi.org/10.22201/ia.14052059p.2025.59.30

DEVELOPING SCHOOL SCIENCE SKILLS THROUGH THE SCIENCE-IES ROBOTIC TELESCOPE PROJECTS

J. R. Girón-Gambero[1]

RESUMEN

Desde 2013, algunos de los proyectos Science-IES en Institutos de Enseñanza Secundaria en Málaga y provincia (España) se centran en el uso de telescopios robóticos y conjuntamente con el resto de proyectos, y se presentan como oportunidades para el desarrollo de habilidades científicas escolares en estudiantes de secundaria y bachillerato, especialmente en lo que respecta a la explicación de fenómenos científicos. También están conectados con el conocimiento de las disciplinas que conforman el enfoque STEM (Ciencia, Tecnología, Ingeniería y Matemáticas), manifestándose esta conexión en mayor medida con la parte científica y matemática.

ABSTRACT

Scince 2013, some of Science-IES (high-schools) projects in Málaga and its province (Spain) focus on the use of robotic telescopes and together with all the other projects are presented as opportunities for the development of school science skills in secondary and high school students, especially with regard to the explanation of scientific phenomena. They are also connected with knowledge of the disciplines that make up the STEM (Science, Technology, Engineering & Mathematics) approach, this connection being manifested to a greater extent with the scientific and mathematical part.

Key Words: education — instrumentation: detectors — methods: observational — telescopes

1. INTRODUCTION

The competency-based vision of education guided by international standards (OECD 2023), aims for students to develop specific competences and STEM competences (mathematical competence and competence in science, technology and engineering) at school stages (MECyD 2022). This development can take place through formal education in the classroom or through school science programmes (Pérez-Cáceres et al. 2017). One of the best known in Andalusia is Science-IES, formerly known as PIIISA (Lupión and Pérez-Cáceres 2017), in which secondary school students work together with scientists from universities or research centres.

ScienceIES is a distinctive way to teach Astronomy and other scientific disciplines, focusing in high-school students (age 15-17). ScienceIES is the name of the project started in 2010 at regional level in Andaluca (south Spain) pulling together the educational and scientific systems with students in the target[2]. Some of the Astronomy projects are based on the use of robotic telescopes (Castro-Tirado et al. 2021), such as the ones of the BOOTES worldwide network (Castro-Tirado 2023).

The approach in the secondary school classroom of transversal practices that integrate Science, Technology, Engineering and Mathematics (STEM) disciplines is complicated and not very viable due to the organisation of the curriculum (Gardner & Tillotson 2019; Toma & Greca 2018), therefore the Science-IES programme is an interesting approach for the development of transdisciplinary STEM scientific knowledge as it is oriented towards problem solving and contextualised in diverse and real situations (Aguilera et al. 2022). While it is true that the programme as a whole was assessed from an educational perspective in a previous edition (Lupión et al. 2022), this is the first time that projects using robotic telescopes are specifically analysed for a wide range of years, in order to determine the degree to which they develop scientific skills (OECD 2023) and contribute to the knowledge of the different disciplines that constitute the STEM educational approach.

2. METHODOLOGY

Since 2013, some of the annual Science-IES projects have been developed with robotic telescopes as the focus (Castro-Tirado et al. 2021). A total of 121 secondary and high school students from secondary schools in Málaga (including the

[1]Facultad de Ciencias de la Educación, Departamento de Didáctica de la Matemática, Didáctica de las Ciencias Sociales y de las Ciencias Experimentales, Universidad de Málaga, Boulevard Louis Pasteur 25, 29010 Málaga, Spain (jrgiron@uma.es).

[2]https://piiisaandalucia.blogspot.com/

VII Workshop on Robotic Autonomous Observatories (October 16-20, 2023)
Editors: Maria Gritsevich, Alberto J. Castro-Tirado, Petr Kubánek, Shashi B. Pandey, and David Hiriart - DOI: https://doi.org/10.22201/ia.14052059p.2025.59.30



Fig. 1. *Left:* Flare stars high-school students' ScienceIES poster. *Right:* Pluto's atmosphere high-school students' ScienceIES poster.



Fig. 2. *Left:* Meteors and fireballs high-school students' ScienceIES poster. *Right:* The Local Group of Galaxies high-school students' ScienceIES poster.

province) and 11 scientists from two research centres in Málaga and Granada have collaborated closely. The three research centres are: University of Málaga (UMA), Institute of Astrophysics of Andalucía of the State Agency Spanish Research Council (IAA-CSIC) and Institute of Subtropical and Mediter-

VII Workshop on Robotic Autonomous Observatories (October 16-20, 2023)
Editors: Maria Gritsevich, Alberto J. Castro-Tirado, Petr Kubánek, Shashi B. Pandey, and David Hiriart - DOI: https://doi.org/10.22201/ia.14052059p.2025.59.30



Fig. 3. *Left:* Astrobiology and exoplanets high-school students' ScienceIES poster. *Right:* Solar activity high-school students' ScienceIES poster.

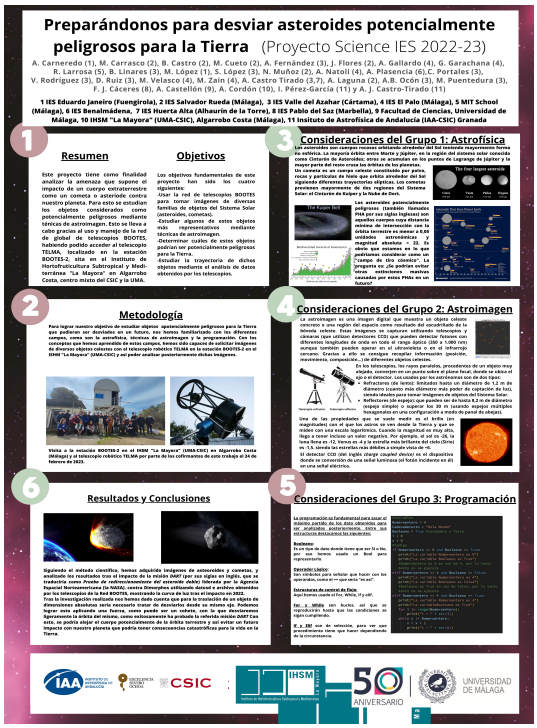


Fig. 4. Potentially hazardous asteroids high-school students' ScienceIES poster. This one and the above mentioned projects have been conducted under the supervision of A. J. Castro-Tirado (IAA-CSIC and UMA).

ranean Hortofruticulture La Mayora (IHSM\UMA-CSIC). In order to assess the educational interest of these projects, the scientific posters (Figures 1-7) were used as a source of data, as they had been prepared by the students following the usual scientific dissemination structure of real science congresses. In the didactic analysis procedure, the PISA 2025 Framework (OECD 2023) is taken as a reference, which establishes three main scientific competences that, in turn, are broken down into skills that, as a whole, determine the students' degree of competence. In this research, achievement indicators have been designed for each of the Framework´s competences, so that the contribution of the projects as a whole to the development of scientific competences can be studied (Tables 1-3). Moreover, due to the specific nature of the procedures followed in the robotic telescope projects, it is possible to link these indicators to dimensions of the STEM competence, for example: the use of specific software is linked to the "E" of Engineering or the use of astronomical magnitudes to the "M" of Mathematics (Tables 1-3).

3. RESULTS

All the projects develop the capacities established by the PISA 2025 Framework, based on the indicators detected in each of them (Tables 1-3).

VII Workshop on Robotic Autonomous Observatories (October 16-20, 2023)
Editors: Maria Gritsevich, Alberto J. Castro-Tirado, Petr Kubánek, Shashi B. Pandey, and David Hiriart - DOI: https://doi.org/10.22201/ia.14052059p.2025.59.30

Table 1. Contribution of the projects to the development of the scientific competence "Explaining phenomena scientifically".

1. Explaining phenomena scientifically		
Capacities	*Indicators*	*STEM*
Recall and apply appropriate scientific knowledge	Uses laws and theories of astronomy	S
	Uses astronomical magnitudes and units of measure	M
	Describes telescopes according to their technical characteristics	E
	Applies specific formulas	S
Use different forms of representations and alternate between them.	It represents complex parameters (light curve, Wolf number...) and corresponds to real images provided by telescopes.	E
		M
Recognise and develop explanatory hypotheses for phenomena in the material world	Indicates problem or hypothesis in introductory part	S
Explain the potential implications of scientific knowledge for society.	Outlines in conclusions the implications for society	T
		S

Fig. 5. Contribution of the projects to the development of the scientific competence “Explaining phenomena scientifically”.

Table 2. Contribution of the projects to the development of the scientific competence "Constructing and evaluating scientific research designs and interpreting scientific data and evidence critically".

2. Construct and evaluate designs for scientific research and interpret scientific data and evidence critically.		
Capacities	*Indicators*	*STEM*
Identifying the question in a specific scientific study	Set concise objectives	S
	It draws conclusions that respond to the objectives	S
		E
Interpret data presented in different representations, draw appropriate conclusions from the data and evaluate their relative merits.	Analyses telescope images of celestial bodies	S
	Includes and interprets electromagnetic spectra or complex graphs	M
	Specifies a procedure in methodology for analysing data	T
	Uses specialised software to obtain data	E
	Drawing conclusions based on astronomical data	M

Fig. 6. Contribution of the projects to the development of the scientific competence “Constructing and evaluating scientific research designs and interpreting scientific data and evidence critically”.

The most important skill to develop is “remembering and applying appropriate scientific knowledge”, which transcends school science and is specific to the researchers with whom the pupils collaborated.

The skill it contributes most to developing is “Interpret data presented in different representations, draw appropriate conclusions from the data and evaluate their relative merits”, extracted from complex measuring devices used by scientists in their research.

This competence is developed to a lesser extent, with scientific arguments constructed using complex scientific data appearing.

The projects contribute to the development of the three scientific competences, but when analysed

VII Workshop on Robotic Autonomous Observatories (October 16-20, 2023)
Editors: Maria Gritsevich, Alberto J. Castro-Tirado, Petr Kubánek, Shashi B. Pandey, and David Hiriart - DOI: https://doi.org/10.22201/ia.14052059p.2025.59.30

Table 3. Contribution of the projects to the development of the scientific competence "Investigate, evaluate and use scientific information to make decisions and take action".

3. Research, evaluate and use scientific information to make decisions and take action.		
Capacities	*Indicators*	*STEM*
Construct an argument to support an appropriate scientific conclusion from a set of data.	Includes sentences with scientific arguments	S

Fig. 7. Contribution of the projects to the development of the scientific competence “Investigate, evaluate and use scientific information to make decisions and take action”.

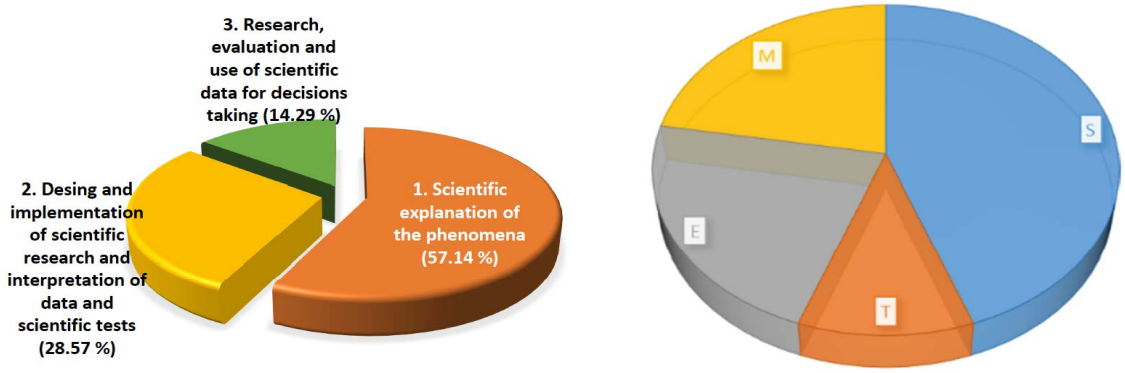


Fig. 8. *Left:* Overview of the contribution of projects to the development of scientific competences. *Right:* Connecting the projects to the different disciplines of the STEM education approach.

on the basis of the indicators, the relative weight between them is unequal (Figure 8, left).

Finally, the analysis of the indicators also provides information regarding the connection of the projects with the different disciplines of the STEM education approach (Figure 8, right).

It appears that these projects are connected to a greater extent with the scientific and mathematical part of STEM.

4. CONCLUSIONS

Science-IES projects that focus on the use of robotic telescopes are presented as opportunities for the development of school science skills in secondary and high school students, especially with regard to the explanation of scientific phenomena. They are also connected with knowledge of the disciplines that make up the STEM approach, this connection being manifested to a greater extent with the scientific and mathematical part. It is therefore necessary to continue this collaboration between astrophysicists and schoolchildren in order to provide a stable framework for the development of scientific skills in the context of astronomy.

Acknowledgements: I want to thank F. J. Pérez-Cáceres and A. J. Castro-Tirado for very useful conversations. I also acknowledge the support of the Spanish Ministry Project PID 2023-147028NB-I00 “STE(A)M y CIUDADANÍA. Desarrollo con procesos de indagación y argumentación en la formación del docente de ciencias y su enseñanza. Estudio identitario, entornos y género” (EduCA-STE(A)M).

REFERENCES

Aguilera, D., García-Yeguas, A., Perales-Palacios, F. J., & Vílchez-González, J. M. 2022, “Diseño y validación de una rúbrica para la evaluación de propuestas didácticas STEM (RUBESTEM)”, Revista Interuniversitaria de Formación del Profesorado (continuation of the former Revista de Escuelas Normales), 97 (36.1)

Castro-Tirado, A. J., Pérez-Cáceres, F. J., Castellón, A., et al. 2021, RMxAC, 53, 151

Castro-Tirado, A. J. 2023, Nat Astron, 7, 1136

Gardner, M. & Tillotson, J. W. 2019, International Journal of Science and Mathematics Education, 17, 1283

Lupión, T. & Pérez-Cáceres, F.J. 2017, Apostando por las vocaciones científicas desde la Educación Secun-

daria. Oportunidades mediante investigaciones con el programa Science-IES (PIIISA), UMA Editorial, Universidad de Málaga, Málaga

MECyD 2022, Real Decreto 217/2022, de 29 de marzo, por el que se establece la ordenación y las enseñanzas mínimas de la Educación Secundaria Obligatoria. Boletín Oficial del Estado, 76, de 30 de marzo de 2022, pp. 41571-41789 (https://www.boe.es/eli/es/rd/2022/03/29/217)

OECD 2023, Programme for International Student Assessment (PISA) 2025 Science Framework. OECD Publishing (https://www.oecd.org/en/about/programmes/pisa.html)

Pérez-Cáceres, F. J, Vílchez, J. M., & González, F. 2017, "La colaboración científicos-profesores-estudiantes (STSPs) para mejorar la alfabetización científica. Los contenidos procedimentales y actitudinales en las leyes educativas en España", Enseñanza de las ciencias: revista de investigación y experiencias didácticas (Extra Issue), pp. 555-560

Toma, R. B. & Greca, I. M. 2018, Eurasia Journal of Mathematics, Science and Tecnology Education, 14(4), 1383

VII Workshop on Robotic Autonomous Observatories (October 16-20, 2023)
Editors: Maria Gritsevich, Alberto J. Castro-Tirado, Petr Kubánek, Shashi B. Pandey, and David Hiriart - DOI: https://doi.org/10.22201/ia.14052059p.2025.59.30

Revista Mexicana de Astronomía y Astrofísica Serie de Conferencias (RMxAC), **59**, 193–195 (2025)
© 2025: Instituto de Astronomía, Universidad Nacional Autónoma de México
https://doi.org/10.22201/ia.14052059p.2025.59.31

VII Workshop on Robotic Autonomous Observatories (October 16-20, 2023)
Editors: Maria Gritsevich, Alberto J. Castro-Tirado, Petr Kubánek, Shashi B. Pandey, and David Hiriart - DOI: https://doi.org/10.22201/ia.14052059p.2025.59.31

TULANCINGO-I: THE K BAND MEXICAN RADIOTELESCOPE

D. Hiriart[1], E. Colorado[1], F. Diaz[1], T. Calvario[1], H. Serrano[1], D. Rojas[1], and S. Kurtz[2]

RESUMEN

En este artículo presentamos un proyecto en proceso para la conversión de una antena de telecomunicaciones de 32 m de diámetro para investigación en astronomía. La antena está localizada cerca del poblado de Tulancingo, Hidalgo, en la parte central de México. Operando originalmente en la banda C, las pruebas de la superficie han demostrado que su superficie es útil hasta la banda K. Presentamos los resultados principales que avalan la realización de este proyecto.

ABSTRACT

In this paper, we present an ongoing initiative to convert a 32-meter diameter communication antenna into a radiotelescope for astronomy studies. The antenna is located in central México's state of Hidalgo at the town of Tulancingo. Originally operating at the C-band, its surface accuracy as been probed to be useful up to K-band. We present the main results that points to the feasibility of this project.

Key Words: Radiotelescopes — radio continuum:ISM — radio lines: General

1. INTRODUCTION

The Tulancingo earth station was constructed in Tulancingo, Hidalgo, México, as a part of a project to transmit the 1968 Summer Olympic Games worldwide. The design and construction of the antenna were managed by Mitsubishi Industries. It consists of a 32-m diameter, Cassegrain shaped, parabolic antenna located at then newly established Tulancingo ground station. The station was the principal satellite ground station in México used by the Mexican satellite communication network. From 1986 on, the site was managed by TELECOMM, a decentralized public institution that managed the telegraphic, satellite, and other telecommunication services. During almost 40 years of service, the antenna was maintained in optimal condition and was finally decommissioned in 2010.

The Tulancingo-I antenna (TUL-I) is now part of a project to convert the old satellite infrastructure into a radiotelescope capable of performing radio astronomical observations (Kurtz et al. 2022). The project began in 2018 as a collaboration between the National Autonomous University of México and the University of Oxford, through financial support from the Newton Fund (STFC-UKRI), in collaboration with TELECOMM, the Mexican Space Agency, and the State Government of Hidalgo. The goal of the project is to provide the Mexican research and a teaching community with infrastructure to train students in radio astronomy and carry out astronomical research. Figure 1 shows a photograph of the antenna and Table 1 presents the main characteristics of the telescope. Details of the antenna optical system can be found at Velazquez et al. (2022).



Fig. 1. The TUL-I antenna at Tulancingo earth station (Velazquez et al. 2022).

[1]Instituto de Astronomía, UNAM, Campus Ensenada, Apartado Postal 106, 22860, Ensenada, Baja California, México (hiriart@astro.unam.mx).
[2]Centro de Radioastronomía y Astrofísica, UNAM, Campus Morelia, Apartado Postal 3–72, 58090, Morelia, Michoacán, México (s.kurtz@irya.unam.mx).

VII Workshop on Robotic Autonomous Observatories (October 16-20, 2023)
Editors: Maria Gritsevich, Alberto J. Castro-Tirado, Petr Kubánek, Shashi B. Pandey, and David Hiriart - DOI: https://doi.org/10.22201/ia.14052059p.2025.59.31

TABLE 1

CHARACTERISTICS OF THE TUL-I ANTENNA

Specification	**Description**
Optical System	Cassegrain
Diameter	32 m
Focal length	9.6 m
Focal ratio	f/D=0.3
Diameter	2.8 m
Weight	350 tons
Angular Travel in Acimut	$\pm$ 200°
Angular Travel in Elevation	0– 92°
Maximum velocity in Acimut	$1°s^{-1}$
Maximum velocity in Elevation	$1°s^{-1}$

The telescope will operate in the 1.4–24 GHz range (from L to K bands), both as a stand-alone facility and potentially as part of an international VLBI network. The extension to K-Band is particularly important for radio astronomical studies, because this band includes the water line at 22.235 GHz and the ammonia lines from 23.693 to 24.5 GHz. It would also allow the telescope to participate in the Third International Celestial Reference Frame project (ICRF-3) to determine the galactic acceleration and source positions at 8, 24, and 32 GHz (Charlot et al. 2020).

In this work we present a summary of the works that have been made in the antenna in order to turn it into a radiotelescope.

2. ANTENNA SURFACE

Initially, the TUL-I antenna operated in the C-band, ranging from 4 to 6 GHz. The initial goal was to find out if the antenna surface was good enough to work at K-band (24 GHz) for radio astronomy use. The characterization of the antenna surface was made by the Large Millimeter Telescope National Laboratory in 2020 (Gale 2020). The objective was to know the shape and errors of the main reflector, the subreflector and the tertiary reflector. It was found that the error of primary reflector at zenith (1.094 mm) and 60° elevation (1.305 mm).

A simulation of the electromagnetic antenna patterns based on the results of the optical study were made by Velazquez et al. (2022). The electromagnetic analysis indicates that the antenna is capable of performing observations in the L, C, and X bands without systematic reductions in efficiency. On the other hand, at K-Band, the antenna can perform observations but is limited by rms errors presented at the main reflector surface (Velazquez et al. 2022).

3. TUL-I RECEIVERS

Currently, we have three receivers for use at the TUL-I radio telescope:

- L–Band receiver from the Instituto de Radioastronomía y Astrofísica (IRyA-UNAM);
- C–Band receiver from the University of Oxford (U-Oxford);
- K–Band receiver from the Hartebeesthoek Radio Astronomy Observatory (HartRAO).

The backend of the IRyA receiver is based on a Software-Defined Radio (SDR) (Dillinger, Mandani & Alonistoti 2003), while for the other two receivers, the backends are based on a Xilinx-Zynq®(Churiwala 2017). We intend to standardize all backends to a system based on a Radio Frequency System-on-Chip, known as RFSoC (Liu 2021). Table 2 provides a concise summary of the receiver characteristics that will be employed in the TUL-I radiotelescope.

As a part of this project, we are also developing a dual K-band radiometer at 20/25.5 GHz to measure atmospheric water vapor and to determine the path delay of electromagnetic signals (Claflin, Wu & Resch 1978). This radiometer will be installed at the TUL-I site and potential sites for the new antennas of the new generation Very Large Array (ngVLA) in Northern México to characterize this parameters at those sites.

4. ANTENNA MOTIONS

The Tulancingo I and II antennas have not been used for more than a decade. That causes many problems, such as oxidation of the building's metallic structures and antenna, damage to the concrete, oil leaks, etc. After initializing the project, there was a renewal of the lubrication systems and hydraulic pumps, new seals, and the cleaning of rust from gears, etc. These essential jobs were done before trying to move the antenna. The elevation and azimuth gears were in excellent condition, as the antennas did not move too much since they did not need to follow a geostationary satellite. Since the antenna pointed in a single direction in the sky, it was not equipped with a tracking system. Pointing of the antenna in azimuth and elevation was done by electric motors by pushing buttons on a handset.

The State of Hidalgo Government hired the company to install new servomotors, new encoders, and new control electronics for the antenna. Based on this system, we developed the control software for

VII Workshop on Robotic Autonomous Observatories (October 16-20, 2023)
Editors: Maria Gritsevich, Alberto J. Castro-Tirado, Petr Kubánek, Shashi B. Pandey, and David Hiriart - DOI: https://doi.org/10.22201/ia.14052059p.2025.59.31

TABLE 2

RECEIVERS FOR THE TUL-I ANTENNA

Institution	Band	Freq. Range (MHz)	IF Badnwidth (MHZ)	Backend	Type
IRyA-UNAM	L-Band	1,400–1,800	160	SDR	Room Temp.
Oxford	C-Band	4,000–8,500	4,000–8,500	Xilinx Zynq®	Cryogenic
HartRAO	K-Band	20,500-24,500	3,100–7,100	Xilinx Zynq®	Room Temp

the pointing and tracking of the alt-azimuth mount of the radiotelescope. We also design the user graphical interface for the user.

5. ANTENNA POINTING AND TRACKING TESTS

We will use a small optical telescope mounted on the antenna to look at stars to create the antenna pointing model (Carsltrom 2011; Magnum 2000; Magnum et al. 2006). We will use a telescope and camera to check how well the antenna is pointing and tracking. The direction in which the antenna points is determined by the astrometry of the optical images obtained by the camera(Ramos-Alcaraz, Alonso-Arévalo, & Nuñez-Alfonso 2023). This optical system will be also used for testing the rms tracking of the antenna.

Once the pointing of the antenna has been tested with the optical telescope, we will proceed to determine the offset between the optical axis and the radio axis of the antenna. This small optical telescope It may also be used as an offset guide for the radio telescope at night provided it has a large enough field of view (Assawaworrart & Padin 2012). It can also help in determining the flexure of the radio telescope mount and possible problems with the control system.

Acknowledgements: The Tulancingo-I conversion project is supported by grants from the Newton Fund (Science and Technology Facilities Council, UKRI), the Government of the State of Hidalgo, the Institute of Radioastronomy & Astrophysics (IRyA) and the Institute of Astronomy (IA) of the National Autonomous University of México (UNAM), as well as the San Pedro Martyr National Astronomical Observatory, which is operated by the IA-UNAM. D.H. and S.K. thank DGAPA-UNAM for providing financial assistance through grant PAPIIT # IT101622. We have received additional support from the Ministry of Telecommunications of México, the Mexican Space Agency, and the Oxford University Physics Department.

REFERENCES

Assawaworrart, S. & Padin, S. 2012, PASP, 124, 242
Charlot, P. et al. 2020, A&A, 644, 159
Carlstrom, J. E., Ade, P. A. R., Aird, K. A., et al. 2011, PASP, 123, 568
Claflin, E.S., Wu, S. C. & Resch, G. M. in Microwave Radiometer Measurementof Water Vapor Path Delay: Data Reduction Techniques, DSN, Progress Report 42-43, Jet Propulsion Laboratory, Pasadena, CA. pp.22
Churiwala, S. 2017, Editor of Designing with Xilinx FPGAs, Springer
Dillinger, M., Madani, K., & Nancy Alonistioti, N., 2003, Software Defined Radio: Architectures, Systems and Functions. Wiley & Sons
Gale, D.,2020, LNAGTM report, "Antena Tulancingo-1: Estudio del sistema óptico." Convenio Específico INAOE-2019-OPT-102 Entregable IV
Kurtz, S., Taylor, A. C., Jones, M. E., et al. 2022, SPIE, 12182, 9
Liu, C., Jones, M. E., & Taylor A. C. 2021, MNRAS, 50, 5096
Magnum, J. G. 2000, ALMA Memo 288, An Optical Pointing Systema for the ALMA Prototype Antennas (Charlottesville: NRAO)
Magnum, J. G., Baars, J. W. M., Greve, A., et al. 2006, PASP, 118, 1257
Ramos-Alcaraz, G. E., Alonso-Arévalo, M. A. & Nuñez-Alfonso, J. M., 2023, Aerospace, 10, 9
Velázquez, M., Ibarra-Medel, E., De Villiers, D., et al. 2022, SPIE, 12182, 121822

Revista Mexicana de Astronomía y Astrofísica Serie de Conferencias (RMxAC), **59**, 197–199 (2025)
© 2025: Instituto de Astronomía, Universidad Nacional Autónoma de México
https://doi.org/10.22201/ia.14052059p.2025.59.32

VII Workshop on Robotic Autonomous Observatories (October 16-20, 2023)
Editors: Maria Gritsevich, Alberto J. Castro-Tirado, Petr Kubánek, Shashi B. Pandey, and David Hiriart - DOI: https://doi.org/10.22201/ia.14052059p.2025.59.32

IMAGING STOKES PHOTOMETER-POLARIMETER FOR THE BOOTES GLOBAL TELESCOPE NETWORK

S. Guziy[1,5], I. Syniavskyi[2,3], Ye. Oberemok[2,4], O. Ivanova[5], and A. J. Castro-Tirado[1]

RESUMEN

La idea principal y algunos detalles del fotómetro-polarímetro de Stokes se presentan en este artículo. El fotómetro-polarímetro está diseñado para observaciones muy tempranas de estallidos cósmicos de rayos gamma, seguimiento regular de objetos peculiares, de la coma de cometas, de asteroides activos y de Centauros (también en el Sistema Solar). Las observaciones polarimétricas se optimizarán para dos regiones espectrales: 400-550 nm y 550-1100 nm, haciendo así posible medir los parámetros de Stokes de dos maneras: mediante polarizadores con acimutes 0°, 60°, 120° y polarizadores con acimutes 0°, 45°, 90°, 135° y una placa de cuarto de onda. Esto proporcionará mediciones para polarizaciones lineales y circulares. Algunos detalles de este proyecto se presentan en este artículo.

ABSTRACT

The main idea and some details of Imaging Stokes photometer-polarimeter are presented. The photometer-polarimeter is designed for very early observations of gamma-ray bursts afterglows, regular monitoring of the peculiar objects, cometary comae, active asteroids and Centaurs. Polarimetric observations will be optimized for two spectral regions: 400-550 nm and 550-1100 nm, thus making possible to measure the Stokes parameters on two ways: by means of polarizers with azimuths 0°, 60°, 120° and polarizers with azimuths 0°, 45°, 90°, 135° and a quarter-wave plate. This will provide measurements for linear and circular polarizations. Some details of this project are presented in the paper.

Key Words: Imaging-Polarimetery — Stokes parameters — BOOTES — Robotic Telescope — GRB

1. INTRODUCTION

Polarimetry plays an increasingly important role in visible and infrared astronomical observations since it provides a wealth of information: on the nature of radiation sources, on the geometrical and velocity relationship between a radiation source, scatterer and observer, on the chemical and physical properties of the dust grains, on the direction of the magnetic field as projected on the plane of the sky (for the case where these are aligned).

Linear polarization dependencies on phase angle and wavelength also serve as reliable sources of information about the properties of dust particles in cometary comae and active asteroids and Centaurs. Analysing not only brightness measurements and their spectral dependencies but also the phase dependence of linear polarization, which is particularly sensitive to scattering object properties such as size, shape, structure, and refractive index, remains a relevant task for remote sensing of celestial bodies to investigate their origin and evolution. The past two decades have seen significant advancements in ground-based polarimetry of small solar system bodies. Notably, it has been observed that the negative polarization branch of scattered light (a 90° rotation of the plane of polarization at small phase angles) for distant comets significantly differs from comets at closer solar distances. The 2.0m Liverpool Telescope (+RINGO) already responded to two gamma ray bursts (GRBs): GRB 060418 in ≈200s imposing a 2-σ limit of polrization degree $< 8\%$ and detecting significant polarization (10%) for GRB 090102 in a 60s exposure taken 150s after the event (Steele et al. 2009). Support is given to a higher polarization which may be highly variable (as might have seen in γ-rays for GRB 041219A; (see also (Gtz et al. 2009)).

However, monitoring polarization observations in conjunction with photometric studies, feasible only

[1]Instituto de Astrofísica de Andalucía, Granada, Glorieta de la Astronomía s/n, 18008, Spain (gssgrb@gmail.com).
[2]Main Astronomical Observatory of NAS of Ukraine, Kyiv, 27 Akademika Zabolotnoho Street, 03143, Ukraine (syn@mao.kiev.ua).
[3]Igor Sikorsky Kyiv Polytechnic Institute, Kyiv, Beresteiskyi Ave., 37, 03056, Ukraine.
[4]Taras Shevchenko National University of Kyiv, Kyiv, 60 Volodymyrska Street, 01033, Ukraine (oberemok@knu.ua).
[5]Astronomical Institute of the Slovak Academy of Sciences, Tatranská Lomnica 05960 Vysoké Tatry, Slovak Republic (oivanova@ta3.sk).
[5]Petro Mohyla Black Sea National University, Mykolaiv, 68 Desantnikiv Street, 54000 , Ukraine (gssgrb@gmail.com).

VII Workshop on Robotic Autonomous Observatories (October 16-20, 2023)
Editors: Maria Gritsevich, Alberto J. Castro-Tirado, Petr Kubánek, Shashi B. Pandey, and David Hiriart - DOI: https://doi.org/10.22201/ia.14052059p.2025.59.32

with small telescopes, is required for a more detailed investigation. Additionally, monitoring polarimetric observations of Centaurs and asteroids is necessary for detecting activity. Only one active asteroid and two active Centaurs have been observed in polarimetric mode. Therefore, using small telescopes for polarimetric monitoring represents an essential tool in advancing our understanding of these celestial objects, shedding light on their physical properties, origins, and evolutionary processes.

One of the most significant factors limiting the accuracy of ground-based polarization observations is the influence of Earth's atmosphere. Simple changes in transparency in the case of a two-beam polarization measurement scheme have little effect on the accuracy of normalized Stokes parameter measurements. However, variations in radiative transfer parameters in the atmosphere lead to changes in the depolarization coefficient D = Io/Ie in different exposures. The primary cause of depolarization is selective scattering on microparticles whose size is smaller than the wavelength of the observed radiation and non-selective scattering on aerosols. Moreover, the characteristic times of rapid depolarization changes in the atmosphere are comparable to the freezing time and can vary depending on the atmospheric conditions during observations, typically ranging from 10 to 30 ms. Usually, schemes with fast modulation or switching of polarization channels are used to suppress depolarization effects, which are referred to as flickering effects. We need to measure linear polarization with an accuracy of not less than 0.10.2 %. Also important to have a detector that allows fast acquisition of images, which is necessary for suppressing atmospheric flux scintillation in polarized light.

It is crucial to conduct obsevations during photometric nights with low values of seeing, absence of clouds, and dark nights with no moonlight or preferably during gray nights (during the small phases of the Moon). During data processing, proper consideration of the background (e.g., using histogram methods) and the correct removal of stars from the field is essential, especially for extended objects like comets and active asteroids.

2. BURST OBSERVER AND OPTICAL TRANSIENT EXPLORING SYSTEM

The Burst Observer and Optical Transient Exploring System (BOOTES), started in 1998 as a Spanish-Czech collaboration devoted to study optical emissions from gamma ray bursts (GRBs). The BOOTES global network of robotic telescopes is constantly watching the sky for astronomical transients, from its seven locations spread across both hemispheres. With them, Spain celebrated the beginning of a transformative era in ground-based observations with the successful completion of the BOOTES Network (Castro-Tirado 2023). Studies of astrophysical transients, such as GRBs and other high-energy phenomena, have long been hindered by their elusive and unpredictable nature. BOOTES can track and monitor suspected neutrino sources and gravitational wave emitters, as well as nearby objects like fireballs, comets, asteroids, or trans-Neptunian objects in the Solar System, variable stars in our Galaxy, supernovae in distant galaxies or blazars. Moreover, BOOTES may diligently commit to space debris monitoring and may survey the sky to identify potentially dangerous objects posing a threat to humanity. Very few telescopes can obtain polarimetric observations on a regular basis. In our case, we can very simply and without much expense add the ability to do polarimetric observations using BOOTES network telescopes. Thus, we have designed a photometer-polarimeter optimised for very early observations of gamma-ray bursts afterglows, regular monitoring of the peculiar objects, cometary comae, active asteroids and Centaurs.

3. INSTRUMENTATION

The optical wavelength range of the BOOTES telescopes is determined by the sensitivity of the detector. It spans from 350 to 1000 nm, with all six 0.6 m telescopes (100 deg/s slewing speed) being equipped with identical high-speed, highly sensitive electron multiplying EMCCD cameras iKon-L. These cameras offer a 10 arcmin field of view and employ Sloan ugri and ZY WFCAM filters, enabling seamless data fusion from various observation sites (Hu et al. 2023). Sloan Digital Sky Survey (SDSS) is one of the most common and important photometric systems in modern astronomy. The filters are placed in the holes of the rotateing wheel (Fig. 1.a). Five u, g, r, i, z band filters are for cover camera spectral range. Sixth hole place quartz window (to compensate optical ray path in filters for no defocusing when changing wheel position).

To provide polarization measurements, it is planned to add an additional wheel with 8 holes into the telescope path. The first three holes is for linear polarizers with optimal set of azimuths of 0°, 60° and 120°. These will allow determining the linear polarization of the input scene in the 400-550 nm spectral range. The next four holes is for three linear polarizers with azimuths of 0°, 45°, 90° and one for a circular polarizer, built of sequence of achromatic quarter-wave plate and a 135° linear polarizer.

VII Workshop on Robotic Autonomous Observatories (October 16-20, 2023)
Editors: Maria Gritsevich, Alberto J. Castro-Tirado, Petr Kubánek, Shashi B. Pandey, and David Hiriart - DOI: https://doi.org/10.22201/ia.14052059p.2025.59.32

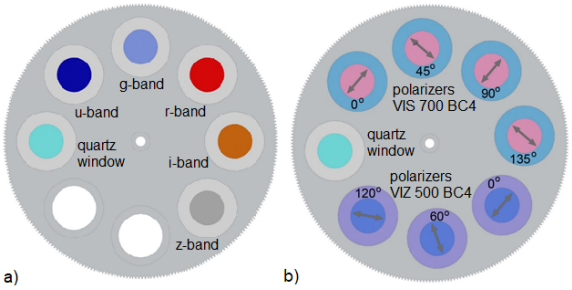


Fig. 1. a) Filter wheel of BOOTES telescope; b) additional polarizer wheel.

These will allow determining the linear polarization of the input scene in the 550-1100 nm spectral range (Fig. 1.b). We plan to use a highly efficient CODIXX polarizers. One set of VIS 500 BC4 polarizers to cover the g band. Second set of VIS 700 BC4 polarizers with achromatic quarter-wave plate to cover the r - band, I - band, z - band. The principle of design an imaging polarimeter for BOOTES telescope is shown in Figure 2.

4. MEASUREMENT AND CALIBRATION APPROACH

Above set of polarization elements will make it possible to determine Stokes parameters of the input scene in the spectral range 550-1100 nm. For example, an expression for determining the first three Stokes parameters I, Q, U of radiation in the first case is given below:

$$\begin{bmatrix} I \\ Q \\ U \end{bmatrix} = \frac{1}{2} \begin{bmatrix} 1 & \cos(\theta_1)a_1 & \sin(\theta_1)a_1 \\ 1 & \cos(\theta_2)a_2 & \sin(\theta_2)a_2 \\ 1 & \cos(\theta_3)a_3 & \sin(\theta_3)a_3 \end{bmatrix}^{-1} \begin{bmatrix} I_1 \\ I_2 \\ I_3 \end{bmatrix} \quad (1)$$

where θ_n - azimuth of polarizers; I_n intensity at the output of polarizer with azimuth θ_n; $a_n = (e_n - 1)/(e_n + 1)$ polarizations scale factor, e_n extinction ratio of n-th polarizing film; "-1" inversion of matrix.

From eqn. 1 it is clear that the above mentioned parameters of polarizert (as well as the parameters of wave plate) are not mandatory, although they are optimal from the point of view of minimizing the measurement error. Therefore, some dispersion of extinction ratio of polarizing films and birefringence of wave plate are acceptable. The eighth hole of the additional wheel will be free of optical elements to ensure optical observations with the telescope in normal mode at the appropriate angle of rotation of the wheel.

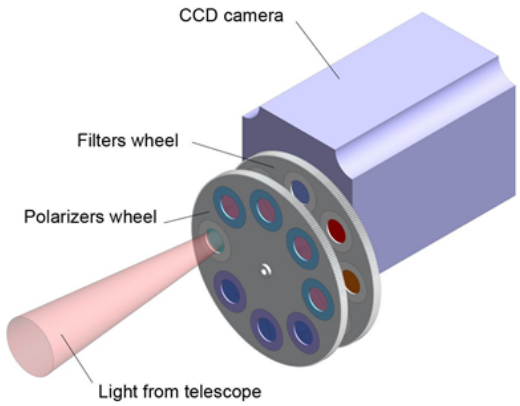


Fig. 2. The principle of design an imaging polarimeter for BOOTES telescope.

Each cycle of linear polarization measurements consists of a series of images obtained at fixed positional angles of polarisation wheel, for instance, 0°, 60° and 120°. Instrumental polarization is determined through observations of standard stars with low polarization (Heiles (2000): 9286 Stars: An agglomeration of Stellar Polarization Catalogs./ Heiles C(2000): standard s, rs should deviate from catalog values by an average of 0.1-0.3 % and the position angle of the polarization plane should shift by 0.5-0.7°. These values are considered the accuracy of a comet's integral polarimetric data. Binning 2×2 pixels is applied to the polarimetric images to enhance the measured signal's signal-to-noise (S/N) ratio.

5. CONCLUSION

In our project we showed how, with simple means and little funding, can upgrade existing photometers with the using of an additional wheel with polarizer films. This Photometer-polarimeter designed for BOOTES telescopes network for very early observations of gamma-ray bursts (afterglow), regular monitoring of the peculiar objects, cometary comae, active asteroids and Centaurs. Polarimetric observations will be on the two spectral regions 400-550 and 550-1100 nm, using two set of polarizers and one quarter-wave plate. This will provide measurements circular and linear polarizations in considered bands correspondingly.

REFERENCES

Castro-Tirado, A. J. 2023, NatAstro, 7, 1136
Götz,D., Laurent, P., Lebrun, F., Daigne, F., & Bošnjak, Ž. 2009, ApJ, 695, L208
Hu, Y.-D., Fernández-García, E., Caballero-García, D., et al. 2023, Front. Astron. Space Sci., 10, 952887
Steele, I., Mundell, C., Smith, R., Kobayashi, S., & Guidorzi, C. 2009, Nat, 462, 767

Revista Mexicana de Astronomía y Astrofísica Serie de Conferencias (RMxAC), **59**, 201–207 (2025)
© 2025: Instituto de Astronomía, Universidad Nacional Autónoma de México
https://doi.org/10.22201/ia.14052059p.2025.59.33

VII Workshop on Robotic Autonomous Observatories (October 16-20, 2023)
Editors: Maria Griffsevich, Alberto J. Castro-Tirado, Petr Kubánek, Shashi B. Pandey, and David Hiriart - DOI: https://doi.org/10.22201/ia.14052059p.2025.59.33

THE INTELLIGENT OBSERVATORY

N. Erasmus[1,2], S. B. Potter[1,3], C. H. D. van Gend[1], S. Chandra[1], H. L. Worters[1], M. Hlakola[1], and R. Julie[1,4]

RESUMEN

El Observatorio Astronómico de Sudáfrica (SAAO) se ha embarcado en un programa para mejorar tanto sus telescopios e instrumentos como el análisis de datos para que trabajen juntos de manera inteligente y coordinada. El objetivo no solo es ofrecer mayor eficiencia y agilidad, sino también permitir la exploración de nuevas oportunidades científicas, particularmente en esta era de la astronomía de multi-mensajeros y del dominio temporal.

ABSTRACT

The South African Astronomical Observatory (SAAO) has embarked on a programme to upgrade its telescopes, instruments and data analysis to have them intelligently working together in a coordinated fashion. The objective is to not only deliver greater efficiency and agility but to enable the exploration of new science opportunities particularly in the era of multi-messenger and time-domain astronomy.

Key Words: Robotic observatories — Autonomous follow-up — Transient Alerts — Multi-messenger astronomy

1. INTRODUCTION

The rate of astronomical transient discoveries and alerts is poised to increase dramatically in the coming years, driven by data-intensive surveys such as the Legacy Survey of Space and Time (LSST) at the Vera C. Rubin Observatory. In anticipation of this influx of transient alerts, the South African Astronomical Observatory (SAAO) has initiated the "Intelligent Observatory" or "IO" project (Väisänen et al. 2018; Potter 2021). The program involves the upgrading of the hardware of all the telescopes to permit autonomous operations with the corresponding development of software. Intelligent algorithms have also been developed in order to intelligently and autonomously respond to real-time alerts from other telescopes across the world and space based observatories. All this is overseen by an Observatory Control System that actively manages an observing queue in real-time. Here we summarize the achievements so far, particularly with the completion of one such SAAO telescope that is now fully integrated into the IO's daily operations[5].

2. DIVERSITY OF FACILITIES AND INSTRUMENTS AT THE SAAO

Situated at the southern tip of the Northern Cape province in South Africa, the South African Astronomical Observatory (SAAO) owns and operates four telescopes while serving as host to over 15 telescopes from various international partners. The SAAO-owned telescopes alone present a reasonable diversity, featuring instruments and aperture sizes ranging from the 1-meter Lesedi telescope to the impressive 10-meter South African Large Telescope (SALT). This diversity encompasses a broad spectrum of instrument capabilities, including optical imaging, optical and near-infrared spectroscopy, polarimetry, spectro-polarimetry, and high-speed photometry (refer to Figure 1). When including the capabilities of the various hosted facilities, the scientific endeavors at the observatory span a multifaceted array, encompassing transient science, near-Earth asteroid surveys, microlensing detection, exoplanet discovery, solar monitoring, to name just a few. The unique strengths of each telescope position the observatory to collectively serve as a potent "follow-up machine", particularly if autonomous robotic observing becomes the norm for each facility, supported by more cohesive and coordinated observing strategies.

3. THE IO PROJECT AND ITS VISION

The IO project is a comprehensive initiative within the SAAO that spans across all divisions, including astronomy, software, engineering, and instrumentation. The primary objective is to future-proof the SAAO and ensure its relevance in the

[1]South African Astronomical Observatory, 1 Observatory Road, Cape Town, 7925, South Africa (n.erasmus@saao.nrf.ac.za).
[2]Department of Physics, Stellenbosch University, Stellenbosch, 7602, South Africa.
[3]Department of Physics, University of Johannesburg, Auckland Park, Johannesburg, 2006, South Africa.
[4]South African Radio Astronomy Observatory, 2 Fir Street, Cape Town, 7925, South Africa.
[5]`https://io.saao.ac.za/`

VII Workshop on Robotic Autonomous Observatories (October 16-20, 2023)
Editors: Maria Gritsevich, Alberto J. Castro-Tirado, Petr Kubánek, Shashi B. Pandey, and David Hiriart - DOI: https://doi.org/10.22201/ia.14052059p.2025.59.33

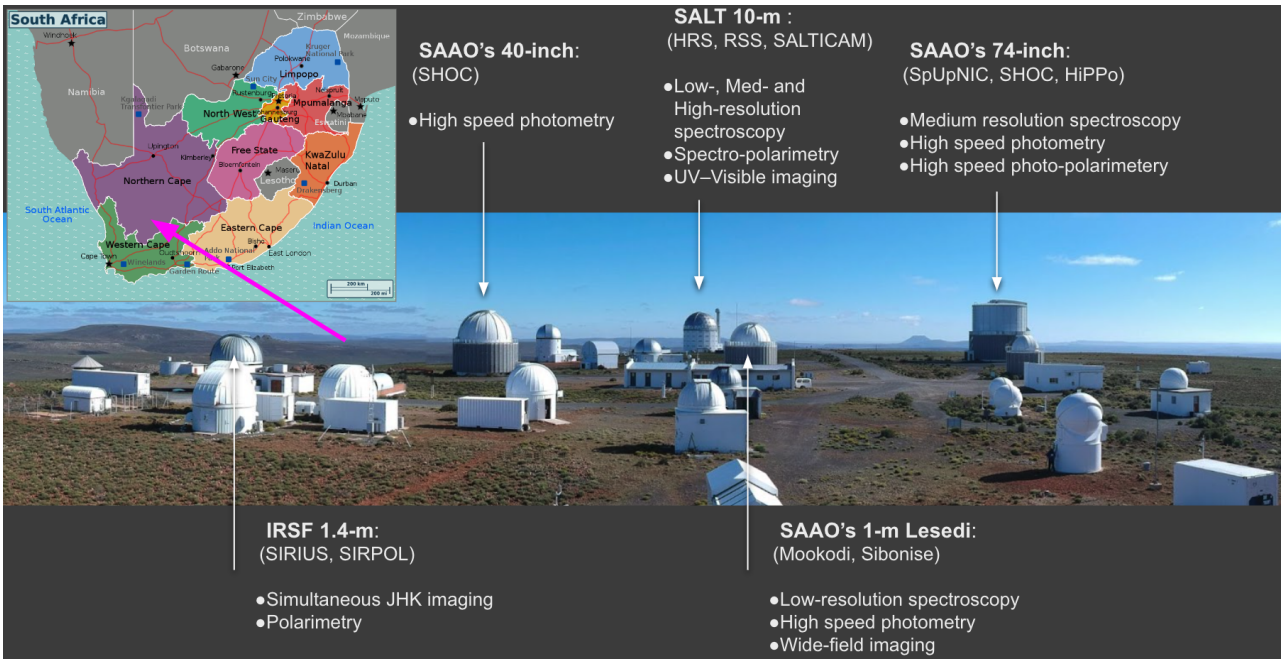


Fig. 1. Panoramic view of the South African Astronomical Observatory's site in Sutherland, Northern Cape, showcasing the 40-inch, Lesedi, and 74-inch telescopes under the ownership and operation of the SAAO. Additionally, the Southern African Large Telescope (SALT) and InfraRed Survey Facility (IRSF) are also highlighted with their respective available instruments and capabilities. The photograph captures the presence of many of the other telescopes from international partners contributing to the collaborative astronomical efforts at the site.

rapidly evolving astronomical landscape (Buckley 2019). Open to all capable contributors within the organization, the project maintains a core IO team utilizing a modified "Scrum" methodology as a framework for effective work execution toward the ultimate goal. The project envisions the integration of as many telescopes as possible into the IO system, fostering more coordinated scientific efforts across telescopes in the era of multi-messenger astronomy. This integration aims to strengthen national and international partnerships while propelling the SAAO into the realm of the fourth industrial revolution (4IR). Such advancements will enhance the SAAO's service to the astronomy community and users, enabling features such as the submission of proposals at any time, science on various timescales (i.e. not restricted to the classical 1-week blocks), manually performing remote observing from Sutherland, Cape Town, or anywhere globally, robotically queued observations, improved responsiveness to transient alerts, and the facilitation of computer-generated observing requests for rapid response.

4. CURRENT STATE OF THE IO PROJECT

While we envisions the integration of as many telescopes as possible into the IO system, for now the IO activities have mainly focused on the telescopes fully owned by the SAAO with no external partners. This mainly includes the almost 80-year old 74-inch telescope, the roughly 60-year old 40-inch telescope, and the newly installed 1-m Lesedi telescope that was purchased and installed with robotic operation in mind from the onset.

4.1. *Remote Observing*

A crucial initial stride towards achieving fully autonomous observing, particularly with the two older telescopes, involves the implementation of remote observing capabilities. Over the past decade, a concerted effort has been dedicated to upgrading various electronic and mechanical components, as well as control software for the telescopes and domes, to facilitate remote observing. Currently, all telescopes operated by the SAAO are accessible remotely from the dedicated remote observing room at the SAAO's headquarters in Cape Town. In principle, they are remotely operable from any computer worldwide equipped with a web browser and appropriate access credentials. It's noteworthy that this is not merely through desktop remote connections to the control PCs but via web-based graphical user interfaces (GUIs) that communicate with GUI-independent back-end software services running

VII Workshop on Robotic Autonomous Observatories (October 16-20, 2023)
Editors: Maria Griffsevich, Alberto J. Castro-Tirado, Petr Kubánek, Shashi B. Pandey, and David Hiriart - DOI: https://doi.org/10.22201/ia.14052059p.2025.59.33

on the control PCs. The back-ends are accessible through an application programming interface (API), future-proofing for robotic algorithmic control of the telescopes and instruments.

The implementation of remote observing has already proven valuable for certain science programs that require only a single night or even a portion of a night (e.g stellar occultations of solar system bodies), rather than an entire week, demonstrating the flexibility and more efficient use of telescope time of the upgraded system.

4.2. *Robotic Observing with Lesedi*

Lesedi (Worters et al. 2016) meaning "light" or "enlightenment" in Sesotho, is the name of the SAAO's 1-m alt-az telescope, which features two Nasmyth ports equipped with field derotating and autoguiding capabilities. Installed on one of the ports is Mookodi (Erasmus et al. 2024) - meaning "rainbow" in Sesotho a low-resolution ($R = 300$) spectrograph operating in the visible wavelength range ($400-800$ nm). Both Lesedi and Mokoodi were designed and constructed with robotic operation in mind from the outset, making them the obvious initial telescope and instrument combination for full integration into the IO's system. Mokoodi utilizes an imaging mode for astrometrically-driven automated target acquisition[6] on the spectrograph's slit, and this imaging mode can also be used for scientific operations because it employs the same science-grade detector as the spectroscopy mode. The instrument is equipped with a full Sloan filter set (see caption of Figure 2 for more detail on Mookodi). The capability to rapidly switch between spectroscopy mode and photometric imaging mode makes Mokoodi an attractive instrument for the SAAO's IO initiative since this is essentially two instruments in one that can cater for various science cases. The telescope and instrument have been in full robotic operation for over a year, and the science cases presented in Section 5 are performed by this duo.

4.3. *Observatory Control System*

The IO Project has chosen to leverage proven technology, utilizing the recently open-sourced Observatory Control System software (OCS) [7] developed by the Las Cumbres Observatory (LCO)

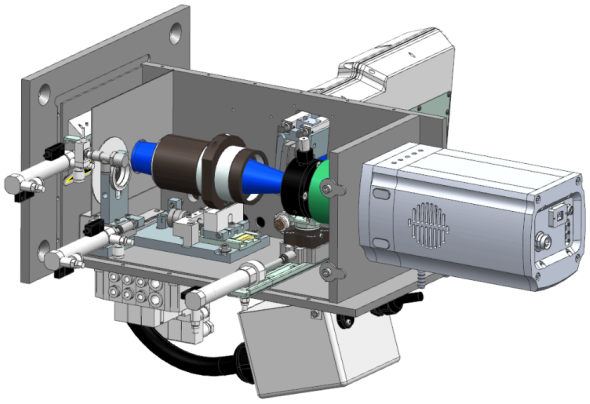


Fig. 2. CAD render of the Mookodi instrument (Erasmus et al. 2024), a low-resolution spectrograph. The incorporation of a grism enables a linear optical design, facilitating the movement of specific optical components (such as the slit and grism) out of the beam without beam deflection, transforming the instrument into an imager. The inclusion of photometric filters (cover of filter slides visible protruding into the page at the back) allows for multi-filter imaging. This dual functionality makes the instrument versatile, serving as both a low-resolution spectrograph and a multi-filter imager.

to manage user-submitted observing requests and schedule observations into a dynamic queue. The LCO's OCS is already AEON (Astronomical Event Observatory Network) compatible, aligning well with the goals of the SAAO's IO project. AEON aims to create a network of world-class telescopes accessible on demand, specifically for swift follow-up observations in the LSST-like survey era. Currently, the SAAO's version of the OCS has implemented the Mookodi instrument, with plans for more instruments in the future. Users can submit observation requests manually through a web form or programmatically via the provided API. Figure 3 shows a screenshot of the web-front end of the OCS showing the submitted observation requests. The OCS dynamically schedules requests into a queue that can be rearranged or appended as new requests are submitted. A continuous-running in-house developed "poller" on the observation control PC retrieves the latest version of the queue every minute, executing the top request by translating observation details into commands for our developed back-end software for Mookodi and the Lesedi telescope.

4.4. *Monitoring of hardware, software services and observations*

In addition to the control software for the telescopes and instruments we have developed, we have

[6] Two options are available for automated target acquisition: 1) acquisition based on the astrometric solution of the acquisition frame and the provided RA and Dec, and 2) the same as option 1 with an additional search for any nearby detected source. The second option is recommended when the exact coordinates are uncertain.

[7] `https://observatorycontrolsystem.github.io/`

VII Workshop on Robotic Autonomous Observatories (October 16-20, 2023)
Editors: Maria Gritsevich, Alberto J. Castro-Tirado, Petr Kubánek, Shashi B. Pandey, and David Hiriart - DOI: https://doi.org/10.22201/ia.14052059p.2025.59.33

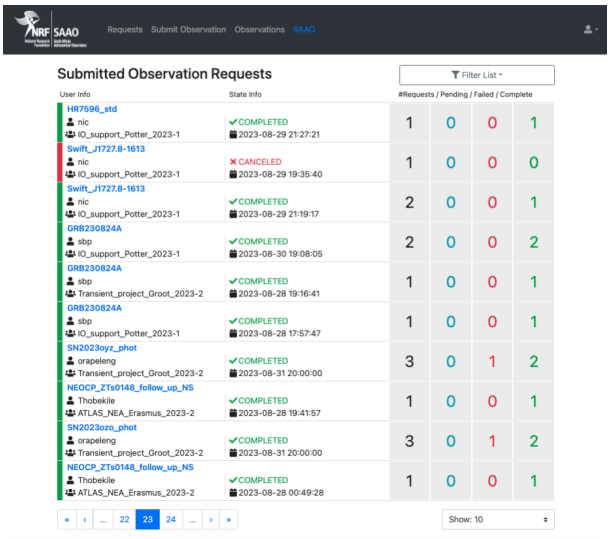


Fig. 3. Displayed is the web-based user interface of the Observatory Control Software (refer to Section 4.3 for implementation details), enabling registered users with approved proposals to submit observing requests through a web-form. Additionally, this platform allows users to monitor the status of submitted requests.

also created user-friendly overview platforms to monitor the state of hardware and services crucial for successful autonomous observing. Our team has access to an "overview dashboard" (refer to Figure 4), which serves as a centralized tool for monitoring. This dashboard enables us to intervene promptly when a specific service is disrupted or hardware is in a faulty state, ensuring the smooth operation of the observing system.

Finally, we have also developed a "schedule viewer" that enables operators and astronomers to visualize the observing queue generated by the Observatory Control System (OCS), indicating the status of each observation as "COMPLETED", "PENDING", or "IN PROGRESS" (refer to Figure 5). Currently, this feature is available for Lesedi, but there are plans to implement separate viewers for each telescope in the near future.

5. SOME EXAMPLE USE CASES

While the telescopes incorporated into the IO project will remain available (with sufficient motivation) for manual observing by astronomers in the more traditional week-long blocks, particularly for science cases better suited to such an approach, the showcased use cases here emphasize the system's true power and efficiency in fully automated robotic operations.

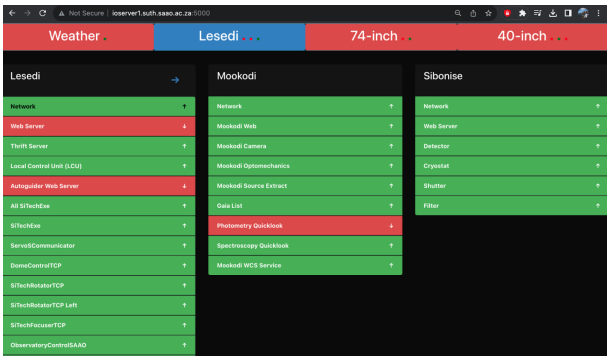


Fig. 4. The "overview dashboard" designed for monitoring the status of all hardware and software services. A color-coded system is employed, where green signifies normal operation, while red indicates a potential fault. Each telescope is organized into distinct tabs, offering dedicated sections for different instruments and relevant components related to that telescope. In this example, the Lesedi telescope's tab is selected (indicated with a blue color).

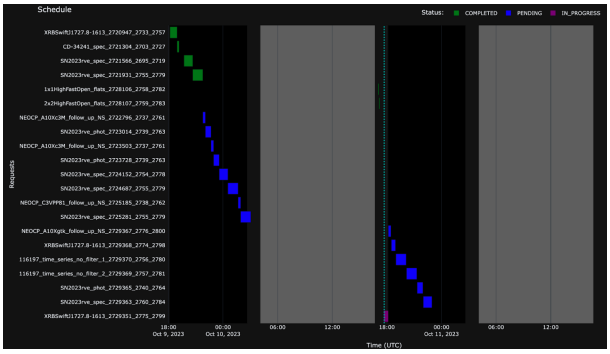


Fig. 5. An overview of the observing queue for the Lesedi telescope, depicting the past and upcoming 24 hours. Daytime is represented by light gray areas, twilight in dark gray, and black areas indicate available observing hours. The vertical cyan dotted line denotes the present time. Hovering over each block, which represents a scheduled observing request, provides additional details such as exposure times, the number of exposures, and selected filters. Completed, pending, and ongoing observations are denoted by green, blue, and purple blocks, respectively.

5.1. *near-Earth asteroid follow-up*

One of the best use cases that demonstrates the full capability of the systems developed by the IO is the swift follow-up of newly discovered near-Earth asteroids (NEAs). In this program, a "watchdog service" continually queries the publicly available Near-Earth Object Confirmation page[8] (NEOCP)

[8] `https://www.minorplanetcenter.net/iau/NEO/toconfirm_tabular.html`

VII Workshop on Robotic Autonomous Observatories (October 16-20, 2023)
Editors: Maria Gritsevich, Alberto J. Castro-Tirado, Petr Kubánek, Shashi B. Pandey, and David Hiriart - DOI: https://doi.org/10.22201/ia.14052059p.2025.59.33

of the Minor Planet Centre (MPC), which consolidates discoveries from various asteroid surveys and serendipitous discoveries by others. These automated queries don't query the MPC directly but rather utilize NASA's JPL Centre for Near-Earth Studies (CNEOS) Scout service[9], offering real-time NEOCP updates but with more easily accessible additional information, such as on-sky uncertainties, through a well-documented API. When a new discovery appears on CNEOS Scout that is observable from Sutherland using Mookodi (filtered based on magnitude and on-sky position uncertainty limits), the service promptly sends an observing request to the IO's Observatory Control System (OCS) also via a well documented API provided by developers at LCO. Since the OCS is able to receive observing requests for non-sidereal objects as well, the autonomous "watchdog service" only needs to provide the orbital parameters, and the OCS dynamically calculates RA and DEC on-the-fly to accommodate non-sidereal objects in a dynamic observing queue. Figure 5 illustrates some of these "NEOCP observing requests" in a queue.

Operating since early 2023, this program has successfully executed follow-up observations for nearly 300 near-Earth Asteroids (NEAs) in its inaugural year, all without human intervention, including the submission of observing requests to the OCS. Approximately 63% of these completed observations were deemed successful, meaning the asteroid was captured in the frame and sufficiently bright for detection in the reduction pipeline. Of these successful observations, the astrometry of 75% was submitted to the Minor Planet Center (MPC) in time to contribute to the Minor Planet Electronic Circular (MPEC) demonstrating the program's rapid end-to-end success from triggering on a discovery to submitting measurements to the MPC. Many of these follow-ups and subsequent submission occurred within the same night as the discovery.

The remaining 37% of unsuccessful observations were attributed to various factors: 1) faint objects not detectable in the frame despite correct exposure (14%), 2) incorrect telescope pointing leading to the asteroid being out of frame, mostly due to growing on-sky uncertainty and a large delay in the observations since the observing request was sent (13%), 3) lack of visible stars in frames due to weather or technical issues, such as unexpected dome closure or clouds appearing without timely automated shutdown (7%), and 4) cases where the discovery was suspected to be artificial (e.g a satellite) or not real, subsequently removed from the NEOCP but unfortunately only after our observation request trigger (2%).

Impressively, these 300 completed observations only consumed approximately 75 hours of telescope time (15 minutes per observation), equivalent to about one traditional one-week block. Achieving this volume of observations in a traditional one-week block would have been totally unfeasible.

5.2. *Transient Name Server follow-up*

Another use case aligned precisely with the IO's vision of rapid follow-up characterizations involves triggering spectroscopic observations of transients reported to the Transient Name Server (TNS). To provide an additional service to the SAAO transient astronomer community, we developed an additional "TNS watchdog" that continuously queries the TNS for any transients discovered in the past 24 hours within the limiting magnitude of a 600-second exposure of the Mookodi instrument in spectroscopy mode. The concept is that these quick-look, low-resolution spectra from Mookodi can better inform the community about the likely type of transient and whether further follow-up, such as with the high-resolution spectrograph (HRS) on the 10-m SALT, is warranted. Although this specific case wasn't triggered by our autonomous "TNS watchdog", the workflow and methodology described in the Astronomer's Telegram #16369 (Buckley et al. 2023), involving quick-look follow-up spectra of the LMC transient ASASSN-23ii (AT 2023ygp) with Mookodi superseded by more detailed follow-up spectroscopy using SALT's HRS, perfectly exemplified the type of use case envisioned by this program.

Figure 6 depicts the acquisition image illustrating an instance of fully automated spectroscopic follow-up for SN 2023yoo conducted by our "TNS watchdog." This supernova was discovered by ATLAS on 2023-11-28 at 00:50:48 UT, with a magnitude of 17.3. Our systems promptly triggered a spectroscopic observing request at 2023-11-28 11:00 UT[10] following the ATLAS team's report of the discovery to the TNS at 2023-11-28 10:36:43 UT[11]. The observation was submitted as a "rapid-response" request, prioritized at the forefront of the queue and

[9] `https://cneos.jpl.nasa.gov/scout/#/`

[10] at the time of this trigger the TNS was being queried every 30 min but this interval can be reduced for more rapid response in future

[11] we rely on TNS alerts for triggering so our response time is constrained by the reporting timeline of the relevant discovery team. In this instance, the ATLAS team reported the discovery to the TNS several hours after the discovery exposure.

VII Workshop on Robotic Autonomous Observatories (October 16-20, 2023)
Editors: Maria Gritsevich, Alberto J. Castro-Tirado, Petr Kubánek, Shashi B. Pandey, and David Hiriart - DOI: https://doi.org/10.22201/ia.14052059p.2025.59.33

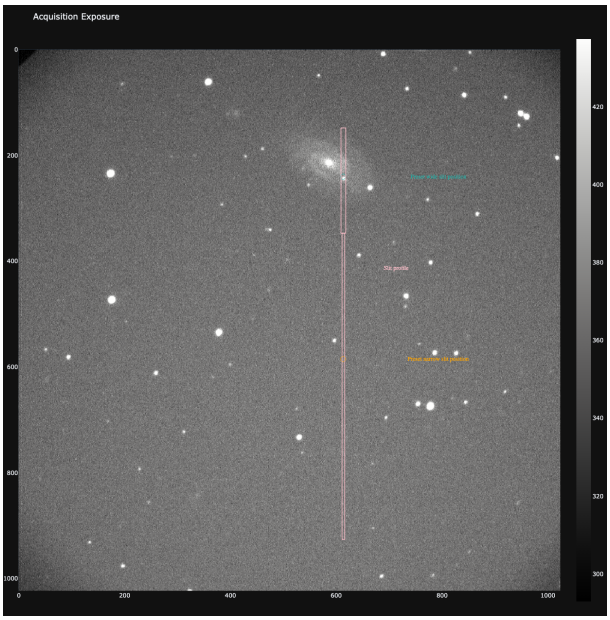


Fig. 6. Presented is the acquisition image from the rapid spectroscopic follow-up of SN 2023yoo using Mookodi. The robotic system utilizes Mookodi in imaging mode, coupled with astrometric calibration to precisely and automated position the requested RA and DEC within the appropriate section of the spectrograph's slit. In this instance, RA=22:01:03.150 and DEC=-13:16:28.99, and the request specified the use of the "wide slit" (depicted by the pink outline, illustrating the location of Mookodi's stepped-slit, with a ∼6-arcmin-long "narrow slit" of 2 arcseconds and ∼2-arcmin-long "wide slit" of 4 arcseconds). The resulting spectrum can be viewed on the Transient Name Server (TNS) at: `https://www.wis-tns.org/object/2023yoo`.

executed immediately after twilight on 2023-11-28 at 18:57:23.939 UT. Subsequently, the spectra were processed, and a classification report[12] was submitted to the TNS (Mogawana et al. 2023). We aim to streamline and automate certain aspects of the reduction and TNS reporting processes in the future.

5.3. *General Coordinates Network follow-up*

Similar to the the "TNS watchdog" discussed in section 5.2, we have established a service that monitors notifications from the General Coordinates Network (GCN) operated by NASA. To achieve this, we utilized and expanded the provided example Kafka Client Python code with the instructions outlined by GCN[13]. While the GCN offers real-time notices for various instruments our current focus, for testing purposes, is on alerts generated by the instruments of the *Neil Gehrels Swift Observatory*: the Burst Alert Telescope (BAT) with multi-filter photometry follow-up, the X-Ray Telescope (XRT), and the Ultraviolet/Optical Telescope (UVOT) with spectroscopy follow-up. The decision between whether to purse photometry or spectroscopy follow-up is determined by the source position accuracy provided by each instrument. Only XRT and UVOT offer source location accuracies sufficient for positioning the source within our widest selectable 4-arcsec slit of Mookodi when in spectroscopy mode. In the future, we aspire to broaden our scope by responding to additional alerts provided by the GCN (e.g., from instruments on the Fermi Gamma-ray Space Telescope). The future strategy would also involve submitting requests to instruments/telescopes integrated into the IO project best suited to meet the specific alert constraints (e.g., factors like magnitude and position uncertainty).

6. WORK IN PROGRESS, FUTURE PLANS AND CONCLUSION

Our future focus is on seamlessly integrating more SAAO-operated telescopes into our IO system, likely starting with the larger 74-inch telescope. This telescope will soon feature a remotely operated "instrument selector", allowing the permanent pairing of the SHOC (imager) instrument with either SpUpNIC (spectrograph) or HiPPo (photo-polarimeter). Our initial objective is to establish the 74-inch telescope, along with SHOC, as a fully robotic-enabled system, enhancing our automated photometric follow-up capabilities for fainter objects. Simultaneously, we aim to optimize rapid-response observations for Supernovae and Gamma-Ray Bursts, collaborating with experts within the SAAO. Looking ahead, we plan to diversify our observational portfolio with time-critical but not necessarily rapid-response projects that could benefit from robotic automation, such as occultations of Solar System objects and exoplanet transits.

Currently, we support several data pipelines for our various instruments, enabling users to manually extract calibrated spectra and photometry from images. In the future, we aim to automate some of these processes to provide users with publish-ready data products. For example, we plan to implement real-time astrometric and photometric calibration for each frame as it is created, thereby generating corresponding catalog files containing calibrated photometric data for all detected sources. We are actively exploring several approaches to achieve this.

[12] `https://www.wis-tns.org/object/2023yoo/classification-cert`

[13] `https://gcn.nasa.gov/docs/client`

VII Workshop on Robotic Autonomous Observatories (October 16-20, 2023)
Editors: Maria Gritsevich, Alberto J. Castro-Tirado, Petr Kubánek, Shashi B. Pandey, and David Hiriart - DOI: https://doi.org/10.22201/ia.14052059p.2025.59.33

In conclusion, we have successfully demonstrated an end-to-end telescope and instrument system that aligns with the SAAO's "Intelligent Observatory" vision of fully automated, rapid-response of transient objects. This achievement paves the way for future integration of additional telescopes into the IO framework, further advancing astronomical research at the SAAO.

Acknowledgments: This work is supported by the South African National Research Foundation (NRF).

REFERENCES

Buckley, D. A. H. 2019, NatAs, 3, 369-373
Buckley, D. A. H., Aydi, E., Groot, P., et al. 2023, ATel, 16369, 1
Erasmus, N., Steele, I. A., Piascik, A. S., et al. 2024, JATIS, 10, 025005
Mogawana, O., Groot, P., Erasmus, N. 2023, Transient Name Server Classification Report, 2023-3111, 1
Potter, S. B. 2021, Anais da Academia Brasileira de Ciências, 93, SciELO Brasil
Väisänen, P., Crause, L., Gilbank, D., et al. 2018, SPIE, 10704, 107040A
Worters, H. L., O'Connor, J. E., Carter, D. B., et al. 2016, SPIE, 9908, 99083Y

Revista Mexicana de Astronomía y Astrofísica Serie de Conferencias (RMxAC), **59**, 209–215 (2025)
© 2025: Instituto de Astronomía, Universidad Nacional Autónoma de México
https://doi.org/10.22201/ia.14052059p.2025.59.34

VII Workshop on Robotic Autonomous Observatories (October 16-20, 2023)
Editors: Maria Griffsevich, Alberto J. Castro-Tirado, Petr Kubánek, Shashi B. Pandey, and David Hiriart - DOI: https://doi.org/10.22201/ia.14052059p.2025.59.34

SOFTWARE COMPONENTS OF THE INTELLIGENT OBSERVATORY

C. H. D. van Gend[1], S. B. Potter[1,2], N. Erasmus[1], S. Chandra[1], M. Hlakola[1], H. Worters[1], and R. Julie[3]

RESUMEN

El Observatorio Inteligente (OI) es un proyecto del Observatorio Astronómico de Sudáfrica (SAAO) para optimizar la flexibilidad y eficacia de los telescopios e instrumentos en el lugar de observación. Destacamos dos aspectos del proyecto OI: la actualización del software de control y la supervisión de instrumentos y telescopios, y permitir programar y ejecutar observaciones de forma dinámica.

En cuanto al primer aspecto, analizamos la arquitectura del software que hemos desarrollado para conectar los instrumentos y telescopios, así como su compatibilidad con las aplicaciones de la red telescopios y cómo esto soporta interfaces remotas y automatizadas con ellos. A partir de esta arquitectura, hemos desarrollado una Unidad de Control Local (UCL) para cada telescopio, responsable de la seguridad del mismo, interfaces web para cada instrumento y telescopio para permitir el control directo y la supervisión de los mismos, así como un componente de secuencia de comandos (*scripting*) que permite la operación automatizada.

Para la programación de solicitudes de observación utilizamos el componente denominado *Adaptive Scheduler del Observatory Control System* (OCS), desarrollado por el Observatorio Las Cumbres. Esto permite que los observadores envíen solicitudes de observación y produce un cronograma de observaciones que puede cambiar dinámicamente durante la noche.

El sistema de secuencia de comandos sirve de unión entre el programador, por un lado, y los instrumentos y el telescopio, por el otro. Un sondeador de horarios consulta periódicamente a la UCL para obtener permiso para observar y, si se le otorga, recupera la programación más reciente del programador OCS y pasa los elementos de programación individuales a un ejecutor de secuencias de comandos. El ejecutor de la secuencia de comandos configura los instrumentos y el telescopio de acuerdo con la solicitud de observación y a continuación, ejecuta las observaciones. Una vez completadas o fallidas, el estado se devuelve al OCS para que el programa pueda actualizarse.

ABSTRACT

The Intelligent Observatory (IO) is a project of the South African Astronomical Observatory (SAAO) to optimise the flexibility and efficiency of the telescopes and instruments at the observing site. We highlight two aspects of the IO project: updating the control and monitoring software for instruments and telescopes, and allowing observations to be scheduled and executed dynamically.

For the first, we discuss the architecture of the software we have developed to connect instruments and telescopes, and how this supports remote and automated interfaces to these. Using this architecture, we have developed a Local Control Unit (LCU) for each telescope responsible for the safety of that telescope, web interfaces for each instrument and telescope to allow direct control and monitoring of these, and a scripting component which allows automated operation.

For the scheduling of observation requests, we use the Adaptive Scheduler component of the Observatory Control System (OCS), developed by the Las Cumbres Observatory. This allows observation requests to be submitted by observers, and produces a schedule for observations which may change dynamically in the night.

The scripting system provides the glue between the scheduler on the one hand and the instruments and telescope on the other. A schedule poller regularly queries the LCU for permission to observe, and if this is given, retrieves the latest schedule from the OCS scheduler and passes the individual schedule items to a script runner. The script runner configures the instruments and telescope according to the observation request, then executes the observations. On completion or failure the status is returned to the OCS so that the schedule may be updated.

Key Words: Robotic observatory — Autonomous observing — Software architecture — Intelligent Observatory

[1]South African Astronomical Observatory, 1 Observatory Rd, Observatory, Cape Town 7925, South Africa (c.vangend@saao.nrf.ac.za).

[2]Department of Physics, University of Johannesburg, Auckland Park, Johannesburg, 2006 South Africa.

[3]South African Radio Astronomy Observatory, 2 Fir Street, Observatory, Cape Town 7925, South Africa.

VII Workshop on Robotic Autonomous Observatories (October 16-20, 2023)
Editors: Maria Gritsevich, Alberto J. Castro-Tirado, Petr Kubánek, Shashi B. Pandey, and David Hiriart - DOI: https://doi.org/10.22201/ia.14052059p.2025.59.34

1. INTRODUCTION

The South African Astronomical Observatory (SAAO) operates a diverse range of telescopes at its observing station near the town of Sutherland, in South Africa's arid Karoo region. These include the 10-metre class Southern African Large Telescope (SALT), the newly acquired 1.0-metre Lesedi telescope (Worters et al (2016)), as well as the two older 1.9- and 1.0-metre telescopes (the latter two commissioned in 1948 and 1964 respectively). Additionally the SAAO shares ownership or has access to observing time on several other telescopes on the observing plateau. The telescopes are equipped with a range of instruments, including high speed cameras, low and medium resolution spectrographs, and polarimeters.

The older telescopes and instruments each had their own specific control software, interfaces, data pipelines and operating procedures, and there was no common approach to interacting with these. As we developed control software for and interfaces to newer telescopes and instruments, we wanted to follow a more uniform approach and adopt common standards for development of control and access software. We also wanted to apply these to the older telescopes and instruments.

In addition, the requirements of observers and the observatory have changed over the years. It is no longer the best use of telescope time to grant a full week or more to an observer who then travels to the Sutherland observatory and spends each night (weather permitting) at the the allocated telescope. A target might only be visible for part of the evening, or an observer might equally well prefer to observe a given target over several months. With new telescopes such as the Legacy Survey of Space and Time (LSST) and the Square Kilometre Array (SKA) we expect many new targets meriting follow-up observations to be discovered each night, and we would like our systems and procedures to have the flexibility and capability of taking advantage of these.

The Intelligent Observatory (IO) project of the South African Astronomical Observatory was set up to address these issues (Väisänen et al. 2018; Potter 2021). The IO is an effort to systematically modernize and improve the efficiency of the SAAO's telescopes and instruments. It envisages a central control system (CCS) which has oversight of all telescopes and their associated instruments, and is able to send observation requests to each telescope, and receive status updates from these.

The project requires changes to hardware, software and procedures. Among the hardware updates are those allowing remote control and instrument selection by software alone. The software updates include changes to allow safe programmatic operability, following a uniform approach. This has allowed us to build a system to receive and execute remote observation requests, and a scheduler which can produce a dynamic queue of observations to be performed.

The IO is a project with many aspects, and in this paper we will concentrate here on control software, software providing auxiliary functions, and software required for autonomous operations.

2. SOFTWARE ARCHITECTURE

A fundamental need for the IO project is that instruments and telescopes be safely operable both remotely and autonomously.

To enable this, we need a software system which allows diverse hardware components and software services to communicate with one another. These should be accessible to other software which can receive observation requests and translate these into a set of operations which result in these requests being executed.

In the absence of human control, we need to ensure system safety. An independent system able to monitor weather should be able to take control of the telescope and issue a shutdown command, regardless of other applications which might be preparing for or taking observations. This implies that multiple applications should be able to access the hardware simultaneously.

The system should be modular and extensible, allowing new components to be added without requiring significant code changes in existing systems, and it should also be possible for application-level software to be developed without extensive knowledge of the lower-level software.

To accommodate these requirements we have chosen a modular, layered, and distributed architecture (Richards (2022)). In this context, modular means that the software consists of independently developed units which can be plugged together into larger aggregations. A layered architecture is one in which communication from hardware to control passes through a number of layers, each additional layer adding different functionality. Layers typically only communicate directly with the adjacent layers above and below. A distributed architecture, in this context, is one in which an entity can be built from several independent hardware components which don't necessarily need to be on the same host.

Figure 1 illustrates such an architecture.

The instruments and telescopes typically comprise several components. The required functionality

VII Workshop on Robotic Autonomous Observatories (October 16-20, 2023)
Editors: Maria Griffsevich, Alberto J. Castro-Tirado, Petr Kubánek, Shashi B. Pandey, and David Hiriart - DOI: https://doi.org/10.22201/ia.14052059p.2025.59.34

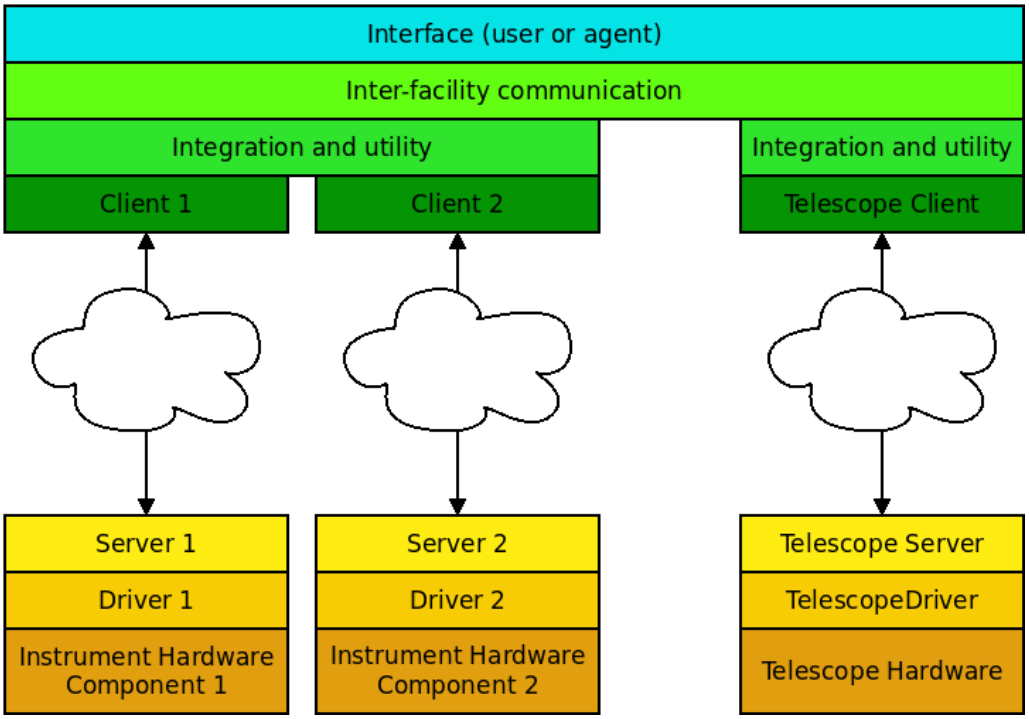


Fig. 1. A layered, distributed modular architecture.

of each hardware component is provided by a driver, embedded in server software allowing network access to these capabilities. A corresponding client for each component is able to access these capabilities. The client can be embedded in any software which requires access to the hardware item.

An integration and utility layer instantiates each of the clients representing the hardware components of the system. This layer also provides functions which depend on multiple components - for example, setting up an instrument to use frame transfer mode might require configuration of both a detector and a shutter.

Above the integration and utility layer, an inter-facility communication layer allows communication between facilities like telescopes and instruments. So for example if an instrument needs current pointing information from the telescope to populate FITS file headers, it could make a call to a `get_fits_info()` function in the telescope's integration and utility layer, via the top-level controller.

Finally, user or machine interfaces to the instrument can be built above the interfacility communication layer. Examples of these will be discussed later.

3. IMPLEMENTATION OF COMPONENTS

The architecture depicted above describes the pattern used for the interaction between hardware components and higher-level software, and the way in which we may assemble more complex software from more basic building blocks. When implementing the design, we need to make some concrete decisions.

A benefit of a distributed architecture is that the various components can be written in whichever programming language is most suitable for the task at hand. For hardware items like detectors, the driver software needs to be able to read data rapidly, and for these we use C++. Everywhere else, we have built our stack in Python.

For the client-server interaction, it would certainly be possible to develop the client and server code using low-level TCP/IP. However, there exist several packages which allow remote procedure calls (RPCs) and inter-process communication (IPC). We chose to use Apache Thrift[4] because it is a lightweight framework that makes such RPC/IPC easy. Thrift allows an interface consisting of functions and data structures to be specified in an intuitive interface definition language as shown in figure 2. The Thrift package includes a compiler which takes this interface definition and outputs server and client stub code in the languages of choice. In this case, the stub code consists of a set of empty function calls for each function defined in the interface, and

[4] `https://thrift.apache.org/`

VII Workshop on Robotic Autonomous Observatories (October 16-20, 2023)
Editors: Maria Gritsevich, Alberto J. Castro-Tirado, Petr Kubánek, Shashi B. Pandey, and David Hiriart - DOI: https://doi.org/10.22201/ia.14052059p.2025.59.34

the work to be done is mostly filling these in with working code. Thrift provides middleware modules (for Python) and libraries (for C++) which do the work of serializing and transporting function calls and data between client and server. Developers implementing clients and servers do not need to concern themselves with the details of the middleware code. Calls made on the client side are executed on the server side, and the results returned to the client.

Building the software components of the IO, following the architecture we have chosen, is a three-stage process: creating interfaces to hardware components, combining and extending individual hardware interfaces to form instrument or telescope interfaces, and finally, developing the end components.

The first stage, creating interfaces to each hardware item, means deciding which hardware functionality to make available, creating a Thrift interface definition reflecting this, compiling this to generate the stub code, and fleshing out the code to create working drivers. The drivers are wrapped in server code (also using a Thrift template) and then become stand-alone processes, listening for connections from their corresponding clients.

The second stage is to develop the integration and utility layer modules for the instruments or telescope. These modules include the client code for each associated hardware item but also functions which apply to more than one hardware item, and functions which contain business logic which is not specific to any particular hardware item. The functions of the integration and utility module, including those of the clients the module includes, form an application programming interface (API) to the particular instrument or telescope they describe.

As discussed in the architecture description, we use an interfacility communication layer above the integration and utility layer to allow telescopes, instruments and weather services to communicate with one another. This enables utility functions in the integration and utility layer to use more than one facility. Which of these get included is configured at run time by the software application.

The third and final stage is the development of these specific applications, using the interfaces to the various instrument, telescope and weather services.

It is important to note that there is a single instance of each hardware component server running at any time. The higher layers are software which provide access to the hardware, and multiple applications using these layers may be built, and may run simultaneously.

The applications we have built include:

- Command line tools to view and operate instruments and telescopes (used mostly for testing)
- Web interfaces for instruments and telescopes (providing a more user-friendly interface)
- Monitoring and safety tools
- Autonomous agents

We use the git (Chacon (2014)) version control system during development and deployment, with code stored in a central repository. Code to be deployed is tagged, and the tagged version is checked out onto the target machine. C++ code is compiled and installed using a Makefile. Where Python code is used, each subsystem has a dedicated Python virtual environment, and deployment entails installing the code into that environment. The Python setuptools package is used for overall controll of the build and deployment system.

Extensive logging is performed during runtime as an aid to monitoring, debugging and analysis of software and hardware. We also check for exceptional behaviour in code (operations timing out, system calls failing, etc) and propagate these exceptions upwards to where they can be best handled. A feature of Apache Thrift is that exceptions may be propagated across the interface; this enables exceptions arising in a driver process to be caught and displayed in a user interface. When this occurs a message can be displayed in the user interface and users may take corrective action before continuing with observations.

4. UTILITY FUNCTIONS

As part of the IO project, we have developed various functions which make life easier for astronomers observing manually, and which are necessary when observing in autonomous mode.

An example of this is an autofocus function. Previously, finding the best focus position required iterating through a list of focus positions using the telescope control, taking an image with the currently selected instrument at each position, and finally selecting the focus position which gave the best-focussed image.

If the temperature changes enough, if a filter is changed, or of course if a different instrument is selected, the best focus position needs to be determined again.

Since the software now allows instruments to communicate with and send commands to the telescope, we have been able to produce an autofocus() function in the instrument service. This iterates

VII Workshop on Robotic Autonomous Observatories (October 16-20, 2023)
Editors: Maria Griffsevich, Alberto J. Castro-Tirado, Petr Kubánek, Shashi B. Pandey, and David Hiriart - DOI: https://doi.org/10.22201/ia.14052059p.2025.59.34

```
service CameraService
{
    void set_binning(1: i8 xbin, 2: i8 ybin) throws (1: CameraException e);
    void set_readout_speed(1: ReadoutSpeed speed) throws (1: CameraException e);
    void set_gain(1: Gain gain_number) throws (1: CameraException e);
    void set_exposure_length(1: i32 exposure_length) throws (1: CameraException e);
    void start_expose() throws (1: CameraException e);
    void abort_exposure() throws (1: CameraException e);
    CameraState get_state() throws (1: CameraException e);
}
```

Fig. 2. An example of a basic Thrift interface definition

through the range of focus positions, obtaining an image at each. A source extraction is performed on each image, the full width at half maximum (FWHM) is then obtained for each source, and the average of these calculated. After iterating through the range a quadratic is fitted to the plot of mean FWHM vs focus position, and the best focus position is that which minimizes the focus measure.

For a given instrument and filter, the focus position depends linearly on the ambient temperature. Over time, using the autofocus function at a range of temperatures, we are able to acquire enough data to determine the parameters of this linear fit. This enables us to set the correct focus immediately, given the measured ambient temperature, the filter and the instrument.

A further utility function which relieves manual observers of some tedium but which is necessary for autonomous observations, is moving the telescope so that the light from the target falls on a specific pixel. This is particularly important in spectroscopy, where the light from the target must fall on the slit.

Our Mookodi instrument is both an imager and spectrograph (Erasmus et al. submitted). The spectrograph design is such that the beam is not deflected by the spectrograph optics grism and slit). These may be moved out of the beam, so that the CCD is directly illuminated.

The slit has a narrow and a wide section, the latter used when the seeing is high. The column of pixels corresponding to the slit position is known, and we have chosen two "magic pixels" corresponding to points under the narrow or wide slit sections. Pointing the telescope such that the target falls on either of these guarantees that when the spectrograph optical elements are placed in the beam, the light from the target will pass through the slit.

To achieve this, a `drop_star_on_slit()` function in the instrument service is used. This ensures that the optical elements are moved out of the beam. then makes a best effort to point the telescope in the right direction. Thereafter an image is obtained and the sources extracted. This list of sources is then sent to a WCS service - we use astrometry.net (Lang et al (2010)) - which returns the actual coordinates of the image centre. Comparing these with the coordinates of the best effort pointing, and knowing the offset of the magic pixel, we can calculate the direction and distance to nudge the telescope so that the light from the target falls directly on the magic pixel.

Again this is possible because the instrument and telescope can communicate with one another.

5. AUTONOMOUS OPERATIONS

Finally, our goal has been to prepare instruments and telescopes for autonomous observing. We have the building blocks in place, in the sense that we have interfaces to each of the instruments and the telescope, and we can do all of the tasks of pointing, focusing, acquiring a target, and taking exposures.

The general health and functioning of the IO ecosystem is made visible through a web-based dashboard, which shows the status of each service on each telescope. An alerting system sends text messages or emails to relevant parties in the event of critical processes failing. A "pre-flight" test is run in the late afternoon, ensuring that all relevant subsystems are functional, and the results mailed to the overseers of the IO.

Telescope and instrument safety is a primary concern when the telescope is operating autonomously. To address this we have a Local Control Unit (LCU) (van Gend et al (2022)) which monitors external conditions, and shuts the telescope down if required.

For the scheduling of observation requests, we use the Adaptive Scheduler component of the Observatory Control System (OCS) (Nation et al (2022)),

VII Workshop on Robotic Autonomous Observatories (October 16-20, 2023)
Editors: Maria Gritsevich, Alberto J. Castro-Tirado, Petr Kubánek, Shashi B. Pandey, and David Hiriart - DOI: https://doi.org/10.22201/ia.14052059p.2025.59.34

developed by the Las Cumbres Observatory[5]. This allows observation requests to be submitted by observers, and produces a schedule for observations which may change dynamically in the night

As observations are marked as completed, they are removed from the queue, while those marked as having failed may be rescheduled. The queue may be adjusted as new observation requests are added. Each observation request in the queue contains details about the telescope pointing, instrument configuration and observation requirements, and the time at which the observation is to be started.

We have developed a service which polls the scheduler, retrieving the queue at regular intervals (we use intervals of 1 minute). The queue is then examined to determine when the next observation is scheduled. If a previously scheduled observation is already running, the polling software does nothing and sleeps until the next interval elapses. If no observation is due in the next 20 minutes, and the telescope is open, a command is sent to shut down the telescope. If the next observation is due within the next 10 minutes, a command is sent to open the telescope. Finally, if the time for the next observation has been reached, the observation request is sent to the software which oversees its execution.

The first step in executing the observation is to translate the XML-format observation request, as sent by the OCS scheduler, to a form that our software (instrument and telescope) can act on. We produce two JSON format scripts: a setup script for the pointing of the telescope and target acquisition, and an execution script with the details of each observation to be made at the given telescope setup.

The telescope setup script contains the target right ascension and declination, the required tracking type (sidereal, non-sidereal or none) and for non-sidereal tracking, the parameters for this. For non-sidereal tracking, we currently support MPC[6] orbital elements to specify this, but we plan to extend this support to use JPL[7] orbital elements too (the latter is already supported by the OCS. If the telescope pointing needs to be finely adjusted (e.g. to put a star on a given pixel, as is required for spectroscopy, the details required for that are included.

The setup script is passed to a `run_script()` function, which passes the telescope and instrument specific parts of the script to the `stage_script()` functions in the telescope and instrument. These functions move the telescope or configure the instrument as required, but do not start any observations. When these functions have returned, the telescope is in position to begin observing .

The second script contains details of the exposures to be taken at that telescope position, including exposure time, number of observations, binning, gains, and filters. This script is passed to the instrument's `stage_script()` and after this a call is made to the instrument's `start_exposure()` function. There may be multiple such sets of exposures specified, in each case they are executed in succession.

At the beginning of each observation attempt, the OCS is notified and the observation is marked as attempted. After the observation is completed, the OCS is again notified and the observation is marked as complete. If instead the observation is unable to be completed, the OCS is notified and the observation is marked as failed, and possibly rescheduled.

6. CONCLUSIONS

We have developed a simple and flexible software architecture which we have applied to our systems, enabling remote and robotic operations

Various utility functions have been developed to replace formerly tedious and time consuming steps.

We have successfully applied this to the Lesedi telescope and the Mookodi instrument.

The telescope runs in queue scheduled mode, fully autonomously:

- The LCU enforces safe operation
- Biases are taken in the late afternoon
- Flats are taken immediately after sunset
- Items in the schedule queue are executed at the prescribed time
- We are able to observe sidereal and non-sidereal objects

We are currently commissioning Sibonise, a wide field imager on the same telescope, and will incorporate it into our autonomous observing plan when commissioning is finished.

We will then roll out fully autonomous observing to our 74-inch telescope, using the instrument selector currently being commissioned. Observations will use SHOC, a high speed camera, and SpUPNic, a medium resolution spectrograph. Following that we will turn our attention to the 40-inch telescope, and then to other telescopes.

Lastly, we have developed systems which listen for alerts of events meriting follow-up observations,

[5] `https://observatorycontrolsystem.github.io/`
[6] `https://www.minorplanetcenter.net/`
[7] `https://ssd.jpl.nasa.gov/orbits.html`

and when these are received the observation requests are added to the queue. We will be expanding these, and intend to be ready to react to alerts issued by the LSST when it comes online later in 2024.

REFERENCES

Chacon, S., Straub, B. 2014, Pro git, Apress
Erasmus, N., Steele, I. A., Piascik, A. S., et al. submitted
Lang, D., Hogg, D. W., Mierle, K., Blanton, M., & Roweis, S. 2010, AJ, 139, 1782
Nation, J., Bowman, M., Daily, M., et al. Proc. SPIE, 12186, 121860Q
Potter, S. B. 2021, Anais da Academia Brasileira de Cincias, 93, SciELO Brasil
Richards, M., 2022, Software Architecture Patterns, O'Reilly Media Inc.
Väisänen, P., Crause, L., Gilbank, D., et al. Proc. SPIE, 10704, 107040A
van Gend, C. H. D., Potter, S. B., Julie, R., et al. Proc. SPIE, 12189, 121890R
Worters, H. L., O'Connor, J. E., Carter, D. B., et al. Proc. SPIE, 9908, 99083Y

VII Workshop on Robotic Autonomous Observatories (October 16-20, 2023)
Editors: Maria Gritsevich, Alberto J. Castro-Tirado, Petr Kubánek, Shashi B. Pandey, and David Hiriart - DOI: https://doi.org/10.22201/ia.14052059p.2025.59.34

Revista Mexicana de Astronomía y Astrofísica Serie de Conferencias (RMxAC), **59**, 217–223 (2025)
© 2025: Instituto de Astronomía, Universidad Nacional Autónoma de México
https://doi.org/10.22201/ia.14052059p.2025.59.35

VII Workshop on Robotic Autonomous Observatories (October 16-20, 2023)
Editors: Maria Gritsevich, Alberto J. Castro-Tirado, Petr Kubánek, Shashi B. Pandey, and David Hiriart - DOI: https://doi.org/10.22201/ia.14052059p.2025.59.35

NEW ROBOTIC TELESCOPE: THE BIG EYE TO OBSERVE THE TRANSIENT UNIVERSE

C. M. Gutiérrez[1,2], J. Barrera[1,2], J. Bento[3], D. Copley[3], C. M. Copperwheat[3], F. J. De Cos[4,5], M. Escriche[1,2], J. J. Fernández-Valdivia[1,2], A. P. Garner[3], J. Gracia[4,6], D. G. Heffernan-Clarke[3], H. E. Jermak[3], J. León Gil[1,2], A. M. McGrath[3], C. Miossec[3], A. Oria[1,2], A. Ranjbar[3], R. Rebolo[1,2], C. Rodríguez-Pereira[4], F. Sánchez-Lasheras[4,7], R. J. Smith[3], I. A. Steele[3], and M. Torres[1,2]

RESUMEN

NRT es un proyecto internacional para construir y operar el mayor telescopio robótico del mundo. El telescopio tendrá un espejo primario segmentado con un diámetro equivalente de 4 m, un conjunto de instrumentos ópticos y de infrarrojo cercano montados simultáneamente, y un tiempo de respuesta inferior a 30 segundos. El proyecto se basa en la experiencia adquirida con el exitoso funcionamiento durante veinte años del telescopio de Liverpool, y con la óptica y el sistema de control del telescopio GTC. Todo ello, unido a las excelentes condiciones para la observación astronómica de La Palma, representa una base sólida y garantiza que el NRT será una de las instalaciones punteras en el campo de la astronomía en el dominio temporal. Esta contribución analiza el estado actual del proyecto, con especial énfasis en el desarrollo de su óptica, y los planes para su construcción y operación.

ABSTRACT

NRT is an international project to build and operate the world's largest robotic telescope. The telescope will have a segmented primary mirror with an equivalent diameter of 4 m, a set of simultaneously mounted optical and near-infrared instruments, and a response time of less than 30 seconds. The project builds on the experience gained with the successful twenty-year operation of the Liverpool telescope, and with the GTC optics and control system. All of the above together with the excellent conditions for astronomical observation of La Palma, represents a solid base and guarantees that NRT will be one of the leading facilities in the field of time domain astronomy. This contribution will analyze the current status of the project with special emphasis on the development of its optics, and the plans for its construction and operation.

Key Words: robotic telescopes — time-domain astronomy

1. INTRODUCTION

Astronomical observations in recent years are showing a changing face of the Universe, where sudden transient phenomena have been discovered on timescales that can be studied with the telescopes and instrumentation available nowdays. This has been made possible by advances in instrumentation and the design of increasingly versatile telescopes both on the ground and in space. Many of these telescopes allow efficient mapping of large regions of the sky and the access to unexplored ranges of the electromagnetic spectrum. These observations show a dynamic Universe spanning a wide range of spatial and temporal scales, encompassing from the discovery of new objects in the solar system, to galactic phenomena, such as novae, supernovae or tidal disruption events, to those of cosmological interest such as gamma-ray bursts or gravitational waves. Those phenomena open the door to the observation of new physical phenomena and to study the properties of matter and energy in extreme conditions, offering the possibility of discovering and extending our knowledge of the laws of nature.

A large number of telescopes have played a leading role in this progress, from those that act as discoverers of events, to those that are able to precisely locate and associate them with a particular astro-

[1]Instituto de Astrofísica de Canarias, E-38205 Tenerife, Spain.
[2]University of La Laguna, E-38206 Tenerife, Spain.
[3]Astrophysics Research Institute, Liverpool John Moores University, IC2, Liverpool Science Park, 146 Brownlow Hill, Liverpool, L3 5RF, UK.
[4]Instituto Universitario de Ciencias y Tecnologías Espaciales de Asturias (ICTEA), c/Independencia 13, 33004 Oviedo, Spain.
[5]Department of Prospecting and Exploitation of Mines, University of Oviedo, 33004 Oviedo, Spain.
[6]Department of Construction and Manufacturing Engineering, Oviedo University, c/ Pedro Puig Adam, 33203 Gijón, Spain.
[7]Department of Mathematics, Oviedo University, Oviedo, c/ Leopoldo Calvo Sotelo 18, 33007 Oviedo, Spain.

VII Workshop on Robotic Autonomous Observatories (October 16-20, 2023)
Editors: Maria Griffsevich, Alberto J. Castro-Tirado, Petr Kubánek, Shashi B. Pandey, and David Hiriart - DOI: https://doi.org/10.22201/ia.14052059p.2025.59.35

nomical source, to those that subsequently classify and characterise such events. As the number of discoveries of these transient phenomena is increasing, it is desirable to have telescopes that are fully dedicated to their study. Rapid localisation and classification is essential to exploit the full potential of these phenomena, so such facilities must be able to respond rapidly to a given alert and provide the data quickly and efficiently to the community. Automated operation of all these processes is desirable. That was the starting point almost twenty years ago for the Liverpool telescope (Steele 2004) which represented the first step towards a generation of large aperture telescopes operating in robotic mode and whose impact over the years has been demonstrated through a large number of leading scientific publications.

The new era of transient discoveries to be led among others by the Rubin Observatory (`https://rubinobservatory.org`), which will be able to make deep mappings of a representative part of the sky with cadences of a few days, makes the need for facilities capable of classifying and characterising these phenomena urgent. A detailed study of each of these phenomena would require a titanic observational task and an unfeasible number of facilities in the world. Therefore, robotic telescopes with relatively large apertures are essential to perform a selection of the most interesting cases and an optimal observation of them, allowing a rapid classification of the phenomena and their subsequent study with large telescopes. That was the motivation of the project presented in this contribution. Building on the experience gained during almost two decades of successful operation of the Liverpool telescope, we proposed to take the first step towards a new generation of 4-metre class robotic telescopes, with the New Robotic Telescope (NRT) project as the first representative and guide of this new generation. The concept study and the main scientific drivers were presented in Copperwheat et al. (2015). Here, we present an update to those presented in past years (Gutiérrez et al. 2019, 2021), highlighting the current status of the project, its plans until first light, and emphasising the optical, mechanical and control system solutions adopted.

2. THE PROJECT

The technological development of the project began in 2018 promoted by the University of Liverpool (LJMU), in collaboration with the Instituto de Astrofísica de Canarias (IAC) and soon joined by the University of Oviedo (UoO). The basic requirements were fully robotic operation, aperture size, operation in the optical and infrared ranges, a response time to an alert of interest of less than 30 seconds, a Ritchey-Chretien optical configuration with a field of view of 15 arcmin, and six focal stations allowing the simultaneous mounting of several instruments. The image quality requirement implied a deterioration with respect to seeing of no more than 0.2 arcseconds at 80 % fraction of enclosed energy for long exposures.

The project has gone through its different design phases culminating in its Preliminar Design Review (PDR) Design Review) at the end of 2021, and is currently in the phase of detailed design in order to carrying out a Critical Design Review (CDR) in 2025. At the same time, the corresponding studies and environmental impact assessments are being carried out and the corresponding administrative permits are being obtained. The agreements for the construction and operation of the telescope are also being formalised, setting out the rights and obligations of each of the parties. We estimate that the first light will take place in 2028.

The telescope will be installed in the Roque de los Muchachos Observatory (La Palma, Spain), complementing and adding value to the existing facilities at the observatory, which make it one of the most important sites in the world for astronomical observations. The Observatory combines this excellent quality for observation with a set of logistical advantages, including the existence of an international airport just over an hour's drive from the observatory, which can be accessed by several paved roads that are open almost 365 days a year, as well as the existence of a set of infrastructures, technical support and specialised personnel that facilitate the effective operation of the telescope. To all this must be added the European Union (EU) own legal framework, which guarantees stability and legal certainty.

Within the observatory, a location previously occupied by a now decomissioned facility (the Carlsberg Meridian Telescope) has been chosen to minimise the environmental and landscape impact and to optimise resources in an efficient way. Atmospheric data collected over the years near to that location show very good conditions in terms of seeing (median 0.7 arcseconds), useful observing hours, humidity, sky darkness, etc. Figure 1 shows a view of such location at the Roque de los Muchachos Observatory.

For the building and enclosure, a functional design concept (Gradisar et al. 2022) has been pursued to house the telescope, as well as facilities such as workshops and storage areas, in line with the min-

VII Workshop on Robotic Autonomous Observatories (October 16-20, 2023)
Editors: Maria Gritsevich, Alberto J. Castro-Tirado, Petr Kubánek, Shashi B. Pandey, and David Hiriart - DOI: https://doi.org/10.22201/ia.14052059p.2025.59.35



Fig. 1. View of the Roque de los Muchachos Observatory (La Palma, Spain) with the WHT telescope in front. The planned location of NRT is indicated by a blue ellipse.

imal interaction required for such a telescope. Figure 2 shows an artistic simulation of what the enclosure will look like. A clam-shell solution has been chosen. This solution allows full all-sky observation above a height of 20 degrees, facilitates operation and maintenance, reduces dome seeing by allowing rapid heat dissipation before observations start, and is a solution that has proven successful over many years at the Liverpool telescope. On the downside, the permanent and complete exposure of the telescope to the atmosphere must be taken into account in the design and operation of the telescope.

3. STRUCTURE

The design of the NRT structure has undergone multiple iterations and analyses to optimise its performance (Rodríguez Pereira et al. 2022). Special attention was paid to achieving a fast response time, sufficient stiffness, and quick settling time for the telescope in order to accurately observe and respond to quickly fading transient events. The original design based on a Serrurier truss showed the feasibility of the quick movements required for NRT, and determined that a locked rotor frequency resonance of 10 Hz was needed (Ranjbar et al. 2020).

In subsequent analysis that design was changed to a Multibay Truss (Fig. 3), which provides greater stiffness at a lower weight compared to the original Serrurier Truss, and the primary cell was reconfigured. This change enabled a reduction in the overall weight of the optical support system by about 25 tonnes (33 % from the original design), thus lowering torque requirements for the drive systems while maintaining the same performance objectives of the Serrurier truss. In addition, this modification enabled a change in the configuration of the secondary structure, allowing a configuration of secondary support vanes overlapping the gaps in the primary inner segments, thus reducing the obstruction of the primary mirror. This Multibay truss provided also great accessibility for mirror segment handling, although it introduces some susceptibility to torsional motion, which was resolved by applying pre-stresses to the secondary mirror system vanes.

The drive system solution will use hydrostatic bearings and direct drive motors, which will be segmented in the azimuth axis. The low friction afforded by the hydrostatic bearings allows for good performance at low speeds for tracking, despite the high slewing speeds achieved during pointing operations. The direct drives will provide a smooth input torque, avoiding the noise a mechanical transmission would introduce into the system.

To study the static behaviour a finite element model was applied obtaining a maximum offset (at the lowest elevation) between the primary and secondary mirrors of 0.083 mm and a defocus of 0.095 mm, which are within the requirements. In terms of dynamic behaviour, analyses have been carried out to estimate the natural frequencies of the structure which demonstrate its ability to move and stabilise within an acceptable range of vibration amplitude, in less than 30 seconds. As a whole, all these analyses show promising results in terms of low deformations and good optical, vibration, pointing, and tracking performance. In successive analyses we plan to include factors such as wind shaking or vibrations induced by the drive system during tracking.

4. OPTICS AND OPTOMECHANICS

The telescope will be a Ritchey-Chretien with F/10.6 in which the primary mirror consists of a set of 18 hexagonal mirrors of 96 cm placed in three concentric rings (Harvey et al. 2022). This gives a collecting surface which is equivalent to that of a 4 m diameter telescope. The secondary mirror is a lightened hyperbolic mirror with a diameter of 91 cm. Additionally, there is a mirror centred on the optical axis which allows the direct Cassegrain focal station to be exchanged for one of a set of 6 folded focal stations on which different instruments will be mounted simultaneously.

Figure 3 shows the topological configuration adopted for the primary mirror of NRT. Each of the segments will be an off-axis section of the nominal hyperboloid mounted on to an identical optomechanical support structure independently of their type. Each set of mirrors (of the same type) will be composed of 6 identical segments. This configuration requires three types of mirrors, due to the different radial positions of these groups with respect to the optical axis and the asphericity of the optical surface.

VII Workshop on Robotic Autonomous Observatories (October 16-20, 2023)
Editors: Maria Gritsevich, Alberto J. Castro-Tirado, Petr Kubánek, Shashi B. Pandey, and David Hiriart - DOI: https://doi.org/10.22201/ia.14052059p.2025.59.35

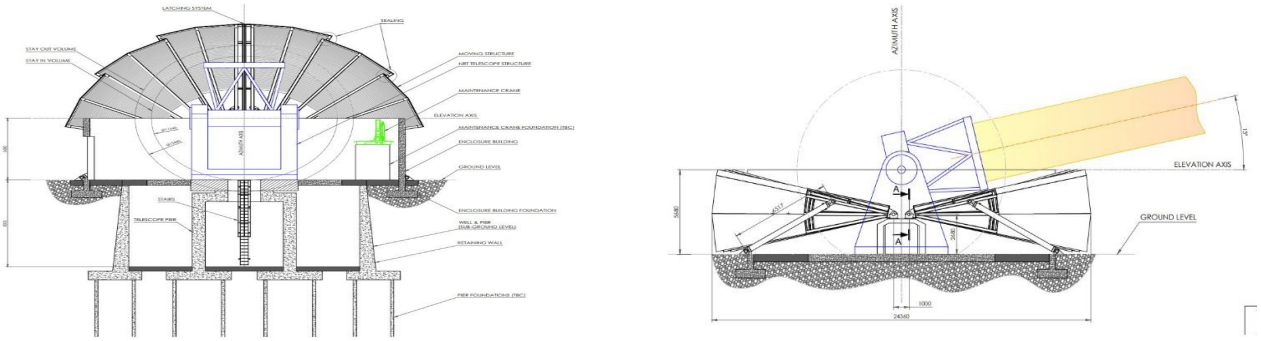


Fig. 2. Enclosure of NRT.

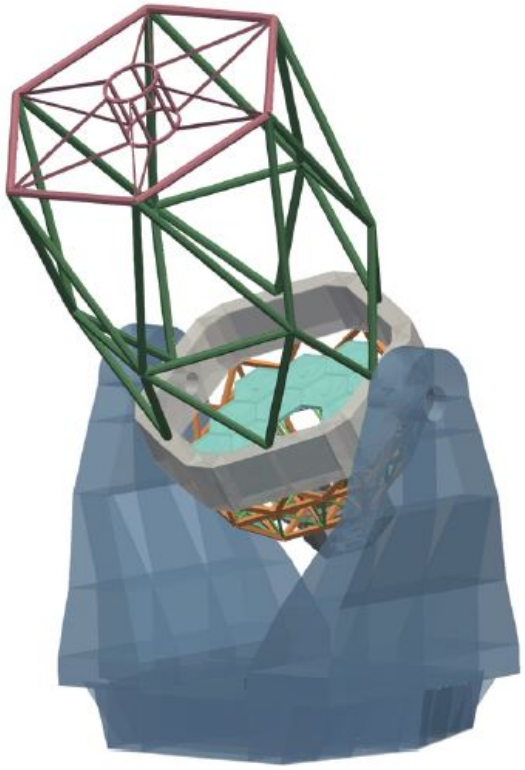


Fig. 3. Artistic view of the concept for the mechanical structure of the NRT telescope.

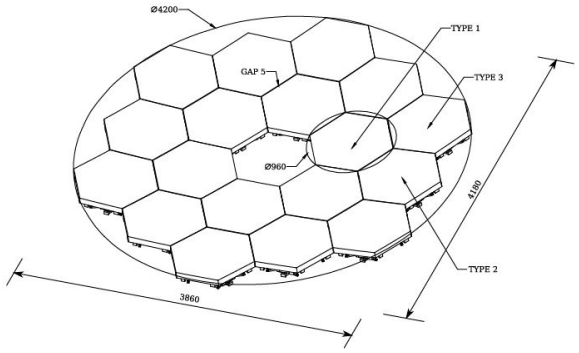


Fig. 4. NRT primary mirror topology.

Although that type of segmented topology is typical of large telescopes such as GTC (www.gtc.iac.es), Keck (www.keckobservatory.org), and SALT (www.salt.ac.za), and of the new generation of large telescopes such as ELT (www.elt.eso.org) or TMT (www.tmt.org), there are some cases of smaller telescopes such as SEIMEI (Kurita et al. 2020) or LAMOST (www.lamost.org) that also use this type of solution. There were several reasons that led us to select a segmented configuration; firstly the segments allow for a weight reduction of several tons, in addition it allows the mirrors to be manufactured within the consortium; in fact, the IAC is developing an optics centre for the production of optical elements with the equipment and metrology tools to manufacture mirrors with diameters up to 1.5 m. The configuration chosen is similar to that of GTC, and it is therefore to be expected that the optomechanical and control system for NRT could be based on the solutions adopted by GTC. Furthermore, NRT will represent the pioneer for new generations of robotic telescopes with progressively larger apertures that will necessarily have to adopt segmented solutions above a given diameter.

On the other hand, this solution poses additional problems such as the higher complexity of the positioning system, and the logistical difficulty of the recoating process in which a strategy of realuminisations by groups of three segments every several months is foreseen, instead of a single aluminisation every two years as would be necessary for a monolithic mirror.

Each primary mirror segment system will be composed of the substrate, and the axial and lateral pads as shown in Figure 5. The substrate will be a plano-

VII Workshop on Robotic Autonomous Observatories (October 16-20, 2023)
Editors: Maria Gritsevich, Alberto J. Castro-Tirado, Petr Kubánek, Shashi B. Pandey, and David Hiriart - DOI: https://doi.org/10.22201/ia.14052059p.2025.59.35

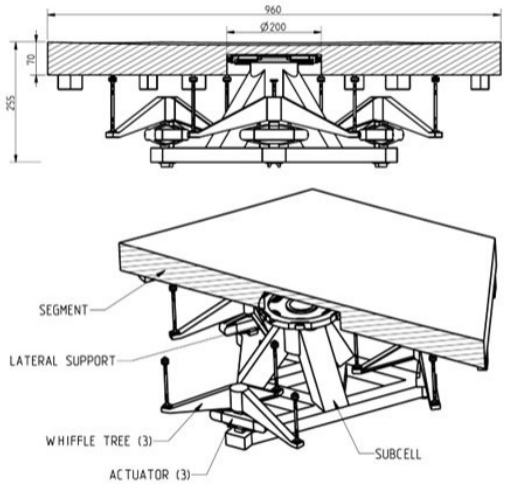


Fig. 5. Primary mirror segment support assembly.

concave hexagon with a mean size of 960 mm point-to-point and about 70 mm of maximum thickness (Oria 2022). The active optics implements actuators to move the mirrors (in piston, tip and tilt) maintaining the shape of the M1 optical surface in the presence of different perturbations such as gravity, thermal changes or wind effects. The axial and lateral supports, and the actuators will be mounted on a common structure, the subcell that will hold both supports and actuators during segment handling. The axial load of each actuator will be distributed to three support points on the back plane of the substrate to reduce the segment gravity print-through. The load spreading element performing this function is called the whiffletree. The three different whiffletrees of the segment constitute its axial support system. The lateral support consists of a central diaphragm-like element located approximately at the segment center of gravity. The assembly is composed of a membrane, a monolithic outer frame including the radial vanes, a central hub and a mechanical safety limit to restrict the maximum motion range. This solution can take the lateral loads while remaining axially and tip/tilt compliant to decouple from the axial support.

An overview of the preliminary design of the secondary mirror system is shown in Figure 6. It is made up of the secondary mirror itself, its support system, and an active slow positioning stage to maintain the optical alignment with respect to the primary mirror. This unit can be precisely positioned in its six rigidbody degrees of freedom by means of a hexapod (see Fig. 6 bottom). As the secondary has to be supported by all the structural elements of the telescope, it is convenient to reduce its mass as much as possible to minimise the overall weight of the complete system. Figure 6 (top) shows the back side of the secondary mirror and the geometrical solution proposed for this weight reduction.

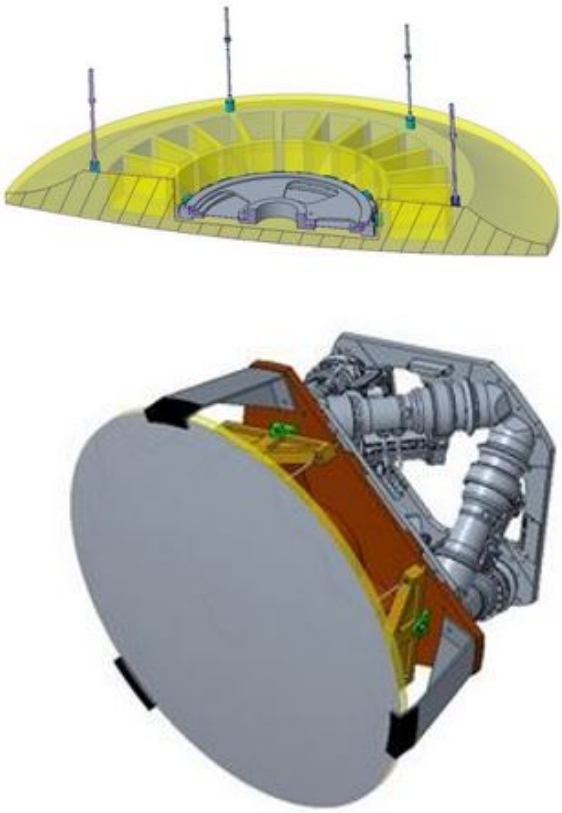


Fig. 6. NRT secondary mirror system.

5. CONTROL SYSTEM

The NRT project implements a software architecture (Bento et al. 2022a) designed to support high-precision astronomical observations and user interactions with the telescope. A distributed architecture across two environments optimizes performance and accessibility, allowing for reliable nightly fully robotic operations and remote user interactions. A first environment, located on the observatory forms the basis for a reliable software platform for nightly fully robotic operations. Containerized applications (Fernández-Valdivia et al. 2022) are used to manage and process data directly from the telescope, enabling real-time analysis and immediate feedback on observations. The second environment will be hosted on Google Cloud, providing secure and scalable access to telescope data, analytical tools, and computational resources.

VII Workshop on Robotic Autonomous Observatories (October 16-20, 2023)
Editors: Maria Gritsevich, Alberto J. Castro-Tirado, Petr Kubánek, Shashi B. Pandey, and David Hiriart - DOI: https://doi.org/10.22201/ia.14052059p.2025.59.35

GitLab[1] is leveraged for version control, providing efficient code management and collaboration, while DevOps pipelines automate building, testing, and deployment processes. This automation is crucial for rapid iterate on the software, and reduces the time and effort required to bring new features and updates to the infrastructure. Harbor[2] is used as an artifact repository, ensuring secure storage and management of Docker images[3] and Helm charts[4] used in Kubernetes deployments.

The software control topology is split into three layers: the Science Operations Data Centre (SODC), the Robotic Control System (RCS), and the Telescope Level Systems (TLS). The SODC layer (Jermak et al. 2022) handles user-facing functionality, including proposal submission, observation planning, data reduction pipelines, and access to data archives. The RCS layer is the equivalent to a human astronomer, making scientific decisions based on live conditions, prioritizing and scheduling observations, and providing fast-follow-up functionality. The Master Control Process acts as the ultimate decision maker within the RCS layer and communicates with the SODC layer through an application programming interface (API).

The TLS layer is the link between the low-level hardware and the RCS. The TLS encompasses everything that directly controls hardware within the observatory and therefore, handles control of slewing, pointing, segmented mirror alignment, dome control and instrument interface. It contains the observing engine which allows targets requested by the RCS to be captured. The TLS is based (Bento et al. 2022b) on the existing GTC control system (GCS) that allows a ready-made functionality for key telescope behaviours such as segmented mirror alignment. Another key benefit of the GCS is that devices can be created to communicate to a wide variety of other systems and field busses. This means that both, instruments and control hardware can be operated directly by GCS without incorporating low level control within the TLS.

Finally, the architecture for the low-level hardware control utilizes a distributed industrial network with Beckhoff PLCs and Ethercat data bus for robust and reliable control and communication between systems. The PLCs are controlled by a Kubernetes Cluster using the OPCUA[5] protocol.

[1] https://about.gitlab.com/
[2] https://goharbor.io/
[3] https://hub.docker.com/
[4] https://helm.sh/
[5] https://opcfoundation.org/about/opc-technologies/opc-ua/

6. CONCLUSIONS

NRT is an ambitious initiative that is set to play a key role in the new era of time domain astronomy, acting both as a pioneer and as an example of a generation of new telescopes extending robotic operation from the current 2-metre to 4-metre telescopes. This contribution has presented the motivation, objectives and main features of the project, as well as its current status and the plans until its commissioning. The main features of the project are its relatively low cost of construction and operation, and its high efficiency and versatility that will allow it to address studies of a large number of transient phenomena by acting as a necessary link between the discovery instruments and the larger, traditionally operated telescopes that can carry out more detailed studies. With this approach, NRT aims to develop technological standards to guide this fascinating adventure to understand the world of transient phenomena in the universe.

Acknowledgements: This Project has received funding from the Canary Islands Government under a direct grant awarded on grounds of public interest (Order N 185 August 2017). We also thank the support of the Spanish Ministerio de Ciencia, Innovación y Universidades, Fondo Europeo de Desarrollo Regional (FEDER), Agencia Canaria de Investigación, Innovación y Sociedad de la Información (ACIISI) and the programmes Canarias Avanza con Europa and Tenerife Innova, Cabildo de Tenerife. The project is also supported by a UKRI grant from STFC (ST/V003828/1) and by the University of Oviedo, Project FUO-20-362.

REFERENCES

Bento, J., Smith, R. J., Arnold, D. M., et al. 2022a, Proc. SPIE, 12189, 121890C
Bento, J., Arnold, D. M., Smith, R. J., et al. 2022b, Proc. SPIE, 12189, 1218905
Copperwheat, C. M., Steele, I. A., Barnsley, R. M., et al. 2015, ExA, 39, 119
Fernández-Valdivia, J. J., Barrera Martín, J., Torres, M., et al. 2022, Proc. SPIE, 12189, 121890S
Gradišar, L., Copley, D., McGrath, A., et al. 2022, Proc. SPIE, 12182, 121821O
Gutiérrez, C. M., Arnold, D., Copley, D., et al. 2019, AN, 340, 40
Gutiérrez, C. M., Torres, M., Oria, A., et al. 2021, RMxAC, 53, 8
Harvey, É. J., Steele, I. A., Torres, M., et al. 2022, Proc. SPIE, 12182, 121821Z
Jermak, H., Law, D., Buntin, S., et al. 2022, Proc. SPIE, 12182, 121824G

Kurita, M., Kino, M., Iwamuro, F. et al. 2020, PASJ, 72, 48
Oria, A. 2022, PhDThesis, Universidad de La Laguna
Ranjbar, A., Copley, D., Steele, I. A., et al. 2020, Proc. SPIE, 11445, 1144556
Rodríguez Pereira, C., de la Roza Palicio, F., Gracia Rodríguez, J., et al. 2022, Proc. SPIE, 12182, 121823R
Steele, I. 2004, AN, 325, 519

VII Workshop on Robotic Autonomous Observatories (October 16-20, 2023)
Editors: Maria Gritsevich, Alberto J. Castro-Tirado, Petr Kubánek, Shashi B. Pandey, and David Hiriart - DOI: https://doi.org/10.22201/ia.14052059p.2025.59.35

VII Workshop on Robotic Autonomous Observatories (October 16-20, 2023)
Editors: Maria Gritsevich, Alberto J. Castro-Tirado, Petr Kubánek, Shashi B. Pandey, and David Hiriart

AUTHOR INDEX

Abdikamalov, E. Early-Time Optical Spectral Shape Measurements of GRB 200925B. *Z. Abdullayev, T. Komesh, B. Grossan, E. Abdikamalov, Z. Maksut, M. Krugov, S. Myrzakul, D. Tuiakbayeva, & A. Kostangeldinova*, 109

Abdullayev, Z. Early-Time Optical Spectral Shape Measurements of GRB 200925B. *Z. Abdullayev, T. Komesh, B. Grossan, E. Abdikamalov, Z. Maksut, M. Krugov, S. Myrzakul, D. Tuiakbayeva, & A. Kostangeldinova*, 109

Alcaraz, C. Unsynchronized Fireball Analysis and Challenges in Dimensionless Atmospheric Flight Parametrization:The SPMN230522 Superbolide as a Case Study. *E. Peña-Asensio, P. Grèbol-Tomàs, J.M. Trigo-Rodríguez, M. Gritsevich, A. Rimola, M. Corretgé-Gilart, C. Guasch, C. Alcaraz, V. Ibáñez, A. Gómez, & J. Gómez*, 87

Aryan, A. An Intermediate Luminosity GRB 210210A: The Early Onset of the External Forward Shock in the X-ray?. *R. Gupta, A. K. Ror, S. B. Pandey, J. Racusin, M. Moss, A. Aryan, N. Klingler, & A. J. Castro-Tirado*, 115

Aryan, A. Prompt and Afterglow Analysis of the *Fermi-LAT detected GRB 230812B.* *A. K. Ror, S. B. Pandey, A. Aryan, S. Kumar, and A. J. Castro-Tirado*, 133

Aryan, A. The Core Collapse of a 16.5 $M_\odot$ Star. *A. Aryan, S. B. Pandey, R. Gupta, A. K. Ror, & A. J. Castro-Tirado*, 145

Bahrani, F. Using Artificial Intelligence and Machine Learning in Education of Astronomy, Physics and Mathematics. *F. Bahrani*, 183

Baroch, D. Advanced Weather Control System at the TJO Telescope. *F. Domene, E. Herrero, P. Gil, D. Baroch, & A. Rojas*, 55

Baroch, D. Autonomous Scheduling at the TJO Telescope. *D. Baroch, E. Herrero, P. Gil, F. Domene, A. Rojas, & N. Ribó*, 81

Barrera, J. New Robotic Telescope: The Big Eye to Observe the Transient Universe. *C. M. Gutiérrez, J. Barrera, J. Bento, D. Copley, C. M. Copperwheat, F. J. De Cos, M. Escriche, J. J. Fernández-Valdivia, A. P. Garner, J. Gracia, D. G. Heffernan-Clarke, H. E. Jermak, J. León Gil, A. M. McGrath, C. Miossec, A. Oria, A. Ranjbar, R. Rebolo, C. Rodríguez-Pereira, F. Sánchez-Lasheras, R. J. Smith, I. A. Steele, & M. Torres*, 217

Bento, J. New Robotic Telescope: The Big Eye to Observe the Transient Universe. *C. M. Gutiérrez, J. Barrera, J. Bento, D. Copley, C. M. Copperwheat, F. J. De Cos, M. Escriche, J. J. Fernández-Valdivia, A. P. Garner, J. Gracia, D. G. Heffernan-Clarke, H. E. Jermak, J. León Gil, A. M. McGrath, C. Miossec, A. Oria, A. Ranjbar, R. Rebolo, C. Rodríguez-Pereira, F. Sánchez-Lasheras, R. J. Smith, I. A. Steele, & M. Torres*, 217

Boaca, I. Cometary Outbursts and Evolution of Ejected Particles. *M. Gritsevich, M. Nissinen, J. Ryske, A. J. Castro-Tirado, I. Pérez-García, M. Weso, J. M. Trigo-Rodríguez, E. Peña-Asensio, I. Boaca, T. Prystavski, M. Husárik, O. Ivanova, A. Sánchez, & J. M. Llenas*, 93

Calvario, T. Tulancingo-I: The K Band Mexican Radiotelescope. *D. Hiriart, E. Colorado, F. Diaz, T. Calvario, H. Serrano, D. Rojas, & S. Kurtz*, 193

Castro Tirado, M. A. Development of astronomical observatories from the late 19th to the 21st Century. *M. A. Castro Tirado*, 1

Castro-Tirado, A. J. An Intermediate Luminosity GRB 210210A: The Early Onset of the External Forward Shock in the X-ray?. *R. Gupta, A. K. Ror, S. B. Pandey, J. Racusin, M. Moss, A. Aryan, N. Klingler, & A. J. Castro-Tirado*, 115

Castro-Tirado, A. J. Cometary Outbursts and Evolution of Ejected Particles. *M. Gritsevich, M. Nissinen, J. Ryske, A. J. Castro-Tirado, I. Pérez-García, M. Weso, J. M. Trigo-Rodríguez, E. Peña-Asensio, I. Boaca, T. Prystavski, M. Husárik, O. Ivanova, A. Sánchez, & J. M. Llenas*, 93

Castro-Tirado, A. J. Early Emission of Short Optical Transients. *S. Wu, V. M. Lipunov, A. J. Castro-Tirado, Y.-D. Hu, K. Zhirkov, & N. V. Tyurina*, 153

Castro-Tirado, A. J. Imaging Stokes Photometer-Polarimeter for the BOOTES Global Telescope Network. *S. Guziy, I. Syniavsky, Ye. Oberemok, O. Ivanova, & A. J. Castro-Tirado*, 197

Castro-Tirado, A. J. Prompt and Afterglow Analysis of the *Fermi-LAT detected GRB 230812B.* *A. K. Ror, S. B. Pandey, A. Aryan, S. Kumar, and A. J. Castro-Tirado*, 133

Castro-Tirado, A. J. The Core Collapse of a 16.5 $M_\odot$ Star. *A. Aryan, S. B. Pandey, R. Gupta, A. K. Ror, & A. J. Castro-Tirado*, 145

Castro-Tirado, A. J. Preface. *Maria Gritsevich, Alberto J. Castro-Tirado, Petr Kubánek, Shashi B. Pandey, and David Hiriart*, vii

VII Workshop on Robotic Autonomous Observatories (October 16-20, 2023)
Editors: Maria Gritsevich, Alberto J. Castro-Tirado, Petr Kubánek, Shashi B. Pandey, and David Hiriart

Chandra, S. Observatory Control System at South African Astronomical Observatory. *Sunil Chandra, Steve B. Potter, Carel van Gend, Nicolas Erasmus, & Roufurd Julie*, 71

Chandra, S. Software Components of the Intelligent Observatory. *C. H. D. van Gend, S. B. Potter, N. Erasmus, S. Chandra, M. Hlakola, H. Worters, & R. Julie*, 209

Chandra, S. The Intelligent Observatory. *N. Erasmus, S. B. Potter, C. H. D. van Gend, S. Chandra, H. L. Worters, M. Hlakola, & R. Julie*, 201

Colorado, E. Tulancingo-I: The K Band Mexican Radiotelescope. *D. Hiriart, E. Colorado, F. Diaz, T. Calvario, H. Serrano, D. Rojas, & S. Kurtz*, 193

Copley, D. New Robotic Telescope: The Big Eye to Observe the Transient Universe. *C. M. Gutiérrez, J. Barrera, J. Bento, D. Copley, C. M. Copperwheat, F. J. De Cos, M. Escriche, J. J. Fernández-Valdivia, A. P. Garner, J. Gracia, D. G. Heffernan-Clarke, H. E. Jermak, J. León Gil, A. M. McGrath, C. Miossec, A. Oria, A. Ranjbar, R. Rebolo, C. Rodríguez-Pereira, F. Sánchez-Lasheras, R. J. Smith, I. A. Steele, & M. Torres*, 217

Copperwheat, C. M. New Robotic Telescope: The Big Eye to Observe the Transient Universe. *C. M. Gutiérrez, J. Barrera, J. Bento, D. Copley, C. M. Copperwheat, F. J. De Cos, M. Escriche, J. J. Fernández-Valdivia, A. P. Garner, J. Gracia, D. G. Heffernan-Clarke, H. E. Jermak, J. León Gil, A. M. McGrath, C. Miossec, A. Oria, A. Ranjbar, R. Rebolo, C. Rodríguez-Pereira, F. Sánchez-Lasheras, R. J. Smith, I. A. Steele, & M. Torres*, 217

Corretgé-Gilart, M. Unsynchronized Fireball Analysis and Challenges in Dimensionless Atmospheric Flight Parametrization:The SPMN230522 Superbolide as a Case Study. *E. Peña-Asensio, P. Grèbol-Tomàs, J.M. Trigo-Rodríguez, M. Gritsevich, A. Rimola, M. Corretgé-Gilart, C. Guasch, C. Alcaraz, V. Ibáñez, A. Gómez, & J. Gómez*, 87

Coward, D. Management of a Multi-User Robotic Observatory. *J. Moore, B. Gendre, D. Coward, F. Panther, & E. Moore*, 77

Coward, D. The Impact of the Site Quality of the Zadko Observatory on its Scientific Results. *B. Gendre, R. Tonello, M. Studdert, D. Coward, A. Klotz, E. Moore, J. Moore, & F. Panther*, 49

Cristarella Orestano, P. Modernization of Coloti Optical Observatory: Remote Control and Automation for Multimessenger Follow-Up. *P. Cristarella Orestano, S. Cutini, S. Germani, S. Palmerini, & G. Tosti*, 19

Cutini, S. Modernization of Coloti Optical Observatory: Remote Control and Automation for Multimessenger Follow-Up. *P. Cristarella Orestano, S. Cutini, S. Germani, S. Palmerini, & G. Tosti*, 19

Díaz, F. Tulancingo-I: The K Band Mexican Radiotelescope. *D. Hiriart, E. Colorado, F. Diaz, T. Calvario, H. Serrano, D. Rojas, & S. Kurtz*, 193

De Cos, F. J. New Robotic Telescope: The Big Eye to Observe the Transient Universe. *C. M. Gutiérrez, J. Barrera, J. Bento, D. Copley, C. M. Copperwheat, F. J. De Cos, M. Escriche, J. J. Fernández-Valdivia, A. P. Garner, J. Gracia, D. G. Heffernan-Clarke, H. E. Jermak, J. León Gil, A. M. McGrath, C. Miossec, A. Oria, A. Ranjbar, R. Rebolo, C. Rodríguez-Pereira, F. Sánchez-Lasheras, R. J. Smith, I. A. Steele, & M. Torres*, 217

Denneau, L. Zero Point Magnitudes of All-Sky Images for Determining Cloud Conditions. *C. H. D. van Gend, N. Erasmus, J. Tonry, L. Denneau, M. Hlakola, & S. B. Potter*, 69

Domene, F. Advanced Weather Control System at the TJO Telescope. *F. Domene, E. Herrero, P. Gil, D. Baroch, & A. Rojas*, 55

Domene, F. Autonomous Scheduling at the TJO Telescope. *D. Baroch, E. Herrero, P. Gil, F. Domene, A. Rojas, & N. Ribó*, 81

Erasmus, N. Observatory Control System at South African Astronomical Observatory. *Sunil Chandra, Steve B. Potter, Carel van Gend, Nicolas Erasmus, & Roufurd Julie*, 71

Erasmus, N. Software Components of the Intelligent Observatory. *C. H. D. van Gend, S. B. Potter, N. Erasmus, S. Chandra, M. Hlakola, H. Worters, & R. Julie*, 209

Erasmus, N. The Intelligent Observatory. *N. Erasmus, S. B. Potter, C. H. D. van Gend, S. Chandra, H. L. Worters, M. Hlakola, & R. Julie*, 201

Erasmus, N. Zero Point Magnitudes of All-Sky Images for Determining Cloud Conditions. *C. H. D. van Gend, N. Erasmus, J. Tonry, L. Denneau, M. Hlakola, & S. B. Potter*, 69

Erece, O. Autonomous Telescope and Scientific Infrastructure Developments at TUG. *O. Erece, Y. Kilic, & K. Uluc*, 27

Escriche, M. New Robotic Telescope: The Big Eye to Observe the Transient Universe. *C. M. Gutiérrez, J. Barrera, J. Bento, D. Copley, C. M. Copperwheat, F. J. De Cos, M. Escriche, J. J. Fernández-Valdivia, A. P. Garner, J. Gracia, D. G. Heffernan-Clarke, H. E. Jermak, J. León Gil, A. M. McGrath, C. Miossec, A. Oria, A. Ranjbar, R. Rebolo, C. Rodríguez-Pereira, F. Sánchez-Lasheras, R. J. Smith, I. A. Steele, & M. Torres*, 217

Fernández-Valdivia, J. J. New Robotic Telescope: The Big Eye to Observe the Transient Universe. *C. M. Gutiérrez, J. Barrera, J. Bento, D. Copley, C. M. Copperwheat, F. J. De Cos, M. Escriche, J. J. Fernández-Valdivia, A. P. Garner, J. Gracia, D. G. Heffernan-Clarke, H. E. Jermak, J. León Gil, A. M. McGrath, C. Miossec, A. Oria, A. Ranjbar, R.*

VII Workshop on Robotic Autonomous Observatories (October 16-20, 2023)
Editors: Maria Gritsevich, Alberto J. Castro-Tirado, Petr Kubánek, Shashi B. Pandey, and David Hiriart

Rebolo, C. Rodríguez-Pereira, F. Sánchez-Lasheras, R. J. Smith, I. A. Steele, & M. Torres, 217

Gómez, A. Unsynchronized Fireball Analysis and Challenges in Dimensionless Atmospheric Flight Parametrization:The SPMN230522 Superbolide as a Case Study. *E. Peña-Asensio, P. Grèbol-Tomàs, J.M. Trigo-Rodríguez, M. Gritsevich, A. Rimola, M. Corretgé-Gilart, C. Guasch, C. Alcaraz, V. Ibáñez, A. Gómez, & J. Gómez*, 87

Gómez, J. Unsynchronized Fireball Analysis and Challenges in Dimensionless Atmospheric Flight Parametrization:The SPMN230522 Superbolide as a Case Study. *E. Peña-Asensio, P. Grèbol-Tomàs, J.M. Trigo-Rodríguez, M. Gritsevich, A. Rimola, M. Corretgé-Gilart, C. Guasch, C. Alcaraz, V. Ibáñez, A. Gómez, & J. Gómez*, 87

Gabor, P. Don: Automation of the Vatican Advanced Technology Telescope. *P. Gabor*, 23

Garner, A. P. New Robotic Telescope: The Big Eye to Observe the Transient Universe. *C. M. Gutiérrez, J. Barrera, J. Bento, D. Copley, C. M. Copperwheat, F. J. De Cos, M. Escriche, J. J. Fernández-Valdivia, A. P. Garner, J. Gracia, D. G. Heffernan-Clarke, H. E. Jermak, J. León Gil, A. M. McGrath, C. Miossec, A. Oria, A. Ranjbar, R. Rebolo, C. Rodríguez-Pereira, F. Sánchez-Lasheras, R. J. Smith, I. A. Steele, & M. Torres*, 217

Gend, C. V. Observatory Control System at South African Astronomical Observatory. *Sunil Chandra, Steve B. Potter, Carel van Gend, Nicolas Erasmus, & Roufurd Julie*, 71

Gendre, B. Management of a Multi-User Robotic Observatory. *J. Moore, B. Gendre, D. Coward, F. Panther, & E. Moore*, 77

Gendre, B. The Impact of the Site Quality of the Zadko Observatory on its Scientific Results. *B. Gendre, R. Tonello, M. Studdert, D. Coward, A. Klotz, E. Moore, J. Moore, & F. Panther*, 49

Germani, S. Modernization of Coloti Optical Observatory: Remote Control and Automation for Multimessenger Follow-Up. *P. Cristarella Orestano, S. Cutini, S. Germani, S. Palmerini, & G. Tosti*, 19

Gil, P. Advanced Weather Control System at the TJO Telescope. *F. Domene, E. Herrero, P. Gil, D. Baroch, & A. Rojas*, 55

Gil, P. Autonomous Scheduling at the TJO Telescope. *D. Baroch, E. Herrero, P. Gil, F. Domene, A. Rojas, & N. Ribó*, 81

Girón-Gambero, J. R. Developing School Science Skills Through the Science-IES Robotic Telescope Projects. *J. R. Girón-Gambero*, 187

Grèbol-Tomàs, P. Unsynchronized Fireball Analysis and Challenges in Dimensionless Atmospheric Flight Parametrization:The SPMN230522 Superbolide as a Case Study. *E. Peña-Asensio, P. Grèbol-Tomàs, J.M. Trigo-Rodríguez, M. Gritsevich, A. Rimola, M. Corretgé-Gilart, C. Guasch, C. Alcaraz, V. Ibáñez, A. Gómez, & J. Gómez*, 87

Gracia, J. New Robotic Telescope: The Big Eye to Observe the Transient Universe. *C. M. Gutiérrez, J. Barrera, J. Bento, D. Copley, C. M. Copperwheat, F. J. De Cos, M. Escriche, J. J. Fernández-Valdivia, A. P. Garner, J. Gracia, D. G. Heffernan-Clarke, H. E. Jermak, J. León Gil, A. M. McGrath, C. Miossec, A. Oria, A. Ranjbar, R. Rebolo, C. Rodríguez-Pereira, F. Sánchez-Lasheras, R. J. Smith, I. A. Steele, & M. Torres*, 217

Gritsevich, M. A Unique Look on Micrometeorites: When Spectroscopy Meets Citizen Science. *M. R. López-Ramírez, J. Laserna, M. Hanna, J. Moilanen, & M. Gritsevich*, 179

Gritsevich, M. Cometary Outbursts and Evolution of Ejected Particles. *M. Gritsevich, M. Nissinen, J. Ryske, A. J. Castro-Tirado, I. Pérez-García, M. Weso, J. M. Trigo-Rodríguez, E. Peña-Asensio, I. Boaca, T. Prystavski, M. Husárik, O. Ivanova, A. Sánchez, & J. M. Llenas*, 93

Gritsevich, M. Interstellar Visitors and Elusive Extrasolar Meteorites. *E. Peña-Asensio, J. M. Trigo-Rodr', M. Gritsevich, H. Socas-Navarro, J. Visuri, & A. Rimola*, 101

Gritsevich, M. Unsynchronized Fireball Analysis and Challenges in Dimensionless Atmospheric Flight Parametrization:The SPMN230522 Superbolide as a Case Study. *E. Peña-Asensio, P. Grèbol-Tomàs, J.M. Trigo-Rodríguez, M. Gritsevich, A. Rimola, M. Corretgé-Gilart, C. Guasch, C. Alcaraz, V. Ibáñez, A. Gómez, & J. Gómez*, 87

Gritsevich, M. Preface. *Maria Gritsevich, Alberto J. Castro-Tirado, Petr Kubánek, Shashi B. Pandey, and David Hiriart*, vii

Grossan, B. Early-Time Optical Spectral Shape Measurements of GRB 200925B. *Z. Abdullayev, T. Komesh, B. Grossan, E. Abdikamalov, Z. Maksut, M. Krugov, S. Myrzakul, D. Tuiakbayeva, & A. Kostangeldinova*, 109

Guasch, C. Unsynchronized Fireball Analysis and Challenges in Dimensionless Atmospheric Flight Parametrization:The SPMN230522 Superbolide as a Case Study. *E. Peña-Asensio, P. Grèbol-Tomàs, J.M. Trigo-Rodríguez, M. Gritsevich, A. Rimola, M. Corretgé-Gilart, C. Guasch, C. Alcaraz, V. Ibáñez, A. Gómez, & J. Gómez*, 87

Gupta, R. An Intermediate Luminosity GRB 210210A: The Early Onset of the External Forward Shock in the X-ray?. *R. Gupta, A. K. Ror, S. B. Pandey, J. Racusin, M. Moss, A. Aryan, N. Klingler, & A. J. Castro-Tirado*, 115

Gupta, R. The Core Collapse of a 16.5 $M_\odot$ Star. *A. Aryan, S. B. Pandey, R. Gupta, A. K. Ror, & A. J. Castro-Tirado*, 145

Gutiérrez, C. M. New Robotic Telescope: The Big Eye to Observe the Transient Universe. *C. M. Gutiérrez, J. Barrera, J. Bento, D. Copley,*

VII Workshop on Robotic Autonomous Observatories (October 16-20, 2023)
Editors: Maria Gritsevich, Alberto J. Castro-Tirado, Petr Kubánek, Shashi B. Pandey, and David Hiriart

C. M. Copperwheat, F. J. De Cos, M. Escriche, J. J. Fernández-Valdivia, A. P. Garner, J. Gracia, D. G. Heffernan-Clarke, H. E. Jermak, J. León Gil, A. M. McGrath, C. Miossec, A. Oria, A. Ranjbar, R. Rebolo, C. Rodríguez-Pereira, F. Sánchez-Lasheras, R. J. Smith, I. A. Steele, & M. Torres, 217

Guziy, S. Imaging Stokes Photometer-Polarimeter for the BOOTES Global Telescope Network. *S. Guziy, I. Syniavsky, Ye. Oberemok, O. Ivanova, & A. J. Castro-Tirado*, 197

Haislip, J. B. OAUJ-CDK500: A New Kraków Robotic Telescope. *S. Zola, G. Stachowski, S. Kurowski, T. Kundera, W. Waniak, D. E. Reichart, V. Kouprianov, J. B. Haislip, Ł. Wyrzykowski, & P. J. Mikołajczyk*, 31

Hanna, M. A Unique Look on Micrometeorites: When Spectroscopy Meets Citizen Science. *M. R. López-Ramírez, J. Laserna, M. Hanna, J. Moilanen, & M. Gritsevich*, 179

Heffernan-Clarke, D. G. New Robotic Telescope: The Big Eye to Observe the Transient Universe. *C. M. Gutiérrez, J. Barrera, J. Bento, D. Copley, C. M. Copperwheat, F. J. De Cos, M. Escriche, J. J. Fernández-Valdivia, A. P. Garner, J. Gracia, D. G. Heffernan-Clarke, H. E. Jermak, J. León Gil, A. M. McGrath, C. Miossec, A. Oria, A. Ranjbar, R. Rebolo, C. Rodríguez-Pereira, F. Sánchez-Lasheras, R. J. Smith, I. A. Steele, & M. Torres*, 217

Herrero, E. Advanced Weather Control System at the TJO Telescope. *F. Domene, E. Herrero, P. Gil, D. Baroch, & A. Rojas*, 55

Herrero, E. Autonomous Scheduling at the TJO Telescope. *D. Baroch, E. Herrero, P. Gil, F. Domene, A. Rojas, & N. Ribó*, 81

Hiriart, D. Tulancingo-I: The K Band Mexican Radiotelescope. *D. Hiriart, E. Colorado, F. Diaz, T. Calvario, H. Serrano, D. Rojas, & S. Kurtz*, 193

Hiriart, D. Preface. *Maria Gritsevich, Alberto J. Castro-Tirado, Petr Kubánek, Shashi B. Pandey, and David Hiriart*, vii

Hlakola, M. The Intelligent Observatory. *N. Erasmus, S. B. Potter, C. H. D. van Gend, S. Chandra, H. L. Worters, M. Hlakola, & R. Julie*, 201

Hlakola, M. Zero Point Magnitudes of All-Sky Images for Determining Cloud Conditions. *C. H. D. van Gend, N. Erasmus, J. Tonry, L. Denneau, M. Hlakola, & S. B. Potter*, 69

Hlakols, M. Software Components of the Intelligent Observatory. *C. H. D. van Gend, S. B. Potter, N. Erasmus, S. Chandra, M. Hlakola, H. Worters, & R. Julie*, 209

Hu, Y.-D. Early Emission of Short Optical Transients. *S. Wu, V. M. Lipunov, A. J. Castro-Tirado, Y.-D. Hu, K. Zhirkov, & N. V. Tyurina*, 153

Husárik, M. Cometary Outbursts and Evolution of Ejected Particles. *M. Gritsevich, M. Nissinen, J. Ryske, A. J. Castro-Tirado, I. Pérez-García, M. Weso, J. M. Trigo-Rodríguez, E. Peña-Asensio, I. Boaca, T. Prystavski, M. Husárik, O. Ivanova, A. Sánchez, & J. M. Llenas*, 93

Husser, T. O. Sky Brightness Measurements with the Allsky Camera at the University of Göttingen. *K. J. Schimpf & T. O. Husser*, 63

Husser, T. O. Towards a Fully Robotic Solar Observatory at the University of Göttingen. *S. Martens & T. O. Husser*, 43

Ibáñez, V. Unsynchronized Fireball Analysis and Challenges in Dimensionless Atmospheric Flight Parametrization:The SPMN230522 Superbolide as a Case Study. *E. Peña-Asensio, P. Grèbol-Tomàs, J.M. Trigo-Rodríguez, M. Gritsevich, A. Rimola, M. Corretgé-Gilart, C. Guasch, C. Alcaraz, V. Ibáñez, A. Gómez, & J. Gómez*, 87

Ivanova, O. Cometary Outbursts and Evolution of Ejected Particles. *M. Gritsevich, M. Nissinen, J. Ryske, A. J. Castro-Tirado, I. Pérez-García, M. Weso, J. M. Trigo-Rodríguez, E. Peña-Asensio, I. Boaca, T. Prystavski, M. Husárik, O. Ivanova, A. Sánchez, & J. M. Llenas*, 93

Ivanova, O. Imaging Stokes Photometer-Polarimeter for the BOOTES Global Telescope Network. *S. Guziy, I. Syniavsky, Ye. Oberemok, O. Ivanova, & A. J. Castro-Tirado*, 197

Jermak, H. E. New Robotic Telescope: The Big Eye to Observe the Transient Universe. *C. M. Gutiérrez, J. Barrera, J. Bento, D. Copley, C. M. Copperwheat, F. J. De Cos, M. Escriche, J. J. Fernández-Valdivia, A. P. Garner, J. Gracia, D. G. Heffernan-Clarke, H. E. Jermak, J. León Gil, A. M. McGrath, C. Miossec, A. Oria, A. Ranjbar, R. Rebolo, C. Rodríguez-Pereira, F. Sánchez-Lasheras, R. J. Smith, I. A. Steele, & M. Torres*, 217

Julie, R. Observatory Control System at South African Astronomical Observatory. *Sunil Chandra, Steve B. Potter, Carel van Gend, Nicolas Erasmus, & Roufurd Julie*, 71

Julie, R. Software Components of the Intelligent Observatory. *C. H. D. van Gend, S. B. Potter, N. Erasmus, S. Chandra, M. Hlakola, H. Worters, & R. Julie*, 209

Julie, R. The Intelligent Observatory. *N. Erasmus, S. B. Potter, C. H. D. van Gend, S. Chandra, H. L. Worters, M. Hlakola, & R. Julie*, 201

Kilic, Y. Autonomous Telescope and Scientific Infrastructure Developments at TUG. *O. Erece, Y. Kilic, & K. Uluc*, 27

VII Workshop on Robotic Autonomous Observatories (October 16-20, 2023)
Editors: Maria Gritsevich, Alberto J. Castro-Tirado, Petr Kubánek, Shashi B. Pandey, and David Hiriart

Klingler, N. An Intermediate Luminosity GRB 210210A: The Early Onset of the External Forward Shock in the X-ray?. *R. Gupta, A. K. Ror, S. B. Pandey, J. Racusin, M. Moss, A. Aryan, N. Klingler, & A. J. Castro-Tirado*, 115

Klotz, A. The Impact of the Site Quality of the Zadko Observatory on its Scientific Results. *B. Gendre, R. Tonello, M. Studdert, D. Coward, A. Klotz, E. Moore, J. Moore, & F. Panther*, 49

Komesh, T. Early-Time Optical Spectral Shape Measurements of GRB 200925B. *Z. Abdullayev, T. Komesh, B. Grossan, E. Abdikamalov, Z. Maksut, M. Krugov, S. Myrzakul, D. Tuiakbayeva, & A. Kostangeldinova*, 109

Kostangeldinova, A. Early-Time Optical Spectral Shape Measurements of GRB 200925B. *Z. Abdullayev, T. Komesh, B. Grossan, E. Abdikamalov, Z. Maksut, M. Krugov, S. Myrzakul, D. Tuiakbayeva, & A. Kostangeldinova*, 109

Kotysz, K. Black Hole TOM – an Automatic Tool for Photometric Time-Domain Data. *P. J. Mikołajczyk, P. Zieliński, Ł. Wyrzykowski, A. Krawczyk, & K. Kotysz*, 167

Kouprianov, V. OAUJ-CDK500: A New Kraków Robotic Telescope. *S. Zola, G. Stachowski, S. Kurowski, T. Kundera, W. Waniak, D. E. Reichart, V. Kouprianov, J. B. Haislip, Ł. Wyrzykowski, & P. J. Mikołajczyk*, 31

Krawczyk, A. Black Hole TOM – an Automatic Tool for Photometric Time-Domain Data. *P. J. Mikołajczyk, P. Zieliński, Ł. Wyrzykowski, A. Krawczyk, & K. Kotysz*, 167

Krugov, M. Early-Time Optical Spectral Shape Measurements of GRB 200925B. *Z. Abdullayev, T. Komesh, B. Grossan, E. Abdikamalov, Z. Maksut, M. Krugov, S. Myrzakul, D. Tuiakbayeva, & A. Kostangeldinova*, 109

Kubánek, P. Preface. *Maria Gritsevich, Alberto J. Castro-Tirado, Petr Kubánek, Shashi B. Pandey, and David Hiriart*, vii

Kumar, S. Prompt and Afterglow Analysis of the *Fermi-LAT detected GRB 230812B.* *A. K. Ror, S. B. Pandey, A. Aryan, S. Kumar, and A. J. Castro-Tirado*, 133

Kundera, T. OAUJ-CDK500: A New Kraków Robotic Telescope. *S. Zola, G. Stachowski, S. Kurowski, T. Kundera, W. Waniak, D. E. Reichart, V. Kouprianov, J. B. Haislip, Ł. Wyrzykowski, & P. J. Mikołajczyk*, 31

Kurowski, S. OAUJ-CDK500: A New Kraków Robotic Telescope. *S. Zola, G. Stachowski, S. Kurowski, T. Kundera, W. Waniak, D. E. Reichart, V. Kouprianov, J. B. Haislip, Ł. Wyrzykowski, & P. J. Mikołajczyk*, 31

Kurtz, S. Tulancingo-I: The K Band Mexican Radiotelescope. *D. Hiriart, E. Colorado, F. Diaz, T. Calvario, H. Serrano, D. Rojas, & S. Kurtz*, 193

López-Ramírez, M. R. A Unique Look on Micrometeorites: When Spectroscopy Meets Citizen Science. *M. R. López-Ramírez, J. Laserna, M. Hanna, J. Moilanen, & M. Gritsevich*, 179

Laserna, J. A Unique Look on Micrometeorites: When Spectroscopy Meets Citizen Science. *M. R. López-Ramírez, J. Laserna, M. Hanna, J. Moilanen, & M. Gritsevich*, 179

León Gil, J. New Robotic Telescope: The Big Eye to Observe the Transient Universe. *C. M. Gutiérrez, J. Barrera, J. Bento, D. Copley, C. M. Copperwheat, F. J. De Cos, M. Escriche, J. J. Fernández-Valdivia, A. P. Garner, J. Gracia, D. G. Heffernan-Clarke, H. E. Jermak, J. León Gil, A. M. McGrath, C. Miossec, A. Oria, A. Ranjbar, R. Rebolo, C. Rodríguez-Pereira, F. Sánchez-Lasheras, R. J. Smith, I. A. Steele, & M. Torres*, 217

Lipunov, V. M. Early Emission of Short Optical Transients. *S. Wu, V. M. Lipunov, A. J. Castro-Tirado, Y.-D. Hu, K. Zhirkov, & N. V. Tyurina*, 153

Llenas, J. M. Cometary Outbursts and Evolution of Ejected Particles. *M. Gritsevich, M. Nissinen, J. Ryske, A. J. Castro-Tirado, I. Pérez-García, M. Weso, J. M. Trigo-Rodríguez, E. Peña-Asensio, I. Boaca, T. Prystavski, M. Husárik, O. Ivanova, A. Sánchez, & J. M. Llenas*, 93

Maksut, Z. Early-Time Optical Spectral Shape Measurements of GRB 200925B. *Z. Abdullayev, T. Komesh, B. Grossan, E. Abdikamalov, Z. Maksut, M. Krugov, S. Myrzakul, D. Tuiakbayeva, & A. Kostangeldinova*, 109

Martínez, R. Attitude Control Study on Artificial Satellites and Space Debris using Laser Data. *R. Martínez & M. Á. Sánchez*, 173

Martens, S. Towards a Fully Robotic Solar Observatory at the University of Göttingen. *S. Martens & T. O. Husser*, 43

McGrath, A. M. New Robotic Telescope: The Big Eye to Observe the Transient Universe. *C. M. Gutiérrez, J. Barrera, J. Bento, D. Copley, C. M. Copperwheat, F. J. De Cos, M. Escriche, J. J. Fernández-Valdivia, A. P. Garner, J. Gracia, D. G. Heffernan-Clarke, H. E. Jermak, J. León Gil, A. M. McGrath, C. Miossec, A. Oria, A. Ranjbar, R. Rebolo, C. Rodríguez-Pereira, F. Sánchez-Lasheras, R. J. Smith, I. A. Steele, & M. Torres*, 217

Meintjes, P. J. Considerations on automating older telescopes: The Boyden 1.5 m telescope. *H. J. van Heerden, P. J. Meintjes, B. van Soelen, W. Smit, I. P. van der Westhuizen, & H. Szegedi*, 13

Mikołajczyk, P. J. Black Hole TOM – an Automatic Tool for Photometric Time-Domain Data. *P. J. Mikołajczyk, P. Zieliński, Ł. Wyrzykowski, A. Krawczyk, & K. Kotysz*, 167

Mikołajczyk. P. J. OAUJ-CDK500: A New Kraków Robotic Telescope. *S. Zola, G. Stachowski, S. Kurowski, T. Kundera, W. Waniak, D. E. Reichart, V. Kouprianov, J. B. Haislip, Ł. Wyrzykowski, & P. J. Mikołajczyk*, 31

Miossec, C. New Robotic Telescope: The Big Eye to Observe the Transient Universe. *C. M. Gutiérrez, J. Barrera, J. Bento, D. Copley, C. M. Copperwheat, F. J. De Cos, M. Escriche, J. J. Fernández-Valdivia, A. P. Garner, J. Gracia, D. G. Heffernan-Clarke, H. E. Jermak, J. León Gil, A. M. McGrath, C. Miossec, A. Oria, A. Ranjbar, R. Rebolo, C. Rodríguez-Pereira, F. Sánchez-Lasheras, R. J. Smith, I. A. Steele, & M. Torres*, 217

Molainen, J. A Unique Look on Micrometeorites: When Spectroscopy Meets Citizen Science. *M. R. López-Ramírez, J. Laserna, M. Hanna, J. Moilanen, & M. Gritsevich*, 179

Moore, E. Management of a Multi-User Robotic Observatory. *J. Moore, B. Gendre, D. Coward, F. Panther, & E. Moore*, 77

Moore, E. The Impact of the Site Quality of the Zadko Observatory on its Scientific Results. *B. Gendre, R. Tonello, M. Studdert, D. Coward, A. Klotz, E. Moore, J. Moore, & F. Panther*, 49

Moore, J. Management of a Multi-User Robotic Observatory. *J. Moore, B. Gendre, D. Coward, F. Panther, & E. Moore*, 77

Moore, J. The Impact of the Site Quality of the Zadko Observatory on its Scientific Results. *B. Gendre, R. Tonello, M. Studdert, D. Coward, A. Klotz, E. Moore, J. Moore, & F. Panther*, 49

Moss, M. An Intermediate Luminosity GRB 210210A: The Early Onset of the External Forward Shock in the X-ray?. *R. Gupta, A. K. Ror, S. B. Pandey, J. Racusin, M. Moss, A. Aryan, N. Klingler, & A. J. Castro-Tirado*, 115

Myrzakul, S. Early-Time Optical Spectral Shape Measurements of GRB 200925B. *Z. Abdullayev, T. Komesh, B. Grossan, E. Abdikamalov, Z. Maksut, M. Krugov, S. Myrzakul, D. Tuiakbayeva, & A. Kostangeldinova*, 109

Nissinen, M. Cometary Outbursts and Evolution of Ejected Particles. *M. Gritsevich, M. Nissinen, J. Ryske, A. J. Castro-Tirado, I. Pérez-García, M. Weso, J. M. Trigo-Rodríguez, E. Peña-Asensio, I. Boaca, T. Prystavski, M. Husárik, O. Ivanova, A. Sánchez, & J. M. Llenas*, 93

O'Neill, D. GERry : Finding Electromagnetic Counterparts in Gravitational Waves Follow-Up Campaigns. *D. O'Neill*, 161

Oberemok, Ye. Imaging Stokes Photometer-Polarimeter for the BOOTES Global Telescope Network. *S. Guziy, I. Syniavsky, Ye. Oberemok, O. Ivanova, & A. J. Castro-Tirado*, 197

Odeh, M. Building A limited budget Robotic Observatory. *M. Odeh*, 37

Oria, A. New Robotic Telescope: The Big Eye to Observe the Transient Universe. *C. M. Gutiérrez, J. Barrera, J. Bento, D. Copley, C. M. Copperwheat, F. J. De Cos, M. Escriche, J. J. Fernández-Valdivia, A. P. Garner, J. Gracia, D. G. Heffernan-Clarke, H. E. Jermak, J. León Gil, A. M. McGrath, C. Miossec, A. Oria, A. Ranjbar, R. Rebolo, C. Rodríguez-Pereira, F. Sánchez-Lasheras, R. J. Smith, I. A. Steele, & M. Torres*, 217

Pérez-García, I. Cometary Outbursts and Evolution of Ejected Particles. *M. Gritsevich, M. Nissinen, J. Ryske, A. J. Castro-Tirado, I. Pérez-García, M. Weso, J. M. Trigo-Rodríguez, E. Peña-Asensio, I. Boaca, T. Prystavski, M. Husárik, O. Ivanova, A. Sánchez, & J. M. Llenas*, 93

Palmerini, S. Modernization of Coloti Optical Observatory: Remote Control and Automation for Multimessenger Follow-Up. *P. Cristarella Orestano, S. Cutini, S. Germani, S. Palmerini, & G. Tosti*, 19

Pandey, S. B. An Intermediate Luminosity GRB 210210A: The Early Onset of the External Forward Shock in the X-ray?. *R. Gupta, A. K. Ror, S. B. Pandey, J. Racusin, M. Moss, A. Aryan, N. Klingler, & A. J. Castro-Tirado*, 115

Pandey, S. B. Prompt and Afterglow Analysis of the *Fermi-LAT detected GRB 230812B.* *A. K. Ror, S. B. Pandey, A. Aryan, S. Kumar, and A. J. Castro-Tirado*, 133

Pandey, S. B. The Core Collapse of a 16.5 $M_\odot$ Star. *A. Aryan, S. B. Pandey, R. Gupta, A. K. Ror, & A. J. Castro-Tirado*, 145

Pandey, S. B. Preface. *Maria Gritsevich, Alberto J. Castro-Tirado, Petr Kubánek, Shashi B. Pandey, and David Hiriart*, vii

Panther, F. Management of a Multi-User Robotic Observatory. *J. Moore, B. Gendre, D. Coward, F. Panther, & E. Moore*, 77

Panther, F. The Impact of the Site Quality of the Zadko Observatory on its Scientific Results. *B. Gendre, R. Tonello, M. Studdert, D. Coward, A. Klotz, E. Moore, J. Moore, & F. Panther*, 49

Peña-Asensio, E. Cometary Outbursts and Evolution of Ejected Particles. *M. Gritsevich, M. Nissinen, J. Ryske, A. J. Castro-Tirado, I. Pérez-García, M. Weso, J. M. Trigo-Rodríguez, E. Peña-Asensio, I. Boaca, T. Prystavski, M. Husárik, O. Ivanova, A. Sánchez, & J. M. Llenas*, 93

Peña-Asensio, E. Interstellar Visitors and Elusive Extrasolar Meteorites. *E. Peña-Asensio, J. M. Trigo-Rodr', M. Gritsevich, H. Socas-Navarro, J. Visuri, & A. Rimola*, 101

Peña-Asensio, E. Unsynchronized Fireball Analysis and Challenges in Dimensionless Atmospheric Flight Parametrization:The SPMN230522 Superbolide as a Case Study. *E. Peña-Asensio, P. Grèbol-Tomàs,*

VII Workshop on Robotic Autonomous Observatories (October 16-20, 2023)
Editors: Maria Gritsevich, Alberto J. Castro-Tirado, Petr Kubánek, Shashi B. Pandey, and David Hiriart

VII Workshop on Robotic Autonomous Observatories (October 16-20, 2023)
Editors: Maria Gritsevich, Alberto J. Castro-Tirado, Petr Kubánek, Shashi B. Pandey, and David Hiriart

J.M. Trigo-Rodríguez, M. Gritsevich, A. Rimola, M. Corretgé-Gilart, C. Guasch, C. Alcaraz, V. Ibáñez, A. Gómez, & J. Gómez, 87

Potter, S. B. Observatory Control System at South African Astronomical Observatory. *Sunil Chandra, Steve B. Potter, Carel van Gend, Nicolas Erasmus, & Roufurd Julie*, 71

Potter, S. B. Software Components of the Intelligent Observatory. *C. H. D. van Gend, S. B. Potter, N. Erasmus, S. Chandra, M. Hlakola, H. Worters, & R. Julie*, 209

Potter, S. B. The Intelligent Observatory. *N. Erasmus, S. B. Potter, C. H. D. van Gend, S. Chandra, H. L. Worters, M. Hlakola, & R. Julie*, 201

Potter, S. B. Zero Point Magnitudes of All-Sky Images for Determining Cloud Conditions. *C. H. D. van Gend, N. Erasmus, J. Tonry, L. Denneau, M. Hlakola, & S. B. Potter*, 69

Prystavski, T. Cometary Outbursts and Evolution of Ejected Particles. *M. Gritsevich, M. Nissinen, J. Ryske, A. J. Castro-Tirado, I. Pérez-García, M. Weso, J. M. Trigo-Rodríguez, E. Peña-Asensio, I. Boaca, T. Prystavski, M. Husárik, O. Ivanova, A. Sánchez, & J. M. Llenas*, 93

Racusin, J. An Intermediate Luminosity GRB 210210A: The Early Onset of the External Forward Shock in the X-ray?. *R. Gupta, A. K. Ror, S. B. Pandey, J. Racusin, M. Moss, A. Aryan, N. Klingler, & A. J. Castro-Tirado*, 115

Ranjbar, A. New Robotic Telescope: The Big Eye to Observe the Transient Universe. *C. M. Gutiérrez, J. Barrera, J. Bento, D. Copley, C. M. Copperwheat, F. J. De Cos, M. Escriche, J. J. Fernández-Valdivia, A. P. Garner, J. Gracia, D. G. Heffernan-Clarke, H. E. Jermak, J. León Gil, A. M. McGrath, C. Miossec, A. Oria, A. Ranjbar, R. Rebolo, C. Rodríguez-Pereira, F. Sánchez-Lasheras, R. J. Smith, I. A. Steele, & M. Torres*, 217

Rebolo, R. New Robotic Telescope: The Big Eye to Observe the Transient Universe. *C. M. Gutiérrez, J. Barrera, J. Bento, D. Copley, C. M. Copperwheat, F. J. De Cos, M. Escriche, J. J. Fernández-Valdivia, A. P. Garner, J. Gracia, D. G. Heffernan-Clarke, H. E. Jermak, J. León Gil, A. M. McGrath, C. Miossec, A. Oria, A. Ranjbar, R. Rebolo, C. Rodríguez-Pereira, F. Sánchez-Lasheras, R. J. Smith, I. A. Steele, & M. Torres*, 217

Reichart, D. E. OAUJ-CDK500: A New Kraków Robotic Telescope. *S. Zola, G. Stachowski, S. Kurowski, T. Kundera, W. Waniak, D. E. Reichart, V. Kouprianov, J. B. Haislip, Ł. Wyrzykowski, & P. J. Mikołajczyk*, 31

Ribó, N. Autonomous Scheduling at the TJO Telescope. *D. Baroch, E. Herrero, P. Gil, F. Domene, A. Rojas, & N. Ribó*, 81

Rimola, A. Interstellar Visitors and Elusive Extrasolar Meteorites. *E. Peña-Asensio, J. M. Trigo-Rodr', M. Gritsevich, H. Socas-Navarro, J. Visuri, & A. Rimola*, 101

Rimola, A. Unsynchronized Fireball Analysis and Challenges in Dimensionless Atmospheric Flight Parametrization:The SPMN230522 Superbolide as a Case Study. *E. Peña-Asensio, P. Grèbol-Tomàs, J.M. Trigo-Rodríguez, M. Gritsevich, A. Rimola, M. Corretgé-Gilart, C. Guasch, C. Alcaraz, V. Ibáñez, A. Gómez, & J. Gómez*, 87

Rodríguez-Pereira, C. New Robotic Telescope: The Big Eye to Observe the Transient Universe. *C. M. Gutiérrez, J. Barrera, J. Bento, D. Copley, C. M. Copperwheat, F. J. De Cos, M. Escriche, J. J. Fernández-Valdivia, A. P. Garner, J. Gracia, D. G. Heffernan-Clarke, H. E. Jermak, J. León Gil, A. M. McGrath, C. Miossec, A. Oria, A. Ranjbar, R. Rebolo, C. Rodríguez-Pereira, F. Sánchez-Lasheras, R. J. Smith, I. A. Steele, & M. Torres*, 217

Rojas, A. Advanced Weather Control System at the TJO Telescope. *F. Domene, E. Herrero, P. Gil, D. Baroch, & A. Rojas*, 55

Rojas, A. Autonomous Scheduling at the TJO Telescope. *D. Baroch, E. Herrero, P. Gil, F. Domene, A. Rojas, & N. Ribó*, 81

Rojas, D. Tulancingo-I: The K Band Mexican Radiotelescope. *D. Hiriart, E. Colorado, F. Diaz, T. Calvario, H. Serrano, D. Rojas, & S. Kurtz*, 193

Ror, A. K. An Intermediate Luminosity GRB 210210A: The Early Onset of the External Forward Shock in the X-ray?. *R. Gupta, A. K. Ror, S. B. Pandey, J. Racusin, M. Moss, A. Aryan, N. Klingler, & A. J. Castro-Tirado*, 115

Ror, A. K. Prompt and Afterglow Analysis of the *Fermi-LAT detected GRB 230812B*. *A. K. Ror, S. B. Pandey, A. Aryan, S. Kumar, and A. J. Castro-Tirado*, 133

Ror, A. K. The Core Collapse of a $16.5\,M_\odot$ Star. *A. Aryan, S. B. Pandey, R. Gupta, A. K. Ror, & A. J. Castro-Tirado*, 145

Ryske, J. Cometary Outbursts and Evolution of Ejected Particles. *M. Gritsevich, M. Nissinen, J. Ryske, A. J. Castro-Tirado, I. Pérez-García, M. Weso, J. M. Trigo-Rodríguez, E. Peña-Asensio, I. Boaca, T. Prystavski, M. Husárik, O. Ivanova, A. Sánchez, & J. M. Llenas*, 93

Sánchez, A. Cometary Outbursts and Evolution of Ejected Particles. *M. Gritsevich, M. Nissinen, J. Ryske, A. J. Castro-Tirado, I. Pérez-García, M. Weso, J. M. Trigo-Rodríguez, E. Peña-Asensio, I. Boaca, T. Prystavski, M. Husárik, O. Ivanova, A. Sánchez, & J. M. Llenas*, 93

Sánchez, M. Á. Attitude Control Study on Artificial Satellites and Space Debris using Laser Data. *R. Martínez & M. Á. Sánchez*, 173

VII Workshop on Robotic Autonomous Observatories (October 16-20, 2023)
Editors: Maria Gritsevich, Alberto J. Castro-Tirado, Petr Kubánek, Shashi B. Pandey, and David Hiriart

Sánchez-Lasheras, F. New Robotic Telescope: The Big Eye to Observe the Transient Universe. *C. M. Gutiérrez, J. Barrera, J. Bento, D. Copley, C. M. Copperwheat, F. J. De Cos, M. Escriche, J. J. Fernández-Valdivia, A. P. Garner, J. Gracia, D. G. Heffernan-Clarke, H. E. Jermak, J. León Gil, A. M. McGrath, C. Miossec, A. Oria, A. Ranjbar, R. Rebolo, C. Rodríguez-Pereira, F. Sánchez-Lasheras, R. J. Smith, I. A. Steele, & M. Torres*, 217

Schimpf, K. J. Sky Brightness Measurements with the Allsky Camera at the University of Göttingen. *K. J. Schimpf & T. O. Husser*, 63

Serrano, H. Tulancingo-I: The K Band Mexican Radiotelescope. *D. Hiriart, E. Colorado, F. Diaz, T. Calvario, H. Serrano, D. Rojas, & S. Kurtz*, 193

Smit, W. Characterization of the KL4040 sCMOS for use on the Boyden Research Telescopes. *W. Smit, H. J. van Heerden, & B. van Soelen*, 9

Smit, W. Considerations on automating older telescopes: The Boyden 1.5 m telescope. *H. J. van Heerden, P. J. Meintjes, B. van Soelen, W. Smit, I. P. van der Westhuizen, & H. Szegedi*, 13

Smith, R. J. New Robotic Telescope: The Big Eye to Observe the Transient Universe. *C. M. Gutiérrez, J. Barrera, J. Bento, D. Copley, C. M. Copperwheat, F. J. De Cos, M. Escriche, J. J. Fernández-Valdivia, A. P. Garner, J. Gracia, D. G. Heffernan-Clarke, H. E. Jermak, J. León Gil, A. M. McGrath, C. Miossec, A. Oria, A. Ranjbar, R. Rebolo, C. Rodríguez-Pereira, F. Sánchez-Lasheras, R. J. Smith, I. A. Steele, & M. Torres*, 217

Socas-Navarro, H. Interstellar Visitors and Elusive Extrasolar Meteorites. *E. Peña-Asensio, J. M. Trigo-Rodr', M. Gritsevich, H. Socas-Navarro, J. Visuri, & A. Rimola*, 101

Stachowski, G. OAUJ-CDK500: A New Kraków Robotic Telescope. *S. Zola, G. Stachowski, S. Kurowski, T. Kundera, W. Waniak, D. E. Reichart, V. Kouprianov, J. B. Haislip, Ł. Wyrzykowski, & P. J. Mikołajczyk*, 31

Steele, I. A. New Robotic Telescope: The Big Eye to Observe the Transient Universe. *C. M. Gutiérrez, J. Barrera, J. Bento, D. Copley, C. M. Copperwheat, F. J. De Cos, M. Escriche, J. J. Fernández-Valdivia, A. P. Garner, J. Gracia, D. G. Heffernan-Clarke, H. E. Jermak, J. León Gil, A. M. McGrath, C. Miossec, A. Oria, A. Ranjbar, R. Rebolo, C. Rodríguez-Pereira, F. Sánchez-Lasheras, R. J. Smith, I. A. Steele, & M. Torres*, 217

Studdert, M. The Impact of the Site Quality of the Zadko Observatory on its Scientific Results. *B. Gendre, R. Tonello, M. Studdert, D. Coward, A. Klotz, E. Moore, J. Moore, & F. Panther*, 49

Syniavskyi, I. Imaging Stokes Photometer-Polarimeter for the BOOTES Global Telescope Network. *S. Guziy, I. Syniavsky, Ye. Oberemok, O. Ivanova, & A. J. Castro-Tirado*, 197

Szegedi, H. Considerations on automating older telescopes: The Boyden 1.5 m telescope. *H. J. van Heerden, P. J. Meintjes, B. van Soelen, W. Smit, I. P. van der Westhuizen, & H. Szegedi*, 13

Tonello, R. The Impact of the Site Quality of the Zadko Observatory on its Scientific Results. *B. Gendre, R. Tonello, M. Studdert, D. Coward, A. Klotz, E. Moore, J. Moore, & F. Panther*, 49

Tonry, J. Zero Point Magnitudes of All-Sky Images for Determining Cloud Conditions. *C. H. D. van Gend, N. Erasmus, J. Tonry, L. Denneau, M. Hlakola, & S. B. Potter*, 69

Torres, M. New Robotic Telescope: The Big Eye to Observe the Transient Universe. *C. M. Gutiérrez, J. Barrera, J. Bento, D. Copley, C. M. Copperwheat, F. J. De Cos, M. Escriche, J. J. Fernández-Valdivia, A. P. Garner, J. Gracia, D. G. Heffernan-Clarke, H. E. Jermak, J. León Gil, A. M. McGrath, C. Miossec, A. Oria, A. Ranjbar, R. Rebolo, C. Rodríguez-Pereira, F. Sánchez-Lasheras, R. J. Smith, I. A. Steele, & M. Torres*, 217

Tosti, G. Modernization of Coloti Optical Observatory: Remote Control and Automation for Multimessenger Follow-Up. *P. Cristarella Orestano, S. Cutini, S. Germani, S. Palmerini, & G. Tosti*, 19

Trigo-Rodríguez, J. M. Cometary Outbursts and Evolution of Ejected Particles. *M. Gritsevich, M. Nissinen, J. Ryske, A. J. Castro-Tirado, I. Pérez-García, M. Weso, J. M. Trigo-Rodríguez, E. Peña-Asensio, I. Boaca, T. Prystavski, M. Husárik, O. Ivanova, A. Sánchez, & J. M. Llenas*, 93

Trigo-Rodríguez, J. M. Interstellar Visitors and Elusive Extrasolar Meteorites. *E. Peña-Asensio, J. M. Trigo-Rodr', M. Gritsevich, H. Socas-Navarro, J. Visuri, & A. Rimola*, 101

Trigo-Rodríguez, J.M. Unsynchronized Fireball Analysis and Challenges in Dimensionless Atmospheric Flight Parametrization:The SPMN230522 Superbolide as a Case Study. *E. Peña-Asensio, P. Grèbol-Tomàs, J.M. Trigo-Rodríguez, M. Gritsevich, A. Rimola, M. Corretgé-Gilart, C. Guasch, C. Alcaraz, V. Ibáñez, A. Gómez, & J. Gómez*, 87

Tuiakbayeva, D. Early-Time Optical Spectral Shape Measurements of GRB 200925B. *Z. Abdullayev, T. Komesh, B. Grossan, E. Abdikamalov, Z. Maksut, M. Krugov, S. Myrzakul, D. Tuiakbayeva, & A. Kostangeldinova*, 109

Tyurina, N. V. Early Emission of Short Optical Transients. *S. Wu, V. M. Lipunov, A. J. Castro-Tirado, Y.-D. Hu, K. Zhirkov, & N. V. Tyurina*, 153

Uluc, K. Autonomous Telescope and Scientific Infrastructure Developments at TUG. *O. Erece, Y. Kilic, & K. Uluc*, 27

VII Workshop on Robotic Autonomous Observatories (October 16-20, 2023)
Editors: Maria Gritsevich, Alberto J. Castro-Tirado, Petr Kubánek, Shashi B. Pandey, and David Hiriart

van der Westhuizen, I. P. Considerations on automating older telescopes: The Boyden 1.5 m telescope. *H. J. van Heerden, P. J. Meintjes, B. van Soelen, W. Smit, I. P. van der Westhuizen, & H. Szegedi*, 13

van Gend, C. H. D. Software Components of the Intelligent Observatory. *C. H. D. van Gend, S. B. Potter, N. Erasmus, S. Chandra, M. Hlakola, H. Worters, & R. Julie*, 209

van Gend, C. H. D. The Intelligent Observatory. *N. Erasmus, S. B. Potter, C. H. D. van Gend, S. Chandra, H. L. Worters, M. Hlakola, & R. Julie*, 201

van Gend, C. H. D. Zero Point Magnitudes of All-Sky Images for Determining Cloud Conditions. *C. H. D. van Gend, N. Erasmus, J. Tonry, L. Denneau, M. Hlakola, & S. B. Potter*, 69

van Heerden, H. J. Characterization of the KL4040 sCMOS for use on the Boyden Research Telescopes. *W. Smit, H. J. van Heerden, & B. van Soelen*, 9

van Heerden, H. J. Considerations on automating older telescopes: The Boyden 1.5 m telescope. *H. J. van Heerden, P. J. Meintjes, B. van Soelen, W. Smit, I. P. van der Westhuizen, & H. Szegedi*, 13

van Soelen, B. Characterization of the KL4040 sCMOS for use on the Boyden Research Telescopes. *W. Smit, H. J. van Heerden, & B. van Soelen*, 9

van Soelen, B. Considerations on automating older telescopes: The Boyden 1.5 m telescope. *H. J. van Heerden, P. J. Meintjes, B. van Soelen, W. Smit, I. P. van der Westhuizen, & H. Szegedi*, 13

Visuri, J. Interstellar Visitors and Elusive Extrasolar Meteorites. *E. Peña-Asensio, J. M. Trigo-Rodr', M. Gritsevich, H. Socas-Navarro, J. Visuri, & A. Rimola*, 101

Waniak, W. OAUJ-CDK500: A New Kraków Robotic Telescope. *S. Zola, G. Stachowski, S. Kurowski, T. Kundera, W. Waniak, D. E. Reichart, V. Kouprianov, J. B. Haislip, Ł. Wyrzykowski, & P. J. Mikołajczyk*, 31

Weso, M. Cometary Outbursts and Evolution of Ejected Particles. *M. Gritsevich, M. Nissinen, J. Ryske, A. J. Castro-Tirado, I. Pérez-García, M. Weso, J. M. Trigo-Rodríguez, E. Peña-Asensio, I. Boaca, T. Prystavski, M. Husárik, O. Ivanova, A. Sánchez, & J. M. Llenas*, 93

Worters, H. Software Components of the Intelligent Observatory. *C. H. D. van Gend, S. B. Potter, N. Erasmus, S. Chandra, M. Hlakola, H. Worters, & R. Julie*, 209

Worters, H. L. The Intelligent Observatory. *N. Erasmus, S. B. Potter, C. H. D. van Gend, S. Chandra, H. L. Worters, M. Hlakola, & R. Julie*, 201

Wu, S. Early Emission of Short Optical Transients. *S. Wu, V. M. Lipunov, A. J. Castro-Tirado, Y.-D. Hu, K. Zhirkov, & N. V. Tyurina*, 153

Wyrzykowski, Ł. Black Hole TOM – an Automatic Tool for Photometric Time-Domain Data. *P. J. Mikołajczyk, P. Zieliński, Ł. Wyrzykowski, A. Krawczyk, & K. Kotysz*, 167

Wyrzykowski, Ł. OAUJ-CDK500: A New Kraków Robotic Telescope. *S. Zola, G. Stachowski, S. Kurowski, T. Kundera, W. Waniak, D. E. Reichart, V. Kouprianov, J. B. Haislip, Ł. Wyrzykowski, & P. J. Mikołajczyk*, 31

Zhirkov, K. Early Emission of Short Optical Transients. *S. Wu, V. M. Lipunov, A. J. Castro-Tirado, Y.-D. Hu, K. Zhirkov, & N. V. Tyurina*, 153

Zieliński, P. Black Hole TOM – an Automatic Tool for Photometric Time-Domain Data. *P. J. Mikołajczyk, P. Zieliński, Ł. Wyrzykowski, A. Krawczyk, & K. Kotysz*, 167

Zola, S. OAUJ-CDK500: A New Kraków Robotic Telescope. *S. Zola, G. Stachowski, S. Kurowski, T. Kundera, W. Waniak, D. E. Reichart, V. Kouprianov, J. B. Haislip, Ł. Wyrzykowski, & P. J. Mikołajczyk*, 31